Eirik Erlandsen

Magnon-mediated superconductivity and other collective phenomena in heterostructures of magnets and conductors

NTNU
Norwegian University of
Science and Technology

Eirik Erlandsen

Magnon-mediated superconductivity and other collective phenomena in heterostructures of magnets and conductors

Thesis for the Degree of Philosophiae Doctor

Trondheim, September 2022

Norwegian University of Science and Technology
Faculty of Natural Sciences
Department of Physics

NTNU

Norwegian University of
Science and Technology

Abstract

In many cases, magnetic materials, such as ferromagnets and antiferromagnets, and conductors, such as normal metals and superconductors, represent quite well-understood systems that condensed matter physicists are able to effectively model and describe. While e.g. the conducting properties of normal metals can be predicted from their band-filling and the superconducting properties of conventional superconductors can be derived from the interplay between electrons and phonons, the magnetic properties of magnetic insulators can often be understood in terms of localized spins interacting through exchange interactions. Rather than directly contributing to the understanding of such materials, or their more complicated and more mysterious relatives, this thesis is focused on the physics that arise when magnets and conductors are joined together in heterostructures. However, as such heterostructures involve itinerant electrons coupled to magnetism, they might, in addition to being interesting or useful in themselves, also be capable of shedding some light on the physics of interesting single-material systems such as material featuring unconventional superconductivity.

The thesis itself consists of seven research papers, preceded by a presentation of background material, as well as a discussion of the included articles. The first four papers consider the possibility of inducing superconductivity in a conductor through spatial proximity to magnetic insulators. While the second paper is concerned with coupling of the conducting surface states of a topological insulator to both ferromagnetic and antiferromagnetic insulators, the three other articles focus on normal metals proximitized by antiferromagnetic insulators.

The first paper reveals the importance of the magnetic structure at the antiferromagnet/metal interface. If both the spin-up and spin-down sublattices of the antiferromagnet are exposed at the interface, the effective electron-magnon scattering can be suppressed compared to the case where only one of the two antiferromagnetic sublattices couple to the itinerant electrons in the normal metal. In the latter case of an uncompensated antiferromagnetic interface, it is concluded that realization of magnon-mediated superconductivity could be possible.

In the second paper, the ideas of the first paper are extended to the case of magnon-mediated superconductivity on the surface of a topological insulator. It is once again found that an asymmetric coupling to the two antiferromagnetic sublattices could be beneficial for superconductivity.

In this paper, we also introduce next-nearest neighbor frustration in the antiferromagnet, enhancing the spin-fluctuations and potentially also the superconductivity.

In the third paper, we return to the simpler antiferromagnet/normal metal system in order to expand on the effect of adding frustration to the antiferromagnet. Adjusting the next-nearest neighbor interaction, we tune our way from a normal antiferromagnetic checkerboard phase to a stripe phase, finding that approaching the transition point between the two phases is generally favorable for superconductivity as long as magnetic order can be preserved.

The fourth paper builds on paper 1 and 3, solidifying earlier obtained results through investigating the system using Eliashberg theory rather than BCS theory. This study also considers the impact of non-isotropic Fermi surfaces and concludes that the frequency dependence of the effective magnon-mediated interaction should be properly taken into account when determining the energy scale for the superconducting critical temperature.

In the fifth paper, we study indirect magnetic exchange interaction between two ferromagnets mediated by an unconventional superconductor. While such indirect interaction mediated by superconductors normally has a preference for anti-alignment of the magnetization in the ferromagnets, we find that the presence of zero-energy bound states on the surface of the superconductor can lead to a preference for alignment of the ferromagnets.

The sixth paper is concerned with the maximum spin-splitting field that spin-singlet superconductivity can survive. This spin-splitting field is typically restricted to a fraction of the superconducting gap at zero field. For a system with a dispersive energy band crossing the Fermi level as well as a completely flat band located slightly away from the Fermi level, we predict that it could be possible for the superconductivity to survive spin-splitting fields larger than the superconducting gap at zero field.

Finally, in the seventh paper, we return to our antiferromagnet/normal metal system in order to investigate whether an electron charge current, flowing parallel to the interface, in the normal metal can induce a magnon spin-current in the antiferromagnet. For an uncompensated antiferromagnetic interface, we find that inducing such a spin-polarized magnon current could be possible even if the antiferromagnet hosts two degenerate and oppositely spin-polarized magnon modes.

Preface

This thesis is submitted to the Norwegian University of Science and Technology (NTNU) in Trondheim, Norway as a partial fulfillment of the requirements for the degree of Philosophiae Doctor. The performed work, resulting in seven research articles, was done under supervision of Professor Asle Sudbø and co-supervision of Professor Jacob Linder from August 2018 until June 2022. The work was funded by The Research Council of Norway through its Centres of Excellence funding scheme Project No. 262633 "QuSpin". The candidate has further completed 30 ECTS credits of coursework, as well as teaching duties corresponding to one year of work. The teaching duties consisted of six semesters of teaching student labs.

<div align="right">

Eirik Erlandsen
Trondheim, Norway
June 2022

</div>

Acknowledgements

My four years as a PhD Candidate have involved a lot of hard work, but also a lot of fun. The fun parts were largely due to the great people I met along the way.

First, I would like to thank my supervisor Asle Sudbø who has been providing guidance and insight throughout my master's degree and PhD. I am grateful that you accepted to supervise me when I, as an overworked exchange student abroad, contacted you because I needed a supervisor, charming you with the statement that I was under the impression that you were doing "real stuff". Since then, we have worked together on a long list of challenging and rewarding projects. We have had many interesting conversations, both in your office and e.g. on fast-paced and never-ending QuSpin workshop walks. I am thankful that you put your trust in me and let me work very independently on many of my projects, but that you have also been there when I have been stuck and always helped me find a way out of my problems.

I would also like to thank my co-supervisor Jacob Linder for answering the many, both naive and advanced, questions I had while trying to contribute to the projects we worked on together. I especially appreciate all the times you answered my long emails with even longer emails, bringing us closer to an understanding of what was going on in our system.

During my PhD, I also got the opportunity to work directly with Arne Brataas, Akashdeep Kamra, and Even Thingstad. In particular, Arne's feedback on my writing in the articles we wrote together deserves recognition for why many of the sentences in this thesis, despite still long, are not even longer. I also want to thank Akash for all the fun times we had together and for all the advice he gave me at the beginning of my PhD. Further, thank you Even for acting as my oracle. I am grateful for everything I learned from working together with you and for all the wisdom you bestowed upon me during my frequent visits to your office. I also want to thank you for being a great friend and for the terrific time we had in Denver, despite the fact that the March Meeting was cancelled upon our arrival.

I also want to thank the rest of my colleagues and friends at QuSpin. Håvard has been an excellent office mate and soothed my soul with "the sound of Monte Carlo". Nicolai always managed to infect me with his energy and enthusiasm, and was a driving force behind the QuSpin LAN parties which will always stay close to my heart. Matthias and Payel have been

Publications

Paper 1:
E. Erlandsen, A. Kamra, A. Brataas, and A. Sudbø,
Enhancement of superconductivity mediated by antiferromagnetic squeezed magnons,
Phys. Rev. B **100**, 100503(R) (2019) [1].

Paper 2:
E. Erlandsen, A. Brataas, and A. Sudbø,
Magnon-mediated superconductivity on the surface of a topological insulator,
Physical Review B **101**, 094503 (2020) [2].

Paper 3:
E. Erlandsen and A. Sudbø,
Schwinger boson study of superconductivity mediated by antiferromagnetic spin fluctuations,
Physical Review B **102**, 214502 (2020) [3].

Paper 4:
E. Thingstad*, E. Erlandsen*, and A. Sudbø,
Eliashberg study of superconductivity induced by interfacial coupling to antiferromagnets,
Physical Review B **104**, 014508 (2021) [4].

Paper 5:
A. Ghanbari, E. Erlandsen, and J. Linder,
The effect of midgap states on the magnetic exchange interaction mediated by a d-wave superconductor,
Physical Review B **104**, 054502 (2021) [5].

Paper 6:
A. Ghanbari*, E. Erlandsen*, A. Sudbø, and J. Linder,
Going beyond the Chandrasekhar-Clogston limit in a flatband superconductor,
Physical Review B **105**, L060501 (2022) [6].

My contributions to the publications

For Paper 1, I performed the analytical and numerical calculations, in addition to making the main figures. The results were discussed and the manuscript was written in collaboration with the coauthors, with significant contributions from Akashdeep Kamra. For Paper 2 and 3, I performed the analytical and numerical calculations, made the figures, and wrote the first draft of the manuscript. For Paper 4, I worked closely with Even Thingstad, both of us contributing equally to the paper. Together we performed the analytical and numerical calculations and wrote the first draft of the manuscript. For paper 5, I helped interpret the results and contributed significantly to the first draft of the manuscript. For Paper 6, I worked closely with Atousa Ghanbari, who was responsible for most of the analytical calculations. Together, we performed the numerical calculations, created the figures, interpreted the results and wrote the first draft of the manuscript. In total we contributed equally to the paper. For Paper 7, I performed the analytical and numerical calculations, created the figures, and wrote the first draft of the manuscript. For all papers, all authors contributed in discussions and by providing feedback on the manuscript.

Contents

1

Introduction

One of the great challenges of our time is to reduce climate gas emissions while simultaneously meeting the energy needs of tomorrow. As scaling up the production of clean electricity at a sufficient speed can prove to be challenging, limiting the amount of wasted energy is likely to be an important part of the solution. Entering a continuously more data-driven future, reducing e.g. the energy spent running and cooling computers can be a substantial contribution [8, 9].

Superconductors, featuring zero electrical resistance, could hold the key to reducing energy losses within many different areas of society. Superconducting wires can e.g. remove the energy loss associated with electrical power transmission. They can also increase the efficiency of electrical devices, including computers where much energy is lost as heat during the transport of electrical signals. Moreover, currents carried by superconductors can be used to generate strong magnetic fields, or even to store energy through currents that run in a loop without slowing down.

While this sounds very promising, there is, of course, a reason why we are currently not completely surrounded by such applications of superconductors. Superconducting materials unfortunately lose their special properties above a critical temperature which is normally considerably below room temperature. Some of the materials we normally surround ourselves with, such as aluminium, can in fact become superconducting, but only if they are cooled down sufficiently. The advantages of using superconductors in applications are therefore often out-weighted by the cost of cooling. An important exception is the use of superconductors as electromagnets in MRI devices [10]. Similarly, superconductors are used to generate large magnetic fields to guide the particle beams in particle accelerators [11]. Reversely, superconductors can also be used in sensitive magnetometers, able to measure the strength of very weak magnetic fields [12]. There are actually also e.g. some existing superconducting cables in use for power transmission [13].

Releasing the true potential of superconductivity clearly requires the discovery or construction of a room-temperature (or at least close to room-temperature) superconductor, which preferably also should be easy to produce and shape. The probability of reaching this goal can be increased if the search is guided by a solid theoretical understanding of superconductors, including both why superconductivity arises and which properties that determine the critical temperature of a superconducting material. A large class of superconductors are currently well-understood as arising from electrons in a metal interacting with spatial fluctuations in the ionic lattice. Such superconductors are often referred to as conventional superconductors and examples include many elemental superconductors such as aluminium and lead. Their critical temperatures are typically of the order $0.1 - 10\,\mathrm{K}$. There are, however, also superconductors with larger critical temperatures, all the way up towards $140\,\mathrm{K}$ [14]. The mechanism leading to superconductivity in these types of superconductors is less understood. As we will return to later, it is generally believed that magnetic fluctuations play an important role.

Building a better understanding of currently known high-temperature superconductors could be a pathway towards further optimization leading to realization of a room-temperature superconductor. Another, more recent, potential pathway towards room-temperature superconductivity relies on large pressures to stabilize new materials containing light elements such as hydrogen. The presence of the light ions can lead to a very large energy scale for the associated lattice vibrations, which can set a large energy scale for the superconducting critical temperature [15]. In such systems, room-temperature superconductivity, at least for a somewhat chilly room keeping 15℃, has recently been achieved [16]. Unfortunately, the somewhat chilly room also needs to have a pressure six order of magnitude larger than atmospheric pressure. Rather than trying to increase the critical temperature, the new challenge is then to be able to lower the necessary pressure.

In addition to the potential applications listed above, superconductors can also be useful within the field of spintronics. This field aims to use spin, rather than charge, to store and transport information for computational purposes [17]. Spins have actually already been used to store information for quite a long time. In normal hard drives, information is encoded through the direction of the magnetization in magnetic domains, determined by the direction of the spins in the domain which align to create the magnetization. Information can then be written to the hard-drive by driving a current, pro-

ducing a magnetic field that can switch the direction of a magnetic domain. Reading of the encoded information can be achieved through the use of a material with large magnetoresistance, i.e. a material whose electrical resistance is strongly influenced by the presence of a magnetic field. Placing such a material close to a magnetic domain and attempting to drive a current through the material, one can then obtain information about the magnetic domain. Large magnetoresistance can be achieved in structures consisting of metallic magnets separated by nonmagnetic metals. This effect is named giant magnetoresistance (GMR) and was discovered by Fert and Grünberg, leading to them being awarded the Nobel prize in physics in 2007 [18, 19].

GMR relies on electrons experiencing spin-dependent scattering when moving through a magnetic metal. If e.g. electrons with spins aligned with the background field in the magnetic material tend to scatter more, electrons with spins anti-aligned with the background field will easier move through the material and better contribute to the conductivity. In a structure consisting of a single nonmagnetic metal sandwiched between two magnetic metals that prefer to have anti-aligned magnetization, both spin-up and spin-down electrons will scatter strongly on their way through the structure, leading to a large resistance. However, if an external field is used to align the magnetization in the two materials, the structure will have a lower resistance as electrons with a specific spin-direction are able to float through the system without experiencing strong scattering. The resistance of the structure can, in other words, be strongly affected by an applied magnetic field. If we further fix the direction of one of the magnets, the resistance becomes dependent on the direction of the applied field: The field can either leave the magnetization of the second magnet unchanged, or it can reverse it. Bringing such a structure close to a magnetic domain in a hard drive, the resistance through the structure will then depend on the direction of the magnetic domain and we are able to read out information from the hard-drive.

The spin-property of electrons is clearly already of importance for information storage. It is, however, also possible to use spin signals to transport information through so-called spin currents. A spin current can simply be a spin-polarized version of a normal electron current, meaning an electron current consisting of e.g. more electrons with spin-up than spin-down. Such a spin current is naturally realized in magnetic metals. Similarly, it is also possible to realize an electronic pure spin current where electrons with opposite spins move in opposite directions. This can e.g. be realized in heavy

metals where electrons can be viewed as following curved trajectories where the direction of deviation from a straight line depends on the spin of the electrons. A charge current will then lead to a transverse pure spin current, which is known as the spin Hall effect [20, 21]. The reverse process, where a spin current generates a transverse charge current is known as the inverse spin Hall effect [21]. The inverse spin Hall effect is useful for indirectly detecting spin currents through their associated transverse charge currents.

An alternative way of transporting spin signals is through spin currents in magnetic insulators. There are then no moving electrons that can carry spin through the system, only localized spins that can fluctuate around their preferred direction. The spin signal then travels through the system like the effect of a puff of wind travelling through a grain field. As the signal is transported without any moving charge carriers, magnetic insulators can allow for low-loss transfer of information [22]. Spin currents in magnetic insulators can be generated by subjecting the magnet to an incoming electron spin current from a neighboring heavy metal, or by applying a temperature gradient to the system. In the latter case, more spin-fluctuations will be present in the warmer part of the system which will then spread out to the colder part of the system, giving rise to a spin current. Moreover, regardless of their origin, spin currents in magnetic insulators can be sent into a neighboring heavy metal where they can be detected through the inverse spin Hall effect.

Finally, another alternative for low-loss transportation of spin signals is superconducting spin currents. Such spin currents are of interest within the field of superconducting spintronics which aims to use the special properties of superconductors to improve the efficiency of spintronics devices [23, 24]. Combining superconductivity and spintronics does, however, typically also mean combining superconductivity and magnetism. As we will see later, superconductivity and magnetism are, unfortunately, normally not the best of friends. An important question within the field is therefore under what circumstances superconductivity and magnetism can coexists, as well as which interesting, and potentially useful, effects that can arise when such coexistence is achieved.

In this thesis, we first attempt to better understand how spin fluctuations can give rise to superconductivity. High-temperature superconductors, where spin fluctuations appear to be of importance, typically represent complex systems that it can be difficult to understand even when they are in their "normal" state above the superconducting critical temperature.

This motivates studying spin-fluctuation mediated superconductivity in systems that it might be easier to understand. We approach the problem of spin-fluctuations mediated superconductivity from the perspective of heterostructures consisting of magnetic insulators and conductors. Although the presence of an interface between two different materials in one way complicates the system, this approach to the problem also introduces certain clear advantages. The conduction electrons and magnetic fluctuations now have completely separate origin, in fact being hosted by two separate materials. It is then possible, both theoretically and experimentally, to pick the heterostructure apart to investigate the properties of the electrons and magnetic fluctuations decoupled from each other. This can aid in understanding the, potentially complex, physics that arise when they are brought together. Heterostructures also provide large possibilities for separately adjusting the properties of the metallic and magnetic materials, as well as how they couple to each other. This can increase the chance of realizing a parameter regime which is favorable for superconductivity, and also means that such heterostructures might provide a potential playground for gaining a better understanding of the relationship between superconductivity and spin fluctuations.

Further, in this thesis, we also study interplay between magnetism and different types of superconductors, as well as new ways of generating spin currents in magnetic insulators. We start the thesis by providing an introduction to magnetism and magnetic fluctuations in chapter 2. We then dive into superconductivity in chapter 3, also introducing the effect of magnetic fields on superconductors and briefly commenting on spin-fluctuation mediated superconductivity. In chapter 4, we move on to discussing in detail spin-fluctuation mediated superconductivity in heterostructures, which brings us to Papers [1–4]. Next, we introduce the concept of indirect exchange interaction in chapter 5 and make our way to Paper [5], discussing magnetic exchange interaction between ferromagnets mediated by a superconductor. We then further consider flatband systems and flatband superconductivity in chapter 6, leading up to the discussion of the critical magnetic field of flatband superconductors in Paper [6]. In chapter 7, we consider transport theory and coupling between flow of electrons and spin fluctuations, bringing us to Paper [7]. We end with concluding and highlighting possible paths for future work in chapter 8.

2

Magnetism

When applying a magnetic field to a material, the response of the material can differ. Considering a solid material consisting of periodically spaced atom cores with associated electrons, the atom cores themselves can provide magnetic moments that can interact with a magnetic field. More importantly, the electrons associated with the atoms carry a spin, which can provide the atoms with a much larger nonzero magnetic moment if there are one or more unpaired electrons, i.e. electrons in states that are not doubly occupied by electrons with opposite spin directions. Similarly, the orbital motion of electrons around the atom cores can also contribute to the net magnetic moment if such contributions do not sum up to zero. In a paramagnetic material, the dominant effect is that magnetic moments in the system align with an external magnetic field, making the material strengthen the applied field. The presence of a magnetic field can, however, also influence the orbital motion of electrons around the atom cores, setting up a magnetic field in the opposite direction of the applied field. This effect can be dominant if e.g. the electron contributions to the net magnetic moments of the atoms vanish. The material then becomes a diamagnet, which is a material that works against an applied magnetic field. Taking into account that the material may feature itinerant electrons, these electrons can also have their motion altered by an external field or align their magnetic moments with the field. The paramagnetic contributions from itinerant electrons are, however, limited by the fact that the magnetic field is only able to spin-polarize electrons close to the Fermi level. Despite this, such contributions can e.g. be important for the critical magnetic field of superconductors, which we will see in Chap. 3. The diamagnetic contributions from itinerant electrons are, normally, also small [25].

Both paramagnetic and diamagnetic materials become magnetized when exposed to a magnetic field. Another class of materials, ferromagnets, can host a net magnetic moment in the absence of an external field. Ferromagnetic insulators consist of localized magnetic moments that interact

with each other in a way that favors alignment of the magnetic moments. Although magnetic moments can simply interact with each other through dipole-dipole interactions, the dominant interactions in ferromagnetic insulators are so-called exchange interactions [26].

Exchange interactions arise from the symmetry restrictions of identical particles under exchange, allowing e.g. the spin state of a system to influence the spatial state. Considering for instance some two-electron system where the electrons repel each other through the Coulomb interaction, whether the electrons are in a spin-singlet or spin-triplet state will dictate whether their combined wave function is odd or even under exchange of their spatial coordinates. Even if the Hamiltonian is not spin-dependent, the energy of the two-particle system can depend on the affected spatial properties of the wave function, giving rise to an energy difference between the singlet and triplet states [25, 26]. The Hamiltonian describing the system can then be expressed in terms of dot product between the two spin operators $H \sim J\boldsymbol{S}_1 \cdot \boldsymbol{S}_2$, where the exchange coupling J is determined by the difference in energy between the singlet and triplet states.

In general, exchange couplings can favor both ferromagnetic and antiferromagnetic alignment of neighboring spins. They can arise from direct exchange as in the above example, but we can also have more complicated indirect interactions, which we will return to in Chap. 5. If the interaction between neighboring magnetic moments favors anti-alignment, rather than alignment, the material can be an antiferromagnet where neighboring spins are anti-aligned. The material does then not feature a net magnetic moment, but there is still magnetic order in the system. Although antiferromagnets may seem like simply a combination of two oppositely aligned ferromagnets, we will see in this chapter that this is far from the full story. Similarly, other types of interaction or additional interaction between e.g. next-nearest neighbors can give rise to different types of magnetic order. One example is Dzyaloshinskii-Moriya interaction, normally arising due to the presence of spin-orbit coupling in the system, which favors neighboring spins to be orthogonal to each other.

Moreover, metallic systems can also feature magnetic order. The magnetic order can arise from localized magnetic moments as before, or from the itinerant electrons themselves. Similarly to localized electrons, the spins of itinerant electrons may interact in ways favoring e.g. alignment of spins, which can make the electrons stay more away from each other and thereby reduce the effect of Coulomb repulsion. Starting with a spin-degenerate sys-

tem of itinerant electrons filling up the states below the Fermi level, spin-polarizing the system requires emptying e.g. spin-down states below the Fermi level and filling spin-up states above the Fermi level. This leads to a kinetic energy cost which, in order for magnetization to take place, must be compensated by the potential energy gain associated with the spin-polarized state. While the potential energy gain will increase with the strength of the spin-dependent interaction, the associated kinetic energy cost will be lower for a larger density of states at the Fermi level, allowing more states to be filled above the Fermi level at a lower energy cost. The combination of sufficiently strong spin-dependent interaction and a sufficiently large density of states at the Fermi level can therefore lead to a magnetic state. This gives rise to the Stoner criterion for itinerant ferromagnetism [27]. For real materials, properly evaluating and satisfying this, seemingly simple, criterion for itinerant ferromagnetism may necessitate taking into account detailed band structures featuring more or less localized/itinerant electrons [25]. When modelling metallic ferromagnets, one often considers a system consisting of itinerant electrons coupled to fully localized spins displaying magnetic order, or simply itinerant electrons coupled to a background field of unspecified origin. As we will see in Chap. 5, the latter case is applied in Paper [5] where we consider ferromagnetic metals coupled together by a superconductor.

The focus of this chapter will be on magnetic insulators, which play an integral part in most of the papers included in this thesis. We start by discussing ferromagnetism in Sec. 2.1, where we introduce a spin-model for ferromagnetic insulators and investigate the excitations of this model within both a linear spin-wave and Schwinger boson framework. We then move on to an analogous discussion of antiferromagnetism in Sec. 2.2.

2.1 Ferromagnetism

As described above, ferromagnetic materials contain magnetic moments that can spontaneously align in the absence of a magnetic field. An example of localized spins that align due to a ferromagnetic nearest-neighbor interaction, forming a net magnetization, is shown in Fig. 2.1(a). Further, as displayed in Fig. 2.1 (b), the magnetic order is stable below some critical temperature T_C, which is called the Curie temperature of the material. Above this temperature, thermal fluctuations become too strong and over-
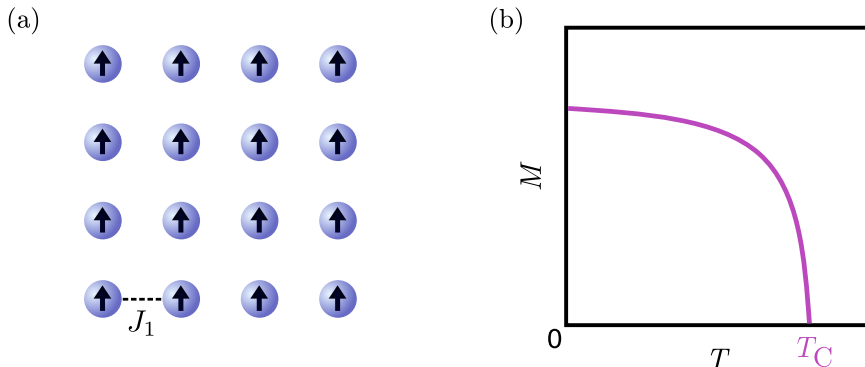
Figure 2.1: (a) Ferromagnet with localized spins that interact with nearest neighbors through an exchange interaction J_1. In (b), we show a sketch of the magnetization M as a function of temperature T for a ferromagnet. The magnetization decays with temperature, until it vanishes at the Curie temperature T_C.

power the tendency of ordering in the system.

Rather than all spin being aligned in the same direction, ferromagnets in reality often break up into domains with different direction of magnetization. We will in the following consider the physics of a single uniform domain. Further, ferromagnetic insulators often include nonmagnetic atoms in addition to the atoms giving rise to the localized magnetic moments. When modelling the system, we simply focus on the localized spins and the interaction between them.

To describe a ferromagnetic insulator of the type in Fig. 2.1(a), we will start out from a spin Hamiltonian on the form

$$H_{\mathrm{FMI}} = -J_1 \sum_{\langle \boldsymbol{i}, \boldsymbol{j} \rangle} \boldsymbol{S_i} \cdot \boldsymbol{S_j} - K \sum_{\boldsymbol{i}} S_{\boldsymbol{i}z}^2 - h \sum_{\boldsymbol{i}} S_{\boldsymbol{i}z}. \tag{2.1}$$

Here, $\boldsymbol{S_i}$ represents a localized quantum spin located at lattice site $\boldsymbol{i}$ which interacts with its nearest neighbors $\boldsymbol{S_j}$ in all directions so that each nearest neighbor bond is double-counted when we sum over the lattice sites. We will, for simplicity, assume that the lattice is a simple d-dimensional cubic lattice. We have also added the potential effect of an external magnetic field favoring the spins to align in the z-direction, as well as an easy-axis anisotropy term

proportional to K. This anisotropy term captures the possibility that some specific ordering axis can be more favorable than others. Such spin-space anisotropy can originate with e.g. spin-orbit coupling arising from the orbital motion of electrons in the electric field of the crystal, whose effect will be influenced by the crystal symmetry [28].

In order to analyze the above spin Hamiltonian, one often attempts to simplify the problem through some approximate procedure. We start with introducing the approach to the problem which is referred to as linear spin-wave theory.

2.1.1   Linear spin wave theory

We start out from an assumption that the ferromagnetic system is close to a fully ordered state where all spins point in the same direction, representing the ground state of the system. It should then be possible to describe the system as a fully ordered state combined with deviations away from the fully ordered state. This is achieved through the linearized Holstein-Primakoff transformation [29]

$$S_{i+} = \sqrt{2S - a_i^\dagger a_i}\, a_i \approx \sqrt{2S}\, a_i, \tag{2.2a}$$

$$S_{i-} = a_i^\dagger \sqrt{2S - a_i^\dagger a_i} \approx \sqrt{2S}\, a_i^\dagger, \tag{2.2b}$$

$$S_{iz} = S - a_i^\dagger a_i, \tag{2.2c}$$

where $a_i^\dagger$ is a bosonic creation operator, lowering the z-direction spin quantum number at lattice site i. In the absence of of such bosons, the system is simply in its fully ordered state with $S_{iz} = S$. Assuming that deviations away from this state are small, we have expanded the square roots to linear order in the boson operators.

For a spin-$\frac{1}{2}$ system, a lowering of the z-direction spin quantum number leads to a complete flip of the localized spin. Although such localized spin-flips (or partly flips for $S > 1/2$) may seem like natural excitations of an ordered ferromagnet, such spin-flips are energetically costly due to the ferromagnetic exchange interaction between nearest neighbors, and they are not eigenexcitations of the system. In order to obtain the eigenexcitations, we need to introduce Fourier-transformed bosonic operators

$$a_{\boldsymbol{q}} = \frac{1}{\sqrt{N}} \sum_{\boldsymbol{i}} a_{\boldsymbol{i}} e^{i\boldsymbol{q}\cdot\boldsymbol{r_i}}, \tag{2.3}$$

where N is the number of lattice sites in the system. These new excitations represent delocalized spin-flips, which are collective excitations referred to as magnons. While magnons carrying finite momentum $\boldsymbol{q}$ represent spin-waves travelling through the system, the special case of a magnon with $\boldsymbol{q} \to 0$ corresponds to a macroscopically small uniform deviation of the spin-direction. The latter type of excitations have an energy cost of the order K or h in the presence of easy-axis anisotropy or a magnetic field. Such excitations can be much less costly than localized spin-flip excitations that come with an energy cost of the order J_1.

Inserting the linearized Holstein-Primakoff transformation, Fourier transforming the original spin-flip operators, and disregarding constant terms, our initial spin Hamiltonian can be expressed as

$$H_{\mathrm{FMI}} = \sum_{\boldsymbol{q}} \omega_{\boldsymbol{q}} \, a_{\boldsymbol{q}}^{\dagger} a_{\boldsymbol{q}}, \tag{2.4}$$

where

$$\omega_{\boldsymbol{q}} = 2KS + 2SJ_1 z_1 (1 - \gamma_{\boldsymbol{q}}) + h, \tag{2.5}$$

and $\gamma_{\boldsymbol{q}} = \frac{1}{z_1} \sum_{\boldsymbol{\delta}_1} e^{i\boldsymbol{q}\cdot\boldsymbol{\delta}_1}$. Here, we have denoted the number of nearest neighbors by z_1, while the sum over $\boldsymbol{\delta}_1$ is a sum over nearest neighbor vectors. The magnon excitation energies $\omega_{\boldsymbol{q}}$ are presented as a function of momentum in Fig. 2.2 (a) and (b). Around the Brillouin zone center, we see that the magnons follow a quadratic dispersion relation. In (b), we highlight that taking $K > 0$ opens a gap in the magnon spectrum. The quantity a is here the lattice constant.

The magnetization in the system can further be expressed as

$$M = \frac{1}{N} \sum_{\boldsymbol{i}} \langle S_{\boldsymbol{i},z} \rangle = S - \frac{1}{N} \sum_{\boldsymbol{q}} b(\omega_{\boldsymbol{q}}), \tag{2.6}$$

where $b(\omega_{\boldsymbol{q}})$ is a Bose-distribution. Assuming a gapless magnon spectrum, one can then show that the correction term to the magnetization diverges at
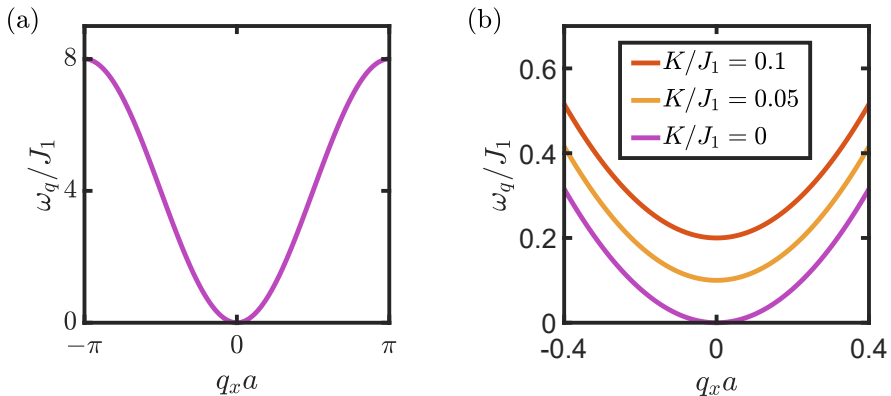
Figure 2.2: Dispersion relation for ferromagnetic magnons living in two dimensions with $q_y a = 0$, $S = 1$, and $h = 0$. For the purple curves in (a) and (b), we have set the easy-axis anisotropy to zero. In (b), we also show that a nonzero easy-axis anisotropy opens a gap in the magnon spectrum.

finite temperature for dimensions smaller than 3, indicating that there is no magnetic order in this case. This is consistent with the Hohenberg-Mermin-Wagner theorem [30, 31], which states that continuous symmetries cannot be spontaneously broken at finite temperatures if the system is one- or two-dimensional and the involved interactions are sufficiently short-ranged. As a gapless magnon spectrum corresponds to our spin Hamiltonian featuring a continuous spin-rotational symmetry, this symmetry of the Hamiltonian must be spontaneously broken for the spins of the system to order in a specific direction. We then need a three-dimensional system to achieve long-range order above zero temperature. The Hohenberg-Mermin-Wagner theorem can, however, be circumvented by explicitly breaking the continuous spin-rotational symmetry through e.g. introducing easy-axis anisotropy in the system. Magnetic ordering at nonzero temperatures is then no longer restricted to three-dimensional systems.

2.1.2   Schwinger bosons

The spin Hamiltonian in Eq. (2.1) can also be treated by rewriting the spin operators in terms of Schwinger bosons operators. A potential advantage of this approach is that we are not restricted to studying the system close to a fully ordered state. Through this approach, one can, in fact, even study
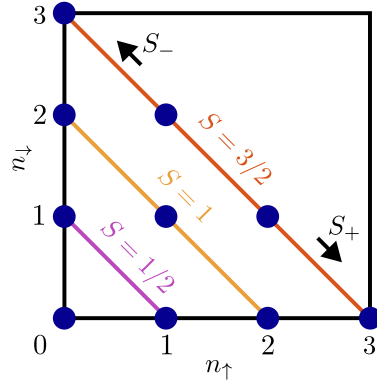
Figure 2.3: Spin state at a lattice site as a function of the occupation of Schwinger bosons with spin ↑ and ↓. For a given spin quantum number S, the state where the z-component of the spin is maximized is located along the x-axis of the figure.

disordered magnetic phases. Schwinger bosons also allow for a straightforward generalization from spin-systems with $SU(2)$ symmetries to systems with $SU(N')$ symmetry. In contrast to the spin wave approach, which relies on a sufficiently large S, Schwinger bosons approaches are large N' approximations [32].

In terms of Schwinger bosons, the spin operators take the form

$$S_{i+} = a_{i\uparrow}^\dagger a_{i\downarrow}, \tag{2.7a}$$

$$S_{i-} = a_{i\downarrow}^\dagger a_{i\uparrow}, \tag{2.7b}$$

$$S_{iz} = \frac{1}{2}(a_{i\uparrow}^\dagger a_{i\uparrow} - a_{i\downarrow}^\dagger a_{i\downarrow}), \tag{2.7c}$$

where $a_{i\sigma}^\dagger$ creates a Schwinger boson with spin σ. How the spin state at a given lattice site depends on the occupation of Schwinger bosons is displayed in Fig. 2.3. It further follows that

$$a_{i\uparrow}^\dagger a_{i\uparrow} + a_{i\downarrow}^\dagger a_{i\downarrow} = 2S, \tag{2.8}$$

on each lattice site. Notably, this restriction on the total boson number associated with a lattice site is an equality, rather than the inequality $0 \leq$

$a_i^\dagger a_i \leq 2S$ that restricts the number of bosons per site within the spin-wave framework.

In order to analyze the ferromagnet Hamiltonian, we next introduce the ferromagnetic bond operators [33, 34]

$$B_{ij} = \frac{1}{2}(a_{i\uparrow}a_{j\uparrow}^\dagger + a_{i\downarrow}a_{j\downarrow}^\dagger), \tag{2.9}$$

allowing us to write

$$H_{\text{FMI}} = Nz_1 J_1 S(S+1) - 2J_1 \sum_{\langle i,j \rangle} B_{ij}^\dagger B_{ij} - K \sum_i S_{iz}^2 - h \sum_i S_{iz}. \tag{2.10}$$

We then express the bond operators in terms of mean-field values and deviations

$$B_{ij} = \langle B_{ij} \rangle + (B_{ij} - \langle B_{ij} \rangle) = \langle B_{ij} \rangle + \delta B_{ij}. \tag{2.11}$$

Neglecting quadratic terms in the deviations, we can then write

$$B_{ij}^\dagger B_{ij} \approx \langle B_{ij}^\dagger \rangle B_{ij} + \langle B_{ij} \rangle B_{ij}^\dagger - \langle B_{ij}^\dagger \rangle \langle B_{ij} \rangle. \tag{2.12}$$

Similarly, we can also introduce a similar mean-field decoupling for $S_{i,z}$ in order to treat the easy-axis anisotropy term. Relaxing the constraint in (2.8) to only hold for the average values of the Schwinger boson numbers, and enforcing this constraint through the introduction of a Lagrange multiplier λ, the Hamiltonian can now be expressed as

$$\begin{aligned} H_{\text{FMI}} = {} & \lambda \sum_i (a_{i\uparrow}^\dagger a_{i\uparrow} + a_{i\downarrow}^\dagger a_{i\downarrow} - 2S) + Nz_1 J_1 S(S+1) \\ & - 2J_1 \sum_{\langle i,j \rangle} \left[\langle B_{ij}^\dagger \rangle B_{ij} + \langle B_{ij} \rangle B_{ij}^\dagger \right] + 2J_1 \sum_{\langle i,j \rangle} \langle B_{ij}^\dagger \rangle \langle B_{ij} \rangle \\ & - 2K \sum_i \langle S_{iz} \rangle S_{iz} + K \sum_i \langle S_{iz} \rangle^2 - h \sum_i S_{iz}. \end{aligned} \tag{2.13}$$

We then take $\langle B_{ij} \rangle = \langle B_{ij}^\dagger \rangle = \mathcal{B}$, where $\mathcal{B}$ is constant and real. Similarly, we also take $\langle S_{i,z} \rangle = M$. We can then insert the expression for B_{ij} in terms of

the Schwinger boson operators and introduce the Fourier transformation of the operators. This leads us to the diagonalized Hamiltonian

$$
\begin{aligned}
H_{\text{FMI}} = {} & N z_1 J_1 S(S+1) + 2 J_1 N z_1 \mathcal{B}^2 - 2S\lambda N + N K M^2 \\
& + \sum_{\boldsymbol{q}\sigma} \omega_{\boldsymbol{q}\sigma} a_{\boldsymbol{q}\sigma}^\dagger a_{\boldsymbol{q}\sigma},
\end{aligned}
\tag{2.14}
$$

where

$$
\omega_{\boldsymbol{q}\sigma} = \lambda - 2\mathcal{B} J_1 z_1 \gamma_{\boldsymbol{q}} - \frac{\sigma}{2}(2KM + h).
\tag{2.15}
$$

The Lagrange multiplier λ, and the mean-field parameters $\mathcal{B}$ and M should be determined by minimizing the free energy. Several of the terms not involving any operators are therefore still of relevance. We will go more into the minimization of the free energy when we get to the antiferromagnetic case. Here, we only quickly note that the magnetization can be expressed as

$$
M = \frac{1}{N} \sum_{\boldsymbol{i}} \langle S_{\boldsymbol{i}z} \rangle = \frac{1}{2N} \sum_{\boldsymbol{q}} \left(\langle a_{\boldsymbol{q}\uparrow}^\dagger a_{\boldsymbol{q}\uparrow} \rangle - \langle a_{\boldsymbol{q}\downarrow}^\dagger a_{\boldsymbol{q}\downarrow} \rangle \right).
\tag{2.16}
$$

Within this framework, ferromagnetic order is, in the thermodynamic limit, signalled by Bose-Einstein condensation of Schwinger bosons with $\boldsymbol{q} = \boldsymbol{0}$. For ordering along the z-axis, we then have condensation of either spin-$\uparrow$ or spin-$\downarrow$ Schwinger bosons. A macroscopic number of e.g. spin-$\uparrow$ magnons with $\boldsymbol{q} = \boldsymbol{0}$ and no spin-$\downarrow$ magnons then corresponds to a uniform state where all spins point in the positive z-direction.

2.2   Antiferromagnetism

After having introduced ferromagnetism and ferromagnetic excitations, we are ready to move on to antiferromagnetism. In Fig. 2.4 (a), we show an example of localized spins that interact with nearest and next-nearest neighbors, forming an antiferromagnetic state. For a dominant antiferromagnetic nearest neighbor interaction, a ferromagnetic next-nearest neighbor interaction will help stabilize the antiferromagnetic state, while an antiferromagnetic next-nearest neighbor interaction acts as a frustration. The
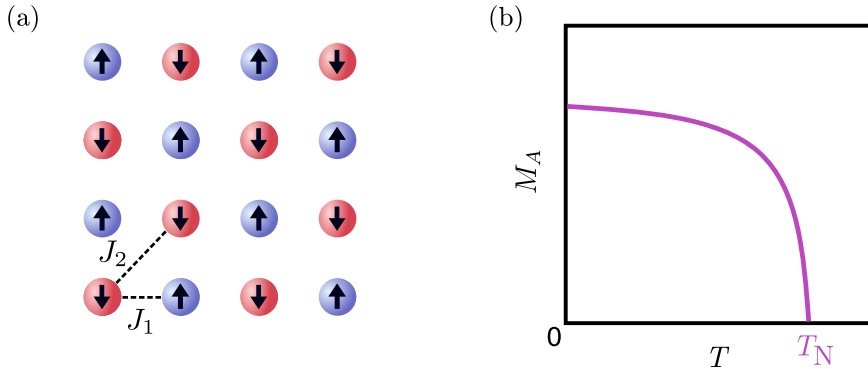
Figure 2.4: (a) Antiferromagnet with localized spins that interact with nearest neighbors and next-nearest neighbors through exchange interactions J_1 and J_2. In (b), we show a sketch of the sublattice magnetization M_A as a function of temperature T for an antiferromagnet. Similar to the ferromagnet, the magnetization decays with temperature. The critical temperature where magnetic ordering is lost is called the Néel temperature T_N.

checkerboard antiferromagnetic state shown in this figure is known as a Néel state. Although the net magnetization vanishes, we can divide the lattice up into two sublattices (A and B) which each features a nonzero sublattice magnetization. As displayed in Fig. 2.4 (b), the sublattice magnetization vanishes above a critical temperature referred to as the Néel temperature T_N.

In order to model an antiferromagnetic insulator, we start out from a spin Hamiltonian similar to the one we used in the previous section

$$H_{\mathrm{AFMI}} = J_1 \sum_{\langle \boldsymbol{i},\boldsymbol{j} \rangle} \boldsymbol{S_i} \cdot \boldsymbol{S_j} + J_2 \sum_{\langle\langle \boldsymbol{i},\boldsymbol{j} \rangle\rangle} \boldsymbol{S_i} \cdot \boldsymbol{S_j} - K \sum_{\boldsymbol{i}} S_{\boldsymbol{i}z}^2 - h \sum_{\boldsymbol{i}} S_{\boldsymbol{i},z}, \qquad (2.17)$$

where the spin are, again, taken to live on a d-dimensional simple cubic lattice. We have now introduced an additional interaction between next-nearest neighbors and reversed the sign in front of the first term in order for $J_1 > 0$ to correspond to an antiferromagnetic coupling between nearest neighbors.

The fully ordered Néel state is, indeed, the classical ground state of the system. However, in contrast to the situation we had for the ferromag-

net, the classical ground state is in this case not the ground state, or even an eigenstate, of the quantum Hamiltonian. This is easily seen by writing $\boldsymbol{S_i} \cdot \boldsymbol{S_j} = \frac{1}{2}(S_{i+}S_{j-} + S_{i-}S_{j+}) + S_{iz}S_{jz}$ and inspecting the nearest neighbor term. For a ferromagnet state, combinations of ladder operators such as $S_{i+}S_{j-}$ give vanishing contributions when acting on two neighboring spins polarized in the same direction. However, for a Néel state, $S_{i+}S_{j-}$ may change the state of the system when acting on two oppositely polarized spins, making the Néel state not an eigenstate of the quantum Hamiltonian.

Despite the fact that the Néel state is not an eigenstate of the Hamiltonian, we must keep in mind that we are trying to describe an antiferromagnet featuring a net magnetization on each sublattice. In order for our choice of Hamiltonian to be sensible, the ground state should also feature a net magnetization associated with each sublattice and therefore not be too different from a Néel state. When treating the Hamiltonian within the linear spin wave framework, we therefore consider a fully ordered checkerboard state combined with small deviations away from this state.

2.2.1   Linear spin wave theory

For each sublattice, the linearized Holstein-Primakoff transformation now takes the form

$$S_{i+}^A = \sqrt{2S - a_i^\dagger a_i}\, a_i \approx \sqrt{2S}\, a_i, \qquad S_{j+}^B = b_j^\dagger \sqrt{2S - b_j^\dagger b_j} \approx \sqrt{2S}\, b_j^\dagger, \quad (2.18a)$$

$$S_{i-}^A = a_i^\dagger \sqrt{2S - a_i^\dagger a_i} \approx \sqrt{2S}\, a_i^\dagger, \qquad S_{j-}^B = \sqrt{2S - b_j^\dagger b_j}\, b_j \approx \sqrt{2S}\, b_j, \quad (2.18b)$$

$$S_{iz}^A = S - a_i^\dagger a_i, \qquad\qquad\qquad S_{jz}^B = -S + b_j^\dagger b_j. \qquad\qquad (2.18c)$$

Using this transformation, we rewrite the spin operators in our Hamiltonian in terms of bosonic operators before we, once again, introduce the Fourier transformation of the localized bosonic operators

$$a_{\boldsymbol{i}} = \frac{1}{\sqrt{N_A}} \sum_{\boldsymbol{q}} a_{\boldsymbol{q}} e^{-i\boldsymbol{q}\cdot\boldsymbol{r_i}}, \qquad b_{\boldsymbol{i}} = \frac{1}{\sqrt{N_B}} \sum_{\boldsymbol{q}} b_{\boldsymbol{q}} e^{-i\boldsymbol{q}\cdot\boldsymbol{r_i}}, \qquad (2.19)$$

where $N_A = N_B = N/2$. As the localized bosonic operators, in this case, are associated with the sublattices of the full lattice, the delocalized spin-flip
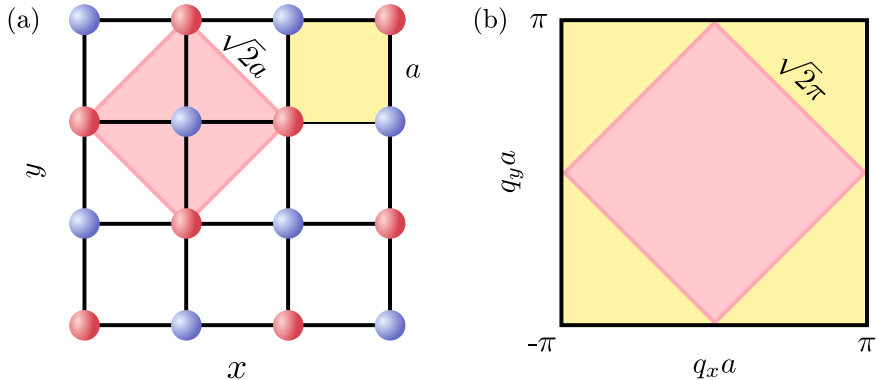
Figure 2.5: (a) Unit cell for the full lattice and a sublattice, with corresponding Brillouin zones in (b). The Brillouin zone corresponding to the sublattices is rotated and shrunk by a factor $\sqrt{2}$.

magnons live in a reduced Brillouin zone, as displayed in Fig. 2.5.

Neglecting constant terms, we now have

$$
\begin{aligned}
H_{\mathrm{AFMI}} = \sum_{\boldsymbol{q}} \Big[&C_{\boldsymbol{q}}(a_{\boldsymbol{q}}^{\dagger}a_{\boldsymbol{q}} + b_{\boldsymbol{q}}^{\dagger}b_{\boldsymbol{q}}) + h(a_{\boldsymbol{q}}^{\dagger}a_{\boldsymbol{q}} - b_{\boldsymbol{q}}^{\dagger}b_{\boldsymbol{q}}) \\
&+ D_{\boldsymbol{q}}(a_{\boldsymbol{q}}^{\dagger}b_{-\boldsymbol{q}}^{\dagger} + a_{\boldsymbol{q}}b_{-\boldsymbol{q}}) \Big],
\end{aligned}
\tag{2.20}
$$

where

$$
C_{\boldsymbol{q}} = 2SJ_1 z_1 + 2SK - 2SJ_2 z_2(1 - \tilde{\gamma}_{\boldsymbol{q}}), \tag{2.21a}
$$
$$
D_{\boldsymbol{q}} = 2SJ_1 z_1 \gamma_{\boldsymbol{q}}. \tag{2.21b}
$$

Here, $\tilde{\gamma}_{\boldsymbol{q}} = \frac{1}{z_2} \sum_{\boldsymbol{\delta}_2} e^{i\boldsymbol{q}\cdot\boldsymbol{\delta}_2}$ where the sum covers next-nearest neighbor vectors. As we now see, a Fourier transformation is not sufficient to diagonalize our antiferromagnetic Hamiltonian. If we had taken $J_1 = 0$ and relied on a ferromagnetic next-nearest neighbor interaction $J_2 < 0$ as well as e.g. some staggered magnetic field to produce a Néel phase, the story would have ended here. Our system would simply consist of two decoupled ferromagnets. As we, instead, are studying two strongly coupled sublattices, we need to introduce an additional Bogoliubov transformation
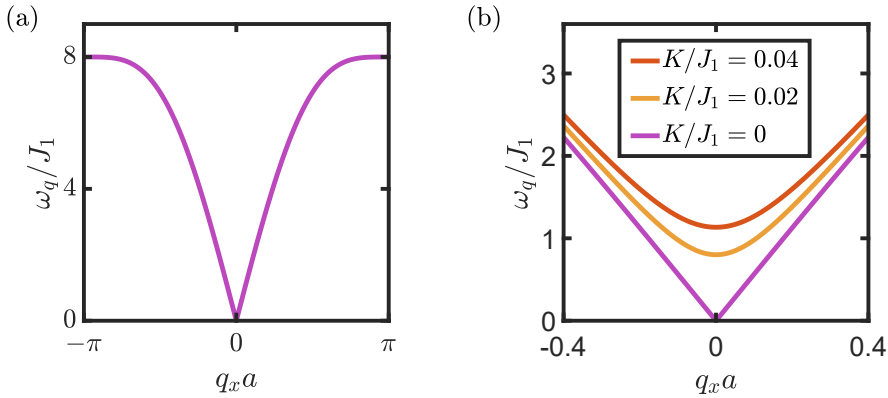
Figure 2.6: Dispersion relation for antiferromagnetic magnons living in two dimensions with $q_y a = 0$, $S = 1$, and $h = 0$. For the purple curves in (a) and (b), we have set the easy-axis anisotropy to zero. In (b), we show that a nonzero easy-axis anisotropy now not only opens a gap in the magnon spectrum, but also leads to the dispersion relation being quadratic instead of linear around the Brillouin zone center.

$$a_{\boldsymbol{q}} = u_{\boldsymbol{q}}\alpha_{\boldsymbol{q}} + v_{\boldsymbol{q}}\beta^{\dagger}_{-\boldsymbol{q}}, \tag{2.22a}$$

$$b^{\dagger}_{-\boldsymbol{q}} = u_{\boldsymbol{q}}\beta^{\dagger}_{-\boldsymbol{q}} + v_{\boldsymbol{q}}\alpha_{\boldsymbol{q}}, \tag{2.22b}$$

where $u_{\boldsymbol{q}}^2 - v_{\boldsymbol{q}}^2 = 1$. Inverting these expressions, we obtain

$$\alpha_{\boldsymbol{q}} = u_{\boldsymbol{q}}a_{\boldsymbol{q}} - v_{\boldsymbol{q}}b^{\dagger}_{-\boldsymbol{q}} \tag{2.23a}$$

$$\beta^{\dagger}_{-\boldsymbol{q}} = u_{\boldsymbol{q}}b^{\dagger}_{-\boldsymbol{q}} - v_{\boldsymbol{q}}a_{\boldsymbol{q}}, \tag{2.23b}$$

showing that e.g. annihilating an α magnon is a combination of removing a delocalized spin-flip from the A-sublattice and adding a delocalized spin-flip to the B-sublattice. Both these processes increase the z-direction spin quantum number, meaning that α magnons carry a spin polarized in the negative z-direction. Similarly, we see that β magnons carry a spin polarized in the positive z-direction.

Taking
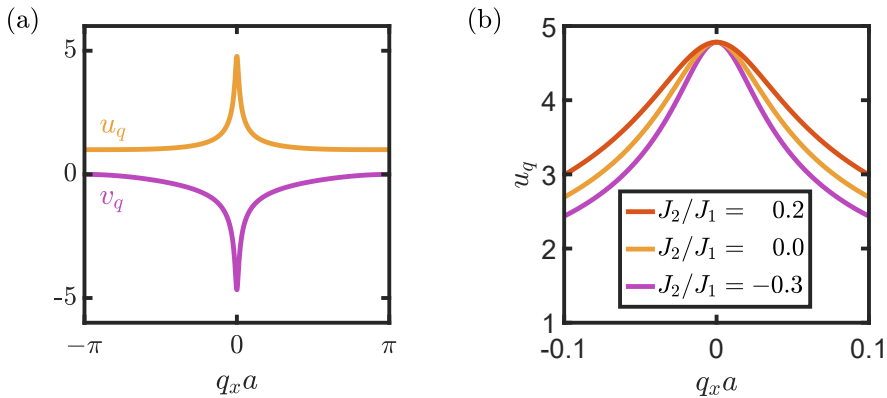
Figure 2.7: (a) Coherence factors $u_{\boldsymbol{q}}$ and $v_{\boldsymbol{q}}$ for antiferromagnetic magnons living in two dimensions with $q_y a = 0$, $S = 1$, and $K/J_1 = 10^{-3}$. In (b), we show how $u_{\boldsymbol{q}}$ varies with the next-nearest neighbor interaction J_2. For $J_2 > 0$, acting as a frustration, the curve becomes flatter.

$$u_{\boldsymbol{q}} = \frac{1}{\sqrt{2}}\sqrt{\frac{C_{\boldsymbol{q}}}{\omega_{\boldsymbol{q}}} + 1}, \qquad v_{\boldsymbol{q}} = \frac{-1}{\sqrt{2}}\sqrt{\frac{C_{\boldsymbol{q}}}{\omega_{\boldsymbol{q}}} - 1}, \tag{2.24}$$

the Hamiltonian is finally diagonalized and put on the form

$$H_{\mathrm{AFMI}} = \sum_{\boldsymbol{q}}(\omega_{\boldsymbol{q}\alpha}\alpha_{\boldsymbol{q}}^{\dagger}\alpha_{\boldsymbol{q}} + \omega_{\boldsymbol{q}\beta}\beta_{\boldsymbol{q}}^{\dagger}\beta_{\boldsymbol{q}}), \tag{2.25}$$

where $\omega_{\boldsymbol{q}\alpha} = \omega_{\boldsymbol{q}} + h$, $\omega_{\boldsymbol{q}\beta} = \omega_{\boldsymbol{q}} - h$, and

$$\omega_{\boldsymbol{q}} = \sqrt{C_{\boldsymbol{q}}^2 - D_{\boldsymbol{q}}^2}. \tag{2.26}$$

The excitation energies for the α and β magnons are presented as a function of momentum in Fig. 2.6 (a) and (b). When gapless, the dispersion relation is now linear, rather than quadratic, around the Brillouin zone center. When a gap in the spectrum is introduced through easy-axis anisotropy, the spectrum becomes quadratic in a region of size $qa \sim \sqrt{K/J_1}$ around the Brillouin zone center, before the linear behavior takes over.

Further, in Fig. 2.7 (a), we show how the Bogoliubov coefficients $u_{\boldsymbol{q}}$ and $v_{\boldsymbol{q}}$, also referred to as coherence factors, depend on momentum. As

seen from this figure, $|u_{\boldsymbol{q}}|$ and $|v_{\boldsymbol{q}}|$ are both peaked at zero momentum, with opposite sign for $u_{\boldsymbol{q}}$ and $v_{\boldsymbol{q}}$. At the peak, their magnitudes are similar and of the order $(\frac{J_1}{K})^{1/4}$, diverging as $K \to 0$. For larger q, they approach $u_{\boldsymbol{q}} = 1$ and $v_{\boldsymbol{q}} = 0$. Introducing $J_2 > 0$, we further see in Fig. 2.7 (b) that the coherence factors decay more slowly as we move away from zero momentum.

As the coherence factors approach $u_{\boldsymbol{q}} = 1$ and $v_{\boldsymbol{q}} = 0$ for large q, we then simply have that $\alpha_{\boldsymbol{q}} \approx a_{\boldsymbol{q}}$ and $\beta_{\boldsymbol{q}} \approx b_{\boldsymbol{q}}$. The eigenexcitations of the antiferromagnet are then simply delocalized spin-flip excitations associated with a single sublattice. However, for small q the coupling between the two sublattices makes its mark on the physics of the system, and the antiferromagnetic eigenexcitations are associated with spin fluctuations on both sublattices. The corresponding potential largeness of the magnitude of the magnon coherence factors for small q can be of interest for the following reason. When coupling the spins of an antiferromagnet to some external system, the spin operators may be expressed in terms of sublattice spin-flip magnons, which again should be expressed in terms of the antiferromagnetic α and β magnons. This introduces magnon coherence factors in the coupling to the external system, which may lead to a large coupling between the external system and the long-wavelength magnons of the antiferromagnet. As we will see when discussing the results of Paper [1], this effect relies on avoiding destructive interference between contributions from the two sublattices of the antiferromagnet. One way of avoiding such destructive interference is by coupling the external system to only one of the two sublattices of the antiferromagnet. This can be achieved through so-called uncompensated antiferromagnetic interfaces where only one of the two sublattices is exposed.

A simple picture for why it can be favorable to couple asymmetrically to the two sublattices of an antiferromagnet relies on expressing the vacuum state of antiferromagnetic eigenexcitations in terms of states produced by adding delocalized sublattice spin-flip excitations to the Néel state [35]. The antiferromagnetic vacuum state, as well as e.g. a state hosting a single antiferromagnetic magnon, can then be expressed as a superposition of states with increasing number of sublattice spin-flip excitations of the type that diagonalized the ferromagnetic Hamiltonian. Sketches of the general structure of these superpositions are displayed in Fig. 2.8. As outlined in Ref. [35], these antiferromagnetic states can be viewed as so-called squeezed states. Importantly, large magnon coherence factors are associated with the superpositions having significant contributions from states featuring a large
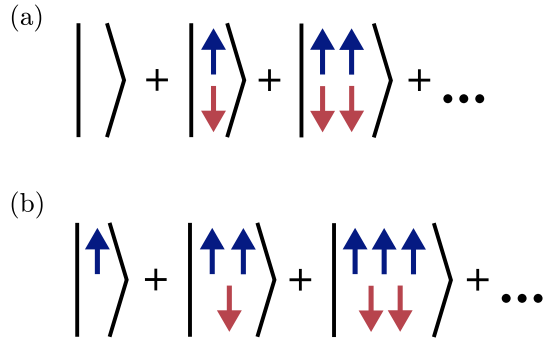
Figure 2.8: (a) Simple sketch of the general structure of the antiferromagnetic vacuum state expressed as a superposition of states arising from adding delocalized sublattice spin-flip excitations to the Néel state. Blue arrows here represent delocalized spin-flip excitations carrying spin polarized in the positive z-direction, corresponding to spin-flips on the B sublattice. In (b), we similarly sketch the structure of an antiferromagnetic eigenstate featuring a single β magnon. The figure is adapted from Refs. [1] and [35].

number of sublattice spin-flip magnons. A simple picture is then that a state with a single long-wavelength antiferromagnetic magnon may be associated with a large number of oppositely acting spin-flip excitations living on the two sublattices of the antiferromagnet, which can give rise to a strong interaction when coupling to only one of the two sublattices.

Finally, we also note that the magnetization on sublattice A can be expressed as

$$M_A = \frac{1}{N_A} \sum_{i \in A} \langle S^A_{i,z} \rangle = S - \frac{1}{N_A} \sum_{\boldsymbol{q}} \langle a^\dagger_{\boldsymbol{q}} a_{\boldsymbol{q}} \rangle. \tag{2.27}$$

We then need to insert the additional Bogoliubov transformation, leading to

$$M_A = S - \frac{1}{N_A} \sum_{\boldsymbol{q}} [u^2_{\boldsymbol{q}} \langle \alpha^\dagger_{\boldsymbol{q}} \alpha_{\boldsymbol{q}} \rangle + v^2_{\boldsymbol{q}} \langle \beta^\dagger_{\boldsymbol{q}} \beta_{\boldsymbol{q}} \rangle + v^2_{\boldsymbol{q}}]. \tag{2.28}$$

Unlike for the ferromagnet, we now have quantum fluctuations in the system. For a spin-space isotropic and two-dimensional antiferromagnet with

$J_2 = 0$, the zero-temperature correction to the sublattice magnetization is around 0.2 [36]. For the same system in one dimension, the zero-temperature corrections diverge. Going to nonzero temperature, one can further, similarly to the case of the ferromagnet, show that the correction terms diverge for spin-space isotropic antiferromagnets in dimensions less than 3.

2.2.2 Schwinger bosons

As we did for the ferromagnet, we will also treat the antiferromagnetic Hamiltonian in Eq. (2.17) within a Schwinger boson framework. We will here follow the approach in Paper [3], neglecting the effect of a magnetic field. In this paper, we considered the effect of coupling an external system, symmetrically or asymmetrically, to the two sublattices of the AFMI. We then found it useful to define different Schwinger bosons for the two sublattices of the AFMI [37], simplifying the treatment of the separate scattering terms arising from each sublattice. When describing an isolated antiferromagnetic system, one normally works with Schwinger bosons that are defined equally on all lattice sites, elegantly describing different magnetic phases within a unified framework [38–41].

In Paper [3], varying the definition of the two sublattices, we provided two separate treatments of a Néel phase and a so-called stripe phase. The latter phase arises from a dominant antiferromagnetic next-nearest neighbor interaction, forcing next-nearest neighboring spins to be anti-aligned. For $J_1 = 0$, the system can then be divided up into two decoupled Néel antiferromagnets where each Néel antiferromagnet lives on a set of lattice sites that are connected by next-nearest neighbor vectors. Introducing nearest neighbor interaction in the system, the two Néel antiferromagnets are coupled together, giving rise to a stripe pattern [39]. An example of such a pattern is shown in Fig. 2.9. In the following discussion we, however, restrict ourselves to a Schwinger boson treatment of the Néel phase.

For the two sublattices of the antiferromagnet, we introduce

$$S_{i+}^A = a_{i\uparrow}^\dagger a_{i\downarrow}, \qquad\qquad S_{i+}^B = -b_{i\downarrow}^\dagger b_{i\uparrow}, \qquad\qquad (2.29a)$$

$$S_{i-}^A = a_{i\downarrow}^\dagger a_{i\uparrow}, \qquad\qquad S_{i-}^B = -b_{i\uparrow}^\dagger b_{i\downarrow}, \qquad\qquad (2.29b)$$

$$S_{iz}^A = \frac{1}{2}(a_{i\uparrow}^\dagger a_{i\uparrow} - a_{i\downarrow}^\dagger a_{i\downarrow}), \qquad S_{iz}^B = -\frac{1}{2}(b_{i\uparrow}^\dagger b_{i\uparrow} - b_{i\downarrow}^\dagger b_{i\downarrow}). \qquad (2.29c)$$

On each site of the A-sublattice, we now have
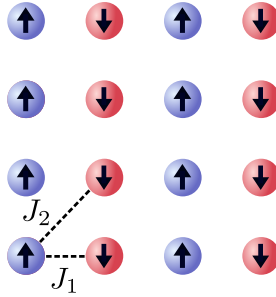
Figure 2.9: Example of a stripe phase where next-nearest neighbors are anti-aligned due to a dominant antiferromagnetic next-nearest neighbor interaction J_2. In this section, we focus on the Néel phase.

$$2S = \sum_\alpha a_{\boldsymbol{i}\alpha}^\dagger a_{\boldsymbol{i}\alpha}, \tag{2.30}$$

while we similarly, on each site of the B-sublattice, have

$$2S = \sum_\alpha b_{\boldsymbol{i}\alpha}^\dagger b_{\boldsymbol{i}\alpha}. \tag{2.31}$$

The Hamiltonian can be expressed in terms of a set of bond operators

$$A_{\boldsymbol{ij}}^{1,A} = \frac{1}{2}\big(a_{\boldsymbol{i}\uparrow}b_{\boldsymbol{j}\uparrow} + a_{\boldsymbol{i}\downarrow}b_{\boldsymbol{j}\downarrow}\big), \qquad A_{\boldsymbol{ij}}^{2,A} = \frac{1}{2}\big(a_{\boldsymbol{i}\uparrow}a_{\boldsymbol{j}\downarrow} - a_{\boldsymbol{i}\downarrow}a_{\boldsymbol{j}\uparrow}\big), \tag{2.32a}$$

$$B_{\boldsymbol{ij}}^{1,A} = \frac{1}{2}\big(a_{\boldsymbol{i}\downarrow}b_{\boldsymbol{j}\uparrow}^\dagger - a_{\boldsymbol{i}\uparrow}b_{\boldsymbol{j}\downarrow}^\dagger\big), \qquad B_{\boldsymbol{ij}}^{2,A} = \frac{1}{2}\big(a_{\boldsymbol{i}\uparrow}a_{\boldsymbol{j}\uparrow}^\dagger + a_{\boldsymbol{i}\downarrow}a_{\boldsymbol{j}\downarrow}^\dagger\big), \tag{2.32b}$$

$$A_{\boldsymbol{ij}}^{1,B} = \frac{1}{2}\big(-b_{\boldsymbol{i}\downarrow}a_{\boldsymbol{j}\downarrow} - b_{\boldsymbol{i}\uparrow}a_{\boldsymbol{j}\uparrow}\big), \qquad A_{\boldsymbol{ij}}^{2,B} = \frac{1}{2}\big(b_{\boldsymbol{i}\uparrow}b_{\boldsymbol{j}\downarrow} - b_{\boldsymbol{i}\downarrow}b_{\boldsymbol{j}\uparrow}\big), \tag{2.32c}$$

$$B_{\boldsymbol{ij}}^{1,B} = \frac{1}{2}\big(b_{\boldsymbol{i}\uparrow}a_{\boldsymbol{j}\downarrow}^\dagger - b_{\boldsymbol{i}\downarrow}a_{\boldsymbol{j}\uparrow}^\dagger\big), \qquad B_{\boldsymbol{ij}}^{2,B} = \frac{1}{2}\big(b_{\boldsymbol{i}\uparrow}b_{\boldsymbol{j}\uparrow}^\dagger + b_{\boldsymbol{i}\downarrow}b_{\boldsymbol{j}\downarrow}^\dagger\big). \tag{2.32d}$$

Here, the A operators describe antiferromagnetic bonds, while the B operators describe ferromagnetic bonds [39, 40]. The index 1, 2 refers to nearest

neighbor and next-nearest neighbor bonds, while the index A, B refers to whether the bond starts at the A or B sublattice. For instance, $A_{ij}^{1,A}$ represents an antiferromagnetic bond between nearest neighbors starting at the A sublattice. For the Néel phase, the relevant bonds will be assumed to be antiferromagnetic bonds between nearest neighbors and frustrating (for $J_2 > 0$) ferromagnetic bonds between next-nearest neighbors. Performing the usual mean-field decoupling, we take the Ansatz

$$
\begin{aligned}
\langle B_{ij}^{1,A} \rangle &= \langle B_{ij}^{1,B} \rangle = 0, \\
\langle A_{ij}^{1,A} \rangle &= -\langle A_{ij}^{1,B} \rangle = \mathcal{A}_{\boldsymbol{\delta}_1}, \\
\langle B_{ij}^{2,A} \rangle &= \langle B_{ij}^{2,B} \rangle = \mathcal{B}_{\boldsymbol{\delta}_2}, \\
\langle A_{ij}^{2,A} \rangle &= \langle A_{ij}^{2,B} \rangle = 0,
\end{aligned}
\tag{2.33}
$$

together with $\langle A_{ij}^\dagger \rangle = \langle A_{ij} \rangle$ and $\langle B_{ij}^\dagger \rangle = \langle B_{ij} \rangle$ in all cases. We have here assumed that, for a given sublattice, expectation values of bond operators only depend on $\boldsymbol{\delta}_l = \boldsymbol{j} - \boldsymbol{i}$, and not on the overall spatial position. From the identity $(B_{i,j}^{2,\eta})^\dagger = B_{j,i}^{2,\eta}$, we now have that $\mathcal{B}_{\boldsymbol{\delta}_2} = \mathcal{B}_{-\boldsymbol{\delta}_2}$. Similarly, for our choice of Ansatz, the identity $A_{ij}^{1,A} = -A_{ji}^{1,B}$ implies that $\mathcal{A}_{\boldsymbol{\delta}_1} = \mathcal{A}_{-\boldsymbol{\delta}_1}$. If we had instead chosen e.g. $\langle A_{ij}^{1,A} \rangle = \langle A_{ij}^{1,B} \rangle$, we would have had to work with $\mathcal{A}_{\boldsymbol{\delta}_1} = -\mathcal{A}_{-\boldsymbol{\delta}_1}$.

In order to deal with the easy-axis anisotropy term, we perform a similar mean-field decoupling where we introduce $\langle S_{iz}^A \rangle = M_A$ and $\langle S_{iz}^B \rangle = M_B$. Rewriting the remaining bond operators in terms of the Schwinger boson operators and further introducing Fourier transformed Schwinger boson operators, we can then express the Hamiltonian as $H_{\mathrm{AFMI}} = E_0 + H^\uparrow + H^\downarrow$ where

$$
\begin{aligned}
E_0 = {}& 2N_A \Big[J_1 \sum_{\boldsymbol{\delta}_1} \left(\mathcal{A}_{\boldsymbol{\delta}_1} \right)^2 - J_2 \sum_{\boldsymbol{\delta}_2} \left(\mathcal{B}_{\boldsymbol{\delta}_2} \right)^2 \Big] \\
& - 2N_A \lambda(\kappa + 1) + K N_A (M_A^2 + M_B^2),
\end{aligned}
\tag{2.34}
$$

and

$$
\begin{aligned}
H^\sigma = {}& \sum_{\boldsymbol{q}} \left(\lambda + \gamma_{\boldsymbol{q}}^{B_2} - \sigma K M_A \right) a_{\boldsymbol{q}\sigma}^\dagger a_{\boldsymbol{q}\sigma} + \sum_{\boldsymbol{q}} \left(\lambda + \gamma_{\boldsymbol{q}}^{B_2} + \sigma K M_B \right) b_{\boldsymbol{q}\sigma} b_{\boldsymbol{q}\sigma}^\dagger \\
& - \sum_{\boldsymbol{q}} \gamma_{\boldsymbol{q}}^{A_1} \left(b_{\boldsymbol{q}\sigma}^\dagger a_{-\boldsymbol{q}\sigma}^\dagger + a_{\boldsymbol{q}\sigma} b_{-\boldsymbol{q}\sigma} \right).
\end{aligned}
\tag{2.35}
$$

We have here, again, introduced a Lagrange multiplier $\lambda = \lambda_A = \lambda_B$ to enforce a constraint on the average number of Schwinger boson number per lattice site. As is often done in the literature [41, 42], we have set the average number of Schwinger bosons per site equal to a parameter κ. Like we did for the ferromagnet, we will simply take $\kappa = 2S$, which fixes the magnitude of the spins to the correct value. This choice does, however, not produce the correct value for $\langle \boldsymbol{S}_{\boldsymbol{i}}^2 \rangle$ [43], which may motivate other choices of κ [41, 42] as well as remind us that one should careful about putting too much emphasis on the quantitative results obtained from Schwinger boson mean-field theory. We have further taken $\lambda' = \lambda - \frac{1}{4}\left(J_1 z_1 + J_2 z_2\right)$ and renamed $\lambda' \to \lambda$, as well as neglected constant terms that do not contain any of the mean-field parameters. We have also defined

$$\gamma_{\boldsymbol{q}}^{A_1} = J_1 \sum_{\boldsymbol{\delta_1}} \mathcal{A}_{\boldsymbol{\delta_1}} \cos(\boldsymbol{q} \cdot \boldsymbol{\delta_1}), \tag{2.36a}$$

$$\gamma_{\boldsymbol{q}}^{B_2} = J_2 \sum_{\boldsymbol{\delta_2}} \mathcal{B}_{\boldsymbol{\delta_2}} \cos(\boldsymbol{q} \cdot \boldsymbol{\delta_2}). \tag{2.36b}$$

In order to diagonalize the Hamiltonian, we need to perform a Bogoliubov transformation. Following the notation in [41], which we did in Paper [3], we here introduce

$$\begin{aligned}
a_{\boldsymbol{q}\sigma} &= u_{\boldsymbol{q}\sigma}\alpha_{\boldsymbol{q}\sigma} - v_{\boldsymbol{q}\sigma}\beta_{-\boldsymbol{q}\sigma}^\dagger, \\
b_{-\boldsymbol{q}\sigma}^\dagger &= v_{\boldsymbol{q}\sigma}\alpha_{\boldsymbol{q}\sigma} - u_{\boldsymbol{q}\sigma}\beta_{-\boldsymbol{q}\sigma}^\dagger.
\end{aligned} \tag{2.37}$$

It should be noted that the sign of $v_{\boldsymbol{q}\sigma}$ is here reversed to our linear spin wave treatment of the problem. Simplifying the expressions by assuming $M_B = -M_A$ and choosing to work with $A_{\boldsymbol{\delta_1}}$ positive, we can take

$$u_{\boldsymbol{q}\sigma} = \frac{1}{\sqrt{2}}\sqrt{\frac{\lambda + \gamma_{\boldsymbol{q}}^{B_2} - \sigma K M_A}{\omega_{\boldsymbol{q}\sigma}} + 1}, \tag{2.38a}$$

$$v_{\boldsymbol{q}\sigma} = \frac{1}{\sqrt{2}}\sqrt{\frac{\lambda + \gamma_{\boldsymbol{q}}^{B_2} - \sigma K M_A}{\omega_{\boldsymbol{q}\sigma}} - 1}, \tag{2.38b}$$

leading to

$$H_{\text{AFMI}} = E_0' + \sum_{\boldsymbol{q}\sigma} \omega_{\boldsymbol{q}\sigma}\left(\alpha_{\boldsymbol{q}\sigma}^\dagger\alpha_{\boldsymbol{q}\sigma} + \beta_{\boldsymbol{q}\sigma}^\dagger\beta_{\boldsymbol{q}\sigma}\right), \tag{2.39}$$

where

$$\omega_{\boldsymbol{q}\sigma} = \sqrt{\left(\lambda + \gamma_{\boldsymbol{q}}^{B_2} - \sigma K M_A\right)^2 - \left(\gamma_{\boldsymbol{q}}^{A_1}\right)^2}, \tag{2.40}$$

and $E_0' = E_0 + \sum_{\boldsymbol{k}\sigma} \omega_{\boldsymbol{k}\sigma}$.

As mentioned in the previous discussion of Schwinger boson treatment of a ferromagnet, we now need to determine the parameters λ, $\mathcal{A}_{\boldsymbol{\delta}_1}$, $\mathcal{B}_{\boldsymbol{\delta}_2}$, and M_A by minimizing the free energy. The free energy per lattice site can be expressed as

$$f = \frac{E_0'}{N} + \frac{2}{\beta N} \sum_{\boldsymbol{q}\sigma} \ln\left(1 - e^{-\beta\omega_{\boldsymbol{q}\sigma}}\right), \tag{2.41}$$

where $\beta = 1/(k_B T)$, k_B is the Boltzmann constant, and T is the system temperature. Minimizing this free energy with respect to the above mentioned parameters produces the set of equations

$$\mathcal{A}_{\boldsymbol{\delta}_1} = \frac{1}{2N} \sum_{\boldsymbol{q}\sigma} \frac{\gamma_{\boldsymbol{q}}^{A_1}}{\omega_{\boldsymbol{q}\sigma}} \left[1 + 2b(\omega_{\boldsymbol{q}\sigma})\right] \cos(\boldsymbol{q} \cdot \boldsymbol{\delta}_1), \tag{2.42a}$$

$$\mathcal{B}_{\boldsymbol{\delta}_2} = \frac{1}{2N} \sum_{\boldsymbol{q}\sigma} \frac{\left(\lambda + \gamma_{\boldsymbol{q}}^{B_2} - \sigma K M_A\right)}{\omega_{\boldsymbol{q}\sigma}} \left[1 + 2b(\omega_{\boldsymbol{q}\sigma})\right] \cos(\boldsymbol{q} \cdot \boldsymbol{\delta}_2), \tag{2.42b}$$

$$\bar{\kappa} = \frac{1}{2N} \sum_{\boldsymbol{q}\sigma} \frac{\left(\lambda + \gamma_{\boldsymbol{q}}^{B_2} - \sigma K M_A\right)}{\omega_{\boldsymbol{q}\sigma}} \left[1 + 2b(\omega_{\boldsymbol{q}\sigma})\right], \tag{2.42c}$$

$$M_A = \frac{1}{2N} \sum_{\boldsymbol{q}\sigma} \frac{\sigma\left(\lambda + \gamma_{\boldsymbol{q}}^{B_2} - \sigma K M_A\right)}{\omega_{\boldsymbol{q}\sigma}} \left[1 + 2b(\omega_{\boldsymbol{q}\sigma})\right], \tag{2.42d}$$

where we have defined $\bar{\kappa} = \frac{1}{2}(\kappa + 1)$. Expecting no directional dependence, we introduce $\mathcal{A} = \mathcal{A}_{\boldsymbol{\delta}_1}$ and $\mathcal{B} = \mathcal{B}_{\boldsymbol{\delta}_2}$, before we go to zero temperature where contributions from the Bose-distributions are limited to contributions from condensation of Schwinger bosons. As we have defined the Schwinger bosons differently on the two sublattices, magnetic ordering is again signalled by Bose-Einstein condensation of magnons with zero momentum, corresponding to a uniform magnetization on each sublattice. Assuming the magnetization to be positive on the A-sublattice, we then need $\lambda + \gamma_0^{B_2} - K m_A = \gamma_0^{A_1}$ in order for condensation of $\uparrow$-bosons to take place. In order to deal with the contributions from the condensate, we take the term corresponding to $\boldsymbol{q} = 0$ and $\sigma = \uparrow$ out of the sums. As this special term takes the same form
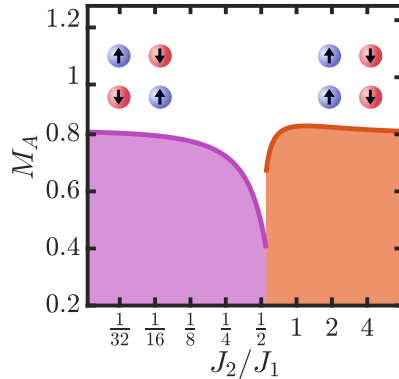
Figure 2.10: Sublattice magnetization M_A as a function of the ratio of next-nearest neighbor to nearest neighbor antiferromagnetic interaction J_2/J_1 for the Néel and stripe phase. We have gone to zero temperature, taken an easy-axis anisotropy $K/J_1 = 10^{-3}$ and set the spin quantum number to $S = 1$. We obtain a first-order phase transition between the two phases slightly above $J_2/J_1 = 0.5$.

for all of the four above equations, we can use Eq. (2.42c) to eliminate the term from the coupled set of equations. That this term is missing from the sums will be denoted by a prime. Defining $\zeta_{\boldsymbol{k}\sigma} = \gamma_0^{A_1} - \gamma_0^{B_2} + \gamma_{\boldsymbol{k}}^{B_2} + 2K m_A \delta_{\sigma,\downarrow}$, we are left with a coupled set of self-consistent equations on the form

$$M_A - \bar{\kappa} + \frac{1}{N} \sideset{}{'}\sum_{\boldsymbol{q}} \frac{\zeta_{\boldsymbol{q}\downarrow}}{\omega_{\boldsymbol{q}\downarrow}} = 0, \tag{2.43a}$$

$$\mathcal{A} - \bar{\kappa} - \frac{1}{2N} \sideset{}{'}\sum_{\boldsymbol{q}\sigma} \frac{\gamma_{\boldsymbol{q}}^{A_1} \cos(k_x) - \zeta_{\boldsymbol{q}\sigma}}{\omega_{\boldsymbol{q}\sigma}} = 0, \tag{2.43b}$$

$$\mathcal{B} - \bar{\kappa} - \frac{1}{2N} \sideset{}{'}\sum_{\boldsymbol{q}\sigma} \frac{\zeta_{\boldsymbol{q}\sigma}}{\omega_{\boldsymbol{q}\sigma}} \Big[\cos(k_x + k_y) - 1 \Big] = 0. \tag{2.43c}$$

This set of equations can be solved numerically for a given set of system parameters.

A similar treatment of the stripe phase is performed in Paper [3]. Calculating the sublattice magnetization M_A as a function of J_2/J_1 for both the Néel and stripe phase, as well as comparing the free energies of the two phases, we obtain the diagram presented in Fig. 2.10. For $S = 1$ and

$J_2/J_1 = 0$, the sublattice magnetization of the Néel phase is around $S - 0.2$. Then, as we increase J_2/J_1, the sublattice magnetization decreases. However, before the sublattice magnetization vanishes, the systems performs a transition to a stripe phase. For $K \to 0$, we find the transition point to be around the expected value of $J_2/J_1 = 0.549$ [44]. For $S = 1/2$, our treatment of the system would indicate a direct transition between the two phases around $J_2/J_1 = 0.595$. More refined approaches do, however, indicate that the system in this cases loses magnetic order in an intermediate region between the two ordered phases [45].

3

Superconductivity

As mentioned in the introduction chapter, superconducting materials feature a vanishing electrical resistance below some critical temperature. This property was first discovered in 1911 in mercury cooled down to liquid Helium temperatures [46]. Superconductors do, however, also have another defining property which was not discovered until 1933 [47]. If placed in a magnetic field and cooled down, magnetic flux is expelled from the interior of a superconducting material at the transition temperature. This is referred to as the Meissner effect. In Fig. 3.1, we show a sketch of how the electrical resistance of a superconductor can depend on temperature, and how magnetic field lines bend around a superconducting material.
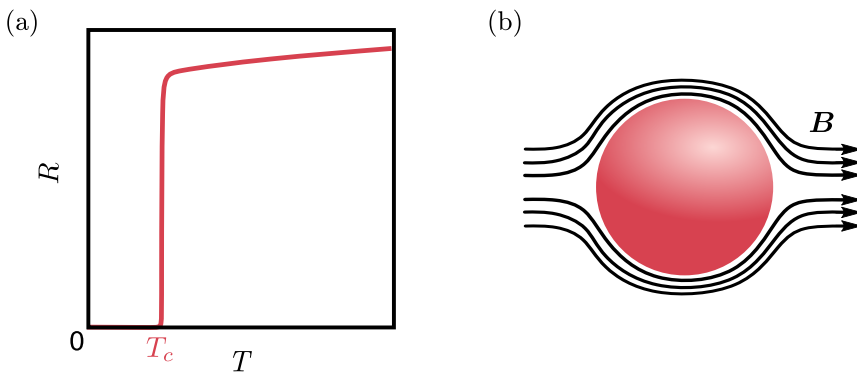
Figure 3.1: (a) Sketch of the electrical resistance of a superconductor as a function of temperature. The resistance vanishes at a critical temperature T_c. (b) At the critical temperature, magnetic flux is expelled from a superconductor subjected to a magnetic field. Magnetic field lines are then no longer able to penetrate the superconductor.
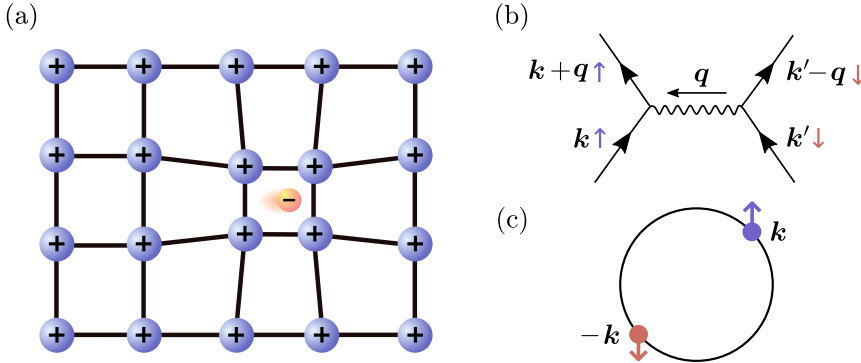
Figure 3.2: (a) A negatively charged electron travelling through the system will pull positively charged ions towards itself. (b) Another electron can be attracted to the area with increased density of positive charge left behind by the first electron, giving rise to an effective attractive interaction between electrons. (c) This can give rise to formation of Cooper pairs consisting of electrons from opposite sides of the Fermi surface.

In 1957, a microscopic theory of superconductivity was presented [48], known as the BCS theory. In this theory, superconductivity arises from attractive interaction between electrons mediated by phonons. This leads to formation of a state where electrons pair up in so-called Cooper pairs, each consisting of two electrons with opposite spins and momenta. These Cooper pairs are responsible for carrying supercurrents that flow without resistance. The BCS theory arose from existing ideas concerning e.g. the existence of attractive interaction between electrons mediated by phonons [49], and the formation of Cooper pairs in response to an attractive interaction [50]. A key for making the connection between ion fluctuations and superconductivity was the observation that the critical temperature of elemental superconductors varied with the isotope, decreasing with increased ion mass [51, 52]. This is referred to as the isotope effect.

A simple picture for how spatial fluctuations of ions can give rise to superconductivity is illustrated in Fig. 3.2 (a). A negatively charged electron moving through the system will attract positively charged ions. As the electron motion is much faster than the ion motion, the electron will leave behind an area with increased positive charge density that remains long after the electron is gone. Another electron may then be attracted to

this area, representing an attractive interaction between electrons [53]. This effective interaction mediated by a phonon, can be depicted by a diagram of the type in Fig. 3.2 (b). Here, two incoming electrons, assumed to have opposite spins, are scattered by exchange of a phonon carrying a momentum q from one side of the diagram to the other. Electrons on opposite sides of the Fermi surface, as displayed in Fig. 3.2 (c), can through this interaction form Cooper pairs.

Although BCS theory captures how superconductivity can arise from electron-phonon interaction, it eventually became clear that the theory is not able to quantitatively describe the properties of all phonon-driven superconductors [54]. This especially applies to the case of superconductors featuring strong electron-phonon coupling. It was therefore necessary with a new theory better capturing the details of the electron-phonon interaction. Such a theory, utilizing the many-body Green's functions framework, was eventually developed, typically referred to as Eliashberg theory [55] or Migdal-Eliashberg theory [56]. This theory has, however, not been able to successfully describe all superconductors that have been discovered. The superconductivity in many unconventional superconductors, with at least partly non-phononic origin, has proven to be challenging to understand [57, 58].

The above theories introduce an order parameter representing pairing of electrons, suitable for describing the superconducting transition in three-dimensional systems. In two dimensions, such as in superconducting thin-films, the phase transition is, however, in reality a topological phase transition, often referred to as a Berezinskii-Kosterlitz-Thouless (BKT) transition [59–61]. The order parameter is then instead a non-local stiffness. The existence of such a transition relies on a sufficiently thin superconducting film [57, 62], in which case one can have ordering across a thin-film of finite in-plane size. The BKT transition temperature can further be expressed as a system-dependent fraction of the mean-field critical temperature [62]. A finite critical temperature obtained within e.g. BCS theory can therefore serve as an indication of a superconducting instability also for superconducting thin-films.

We start the chapter by discussing the BCS theory of superconductivity, performing a generalized treatment, before we focus on the case of phonon-mediated superconductivity. We also comment on the effect of Coulomb interaction on superconductivity. We then move on to discussing superconductors in magnetic fields, focusing on the critical magnetic field where su-

perconductivity breaks down. Next, we turn to Eliashberg theory where we, similarly to what we did for BCS theory, start with a generalized treatment before specializing to phonon-mediated superconductivity and commenting on the effect of Coulomb interaction. We also provide a brief discussion of what is known as Migdal's theorem. We end the chapter by commenting on superconductivity mediated by spin fluctuations and its connection to e.g. high-T_c superconductivity.

3.1 BCS theory

As stated above, the BCS theory introduced how attractive interaction between electrons, mediated by phonons, can give rise to superconductivity. Rather than starting from a coupled system of electron and phonons, we will instead start out from a more general Hamiltonian featuring electrons that can interact attractively with each other. After outlining what is often referred to as generalized BCS theory [63], we will then return to the coupled electron-phonon system and discuss phonon-mediated superconductivity. The generalized formalism will be useful when we discuss magnon-mediated superconductivity in the next chapter.

Outlining the generalized formalism, we will more or less follow the derivation in Ref. [63], which is also similarly presented in Ref. [64]. We start out from a Hamiltonian

$$H = \sum_{\boldsymbol{k}\sigma} \epsilon_{\boldsymbol{k}\sigma} c_{\boldsymbol{k}\sigma}^{\dagger} c_{\boldsymbol{k}\sigma} + \frac{1}{2} \sum_{\boldsymbol{k}\boldsymbol{k}'} \sum_{\sigma_1\sigma_2\sigma_3\sigma_4} V_{\boldsymbol{k}\boldsymbol{k}'}^{\sigma_1\sigma_2\sigma_3\sigma_4} c_{\boldsymbol{k}\sigma_1}^{\dagger} c_{-\boldsymbol{k}\sigma_2}^{\dagger} c_{-\boldsymbol{k}'\sigma_3} c_{\boldsymbol{k}'\sigma_4}. \tag{3.1}$$

where we have itinerant electrons with energy spectrum $\epsilon_{\boldsymbol{k}\sigma}$ and scattering of electrons with opposite momenta into new states with opposite momenta. The spin is here denoted by σ, and we allow for all possible spin combinations in the interaction. From fermionic anti-commutation relations, it follows that

$$V_{\boldsymbol{k}\boldsymbol{k}'}^{\sigma_1\sigma_2\sigma_3\sigma_4} = -V_{-\boldsymbol{k}\boldsymbol{k}'}^{\sigma_2\sigma_1\sigma_3\sigma_4} = -V_{\boldsymbol{k},-\boldsymbol{k}'}^{\sigma_1\sigma_2\sigma_4\sigma_3} = V_{-\boldsymbol{k},-\boldsymbol{k}'}^{\sigma_2\sigma_1\sigma_4\sigma_3}. \tag{3.2}$$

Further, assuming that the Hamiltonian is hermitian and that the potential is real, we further have that $V_{\boldsymbol{k}'\boldsymbol{k}}^{\sigma_4\sigma_3\sigma_2\sigma_1} = V_{\boldsymbol{k}\boldsymbol{k}'}^{\sigma_1\sigma_2\sigma_3\sigma_4}$.

We then perform a mean-field treatment of the Hamiltonian where we, inspired by the idea of formation of Cooper pairs consisting of electrons

with opposite momenta, introduce $b_{\boldsymbol{k},\sigma'\sigma} = \langle c_{-\boldsymbol{k}\sigma} c_{\boldsymbol{k}\sigma'} \rangle$. Similarly to what we did in the previous chapter, we then write

$$c_{-\boldsymbol{k}'\sigma_3} c_{\boldsymbol{k}'\sigma_4} = b_{\boldsymbol{k}',\sigma_4\sigma_3} + \left(c_{-\boldsymbol{k}'\sigma_3} c_{\boldsymbol{k}'\sigma_4} - b_{\boldsymbol{k}',\sigma_4\sigma_3} \right) = b_{\boldsymbol{k}',\sigma_4\sigma_3} + \delta b_{\boldsymbol{k}',\sigma_4\sigma_3}, \quad (3.3)$$

and

$$c_{\boldsymbol{k}\sigma_1}^\dagger c_{-\boldsymbol{k}\sigma_2}^\dagger = b_{\boldsymbol{k},\sigma_1\sigma_2}^\dagger + \left(c_{\boldsymbol{k}\sigma_1}^\dagger c_{-\boldsymbol{k}\sigma_2}^\dagger - b_{\boldsymbol{k},\sigma_1\sigma_2}^\dagger \right) = b_{\boldsymbol{k},\sigma_1\sigma_2}^\dagger + \delta b_{\boldsymbol{k},\sigma_1\sigma_2}^\dagger. \quad (3.4)$$

Neglecting quadratic terms in the deviations away from the mean-field values, we can then write

$$\begin{aligned}
H = \sum_{\boldsymbol{k}\sigma} \epsilon_{\boldsymbol{k}\sigma} c_{\boldsymbol{k}\sigma}^\dagger c_{\boldsymbol{k}\sigma} + \frac{1}{2} \sum_{\boldsymbol{k}\boldsymbol{k}'} \sum_{\sigma_1\sigma_2\sigma_3\sigma_4} V_{\boldsymbol{k}\boldsymbol{k}'}^{\sigma_1\sigma_2\sigma_3\sigma_4} \\
\times \left[b_{\boldsymbol{k},\sigma_1\sigma_2}^\dagger c_{-\boldsymbol{k}'\sigma_3} c_{\boldsymbol{k}'\sigma_4} + c_{\boldsymbol{k}\sigma_1}^\dagger c_{-\boldsymbol{k}\sigma_2}^\dagger b_{\boldsymbol{k}',\sigma_4\sigma_3} - b_{\boldsymbol{k},\sigma_1\sigma_2}^\dagger b_{\boldsymbol{k}',\sigma_4\sigma_3} \right].
\end{aligned} \quad (3.5)$$

We next introduce a gap function

$$\Delta_{\boldsymbol{k},\sigma_1\sigma_2} = - \sum_{\boldsymbol{k}',\sigma_3\sigma_4} V_{\boldsymbol{k}\boldsymbol{k}'}^{\sigma_1\sigma_2\sigma_3\sigma_4} b_{\boldsymbol{k}',\sigma_4\sigma_3}. \quad (3.6)$$

As seen from this equation, the gap function inherits its symmetries from the interaction potential. As the interaction potential needs to be odd under the combined operation of $\boldsymbol{k} \to -\boldsymbol{k}$ and $\sigma_1 \leftrightarrow \sigma_2$, the gap function will also be odd under this combined operation. A gap function (or the part of a gap function) which is even in momentum will therefore have to be odd in spin (spin-singlet), and a gap equation which is odd in momentum will have to be even in spin (spin-triplet). This reflects the fact that the particles that pair up to give a nonzero gap function are fermions.

Writing explicitly out the matrix structure of the gap function, we have

$$\hat{\Delta}_{\boldsymbol{k}} = \begin{pmatrix} \Delta_{\boldsymbol{k},\uparrow\uparrow} & \Delta_{\boldsymbol{k},\uparrow\downarrow} \\ \Delta_{\boldsymbol{k},\downarrow\uparrow} & \Delta_{\boldsymbol{k},\downarrow\downarrow} \end{pmatrix}, \quad (3.7)$$

where we have put a hat on $\hat{\Delta}_{\boldsymbol{k}}$ in order to highlight that it is a matrix. Assuming that the gap function is even in momentum, we can then write

$$\hat{\Delta}_{\boldsymbol{k}}^{s} = \begin{pmatrix} 0 & \Delta_{\boldsymbol{k},\uparrow\downarrow} \\ -\Delta_{\boldsymbol{k},\uparrow\downarrow} & 0 \end{pmatrix}. \tag{3.8}$$

We then see that $\hat{\Delta}_{\boldsymbol{k}}^{s}(\hat{\Delta}_{\boldsymbol{k}}^{s})^{\dagger} = |\Delta_{\boldsymbol{k},\uparrow\downarrow}|^{2}I$ is proportional to the identity matrix I. Spin-singlet pairing is therefore an example of so-called unitary pairing. If we instead consider consider that the gap function is odd in momentum, the matrix can be expressed as [63]

$$\hat{\Delta}_{\boldsymbol{k}}^{t} = \begin{pmatrix} \Delta_{\boldsymbol{k},\uparrow\uparrow} & \Delta_{\boldsymbol{k},\uparrow\downarrow} \\ \Delta_{\boldsymbol{k},\uparrow\downarrow} & \Delta_{\boldsymbol{k},\downarrow\downarrow} \end{pmatrix} = \begin{pmatrix} -d_{\boldsymbol{k},x} + id_{\boldsymbol{k},y} & d_{\boldsymbol{k},z} \\ d_{\boldsymbol{k},z} & d_{\boldsymbol{k},x} + id_{\boldsymbol{k},y} \end{pmatrix} = i(\boldsymbol{d}_{\boldsymbol{k}} \cdot \boldsymbol{\sigma})\sigma_{y}, \tag{3.9}$$

where $\boldsymbol{\sigma}$ is the vector of Pauli matrices and $\boldsymbol{d}$ is referred to as the d-vector. Using the identity $(\boldsymbol{a} \cdot \boldsymbol{\sigma})(\boldsymbol{b} \cdot \boldsymbol{\sigma}) = (\boldsymbol{a} \cdot \boldsymbol{b})I + i(\boldsymbol{a} \times \boldsymbol{b}) \cdot \boldsymbol{\sigma}$, where $\boldsymbol{a}$ and $\boldsymbol{b}$ are vectors, we can compute $\hat{\Delta}_{\boldsymbol{k}}^{t}(\hat{\Delta}_{\boldsymbol{k}}^{t})^{\dagger} = |\boldsymbol{d}_{\boldsymbol{k}}|^{2}I + i(\boldsymbol{d}_{\boldsymbol{k}} \times \boldsymbol{d}_{\boldsymbol{k}}^{*}) \cdot \boldsymbol{\sigma}$. We then see that spin-triplet pairing is not necessarily unitary. Non-unitary pairing is associated with some spin-polarization of the pairing and requires broken time-reversal symmetry [63]. In this thesis, we will mostly focus on different types of unitary pairing.

We may further write

$$\Delta_{\boldsymbol{k}',\sigma_{4}\sigma_{3}}^{*} = -\sum_{\boldsymbol{k},\sigma_{1}\sigma_{2}} V_{\boldsymbol{k}\boldsymbol{k}'}^{\sigma_{1}\sigma_{2}\sigma_{3}\sigma_{4}} b_{\boldsymbol{k},\sigma_{1}\sigma_{2}}^{\dagger}, \tag{3.10}$$

which allows us to express the Hamiltonian as

$$\begin{aligned} H = &\sum_{\boldsymbol{k}\sigma} \epsilon_{\boldsymbol{k}\sigma} c_{\boldsymbol{k}\sigma}^{\dagger} c_{\boldsymbol{k}\sigma} \\ &- \frac{1}{2} \sum_{\boldsymbol{k}} \sum_{\sigma_{1}\sigma_{2}} \left[\Delta_{\boldsymbol{k},\sigma_{2}\sigma_{1}}^{*} c_{-\boldsymbol{k}\sigma_{1}} c_{\boldsymbol{k}\sigma_{2}} + \Delta_{\boldsymbol{k},\sigma_{1}\sigma_{2}} c_{\boldsymbol{k}\sigma_{1}}^{\dagger} c_{-\boldsymbol{k}\sigma_{2}}^{\dagger} - b_{\boldsymbol{k},\sigma_{1}\sigma_{2}}^{\dagger} \Delta_{\boldsymbol{k},\sigma_{1}\sigma_{2}} \right]. \end{aligned} \tag{3.11}$$

Putting this on a more compact form, we obtain

$$H = \tilde{H}_{0} + \frac{1}{2} \sum_{\boldsymbol{k}} \phi_{\boldsymbol{k}}^{\dagger} M_{\boldsymbol{k}} \phi_{\boldsymbol{k}}, \tag{3.12}$$

where $\tilde{H}_{0} = \frac{1}{2} \sum_{\boldsymbol{k}} \sum_{\sigma_{1}\sigma_{2}} b_{\boldsymbol{k},\sigma_{1}\sigma_{2}}^{\dagger} \Delta_{\boldsymbol{k},\sigma_{1}\sigma_{2}} + \frac{1}{2} \sum_{\boldsymbol{k}\sigma} \epsilon_{\boldsymbol{k}\sigma}$,

$$\phi_{\bm{k}}^{\dagger} = \begin{pmatrix} c_{\bm{k}\uparrow}^{\dagger} & c_{\bm{k}\downarrow}^{\dagger} & c_{-\bm{k}\uparrow} & c_{-\bm{k}\downarrow} \end{pmatrix}, \tag{3.13}$$

and

$$M_{\bm{k}} = \begin{pmatrix} \epsilon_{\bm{k}\uparrow} & 0 & -\Delta_{\bm{k},\uparrow\uparrow} & -\Delta_{\bm{k},\uparrow\downarrow} \\ 0 & \epsilon_{\bm{k}\downarrow} & -\Delta_{\bm{k},\downarrow\uparrow} & -\Delta_{\bm{k},\downarrow\downarrow} \\ -\Delta_{\bm{k},\uparrow\uparrow}^{*} & -\Delta_{\bm{k},\downarrow\uparrow}^{*} & -\epsilon_{\bm{k}\uparrow} & 0 \\ -\Delta_{\bm{k},\uparrow\downarrow}^{*} & -\Delta_{\bm{k},\downarrow\downarrow}^{*} & 0 & -\epsilon_{\bm{k}\downarrow} \end{pmatrix}. \tag{3.14}$$

We then need to diagonalize this Hamiltonian. For simplicity, we take $\epsilon_{\bm{k}\uparrow} = \epsilon_{\bm{k}\downarrow} = \epsilon_{\bm{k}}$ and assume that the pairing is unitary. We then introduce a unitary matrix $U_{\bm{k}}$ to write

$$
\begin{aligned}
H &= \tilde{H}_0 + \frac{1}{2} \sum_{\bm{k}} (\phi_{\bm{k}}^{\dagger} U_{\bm{k}})(U_{\bm{k}}^{\dagger} M_{\bm{k}} U_{\bm{k}})(U_{\bm{k}}^{\dagger} \phi_{\bm{k}}) \\
&= \tilde{H}_0 + \frac{1}{2} \sum_{\bm{k}} \Psi_{\bm{k}}^{\dagger} W_{\bm{k}} \Psi_{\bm{k}},
\end{aligned}
\tag{3.15}
$$

where the new quasiparticle operators contained in

$$\Psi_{\bm{k}}^{\dagger} = \begin{pmatrix} \gamma_{\bm{k}\uparrow}^{\dagger} & \gamma_{\bm{k}\downarrow}^{\dagger} & \gamma_{-\bm{k}\uparrow} & \gamma_{-\bm{k}\downarrow} \end{pmatrix}, \tag{3.16}$$

are related to the original electron operators through $\Psi_{\bm{k}} = U_{\bm{k}}^{\dagger} \phi_{\bm{k}}$. As now

$$M_{\bm{k}} = \begin{pmatrix} \epsilon_{\bm{k}} I & -\hat{\Delta}_{\bm{k}} \\ -\hat{\Delta}_{\bm{k}}^{\dagger} & -\epsilon_{\bm{k}} I \end{pmatrix}. \tag{3.17}$$

taking

$$U_{\bm{k}} = \begin{pmatrix} \upsilon_{\bm{k}} & \nu_{\bm{k}} \\ -\nu_{\bm{k}}^{\dagger} & \upsilon_{\bm{k}} \end{pmatrix}, \tag{3.18}$$

with

$$v_{\boldsymbol{k}} = \frac{E_{\boldsymbol{k}} + \epsilon_{\boldsymbol{k}}}{\sqrt{(E_{\boldsymbol{k}} + \epsilon_{\boldsymbol{k}})^2 + \frac{1}{2}\mathrm{Tr}[\hat{\Delta}_{\boldsymbol{k}}(\hat{\Delta}_{\boldsymbol{k}})^{\dagger}]}} I, \tag{3.19}$$

$$\nu_{\boldsymbol{k}} = \frac{\hat{\Delta}_{\boldsymbol{k}}}{\sqrt{(E_{\boldsymbol{k}} + \epsilon_{\boldsymbol{k}})^2 + \frac{1}{2}\mathrm{Tr}[\hat{\Delta}_{\boldsymbol{k}}(\hat{\Delta}_{\boldsymbol{k}})^{\dagger}]}}, \tag{3.20}$$

and $E_{\boldsymbol{k}} = \sqrt{\epsilon_{\boldsymbol{k}}^2 + \frac{1}{2}\mathrm{Tr}[\hat{\Delta}_{\boldsymbol{k}}(\hat{\Delta}_{\boldsymbol{k}})^{\dagger}]}$, diagonalizes our matrix

$$W_{\boldsymbol{k}} = U_{\boldsymbol{k}}^{\dagger} M_{\boldsymbol{k}} U_{\boldsymbol{k}} = \begin{pmatrix} E_{\boldsymbol{k}} & 0 & 0 & 0 \\ 0 & E_{\boldsymbol{k}} & 0 & 0 \\ 0 & 0 & -E_{\boldsymbol{k}} & 0 \\ 0 & 0 & 0 & -E_{\boldsymbol{k}} \end{pmatrix}. \tag{3.21}$$

One can then check that the new quasiparticle operators satisfy the correct anti-commutation relations. Writing out the diagonalized Hamiltonian, we obtain

$$H = H_0' + \sum_{\boldsymbol{k}\sigma} E_{\boldsymbol{k}} \gamma_{\boldsymbol{k}\sigma}^{\dagger} \gamma_{\boldsymbol{k}\sigma}, \tag{3.22}$$

where $H_0' = \tilde{H}_0 - \sum_{\boldsymbol{k}} E_{\boldsymbol{k}}$. With our definitions, we are now working with only positive quasiparticle energies. Importantly, the new operators are superpositions of creation and annihilation operators. The new quasiparticles are therefore combinations of electrons and holes. Further, for $\boldsymbol{k}$ on the Fermi surface, we have that $\epsilon_{\boldsymbol{k}} = 0$, but $E_{\boldsymbol{k}} = \sqrt{\frac{1}{2}\mathrm{Tr}[\hat{\Delta}_{\boldsymbol{k}}(\hat{\Delta}_{\boldsymbol{k}})^{\dagger}]}$ may still be nonzero. We then see that a nonzero gap function opens a gap in the excitation spectrum around the Fermi level.

Writing explicitly out the expression for the electron annihilation operators in terms of the new quasiparticle operators, we obtain

$$c_{\boldsymbol{k}'\sigma} = \frac{(E_{\boldsymbol{k}'} + \epsilon_{\boldsymbol{k}'})\gamma_{\boldsymbol{k}'\sigma} + \Delta_{\boldsymbol{k}',\sigma\uparrow}\gamma_{-\boldsymbol{k}'\uparrow}^{\dagger} + \Delta_{\boldsymbol{k}',\sigma\downarrow}\gamma_{-\boldsymbol{k}'\downarrow}^{\dagger}}{\sqrt{(E_{\boldsymbol{k}'} + \epsilon_{\boldsymbol{k}'})^2 + \frac{1}{2}\mathrm{Tr}[\hat{\Delta}_{\boldsymbol{k}'}(\hat{\Delta}_{\boldsymbol{k}'})^{\dagger}]}}. \tag{3.23}$$

Inserting this into the definition of the gap function in Eq. (3.6), we obtain the self-consistent gap equation

$$\Delta_{\boldsymbol{k},\sigma_1\sigma_2} = -\sum_{\boldsymbol{k}',\sigma_3\sigma_4} V_{\boldsymbol{k}\boldsymbol{k}'}^{\sigma_1\sigma_2\sigma_3\sigma_4} \Delta_{\boldsymbol{k}',\sigma_4\sigma_3} \chi_{\boldsymbol{k}'}, \tag{3.24}$$

where [63]

$$\chi_{\boldsymbol{k}'} = \frac{1}{2E_{\boldsymbol{k}'}} \tanh\left(\frac{\beta E_{\boldsymbol{k}'}}{2}\right). \tag{3.25}$$

As seen from the gap equation, a vanishing gap function is always a solution, corresponding to the system being in its normal state. If we find a nontrivial solution to the gap equation, the next question is then whether this solution minimizes the free energy of the system.

3.1.1 Condensation energy

The free energy of the system takes the form

$$F = \frac{1}{2}\sum_{\boldsymbol{k}}\sum_{\sigma_1\sigma_2} b_{\boldsymbol{k},\sigma_1\sigma_2}^{\dagger}\Delta_{\boldsymbol{k},\sigma_1\sigma_2} + \sum_{\boldsymbol{k}}(\epsilon_{\boldsymbol{k}} - E_{\boldsymbol{k}}) - \frac{2}{\beta}\sum_{\boldsymbol{k}}\ln\left(1 + e^{-\beta E_{\boldsymbol{k}}}\right). \tag{3.26}$$

We can here again express the original electron operators in terms of the new quasiparticle operators and insert these expressions into $b_{\boldsymbol{k},\sigma_1\sigma_2}^{\dagger}$. Further, we also go to zero temperature ($\beta \to \infty$), in which case the last term in the free energy vanishes as $E_{\boldsymbol{k}'} \geq 0$ for all $\boldsymbol{k}'$. We then obtain

$$F_0 = \frac{1}{2}\sum_{\boldsymbol{k}}\sum_{\sigma_1\sigma_2} \Delta_{\boldsymbol{k},\sigma_1\sigma_2}^{*}\Delta_{\boldsymbol{k},\sigma_1\sigma_2}\chi_{\boldsymbol{k}} + \sum_{\boldsymbol{k}}(\epsilon_{\boldsymbol{k}} - E_{\boldsymbol{k}}). \tag{3.27}$$

As we want to compare the free energy of the superconducting state with the free energy of the normal state, we further introduce

$$F_0^N = F_0(\Delta = 0) = \sum_{\boldsymbol{k}}(\epsilon_{\boldsymbol{k}} - |\epsilon_{\boldsymbol{k}}|). \tag{3.28}$$

The energy gain, relative to the normal state, associated with forming a superconducting state at zero temperature, referred to as the condensation energy, is then

$$E_C = F_0^N - F_0 = \sum_{\boldsymbol{k}}(E_{\boldsymbol{k}} - |\epsilon_{\boldsymbol{k}}|) - \sum_{\boldsymbol{k}}\frac{1}{2}\mathrm{Tr}[\hat{\Delta}_{\boldsymbol{k}}(\hat{\Delta}_{\boldsymbol{k}})^\dagger]\chi_{\boldsymbol{k}}. \tag{3.29}$$

In order to evaluate this expression, we will go to the thermodynamic limit and split the momentum integration into integration along surfaces of constant energy $\epsilon_{\boldsymbol{k}}$ and integration normal to these surfaces. We will refer to this as parallel and perpendicular momentum integration. While we keep the parallel momentum-dependence of the gap function, we will make a simplifying assumption about its perpendicular momentum-dependence. We will take the gap function to not vary with perpendicular momentum in a thin energy shell of width $2\omega_c$ around the Fermi surface. Outside of this thin shell, the gap function will be taken to vanish. We will return to the origin of this assumption in the next section.

We first write

$$E_C = \sum_{\boldsymbol{k}} g(\boldsymbol{k}) = \frac{N}{V_{\mathrm{BZ}}}\int \mathrm{d}k_\perp \int_{S_\perp} \mathrm{d}\boldsymbol{k}_\parallel\, g(k_\perp, \boldsymbol{k}_\parallel), \tag{3.30}$$

where

$$g(\boldsymbol{k}) = (E_{\boldsymbol{k}} - |\epsilon_{\boldsymbol{k}}|) - \frac{1}{2}\mathrm{Tr}[\hat{\Delta}_{\boldsymbol{k}}(\hat{\Delta}_{\boldsymbol{k}})^\dagger]\chi_{\boldsymbol{k}}. \tag{3.31}$$

Performing a change of variable, we can further express the condensation energy as

$$E_C = \frac{N}{V_{\mathrm{BZ}}}\int \mathrm{d}\epsilon_{\boldsymbol{k}} \int_{S(\epsilon_{\boldsymbol{k}})} \mathrm{d}\boldsymbol{k}_\parallel \left|\frac{\mathrm{d}\epsilon_{\boldsymbol{k}}}{\mathrm{d}k_\perp}\right|^{-1} g(\epsilon_{\boldsymbol{k}}, \boldsymbol{k}_\parallel). \tag{3.32}$$

We then introduce $A(\epsilon_{\boldsymbol{k}}) = \int_{S(\epsilon_{\boldsymbol{k}})}\mathrm{d}\boldsymbol{k}_\parallel$, and further the anisotropic density of states

$$D(\epsilon_{\boldsymbol{k}}, \boldsymbol{k}_\parallel) = \frac{N}{V_{\mathrm{BZ}}}A(\epsilon_{\boldsymbol{k}})\left|\frac{\mathrm{d}\epsilon_{\boldsymbol{k}}}{\mathrm{d}k_\perp}\right|^{-1}. \tag{3.33}$$

For the case of an isotropic constant energy surface with associated isotropic energy gradient around the surface, we simply have that $D(\epsilon_{\boldsymbol{k}}, \boldsymbol{k}_\parallel)$ is equal to the normal density of states $D(\epsilon_{\boldsymbol{k}})$, while in general

$$D(\epsilon_{\boldsymbol{k}}) = \frac{1}{A(\epsilon_{\boldsymbol{k}})} \int_{S(\epsilon_{\boldsymbol{k}})} \mathrm{d}\boldsymbol{k}_{\parallel}\, D(\epsilon_{\boldsymbol{k}}, \boldsymbol{k}_{\parallel}). \tag{3.34}$$

We can then express the condensation energy as

$$E_{\mathrm{C}} = \int \mathrm{d}\epsilon_{\boldsymbol{k}} \frac{1}{A(\epsilon_{\boldsymbol{k}})} \int_{S(\epsilon_{\boldsymbol{k}})} \mathrm{d}\boldsymbol{k}_{\parallel} D(\epsilon_{\boldsymbol{k}}, \boldsymbol{k}_{\parallel})\, g(\epsilon_{\boldsymbol{k}}, \boldsymbol{k}_{\parallel}). \tag{3.35}$$

The dependence of $g(\epsilon_{\boldsymbol{k}}, \boldsymbol{k}_{\parallel})$ on $\boldsymbol{k}_{\parallel}$ is contained in the gap function which is assumed to not vary with perpendicular momentum in the region where we have nonzero contributions to the integral. As this region constitutes a thin shell around the Fermi surface, we further approximate the surface $S(\epsilon_{\boldsymbol{k}})$ with the Fermi surface and the derivative of $\epsilon_{\boldsymbol{k}}$ with respect to perpendicular momentum with the derivative taken at the Fermi surface. Denoting the anisotropic density of states at the Fermi level by an index 0, and similarly for A, the condensation energy can then be written on the form

$$E_{\mathrm{C}} = \frac{1}{A_0} \int_{\mathrm{FS}} \mathrm{d}\boldsymbol{k}_{\parallel} D_0(\boldsymbol{k}_{\parallel}) \int \mathrm{d}\epsilon_{\boldsymbol{k}}\, g(\epsilon_{\boldsymbol{k}}, \boldsymbol{k}_{\parallel}), \tag{3.36}$$

which we express as

$$E_{\mathrm{C}} = \langle D_0(\boldsymbol{k}_{\parallel}) \int \mathrm{d}\epsilon_{\boldsymbol{k}}\, g(\epsilon_{\boldsymbol{k}}, \boldsymbol{k}_{\parallel}) \rangle_{\boldsymbol{k}_{\parallel},\mathrm{FS}} = \langle E_C(\boldsymbol{k}_{\parallel}) \rangle_{\boldsymbol{k}_{\parallel},\mathrm{FS}} \tag{3.37}$$

with

$$
\begin{aligned}
E_{\mathrm{C}}(\boldsymbol{k}_{\parallel}) &= D_0(\boldsymbol{k}_{\parallel}) \int_{-\omega_c}^{\omega_c} \mathrm{d}\epsilon \left(\sqrt{\epsilon^2 + \frac{1}{2}\mathrm{Tr}[\hat{\Delta}_{\boldsymbol{k}_{\parallel}}(\hat{\Delta}_{\boldsymbol{k}_{\parallel}})^{\dagger}]} - |\epsilon| \right) \\
&\quad - D_0(\boldsymbol{k}_{\parallel}) \int_{-\omega_c}^{\omega_c} \mathrm{d}\epsilon\, \frac{\frac{1}{2}\mathrm{Tr}[\hat{\Delta}_{\boldsymbol{k}_{\parallel}}(\hat{\Delta}_{\boldsymbol{k}_{\parallel}})^{\dagger}]}{2\sqrt{\epsilon^2 + \frac{1}{2}\mathrm{Tr}[\hat{\Delta}_{\boldsymbol{k}_{\parallel}}(\hat{\Delta}_{\boldsymbol{k}_{\parallel}})^{\dagger}]}}.
\end{aligned}
\tag{3.38}
$$

The integral over momenta running over the Fermi surface divided by A_0 is here referred to as a Fermi surface average. It should be understood that the perpendicular momentum dependence of the density of states and the gap function, in the region with nonzero contributions, has been neglected.

This has allowed us to separate the integration into an integral over $\epsilon_{\boldsymbol{k}}$ and an integral over $\boldsymbol{k}_\parallel$ running over the Fermi surface. As our expression still contains an integration over $\epsilon_{\boldsymbol{k}}$, the momentum $\boldsymbol{k}$ is clearly not restricted to the Fermi surface.

We then divide up the above expression for $E_{\mathrm{C}}(\boldsymbol{k}_\parallel) = E_{\mathrm{C}}^{(1)}(\boldsymbol{k}_\parallel) + E_{\mathrm{C}}^{(2)}(\boldsymbol{k}_\parallel)$ into two parts. Starting with performing the integral over ϵ in the first term and assuming that $\omega_c^2 \gg \frac{1}{2}\mathrm{Tr}[\hat{\Delta}_{\boldsymbol{k}}(\hat{\Delta}_{\boldsymbol{k}})^\dagger]$, we obtain the approximate result

$$
E_{\mathrm{C}}^{(1)}(\boldsymbol{k}_\parallel) = \frac{D_0(\boldsymbol{k}_\parallel)\mathrm{Tr}[\hat{\Delta}_{\boldsymbol{k}_\parallel}(\hat{\Delta}_{\boldsymbol{k}_\parallel})^\dagger]}{4}\left[1 + 2\ln\left(\frac{2\omega_c}{\sqrt{\frac{1}{2}\mathrm{Tr}[\hat{\Delta}_{\boldsymbol{k}_\parallel}(\hat{\Delta}_{\boldsymbol{k}_\parallel})^\dagger]}}\right)\right].
$$
(3.39)

Similarly, for $E_{\mathrm{C}}^{(2)}(\boldsymbol{k}_\parallel)$, we obtain

$$
E_{\mathrm{C}}^{(2)}(\boldsymbol{k}_\parallel) = -\frac{D_0(\boldsymbol{k}_\parallel)\mathrm{Tr}[\hat{\Delta}_{\boldsymbol{k}_\parallel}(\hat{\Delta}_{\boldsymbol{k}_\parallel})^\dagger]}{4}\left[2\ln\left(\frac{2\omega_c}{\sqrt{\frac{1}{2}\mathrm{Tr}[\hat{\Delta}_{\boldsymbol{k}_\parallel}(\hat{\Delta}_{\boldsymbol{k}_\parallel})^\dagger]}}\right)\right].
$$
(3.40)

We then see that the final result for the condensation energy is [63]

$$
E_{\mathrm{C}} = \frac{1}{4}\left\langle D_0(\boldsymbol{k}_\parallel)\mathrm{Tr}[\hat{\Delta}_{\boldsymbol{k}_\parallel}(\hat{\Delta}_{\boldsymbol{k}_\parallel})^\dagger]\right\rangle_{\boldsymbol{k}_\parallel,\mathrm{FS}}.
$$
(3.41)

With our definition, a positive value for the condensation energy, as guaranteed by the above expression for nonzero gap function, implies that the superconducting state is favored.

3.1.2 Critical temperature

Finally, returning to the gap equation, we finish our generalized treatment by attempting to determine the critical temperature T_c where the gap function vanishes. We can in that case neglect the effect of the gap function on $E_{\boldsymbol{k}'}$ and write out the linearized gap equation

$$
\Delta_{\boldsymbol{k},\sigma_1\sigma_2} = -\sum_{\boldsymbol{k}',\sigma_3\sigma_4} V_{\boldsymbol{k}\boldsymbol{k}'}^{\sigma_1\sigma_2\sigma_3\sigma_4}\frac{\Delta_{\boldsymbol{k}',\sigma_4\sigma_3}}{2|\epsilon_{\boldsymbol{k}'}|}\tanh\left(\frac{\beta_c|\epsilon_{\boldsymbol{k}'}|}{2}\right).
$$
(3.42)

Similarly to what we did above, we further assume that we only have contributions from the right-hand-side of the equation in a thin energy shell around the Fermi surface. Within this shell, we neglect the perpendicular momentum dependence of the interaction potential and the gap function, which are assumed to vanish outside of the thin shell. Performing the same steps as above, we can then write

$$\Delta_{\boldsymbol{k}_\parallel,\sigma_1\sigma_2} = -\sum_{\sigma_3\sigma_4} \langle D_0(\boldsymbol{k}'_\parallel)\, V_{\boldsymbol{k}_\parallel \boldsymbol{k}'_\parallel}^{\sigma_1\sigma_2\sigma_3\sigma_4} \Delta_{\boldsymbol{k}'_\parallel,\sigma_4\sigma_3}\rangle_{\boldsymbol{k}'_\parallel,\mathrm{FS}} \int_0^{\omega_c} \mathrm{d}\epsilon\, \frac{1}{\epsilon} \tanh\left(\frac{\beta_c\,\epsilon}{2}\right). \tag{3.43}$$

In order to perform the decoupled integral over ϵ, we introduce $x = \beta_c\epsilon/2$, do integration by parts, and assume $k_B T_c \ll \omega_c$. We then obtain

$$\int_0^{\omega_c} \mathrm{d}\epsilon\, \frac{1}{\epsilon} \tanh\left(\frac{\beta_c\epsilon}{2}\right) = \ln\left(\frac{\beta_c\,\omega_c}{2}\right) + I, \tag{3.44}$$

where [53]

$$I = -\int_0^\infty \mathrm{d}x\, \frac{\ln(x)}{\cosh^2(x)} = -\ln\left(\frac{\pi}{4e^\gamma}\right), \tag{3.45}$$

and γ is the Euler–Mascheroni constant. If we then solve the eigenvalue problem

$$\lambda\Delta_{\boldsymbol{k}_\parallel,\sigma_1\sigma_2} = -\sum_{\sigma_3\sigma_4} \langle D_0(\boldsymbol{k}'_\parallel)\, V_{\boldsymbol{k}_\parallel \boldsymbol{k}'_\parallel}^{\sigma_1\sigma_2\sigma_3\sigma_4} \Delta_{\boldsymbol{k}'_\parallel,\sigma_4\sigma_3}\rangle_{\boldsymbol{k}'_\parallel,\mathrm{FS}}, \tag{3.46}$$

we have that

$$\frac{1}{\lambda} = \ln\left(\frac{\beta_c\,\omega_c e^I}{2}\right). \tag{3.47}$$

Solving for $k_B T_c$ and rounding off, we then obtain

$$k_B T_c = 1.13\,\omega_c\, e^{-\frac{1}{\lambda}}. \tag{3.48}$$

(a)   Singlet   (b)   Triplet

$$\frac{1}{\sqrt{2}}\left(|\!\uparrow\downarrow\rangle - |\!\downarrow\uparrow\rangle\right)$$

$$|\!\uparrow\uparrow\rangle$$
$$\frac{1}{\sqrt{2}}\left(|\!\uparrow\downarrow\rangle + |\!\downarrow\uparrow\rangle\right)$$
$$|\!\downarrow\downarrow\rangle$$

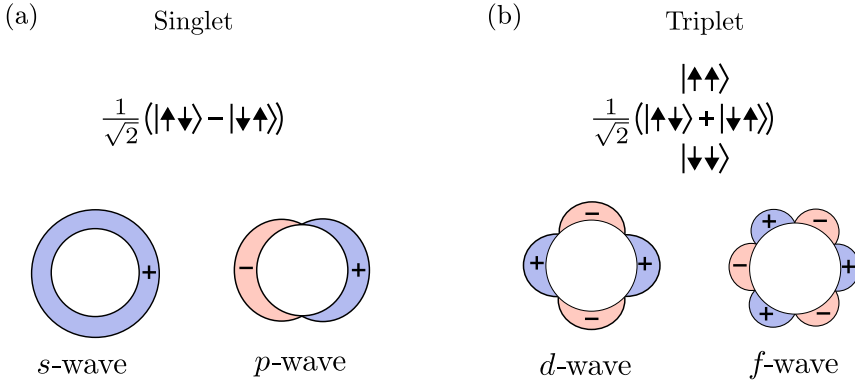s-wave p-wave d-wave f-wave

Figure 3.3: (a) Potential momentum-space symmetries of (a) spin-singlet and (b) spin-triplet gap functions around an isotropic Fermi surface. The differently colored regions correspond to the gap function taking different signs. The width of the colored regions represents the magnitude of the gap function.

In order for $k_B T_c \ll \omega_c$ to hold, we then need λ to be considerably smaller than 1. According to this expression, the critical temperature depends strongly on the parameter λ which, according to Eq. (3.46), increases with the the density of states at the Fermi level and the strength of the interaction potential at the Fermi level. Loosely speaking, the energy scale of the critical temperature is, however, set by the thickness of the shell around the Fermi surface where the interaction has been assumed to be active. We also note that the above formula often instead is presented with a prefactor rounded off to 1.14 rather than 1.13 [63]. Moreover, the eigenvalue problem in Eq. (3.46) will typically have many eigenvalues corresponding to different eigenvectors Δ. The solution preferred by the system is then normally assumed to be the one that has the largest eigenvalue, producing the largest critical temperature.

The symmetries of the gap function that produces the largest critical temperature will be determined by the interaction potential, potentially in collaboration with anisotropy in the density of states. Inspired by the spherical harmonics, gap functions are often identified as s-wave, p-wave, d-wave, or f-wave depending on their sign changes around the Fermi surface. While the gap function in general could be a combination of both spin-singlet and spin-triplet with contributions from different momentum-space

symmetries, it is often assumed that a single symmetry channel dominates. Examples of such symmetry channels for a two-dimensional isotropic Fermi surface are displayed in Fig. 3.3

3.1.3   Phonon-mediated superconductivity

After having introduced the generalized BCS theory, we will now direct our focus towards the electron-phonon system. We then start out from a Hamiltonian describing a coupled system of electrons and phonons

$$H = \sum_{\boldsymbol{k}\sigma} \epsilon_{\boldsymbol{k}} c_{\boldsymbol{k}\sigma}^{\dagger} c_{\boldsymbol{k}\sigma} + \sum_{\boldsymbol{q}} \omega_{\boldsymbol{q}} \Big(a_{\boldsymbol{q}}^{\dagger} a_{\boldsymbol{q}} + \frac{1}{2} \Big) + \sum_{\boldsymbol{k}\boldsymbol{q}\sigma} g_{\boldsymbol{k},\boldsymbol{k}+\boldsymbol{q}} c_{\boldsymbol{k}+\boldsymbol{q}\sigma}^{\dagger} c_{\boldsymbol{k}\sigma} \Big(a_{\boldsymbol{q}} + a_{-\boldsymbol{q}}^{\dagger} \Big), \quad (3.49)$$

where the operator $a_{\boldsymbol{q}}^{\dagger}$ now is a phonon creation operator. We are interested in investigating how the electron system is influenced by the coupling to phonons, and specifically whether this coupling can give rise to attractive interaction between electrons. We therefore take the two first terms in the above Hamiltonian to be the unperturbed Hamiltonian H_0, and treat the last term as a perturbation ηH_1, focusing on how this perturbation influences the electrons. We then perform a Schrieffer-Wolff transformation [29, 49, 65], which starts out with a canonical transformation followed by an expansion in the smallness parameter η [66]

$$\begin{aligned} H' = e^{-\eta \tilde{S}} H e^{\eta \tilde{S}} &= H + \eta \big[H, \tilde{S} \big] + \frac{\eta^2}{2!} \big[\big[H, \tilde{S} \big], \tilde{S} \big] + \mathcal{O}(\eta^3) \\ &= H_0 + \eta \Big(H_1 + \big[H_0, \tilde{S} \big] \Big) + \eta^2 \Big(\big[H_1, \tilde{S} \big] + \frac{1}{2} \big[\big[H_0, \tilde{S} \big], \tilde{S} \big] \Big) + \mathcal{O}(\eta^3). \end{aligned} \quad (3.50)$$

We then choose $\tilde{S}$ so that

$$\eta H_1 + \big[H_0, \eta \tilde{S} \big] = 0, \quad (3.51)$$

producing

$$H' = H_0 + \frac{1}{2} \big[\eta H_1, \eta \tilde{S} \big] + \mathcal{O}(\eta^3). \quad (3.52)$$

In order to achieve this, we take $\tilde{S}$ to be on the form [66]

$$\eta \tilde{S} = \sum_{\boldsymbol{kq\sigma}} g_{\boldsymbol{k},\boldsymbol{k+q}} c^{\dagger}_{\boldsymbol{k+q}\sigma} c_{\boldsymbol{k}\sigma} \left(x_{\boldsymbol{k},\boldsymbol{q}} a_{\boldsymbol{q}} + y_{\boldsymbol{k},\boldsymbol{q}} a^{\dagger}_{-\boldsymbol{q}} \right). \tag{3.53}$$

One can then explicitly work out the commutator in Eq. (3.51) in order to determine $x_{\boldsymbol{k},\boldsymbol{q}}$ and $y_{\boldsymbol{k},\boldsymbol{q}}$. Alternatively, one can sandwich Eq. (3.51) by two eigenstates of the unperturbed Hamiltonian [29], producing

$$\langle n | \eta \tilde{S} | m \rangle = \frac{\langle n | \eta H_1 | m \rangle}{E_m - E_n}, \tag{3.54}$$

where E_l is the energy of the unperturbed electron-phonon system in the state l. Taking the two eigenstates of the unperturbed Hamiltonian to be connected by either electron-phonon scattering involving creation or annihilation of a phonon, one can then show that we must have

$$x_{\boldsymbol{k},\boldsymbol{q}} = \frac{1}{\epsilon_{\boldsymbol{k}} - \epsilon_{\boldsymbol{k+q}} + \omega_{\boldsymbol{q}}}, \qquad y_{\boldsymbol{k},\boldsymbol{q}} = \frac{1}{\epsilon_{\boldsymbol{k}} - \epsilon_{\boldsymbol{k+q}} - \omega_{\boldsymbol{q}}}. \tag{3.55}$$

Working out the commutator in Eq. (3.52), we then obtain an effective interaction between electrons

$$H_{\text{eff}} = \sum_{\substack{\boldsymbol{kqk'} \\ \sigma\sigma'}} g_{\boldsymbol{k},\boldsymbol{k+q}} g_{\boldsymbol{k'},\boldsymbol{k'-q}} \frac{\omega_{\boldsymbol{q}}}{\left(\epsilon_{\boldsymbol{k}} - \epsilon_{\boldsymbol{k'-q}} \right)^2 - \omega_{\boldsymbol{q}}^2} c^{\dagger}_{\boldsymbol{k+q}\sigma} c_{\boldsymbol{k}\sigma} c^{\dagger}_{\boldsymbol{k'-q}\sigma'} c_{\boldsymbol{k'}\sigma'}. \tag{3.56}$$

In order to focus on the possibility of formation of Cooper pairs consisting of electrons with opposite momenta, we restrict the summation to the case of $\boldsymbol{k'} = -\boldsymbol{k}$. We then use the property of the electron-phonon coupling $g_{-\boldsymbol{k},-\boldsymbol{k-q}} = g^{*}_{\boldsymbol{k},\boldsymbol{k+q}}$ [66], juggle around the names of the momenta we sum over, and reorganize the order of the electron operators without keeping generated terms that do not involve four electron operators. We can then express the effective interaction Hamiltonian on the form

$$H_{\text{pair}} = \frac{1}{2} \sum_{\boldsymbol{kk'}} \sum_{\sigma\sigma'} V_{\boldsymbol{kk'}} \, c^{\dagger}_{\boldsymbol{k}\sigma} c^{\dagger}_{-\boldsymbol{k}\sigma'} c_{-\boldsymbol{k'}\sigma'} c_{\boldsymbol{k'}\sigma}, \tag{3.57}$$

with

$$V_{\boldsymbol{k}\boldsymbol{k}'} = |g_{\boldsymbol{k}',\boldsymbol{k}}|^2 \frac{2\omega_{\boldsymbol{k}'-\boldsymbol{k}}}{(\epsilon_{\boldsymbol{k}'} - \epsilon_{\boldsymbol{k}})^2 - \omega_{\boldsymbol{k}'-\boldsymbol{k}}^2}. \tag{3.58}$$

In order to make use of the framework we established in the previous section, we can further rewrite H_{pair} on the more general form

$$H_{\mathrm{pair}} = \frac{1}{2} \sum_{\boldsymbol{k}\boldsymbol{k}'} \sum_{\sigma_1\sigma_2\sigma_3\sigma_4} V_{\boldsymbol{k}\boldsymbol{k}'}^{\sigma_1\sigma_2\sigma_3\sigma_4} c_{\boldsymbol{k}\sigma_1}^\dagger c_{-\boldsymbol{k}\sigma_2}^\dagger c_{-\boldsymbol{k}'\sigma_3} c_{\boldsymbol{k}'\sigma_4}, \tag{3.59}$$

where

$$V_{\boldsymbol{k}\boldsymbol{k}'}^{\sigma\sigma\uparrow\downarrow} = V_{\boldsymbol{k}\boldsymbol{k}'}^{\sigma\sigma\downarrow\uparrow} = V_{\boldsymbol{k}\boldsymbol{k}'}^{\uparrow\downarrow\sigma\sigma} = V_{\boldsymbol{k}\boldsymbol{k}'}^{\downarrow\uparrow\sigma\sigma} = V_{\boldsymbol{k}\boldsymbol{k}'}^{\uparrow\uparrow\downarrow\downarrow} = V_{\boldsymbol{k}\boldsymbol{k}'}^{\downarrow\downarrow\uparrow\uparrow} = 0, \tag{3.60}$$

and

$$V_{\boldsymbol{k}\boldsymbol{k}'}^{\sigma\sigma\sigma\sigma} = V_{\boldsymbol{k}\boldsymbol{k}'}, \qquad V_{\boldsymbol{k}\boldsymbol{k}'}^{\uparrow\downarrow\downarrow\uparrow} = V_{\boldsymbol{k}\boldsymbol{k}'}^{\downarrow\uparrow\uparrow\downarrow} = \frac{1}{2}V_{\boldsymbol{k}\boldsymbol{k}'}, \qquad V_{\boldsymbol{k}\boldsymbol{k}'}^{\uparrow\downarrow\uparrow\downarrow} = V_{\boldsymbol{k}\boldsymbol{k}'}^{\downarrow\uparrow\downarrow\uparrow} = -\frac{1}{2}V_{-\boldsymbol{k}\boldsymbol{k}'} \tag{3.61}$$

covers all 16 terms. It will, in the following, be useful to express the interaction potential $V_{\boldsymbol{k}\boldsymbol{k}'}$ in terms of its even an odd parts with respect to $\boldsymbol{k}$. As $V_{\boldsymbol{k}\boldsymbol{k}'} = V_{-\boldsymbol{k},-\boldsymbol{k}'}$, one can see that these even and odd parts with respect to $\boldsymbol{k}$ will also be even and odd with respect to $\boldsymbol{k}'$. We then write $V_{\boldsymbol{k}\boldsymbol{k}'} = V_{\boldsymbol{k}\boldsymbol{k}',E(\boldsymbol{k})} + V_{\boldsymbol{k}\boldsymbol{k}',O(\boldsymbol{k})}$ where

$$V_{\boldsymbol{k}\boldsymbol{k}',E(\boldsymbol{k})} = \frac{1}{2}(V_{\boldsymbol{k}\boldsymbol{k}'} + V_{-\boldsymbol{k}\boldsymbol{k}'}), \qquad V_{\boldsymbol{k}\boldsymbol{k}',O(\boldsymbol{k})} = \frac{1}{2}(V_{\boldsymbol{k}\boldsymbol{k}'} - V_{-\boldsymbol{k}\boldsymbol{k}'}). \tag{3.62}$$

We can then further express

$$-V_{-\boldsymbol{k}\boldsymbol{k}'} = V_{\boldsymbol{k}\boldsymbol{k}',O(\boldsymbol{k})} - V_{\boldsymbol{k}\boldsymbol{k}',E(\boldsymbol{k})}. \tag{3.63}$$

As we have written the interaction Hamiltonian on the same form as in the previous section, we can now jump straight to the gap equation. Starting with investigating $\Delta_{\uparrow\downarrow}$, we have

$$\Delta_{\boldsymbol{k},\uparrow\downarrow} = -\sum_{\boldsymbol{k}'}\chi_{\boldsymbol{k}'}[V_{\boldsymbol{k}\boldsymbol{k}'}^{\uparrow\downarrow\downarrow\uparrow}\Delta_{\boldsymbol{k}',\uparrow\downarrow} + V_{\boldsymbol{k}\boldsymbol{k}'}^{\uparrow\downarrow\uparrow\downarrow}\Delta_{\boldsymbol{k}',\downarrow\uparrow}]. \qquad (3.64)$$

Writing out the expressions for the components of the spin-dependent interaction potential, we then obtain

$$\Delta_{\boldsymbol{k},\uparrow\downarrow} = -\sum_{\boldsymbol{k}'}\chi_{\boldsymbol{k}'}[V_{\boldsymbol{k}\boldsymbol{k}',E(\boldsymbol{k})}\Delta_{\boldsymbol{k}',\uparrow\downarrow,O(s)} + V_{\boldsymbol{k}\boldsymbol{k}',O(\boldsymbol{k})}\Delta_{\boldsymbol{k}',\uparrow\downarrow,E(s)}]. \qquad (3.65)$$

We have here defined

$$\Delta_{\boldsymbol{k}',\uparrow\downarrow,O(s)} = \frac{1}{2}(\Delta_{\boldsymbol{k}',\uparrow\downarrow} - \Delta_{\boldsymbol{k}',\downarrow\uparrow}), \qquad \Delta_{\boldsymbol{k}',\uparrow\downarrow,E(s)} = \frac{1}{2}(\Delta_{\boldsymbol{k}',\uparrow\downarrow} + \Delta_{\boldsymbol{k}',\downarrow\uparrow}), \quad (3.66)$$

which are naturally even and odd in momentum, respectively. We then see that the gap equation restricted to spin-singlet pairing with $\Delta_{\boldsymbol{k},\uparrow\downarrow} = -\Delta_{\boldsymbol{k},\downarrow\uparrow} = \Delta_{\boldsymbol{k}}^s$ only obtains contributions from the part of the interaction potential which is even in momentum

$$\Delta_{\boldsymbol{k}}^s = -\sum_{\boldsymbol{k}'}V_{\boldsymbol{k}\boldsymbol{k}',E(\boldsymbol{k})}\Delta_{\boldsymbol{k}'}^s\chi_{\boldsymbol{k}'}. \qquad (3.67)$$

Similarly, the gap equation restricted to unpolarized spin-triplet pairing with $\Delta_{\boldsymbol{k},\uparrow\downarrow} = \Delta_{\boldsymbol{k},\downarrow\uparrow} = \Delta_{\boldsymbol{k}}^{t,u}$ only obtains contributions from the part of the interaction potential which is odd in momentum

$$\Delta_{\boldsymbol{k}}^{t,u} = -\sum_{\boldsymbol{k}'}V_{\boldsymbol{k}\boldsymbol{k}',O(\boldsymbol{k})}\Delta_{\boldsymbol{k}'}^{t,u}\chi_{\boldsymbol{k}'}. \qquad (3.68)$$

This is simply an expression of the fact that e.g. the spin-singlet gap function is odd in momentum so that, when multiplied by a potential and summed over momentum, only the part of the potential that is odd in momentum will contribute. We can also consider the gap equation for $\Delta_{\boldsymbol{k},\sigma\sigma}$, which naturally only can obtain contributions from $V_{\boldsymbol{k}\boldsymbol{k}',O(k)}$

$$\Delta_{\boldsymbol{k},\sigma\sigma} = -\sum_{\boldsymbol{k}'}V_{\boldsymbol{k}\boldsymbol{k}',O(k)}\Delta_{\boldsymbol{k}',\sigma\sigma}\chi_{\boldsymbol{k}'}. \qquad (3.69)$$

Now that we have the relevant gap equations, the next step is to judge whether there can be non-trivial solutions to any of these gap equations. This depends on the interaction potential $V_{\boldsymbol{k}\boldsymbol{k}'}$. Investigating the phonon-mediated interaction potential we derived earlier

$$V_{\boldsymbol{k}\boldsymbol{k}'} = |g_{\boldsymbol{k}',\boldsymbol{k}}|^2 \frac{2\omega_{\boldsymbol{k}'-\boldsymbol{k}}}{(\epsilon_{\boldsymbol{k}'} - \epsilon_{\boldsymbol{k}})^2 - \omega_{\boldsymbol{k}'-\boldsymbol{k}}^2},$$

we consider the case of $\boldsymbol{k}$ situated at the Fermi surface which is the relevant case for determining the gap function at the Fermi surface. We denote the largest available phonon energy by ω_c, which e.g. corresponds to the Debye energy in the Debye model for acoustic phonons or the Einstein energy in the Einstein model for optical phonons. As the energy scale for electrons is normally much larger than the energy scale for phonons, the scattering processes where $\epsilon_{\boldsymbol{k}'}$ is smaller than or similar to ω_c constitutes a thin shell around the Fermi surface. When $\boldsymbol{k}'$ is moved outside of this thin shell, the interaction potential is quickly suppressed by the largeness of the electron energy scale through the term $\epsilon_{\boldsymbol{k}'}^2$ in the denominator. This motivates an assumption that the interaction potential will only be providing contributions to the pairing in a thin shell around the Fermi surface.

Inside this thin shell, the above interaction potential can in general vary significantly with $\boldsymbol{k}'$. On the right-hand-side of the gap equation, there is, however, a factor $\chi_{\boldsymbol{k}'}$ which is peaked for $\boldsymbol{k}'$ at the Fermi surface. One would then expect that the most important contributions from the right-hand-side of the gap equation will arise from $\boldsymbol{k}'$ located at the Fermi surface. If one further assumes that the behavior of the potential when integrated over constant energy surfaces inside the thin shell will not vary too quickly also when moving slightly away from the Fermi surface, one might then be able to motivate neglecting the perpendicular momentum dependence of the interaction potential inside the thin shell and simply focus on the behavior at the Fermi surface. We are here simplifying the perpendicular behavior of the interaction potential and treating the eventual decay of the interaction strength when moving from the Fermi surface to some point far away from the Fermi surface as a sudden drop-off. As seen from the gap equation, neglecting all perpendicular momentum dependence of the interaction potential inside the thin shell also leads to a gap function which is constant with respect to perpendicular momentum inside the thin shell. We have then reached the approximation scheme applied when discussing the condensation energy and critical temperature within the generalized BCS

theory outlined in the previous section.

If we then consider the interaction potential with both $\boldsymbol{k}$ and $\boldsymbol{k}'$ located at the Fermi surface, we see that $V_{\boldsymbol{k}\boldsymbol{k}',E(\boldsymbol{k})}$ consists of two terms that both carry a negative sign. This fits nicely with the gap equation for spin-singlet pairing where a negative (attractive) interaction potential then can make both sides of the equation naturally take the same sign. The essence of this possibility can be captured by further neglecting the parallel momentum dependence of the interaction potential. We are then working with an interaction potential that is constant inside a thin shell around the Fermi level [65]

$$V_{\boldsymbol{k}\boldsymbol{k}'} = \begin{cases} -V/N, & |\epsilon_{\boldsymbol{k}}|, |\epsilon_{\boldsymbol{k}'}| \leq \omega_c, \\ 0, & \text{otherwise.} \end{cases} \tag{3.70}$$

For $\boldsymbol{k}$ inside the thin shell around the Fermi surface, the gap equation then takes the form

$$\Delta_{\boldsymbol{k}}^{s} = \frac{V}{N} \sum_{\boldsymbol{k}'}' \Delta_{\boldsymbol{k}'}^{s} \chi_{\boldsymbol{k}'}, \tag{3.71}$$

where now $E_{\boldsymbol{k}'} = \sqrt{\epsilon_{\boldsymbol{k}'}^2 + (\Delta_{\boldsymbol{k}'}^s)^2}$ and the prime on sum over $\boldsymbol{k}'$ indicates that the sum is restricted to a thin shell around the Fermi surface. As the right-hand-side does not depend on $\boldsymbol{k}$, the gap function will also simply be a constant Δ^s inside the thin shell, corresponding to s-wave pairing. Going over to integration over energy, approximating the density of states by the density of states at the Fermi level D_0, and defining $D_0' = D_0/N$, the gap equation takes the form

$$\frac{1}{D_0' V} = 2 \int_0^{\omega_c} \mathrm{d}\epsilon \, \chi(\epsilon), \tag{3.72}$$

where the remaining dependence on Δ^s is now contained in $\chi(\epsilon)$.

Using the critical temperature formula from the previous section, we now obtain right away that

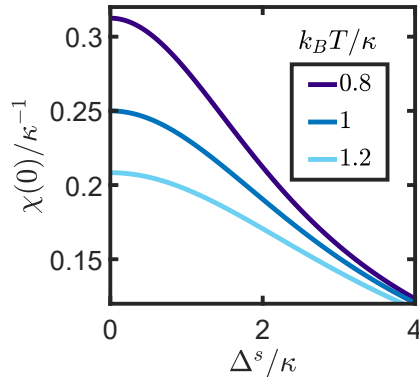$$k_B T_c = 1.13 \, \omega_c \, e^{-1/(D_0' V)}. \tag{3.73}$$

Figure 3.4: The factor $\chi(\epsilon)$ appearing in the gap equation evaluated at the Fermi level as a function of the gap magnitude Δ^s and the temperature T. The quantity κ is an arbitrary energy scale. Increasing the temperature, we see that the important Fermi surface contributions to the right-hand-side of the gap equation are reduced. In order to obtain a solution to the gap equation, a smaller gap is then necessary.

Moreover, for $\Delta_{\boldsymbol{k}}^s = \Delta^s$ inside the thin shell, the condensation energy now becomes $E_{\mathrm{C}} = D_0(\Delta_0^s)^2/2$. Here, we have taken $\Delta^s(T = 0) \equiv \Delta_0^s$. Finally, we attempt to calculate the gap function at zero temperature. As then $E_{\boldsymbol{k}'} > 0$ for all $\boldsymbol{k}'$, we can then take $\tanh(\beta E_{\boldsymbol{k}'}/2) = 1$ when $\beta \to \infty$, producing

$$\frac{1}{D_0' V} = \int_0^{\omega_c} \mathrm{d}\epsilon \frac{1}{\sqrt{\epsilon^2 + (\Delta_0^s)^2}}. \tag{3.74}$$

Introducing $x = \epsilon/\Delta_0^s$, performing the integral over x, and assuming $\Delta^s \ll \omega_c$, we are left with

$$\Delta_0^s = 2\omega_c \, e^{-1/(D_0' V)}. \tag{3.75}$$

Evaluating the ratio between the gap at zero temperature and the critical temperature, without rounding off before reaching the final answer, we then obtain a number

$$\frac{\Delta_0^s}{k_B T_c} = 1.76, \tag{3.76}$$

which is independent on properties of the system such as ω_c and V. Between zero temperature and the critical temperature, the magnitude of the gap function displays a decaying behavior with respect to temperature which can be obtained by solving the gap equation in Eq. (3.72) at arbitrary temperature. As shown in Fig. 3.4, the important Fermi surface contributions to the right-hand-side of this equation decrease with increasing temperature. If the temperature is not too high, one can, however, still obtain a solution to the gap equation by decreasing the gap magnitude.

We finally comment that, with a interaction potential that is even in momentum, there is of course no solution to the gap equations for triplet pairing. If the parallel momentum dependence of the interaction potential is kept, it could in principle be possible to also have triplet solutions depending on the details of the electron-phonon coupling and the phonon dispersion. In order for a triplet state to form, it would, however, have to be more energetically favorable than the typical spin-singlet s-wave state.

3.1.4   Effect of Coulomb interaction

We have discussed attractive interaction between electrons giving rise to formation of Cooper pairs. As electrons repel each other through the Coulomb interaction, a natural question is how Coulomb fits into this picture. Starting from a spatially dependent Coulomb interaction $\sim 1/r$, and Fourier transforming, we obtain a momentum-dependent Coulomb interaction on the form $\sim 1/q^2$. In good metals, the Coulomb interaction is, however, strongly screened. The momentum-dependence is then typically considerably weaker [54]. We will therefore treat the Coulomb interaction as a momentum-independent potential.

For the total interaction potential, we now take $V_{\boldsymbol{k}\boldsymbol{k}'} = V^p_{\boldsymbol{k}\boldsymbol{k}'} + V^C_{\boldsymbol{k}\boldsymbol{k}'}$, where $V^p_{\boldsymbol{k}\boldsymbol{k}'}$ is equal to a constant $-V/N$ in a thin shell of width $2\omega_c$ around the Fermi surface, as introduced in the previous section. The Coulomb potential $V^C_{\boldsymbol{k}\boldsymbol{k}'}$ is taken to simply be on the form

$$V^C_{\boldsymbol{k}\boldsymbol{k}'} = \begin{cases} U/N, & 0 \leq |\epsilon_{\boldsymbol{k}}|, |\epsilon_{\boldsymbol{k}'}| \leq W, \\ 0, & \text{otherwise}, \end{cases} \tag{3.77}$$

where $2W$ is the bandwidth of the relevant electron energy band and we have, for simplicity, assumed that the band is half-filled. This model is often referred to as the Anderson-Morel model [67].

The gap equation

$$\Delta^s_{\boldsymbol{k}} = -\sum_{\boldsymbol{k}'} V_{\boldsymbol{k}\boldsymbol{k}'} \Delta^s_{\boldsymbol{k}'} \chi_{\boldsymbol{k}'}, \tag{3.78}$$

can further be split up into one equation for $\boldsymbol{k}$ inside the thin shell and one equation for $\boldsymbol{k}$ outside the thin shell. For each of these separate cases, the right-hand-side of the equation will not depend on $\boldsymbol{k}$. We then introduce Δ_1 as the constant gap inside the thin shell and Δ_2 as the constant gap outside the thin shell. Going over to an integration over ϵ, we note that, as we have contributions from the whole electron band instead of just a thin shell around the Fermi surface, the density of states can in general vary considerably in the relevant energy region. For simplicity, we still approximate the density of states by the density of states at the Fermi level. The coupled set of self-consistent equations for Δ_1 and Δ_2 can then be expressed as

$$\Delta_1 = -2D'_0 \int_0^{\omega_c} d\epsilon \, (U - V)\Delta_1 \, \chi(\epsilon, \Delta_1) - 2D'_0 \int_{\omega_c}^W d\epsilon \, U\Delta_2 \chi(\epsilon, \Delta_2), \tag{3.79a}$$

$$\Delta_2 = -2D'_0 \int_0^{\omega_c} d\epsilon \, U\Delta_1 \, \chi(\epsilon, \Delta_1) - 2D'_0 \int_{\omega_c}^W d\epsilon \, U\Delta_2 \chi(\epsilon, \Delta_2). \tag{3.79b}$$

Performing the integral over energies outside of the thin shell, one can show that the coupled set of equations has a solution where Δ_1 is, as before, determined by

$$\frac{1}{\lambda} = 2 \int_0^{\omega_c} d\epsilon \, \chi(\epsilon, \Delta_1).$$

with now $\lambda = D'_0 V \rightarrow \lambda' = \lambda - \mu^*$ and [64]

$$\mu^* = \frac{D'_0 U}{1 + D'_0 U \ln(W/\omega_c)}. \tag{3.80}$$

Assuming that $\lambda' \geq 0$, one can then obtain an expression for e.g. the critical temperature

$$k_B T_c = 1.13 \, \omega_c \, e^{-1/(\lambda - \mu^*)}. \tag{3.81}$$

It is then apparent that the effect of Coulomb interaction on the superconductivity depends on how large μ^* is compared to λ. If μ^* is small compared
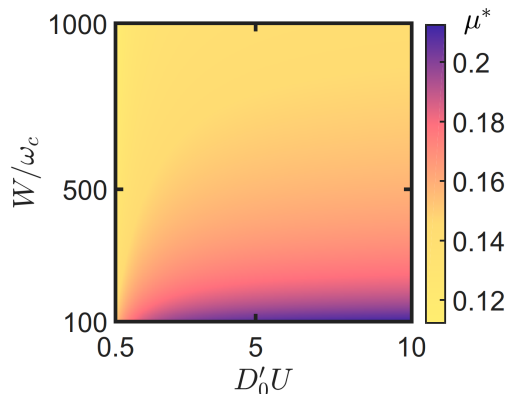
Figure 3.5: The Coulomb pseudo-potential μ^* as a function of $D_0'U$ and W/ω_c.

to λ, the effect of Coulomb interaction will, in fact, be quite limited.

If the Coulomb interaction had also been restricted to a thin shell of width $2\omega_c$ around the Fermi level, the correction to the dimensionless coupling constant λ arising from Coulomb interaction would simply have been $\lambda \to \lambda - D_0'U$. As the Coulomb interaction has been taken to be active across the whole electron band, we have instead ended up with the correction $\lambda \to \lambda - \mu^*$. Inspecting the expression for μ^*, we see that if we take $D_0'U \ll 1$, we will also have $\mu^* \ll 1$ regardless of how large W/ω_c is. If we instead consider $D_0'U = 1$, we obtain $\mu^* = 1/(1 + \ln(W/\omega_c))$. For e.g. $W/\omega_c = 100$, we then have $\mu^* \approx 0.18$, which is significantly better than $\lambda \to \lambda - 1$. Moreover, if we consider $D_0'U \gg 1$, we obtain that $\mu^* = 1/\ln(W/\omega_c)$ regardless of how large $D_0'U$ is. For e.g. $W/\omega_c = 100$, we then have $\mu^* \approx 0.22$, which may still allow for superconductivity to survive. In Fig. 3.5, we further show how μ^* depends more generally on $D_0'U$ and W/ω_c. The picture is then that the effect of Coulomb interaction on the pairing may take the form of an easily incorporated correction to λ, which in many cases is much less dramatic than one might have expected. Although the effect on the critical temperature of including $\lambda \to \lambda - \mu^*$ may not be negligible, this motivates why considering superconductivity without taking Coulomb interaction into account is not necessarily an unreasonable approach to the problem.

The origin of the relatively weak effect of Coulomb interaction becomes clearer if one further derives the expression for Δ_2. From Eq. (3.79b), one can obtain

$$\Delta_2 = -\frac{\mu^*}{\lambda - \mu^*}\Delta_1. \qquad (3.82)$$

We then see that the sign of Δ_2 is the opposite of Δ_1. If we consider the gap equation for $\boldsymbol{k}$ inside the thin shell around the Fermi surface, the Coulomb potential clearly works against the attractive phonon-mediated interaction as long as $\boldsymbol{k}'$ also is inside the thin shell. However, as soon as $\boldsymbol{k}'$ is taken outside the thin shell, the gap equation changes its sign in order to take advantage of the repulsive Coulomb interaction, dramatically reducing Coulomb's destructive effect on superconductivity.

For simplicity, and relevance for phonon-mediated superconductivity, we considered a constant attractive interaction giving rise to spin-singlet s-wave pairing. If one instead considers a gap function that changes sign when moving around the Fermi surface, the effect of Coulomb interaction can be further reduced. Keeping the Coulomb interaction as a momentum-independent constant, its contributions to the gap equation inside the the thin shell can cancel out, leaving the superconductivity untouched.

3.2   Spin-split superconductors

In the beginning of the chapter, we introduced that magnetic fields are not able to penetrate superconductors. As we will see in this section, this is not the full story about superconductors in magnetic fields. It is true that the typical response of a superconductor to a magnetic field is to set up screening currents that counteract the applied field. The magnetic field then decays exponentially inside the superconductor over a length scale referred to as the penetration depth [68]. Considering a bulk superconductor, there is then no magnetic flux penetrating the interior of the superconductor. This picture is, however, only valid up to a certain field strength. If the magnetic field becomes too strong, one out of two things can happen. The first scenario is that the system transitions directly to its normal state as staying in the superconducting state and fighting the magnetic field no longer becomes energetically favorable. These types of superconductors are called type-I superconductors. The alternative is that the system enters an intermediate phase featuring non-superconducting regions circulated by supercurrents, called vortices, where magnetic flux can penetrate the system. Superconductors of this type are called type-II superconductors.

What we will focus on in this section are so-called spin-split superconductors. They can e.g. arise from subjecting thin-film superconductors to magnetic fields. If the magnetic field is applied in-plane, induced orbital motion of electrons can be limited by making the film sufficiently thin. The dominant effect of the magnetic field on the superconductor will then be a spin-splitting effect arising from the interaction of the external field with the spins of the electrons giving rise to the superconducting state [69]. A similar spin-splitting effect can also be achieved by proximity-coupling a thin-film superconductor to a ferromagnetic material. We will, in the following, assume that this spin-splitting is uniform across the thin-film and not be too concerned with its origin.

We include spin-splitting in our model for a superconductor through a spin-splitting field h, so that the electron energies are expressed as $\epsilon_{k\sigma} = \epsilon_k - \sigma h$, where $\sigma = \uparrow, \downarrow = +, -$. We can then return to Eq. (3.12), where we now restrict our analysis to the case of spin-singlet pairing. We then take $\Delta_{k,\uparrow\downarrow} = -\Delta_{k,\downarrow\uparrow} = \Delta_k$ so that the matrix M_k can be expressed as

$$M_{\boldsymbol{k}} = \begin{pmatrix} \epsilon_{\boldsymbol{k}\uparrow} & 0 & 0 & -\Delta_{\boldsymbol{k}} \\ 0 & \epsilon_{\boldsymbol{k}\downarrow} & \Delta_{\boldsymbol{k}} & 0 \\ 0 & \Delta_{\boldsymbol{k}}^* & -\epsilon_{\boldsymbol{k}\uparrow} & 0 \\ -\Delta_{\boldsymbol{k}}^* & 0 & 0 & -\epsilon_{\boldsymbol{k}\downarrow} \end{pmatrix}. \tag{3.83}$$

This matrix can be diagonalized by the transformation we introduced earlier, where the matrix $\hat{\Delta}_{\boldsymbol{k}}$ appearing in $U_{\boldsymbol{k}}$ is now restricted to the case of spin-singlet pairing. We then end up with

$$W_{\boldsymbol{k}} = U_{\boldsymbol{k}}^\dagger M_{\boldsymbol{k}} U_{\boldsymbol{k}} = \begin{pmatrix} E_{\boldsymbol{k}} - h & 0 & 0 & 0 \\ 0 & E_{\boldsymbol{k}} + h & 0 & 0 \\ 0 & 0 & -E_{\boldsymbol{k}} + h & 0 \\ 0 & 0 & 0 & -E_{\boldsymbol{k}} - h \end{pmatrix}, \tag{3.84}$$

producing

$$H = H_0' + \sum_{\boldsymbol{k}\sigma} E_{\boldsymbol{k}\sigma} \gamma_{\boldsymbol{k}\sigma}^\dagger \gamma_{\boldsymbol{k}\sigma}. \tag{3.85}$$

Here, we have defined $E_{\boldsymbol{k}\sigma} = E_{\boldsymbol{k}} - \sigma h$ where still $E_{\boldsymbol{k}} \geq 0$. Further, as before,

$$H_0' = \frac{1}{2} \sum_{\boldsymbol{k}} \sum_{\sigma_1 \sigma_2} b_{\boldsymbol{k},\sigma_1\sigma_2}^\dagger \Delta_{\boldsymbol{k},\sigma_1\sigma_2} + \sum_{\boldsymbol{k}} (\epsilon_{\boldsymbol{k}} - E_{\boldsymbol{k}}).$$

with the first term now taking the form

$$\frac{1}{2} \sum_{\boldsymbol{k}} \sum_{\sigma_1 \sigma_2} \frac{\Delta_{\boldsymbol{k},\sigma_1\sigma_2}^* \Delta_{\boldsymbol{k},\sigma_1\sigma_2}}{4 E_{\boldsymbol{k}}} \Big[\tanh \Big(\frac{\beta E_{\boldsymbol{k}\sigma_1}}{2} \Big) + \tanh \Big(\frac{\beta E_{\boldsymbol{k}\sigma_2}}{2} \Big) \Big],$$

where the only difference from last time is that the quasiparticle energies now are spin dependent, and the gap function should be restricted to spin-singlet pairing. We then obtain the following expression for the free energy

$$F = \frac{1}{2} \sum_{\boldsymbol{k}\sigma} \frac{|\Delta_{\boldsymbol{k}}|^2}{2 E_{\boldsymbol{k}}} \tanh \Big(\frac{\beta E_{\boldsymbol{k}\sigma}}{2} \Big) + \sum_{\boldsymbol{k}} (\epsilon_{\boldsymbol{k}} - E_{\boldsymbol{k}}) - \frac{1}{\beta} \sum_{\boldsymbol{k}\sigma} \ln \Big(1 + e^{-\beta E_{\boldsymbol{k}\sigma}} \Big). \quad (3.86)$$

Similarly, introducing spin-dependent quasiparticle energies and restricting the gap function to spin-singlet pairing, we obtain for the gap equation

$$\Delta_{\boldsymbol{k}} = - \sum_{\boldsymbol{k}'\sigma} V_{\boldsymbol{k}\boldsymbol{k}',E(\boldsymbol{k})} \frac{\Delta_{\boldsymbol{k}'}}{4 E_{\boldsymbol{k}'}} \tanh \Big(\frac{\beta E_{\boldsymbol{k}'\sigma}}{2} \Big). \quad (3.87)$$

Now that we have the relevant expression for the free energy, as well as the gap equation, we make the following observation. If we take the interaction potential to be a constant $-V/N$ inside a thin shell around the Fermi surface, leading to the gap function being a constant Δ inside the thin shell, the gap equation at zero temperature will be unaffected by a spin-splitting field $h < \Delta_0$ as none of the quasiparticle energies will become negative. The solution to the gap equation for $h < \Delta_0$ will therefore still be Δ_0. Similarly, with an unaffected gap, the zero-temperature free energy for $h < \Delta_0$ will also be unaffected by the spin-splitting field. One could therefore imagine that the critical spin-splitting field at zero temperature would have to be larger than or equal to Δ_0. However, we also have to take into account that the free energy of the normal state of the system can be affected by h through the logarithmic term. Since the energy spectrum, in this case, is not gapped, the energies $E_{\boldsymbol{k}\uparrow}$ can now, in fact, become negative. The zero-temperature free energy of the normal state will therefore be lowered by an amount
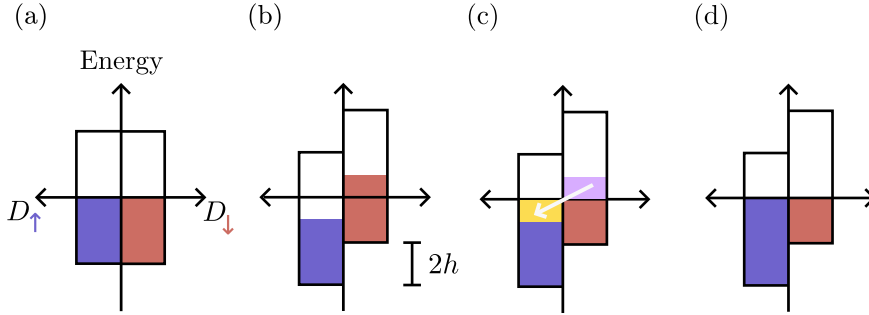
Figure 3.6: Normal state: (a) Density of states, assumed constant, for spin-↑ and spin-↓ energy bands where states below the Fermi level are filled. (b) The introduction of a spin-splitting field h splits the energy bands, pushing spin-↓ electrons above the Fermi level. (c) In order to lower its energy, the system converts spin-↓ electrons situated above the Fermi level to spin-↑ electrons with lower energy, leading to the spin-polarized state in (d). Importantly, the sum over the energies of all colored states is the same in (a) and (b), making the energy of the system in (d) is lower than the energy in (a).

$$F_0^N(h = 0) - F_0^N(h > 0) = \sum_{\boldsymbol{k}}^{|\epsilon_{\boldsymbol{k}}|<h} (h - |\epsilon_{\boldsymbol{k}}|) = D_0 h^2, \tag{3.88}$$

where we have gone over to an integration over energy and approximated the density of states by the density of states at the Fermi level.

As shown earlier, starting out from $h = 0$, the superconducting state is favored by an amount $E_C = D_0 \Delta_0^2 / 2$. Increasing h, but not above Δ_0, the energy of the superconducting state is unaffected, while the normal state energy is reduced by an amount $D_0 h^2$. We then see that the normal state will be favored by the system at a critical spin-splitting field

$$h_c = \frac{\Delta_0}{\sqrt{2}} \approx 0.7\,\Delta_0. \tag{3.89}$$

This result is called the Chandrasekhar-Clogston limit [70, 71] and limits the maximum spin-splitting field that the superconductor can coexist with
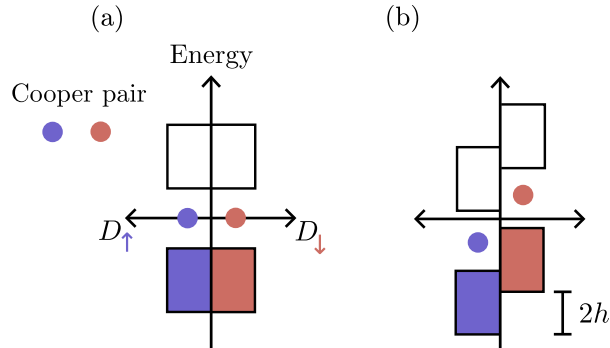
Figure 3.7: Spin-singlet superconductor: (a) Density of states, taken constant with a gap, for energy bands labelled by spin-↑ and spin-↓. States below the Fermi level are filled. We have also included the position along the energy axis of two electrons at the Fermi surface forming a Cooper pair. (b) The introduction of a spin-splitting field h splits the energy bands. In this case, no states are shifted above the Fermi level and the energy of the system is not altered.

to a fraction of the superconducting gap at zero temperature.

The energy gain of the normal state in the presence of a spin-splitting field can be understood from Fig. 3.6. From this figure, we see that the normal state of the system, in the presence of a spin-splitting field, can lower its energy by becoming spin-polarized. We note that connecting this picture with our calculations requires e.g. transforming the hole-like quasiparticles with $\epsilon_{\boldsymbol{k}} < 0$ into electron-like quasiparticles with opposite spin and sending the gap to zero. In the figure, we have further considered the simplest possible case of a constant density of states for both spin-bands, which will then naturally also be equal to the density of states at the Fermi level D_0. The area of the purple rectangle in Fig. 3.6 (c) is then $D_0 h$. Since the yellow rectangle is shifted by an amount h relative to the purple rectangle, we then immediately see that the energy gain of the spin-polarized state is $D_0 h^2$. Importantly, this energy gain relies on having states around the Fermi level.

If we instead consider the effect of a spin-splitting field on the superconducting state, there are no states around the Fermi level due to the gap in the excitations spectrum. This is the reason why the energy of the superconducting state is not affected by a spin-splitting field smaller than the
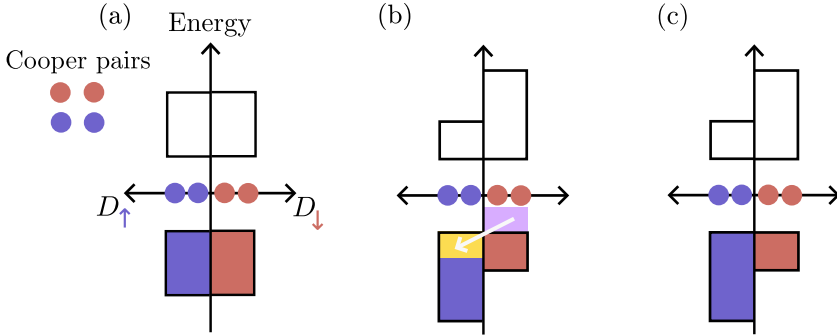
Figure 3.8: Polarized spin-triplet superconductor: (a) Density of states, assumed constant with a gap, for electron-like energy bands labelled by spin-↑ and spin-↓. States below the Fermi level are filled. We have also included the position along the energy axis of two sets of electrons at the Fermi surface forming Cooper pairs. (b) The introduction of a spin-splitting field shifts the bottom and top of the energy bands without affecting the gap around the Fermi surface. Some spin-↓ quasiparticles are therefore converted into spin-↑ quasiparticles. Although the particular electrons going into the Cooper pairs in (a) will be shifted by the field, it is now still possible for electrons at the Fermi surface to form Cooper pairs, as illustrated here. (c) The result is that the system becomes spin-polarized and lowers its energy.

gap. This situations is sketched in Fig. 3.7, where the picture e.g. can be connected to the calculations in the same way as above, but now with a nonzero gap. We have here neglected energy dependence of the density of states, and, for clarity, taken the gap in the spectrum to be enormous. We also show how the electrons going into the Cooper pairs are being separated from each other in energy.

One way of having superconductivity beyond the Chandrasekhar-Clogston limit can be to consider spin-triplet pairing instead of spin-singlet pairing. If we consider what we will refer to as polarized spin-triplet pairing with $\Delta_{\boldsymbol{k},\uparrow\uparrow} = \Delta_{\boldsymbol{k},\downarrow\downarrow}$ and $\Delta_{\boldsymbol{k},\uparrow\downarrow} = \Delta_{\boldsymbol{k},\downarrow\uparrow} = 0$, the quasiparticle energies instead take the form [72]

$$E_{\boldsymbol{k}\sigma} = \sqrt{\epsilon_{\boldsymbol{k}\sigma}^2 + |\Delta_{\sigma\sigma}|^2}. \tag{3.90}$$

We then see that there will be a gap $|\Delta_{\boldsymbol{k},\sigma\sigma}|$ above $E_{\boldsymbol{k}\sigma} = 0$ that does not move in energy with h. This is in contrast to the case of the spin-singlet pairing that we considered above where the energy of the lowest state above the Fermi level took the form $|\Delta| - h$. Describing the system through electron-like quasiparticles labeled by whether they are shifted up or down in energy under $h > 0$, we can then again draw a cartoon picture of the situation, as displayed in Fig. 3.8. We have here introduced a simplified gap rather than the partly gap that arises from a gap-function that change sign around the Fermi surface. From the figure, we see that this simple case captures that a spin-splitting field is able to spin-polarize the system, lowering its energy. Polarized spin-triplet pairing is therefore not restricted by the Chandrasekhar-Clogston limit.

Another way of going above the Chandrasekhar-Clogston limit is so-called FFLO pairing [73, 74]. In this case, electrons with opposite spin and momentum $\boldsymbol{k} + \boldsymbol{q}$ and $-\boldsymbol{k}$ form finite-momentum Cooper pairs with $\boldsymbol{q} \neq 0$ so that the energies of the electrons going into the Cooper pairs can be the same in the presence of spin-splitting. Spin-singlet superconductivity beyond the Chandrasekhar-Clogston limit may also be possible e.g. in the presence of spin-orbit coupling [75] or an applied voltage [76]. Further, in Chap. 6, we will discuss how the presence of a flat energy band in the band structure can influence the critical magnetic field of a superconductor.

3.3   Eliashberg theory

After having provided a thorough introduction to BCS theory and the BCS description of spin-split superconductors, we are now ready to move on to the somewhat more involved Eliashberg theory of superconductivity. We will be following the derivation in Ref. [77], considering a quite general case of electron-boson coupling as well as the specialization to phonon-mediated superconductivity. The general framework will be useful when we, in the next chapter, consider the Eliashberg treatment of magnon-mediated superconductivity presented in Paper [4].

The system is assumed to be described by a Hamiltonian

$$H = \sum_{\boldsymbol{k}\sigma} \epsilon_{\boldsymbol{k}} c^{\dagger}_{\boldsymbol{k}\sigma} c_{\boldsymbol{k}\sigma} + \sum_{\boldsymbol{q}\eta} \omega_{\boldsymbol{q}\eta} a^{\dagger}_{\boldsymbol{q}\eta} a_{\boldsymbol{q}\eta} + \sum_{\boldsymbol{k}\boldsymbol{q}} \sum_{\sigma\sigma'\gamma} f^{\sigma\sigma',\gamma}_{\boldsymbol{k},\boldsymbol{k}+\boldsymbol{q}} B_{\boldsymbol{q}\gamma}\, c^{\dagger}_{\boldsymbol{k}+\boldsymbol{q}\sigma'} c_{\boldsymbol{k}\sigma}, \qquad (3.91)$$

where $B_{\boldsymbol{q}\gamma}$ is a linear combination of boson operators. This equation represents a similar, but more general form, of the Hamiltonian we introduced for

the case of electron-phonon coupling. Similarly to earlier, we will treat the the two first terms as the unperturbed Hamiltonian H_0 and the electron-boson coupling as a perturbation H_1. The difference from our earlier approach is that we will now treat this perturbation in a many-body Green's function framework. We will be using the Matsubara Green's function formalism and a so-called S-matrix expansion to deal with the perturbation term H_1.

3.3.1   Matsubara formalism and S-matrix expansion

In the Matsubara, or imaginary-time, formalism, we can define a single-particle Green's function [78, 79]

$$\mathcal{G}_{\sigma\sigma'}(\boldsymbol{k}, \boldsymbol{k}', \tau) = -\big\langle T_\tau\big[c_{\boldsymbol{k}\sigma}(\tau)\, c^{\dagger}_{\boldsymbol{k}'\sigma'}(0)\big]\big\rangle, \tag{3.92}$$

where $\langle \dots \rangle$ denotes a thermodynamic average. Although we normally use the operators $c_{\boldsymbol{k}\sigma}$ to represent electrons, we, in the following, also comment on the bosonic case. The operators are in the Heisenberg picture and their time dependence is determined by

$$c_{\boldsymbol{k}\sigma}(\tau) = e^{H\tau} c_{\boldsymbol{k}\sigma} e^{-H\tau}, \tag{3.93a}$$

$$c^{\dagger}_{\boldsymbol{k}\sigma}(\tau) = e^{H\tau} c^{\dagger}_{\boldsymbol{k}\sigma} e^{-H\tau}, \tag{3.93b}$$

where τ is a real quantity. Further, the time-ordering operator T_τ puts the operators in order with earliest times furthest to the right

$$T_\tau\big[c_{\boldsymbol{k}\sigma}(\tau)\, c^{\dagger}_{\boldsymbol{k}'\sigma'}(0)\big] = \begin{cases} c_{\boldsymbol{k}\sigma}(\tau)\, c^{\dagger}_{\boldsymbol{k}'\sigma'}(0), & \tau > 0, \\ \xi c^{\dagger}_{\boldsymbol{k}'\sigma'}(0)\, c_{\boldsymbol{k}\sigma}(\tau), & \tau < 0, \end{cases} \tag{3.94}$$

where $\xi = -1$ for fermions and $\xi = +1$ for bosons. Bosonic/fermionic Matsubara Green's functions are further periodic/anti-periodic in imaginary time with period β, and their Fourier transformation can be expressed as

$$\mathcal{G}_{\sigma\sigma'}(\boldsymbol{k}, \boldsymbol{k}', i\omega_n) = \int_0^\beta \mathrm{d}\tau\, e^{i\omega_n\tau} \mathcal{G}_{\sigma\sigma'}(\boldsymbol{k}, \boldsymbol{k}', \tau), \tag{3.95}$$

$$\mathcal{G}_{\sigma\sigma'}(\boldsymbol{k}, \boldsymbol{k}', \tau) = \frac{1}{\beta} \sum_{\omega_n} e^{-i\omega_n\tau} \mathcal{G}_{\sigma\sigma'}(\boldsymbol{k}, \boldsymbol{k}', i\omega_n), \tag{3.96}$$

where ω_n are Matsubara frequencies. For fermions and bosons, they take the form

$$
\omega_n = \begin{cases} (2n+1)\pi/\beta, & \text{for fermions,} \\ 2n\pi/\beta, & \text{for bosons,} \end{cases} \tag{3.97}
$$

where n can take on the value of any integer, both positive and negative. We will, in the following, denote bosonic Matsubara frequencies by ν_m.

For simplicity, we first consider the case of non-interacting fermions, corresponding to the first term of the Hamiltonian in Eq. (3.91). We express the diagonal Green's function as $\mathcal{G}_{\sigma\sigma}(\boldsymbol{k},\boldsymbol{k},\tau) = \mathcal{G}_\sigma(\boldsymbol{k},\tau)$. One can then show that the diagonal, frequency dependent, non-interacting Green's function takes the form

$$
\mathcal{G}_\sigma^{(0)}(\boldsymbol{k}, i\omega_n) = \frac{1}{i\omega_n - \epsilon_{\boldsymbol{k}}}. \tag{3.98}
$$

Defining a Green's function specifically for the boson appearing in the second term of Eq. (3.91)

$$
\mathcal{B}_{\eta\eta'}(\boldsymbol{q}, \boldsymbol{q}', \tau) = -\big\langle T_\tau\big[a_{\boldsymbol{q}\eta}(\tau)\, a_{\boldsymbol{q}'\eta'}^\dagger(0)\big]\big\rangle, \tag{3.99}
$$

the diagonal, frequency dependent, non-interacting Green's function can similarly be expressed as

$$
\mathcal{B}_\eta^{(0)}(\boldsymbol{q}, i\nu_m) = \frac{1}{i\nu_m - \omega_{\boldsymbol{q}\eta}}. \tag{3.100}
$$

In order to deal with the interacting case, we perform an S-matrix expansion. We then rewrite the Green's function

$$
\mathcal{G}_\sigma(\boldsymbol{k}, \tau) = -\big\langle T_\tau\big[c_{\boldsymbol{k}\sigma}(\tau)\, c_{\boldsymbol{k}\sigma}^\dagger(0)\big]\big\rangle, \tag{3.101}
$$

where the operators are in the Heisenberg picture, as

$$
\mathcal{G}_\sigma(\boldsymbol{k}, \tau) = -\frac{\big\langle T_\tau\big[S(\beta)\,\hat{c}_{\boldsymbol{k}\sigma}(\tau)\,\hat{c}_{\boldsymbol{k}\sigma}^\dagger(0)\big]\big\rangle_0}{\big\langle S(\beta)\big\rangle_0}, \tag{3.102}
$$

where the operators are now in the interaction picture, denoted by hats, meaning that they are time-evolved by the unperturbed Hamiltonian H_0. The average is now also evaluated using the unperturbed Hamiltonian. The S matrix itself takes the form

$$S(\tau) = \sum_{n=0}^{\infty} \frac{(-1)^n}{n!} \int_0^\tau \mathrm{d}\tau_1 \ldots \int_0^\tau \mathrm{d}\tau_n \, T_\tau \big[\hat{H}_1(\tau_1) \ldots \hat{H}_1(\tau_n) \big]. \qquad (3.103)$$

Using Wicks theorem to transform average values of many operators into combinations of average values of pairs of operators, one can express the contributions to the interacting Green's function as a series of diagrams. Using the denominator of Eq. (3.102) to cancel contributions from the nominator taking the form of so-called disconnected diagrams, we are further left with only contributions from connected diagrams. Finally, taking into account that many of the diagrams represent identical contributions, the expression for the interacting Green's function is simplified to

$$\mathcal{G}_\sigma(\boldsymbol{k}, \tau) = -\sum_{n=0}^{\infty} (-1)^n \int_0^\beta \mathrm{d}\tau_1 \ldots \int_0^\beta \mathrm{d}\tau_n \left\langle T_\tau \big[\hat{c}_{\boldsymbol{k}\sigma}(\tau) \, \hat{H}_1(\tau_1) \ldots \hat{H}_1(\tau_n) \, \hat{c}^\dagger_{\boldsymbol{k}\sigma}(0) \big] \right\rangle_0', \qquad (3.104)$$

where only contributions from "different", connected diagrams are included [79].

3.3.2 S-matrix expansion in Eliashberg theory

Setting ourselves up for investigating the possibility of superconductivity arising from the Hamiltonian in Eq. (3.91), we define [77]

$$\psi^\dagger_{\boldsymbol{k}} = \begin{pmatrix} c^\dagger_{\boldsymbol{k}\uparrow} & c^\dagger_{\boldsymbol{k}\downarrow} & c_{-\boldsymbol{k}\uparrow} & c_{-\boldsymbol{k}\downarrow} \end{pmatrix}, \qquad (3.105)$$

on the same form as when we did BCS theory. We can then introduce a Green's function matrix

$$\hat{G}(\boldsymbol{k}, \tau) = -\left\langle T_\tau \big[\psi_{\boldsymbol{k}}(\tau) \otimes \psi^\dagger_{\boldsymbol{k}}(0) \big] \right\rangle, \qquad (3.106)$$

which takes the Fourier transformed form

$$\hat{G}(\boldsymbol{k}, i\omega_n) = \begin{pmatrix} G(\boldsymbol{k}, i\omega_n) & F(\boldsymbol{k}, i\omega_n) \\ \bar{F}(\boldsymbol{k}, i\omega_n) & \bar{G}(\boldsymbol{k}, i\omega_n) \end{pmatrix}, \qquad (3.107)$$

where

$$G(\boldsymbol{k}, i\omega_n) = \begin{pmatrix} \mathcal{G}_{\uparrow\uparrow}(\boldsymbol{k}, i\omega_n) & \mathcal{G}_{\uparrow\downarrow}(\boldsymbol{k}, i\omega_n) \\ \mathcal{G}_{\downarrow\uparrow}(\boldsymbol{k}, i\omega_n) & \mathcal{G}_{\downarrow\downarrow}(\boldsymbol{k}, i\omega_n) \end{pmatrix}, \qquad (3.108)$$

and $\bar{G}(\boldsymbol{k}, i\omega_n)$ similarly is a matrix of Fourier transformed Green's functions

$$\bar{\mathcal{G}}_{\sigma\sigma'}(\boldsymbol{k}, \tau) = -\langle T_\tau [c^\dagger_{-\boldsymbol{k}\sigma}(\tau)\, c_{-\boldsymbol{k}\sigma'}(0)]\rangle. \qquad (3.109)$$

The additional anomalous Green's function matrices $F(\boldsymbol{k}, i\omega_n)$ and $\bar{F}(\boldsymbol{k}, i\omega_n)$ are further matrices of the Fourier transformed anomalous Green's functions

$$\mathcal{F}_{\sigma\sigma'}(\boldsymbol{k}, \tau) = -\langle T_\tau [c_{\boldsymbol{k}\sigma}(\tau)\, c_{-\boldsymbol{k}\sigma'}(0)]\rangle, \qquad (3.110)$$

and

$$\bar{\mathcal{F}}_{\sigma\sigma'}(\boldsymbol{k}, \tau) = -\langle T_\tau [c^\dagger_{-\boldsymbol{k}\sigma}(\tau)\, c^\dagger_{\boldsymbol{k}\sigma'}(0)]\rangle. \qquad (3.111)$$

The anomalous Green's functions are included in order to capture the possibility of superconductivity associated with pairing of electrons. From the definition of $F(\boldsymbol{k}, \tau)$ in combination with electrons being fermions, it follows that

$$F(\boldsymbol{k}, i\omega_n) = -F(-\boldsymbol{k}, -i\omega_n)^T, \qquad (3.112)$$

representing that the pairing correlations are odd under the combined operation of exchange of spin, position/momentum, and time/frequency. Compared to the spin and momentum dependent pairing correlations $b_{\boldsymbol{k},s's} = \langle c_{-\boldsymbol{k}s} c_{\boldsymbol{k}s'}\rangle$ we defined earlier, we now have an additional frequency-dependence. This opens up the possibility for odd-frequency pairing [80], allowing for e.g. pairing with spin-triplet s-wave symmetry.

In the same spirit as above, we can also collect the relevant combinations

of boson operators $B_{\boldsymbol{q}}^{\dagger} = \left(\{B_{\boldsymbol{q}\gamma}^{\dagger}\}\right)$ and define a matrix of bosonic Green's functions

$$\hat{D}(\boldsymbol{q},\tau) = -\langle T_{\tau}[B_{\boldsymbol{q}}(\tau) \otimes B_{\boldsymbol{q}}^{\dagger}(0)]\rangle. \tag{3.113}$$

As discussed in Ref. [77], one can further introduce a symmetrized form of the interaction Hamiltonian

$$H_1 = \frac{1}{2} \sum_{\boldsymbol{k}\boldsymbol{q}} \sum_{\delta\epsilon\gamma} f_{\boldsymbol{k},\boldsymbol{k}+\boldsymbol{q}}^{\delta\epsilon,\gamma} B_{\boldsymbol{q}\gamma} \psi_{\boldsymbol{k}+\boldsymbol{q}\delta}^{\dagger}\psi_{\boldsymbol{k}\epsilon}. \tag{3.114}$$

with new coefficients g depending on the indices δ, ϵ instead of spin-indices.

Using the symmetrized expression for H_1 in the expansions for the interacting Green's functions, the expansions can be expressed on the form

$$\hat{G}(k) = \hat{G}_0(k) + \hat{G}_0(k)\,\Sigma(k)\,\hat{G}(k), \tag{3.115a}$$
$$\hat{D}(q) = \hat{D}_0(q) + \hat{D}_0(q)\,\Pi(q)\,\hat{D}(q), \tag{3.115b}$$

with the associated Dyson equations

$$\hat{G}^{-1}(k) = \hat{G}_0^{-1}(k) - \Sigma(k), \tag{3.116a}$$
$$\hat{D}^{-1}(q) = \hat{D}_0^{-1}(q) - \Pi(q). \tag{3.116b}$$

Here, $\hat{G}_0$ and $\hat{D}_0$ are matrices of non-interacting Green's functions and we have introduced the compact notation $k = (\boldsymbol{k}, i\omega_n)$, $q = (\boldsymbol{q}, i\nu_m)$. Further, the expressions for the self-energies take the form

$$\Sigma_{\delta\epsilon}(k) = -\frac{1}{\beta} \sum_{q} \sum_{\gamma\gamma'} \sum_{\delta'\epsilon'} \hat{D}_{\gamma\gamma'}(q)\, f_{\boldsymbol{k},\boldsymbol{k}-\boldsymbol{q}}^{\delta\delta',\gamma}\, \hat{G}_{\delta'\epsilon'}(k-q)\, \Lambda_{k-q,k}^{\epsilon'\epsilon,\gamma'}, \tag{3.117a}$$

$$\Pi_{\gamma\gamma'}(q) = \frac{1}{4\beta} \sum_{k} \sum_{\delta\delta'} \sum_{\epsilon\epsilon'} f_{\boldsymbol{k},\boldsymbol{k}+\boldsymbol{q}}^{\delta\delta',\gamma}\, \hat{G}_{\delta'\epsilon'}(k+q)\, \Lambda_{k+q,k}^{\epsilon'\epsilon,\gamma'}\, \hat{G}_{\epsilon\delta}(k). \tag{3.117b}$$

A diagrammatic representation of the expansions can be found in Paper [4], slightly specialized to the magnon case studied there, while the more general version is presented in Ref. [77]. The expansion for e.g. the elements of

$\hat{G}$ now takes the form of series of self-energy diagrams contained in Σ connected by fermionic Green's functions. Each connection is associated with a factor f and involves two fermionic Green's functions and one bosonic Green's function, corresponding to the structure of the electron-boson interaction in the Hamiltonian. In the absence of so-called vertex corrections, $\Lambda \to f$, and the structure of the self-energy diagrams in terms of interacting Green's functions becomes simple. In the presence of vertex corrections, the self-energy diagrams keep their simple form, but vertices where electron and boson Green's functions meet may be renormalized, capturing contributions from more complicated diagrams. We discuss vertex corrections in more detail later in this chapter.

We then have the foundation that we need in order to investigate superconductivity arising in systems that can be described by a Hamiltonian on the form of Eq. (3.91). In this chapter, we will focus on phonon-mediated superconductivity.

3.3.3 Phonon-mediated superconductivity

We earlier introduced a Hamiltonian for a coupled system of electrons and phonons in Eq. (3.49). Writing the coupling term in this Hamiltonian on the symmetrized form of Eq. (3.114), using the normal symmetry relations for the electron-phonon coupling strength $g_{\boldsymbol{k},\boldsymbol{k}+\boldsymbol{q}}$, we obtain [77]

$$f^{\delta\epsilon,\gamma}_{\boldsymbol{k},\boldsymbol{k}+\boldsymbol{q}} = f^{\delta\epsilon}_{\boldsymbol{k},\boldsymbol{k}+\boldsymbol{q}} = g_{\boldsymbol{k},\boldsymbol{k}+\boldsymbol{q}} \begin{pmatrix} 1 & 0 & 0 & 0 \\ 0 & 1 & 0 & 0 \\ 0 & 0 & -1 & 0 \\ 0 & 0 & 0 & -1 \end{pmatrix}_{\delta\epsilon} = g_{\boldsymbol{k},\boldsymbol{k}+\boldsymbol{q}}(\tau_3 \otimes \sigma_0)_{\delta\epsilon}, \quad (3.118)$$

where τ_3 and σ_0 are Pauli matrices acting on the particle/hole and spin degree of freedom, respectively. Moreover, $B_{\boldsymbol{q}\gamma} = B_{\boldsymbol{q}} = a_{\boldsymbol{q}} + a^{\dagger}_{-\boldsymbol{q}}$, leading to

$$\hat{D}_{\gamma\gamma'}(q) = \mathcal{D}(q), \qquad (3.119)$$

which in the non-interacting case takes the form

$$\mathcal{D}^{(0)}(q) = -\frac{2\omega_{\boldsymbol{q}}}{\nu_m^2 + \omega_{\boldsymbol{q}}^2}. \qquad (3.120)$$

We further neglect the effect of vertex corrections, which we return to in Sec. 3.3.5. We then have, on matrix form,

$$\Sigma(k) = -\frac{1}{\beta} \sum_q |g_{\boldsymbol{k},\boldsymbol{k-q}}|^2 \mathcal{D}(q)\,(\tau_3\sigma_0)\,\hat{G}(k-q)\,(\tau_3\sigma_0), \qquad (3.121\text{a})$$

$$\Pi(q) = \frac{1}{4\beta} \sum_k |g_{\boldsymbol{k},\boldsymbol{k+q}}|^2 \operatorname{Tr}\big[(\tau_3\sigma_0)\,\hat{G}(k+q)\,(\tau_3\sigma_0)\hat{G}(k)\big]. \qquad (3.121\text{b})$$

Although these are less complicated than the more general equations for the self-energies, we still see that we cannot simply calculate the self-energies $\Sigma(k)$ and $\Pi(q)$ as the right-hand sides of the equations involve interacting Green's functions.

From our experience with BCS theory, we expect the pairing to have spin-singlet symmetry, motivating an Ansatz for the electron self-energy matrix

$$\Sigma(k) = [1 - Z(k)]i\omega_n\tau_0\sigma_0 + \chi(k)\,\tau_3\sigma_0 + \phi_s(k)\,\tau_2\sigma_2. \qquad (3.122)$$

The quantity Z here represents a quasiparticle renormalization, while χ is a shift of the quasiparticle energies, and ϕ_s is a pairing amplitude for spin-singlet pairing as σ_2 makes the pairing odd in spin. Using this Ansatz for the electron self-energy matrix, the Dyson equation for the interacting electron Green's function becomes

$$\hat{G}^{-1}(k) = i\omega_n Z(k)\,\tau_0\sigma_0 - \tilde{\xi}_k\,\tau_3\sigma_0 - \phi_s(k)\,\tau_2\sigma_2, \qquad (3.123)$$

where we have used that $\hat{G}_0^{-1} = i\omega_n\tau_0\sigma_0 - \epsilon_{\boldsymbol{k}}\tau_3\sigma_0$ and defined $\tilde{\xi}_k = \epsilon_{\boldsymbol{k}} + \chi(k)$. By inverting this matrix, we can then obtain an expression for the interacting electron Green's function matrix in terms of the different contributions to the electron self-energy matrix. We can then plug this expression for $\hat{G}$ into the expression for the electron self-energy matrix in Eq. (3.121a). The result is then a set of self-consistent equations for the quantities Z, χ, and ϕ_s [77]

$$[1 - Z(k)]i\omega_n = -\frac{1}{\beta}\sum_{k'}|g_{\mathbf{k},\mathbf{k'}}|^2\,\mathcal{D}(k - k')\frac{i\omega_{n'}Z(k')}{\Theta(k')}, \qquad (3.124)$$

$$\chi(k) = -\frac{1}{\beta}\sum_{k'}|g_{\mathbf{k},\mathbf{k'}}|^2\,\mathcal{D}(k - k')\frac{\tilde{\xi}_{k'}}{\Theta(k')}, \qquad (3.125)$$

$$\phi_s(k) = +\frac{1}{\beta}\sum_{k'}|g_{\mathbf{k},\mathbf{k'}}|^2\,\mathcal{D}(k - k')\frac{\phi_s(k')}{\Theta(k')}, \qquad (3.126)$$

which are referred to as the Eliashberg equations. We have here introduced

$$\Theta(k) = [i\omega_n Z(k)]^2 - \tilde{\xi}_k^2 - |\phi_s(k)|^2. \qquad (3.127)$$

In order to start solving these equations, we see that we also need an explicit expression for the interacting phonon propagator $\mathcal{D}(q)$. As this is now a scalar quantity, we simply have from the phonon Dyson equation that

$$\mathcal{D}(q) = \frac{\mathcal{D}^{(0)}(q)}{1 - \Pi(q)\mathcal{D}^{(0)}(q)}. \qquad (3.128)$$

In principle, we should now solve the coupled self-consistent equations for Z, χ, ϕ_s and Π. A common simplification is, however, to neglect the effect of the quasiparticle renormalization χ and the phonon renormalization $\Pi(q)$. In that case, we are left with a coupled set of two self-consistent equations. The first one determines renormalization of the electrons that are being paired, which is an effect of the electron-phonon coupling that we did not capture earlier. The second equation determines the pairing amplitude ϕ_s, and has a structure somewhat similar to the gap equation we encountered within BCS theory. The similarities include the fact that the pairing amplitude for momentum $\mathbf{k}$ is determined by a sum over the pairing amplitudes at other momenta, multiplied by a factor $|g_{\mathbf{k},\mathbf{k'}}|^2\,\mathcal{D}^{(0)}(k - k')$ reminiscent of a interaction potential, and where, simply stated, contributions from momenta far away from the Fermi surface are suppressed by some additional function here taking the form $1/\Theta(k) \sim 1/\epsilon_{\mathbf{k}}^2$. There are, however, also some considerable differences between the BCS gap equation and the pairing amplitude equation we have now encountered. The main difference is that we are now summing the right-hand-side also over frequency as both e.g. the pairing amplitude and the phonon propagator has a

frequency dependence. Importantly, this additional frequency dependence does not represent a small correction to the equation, but instead plays an essential part. This can be seen right away by inspecting the expression for the non-interacting phonon propagator

$$\mathcal{D}^{(0)}(q) = -\frac{2\omega_{\boldsymbol{q}}}{\nu_m^2 + \omega_{\boldsymbol{q}}^2},$$

where we see that rather than coming in as an additional correction, the frequency ν_m appears to have replaced the fermion energies that were present in the effective interaction potential

$$V_{\boldsymbol{k}\boldsymbol{k}'} = -|g_{\boldsymbol{k}',\boldsymbol{k}}|^2 \frac{2\omega_{\boldsymbol{k}'-\boldsymbol{k}}}{-(\epsilon_{\boldsymbol{k}'} - \epsilon_{\boldsymbol{k}})^2 + \omega_{\boldsymbol{k}'-\boldsymbol{k}}^2}.$$

In order to simplify the equations for Z and ϕ_s, we start by working on the momentum dependence. Our strategy will, like earlier, be to go over to an integral over momentum and to divide the integral up into integration along and normal to surfaces of constant energy ϵ. As commented above, we see that the right-hand-side of the equations will be suppressed by the factor $1/\Theta(k')$ when $\boldsymbol{k}'$ is moved far away from the Fermi surface. The phonon-propagator, on the other hand, is not suppressed by the fermionic energy scale when $\boldsymbol{k}'$ is moved away from the Fermi surface. We therefore fully neglect the dependence of the phonon propagator on perpendicular momentum $\boldsymbol{k}'_\perp$, in contrast to the BCS case where the behavior of the interaction potential as a function of perpendicular momentum away from the Fermi surface was assumed to take the form of a constant with a cutoff. We also neglect the perpendicular momentum dependence of the electron-phonon coupling strength g, the pairing amplitude ϕ, and the quasiparticle renormalization Z. Going over to an integral over ϵ, we assume the Fermi surface to be isotropic and approximate the density of states by its value at the Fermi surface. Finally, we also average both sides of the equations over $\boldsymbol{k}$ on the Fermi surface and introduce an s-wave Ansatz for the pairing amplitude and the quasiparticle renormalization. The two remaining Eliashberg equations then take the form

$$[1 - Z(i\omega_n)]i\omega_n = +\frac{1}{\beta}\sum_{i\omega_{n'}}\lambda(i\omega_n - i\omega_{n'})\,i\omega_{n'}Z(i\omega_{n'})\int \frac{\mathrm{d}\epsilon}{\Theta(\epsilon, i\omega_{n'})}, \quad (3.129)$$

$$\phi_s(i\omega_n) = -\frac{1}{\beta}\sum_{i\omega_{n'}}\lambda(i\omega_n - i\omega_{n'})\phi_s(i\omega_{n'})\int \frac{\mathrm{d}\epsilon}{\Theta(\epsilon, i\omega_{n'})}, \quad (3.130)$$

where we now have

$$\Theta(\epsilon, i\omega_{n'}) = [i\omega_{n'}Z(i\omega_{n'})]^2 - \epsilon^2 - |\phi_s(i\omega_{n'})|^2, \quad (3.131)$$

as well as

$$\lambda(i\omega_n - i\omega_{n'}) = -D_0\langle |g_{\boldsymbol{k},\boldsymbol{k}'}|^2\,\mathcal{D}^{(0)}(k - k')\rangle_{\boldsymbol{k},\boldsymbol{k}',\mathrm{FS}}. \quad (3.132)$$

Here, D_0 is the density of states at the Fermi surface. We then take the integration limits for ϵ to $\pm\infty$ and perform the integral, producing

$$Z(\omega_n) = 1 + \frac{\pi}{\beta\omega_n}\sum_{\omega_{n'}}\frac{\lambda(\omega_n - \omega_{n'})}{\sqrt{[\omega_{n'}Z(\omega_{n'})]^2 + |\phi_s(\omega_{n'})|^2}}\omega_{n'}Z(\omega_{n'}), \quad (3.133)$$

$$\phi_s(\omega_n) = \frac{\pi}{\beta}\sum_{\omega_{n'}}\frac{\lambda(\omega_n - \omega_{n'})}{\sqrt{[\omega_{n'}Z(\omega_{n'})]^2 + |\phi_s(\omega_{n'})|^2}}\phi_s(\omega_{n'}). \quad (3.134)$$

We then have two frequency-dependent, coupled, self-consistent equations which should be solved. As $\lambda(\nu_m)$ has been defined to carry a positive sign, it appears that a nontrivial solution for ϕ_s could be possible.

In order to calculate the critical temperature, one can approach this temperature from below, in which case ϕ_s can be neglected in the square roots in the denominator of the right-hand-side of the equations. In that case, the equation for Z no longer depends on ϕ_s, and we can simply calculate Z directly. The problem is then reduced to a single eigenvalue problem. Considering a finite set of Matsubara frequencies, one can then, for a given temperature, find the largest eigenvalue with associated eigenvector through either matrix diagonalization or through iteration. The largest temperature where there is a solution to the equation for ϕ_s with eigenvalue 1 is then the critical temperature.

We will not go more into the details of numerical solutions of these equations. In order to help interpret what is going on, we will instead make

some comments about approximate formulas for the critical temperature. Similarly to what we did for BCS theory, one could, now as a function of frequency, approximate the phonon propagator by a constant with a cutoff at $|\nu_m| = \omega_c$. One can then arrive at an expression [81]

$$T_c^{\text{R}} = 1.13\,\omega_c \exp\left(-\frac{[1 + \lambda(0)]}{\lambda(0)}\right). \tag{3.135}$$

A more refined approximate expression takes the form [82]

$$T_c^{\text{AD}} = \frac{\omega_{\log}}{1.2} \exp\left(-\frac{1.04[1 + \lambda(0)]}{\lambda(0)}\right), \tag{3.136}$$

where $\lambda(0)$ should not be too large for the formula to be accurate. The quantity $\omega_{\log}$ is here an effective cutoff obtained from

$$\omega_{\log} = \omega_a \exp\left(\frac{2D_0}{\lambda(0)}\langle \ln(\omega_{\boldsymbol{k}-\boldsymbol{k}'}/\omega_a)\,|g_{\boldsymbol{k},\boldsymbol{k}'}|^2/\omega_{\boldsymbol{k}-\boldsymbol{k}'}\rangle_{\boldsymbol{k},\boldsymbol{k}',\text{FS}}\right), \tag{3.137}$$

where ω_a is an arbitrary energy scale. As the expression for $\lambda(0)$ takes the form

$$\lambda(0) = 2D_0\langle |g_{\boldsymbol{k},\boldsymbol{k}'}|^2/\omega_{\boldsymbol{k}-\boldsymbol{k}'}\rangle_{\boldsymbol{k},\boldsymbol{k}',\text{FS}}, \tag{3.138}$$

we may interpret $\ln(\omega_{\log})$ as an average over $\ln(\omega_{\boldsymbol{q}})$ weighted by how much the different phonon energies contribute to the zero-frequency electron-phonon interaction. Assuming an Einstein spectrum of phonon with only a single phonon frequency ω_E naturally produces $\omega_{\log} = \omega_E$, leading to a prefactor in the T_c formula of the order ω_E. The above formulas can also be extended to include Coulomb interaction, which is a topic we are saving for the next section.

Going back to our Schrieffer-Wolff/BCS treatment and assuming s-wave pairing as well as a phonon-mediated interaction without neglecting the momentum dependence of the interaction around the Fermi surface, one can put the dimensionless coupling constant λ on exactly the same form as the expression for $\lambda(0)$ in Eq. (3.138). This arises from the fact that the magnon propagator and the fraction in the effective interaction potential we obtained

for phonons are equivalent for the special case of zero frequency/electrons on the Fermi surface. As the additional term $\lambda(0)$ in the numerator of the exponential in the above T_c formulas can be taken to introduce a rescaling of the factor in front of the exponential, we see that the BCS expression

$$T_c^{\mathrm{BCS}} = 1.13\,\omega_c \exp\left(-1/\lambda\right),$$

captures the exponential dependence of T_c on $\lambda(0)$.

We also see that the prefactor in the T_c formula in Eq. (3.136), for the case of the Einstein phonons, turns out to not differ that dramatically between BCS theory and Eliashberg theory. Moreover, we see more generally from Eq. (3.135) that if, simply stated, the behavior of $\lambda(\nu_m)$ with increasing $|\nu_m|$ is somewhat reasonably approximated by a constant with a cutoff determined by the cutoff on the phonon spectrum, Eliashberg theory and the Schrieffer-Wolff/BCS approach we have outlined seem to not disagree strongly on the behavior of the critical temperature. In the BCS framework, this then loosely corresponds to our assumption about contributions to the gap equation from the interaction potential when we move electrons away from the Fermi surface being reasonably approximated by taking the perpendicular momentum dependence of the derived interaction potential on the form of a constant with a cutoff ω_c. If the derived interaction potential somehow differs substantially from this behavior, the outlined BCS approach might not capture the relevant energy scale for the critical temperature. However, as the effective potential still reproduces $\lambda(0)$, the approach is seemingly still capturing an important part of what is going on in the system. Within BCS theory, sticking to our simple Ansatz for the dependence of the interaction potential on perpendicular momentum, even if it does not appear that reasonable, might therefore not necessarily be an inferior approach compared to attempting to use the detailed perpendicular momentum dependence of the effective interaction potential to account for the detailed frequency dependence of $\lambda(\nu_m)$. One could, in addition, also attempt to argue for a different cutoff on the interaction potential than the cutoff on the phonon spectrum. The best option would, of course, be to simply identify that it might be necessary to go to Eliashberg theory.

Above, we have tried to explain why the BCS theory we have outlined sometimes captures more of what is going on in the system, at least for sufficiently small λ, than one might expect based on the roughness of the theory. In order to balance the story, we should also highlight some of the

shortcomings of the theory. In general, it is not necessarily so easy to know, while working within the BCS framework, what parts of the physics of the system the theory is actually accurately capturing without relying on input from more refined approaches. One should therefore clearly be very careful with putting too much faith in the theory's predictive abilities. We are further not able to easily include the effect of e.g. electron and phonon renormalization. In addition to introducing inaccuracies this also contributes to making it more difficult to keep track of whether the theory can be justified or not. For a more accurate, controlled, and thorough description of the properties of superconductors for comparison with experiments, Eliashberg theory is obviously a better option.

3.3.4   Coulomb interaction

As the Eliashberg theory outlined in the previous section neglected Coulomb interaction, there is naturally a question about how the effect of Coulomb interaction enters in Eliashberg theory. In the BCS framework, we saw that the effect of Coulomb interaction turned out to be less destructive than one might have naively expected. The picture for why this happens will become clearer in this section.

   The effect of Coulomb interaction on the system is, in general, hard to take into account [81]. One therefore typically assumes that renormalization due to Coulomb is already included in the starting model and consider the effect of the presence of a repulsive and frequency-independent interaction in the pairing amplitude equations. For simplicity, we further neglect the momentum dependence of the Coulomb interaction. The equation for the pairing amplitude in Eq. (3.130) is then modified to

$$\phi_s(i\omega_n) = -\frac{1}{\beta} \sum_{i\omega_{n'}} [\lambda(i\omega_n - i\omega_{n'}) - \lambda_C]\phi_s(i\omega_{n'}) \int \frac{d\epsilon}{\Theta(\epsilon, i\omega_{n'})}, \qquad (3.139)$$

where $\lambda_C = D_0' U$, or more generally a Fermi surface average if the momentum dependence of the Coulomb interaction around the Fermi surface is kept. As λ and λ_C are both positive quantities, we see that Coulomb repulsion will tend to weaken the pairing. Linearizing the equation and performing the energy integral without taking the integration limits to infinity, we obtain for the case of particle-hole symmetry

$$\phi_s(i\omega_n) = \frac{1}{\beta} \sum_{\omega_{n'}} \left[\lambda(i\omega_n - i\omega_{n'}) - \lambda_C \right] \phi_s(i\omega_{n'})$$

$$\times \frac{1}{\omega_{n'} Z(i\omega_{n'})} \left[\tan^{-1} \left(\frac{\epsilon}{\omega_{n'} Z(i\omega_{n'})} \right) \right]_{-W}^{W} . \tag{3.140}$$

Normally, we have that λ dies off above some frequency $\omega_p \ll W$ representing the phonon energy scale. In that case we can take $\pm W \to \pm\infty$. In the present case, the quantity λ_C does not exhibit such a decay with respect to frequency. We then need to keep the integration limits. We next split the pairing amplitude up into two parts $\phi_s(i\omega_n) = \phi_1(i\omega_n) + \phi_2$ [83]. The first part is assumed to only be nonzero for $|\omega_n| < \omega_p$, while the other part is assumed to not depend on frequency. Above the cutoff frequency, we further expect that $Z \approx 1$. We then split the pairing amplitude equation up into two parts

$$\phi_1(i\omega_n) = \frac{\pi}{\beta} \sum_{|\omega_{n'}| < \omega_p} \lambda(i\omega_n - i\omega_{n'}) \frac{\phi(i\omega_{n'})}{|\omega_{n'}||Z(i\omega_{n'})|}, \tag{3.141}$$

and

$$\phi_2 = -\frac{\lambda_C}{\beta} \left[\pi \sum_{|\omega_{n'}| < \omega_p} \frac{\phi(i\omega_{n'})}{|\omega_{n'}||Z(i\omega_{n'})|} + \sum_{|\omega_{n'}| > \omega_p} \frac{\phi_2}{\omega_{n'}} \left[\tan^{-1} \left(\frac{\epsilon}{\omega_{n'}} \right) \right]_{-W}^{W} \right]. \tag{3.142}$$

Solving this equation for ϕ_2, we obtain

$$\phi_2 = -\frac{\pi}{\beta} \sum_{|\omega_{n'}| < \omega_p} \mu^* \frac{\phi(i\omega_{n'})}{|\omega_{n'}||Z(i\omega_{n'})|}, \tag{3.143}$$

where

$$\mu^* = \frac{\lambda_C}{1 + \frac{\lambda_C}{\beta} \sum_{|\omega_{n'}| > \omega_p} \frac{1}{\omega_{n'}} \left[\tan^{-1} \left(\frac{\epsilon}{\omega_{n'}} \right) \right]_{-W}^{W}} . \tag{3.144}$$

Combining back together the two parts of the pairing amplitude equation, we are then left with

$$\phi(i\omega_n) = \frac{\pi}{\beta} \sum_{|\omega_{n'}|<\omega_p} \left[\lambda(i\omega_n - i\omega_{n'}) - \mu^* \right] \frac{\phi(i\omega_{n'})}{|\omega_{n'}||Z(i\omega_{n'})|}. \tag{3.145}$$

Doing some further work on the expression for μ^* [83], one can then obtain that

$$\mu^* = \frac{\lambda_C}{1 + \lambda_C \ln\left(\frac{W}{\omega_p}\right)}, \tag{3.146}$$

which is simply the expression we obtained within BCS theory for $\omega_p = \omega_c$. We then see that the effect of Coulomb interaction, once again, is suppressed. This time, the suppression arises from the fact that the electron-phonon interaction is only active at low frequencies, determined by the energy scale of the phonons, in contrast to the Coulomb interaction. As small frequencies correspond to large times, a useful picture is then that the electron-phonon interaction acts over much longer time-scales than the Coulomb interaction. Electrons are therefore able to interact with each other attractively through coupling to phonons without having to be close to each other, thereby avoiding the Coulomb repulsion.

3.3.5 Vertex corrections

Vertex corrections are usually neglected on the basis of Migdal's theorem [56], stating that higher-order diagrams are smaller by a factor determined by the phonon energy scale divided by the electron energy scale. In order to see an indication of this, we consider a quick estimate of the type presented in Ref. [78]. Neglecting, for simplicity, the momentum dependence of the unrenormalized vertex $g_{\boldsymbol{k-q},\boldsymbol{k}}$, the renormalized vertex can be expressed as $g[1 + \Gamma(k - q, k)]$. The lowest-order diagram renormalizing the vertex gives a contribution

$$\Gamma_1(k - q, k) = \frac{1}{\beta} \sum_{q'} |g|^2 \mathcal{G}(k - q') \mathcal{G}(k - q' - q) \mathcal{D}(q'), \tag{3.147}$$

and is presented in Fig. 3.9, where we approximate the electron and phonon Green's functions by their non-interacting forms. For the non-interacting phonon Green's function we take $|\mathcal{D}^{(0)}(q)| \sim 1/\omega_p$ for $|\nu_m| < \omega_p$. Above
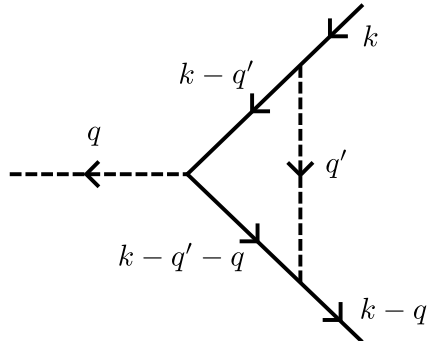
Figure 3.9: Lowest-order diagram correcting the interaction vertices. Dotted lines represent phonon propagators, while solid lines represent electron propagators.

ω_p, the phonon Green's function is assumed to vanish. We will then have contributions from around $\sim \beta\omega_p$ terms in the frequency sum. For the N terms in the momentum sum, the electrons will typically be away from the Fermi level. We therefore approximate the electron Green's functions by $1/E_F$, where the Fermi energy is taken as a measure of the electron energy scale. We then obtain the estimate

$$|\Gamma_1(k-q,k)| \sim \frac{N\,|g|^2}{E_F^2}. \tag{3.148}$$

This estimate would indicate that vertex corrections can be neglected if the energy scale of the electron-phonon coupling is considerably smaller than the electron energy scale. One can further put this estimate on the more famous form [78]

$$|\Gamma_1(k-q,k)| \sim \lambda(0)\frac{\omega_p}{E_F}, \tag{3.149}$$

indicating that vertex corrections can typically be neglected due to the separation of energy scales between phonons and electrons.

In the above estimate, it was assumed that the typical contributions involve the electrons with momentum $\boldsymbol{k}-\boldsymbol{q'}$ and $\boldsymbol{k}-\boldsymbol{q}-\boldsymbol{q'}$ being away from

the Fermi surface. One can also attempt to perform an estimate focusing on
the specific contributions where q' is restricted to keep either $k - q'$ or both
$k - q'$ and $k - q' - q$ close to the Fermi surface [81]. In that case, one typically
finds that the increase provided by the fermion Green's functions is com-
pensated by the reduction of terms in the momentum sum that contribute
to the expression. An exception is the special case of small q, in which case
simply restricting $k - q'$ to be close to the Fermi surface can ensure that
also $k - q' - q$ is kept close to the Fermi surface. Migdal's theorem can
therefore break down for the case of long-wavelength phonons. Luckily, the
importance of such phonons is reduced due to the electron-phonon coupling
vanishing for zero-momentum phonons. Migdal's theorem may also break
down for the case of nested Fermi surfaces [78]. In this case there can be
a substantial number of momenta q where again restricting the momentum
sum to keep one additional electron close to the Fermi surface instead leads
to two additional electrons ending up close to the Fermi surface. More-
over, Migdal originally considered the case of a three-dimensional system,
and vertex corrections can, in general, be of larger importance in lower-
dimensional systems [84, 85].

3.4   Superconductivity from spin fluctuations

Although we have kept parts of the discussion quite general, we have in this
chapter mainly focused on phonon-mediated superconductivity. The simple
picture we presented was that negatively charged electrons can interact at-
tractively with each other with help from the positively charged ionic lattice.
The ionic lattice then acts as a polarizable medium that allows electrons to
interact with each other indirectly. As electrons not only have charge, but
also spin, one could imagine that a collection of spins also could act as a
polarizable medium, giving rise to indirect interaction between electrons.

   The collection of spins could, for instance, be ordered localized spins.
In that case, one could imagine that an itinerant electrons can flip a local-
ized spins, creating a disturbance in the magnetic order that can couple to
another itinerant electron. An illustration of this for the case of ferromag-
netic ordering of the localized spins is shown in Fig. 3.10 (a). The potential
for resulting magnon-mediated superconductivity has e.g. been discussed in
Refs. [86–88]. Indirect interaction between electrons mediated by magnons
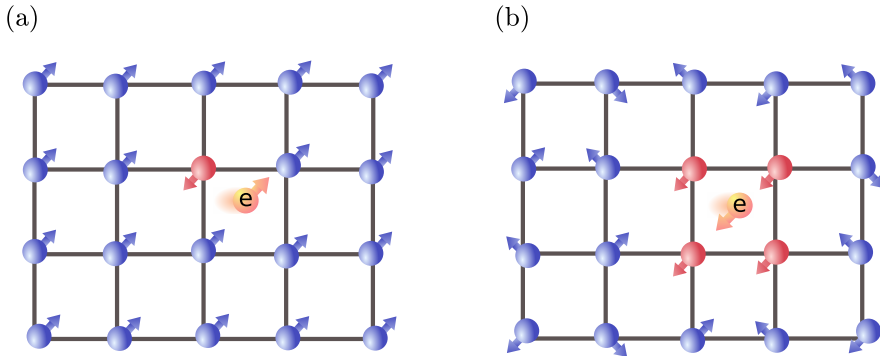could be thought to be of relevance for the observed superconductivity in

Figure 3.10: An itinerant electron interacting with a collection of (a) localized and ferromagnetically ordered spins, and (b) localized and nearly ferromagnetically ordered spins which can easily be polarized by the itinerant electron.

heavy fermion systems, named for their ability to host electrons with large effective mass. In these materials, itinerant electrons can mediate indirect interaction between localized spins, potentially giving rise to antiferromagnetic order [89, 90]. One could then further imagine that fluctuations in the magnetic order could give rise to attractive interaction between itinerant electrons. The picture is, however, not quite as simple as described above as the itinerant electrons themselves are important for establishing magnetic order in the first place. Heavy fermion superconductivity is also typically found to takes place at the brink of magnetic ordering, rather than well inside a magnetic phase [89]. Moreover, the strongly correlated nature of the systems further complicates the problem. Although most likely too simple of a picture to properly describe the origin of superconductivity in typical heavy fermion systems, the magnon-mediated interaction described above could still be a potential mechanism, or at least a useful starting point for describing mechanisms, for superconductivity in systems featuring itinerant electrons and localized magnetic order.

Nearly ordered collections of spins, consisting of localized or delocalized spins, could also provide an indirect interaction between electrons. In this case, one can imagine an itinerant electron polarizing the surrounding spin-system, creating a locally ordered region that can attract another itinerant electron [64]. An illustration of this is presented in Fig. 3.10 (b) for the case

of nearly ferromagnetically ordered localized spins. The interaction is in this case mediated by paramagnons, representing short-ranged spin-waves. Paramagnon exchange was first identified as the pairing mechanism for p-wave superfluidity in ^{3}He [91, 92], and has later been proposed as a potential mechanism for superconductivity in both heavy fermion systems [93–95], as well as in high-T_c cuprates [96, 97]. Similarly to many heavy fermion superconductors, the superconducting phase of cuprates take place in proximity to an antiferromagnetic phase [98]. The antiferromagnetic phase of cuprates can be considered to arise from Coulomb repulsion giving rise to antiferromagnetic Mott insulating behavior, as captured in the Hubbard model close to half-filling. Going away from half-filling in the Hubbard model, paramagnon exchange has, as highlighted in Paper [4], been proposed to give rise to p-wave pairing for small Fermi surfaces and d-wave pairing closer to half-filling [94]. The electrons going into the Cooper pairs are then thought to interact with each other through coupling to their own own collective spin excitations.

The topic of the next chapter will be magnon-mediated superconductivity in heterostructures of magnetic materials and conductors. As discussed earlier, such heterostructures represent customizable systems where itinerant electrons can interact indirectly by coupling to a collection of ordered localized spins. In addition to, compared to single-material systems, more adjustability and potentially clearer separation of the itinerant electrons from the origin of the magnetic order, such heterostructures can also allow for e.g. realization of coupling between itinerant electrons and dominantly only one of the two sublattices of an antiferromagnetic insulator.

4

Magnon-mediated superconductivity

As mentioned in the introduction, one potential pathway to a better understanding of the relationship between spin fluctuations and superconductivity is to study superconductivity in heterostructures of magnets and conductors. This will be the topic of this chapter. We will consider ordered ferromagnetic and antiferromagnetic insulators coupled to normal metals and topological insulator edge states. The coupling between the materials will be considered through an interfacial exchange interaction between the localized spins of the magnet and the spins of the itinerant electrons in the conductor. All details of the interfacial interaction is then baked into an interfacial interaction strength, which in general should be expected to vary substantially depending on the combination of materials as well as the details of the interface. As we will see in this chapter, the interfacial exchange interaction is responsible for both giving rise to electron-magnon coupling, as well as potential spin-splitting of the itinerant electrons in the conductor. In our simple model, the strength of these two effects are then strictly tied together. The electron-magnon coupling will, in the following, be the main star, while the spin-splitting of the electrons, which is typically harmful for superconductivity and can e.g. be cancelled out in trilayer structures, will receive less attention.

The effective electron-magnon coupling experienced by electrons and magnons, as well as the effective spin-splitting experienced by electrons, should further be expected to depend on the thickness of the respective materials. The physical systems we attempt to model in this chapter will indeed in reality typically consists of thin-films of some thickness. In order to ensure magnetic ordering, having a magnet of a certain thickness might be favorable, while the desirable effects of the magnet on the conductor would be expected to be strongest for a thin normal metal layer. Each thin-film

will, however, in the following be modelled as strictly two-dimensional and the effect of finite thickness will be discussed qualitatively. Rather than trying to accurately determine critical temperatures for comparison with experiments, the focus will be on attempting to understand the key physics of the systems and outlining potential mechanisms for superconductivity.

We start the chapter by introducing the physics taking place at interfaces between ferromagnetic insulators and normal metals. For simplicity we, here and in the following, consider square lattices. Similarly to what we did for the case of electron-phonon coupling, we perform a Schrieffer-Wolff transformation in order to obtain an effective interaction between electron mediated by ferromagnetic magnons and comment on the possibility of a superconducting instability. We then move on to the case of interfaces between antiferromagnetic insulators and normal metals, including both the possibility of compensated and uncompensated antiferromagnetic interfaces. We also here derive an effective interaction between electrons, this time mediated by antiferromagnetic magnons. With this background, we are then ready to discuss Paper [1–4], considering the possibility of inducing superconductivity in different types of conductors through proximity coupling to magnetic insulators.

4.1   Ferromagnet-metal interface

An interface between a ferromagnetic insulator and a normal metal is displayed in Fig. 4.1. We stress that the interface itself will be taken to be two-dimensional and that we in our modelling neglect any finite thickness of the two materials, considering square lattice models. We further introduce an interfacial exchange interaction

$$H_{\text{int}} = -2\bar{J}\sum_{\boldsymbol{i}} c_{\boldsymbol{i}}^\dagger \boldsymbol{\sigma} c_{\boldsymbol{i}} \cdot \boldsymbol{S_i}, \tag{4.1}$$

where $c_i^\dagger = (c_{i\uparrow}^\dagger, c_{i\downarrow}^\dagger)$. The ferromagnetic subsystem will be described by a spin Hamiltonian treated through linear spin wave theory, as outlined in Chap. 2. For the normal metal, we take a simple tight-binding model

$$H_{\text{NM}} = -t\sum_{\langle \boldsymbol{i},\boldsymbol{j}\rangle\sigma} c_{\boldsymbol{i}\sigma}^\dagger c_{\boldsymbol{j}\sigma} - \mu\sum_{\boldsymbol{i}\sigma} c_{\boldsymbol{i}\sigma}^\dagger c_{\boldsymbol{i}\sigma}, \tag{4.2}$$
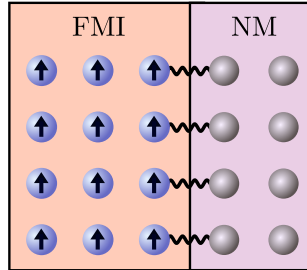
Figure 4.1: Interface between a ferromagnetic insulator (FMI) and a normal metal (NM). Itinerant electrons in the metal interact with the localized spins in the ferromagnet through an interfacial exchange interaction.

which after a Fourier transformation takes the form

$$H_{\text{NM}} = \sum_{\boldsymbol{k}\sigma} \epsilon_{\boldsymbol{k}} c_{\boldsymbol{k}\sigma}^{\dagger} c_{\boldsymbol{k}\sigma}, \tag{4.3}$$

with $\epsilon_{\boldsymbol{k}} = -tz_1\gamma_{\boldsymbol{k}} - \mu$. The sum over momentum here covers a two-dimensional Brillouin zone. The details of the electron dispersion relation will not be focused on in this section, and the choice of tight-binding model is therefore not of significance. Introducing the Holstein-Primakoff transformation in Eq. (4.1), and Fourier transforming both electron and magnon operators, we end up with

$$H_{\text{int}} = \tilde{V} \sum_{\boldsymbol{k}\boldsymbol{q}} (a_{\boldsymbol{q}} c_{\boldsymbol{k}+\boldsymbol{q},\downarrow}^{\dagger} c_{\boldsymbol{k}\uparrow} + a_{-\boldsymbol{q}}^{\dagger} c_{\boldsymbol{k}+\boldsymbol{q}\uparrow}^{\dagger} c_{\boldsymbol{k}\downarrow}) - 2\bar{J}S \sum_{\boldsymbol{k}\sigma} \sigma c_{\boldsymbol{k}\sigma}^{\dagger} c_{\boldsymbol{k}\sigma}, \tag{4.4}$$

where $\tilde{V} = -2\bar{J}\sqrt{2S}/\sqrt{N}$. We have neglected terms of higher order in the magnon operators. The first term in the above equation represents electron-magnon scattering where an incoming electron is scattered off a magnon in a spin-flip process. The second term introduces a spin-splitting of the electrons in the metal. This term will, in the following, be neglected. This can be justified either if the effect of spin-splitting is small, or if one e.g. considers a trilayer structure where a normal metal is sandwiched between

two oppositely magnetized ferromagnets [99].

In order to obtain an effective interaction between electrons mediated by magnons, we perform a Schrieffer-Wolff transformation. The transformation takes the same form as the one introduced for phonons, described in Chap. 3, except that we now take

$$\eta \tilde{S} = \tilde{V} \sum_{\boldsymbol{kq}} \left(x_{\boldsymbol{k,q}} a_{\boldsymbol{q}} c_{\boldsymbol{k+q}\downarrow}^{\dagger} c_{\boldsymbol{k}\uparrow} + y_{\boldsymbol{k,q}} a_{-\boldsymbol{q}}^{\dagger} c_{\boldsymbol{k+q}\uparrow}^{\dagger} c_{\boldsymbol{k}\downarrow} \right), \tag{4.5}$$

with

$$x_{\boldsymbol{k,q}} = \frac{1}{\epsilon_{\boldsymbol{k}} - \epsilon_{\boldsymbol{k+q}} + \omega_{\boldsymbol{q}}}, \qquad y_{\boldsymbol{k,q}} = \frac{1}{\epsilon_{\boldsymbol{k}} - \epsilon_{\boldsymbol{k+q}} - \omega_{\boldsymbol{q}}}. \tag{4.6}$$

The effective interaction Hamiltonian then becomes

$$H_{\text{eff}} = -\frac{\tilde{V}^2}{2} \sum_{\boldsymbol{kqk'}} \left(\frac{1}{\epsilon_{\boldsymbol{k'}} - \epsilon_{\boldsymbol{k'-q}} - \omega_{\boldsymbol{q}}} - \frac{1}{\epsilon_{\boldsymbol{k}} - \epsilon_{\boldsymbol{k+q}} + \omega_{\boldsymbol{q}}} \right) c_{\boldsymbol{k+q}\downarrow}^{\dagger} c_{\boldsymbol{k'-q}\uparrow}^{\dagger} c_{\boldsymbol{k}\uparrow} c_{\boldsymbol{k'}\downarrow}. \tag{4.7}$$

Investigating pairing between electrons with opposite momenta, we further have [99]

$$H_{\text{pair}} = \sum_{\boldsymbol{kk'}} V_{\boldsymbol{kk'}} c_{\boldsymbol{k}\uparrow}^{\dagger} c_{-\boldsymbol{k}\downarrow}^{\dagger} c_{-\boldsymbol{k'}\downarrow} c_{\boldsymbol{k'}\uparrow}, \tag{4.8}$$

with

$$V_{\boldsymbol{kk'}} = -\tilde{V}^2 \frac{\omega_{\boldsymbol{k'+k}}}{(\epsilon_{\boldsymbol{k'}} - \epsilon_{\boldsymbol{k}})^2 - \omega_{\boldsymbol{k'+k}}^2}. \tag{4.9}$$

Here, we have not defined H_{pair} with a factor 1/2 in front of the momentum sums, unlike what we did for the phonon-case, due to a more restricted spin structure.

If we compare our new magnon-mediated potential with the phonon-mediated potential from Chap. 3

$$V_{\boldsymbol{kk'}}^{\text{phonon}} = |g_{\boldsymbol{k'},\boldsymbol{k}}|^2 \frac{2\omega_{\boldsymbol{k'-k}}}{(\epsilon_{\boldsymbol{k'}} - \epsilon_{\boldsymbol{k}})^2 - \omega_{\boldsymbol{k'-k}}^2},$$

(a)

Phonon

$k+q\uparrow$ q $k'-q\downarrow$

$k\uparrow$ $k'\downarrow$

(b)

Magnon

$k+q\downarrow$ q $k'-q\uparrow$

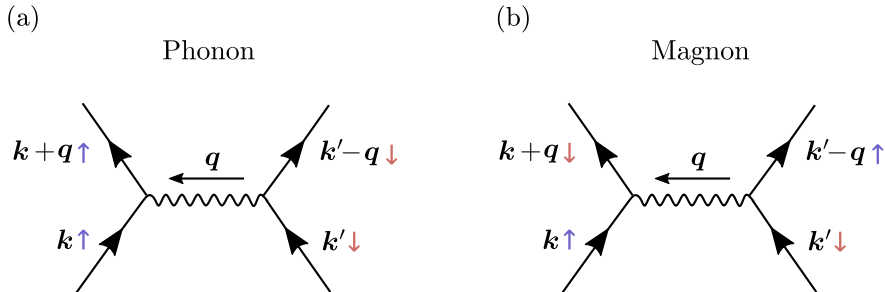$k\uparrow$ $k'\downarrow$

Figure 4.2: Depiction of effective interaction between electrons mediated by (a) a phonon and (b) a magnon. Notably, the interaction vertices in (b) introduce a flip of the electron spin.

we see that there are a few differences. One difference, which we will return more to later, is that the coupling constant appearing as a prefactor in the magnon-mediated potential is momentum independent for the considered electron-magnon coupling, while the prefactor of the phonon-mediated potential has a momentum dependence. Another difference is that the boson energy ω comes with the momentum combination $k' + k$ for the magnon-mediated case, rather than $k' - k$. The most striking difference is that the two potentials have an overall opposite sign. We highlight that such a comparison of interaction potentials, of course, only makes sense if one is careful to place the electron operators following the interaction potential on the same form. An interaction potential, without a specified ordering of the electron operators, is not a basis for discussing the possibility of a super-conducting instability. The two latter differences commented on above can, in fact, be traced back to the spin-flip structure of the magnon scattering producing the need for an additional (or one less) commutation of electron operators in order to obtain the ordering in Eq. (4.8). This commutation leads to a minus sign, as well as an associated redefinition of one of the momenta that we sum over. In Fig. 4.2 (a) and (b), we show illustrative diagrams representing phonon-mediated and magnon-mediated interaction between electrons, highlighting the differences in spin structure.

Based on the above discussion, as well as our experience with phonon-mediated superconductivity from the previous chapter, we can already now

suspect that trying to realize spin-singlet superconductivity with the above magnon-mediated potential is going to be an uphill battle as the prefactor carries the opposite sign of last time. However, before making any further claims about potential superconducting instabilities, we will write our new interaction potential on a more general form and derive the relevant gap equations.

As before, we have that $V_{\boldsymbol{k}\boldsymbol{k}'} = V_{\boldsymbol{k}'\boldsymbol{k}}$ and $V_{\boldsymbol{k}\boldsymbol{k}'} = V_{-\boldsymbol{k},-\boldsymbol{k}'}$. We further express the interaction potential into its even and odd parts with respect to momentum. Dividing our pairing Hamiltonian up into several parts, shuffling around operators, and redefining momenta, we then end up with

$$H_{\text{pair}} = \frac{1}{2} \sum_{\boldsymbol{k}\boldsymbol{k}'} \sum_{\sigma_1\sigma_2\sigma_3\sigma_4} V_{\boldsymbol{k}\boldsymbol{k}'}^{\sigma_1\sigma_2\sigma_3\sigma_4} c_{\boldsymbol{k}\sigma_1}^\dagger c_{-\boldsymbol{k}\sigma_2}^\dagger c_{-\boldsymbol{k}'\sigma_3} c_{\boldsymbol{k}'\sigma_4}. \tag{4.10}$$

Here, like last time,

$$V_{\boldsymbol{k}\boldsymbol{k}'}^{\uparrow\downarrow\downarrow\uparrow} = V_{\boldsymbol{k}\boldsymbol{k}'}^{\downarrow\uparrow\uparrow\downarrow} = \frac{1}{2}\left[V_{\boldsymbol{k}\boldsymbol{k}',O(\boldsymbol{k})} + V_{\boldsymbol{k}\boldsymbol{k}',E(\boldsymbol{k})}\right], \tag{4.11a}$$

$$V_{\boldsymbol{k}\boldsymbol{k}'}^{\uparrow\downarrow\uparrow\downarrow} = V_{\boldsymbol{k}\boldsymbol{k}'}^{\downarrow\uparrow\downarrow\uparrow} = \frac{1}{2}\left[V_{\boldsymbol{k}\boldsymbol{k}',O(\boldsymbol{k})} - V_{\boldsymbol{k}\boldsymbol{k}',E(\boldsymbol{k})}\right], \tag{4.11b}$$

while the rest of the spin combinations are now associated with a vanishing potential.

The general form of the gap equation takes the form of Eq. (3.24). Polarized spin-triplet pairing is not an option this time, but spin-singlet and unpolarized spin-triplet pairing could in principle both be possible. The gap equations for spin-singlet and unpolarized spin-triplet pairing now, once again, take the form

$$\Delta_{\boldsymbol{k}}^s = -\sum_{\boldsymbol{k}'} V_{\boldsymbol{k}\boldsymbol{k}',E(\boldsymbol{k})} \Delta_{\boldsymbol{k}'}^s \chi_{\boldsymbol{k}'}, \tag{4.12}$$

and

$$\Delta_{\boldsymbol{k}}^{t,u} = -\sum_{\boldsymbol{k}'} V_{\boldsymbol{k}\boldsymbol{k}',O(\boldsymbol{k})} \Delta_{\boldsymbol{k}'}^{t,u} \chi_{\boldsymbol{k}'}. \tag{4.13}$$

If we take both $\boldsymbol{k}$ and $\boldsymbol{k}'$ to be on the Fermi surface, we see that the potential in the equation for spin-singlet pairing takes the form

$$V_{\boldsymbol{k}\boldsymbol{k}',E(\boldsymbol{k})} = \tilde{V}^2 \left(\frac{1}{\omega_{\boldsymbol{k}+\boldsymbol{k}'}} + \frac{1}{\omega_{\boldsymbol{k}-\boldsymbol{k}'}} \right).$$

The two sides of the gap equation then have opposite signs unless the gap function changes sign as a function of momentum. By introducing sign changes in the gap function around the Fermi surface, it can in certain cases be possible to obtain superconductivity from a purely "repulsive" potential like the one we have here. A key element is then that the interaction potential should make sure that the largest contributions from the right-hand-side of the gap equation are not associated with the case of $\boldsymbol{k}$ and $\boldsymbol{k}'$ pointing in the same direction, where gap functions on opposite sides of the equations naturally have to carry the same sign. We will see an example of this later. In the present case, one would, quite oppositely, expect $\boldsymbol{k}' = \boldsymbol{k}$ to represent a peak in the interaction potential for a magnon dispersion relation that has a minimum at zero momentum. Spin-singlet pairing does therefore not seem promising.

Considering instead the possibility of unpolarized spin-triplet pairing, we again analyze the case of $\boldsymbol{k}$ and $\boldsymbol{k}'$ on the Fermi surface. The relevant interaction potential then takes the form

$$V_{\boldsymbol{k}\boldsymbol{k}',O(\boldsymbol{k})} = \tilde{V}^2 \left(\frac{1}{\omega_{\boldsymbol{k}+\boldsymbol{k}'}} - \frac{1}{\omega_{\boldsymbol{k}-\boldsymbol{k}'}} \right).$$

We then see that this potential can have a negative sign, as well as be peaked, when $\boldsymbol{k}' = \boldsymbol{k}$. The possibility of spin-triplet pairing therefore seems promising. The potential will also be peaked for $\boldsymbol{k}' = -\boldsymbol{k}$, in which case it carries a positive sign. This is, of course, just a consequence of the potential being odd in momentum. It is also not a problem for the gap equation since the gap functions also has to change sign in this case. In line with this discussion, Ref. [99] concluded that spin-triplet p-wave superconductivity, dominated by contributions from long-wavelength magnons, could be possible in a FMI/NM/FMI trilayer.

4.2 Antiferromagnet-metal interface

We next consider the case of an antiferromagnetic insulator coupled to a normal metal. The case of a compensated antiferromagnetic interface is displayed in Fig. 4.3 (a), while the case of an uncompensated antiferromagnetic interface is shown in Fig. 4.3 (b). Similarly to what we did in the previous section, we capture the coupling between the two materials through an interfacial exchange coupling

$$H_{\text{int}} = -2\bar{J} \sum_{\Upsilon} \sum_{\boldsymbol{i} \in \Upsilon} \Omega_{\Upsilon}\, c_{\boldsymbol{i}}^{\dagger} \boldsymbol{\sigma} c_{\boldsymbol{i}} \cdot \boldsymbol{S_i}. \tag{4.14}$$

The normal metal is assumed to be lattice matched with the full lattice of the antiferromagnet as displayed in Fig. 4.3 (a). We have, however, allowed for the possibility that the coupling of the normal metal electrons to the two sublattices of the antiferromagnet can differ, parameterized through the sublattice dependent parameter $\Omega_{\Upsilon} = \Omega_A, \Omega_B$. Taking $\Omega_A = \Omega_B$ corresponds to a compensated antiferromagnetic interface where the normal metal electrons are coupled equally to both sublattices of the AFMI. Further, by reducing e.g. Ω_B, we can investigate the effect of asymmetry in the coupling to the antiferromagnetic sublattices. The special case of $\Omega_B = 0$ corresponds to a system like in Fig. 4.3 (a), but where the itinerant electrons are only coupled to one of the two sublattices of the antiferromagnet, imitating the uncompensated interface in Fig. 4.3 (b) where the electrons dominantly couple to one of the two sublattices. We are thus able to tune our way from a model for a compensated to an uncompensated interface.

The normal metal is modelled in the same way as in the previous section and the antiferromagnet is treated in a linear spin-wave framework, starting from a spin Hamiltonian, as outlined in Chap. 2. Working on the interaction term, we start by performing a Holstein-Primakoff transformation, as well as Fourier transforming both the electron and magnon operators. As the normal metal is lattice matched with the full lattice of the antiferromagnet, the magnons will live in a reduced Brillouin zone compared to the electrons. The reduced Brillouin zone of the magnons was displayed earlier in Fig. 2.5.

The magnons living in a reduced Brillouin zone means that there will exist two types of scattering processes. One type will be referred to as regular processes and involves the momentum difference between the incoming and outgoing electrons being carried by an incoming or outgoing magnon living in the reduced Brillouin zone. There will also be additional Umklapp

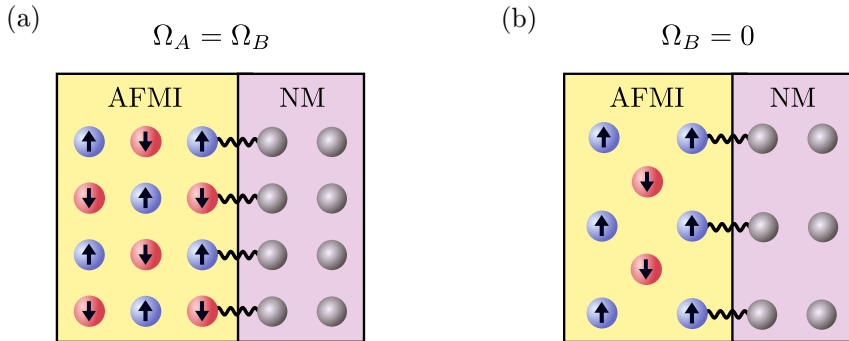(a) $\Omega_A = \Omega_B$ (b) $\Omega_B = 0$

Figure 4.3: (a) Compensated and (b) uncompensated interface between an antiferromagnetic insulator (AFMI) and a normal metal (NM). Our model considers a case like in (a), but allows for the coupling between the itinerant electrons and the antiferromagnet to be sublattice dependent. While $\Omega_A = \Omega_B$ corresponds to a fully compensated interface, $\Omega_B = 0$ corresponds to the itinerant electrons only coupling to one of the two sublattices of the antiferromagnet, similar to an uncompensated interface displayed in (b).

processes where the difference is that the momentum of the outgoing electron is shifted by a reciprocal lattice vector $\boldsymbol{Q} = \pi(\hat{x}+\hat{y})/a$ in addition to the momentum difference carried by a magnon living in the reduced Brillouin zone. Through regular and Umklapp processes, it is possible for magnons to scatter the electrons around in their full Brillouin zone.

One way of keeping track of the different types of processes is to rewrite the Fourier transformation of the electron operators as

$$c_{\boldsymbol{i}\sigma} = \frac{1}{\sqrt{N}} \sum_{\boldsymbol{k}\in\diamond} \left(c_{\boldsymbol{k}\sigma}e^{-i\boldsymbol{k}\cdot\boldsymbol{r_i}} + c_{\boldsymbol{k}+\boldsymbol{Q},\sigma}e^{-i(\boldsymbol{k}+\boldsymbol{Q})\cdot\boldsymbol{r_i}} \right), \qquad (4.15)$$

so that the momentum $\boldsymbol{k}$ is considered to be restricted to the reduced Brillouin zone $\diamond$. When performing sums over only the A sublattice such as

$$\frac{1}{N_A} \sum_{\boldsymbol{i}\in A} e^{i(\boldsymbol{k'}-\boldsymbol{k}-\boldsymbol{q}-\boldsymbol{Q})\cdot\boldsymbol{r_i}} = \delta_{\boldsymbol{k'},\boldsymbol{k}+\boldsymbol{q}},$$

the additional momentum $\boldsymbol{Q}$ does not make any difference. However, as the the lattice sites associated with the B sublattice are shifted e.g. $a\hat{x}$

compared to the A sublattice, the presence of $\boldsymbol{Q}$ leads to a sign change

$$\frac{1}{N_B} \sum_{\boldsymbol{i} \in B} e^{i(\boldsymbol{k}' - \boldsymbol{k} - \boldsymbol{q} - \boldsymbol{Q}) \cdot \boldsymbol{r_i}} = \frac{1}{N_A} \sum_{\boldsymbol{i} \in A} e^{i(\boldsymbol{k}' - \boldsymbol{k} - \boldsymbol{q} - \boldsymbol{Q}) \cdot (\boldsymbol{r_i} + a\hat{x})} = -\delta_{\boldsymbol{k}', \boldsymbol{k} + \boldsymbol{q}},$$

arising from $i\boldsymbol{Q} \cdot a\hat{x} = i\pi$. Performing the full calculations, we end up with $H_{\text{int}} = H_{\text{int}}^V + H_{\text{int}}^h$ with [1, 4]

$$H_{\text{int}}^V = V \sum_{\substack{\boldsymbol{k} \in \square \\ \boldsymbol{q} \in \diamond}} \Big[M_{\boldsymbol{q}}^R c_{\boldsymbol{k}+\boldsymbol{q},\downarrow}^\dagger c_{\boldsymbol{k},\uparrow} + M_{\boldsymbol{q}}^U c_{\boldsymbol{k}+\boldsymbol{q}+\boldsymbol{Q},\downarrow}^\dagger c_{\boldsymbol{k},\uparrow}$$
$$+ (M_{-\boldsymbol{q}}^R)^\dagger c_{\boldsymbol{k}+\boldsymbol{q},\uparrow}^\dagger c_{\boldsymbol{k},\downarrow} + (M_{-\boldsymbol{q}}^U)^\dagger c_{\boldsymbol{k}+\boldsymbol{q}+\boldsymbol{Q},\uparrow}^\dagger c_{\boldsymbol{k},\downarrow} \Big], \qquad (4.16)$$

where we have defined the magnon operators

$$M_{\boldsymbol{q}}^\kappa = \Omega_A a_{\boldsymbol{q}} + \kappa \, \Omega_B b_{-\boldsymbol{q}}^\dagger, \qquad (4.17)$$

as well as $V = -2\bar{J}\sqrt{S/N}$. Here, regular and Umklapp processes are distinguished by $\kappa = R, U = +1, -1$. We see that $M_{\boldsymbol{q}}^\kappa$ for Umklapp scattering processes associated with the B-sublattice of the antiferromagnet carry an opposite sign compared to the regular scattering processes, as discussed above. We have now also combined together terms so that the electron momentum $\boldsymbol{k}$ is no longer restricted to the reduced Brillouin zone. Moreover, the additional terms arising from the interaction Hamiltonian take the form $H_{\text{int}}^h = H_{\text{int}}^{h,A} + H_{\text{int}}^{h,B}$ where [1, 4]

$$H_{\text{int}}^{h,A} = -\bar{J} \Omega_A S \sum_{\boldsymbol{k} \in \square, \sigma} \sigma \Big(c_{\boldsymbol{k}\sigma}^\dagger c_{\boldsymbol{k}\sigma} + c_{\boldsymbol{k}+\boldsymbol{Q},\sigma}^\dagger c_{\boldsymbol{k}\sigma} \Big), \qquad (4.18a)$$

$$H_{\text{int}}^{h,B} = +\bar{J} \Omega_B S \sum_{\boldsymbol{k} \in \square, \sigma} \sigma \Big(c_{\boldsymbol{k}\sigma}^\dagger c_{\boldsymbol{k}\sigma} - c_{\boldsymbol{k}+\boldsymbol{Q},\sigma}^\dagger c_{\boldsymbol{k}\sigma} \Big). \qquad (4.18b)$$

We see that for $\Omega_A \neq \Omega_B$, the electrons will experience a net spin-splitting.

We will next perform some simplifying assumptions. As we did for the ferromagnet, we will assume that the spin-splitting of the electrons is either small or cancelled out in e.g. a trilayer structure. We will further, for the time being, restrict ourselves to small isotropic Fermi surfaces. In that case, Umklapp scattering processes will take electrons close to the Fermi surface away from the Fermi surface, as illustrated in Fig. 4.4. For a sufficiently
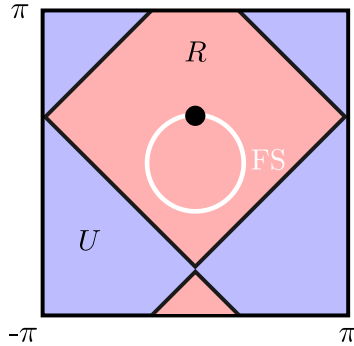
Figure 4.4: An electron situated at the Fermi surface (white circle) can be scattered to the red regions of the Brillouin zone through regular processes and to the blue regions through Umklapp processes. For a small Fermi surface, Umklapp processes always take electrons at the Fermi surface away from the Fermi surface.

small Fermi surface, we therefore neglect the effect of Umklapp scattering processes. We also note that the Umklapp processes in H_{int}^h may be cancelled out in a trilayer structure. Moreover, an experimentally realized uncompensated interface might typically involve lattice matching between the normal metal and the sublattice of the antiferromagnet which is exposed at the interface. In that case, the Umklapp processes are not present in the first place.

From the interaction Hamiltonian, we are now left with the regular electron-magnon scattering terms. Expressing the delocalized spin-flip magnons in terms of the antiferromagnetic magnons, we now obtain

$$H_{int}^V = V \sum_{\substack{\boldsymbol{k}\in\square \\ \boldsymbol{q}\in\diamond}} \left[M_{\boldsymbol{q}} c_{\boldsymbol{k}+\boldsymbol{q},\downarrow}^\dagger c_{\boldsymbol{k},\uparrow} + (M_{-\boldsymbol{q}})^\dagger c_{\boldsymbol{k}+\boldsymbol{q},\uparrow}^\dagger c_{\boldsymbol{k},\downarrow} \right], \qquad (4.19)$$

with

$$M_{\boldsymbol{q}} = \left(\Omega_A u_{\boldsymbol{q}} + \Omega_B v_{\boldsymbol{q}}\right)\alpha_{\boldsymbol{q}} + \left(\Omega_A v_{\boldsymbol{q}} + \Omega_B u_{\boldsymbol{q}}\right)\beta_{-\boldsymbol{q}}^\dagger. \qquad (4.20)$$

As $u_{\boldsymbol{q}}$ and $v_{\boldsymbol{q}}$ carry opposite signs, we see here that the regular electron-magnon scattering strength can be enhanced by introducing an asymmetry

$\Omega_A \neq \Omega_B$. This effect is strongest for long-wavelength magnons associated with coherence factors that grow large in magnitude leading to $|u_{\boldsymbol{q}}| \approx |v_{\boldsymbol{q}}|$.

In order to obtain an effective interaction mediated by magnons, we next perform a Schrieffer-Wolff transformation with

$$\eta \tilde{S} = V \sum_{\substack{\boldsymbol{k}\in\square \\ \boldsymbol{q}\in\diamond}} \left[X_{\boldsymbol{q}}\, c^{\dagger}_{\boldsymbol{k}+\boldsymbol{q},\downarrow} c_{\boldsymbol{k},\uparrow} + Y_{\boldsymbol{q}}\, c^{\dagger}_{\boldsymbol{k}+\boldsymbol{q},\uparrow} c_{\boldsymbol{k},\downarrow} \right], \tag{4.21}$$

where

$$X_{\boldsymbol{q}} = x_{\boldsymbol{k},\boldsymbol{q}}\big(\Omega_A u_{\boldsymbol{q}} + \Omega_B v_{\boldsymbol{q}}\big)\alpha_{\boldsymbol{q}} + y_{\boldsymbol{k},\boldsymbol{q}}\big(\Omega_A v_{\boldsymbol{q}} + \Omega_B u_{\boldsymbol{q}}\big)\beta^{\dagger}_{-\boldsymbol{q}}, \tag{4.22a}$$

$$Y_{\boldsymbol{q}} = y_{\boldsymbol{k},\boldsymbol{q}}\big(\Omega_A u_{\boldsymbol{q}} + \Omega_B v_{\boldsymbol{q}}\big)\alpha^{\dagger}_{-\boldsymbol{q}} + x_{\boldsymbol{k},\boldsymbol{q}}\big(\Omega_A v_{\boldsymbol{q}} + \Omega_B u_{\boldsymbol{q}}\big)\beta_{\boldsymbol{q}}. \tag{4.22b}$$

Here, $x_{\boldsymbol{k},\boldsymbol{q}}$ and $y_{\boldsymbol{k},\boldsymbol{q}}$ are defined in the same way as in the ferromagnetic case. For scattering between pairs of electrons with opposite momenta, we then obtain [1]

$$H_{\text{pair}} = \sum_{\boldsymbol{k}\boldsymbol{k}'} V_{\boldsymbol{k}\boldsymbol{k}'} c^{\dagger}_{\boldsymbol{k}\uparrow} c^{\dagger}_{-\boldsymbol{k}\downarrow} c_{-\boldsymbol{k}'\downarrow} c_{\boldsymbol{k}'\uparrow}, \tag{4.23}$$

where

$$V_{\boldsymbol{k}\boldsymbol{k}'} = -V^2 \frac{2\omega_{\boldsymbol{k}+\boldsymbol{k}'}}{(\epsilon_{\boldsymbol{k}'} - \epsilon_{\boldsymbol{k}})^2 - \omega^2_{\boldsymbol{k}+\boldsymbol{k}'}} A(\boldsymbol{k} + \boldsymbol{k}', \Omega_A, \Omega_B), \tag{4.24}$$

and

$$A(\boldsymbol{q}, \Omega_A, \Omega_B) = \frac{1}{2}(\Omega_A^2 + \Omega_B^2)(u_{\boldsymbol{q}}^2 + v_{\boldsymbol{q}}^2) + 2\,\Omega_A\Omega_B\, u_{\boldsymbol{q}} v_{\boldsymbol{q}}. \tag{4.25}$$

The difference between $\boldsymbol{k}$ and $\boldsymbol{k}'$ is here, naturally, restricted to the reduced Brillouin zone of the antiferromagnetic sublattices as we have only considered regular scattering processes. We now see that we have obtained an interaction potential which is similar to what we obtained for interaction mediated by ferromagnetic magnons in the previous section. The only important difference is the presence of an additional factor $A(\boldsymbol{k} + \boldsymbol{k}', \Omega_A, \Omega_B)$. The effect of this factor on the possibility of superconductivity in the system is the topic of Paper [1].

4.3 Enhancement of superconductivity mediated by antiferromagnetic squeezed magnons

As introduced in the previous section, Paper [1] considers the possibility of superconductivity in a heterostructure of a normal metal and and antiferromagnetic insulator. Specifically, the focus is on how the superconductivity, for a small and isotropic Fermi surface, depends on whether the electrons in the normal metal are coupled symmetrically or asymmetrically to the two sublattices of the antiferromagnet. The study was motivated by previous work on superconductivity in heterostructures of normal metals and ferromagnetic insulators [99], and related [100], as well as superconductivity in heterostructures of ferromagnetic or antiferromagnetic insulators and topological insulators featuring conducting edge states [101, 102]. The study actually grew out of initial investigations of the system of an antiferromagnetic insulator coupled to a topological insulator, combined with the ideas about the difference between coupling to compensated and uncompensated antiferromagnetic interfaces which culminated in Ref. [35]. As it became clear that the effect of asymmetry in the coupling to the two sublattices of the antiferromagnet was quite general, we decided to focus on this effect in a simpler system before we returned to the topological insulator in Paper [2].

The main finding of the article is that coupling a normal metal asymmetrically to the two sublattices of an antiferromagnetic insulator may lead to spin-triplet p-wave superconductivity. The critical temperature is found to increase with the degree of asymmetry, favoring an uncompensated antiferromagnetic interface.

The considered system has already been introduced in the previous section, where we ended up with the effective magnon-mediated interaction potential in Eq. (4.24). As we have already analyzed the interaction mediated by ferromagnetic magnons, the question is now how the additional factor $A(\boldsymbol{k} + \boldsymbol{k}', \Omega_A, \Omega_B)$ changes the picture. Importantly, this factor contains all dependence on Ω_A and Ω_B. Aligning with the notation in the article, we set $\Omega_B = 1$ and $\Omega_A = \Omega$. For the case of $\Omega = 1$, corresponding to a compensated antiferromagnetic interface, we then have

$$A(\boldsymbol{q}, \Omega = 1) = (u_{\boldsymbol{q}} + v_{\boldsymbol{q}})^2. \qquad (4.26)$$

For large $\boldsymbol{q}$, this is expression is simply equal to 1. For small $\boldsymbol{q}$, on the other hand, rewriting the expression on the form $(u_{\boldsymbol{q}} + |v_{\boldsymbol{q}}|)^{-2}$, we see that it is typically much smaller than 1. For large $\boldsymbol{q}$ we then have an interaction potential similar to what we had for the ferromagnet, while for the important small $\boldsymbol{q}$ contributions, the interaction strength is suppressed. Although the coherence factors themselves grow large, contributions from the two separate antiferromagnetic sublattices interfere destructively, limiting the interaction strength.

Considering instead the case of $\Omega = 0$, corresponding to an uncompensated antiferromagnetic interface, we obtain

$$A(\boldsymbol{q}, \Omega = 0) = \frac{1}{2}(u_{\boldsymbol{q}}^2 + v_{\boldsymbol{q}}^2). \tag{4.27}$$

For large $\boldsymbol{q}$, this expression is simply equal to $1/2$. However, for small $\boldsymbol{q}$, the so-called boosting factor A becomes large as the coherence factors are now squared separately. From the discussion of the interaction potential mediated by ferromagnetic magnons, one can now see right away that the potential for interaction mediated by antiferromagnetic magnons, for $\Omega = 0$, also should be able to produce spin-triplet p-wave pairing, where the long-wavelength contributions now obtain an additional boosting from the magnon coherence factors.

In order to calculate the critical temperature as a function of Ω, we can return to the expression

$$k_B T_c = 1.13\, \omega_c\, e^{-\frac{1}{\lambda}},$$

from Chap. 3, where we had

$$\lambda \Delta_{\boldsymbol{k}_\parallel, \sigma_1 \sigma_2} = -\sum_{\sigma_3 \sigma_4} \langle D_0(\boldsymbol{k}'_\parallel)\, V^{\sigma_1 \sigma_2 \sigma_3 \sigma_4}_{\boldsymbol{k}_\parallel \boldsymbol{k}'_\parallel} \Delta_{\boldsymbol{k}'_\parallel, \sigma_4 \sigma_3} \rangle_{\boldsymbol{k}'_\parallel, \mathrm{FS}}.$$

Restricting to unpolarized spin-triplet pairing, we then have to numerically solve the eigenvalue problem

$$\lambda \Delta^{t,u}_{\boldsymbol{k}_\parallel} = -\langle D_0(\boldsymbol{k}'_\parallel)\, V_{\boldsymbol{k}_\parallel \boldsymbol{k}'_\parallel, O(\boldsymbol{k})} \Delta^{t,u}_{\boldsymbol{k}'_\parallel} \rangle_{\boldsymbol{k}'_\parallel, \mathrm{FS}}, \tag{4.28}$$
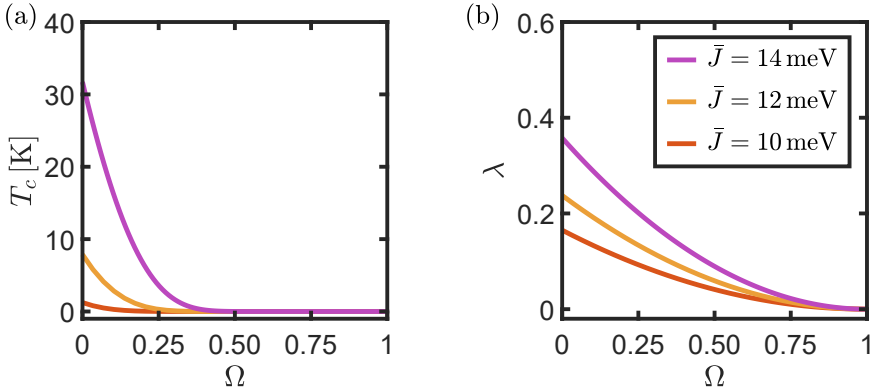
Figure 4.5: (a) Critical temperature T_c and (b) dimensionless coupling constant λ as a function of the asymmetry in the coupling between the normal metal and the two sublattices of the antiferromagnet. Maximum asymmetry is here represented by $\Omega = 0$. The different curves correspond to different values of the interfacial coupling strength $\bar{J}$.

in order to determine the largest eigenvalue λ and its associated eigenvector. The results for the critical temperature T_c and the dimensionless coupling constant λ presented in the article, are here included in Fig. 4.5. The gap function that maximized the critical temperature was found to have a p-wave symmetry, as expected. From Fig. 4.5, we further see that both λ and T_c increase with increased asymmetry in the coupling between the normal metal and the two sublattices of the antiferromagnet.

The above results are only valid if the effect of the spin-splitting of the electrons can be neglected. As highlighted in the article, the effect of spin-splitting is expected to be small if the critical temperature in the absence of spin-splitting is large compared to the spin-splitting. For a given experimental realization of the system, the problem is then relatively simple. If $k_B T_c$ in the absence of spin-splitting is large enough compared to the spin-splitting field, the mechanism is likely to work in a simple bilayer structure. In the opposite case, one has to cancel out the spin-splitting, which e.g. can be done in a trilayer structure. While making the normal metal thick also is a way of reducing the effective spin-splitting experienced by the electrons, one should also expect the effective electron-magnon interaction strength experienced by the electrons to be reduced in this case. As the critical temperature decays quickly with reduced interaction strength,

it is therefore likely that a quite thin normal metal still is favorable. In the article, it was argued that the predicted critical temperatures might be large enough for, if realized in a real system, superconductivity to survive the spin-splitting field arising from the uncompensated antiferromagnetic interface. The highly parameter-dependent critical temperatures resulting from our simple calculation should, however, be viewed as very loose estimates. Based on our results from the Eliashberg treatment of the system in paper [4], we concluded that cancelling out the spin-splitting is likely to be necessary in order for superconductivity to survive.

We also note that, our model of antiferromagnetically ordered, localized spins interacting with itinerant electrons through an exchange interaction does, in fact, take the form of a Hamiltonian that one might write down to describe a single material hosting antiferromagnetically ordered spins interacting with itinerant electrons. For the natural case of $\Omega_A = \Omega_B$, Ref. [88] encountered the destructive interference discussed above, leading to the dominant processes contributing to superconductivity for sufficiently small Fermi surfaces being higher-order processes where the momentum transfer in the effective electron-electron interaction is carried by a pair of magnons rather than a single magnon. Such scattering processes arise from the z-component of the localized spins, e.g. on the form $S - a_{\bm{i}}^{\dagger} a_{\bm{i}}$.

From our above comparisons between the interaction potential mediated by ferromagnetic and antiferromagnetic magnons, it seems quite obvious that the antiferromagnetic potential for $\Omega = 0$ should be better for superconductivity as there is an additional prefactor boosting the interaction. In order to do a more thorough inspection of how the two cases match up, we can consider the situation where the momenta $\bm{k}$ and $\bm{k}'$ are both on the Fermi surface, and write

$$V_{\bm{k}\bm{k}'}^{\mathrm{FM}} = \tilde{V}^2 \frac{1}{\omega_{\bm{k}'+\bm{k}}^{\mathrm{FM}}}, \qquad V_{\bm{k}\bm{k}'}^{\mathrm{AFM}} = V^2 \frac{1}{\omega_{\bm{k}+\bm{k}'}^{\mathrm{AFM}}} \left(u_{\bm{k}+\bm{k}'}^2 + v_{\bm{k}+\bm{k}'}^2 \right). \tag{4.29}$$

If we then inspect the combination of coherence factors, considering $J_2 = 0$, we have

$$u_{\bm{k}+\bm{k}'}^2 + v_{\bm{k}+\bm{k}'}^2 = \frac{2SJ_1 z_1 + 2SK}{\omega_{\bm{k}+\bm{k}'}^{\mathrm{AFM}}}. \tag{4.30}$$

Further, taking the momentum $\bm{k} + \bm{k}'$ to zero, we have

$$\omega_0^{\mathrm{FM}} = 2KS, \qquad \omega_0^{\mathrm{AFM}} = 2S\sqrt{K(K + 2z_1 J_1)}. \qquad (4.31)$$

which, for the case of $J/K \gg 1$, allows us to write

$$V_{\boldsymbol{k}\boldsymbol{k}'}^{\mathrm{FM}} \sim \tilde{V}^2 \frac{1}{K}, \qquad V_{\boldsymbol{k}\boldsymbol{k}'}^{\mathrm{AFM}} \sim V^2 \frac{1}{K}. \qquad (4.32)$$

We then see that the ferromagnet actually can compensate for the missing boosting factor in the potential by having a smaller gap in the magnon spectrum, making the maxima of the two potentials take on similar values for similar easy-axis anisotropy strength K. We will return to this comparison in the discussion of Paper [4], where we will see that the boosting factor of the antiferromagnet, in fact, does provide the antiferromagnet with a potential advantage.

An important reason why the above comparison between the two interaction potentials does not represent the full story is related to our simplified treatment of the magnon-mediated superconductivity. When calculating the superconducting critical temperature, we simply followed the normal approach of assuming that the behavior of the interaction potential and gap function when moving away from the Fermi surface can be treated as constants with a cutoff equal to the cutoff on the boson spectrum. We will return to an evaluation of this approximation later in this chapter, but before we get that far, we will first provide a discussion of Paper [2].

4.4 Magnon-mediated superconductivity on the surface of a topological insulator

In Paper [2], we studied superconductivity on the surface of a topological insulator proximity-coupled to a magnetic insulator. We considered both the case of a ferromagnetic insulator, as well as both compensated and uncompensated antiferromagnetic interfaces. The project was motivated by earlier studies of superconductivity in heterostructures of topological insulators and magnetic insulators [101, 102]. Working in a Green's function framework, Ref. [101] found that superconductivity where the Cooper pairs carry a large finite momentum $2k_F$, so-called Amperean pairing, could be possible on the surface of a topological insulator coupled to a ferromagnetic insulator. Building on this result, Ref. [102] considered both the
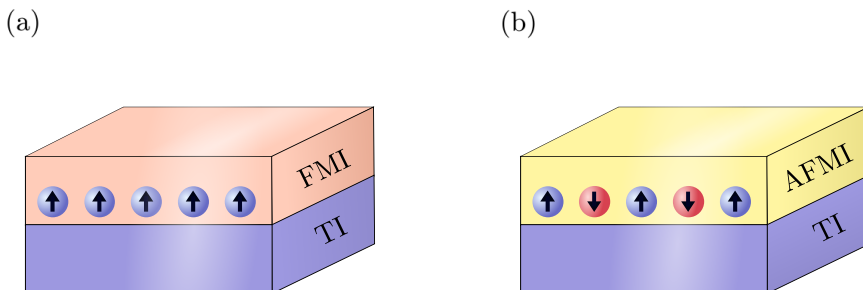
(a)   (b)

Figure 4.6: Heterostructure of topological insulator coupled to (a) a ferro-magnetic insulator (FMI) and (b) an antiferromagnetic insulator (AFMI).

case of coupling to a ferromagnetic and antiferromagnetic insulator. Work-ing within the path integral formalism, they concluded that the resulting effective interaction between helical fermions mediated by both ferromag-netic and antiferromagnetic spin fluctuations had potential for giving rise to superconductivity. The goal of our article was to further investigate the differences between coupling the topological insulator to a ferromagnetic or different types of antiferromagnetic interfaces when the magnets are treated in a quantum mechanical fashion.

The main finding of the article is that the effective interaction po-tential arising from an uncompensated antiferromagnetic interface is quite similar to the potential mediated by ferromagnetic magnons, except that the presence of additional antiferromagnetic coherence factors works to aid in the formation of a superconducting stability. For both the ferromagnetic and the uncompensated antiferromagnetic interface, it was found that the momentum structure of the interaction potential is suitable for Amperean pairing with p-wave symmetry. Similarly to before, a compensated antifer-romagnetic interface leads to destructive interference of the contributions from the two sublattices. Moreover, the study also introduced that adding frustration to the antiferromagnet, generating stronger spin fluctuations, may enhance magnon-mediated superconductivity.

The considered systems are presented in Fig. 4.6. The magnetic insu-lators are treated in the same way as earlier in this chapter with a specific assumption about out-of-plane ordering in this case. The conducting sur-
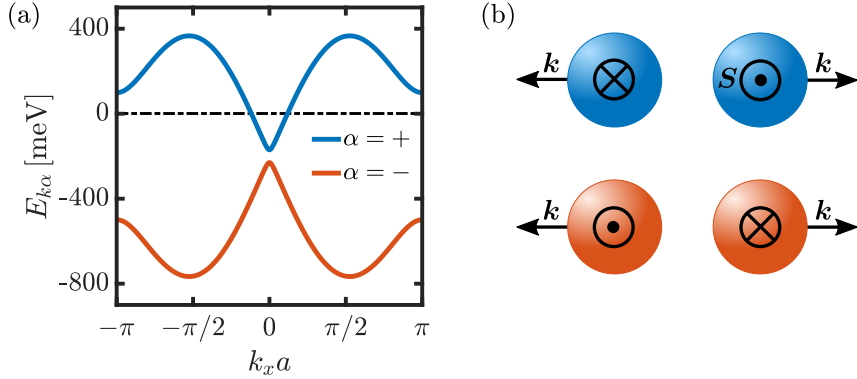
Figure 4.7: (a) Band structure for the surface states of a topological insulator subjected to a an out-of-plane exchange field. We have set $k_y a = 0$. (b) The spins of the surface state fermions lie in-plane with direction perpendicular to the momentum. The direction of the cross product between the spin direction and the momentum direction defines the handedness of the fermions, here referred to as helicity α.

face states of the topological insulator are described through a square lattice model giving rise to a Dirac cone around the center of the Brillouin zone. Interfacial coupling is introduced through an exchange coupling between localized spins in the magnetic insulator and the spins of the electrons going into the lattice model for the surface states of the topological insulator. Similarly to Paper [1], the interfacial exchange coupling to the antiferromagnet is allowed to be sublattice dependent, capturing both the case of a compensated and uncompensated antiferromagnetic interface. The interfacial coupling gives rise to interaction between magnons and helical fermions living on the surface of the topological insulator, as well as a potential spin-splitting of the electrons on the surface of the topological insulator. Taking this spin-splitting into account, the band structure for the helical surface states of the topological insulator takes the form in Fig. 4.7 (a) where a gap has been opened between the bands of opposite helicity [103]. We have here assumed that the Fermi level crosses the upper Dirac cone with positive helicity. The spin-momentum locking of the surfaces states is illustrated in Fig. 4.7 (b).

Working with a small Fermi surface, we neglect Umklapp scattering processes so that the interaction term in the ferromagnetic case takes the form

$$H_{\text{int}}^{\text{FMI},V} = \tilde{V} \sum_{\boldsymbol{kq}} \sum_{\alpha\alpha'} \left[Q_{\downarrow\alpha}^{\dagger}(\boldsymbol{k}+\boldsymbol{q}) Q_{\uparrow\alpha'}(\boldsymbol{k}) a_{\boldsymbol{q}} \, \psi_{\boldsymbol{k}+\boldsymbol{q},\alpha}^{\dagger} \psi_{\boldsymbol{k}\alpha'} + \text{h.c.} \right]. \qquad (4.33)$$

The difference from the case of a ferromagnetic insulator coupled to a normal metal is here that the electron operators have been expressed in terms of the operators $\psi_{\boldsymbol{k}\alpha}$ corresponding to spin-momentum locked fermions with helicity α, introducing some additional prefactors Q. For the antiferromagnetic insulator, the situation is similar. We focus on the expressions for the ferromagnetic case as these are more compact. We next perform a Schrieffer-Wolff transformation in order to obtain an effective magnon-mediated fermion-fermion interaction. We focus on the interaction between fermions with helicity $\alpha = +$, which are the ones living at the Fermi surface. Motivated by the smallness of the Fermi surface, we further approximate the Q-coefficients by their long-wavelength limit expressions. For pairing between fermions with vanishing center-of-mass momentum (BCS-type pairing) and Amperean pairing between fermions with large center-of-mass momentum compared to their relative momentum, we obtain the pairing Hamiltonians

$$H_{\text{pair,FMI}}^{\text{(BCS)}} = \frac{1}{2} \sum_{\boldsymbol{kk'}} V_{\boldsymbol{kk'},\text{FMI}}^{\text{(BCS)}} \psi_{\boldsymbol{k},+}^{\dagger} \psi_{-\boldsymbol{k},+}^{\dagger} \psi_{-\boldsymbol{k'},+} \psi_{\boldsymbol{k'},+}, \qquad (4.34)$$

with

$$\begin{aligned}
V_{\boldsymbol{kk'},\text{FMI}}^{\text{(BCS)}} &= -\frac{V^2}{2} \frac{v_F(k_x - ik_y)}{\sqrt{(2\bar{J}S)^2 + v_F^2 k^2}} \\
&\times \frac{v_F(k_x' + ik_y')}{\sqrt{(2\bar{J}S)^2 + v_F^2 k'^2}} \frac{2\omega_{\boldsymbol{k}-\boldsymbol{k'}}}{(E_{\boldsymbol{k'},+} - E_{\boldsymbol{k},+})^2 - \omega_{\boldsymbol{k}-\boldsymbol{k'}}^2},
\end{aligned} \qquad (4.35)$$

and

$$H_{\text{pair,FMI}}^{\text{(Amp)}} = \frac{1}{2} \sum_{\boldsymbol{Kpp'}} V_{\boldsymbol{pp'},\text{FMI}}^{\text{(Amp)}}(\boldsymbol{K}) \psi_{\boldsymbol{K}+\boldsymbol{p},+}^{\dagger} \psi_{\boldsymbol{K}-\boldsymbol{p},+}^{\dagger} \psi_{\boldsymbol{K}-\boldsymbol{p'},+} \psi_{\boldsymbol{K}+\boldsymbol{p'},+}, \qquad (4.36)$$
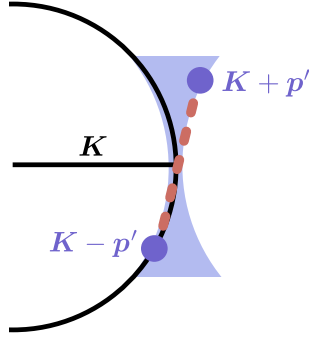
with

Figure 4.8: For Amperean pairing, the most relevant region for contributions to the gap equation is found to take the form of an hourglass around $\boldsymbol{K}$.

$$
\begin{aligned}
V_{\boldsymbol{pp'},\mathrm{FMI}}^{(\mathrm{Amp})}(\boldsymbol{K}) = {} & \frac{V^2}{2} \frac{v_F^2 K^2}{(2\bar{J}s)^2 + v_F^2 K^2} \\
& \times \left(\frac{1}{E_{\boldsymbol{K}-\boldsymbol{p'},+} - E_{\boldsymbol{K}-\boldsymbol{p},+} - \omega_{\boldsymbol{p}-\boldsymbol{p'}}} - \frac{1}{E_{\boldsymbol{K}+\boldsymbol{p'},+} - E_{\boldsymbol{K}+\boldsymbol{p},+} + \omega_{\boldsymbol{p}-\boldsymbol{p'}}} \right).
\end{aligned}
\tag{4.37}
$$

Here, v_F is the Fermi velocity and $2\boldsymbol{K}$ is center-of-mass momentum of the Amperean Cooper pairs. As we only have fermions with helicity $+$ around the Fermi surface, we see immediately that any pairing will have to be even in helicity, and correspondingly odd in momentum. For Amperean pairs, odd in momentum here means odd in relative momentum for a given center of mass momentum. This can easily be seen from the above pairing Hamiltonian by commuting operators and inverting $\boldsymbol{p}$ or $\boldsymbol{p'}$, showing that it is only the part of the interaction potential that is odd in relative momentum that does not vanish.

Performing a mean-field theory as outlined in the article, one can then obtain gap equations for both BCS-type and Amperean pairing in order to analyze whether the interaction potentials may support nontrivial solutions to these gap equations. For BCS-type pairing it was found that the interaction potential had an overall wrong for supporting superconductivity. An indication of this can be seen by taking $\boldsymbol{k}$ and $\boldsymbol{k'}$ on the Fermi surface and inspecting the real part of the part of the potential which is odd in

momentum. Investigation of the gap equation reveals that this part of the potential, whose sign is determined by

$$\sim \boldsymbol{k} \cdot \boldsymbol{k}' \left(\frac{1}{\omega_{\boldsymbol{k}-\boldsymbol{k}'}} + \frac{1}{\omega_{\boldsymbol{k}+\boldsymbol{k}'}} \right),$$

should have been negative for $\boldsymbol{k} = \boldsymbol{k}'$ in order to help produce a nontrivial solution to the gap equation.

We therefore instead consider the possibility of Amperean pairing. Similarly to BCS-type pairing, the gap equation for Amperean pairing contains a factor which ensures that the most important contributions to the gap equation arise from processes where the fermions are kept close to the Fermi surface. For the case of $\boldsymbol{K} = k_F \hat{x}$, Fig. 4.8 shows the most relevant region, which takes the shape of an hourglass around $\boldsymbol{K}$. Sufficiently close to the center of this hourglass, the differences between fermion energies appearing in the interaction potential are small compared to the magnon energies as the magnons have a gap in their excitation spectrum. In this region, the relevant part of the potential that should be negative when $\boldsymbol{p} = \boldsymbol{p}'$ has a simplified dependence

$$\sim \frac{1}{\omega_{\boldsymbol{p}+\boldsymbol{p}'}} - \frac{1}{\omega_{\boldsymbol{p}-\boldsymbol{p}'}}. \tag{4.38}$$

When the fermion energies can be neglected, we see that the potential looks quite promising. In the article, we therefore concluded that, in accordance with earlier findings, the interaction has a suitable momentum structure for p-wave superconductivity to arise. Dividing the area where the fermion energies could be neglected up into a grid of momentum points and attempting to solve the linearized gap equation as a matrix eigenvalue problem, it was found that this area was too small to produce a solution to the gap equation for reasonable parameters. Moving momenta outside of this small region, the sign-changes arising from the fermion energies appearing in the potential make the behavior of the potential quite chaotic and unfavorable for a nontrivial solution to the gap equation. This behavior was interpreted as a result of our effective interaction potential attempting to account for the frequency dependence of the interaction through momentum dependent fermion energies. We did not have much faith in our approach reasonably accounting for the frequency dependence of the interaction, and we were
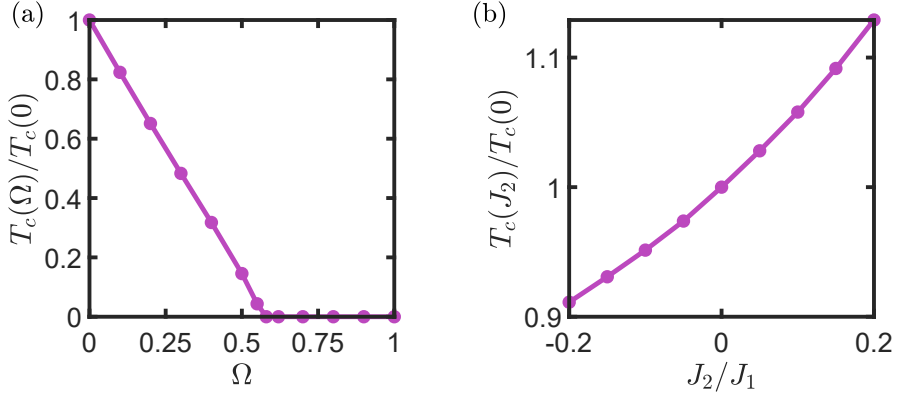
Figure 4.9: Critical temperature as a function of (a) asymmetry in the coupling of the topological insulator to the two sublattices of the antiferromagnet, Ω, and (b) next-nearest neighbor interaction J_2 in the antiferromagnet. Maximum asymmetry is here represented by $\Omega = 0$, and for $J_2/J_1 > 0$ the next-nearest neighbor interaction acts as a frustration.

therefore not able to draw any independent conclusions about whether superconductivity could be realized in this system.

For the antiferromagnet, there are additional scattering processes and additional coherence factors appearing in the effective interaction potential. Apart from this, the situation is very similar to the ferromagnetic case. The interaction is still repulsive for BCS-type pairing. For Amperean pairing, the part of the potential that should be negative for $\boldsymbol{p} = \boldsymbol{p}'$ now has a simplified dependence

$$\sim \frac{1}{\omega_{\boldsymbol{p}+\boldsymbol{p}'}} A(\boldsymbol{p} + \boldsymbol{p}', \Omega) - \frac{1}{\omega_{\boldsymbol{p}-\boldsymbol{p}'}} A(\boldsymbol{p} - \boldsymbol{p}', \Omega). \qquad (4.39)$$

This momentum structure still looks promising for a solution to the gap equation, now with some potential additional boosting of the potential for the case of $\Omega = 0$. Due to this boosting factor we were, in this case, actually able to obtain a solution to the gap equation from the region where the effect of the fermion energies on the interaction potential could be neglected. This should, however, merely be taken as an indication that the momentum structure of the interaction is suitable for realizing superconductivity. The gap function was found to have a p-wave character, and the critical temperature was found to increase with decreasing Ω and increasing next-nearest

neighbor frustration J_2 in the antiferromagnet, as shown in Fig. 4.9.

Based on our results, we concluded that an uncompensated antiferromagnetic interface might be a better candidate than a ferromagnetic interface for realizing superconductivity on the surface of a topological insulator. Looking back at our discussion of the difference between interaction mediated by ferromagnetic and antiferromagnetic magnons in the previous section, it should now be clear that the maximum of the antiferromagnetic potential is not necessarily increased by the presence of the boosting factor A, although it can be viewed in that way for a fixed gap in the magnon spectrum. Another point of view is, however, that the difference introduced by this boosting factor is that the same maximum of the potential obtained for the ferromagnet can be obtained with a larger gap in the magnon spectrum. In Paper [2], for a given maximum of the interaction potential, a larger gap in the magnon spectrum allowed for the fermions to be moved further away from the Fermi surface without the fermion energies dominating over the magnon energies in the interaction potential. The increased region of favorable contributions to the gap equation allowed for a solution to the gap equation in the antiferromagnetic case. Also when the frequency dependence of the interaction is accurately captured, having the same interaction strength with larger magnon energies should be expected to be an advantage as this will allow the interaction strength to be suppressed more slowly with increasing frequency. In order to corroborate these findings, one should properly consider both the momentum and frequency dependence of the interaction between helical fermions mediated by antiferromagnetic magnons, as well as associated fermion and magnon renormalization effects, which is yet to be done.

While the effect of fermion renormalization, in the ferromagnetic case, was found to be important for the superconductivity discussed in Ref. [101], fermion renormalization for the case of an uncompensated antiferromagnetic interface has been discussed in detail in Ref. [104]. Some of the ground work has therefore been laid for a future Eliashberg study of superconductivity arising from a topological insulator coupled to an uncompensated antiferromagnetic interface. For the ferromagnetic case, the effect of tilting the magnetization in-plane has also been considered in Ref. [105]. This study, considering a frequency dependent interaction, but neglecting fermion renormalization, also found that the pairing could be odd in frequency. Restricting to the static case of zero frequency, the gap equation obtained in Ref. [105] displayed very similar behavior to the gap equation in Paper [2], ex-

cept that contributions from a larger momentum region actually allowed for
formation of an Amperean p-wave solution.

In retrospect, performing a BCS-type study to investigate Amperean
pairing on the surface of a topological insulator mediated by magnons ap-
pears somewhat naive. We did, of course, not capture the effect of fermion
renormalization and we were further not able to reasonably capture the
frequency dependence of the interaction. Similarly to what we saw in the
previous chapter, we were, however, when all fermions were kept sufficiently
close to the Fermi surface, able to capture the momentum dependence of
the interaction. We could therefore obtain some useful information about
the difference between coupling the topological insulator to ferromagnetic
and antiferromagnetic interfaces. In particular, we identified that introduc-
ing asymmetry in the coupling to the two sublattices of an antiferromagnet
can be favorable also for the case of superconductivity on the surface of
a topological insulator. Our study also identified that introducing next-
nearest neighbor interaction in the antiferromagnet might be favorable. We
explored this further in Paper [3].

4.5 Schwinger boson study of superconductivity mediated by antiferromagnetic spin fluctuations

In Paper [3], we returned to the coupling between a normal metal and an an-
tiferromagnet. The goal was to better understand the effect of next-nearest
neighbor frustration in the antiferromagnet on the superconductivity medi-
ated by antiferromagnetic spin fluctuations. As the superconductivity arises
from magnetic fluctuations, one would expect that amplification of these
fluctuations would be favorable for the superconductivity. For relatively
weak frustration, this was what we found in Paper [2]. In this project we
wanted to extend these results to the case of larger frustration, investigating
how far this effect could be exploited. We therefore performed a Schwinger
boson study, allowing us to consider the full range from vanishing next-
nearest neighbor interaction to the case where the next-nearest neighbor
interaction dominates, giving rise to a stripe phase as introduced in Chap.
2. As the stripe phases, starting from $J_1 = 0$, arises from two decoupled
Néel antiferromagnets, we had a suspicion that coupling asymmetrically to
the spin-↑ and spin-↓ sites of both of these two Néel antiferromagnets could

give rise to a similar effect as obtained when coupling asymmetrically to the spin-↑ and spin-↓ sites of a normal Néel antiferromagnet. Moreover, although we, in this study, wanted to focus on the case of ordered magnetic phases, we also had hope that the study could provide some pointers for potential future investigation of superconductivity induced by coupling to disordered magnets.

The main finding of the article was that approaching the transition between the Néel and stripe phase from either side generally was favorable for the superconductivity as long as the magnetic order in the magnet was not suppressed too quickly. For the stripe phase, just like the Néel phase, asymmetry in the coupling to the two antiferromagnetic sublattices was found to be necessary in order to avoid destructive interference of contributions to the effective interaction potential.

The considered system, as well as the model for the normal metal, is the same as in Paper [1]. The main difference is that we include a next-nearest neighbor interaction in the antiferromagnet and rewrite the localized spins in terms of Schwinger bosons instead of performing a Holstein-Primakoff transformation. The interfacial coupling is on the same form as before, allowing for an asymmetric coupling to spin-↑ and spin-↓ sites of the antiferromagnet. For the antiferromagnet, we consider the spin quantum number $S = 1$, in which case, depending on the strength of the next-nearest neighbor interaction, our antiferromagnet will be in an ordered Néel or stripe phase. The treatment of the Néel phase is outlined in Chap. 2.

The coupling to e.g. the A-sublattice of the antiferromagnet now takes the form

$$
\begin{aligned}
H_{\text{int}}^{(A)} = {} & -2\bar{J}\,\Omega_A \sum_{\boldsymbol{i}\in A}\big(a_{\boldsymbol{i}\uparrow}^{\dagger}a_{\boldsymbol{i}\downarrow}\,c_{\boldsymbol{i}\downarrow}^{\dagger}c_{\boldsymbol{i}\uparrow} + a_{\boldsymbol{i}\downarrow}^{\dagger}a_{\boldsymbol{i}\uparrow}\,c_{\boldsymbol{i}\uparrow}^{\dagger}c_{\boldsymbol{i}\downarrow}\big) \\
& - \bar{J}\,\Omega_A \sum_{\substack{\boldsymbol{i}\in A \\ \sigma}} \sigma c_{\boldsymbol{i}\sigma}^{\dagger}c_{\boldsymbol{i}\sigma}\big(a_{\boldsymbol{i}\uparrow}^{\dagger}a_{\boldsymbol{i}\uparrow} - a_{\boldsymbol{i}\downarrow}^{\dagger}a_{\boldsymbol{i}\downarrow}\big).
\end{aligned}
\tag{4.40}
$$

The last term may give rise to a spin-splitting of the electron states, which similarly to earlier will be neglected. Introducing Fourier transformations, again neglecting Umklapp processes, and introducing a Bogoliubov transformation for the Schwinger boson operators, we end up with regular electron scattering terms involving two Schwinger boson operators.

In order to obtain an effective interaction between electrons mediated by antiferromagnetic spin fluctuations, we next perform a Schrieffer-Wolff

transformation, as detailed in the article. As the original fermion-boson
coupling now contains two bosonic operators, we will in this case end up
with an "effective interaction" that still involves two bosonic operators. This
additional combination of boson operators is replaced by its ground state
expectation value in order to obtain an effective interaction only involving
electrons. Setting $\Omega_B = 1$ and $\Omega_A = \Omega$ as before and investigating inter-
action between electrons with opposite momentum, the resulting pairing
Hamiltonian takes the form

$$H_{\text{pair}} = \sum_{\boldsymbol{k}\boldsymbol{k}'} V_{\boldsymbol{k}\boldsymbol{k}'} c_{\boldsymbol{k}\uparrow}^\dagger c_{-\boldsymbol{k}\downarrow}^\dagger c_{-\boldsymbol{k}'\downarrow} c_{\boldsymbol{k}'\uparrow}, \tag{4.41}$$

with

$$
\begin{aligned}
V_{\boldsymbol{k}\boldsymbol{k}'} = &-V^2 \frac{\tilde{Q}_0}{S} \frac{2\omega_{\boldsymbol{k}+\boldsymbol{k}'\downarrow}}{(\epsilon_{\boldsymbol{k}'} - \epsilon_{\boldsymbol{k}})^2 - \omega_{\boldsymbol{k}+\boldsymbol{k}'\downarrow}^2} A(\boldsymbol{k}+\boldsymbol{k}', \Omega) \\
&- \frac{V^2}{NS} \sum_{\boldsymbol{h}}' B(\boldsymbol{k}+\boldsymbol{k}'+\boldsymbol{h}, \boldsymbol{h}, \Omega) \frac{2\big(\omega_{\boldsymbol{k}+\boldsymbol{k}'+\boldsymbol{h}\uparrow} + \omega_{\boldsymbol{h}\downarrow}\big)}{\big(\epsilon_{\boldsymbol{k}'} - \epsilon_{\boldsymbol{k}}\big)^2 - \big(\omega_{\boldsymbol{k}+\boldsymbol{k}'+\boldsymbol{h}\uparrow} + \omega_{\boldsymbol{h}\downarrow}\big)^2}.
\end{aligned}
\tag{4.42}
$$

The prime on the sum over $\boldsymbol{h}$ denotes that the term with $\boldsymbol{h} = -\boldsymbol{k} - \boldsymbol{k}'$ has
been taken out of the sum. This interaction potential describes both the
case of a Néel phase and a stripe phase, with e.g. boson dispersion and
coherence factors depending on the phase. We have also defined

$$A(\boldsymbol{q}, \Omega) = \frac{1}{2}\big(\Omega^2 + 1\big)\big(u_{\boldsymbol{q}\downarrow}^2 + v_{\boldsymbol{q}\downarrow}^2\big) - 2\,\Omega\,u_{\boldsymbol{q}\downarrow}v_{\boldsymbol{q}\downarrow}, \tag{4.43}$$

as well as

$$B(\boldsymbol{q}, \boldsymbol{h}, \Omega) = \frac{1}{2}\big(\Omega^2 + 1\big)\big(u_{\boldsymbol{q}\uparrow}^2 v_{\boldsymbol{h}\downarrow}^2 + v_{\boldsymbol{q}\uparrow}^2 u_{\boldsymbol{h}\downarrow}^2\big) - 2\,\Omega\,u_{\boldsymbol{q}\uparrow}v_{\boldsymbol{h}\downarrow}v_{\boldsymbol{q}\uparrow}u_{\boldsymbol{h}\downarrow}. \tag{4.44}$$

For the here undefined factor $\tilde{Q}_0$, we simply note that it is closely related
to the sublattice magnetization of the antiferromagnet. A reduced sublat-
tice magnetization can therefore now lead to a weaker interaction strength.
Apart from this, the first part of the interaction potential $V_{\boldsymbol{k}\boldsymbol{k}'}$ corresponds
quite closely to the interaction potential obtained in Paper [1]. We highlight

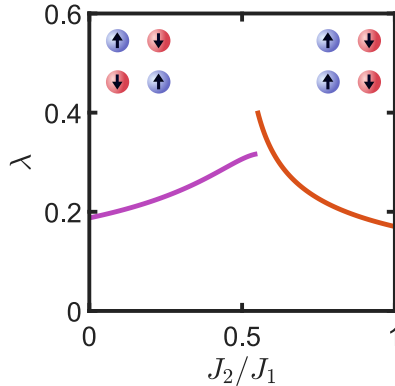Figure 4.10: Dimensionless coupling constant λ, for interaction mediated by antiferromagnetic spin fluctuations, as a function of next-nearest neighbor interaction J_2. We have considered the case where the electrons in the metal are only coupled to one of the two antiferromagnetic sublattices. Approaching the phase transition between the Néel phase and the stripe phase from either side gives rise to an increase in λ, leading to a higher superconducting critical temperature.

that the coherence factors, as mentioned in the Schwinger boson discussion in Chap. 2, have been taken to carry the same sign. For $\Omega = 1$, contributions arising from the two sublattices then interfere destructively in both the case of a Néel phase and a stripe phase. Compared to the case of Paper [1], we now also have an additional type of contributions to the interaction potential which we come back to shortly.

Performing the usual mean-field theory, we can further derive gap equations for spin-singlet and spin-triplet pairing. In the same way as in Paper [1], we can then solve linearized gap equations in order to determine the dimensionless coupling constant λ, as well as the resulting critical temperature and pairing symmetry. For $\Omega = 0$, the first part of the interaction potential naturally prefers p-wave pairing as before. Inspection of the second part of the interaction potential can further reveal that these contributions also contribute favorably to a p-wave solution. Compared to the first part of the potential, these additional contributions, simply summarized, come with an extra factor $1/N$, an extra sum over momentum, and some additional coherence factors. Despite the presence of additional coherence factors, as only a small part of the extra momentum sum contributes significantly to the gap

equation, it was found that the second part of the interaction potential had
little effect on the results.

The results obtained in the article for the dimensionless coupling con-
stant as a function of next-nearest interaction are presented in Fig. 4.10.
We have here set $\Omega = 0$. From this figure, we see that, for both the Néel
and stripe phase, moving in the direction of the phase transition leads to a
larger λ, associated with a larger critical temperature. This behavior arises
from a flattening of the bosonic dispersion relation, associated with gener-
ally larger coherence factors. As shown in Chap. 2, approaching the phase
transition also leads to a reduction of the sublattice magnetization, which
enters the interaction potential through a reduction of the prefactor $\tilde{Q}_0$.
The dominant effect is still that enhancing the magnetic fluctuations leads
to an increase in the dimensionless coupling constant. For the Néel phase,
we can, however, see that the increase in λ as a function of J_2 flattens out
a bit close to the transition point as the sublattice magnetization decays
quite quickly. For the stripe phase, featuring a weaker decay in the sublat-
tice magnetization close to the transition point, we instead see that λ has a
stronger increase close to the transition point.

While the first part of the interaction potential vanishes in the case of
loss of magnetic order, the second part of the interaction potential does not.
As the Schwinger boson formalism can also be used to describe disordered
phases, the second part of the interaction potential might therefore be able
to shed some light on electron-electron interaction induced by coupling to
a disordered antiferromagnet. In the present study, we found that keeping
the magnetic order was essential for the superconductivity, as the contri-
butions from the second part of the potential were small compared to the
contributions from the first part.

Through the work with Paper [1–3], we had started building an under-
standing of how magnetic fluctuations in an antiferromagnet may induce
superconductivity in a neighboring conductor, focusing on the role played
by sublattice interference and frustration. The conclusions obtained so far
where, however, associated with some uncertainty as we could not be con-
fident in how well the superconducting instability was described by our
BCS-like approach. A natural next step was therefore to go to Eliashberg
theory for answers.

4.6 Eliashberg study of superconductivity induced by interfacial coupling to antiferromagnets

In Paper [4], we studied our normal metal-antiferromagnet system using Eliashberg theory. We, this time, considered a trilayer structure and investigated the effect of asymmetry in the coupling to the antiferromagnetic sublattices for both small and larger Fermi surfaces. The extension to larger Fermi surfaces was partly motivated by an earlier BCS study showing that Umklapp scattering processes, for compensated antiferromagnetic interfaces, could give rise to spin-singlet d-wave pairing when the normal metal conduction band is close to half-filled [106]. The Fermi surface can then be approximately square, matching the reduced Brillouin zone of the magnons and allowing long-wavelength Umklapp processes to efficiently scatter electrons between different points on the Fermi surface.

The motivation for investigating the system within Eliashberg theory consisted of several parts. One of them was the following. During the work with the preceding articles, we had started to realize that the case of magnon-mediated superconductivity with dominant contributions from long-wavelength magnons is quite different from the case of phonon-mediated superconductivity, even for the case of acoustic phonons. In the latter case, the potential large contributions from phonons with small energy are suppressed by the electron-phonon coupling vanishing for zero-momentum phonons. Keeping in mind that the magnon case involves large contributions from long-wavelength magnons, one could clearly start questioning the approximation of treating the perpendicular momentum dependence of the interaction potential as a constant with a cutoff equal to the cutoff on the magnon spectrum. As large contributions from long-wavelength magnons rely on small magnon energies in the denominator of the interaction potential, these contributions will start being suppressed as soon as the outgoing electrons are moved a distance away from the Fermi surface larger than the gap in the magnon spectrum. In particular, we expected that the cutoff on the magnon spectrum may then no longer be determining the relevant energy scale for the critical temperature. Taking a quick look at the formula for the effective cutoff $\omega_{\log}$ presented in the previous chapter, we now see clearly that strong electron-boson interaction for long-wavelength bosons should be expected to lead to a smaller effective cutoff in the approximate expression for the critical temperature.

Due to the differences between coupling electrons to magnons and phonons,

we also wanted to consider electron renormalization, magnon renormalization, and vertex corrections in order to attempt to evaluate the importance of these effects. Moreover, based on the prediction that odd-frequency pairing could be possible in the ferromagnetic insulator-topological insulator system [105], we also wanted to look into the possibility of odd-frequency pairing.

The main finding of the study was that we still obtained a spin-triplet p-wave phase for the case of uncompensated antiferromagnetic interfaces and a small Fermi surface, as well as a d-wave phase for the case of compensated antiferromagnetic interfaces and larger Fermi surfaces close to half-filling. Moreover, especially for the p-wave phase, we found, as expected, that the effective cutoff setting the energy scale for the critical temperature was considerably smaller than the cutoff on the magnon spectrum.

The considered system is modelled in the same way as in Paper [1], except that we this time consider a normal metal layer sandwiched between two oppositely ordered antiferromagnets, cancelling out all net and staggered exchange fields. This simplifies the treatment and avoids potential negative effects of such fields on the possibility of superconductivity. Introducing Fourier and Holstein-Primakoff transformations, the interaction term in the Hamiltonian again takes the form of Eq. (4.16)

$$H_{\text{int}} = V \sum_{\substack{\boldsymbol{k}\in\square \\ \boldsymbol{q}\in\diamond}} \Big[M^R_{\boldsymbol{q}} c^\dagger_{\boldsymbol{k}+\boldsymbol{q},\downarrow} c_{\boldsymbol{k},\uparrow} + M^U_{\boldsymbol{q}} c^\dagger_{\boldsymbol{k}+\boldsymbol{q}+\boldsymbol{Q},\downarrow} c_{\boldsymbol{k},\uparrow}$$
$$+ (M^R_{-\boldsymbol{q}})^\dagger c^\dagger_{\boldsymbol{k}+\boldsymbol{q},\uparrow} c_{\boldsymbol{k},\downarrow} + (M^U_{-\boldsymbol{q}})^\dagger c^\dagger_{\boldsymbol{k}+\boldsymbol{q}+\boldsymbol{Q},\uparrow} c_{\boldsymbol{k},\downarrow} \Big],$$

but now with

$$M^\kappa_{\boldsymbol{q}} = \big(\Omega_A u_{\boldsymbol{q}} + \kappa\,\Omega_B v_{\boldsymbol{q}}\big)\big(\alpha_{\boldsymbol{q}H} + \alpha^\dagger_{-\boldsymbol{q}L}\big)$$
$$+ \big(\Omega_A v_{\boldsymbol{q}} + \kappa\,\Omega_B u_{\boldsymbol{q}}\big)\big(\beta^\dagger_{-\boldsymbol{q}H}, + \beta_{\boldsymbol{q}L}\big), \tag{4.45}$$

where H and L refer to the two antiferromagnets with opposite ordering. As we are, this time, also interested in larger Fermi surfaces, we do not throw out the Umklapp processes.

Due to the presence of Umklapp processes, we extend the electron basis that we used when we introduced Eliashberg theory in the previous chapter to

$$\psi_{\boldsymbol{k}}^{\dagger} = \begin{pmatrix} c_{\boldsymbol{k}\uparrow}^{\dagger} & c_{\boldsymbol{k}\downarrow}^{\dagger} & c_{-\boldsymbol{k}\uparrow} & c_{-\boldsymbol{k}\downarrow} & c_{\boldsymbol{k}+\boldsymbol{Q}\uparrow}^{\dagger} & c_{\boldsymbol{k}+\boldsymbol{Q}\downarrow}^{\dagger} & c_{-\boldsymbol{k}-\boldsymbol{Q}\uparrow} & c_{-\boldsymbol{k}-\boldsymbol{Q}\downarrow} \end{pmatrix}, \quad (4.46)$$

while now

$$B_{\boldsymbol{q}}^{\dagger} = \begin{pmatrix} (M_{\boldsymbol{q}}^{R})^{\dagger} & M_{-\boldsymbol{q}}^{R} & (M_{\boldsymbol{q}}^{U})^{\dagger} & M_{-\boldsymbol{q}}^{U} \end{pmatrix}. \qquad (4.47)$$

We can then express the interaction Hamiltonian on the symmetrized form

$$H_{\text{int}} = \frac{V}{4} \sum_{\substack{\boldsymbol{k}\in\square \\ \boldsymbol{q}\in\Diamond}} \sum_{\alpha\beta\gamma} g_{\gamma}^{\alpha\beta} B_{\boldsymbol{q}}^{\gamma} \psi_{\boldsymbol{k}+\boldsymbol{q}\alpha}^{\dagger} \psi_{\boldsymbol{k}\beta}, \qquad (4.48)$$

where the expressions for the matrices g_{γ} are provided in the article. Introducing matrices of Green's functions $\hat{G}(\boldsymbol{k},\tau) = -\langle T_{\tau}[\psi_{\boldsymbol{k}}(\tau) \otimes \psi_{\boldsymbol{k}}^{\dagger}(0)]\rangle$ and $\hat{D}(\boldsymbol{q},\tau) = -\langle T_{\tau}[B_{\boldsymbol{q}}(\tau) \otimes B_{\boldsymbol{q}}^{\dagger}(0)]\rangle$, we can, as before, derive Dyson equations, now with self-energies

$$\Sigma(k) = -\frac{V^2}{2\beta} \sum_{k'} \sum_{\gamma\gamma'} \theta_{\boldsymbol{k}-\boldsymbol{k}'} \hat{D}_{\gamma\gamma'}(k-k') g_{\gamma} \hat{G}(k') g_{\gamma'}, \qquad (4.49\text{a})$$

$$\Pi_{\gamma\gamma'}(q) = \frac{V^2}{4\beta} \sum_{k} \text{Tr}\left[g_{\gamma}\hat{G}(k+q) g_{\gamma'}\hat{G}(k)\right]. \qquad (4.49\text{b})$$

Here, we have neglected the effect of vertex corrections, which we return to later. Further, the factor $\theta_{\boldsymbol{q}}$ is equal to 1 if $\boldsymbol{q}$ is located inside the reduced Brillouin zone of the sublattices, and zero otherwise. This restriction on the sum arises from the magnons living in the reduced Brillouin zone. As magnons living in the reduced Brillouin zone can scatter electrons through regular or Umklapp processes, the presence of $\theta_{\boldsymbol{q}}$ does not put any restrictions on the scattering of electrons around in the full Brillouin zone. Further, the magnon Green's function matrix takes the form

$$\hat{D}(q) = \begin{pmatrix} 0 & \mathcal{D}^{RR}(q) & 0 & \mathcal{D}^{RU}(q) \\ \mathcal{D}^{RR}(-q) & 0 & \mathcal{D}^{UR}(-q) & 0 \\ 0 & \mathcal{D}^{UR}(q) & 0 & \mathcal{D}^{UU}(q) \\ \mathcal{D}^{RU}(-q) & 0 & \mathcal{D}^{UU}(-q) & 0 \end{pmatrix}, \qquad (4.50)$$

where in the non-interacting case

$$\mathcal{D}_0^{\kappa\kappa'}(\boldsymbol{q}, i\nu_m) = -2A_e^{\kappa\kappa'}(\boldsymbol{q})\frac{2\omega_{\boldsymbol{q}}}{\nu_m^2 + \omega_{\boldsymbol{q}}^2}. \tag{4.51}$$

Here, the boosting factors are given by

$$A_e^{RR}(\boldsymbol{q}) = \frac{1}{2}[(\Omega_A u_{\boldsymbol{q}} + \Omega_B v_{\boldsymbol{q}})^2 + (\Omega_A v_{\boldsymbol{q}} + \Omega_B u_{\boldsymbol{q}})^2], \tag{4.52a}$$

$$A_e^{UU}(\boldsymbol{q}) = \frac{1}{2}[(\Omega_A u_{\boldsymbol{q}} - \Omega_B v_{\boldsymbol{q}})^2 + (\Omega_A v_{\boldsymbol{q}} - \Omega_B u_{\boldsymbol{q}})^2], \tag{4.52b}$$

$$A_e^{RU}(\boldsymbol{q}) = A_e^{UR}(\boldsymbol{q}) = \frac{1}{2}(\Omega_A^2 - \Omega_B^2)(u_{\boldsymbol{q}}^2 + v_{\boldsymbol{q}}^2). \tag{4.52c}$$

Starting with the case of only regular scattering processes, we see that $\mathcal{D}_0^{RR}(\boldsymbol{q}, i\nu_m)$ is similar to the corresponding part of the effective interaction potential that we derived earlier

$$V_{\boldsymbol{k}\boldsymbol{k}'} = V^2 \frac{2\omega_{\boldsymbol{k}+\boldsymbol{k}'}}{-(\epsilon_{\boldsymbol{k}'} - \epsilon_{\boldsymbol{k}})^2 + \omega_{\boldsymbol{k}+\boldsymbol{k}'}^2} A(\boldsymbol{k}+\boldsymbol{k}', \Omega_A, \Omega_B),$$

except for, again, the fermion energies being substituted by a frequency dependence. The boosting factors are identical. Inspecting the case of only Umklapp scattering processes, we see that the boosting factor $A_e^{UU}(\boldsymbol{q})$ is actually maximized for $\Omega_A = \Omega_B$. This arises from the earlier discussed sign-change for Umklapp scattering associated with the B-sublattice, which was exploited in Ref. [106].

Due to the structure of $\psi_{\boldsymbol{k}}^\dagger$, the matrix $\hat{G}$ does not only contain correlations between electrons with the same or opposite momentum, starting with momentum $\boldsymbol{k}$ or $\boldsymbol{k}+\boldsymbol{Q}$. It also contains correlations between electrons with e.g. momenta $\boldsymbol{k}$ and $\boldsymbol{k}+\boldsymbol{Q}$, potentially giving rise to a commensurate spin-density wave. As discussed in more detail in the article, away from half-filling, both $\boldsymbol{k}$ and $\boldsymbol{k}+\boldsymbol{Q}$ will not be close to the Fermi surface simultaneously and such correlations may be neglected.

Including the possibility of either spin-singlet or spin-triplet pairing, we can then take an Ansatz for $\Sigma(k)$ similar to what we did in the previous chapter and derive Eliashberg equations

$$[1 - Z(k)]i\omega_n = -V^2 \frac{1}{\beta} \sum_{k'} \mathcal{D}(k - k') \frac{i\omega_{n'} Z(k')}{\Theta(k')}, \tag{4.53a}$$

$$\chi(k) = -V^2 \frac{1}{\beta} \sum_{k'} \mathcal{D}(k - k') \frac{\xi_{k'} + \chi(k')}{\Theta(k')}, \tag{4.53b}$$

$$\phi_s(k) = -V^2 \frac{1}{\beta} \sum_{k'} \mathcal{D}(k - k') \frac{\phi_s(k')}{\Theta(k')}, \tag{4.53c}$$

$$\phi_t(k) = +V^2 \frac{1}{\beta} \sum_{k'} \mathcal{D}(k - k') \frac{\phi_t(k')}{\Theta(k')}, \tag{4.53d}$$

valid for one of ϕ_s and ϕ_t nonzero, corresponding to spin-singlet or spin-triplet pairing. We then have

$$\Theta(k) = [i\omega_n Z(k)]^2 - \tilde{\xi}_k^2 - |\phi_{s,t}(k)|^2, \tag{4.54}$$

where we have also introduced the magnon propagator

$$\mathcal{D}(q) = \theta_{\boldsymbol{q}} \mathcal{D}^{RR}(\boldsymbol{q}, i\nu_m) + \theta_{\boldsymbol{q}+\boldsymbol{Q}} \mathcal{D}^{UU}(\boldsymbol{q} + \boldsymbol{Q}, i\nu_m). \tag{4.55}$$

The momenta $\boldsymbol{k}$ and $\boldsymbol{k}'$ in the Eliashberg equations are allowed to take on values in the full Brillouin zone and depending on whether their difference is located in the reduced Brillouin zone or not, the relevant magnon propagator will be a regular or Umklapp propagator.

Investigating the equations for the pairing amplitudes, we start with the case of a small Fermi surface where regular scattering processes dominate. We first note that the equation for spin-singlet pairing now comes with an opposite sign compared to the phonon-case we considered in the previous chapter. This sign-change arises from the spin-flip structure of the electron-magnon interaction in combination with the oddness of spin-singlet pairing under spin-exchange. Just like we found when working in the BCS framework, spin-singlet pairing does therefore not look so promising for the case of a small Fermi surface. Considering instead the possibility of spin-triplet pairing, $\Theta(k')$ comes in with a negative sign and $\mathcal{D}$ has a negative prefactor. At least for the case of uncompensated antiferromagnetic interfaces, we would further, similarly to in the BCS case, expect $\mathcal{D}^{RR}(k - k')$ to be larger in magnitude when $\boldsymbol{k}$ and $\boldsymbol{k}'$ are parallel than antiparallel. The part
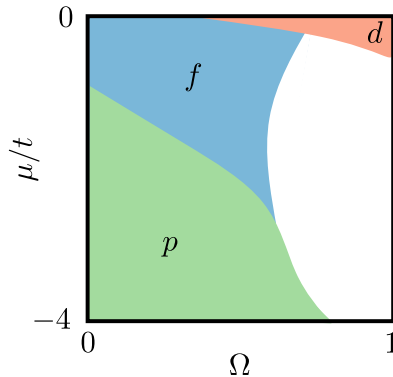
Figure 4.11: Sketch of the phase diagram as a function the sublattice asymmetry of the interfacial coupling, Ω, and chemical potential μ in units of the hopping amplitude t. The regions are colored according to which phase maximizes the critical temperature.

of the propagator which is odd in momentum should then be favorable for spin-triplet p-wave pairing.

If we instead go to the case of a Fermi surface close to half-filling, Umklapp processes start becoming important. This does not rule out the possibility of spin-triplet pairing. It does, however, also introduce the possibility of a spin-singlet d-wave solution where electrons can be Umklapp scattered by long-wavelength magnons from one corner of the almost square Fermi surface to another, introducing a sign-change in the d-wave pairing amplitude. A spin-singlet solution could therefore be possible [106], despite the "interaction potential" seemingly having the wrong sign. Regular scattering processes between points on the Fermi surface where the pairing amplitude has the same sign will, however, still not favor a spin-singlet solution. The importance of sublattice coupling asymmetry then enters the picture through the fact that the regular processes are suppressed for a compensated interface, while the Umklapp processes are not.

In order to simplify the equations, we neglect the effect of χ, renormalization of the magnons, and the momentum dependence of Z. Linearizing the equations close to T_c, we further neglect the perpendicular momentum dependence of the magnon propagator, the pairing amplitudes, and the density of states, allowing us to derive Fermi surface averaged equations. One way of solving these Fermi surface averaged equations is then to assume a

specific Ansatz for the parallel momentum dependence of the pairing amplitude, allowing for explicit evaluation of the Fermi surface averages. The remaining frequency dependent equations can then be dealt with in the same way as described in the previous chapter, allowing for determination of the critical temperature for a given assumption about the spin and momentum symmetries of the pairing amplitude. In order to help interpret the results obtained by solving the Eliashberg equations, the approximate T_c formula introduced in the previous chapter can also be useful, although developed with phonon-mediated superconductivity in mind.

Solving the Fermi surface averaged equations for different pairing symmetries and determining which phase features the largest critical temperature, we obtain the phase diagram in Fig. 4.11. We have here defined $\Omega_A = 1$ and $\Omega_B = \Omega$, in contrast to our earlier choice. This is not of importance. As expected, we obtain a spin-triplet p-wave phase for small Fermi surfaces and small Ω and a spin-singlet d-wave phase close to half-filling and $\Omega = 1$. We also find an additional spin-triplet f-wave phase which is similar to the p-wave phase, but better takes advantage of the Umklapp processes. As mentioned earlier, realistic uncompensated interfaces might, however, typically not give rise to Umklapp processes. Taking out the Umklapp processes from our model by hand for the case of $\Omega = 0$, there is no longer any reason for the f-wave phase to be favored over the p-wave phase.

Another expected finding was that the importance of long-wavelength magnons substantially reduced the effective cutoff setting the energy scale for the critical temperature, especially for the p-wave phase. For the p-wave case, the results presented in the article would indicate that the gap in the magnon spectrum might be a more relevant energy scale than the maximum of the spectrum. The cutoff was found to be somewhat larger for the d-wave phase, allowing for the possibility of higher critical temperatures.

We also tested the BCS theory prediction that next-nearest neighbor frustration can be favorable for superconductivity, finding that this held true also within our Eliashberg approach. Similarly to what we found in BCS theory, the dimensionless coupling constant $\lambda(0)$ was found to increase with frustration. Further, the effect on the effective cutoff was found to be relatively weak, leading to an increased critical temperature for both the p-wave and d-wave phase.

We further considered the effect of magnon renormalization, concluding that the dominant effect on the possibility of superconductivity was a renormalization of the gap in the magnon spectrum. This renormalization
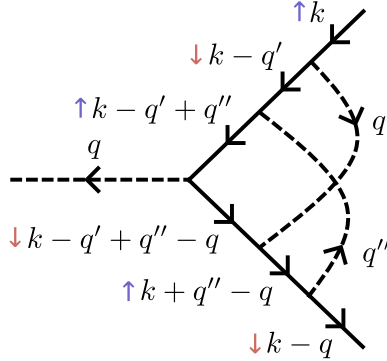
Figure 4.12: Lowest-order diagram correcting the interaction vertices. Dotted lines represent magnon propagators, while solid lines represent electron propagators.

may lead to loss of magnetic ordering if the easy-axis anisotropy in the antiferromagnet is too small. By increasing the easy-axis anisotropy, this effect can however be cancelled out, leaving the possibilities for superconductivity relatively unchanged by magnon renormalization. If the renormalization of the gap is relatively large, this may, on the other hand, pose an experimental challenge of finding a material combination with the fine-tuned property of both avoiding ending up with a too large gap in the magnon spectrum and avoiding ending up with loss of magnetic order.

Finally, we also considered the effect of vertex corrections, motivated by the fact that Migdal's theorem may break down for coupling to long-wavelength phonons or in systems with nested Fermi surfaces. We first considered the case of a circular Fermi surface where regular scattering processes dominate. The lowest-order diagrams correcting the interaction vertices were, due to the spin-structure of the electron-magnon scattering, found to take the form displayed in Fig. 4.12. Vertex corrections should then be expected to be less important than what would have been the case if the simpler diagram of the type considered for the phonons did not vanish in this case. Not taking into account that q could be small, we obtained a simple estimate for the lowest-order corrections to the interaction vertex

$$|\Gamma_1(k,q)| \sim \left(\frac{V^2 N A_e^{RR}(0)}{E_F^2}\right)^2 \sim \left(\frac{1}{100}\right)^2, \qquad (4.56)$$

indicating that vertex corrections are typically negligible due to the energy scale of the electron-magnon coupling being small compared to the electron energy scale.

Considering the possibility that q may be small, we instead obtained a rough estimate

$$|\Gamma_1(k,q)| \sim \left(\frac{N_F V^2 A_e^{RR}(0)}{E_F}\right)^2 \left(\frac{E_F}{\sqrt{v_F^2 q^2 + q_m^2}}\right), \qquad (4.57)$$

for bosonic Matsubara frequency $|q_m| > 0$. This expression was found to be of relevant magnitude for $q = 0$, but, due to the largeness of the Fermi velocity, also found to decay fast with increasing q in the momentum region most relevant for contributions to the pairing amplitude equation. Moreover, while vertex corrections should further be expected to be important exactly at half-filling, we estimated their effect to be considerably reduced when moving away from half-filling.

Throughout the article, a general trend is that our treatment is not valid too close to half-filling. In particular, it is possible that the superconducting instability could be dominated by a spin density wave instability in this region. This represents a potential drawback for the d-wave phase, which otherwise, compared to the p-wave phase, has the advantage of the possibility of larger critical temperatures while being less reliant on realizing a small, but nonzero, renormalized gap in the magnon spectrum. Based on our previous discussion of the comparison of the p-wave phase arising from ferromagnetic and uncompensated antiferromagnetic interfaces, we can now also note the following. The ferromagnetic case would be expected to produce lower critical temperatures as it needs to compensate for the missing boosting factor by relying on contributions from smaller magnon energies, leading to a smaller energy scale for the critical temperature. This advantage of the antiferromagnet over the ferromagnet is similar to what we earlier discussed for the topological insulator system in Paper [2].

As part of the motivation for wanting to extend the study of the p-wave phase to Eliashberg theory was that important contributions to the interaction potential appeared to be quickly suppressed when moving away from

the Fermi surface, one might ask the following question. Is it also important to take into account the behavior of the electron-magnon interaction when moving away from the Fermi surface in Eliashberg theory? In the BCS treatment of the p-wave phase for small Fermi surfaces, the dominant suppression of the interaction potential when moving away from the Fermi surface was that the electron energies in the denominator grew large. When moving away from the Fermi surface in Eliashberg theory, the situations is quite different. Considering the pairing amplitude at the Fermi surface, there will still be a suppression of the contributions from the right-hand-side of the equation when moving electrons away from the Fermi surface as important magnons carrying near-vanishing momentum cannot bring electrons from the Fermi surface to some point away from the Fermi surface. The suppression of the interaction is in this case determined by the magnon energy scale, rather than the electron energy scale. Taking into account the variations in the interaction strength when moving electrons away from the Fermi surface could, however, still lead to a reduction in the obtained critical temperatures. As contributions away from the Fermi surface to the pairing amplitude equation are already suppressed by the electron energy scale, this reduction does not necessarily have to be that large. For the d-wave phase, on the other hand, considering the dependence of the interaction on perpendicular momentum may have a different effect. Slightly away from half-filling, Umklapp scattering off zero-momentum magnons does not connect points on the Fermi surface. Evaluating the interaction also for the case of electrons away from the Fermi surface will then open up the possibility of zero-momentum magnon scattering, which can lead to increased contributions to the pairing amplitude equation. Taking such effects into account represents a substantial complication of the problem, but it should be feasible.

We also note that our magnon propagators ended up even in frequency, meaning that we did not see any opportunities for odd-frequency pairing. This was, at least, the case when all exchange fields were cancelled out. As briefly mentioned in the article, considering e.g. a single antiferromagnetic layer with $\Omega \neq 1$, producing a net exchange field experienced by the normal metal electrons, would produce an odd-frequency term in the magnon propagators. For the case of $\Omega = 0$, we would, however, expect the resulting exchange field to create serious problems for the superconductivity. The topological insulator system [105], where the superconductivity is less strongly affected by spin-splitting, might therefore be a better candidate for

further investigation of magnon-mediated odd-frequency pairing.

Finally, we highlight that an overarching goal of the series of papers discussed in this chapter has been to attempt to identify, as well as compare, types of heterostructures of magnets and conductors that can give rise to magnon-mediated superconductivity. While the first three articles focus largely on the advantage of uncompensated antiferromagnetic interfaces, the last of the articles brought us somewhat closer to the physics of single-material systems through the d-wave superconductivity possible for sublattice symmetric electron-magnon coupling. While additional theoretical investigation can be performed, possibly taking more advantage of the extensive existing literature discussing superconductivity arising from spin fluctuations, collaboration with experiments is likely to be a key for further development.

5

Indirect exchange interaction

Direct exchange interaction was briefly introduced in Chap. 2, taking the form of a spin-spin interaction that in many cases can be stronger than the associated dipole-dipole interaction. We there put forward that the energy of a two-electron system may depend on the symmetry of the total wave function of the system under exchange of the spatial coordinates of the electrons, leading to an effective interaction between the spins of the electrons. However, if the electrons in this example are localized far away from each other, without any overlap of their individual wave functions, the spin configuration of the system will no longer have any real effect on the total spatial wave function. In simple words, forcing the electrons to stay away from each other by putting them in a spin-triplet state does not have any effect if the electrons are never near each other to begin with. While unpaired electrons, giving rise to net magnetic moments, situated at neighboring atoms may have enough wave function overlap to interact directly, exchange interaction over longer distances requires some additional help.

In many magnetic materials, not all atoms are associated with a net magnetic moment. In that case, the interaction between magnetic moments can e.g. be transferred through the help of intermediate non-magnetic atoms [26]. An unpaired electron associated with a given atom can then influence the spatial distribution of spin-↑ and spin-↓ electrons bound to a neighboring non-magnetic atom, which again can influence the spin of an unpaired electron associated with a different magnetic atom. Interaction over even larger distances can also be possible by having itinerant electrons mediate the interaction. This is referred to as Ruderman–Kittel–Kasuya–Yosida (RKKY) interaction [107–109], and will be discussed further in this chapter.

We start the chapter by providing a brief introduction to RKKY interaction, before we move on to indirect interaction mediated by superconductors. We introduce both RKKY interaction between magnetic impurities mediated by the quasiparticles in a superconductor, as well as indirect interaction
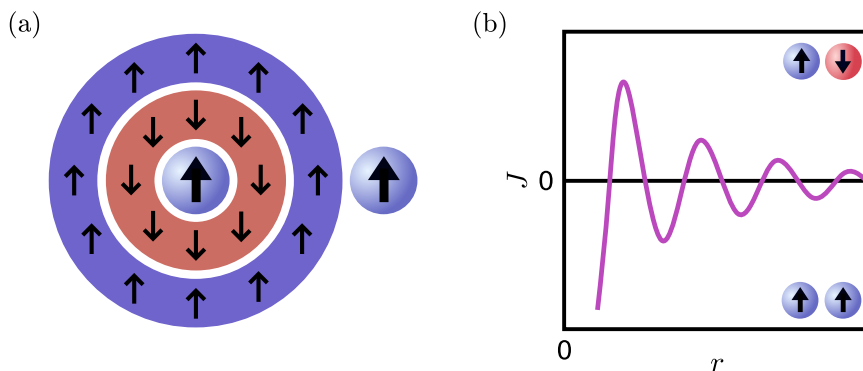
Figure 5.1: (a) Itinerant electrons scattered by a localized spin form an oscillatory pattern of regions with higher density of spin-↑ and spin-↓ electrons. The preferred direction of a second localized spin will then be an oscillating function of the separation distance r between the localized spins. (b) Sketch of the RKKY interaction J between two localized spins, mediated by itinerant electrons, as a function of r.

between ferromagnets connected by a superconductor. In the latter case, the indirect interaction, determining the preferred magnetic configuration of the system, consists of both normal RKKY contributions as well as the effect of the ferromagnets on the energy of the superconductor. We end the chapter by discussing Paper [5], where the considered effect is indirect interaction between two ferromagnets mediated by a d-wave superconductor.

5.1 RKKY interaction

As mentioned above, RKKY interaction is an indirect exchange interaction mediated by itinerant electrons. If we consider a localized spin surrounded by a cloud of electrons, the itinerant electrons will be scattered by the localized spin, giving rise to an oscillatory pattern of regions with higher density of spin-↑ and spin-↓ [26], as shown in Fig. 5.1 (a). A second localized spin located nearby will then feel this generated spin density wave. This gives rise to an effective interaction $J\,\boldsymbol{S_1}\cdot\boldsymbol{S_2}$ between the localized spins, where J exhibits a damped oscillatory behavior with increasing separation distance between the localized spins. A sketch of the interaction strength as a func-

tion of the separation distance r is shown in Fig. 5.1 (b).

RKKY interaction can be of relevance for metallic materials featuring localized magnetic moments as well as itinerant electrons. We can, however, also have RKKY interaction between magnetic materials separated by a nonmagnetic material featuring itinerant electrons [26]. In that case, one can similarly have a situation where the preferred relative magnetization direction of the magnetic materials can vary with the separation distance between them. RKKY interaction therefore plays an important role in realizing giant magnetoresistance (GMR) [110, 111], which we introduced in Chap. 1. In order for us to be able to change the resistance of a GMR structure by applying a magnetic field, it is essential that the magnetization of the magnetic layers are not aligned in the absence of the field. Through the RKKY interaction between the layers, one can then ensure that the magnetizations are anti-aligned by adjusting the separation distance between the magnetic layers.

5.2 Indirect interaction mediated by superconductors

Rather than the interaction between localized spins surrounded by the itinerant electrons in a metal, one could also consider the interaction between localized spins surrounded by the quasiparticles in a conventional superconductor. Then, comparing the RKKY interaction below the superconducting critical temperature with the interaction above the critical temperature, the following simplified picture emerges. For short separation distances, the RKKY interaction is similar, while for larger separation distances the interaction below T_c is suppressed and has a tendency of favoring anti-alignment of the spins [112, 113]. The length scale governing the additional suppression is the superconducting coherence length, which can be thought of as the typical separation between the electrons forming the Cooper pairs. This additional damping for separation distances larger than the coherence length can be understood as arising from the fact that the presence of a gap in the excitation spectrum leads to less particles around the Fermi level that can mediate the interaction. For interaction between localized spins mediated by the quasiparticles of a d-wave superconductor, the picture is similar [114].

Similarly to what we introduced in the previous section, one could also consider interaction between magnetic materials mediated by supercon-

ductors. This interaction could, in itself, present an interesting opportunity to control magnetic configurations through superconductors [115, 116]. Moreover, as heterostructures of superconductors and magnets are essential building blocks within superconducting spintronics, a thorough understanding of how the materials in such heterostructures influence each other is desirable. Before discussing interaction between magnetic materials mediated by superconductors, we first introduce some of the effects that can take place at interfaces between superconductors and magnetic materials.

As introduced in Chap. 3, proximity to a ferromagnetic insulator can induce spin-splitting in a superconductor. Further, an interface between a ferromagnetic metal and a superconductor allows for both itinerant electrons from the ferromagnet to tunnel into the superconductor and for superconducting correlations to leak into the magnet. This can lead to a magnetization being induced at the surface of the superconductor, either directed in the same or opposite direction as the magnetization in the magnet [117, 118]. The leakage of superconducting correlations into the magnet is typically also associated with a reduction in the superconducting gap close to the interface. Further, while itinerant electrons from a metallic ferromagnet with energy within the energy gap of the superconductor normally are not allowed inside the superconductor, when approaching the interface, such electrons can instead experience Andreev reflection [119]. The incoming electron is then reflected back as a hole, leading to generation of a Cooper pair in the superconductor. The reverse process leads to destruction of a Cooper pair in the superconductor.

A typical situation might be that a conventional superconductor sandwiched between two ferromagnetic insulators simply prefers anti-alignment of the ferromagnets [115, 120]. In general, one could, however, have a situation where contributions from RKKY interaction mediated by the itinerant quasiparticles gives rise to sign changes in the effective interaction strength as a function of the separation of the ferromagnets. Considering metallic ferromagnets, instead of ferromagnetic insulators, can also introduce additional effects [121]. The overall picture still seems to be that such systems generally has a preference for anti-alignment of the ferromagnets. For the case of a d-wave superconductor sandwiched between ferromagnetic insulators, it has similarly been observed a preference for anti-alignment of the magnetizations for sufficiently large separation distances [116].

In the upcoming section, we will also be discussing the indirect interaction between ferromagnets mediated by a d-wave superconductor. Instead

of ferromagnetic insulators sandwiching the superconductor, we will consider metallic ferromagnets attached to the same edge of the superconductor. Importantly, we will consider an edge of the superconductor featuring zero-energy surface states, referred to as midgap states. To understand the origin of such surface states, one can consider either a d-wave superconductor/normal metal/insulator trilayer, or e.g. simply a d-wave superconductor next to vacuum where the superconducting gap is suppressed close to the edge producing, simply stated, a "normal region" with both an insulator and a superconductor interface. One may then consider electrons that experience alternating normal and Andreev reflections at the insulator and superconductor interfaces. If the d-wave superconducting order parameter is oriented such that particles involved in subsequent Andreev reflections experience opposite signs of the superconducting gap function, formation of zero-energy bound states may take place [122–124]. The formation of such midgap states has been used as a signature for identifying the cuprates as d-wave superconductors [123, 125].

5.3 Effect of midgap states on the magnetic exchange interaction mediated by a d-wave superconductor

With some background on the physics taking place in systems where ferromagnets are connected by a superconductor, we now move on to discussing Paper [5]. In this article, we considered the indirect interaction between two metallic ferromagnets mediated by a d-wave superconductor. Specifically, we considered the case where the ferromagnets are connected to an edge of the superconductor featuring midgap states. The motivation behind the study was the following. The ability of superconductors to mediate indirect interaction is, as discussed above, influenced by their gapped band structure. How is the indirect interaction altered if one introduces midgap states in the spectrum?

The main finding of the article is that the presence of midgap states can qualitatively change the indirect interaction between the ferromagnets. The interaction is in this case found to vary little with the separation distance between the ferromagnets and to favor alignment of the magnetization of the ferromagnets, rather than anti-alignment.

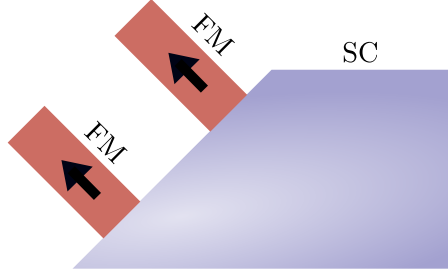The considered system is presented in Fig. 5.2. The structure was de-

Figure 5.2: System setup consisting of two metallic ferromagnets connected to an edge of a d-wave superconductor featuring midgap states.

signed in order to allow for placement of magnets on different types of edges. The article also considered the case where the interaction in this structure is mediated by a normal metal, as well as an s-wave superconductor. In this discussion, we will focus on the case of ferromagnets connected to the diagonal edge of a d-wave superconductor.

The d-wave superconductor is taken to be described by a model

$$H_{\mathrm{SC}} = -\sum_{\langle \boldsymbol{i},\boldsymbol{j}\rangle,\alpha} t_{\boldsymbol{ij}} c_{\boldsymbol{i}\sigma}^{\dagger} c_{\boldsymbol{j}\sigma} - \sum_{\boldsymbol{i},\sigma} \mu_{\boldsymbol{i}} n_{\boldsymbol{i}\sigma} + \sum_{\langle \boldsymbol{i},\boldsymbol{j}\rangle,\sigma\neq\sigma'} V_{\boldsymbol{ij}}\, n_{\boldsymbol{i}\sigma} n_{\boldsymbol{j}\sigma'}, \qquad (5.1)$$

where $n_{\boldsymbol{i}\sigma} = c_{\boldsymbol{i}\sigma}^{\dagger} c_{\boldsymbol{i}\sigma}$ is a number operator and $V_{\boldsymbol{ij}}$ is taken to be a negative constant V for $\boldsymbol{i}$ and $\boldsymbol{j}$ inside the superconductor. The lattice is taken to be a square lattice. This is a simple model which can give rise to a superconducting state with the desired symmetry properties. Further, the metallic ferromagnets are described through an effective model describing itinerant electrons subjected to a spin-splitting

$$H_{\mathrm{FM}} = -\sum_{\langle \boldsymbol{i},\boldsymbol{j}\rangle,\sigma} t_{\boldsymbol{ij}} c_{\boldsymbol{i}\sigma}^{\dagger} c_{\boldsymbol{j}\sigma} - \sum_{\boldsymbol{i},\sigma} \mu_{\boldsymbol{i}} n_{\boldsymbol{i}\sigma} - \sum_{\boldsymbol{i},\sigma\sigma'} h_{i} \left(\sigma_{z}\right)_{\sigma\sigma'} c_{\boldsymbol{i}\sigma}^{\dagger} c_{\boldsymbol{i}\sigma'}. \qquad (5.2)$$

The spin-splitting field is assumed to take on a uniform value inside each ferromagnet. By taking the same/opposite sign of the spin-splitting fields in

the two ferromagnets, we can then model a configuration with aligned/anti-aligned magnetization in the ferromagnets. Further, the coupling between the materials is introduced through a nonzero hopping amplitude across the interfaces, while the vacuum region outside of the superconductor and ferromagnets is simply decoupled from the rest of the system by a vanishing hopping amplitude.

The superconductor is treated in the real-space Bogoliubov-de Gennes framework [126], which involves introducing real-space pairing amplitudes on the form $F_{ij}^{\sigma\sigma'} = \langle c_{i\sigma}c_{j\sigma'}\rangle$. The methodology is outlined in Ref. [124]. The full Hamiltonian of the system can then be expressed in terms of a constant part, as well as a sum over terms quadratic in electron operators. Collecting this together, we can write $H = H_0 + B^\dagger M B$, where M is a large matrix connecting pairs of electron operators. This matrix can be diagonalized numerically for a given set of system parameters and an initial set of values for the pairing amplitudes, leading to the original electron operators being expressed in terms of new quasiparticle operators. Using the relationship between the original electron operators and the new quasiparticle operators, one can then calculate new values of the pairing amplitudes and again diagonalize the Hamiltonian. This procedure is repeated until the values for the pairing amplitudes converge.

Performing the above steps for both the configuration with aligned and anti-aligned ferromagnet magnetization, one can then define an effective interaction between the ferromagnets

$$J = F^{\uparrow\uparrow} - F^{\uparrow\downarrow}, \tag{5.3}$$

where $F^{\uparrow\uparrow}$ is the free energy of the system for the case of aligned ferromagnets, and $F^{\uparrow\downarrow}$ represents the case of anti-aligned ferromagnets. If J is positive, the system then prefers anti-alignment of the ferromagnets, while a negative J corresponds to a preference for alignment of the ferromagnets.

Calculating J for ferromagnets placed with varying separation distance on the diagonal edge of the superconductor in Fig. 5.2, the obtained result is that the system always prefers alignment of the magnetization of the ferromagnets. This result was interpreted in the following way. Although the presence of the ferromagnets would normally suppress the superconducting gap close to the edge, the dominant effect turns out to be suppression of the midgap states, actually allowing for an increase in the superconducting gap along the edge. The aligned magnet configuration produces a more

uniform suppression of the midgap states along the diagonal edge, while the anti-aligned configuration allows for the midgap states to better survive in a region between the two ferromagnets where their respective effects on the system cancel out. The aligned magnet configuration therefore produces the overall largest superconducting gap, leading to this configuration being favored by the system.

As the midgap states provide the superconductor with substantial density of states around the Fermi level, one might imagine that the above discussed preference of alignment of the ferromagnets also could have contributions from a paramagnetic effect. Although we observed an induced magnetization along the diagonal edge, it was hard to find support in the data for this magnetization being directly associated with an energy gain for the system. It was, however, evident that the suppression of the midgap states, which appeared to be the dominant effect of the presence of the ferromagnets, produced an increased superconducting gap.

In general, the study could have benefited from being able to investigate larger system sizes. This could, in general, have made it somewhat easier to interpret the results and, for instance, allowed us to study the decay of the interaction between the magnets as a function of their separation distance. It is also possible that there would be less complications associated with a more symmetric structure than the one considered in this work. A triangular structure could be one option, but the simplest choice might be a structure without different types of edges. When we e.g., for comparison, studied the case where the ferromagnets were connected to a horizontal edge of a d-wave superconductor, avoiding disturbance from interaction with the midgap states located at the diagonal edge was an issue. Moreover, when studying the case of interaction mediated by a normal metal and an s-wave superconductor, the corners of the structure were often a source of difficulty. Luckily, the main result of the paper, the preference of alignment of the ferromagnets when attached to a diagonal edge of a d-wave superconductor, turned out to be a robust result that e.g. was not sensitive to how close to the corners of the structure the ferromagnets were placed.

6

Critical magnetic field of flatband superconductors

In Chap. 3, we showed that the spin-splitting field that a spin-singlet s-wave superconductor can survive is limited to a fraction of the superconducting gap at zero field and temperature. This result can further be generalized to spin-singlet superconductors with other gap symmetries [64]. Superconductivity beyond this limit is therefore often taken as an indication of spin-triplet pairing. In our calculation for the singlet case, we saw that both the condensation energy of the superconducting state and the so-called paramagnetic energy gain of the normal state in the presence of a spin-splitting field had one thing in common: They both increased with the density of states at the Fermi level, which was taken to represent the density of states in the thin shell around the Fermi level that constituted the relevant energy region. In this chapter, we investigate how the critical spin-splitting field of a spin-singlet superconductor may be affected if the density of states varies significantly within the relevant energy region.

Large variations in the density of states can be achieved if the dispersiveness of the relevant energy bands feature large variations. Energy bands that feature flat portions can be an example of this. It is, however, also possible to have energy bands that are completely, or almost completely, flat in the entire, or large parts of, the Brillouin zone. We will here loosely refer to such bands as flatbands. A band structure consisting of e.g. one completely flat band and one more dispersive band can be an example of a system featuring very large variations in the density of states over a small energy range.

We start the chapter by providing a brief introduction to flatband systems, highlighting their recent realization in twisted van der Waals multilayers. We then proceed to discuss superconductivity in flatband systems,

which has been gathering much attention after the observation of super-conductivity in twisted bilayer graphene. We end the chapter by discussing Paper [6], where we consider the critical spin-splitting field of a simple model for a superconductor with both one dispersive band and one flatband near the Fermi level.

6.1   Flatband systems

Completely flat energy bands can result from specific tight-binding models [127–134], which may be realized in different types of artificial systems [135–140]. Such energy bands rely on either protection by lattice symmetry or very specific values of the parameters of the system. They have often been studied in the context of Stoner magnetism due to the large density of states that they provide [127].

Recently, it has also been found that energy bands with very weak momentum dependence can be realized in twisted bilayer graphene [141, 142], consisting of two layers of graphene grown on top of each other with a relative twist-angle. This system represents an example of so-called van der Waals heterostructures [143, 144], consisting of two-dimensional materials which are bound to each other by weak van der Waals forces. In contrast to the typical case, the weak coupling between the layers in these heterostructures allows for the different layers to keep their structure while not being lattice matched with each other. One can then create a large number of combinations of different materials, or combine layers of the same material with a relative twist-angle between them.

Combining two layers that are not lattice matched breaks the normal periodicity of the two-layer structure. A new periodicity over larger length scales can, however, arise, associated with a periodic potential experienced by electrons [145]. This is an example of a Moiré pattern, which is formed when two mismatched patterns interfere with each other. A long-distance superlattice in real space gives rise to a mini Brillouin zone in momentum space with an associated band structure. Both the band structure and the size of the Brillouin zone can be altered by varying the mismatch between the layers. In particular, by varying a relative twist-angle between the layers, one can continuously modify the properties of the system.

For specific twist-angles of bilayer graphene, referred to as magic angles, the band structure has, as mentioned above, been found to feature flatbands. Electrons associated with the flatbands in this case give rise

to a local density of states which is peaked at high-symmetry points with considerable distance and weak tunnelling between each other. One can then realize strongly correlated Hubbard physics. Indications of this was reported through the Mott insulating-like phase observed in magic angle twisted bilayer graphene around half-filling [142]. Interest in twisted bilayer graphene is partly generated by the possibility of studying such strongly correlated physics in a highly tunable system [146]. Moreover, the realization of flatbands and strongly correlated physics could, in general, also be possible in other twisted van der Waals heterostructures [147].

6.2 Flatband superconductivity

As we saw in Chap. 3, the critical temperature of superconductors is normally expected to increase with the density of states at the Fermi level, meaning that there are more available electrons around the Fermi surface that can interact attractively with each other. In the extreme limit of a flatband with a diverging density of states, it has been predicted that the critical temperature may depend linearly on the attractive interaction [148–150], in contrast to the normal exponential behavior that we found in Chap. 3. In general, a flatband could be used to boost the superconductivity in a dispersive band [148, 151], or to be the sole source of superconductivity [152–154].

Flatband superconductivity has especially received much attention after the discovery of a superconducting phase in twisted bilayer graphene [155]. The superconductivity in this case arises in the vicinity of the above mentioned correlated insulating phase, reminiscent of the cuprates. The superconducting state, whose origin and symmetries are still under debate, has been proposed to arise from both strong electron-electron interactions [156–158] or electron-phonon interaction [159–161]. See e.g. Ref. [162] for a long list of additional references.

Superconductivity could in general also be possible in other twisted van der Waals heterostructures [147]. An example is twisted trilayer graphene [163], consisting of three layers of graphene where the middle layer is twisted relative to the other two. The superconductivity has in this case been found to survive considerably larger in-plane magnetic fields than what is expected for a spin-singlet superconductor [164], representing a violation of the Chandrasekhar-Clogston limit. This has been interpreted as an indication of spin-triplet pairing. Such a Chandrasekhar-Clogston limit violation

has not been observed for twisted bilayer graphene [165]. A potential explanation of this finding could be that the pairing is similar in both systems, but that additional symmetries of the trilayer structure allows for the electrons going into the Cooper pairs to not be split apart by an in-plane magnetic field [162].

6.3   Going beyond the Chandrasekhar-Clogston limit in a flatband superconductor

After having provided a brief introduction to flatbands and flatband superconductivity, we are now ready to discuss Paper [6]. We there investigated the effect of a spin-splitting field on a spin-singlet superconductor where a flatband boosts the superconductivity in a dispersive band. The system can e.g. be a thin-film superconductor, with the relevant properties, exposed to an in-plane magnetic field or proximitized to a magnetic material. The focus is on the critical spin-splitting field that the superconductivity can coexist with, motivated by the discussion in the beginning of the chapter about the relationship between the Chandrasekhar-Clogston limit and the density of states around the Fermi level.

Here, we refer to the Chandrasekhar-Clogston limit as the specific restriction $h \leq \Delta_0/\sqrt{2}$. As this limit arises from the paramagnetic energy gain of the normal state compensating the condensation energy of the superconductor, it is often also referred to as the Pauli paramagnetic limit. As long as the transition to the normal state takes place as a result of the paramagnetic energy gain of the normal state becoming too large, one can in principle always define some similar paramagnetic limit. By making the definition general enough, one eventually ends up with the statement that it is not possible to have superconductivity if the normal state minimizes the free energy of the system. A limit of this type will then obviously be impossible to surpass. In the following, we discuss the possibility of going beyond the Chandrasekhar-Clogston limit, as defined above, by shifting the normal power balance between the condensation energy and the paramagnetic energy gain of the normal state so that a larger spin-splitting field per gap is necessary before the paramagnetic energy gain of the normal state becomes larger than the condensation energy.

The main finding of the article is that the presence of a flatband located close to the Fermi level can, in fact, shift the power balance between the condensation energy and the paramagnetic energy gain of the normal state. The

superconductivity can then potentially survive beyond the Chandrasekhar-Clogston limit.

The system is modelled by a Hamiltonian [148]

$$H = \sum_{i,\boldsymbol{k},\sigma} \epsilon_{i,\boldsymbol{k},\sigma} c^{\dagger}_{i,\boldsymbol{k},\sigma} c_{i,\boldsymbol{k},\sigma} - \frac{1}{N} \sum_{i,j,\boldsymbol{k},\boldsymbol{k}'} V_{ij}(\boldsymbol{k},\boldsymbol{k}') \, c^{\dagger}_{i,\boldsymbol{k},\uparrow} c^{\dagger}_{i,-\boldsymbol{k},\downarrow} \, c_{j,-\boldsymbol{k}',\downarrow} c_{j,\boldsymbol{k}',\uparrow}, \quad (6.1)$$

where the index i separates the dispersive band with $i = 1$ from the flatband with $i = 2$. The dispersion relations take the form $\epsilon_{1,\boldsymbol{k},\sigma} = -2t[\cos(k_x a) + \cos(k_y a)] - \mu - \sigma h$ and $\epsilon_{2,\boldsymbol{k},\sigma} = -\mu_0 - \sigma h$. The flatband is here placed μ_0 below the Fermi level, while the dispersive band crosses the Fermi level, generating a Fermi surface depending on the choice of μ. The interaction potential is further taken on the form

$$V_{ij}(\boldsymbol{k},\boldsymbol{k}') = \begin{cases} V_{ij} > 0, & |\epsilon_{i,\boldsymbol{k}}|, |\epsilon_{j,\boldsymbol{k}'}| \leq \omega_c, \\ 0, & \text{otherwise}, \end{cases} \quad (6.2)$$

allowing for both intraband and interband scattering in a thin shell around the Fermi surface [166]. The model we consider is a minimal model capturing the possibility of superconductivity in a dispersive band boosted by a flatband. The band structure is not derived from some underlying lattice model, and we do not consider any hybridization between the two bands. The details of the dispersive band are not very important. The essential part is that the density of states slightly away from the Fermi level should be sufficiently large compared to the density of states at the Fermi level. Our assumed band structure is probably closest to representing a real system when the Fermi level is located towards the bottom of the dispersive band, in which case the flatband is located below the dispersive band instead of crossing through it.

Neglecting any changes to the normal state of the system due to the interaction, one can perform a derivation similar to what we outlined for a spin-split superconductor in Chap. 3. We, this time, end up with a coupled set of gap equations for the gap functions associated with the two bands

$$\Delta_i(\boldsymbol{k}) = \frac{1}{N} \sum_{j,\boldsymbol{k}',\sigma} V_{ij}(\boldsymbol{k},\boldsymbol{k}') \frac{\Delta_j(\boldsymbol{k}')}{4E_{j,\boldsymbol{k}'}} \tanh\left(\frac{\beta}{2} E_{j,\boldsymbol{k}',\sigma}\right). \quad (6.3)$$

Due to the nature of the interaction potential, the gap functions will, once again, be constant in a thin shell around the Fermi surface. We can also

write out the free energy, which is simply a generalization of the expression we obtained in Chap. 3 to the two-band case

$$
\begin{aligned}
F = & \sum_{i,\boldsymbol{k},\sigma} \frac{\Delta_i^2(\boldsymbol{k})}{4E_{i,\boldsymbol{k}}} \tanh\left(\frac{\beta}{2} E_{i,\boldsymbol{k},\sigma}\right) \\
& + \sum_{i,\boldsymbol{k}} \left(\epsilon_{i,\boldsymbol{k}} - E_{i,\boldsymbol{k}}\right) - \frac{1}{\beta} \sum_{i,\boldsymbol{k},\sigma} \ln\left(1 + e^{-\beta E_{i,\boldsymbol{k},\sigma}}\right).
\end{aligned}
\tag{6.4}
$$

The coupled gap equations can be solved numerically for a given set of parameters, and the free energy can be calculated in order to establish whether a superconducting solution to the gap equations actually minimizes the free energy.

Here, we focus on the case of zero temperature and $V_{ij} = V$. A more general discussion can be found in the article. The coupled set of gap equations then reduce to a single gap equation for $\Delta_i = \Delta$, featuring a right-hand-side that obtains contributions from both the dispersive band and the flatband. When the dominant contributions to the gap equation and free energy arise from the flatband due to its large density of states, it is found that the curve for Δ as a function of h can take the form displayed in Fig. 6.1. This behavior can be understood through the following argument.

For $h < |\mu_0|$, the spin-splitting field is not able to change the sign of the quasiparticle energies associated with the flatband, even for $\Delta = 0$. The flatband does then not contribute to the zero-temperature paramagnetic energy gain of the normal state, despite contributing to the condensation energy. This shifts the normal power balance between the condensation energy and the paramagnetic energy gain of the normal state, allowing for superconductivity beyond the Chandrasekhar-Clogston limit. Moreover, as long as $h < \sqrt{\mu_0^2 + \Delta^2}$, the quasiparticle energies in the gap equation associated with the flatband stay positive. The flatband contributions to the gap equation at zero temperature are then unaffected by the spin-splitting field. The contributions from the dispersive band to the gap equation will be reduced for $h > \Delta_0$, as shown in Fig. 6.1. However, relying more and more on the flatband, it is still possible to obtain nontrivial solutions to the gap equation if the flatband is placed sufficiently close to the Fermi level for a given strength of the interaction potential. We can then be in a situation where the superconductivity is not limited by the Chandrasekhar-Clogston limit, but instead survives until $h > |\mu_0|$, when the flatband starts contributing to the paramagnetic energy gain of the normal state and the normal
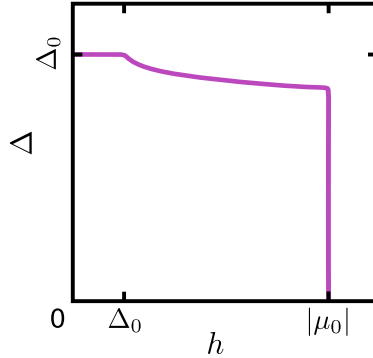
Figure 6.1: Sketch of the gap function Δ as a function of spin-splitting field h for the state of the system that is energetically favored. For $h < \Delta_0$, the gap equation is unaffected by the spin-splitting field. For $\Delta_0 < h < |\mu_0|$, the gap equation loses some contributions originating with the dispersive band. Finally, for $h > |\mu_0|$, the gap function vanishes when the normal state becomes the preferred state of the system.

state eventually becomes favored by the system. If this situation is realized for sufficiently large $|\mu_0|$, it can then be possible to have superconductivity considerably beyond the Chandrasekhar-Clogston limit.

As emphasized earlier, the model and treatment applied in Paper [6] is highly simplified. Although the proposed mechanism for going beyond the Chandrasekhar-Clogston limit is quite general in nature, predicting its realization in a particular real system would require a more detailed study. Potential candidates for real systems could be twisted van der Waals multi-layers, or highly tunable artificial systems where appropriate lattice models may be realized. One specific option could be twisted trilayer graphene, which can host a promising combination of flat and dispersive bands in close proximity to each other [163]. Whether and how far it is possible to go beyond the Chandrasekhar-Clogston limit by tuning $|\mu_0|$ (through the chemical potential) should be expected to depend on e.g. the dispersiveness of the dispersive band, the flatness of the flatband, and the details of the interactions. More realistic studies should therefore be careful to accurately capture these properties. Further guidelines for future studies can be found in the article.

We also highlight that the focus of this study was on whether it is pos-

sible to go beyond the Chandrasekhar-Clogston limit by introducing large variations in the density of states around the Fermi level. The focus was not, in itself, on how to increase the magnitude of the spin-splitting field that spin-singlet superconductivity can coexist with. The Chandrasekhar-Clogston limit does not place any absolute restrictions on the latter quantity, as the magnitude of the critical spin-splitting field can be increased by increasing Δ_0. In that context, one might wonder if the magnitude of the critical spin-splitting field would be larger if one placed the flatband at the Fermi level, leading to a larger superconducting gap, instead of placing it away from the Fermi level in order to increase h_c/Δ_0. In order to shed some light on this question, one can start out from the flatband placed some energy $|\mu_0'|$ away from the Fermi level, giving rise to a gap equation dominated by contributions from the flatband and featuring a solution with substantial $h_c/\Delta_0 \approx |\mu_0'|/\Delta_0$. If one then instead takes $\mu_0 = 0$, placing the flatband at the Fermi level, one will obtain a solution to the gap equation at zero field with $\Delta_0 \approx |\mu_0'|$, making the quasiparticle energies associated with the flatband take on a similar magnitude as before. If we analyze the part of the free energy associated with the flatband, we then see that the critical magnetic field for $\mu_0 = 0$ will be $\Delta_0/2$. This result is lower than the Chandrasekhar-Clogston limit as the considered band is completely flat and all associated quasiparticles with the right spin therefore change their sign as soon as $h > 0$. We then obtain that $h_c \approx |\mu_0'|/2$. Numerical results confirm this to be good estimate. Placing the flatband closer to the Fermi level will then not produce a larger critical spin-splitting field, although the critical temperature naturally will increase.

Transport

We have so far been concerned with systems in equilibrium. In this chapter, we will consider transport, focusing on interplay between electron currents and magnon currents. As discussed in the introduction chapter, magnon spin currents in magnetic insulators can e.g. be induced through the spin Seebeck effect or through injection from a heavy metal exhibiting the spin Hall effect. The resulting magnon currents are then flowing through an insulator without interacting with itinerant electrons. In contrast, interaction with itinerant electrons is naturally present in magnetic metals featuring both conduction electrons and localized spins. As we have seen so far in this thesis, coupling between localized spins and itinerant electrons can, however, also be realized in heterostructures.

We start with introducing the Boltzmann equation in Sec. 7.1, allowing us to describe a nonequilibrium state of electrons or magnons within a semiclassical framework. We also provide a simple calculation of conductivity, serving as an example of how the formalism works. We then move on to discussing Paper [7] in Sec. 7.2, where we consider the interplay between electron and magnon currents in a bilayer structure consisting of an antiferromagnetic insulator and a metal.

7.1 Boltzmann equation

Within the semiclassical Boltzmann formalism, the nonequilibrium distribution of electrons with spin σ at time t is described by a distribution function $f_\sigma(\boldsymbol{r}, \boldsymbol{k}, t)$ [167]. If the electrons simply move through the system without experiencing any collisions, their distribution function has to satisfy the continuity equation

$$\frac{\partial f}{\partial t} + \nabla \cdot (\boldsymbol{u} f) = 0, \tag{7.1}$$

where

$$\boldsymbol{u} = (\dot{x}, \dot{y}, \dot{z}, \dot{k}_x, \dot{k}_y, \dot{k}_z),\tag{7.2}$$

and

$$\nabla = \left(\frac{\partial}{\partial x}, \frac{\partial}{\partial y}, \frac{\partial}{\partial z}, \frac{\partial}{\partial k_x}, \frac{\partial}{\partial k_y}, \frac{\partial}{\partial k_z}\right).\tag{7.3}$$

Considering the electron motion to follow the semiclassical equations of motion

$$\dot{\boldsymbol{r}} = \boldsymbol{v_k} = \frac{1}{\hbar}\frac{\partial \xi_{\boldsymbol{k}}}{\partial \boldsymbol{k}},\tag{7.4}$$

$$\dot{\boldsymbol{k}} = -\frac{e}{\hbar}\big[\boldsymbol{E}(\boldsymbol{r},t) + \boldsymbol{v_k} \times \boldsymbol{B}(\boldsymbol{r},t)\big],\tag{7.5}$$

and taking e.g. $\xi_{\boldsymbol{k}} = \hbar^2 k^2/(2m)$, corresponding to $\boldsymbol{v_k} = \hbar\boldsymbol{k}/m$, we see immediately that $\nabla{\cdot}\boldsymbol{u} = 0$ as the electron energy $\xi_{\boldsymbol{k}}$ is considered to be independent of spatial coordinates, and e.g. the z-component of $\dot{\boldsymbol{k}}$ is independent of k_z. As long as $\nabla \cdot \boldsymbol{u} = 0$, stating that phase space flow is incompressible, the continuity equation can be rewritten as

$$\frac{\partial f}{\partial t} + \dot{\boldsymbol{r}} \cdot \frac{\partial f}{\partial \boldsymbol{r}} + \dot{\boldsymbol{k}} \cdot \frac{\partial f}{\partial \boldsymbol{k}} = 0.\tag{7.6}$$

As soon as we introduce collisions in the system, the above equation no longer holds as the state of an electron can be changed abruptly through a collision. In the presence of collisions we instead have to work with

$$\frac{\partial f}{\partial t} + \dot{\boldsymbol{r}} \cdot \frac{\partial f}{\partial \boldsymbol{r}} + \dot{\boldsymbol{k}} \cdot \frac{\partial f}{\partial \boldsymbol{k}} = \left[\frac{\partial f}{\partial t}\right]_{\text{coll}},\tag{7.7}$$

where the right-hand-side of the equation takes into account sudden scattering into and out of the region surrounding a phase-space point $(\boldsymbol{r}, \boldsymbol{k})$. In general, the collision term considerably complicates the Boltzmann equation as it couples together $f(\boldsymbol{r}, \boldsymbol{k})$ for different point $\boldsymbol{r}$ and $\boldsymbol{k}$ as all possible scattering processes affecting the electron distribution around a specific point in

phase-space needs to be taken into account. The collision term is, however, often treated in the relaxation time approximation, where it e.g. can be written on the simple form [167]

$$\left[\frac{\partial f}{\partial t}\right]_{\text{coll}} = -\frac{f_\sigma(\boldsymbol{r}, \boldsymbol{k}, t) - f_\sigma^0(\boldsymbol{r}, \boldsymbol{k})}{\tau_{\boldsymbol{k}, \sigma}}, \tag{7.8}$$

where the details of the scattering processes are baked into the relaxation time $\tau_{\boldsymbol{k}, \sigma}$. For a normal metal, relevant scattering processes contributing to the relaxation time can be e.g. of the types electron-electron, electron-phonon, and electron-impurity. Further,

$$f_\sigma^0(\boldsymbol{r}, \boldsymbol{k}) = \frac{1}{e^{\beta(\boldsymbol{r})[\xi_{\boldsymbol{k}, \sigma} - \mu(\boldsymbol{r})]} + 1}, \tag{7.9}$$

is the equilibrium distribution function. Taking the distribution of electrons to be independent of position and removing the effect of any external forces, the Boltzmann equation then simply turns into

$$\frac{\partial f_\sigma(\boldsymbol{k}, t)}{\partial t} = -\frac{f_\sigma(\boldsymbol{k}, t) - f_\sigma^0(\boldsymbol{k})}{\tau_{\boldsymbol{k}, \sigma}}, \tag{7.10}$$

which has the solution

$$f_\sigma(\boldsymbol{k}, t) = f_\sigma^0(\boldsymbol{k}) + \delta f_\sigma(\boldsymbol{k}) \, e^{-t/\tau_{\boldsymbol{k}, \sigma}}. \tag{7.11}$$

Assuming $\delta f_\sigma(\boldsymbol{k})$ nonzero, the distribution function at $t = 0$, $f_\sigma(\boldsymbol{k}, 0) = f_\sigma^0(\boldsymbol{k}) + \delta f_\sigma(\boldsymbol{k})$, is perturbed away from the equilibrium distribution. If we then go to $t \gg \tau_{\boldsymbol{k}, \sigma}$, scattering processes bring the electrons back to the equilibrium distribution.

A very simple way of incorporating collision in the description of electron transport is to work in the relaxation time approximation and treat the relaxation time as a phenomenological parameter. A more detailed approach to the problem is to consider the relevant scattering processes and calculating transition rates using Fermi's golden rule. We will see an example of this in Sec. 7.2. Starting from such a microscopic description of the scattering processes, one can then also attempt to write the collision terms on the approximate form in Eq. (7.8), leading to an expression for the relaxation time in terms of the parameters of the system.

7.1.1 Linearized Boltzmann equation for electrons

In the presence of external forces, one approach is to consider their effects to be sufficiently weak for the distribution functions to be expressed on the form

$$f_\sigma(\boldsymbol{r}, \boldsymbol{k}, t) = f_\sigma^0(\boldsymbol{r}, \boldsymbol{k}) + \delta f_\sigma(\boldsymbol{r}, \boldsymbol{k}, t), \qquad (7.12)$$

where $\delta f_\sigma(\boldsymbol{r}, \boldsymbol{k}, t)$ is a small deviation from the equilibrium distribution [167]. As there are now external forces acting, the system will not simply relax to the equilibrium state. Searching for a stationary solution where $\partial f / \partial t = 0$, we start out from the Boltzmann equation in (7.7) and insert the semiclassical equations of motion

$$\boldsymbol{v_k} \cdot \frac{\partial f}{\partial \boldsymbol{r}} - \frac{e}{\hbar} \left(\boldsymbol{E} + \boldsymbol{v_k} \times \boldsymbol{B} \right) \cdot \frac{\partial f}{\partial \boldsymbol{k}} = \left[\frac{\partial f}{\partial t} \right]_{\text{coll}}. \qquad (7.13)$$

Further, inserting the expression for the distribution function in (7.12) and differentiating the equilibrium distribution with respect to $\boldsymbol{r}$, the Boltzmann equation can be written out as

$$
\begin{aligned}
&\boldsymbol{v_k} \cdot \frac{\partial \delta f}{\partial \boldsymbol{r}} + \boldsymbol{v_k} \cdot \left[e \left(\boldsymbol{E} + \frac{\nabla \mu}{e} \right) + \frac{\xi_{\boldsymbol{k}} - \mu}{T} \nabla T \right] \left(-\frac{\partial f^0}{\partial \xi_{\boldsymbol{k}}} \right) \\
&- \frac{e}{\hbar} \left(\boldsymbol{E} + \boldsymbol{v_k} \times \boldsymbol{B} \right) \cdot \frac{\partial \delta f}{\partial \boldsymbol{k}} = \left[\frac{\partial f}{\partial t} \right]_{\text{coll}}.
\end{aligned}
\qquad (7.14)
$$

If we here try to set $\delta f = 0$, this cannot be a solution to the equation due to the driving terms proportional to $\boldsymbol{E}, \nabla \mu$, and ∇T acting to create deviations away from the equilibrium distribution. Using the assumption that δf is small, meaning that the driving terms then also need to be small, we only keep linear terms in δf, $\boldsymbol{E}$, $\nabla \mu$, and ∇T. This leads us to the linearized Boltzmann equation

$$\boldsymbol{v_k} \cdot \frac{\partial \delta f}{\partial \boldsymbol{r}} + \boldsymbol{v_k} \cdot \left[e\left(\boldsymbol{E} + \frac{\nabla \mu}{e} \right) + \frac{\xi_{\boldsymbol{k}} - \mu}{T} \nabla T \right] \left(-\frac{\partial f^0}{\partial \xi_{\boldsymbol{k}}} \right)$$

$$- \frac{e}{\hbar} (\boldsymbol{v_k} \times \boldsymbol{B}) \cdot \frac{\partial \delta f}{\partial \boldsymbol{k}} = \left[\frac{\partial f}{\partial t} \right]_{\text{coll}} . \tag{7.15}$$

7.1.2 DC conductivity

In this section, we consider a simple calculation of conductivity. Starting from the linearized Boltzmann equation, we take the electron distribution to be independent of position and assume vanishing $\boldsymbol{B}$, $\nabla \mu$, and ∇T. Treating the collision term in the relaxation time approximation, we write

$$e(\boldsymbol{v_k} \cdot \boldsymbol{E}) \left(-\frac{\partial f^0(\boldsymbol{k})}{\partial \xi_{\boldsymbol{k}}} \right) = -\frac{f(\boldsymbol{k}) - f^0(\boldsymbol{k})}{\tau_{\boldsymbol{k}}} . \tag{7.16}$$

We then see right away that the solution to the Boltzmann equation is

$$f(\boldsymbol{k}) = f^0(\boldsymbol{k}) - e\,\tau_{\boldsymbol{k}}(\boldsymbol{v_k} \cdot \boldsymbol{E}) \left(-\frac{\partial f^0(\boldsymbol{k})}{\partial \xi_{\boldsymbol{k}}} \right), \tag{7.17}$$

which is a Fermi distribution where the energies are shifted due to the presence of the electric field by an amount depending on the electron relaxation time. We then define the charge current density

$$\boldsymbol{j} = -\frac{e}{Na^d} \sum_{\boldsymbol{k},\boldsymbol{\sigma}} \boldsymbol{v_k}\, f(\boldsymbol{k}) = \frac{2e^2}{Na^d} \sum_{\boldsymbol{k}} \boldsymbol{v_k} \tau_{\boldsymbol{k}} (\boldsymbol{v_k} \cdot \boldsymbol{E}) \left(-\frac{\partial f^0(\boldsymbol{k})}{\partial \xi_{\boldsymbol{k}}} \right), \tag{7.18}$$

where $f^0(\boldsymbol{k}) = f^0(\xi_{\boldsymbol{k}}) = f^0(\xi_{-\boldsymbol{k}})$ and d is the dimensionality of the system. This equation an be expressed as $\boldsymbol{j} = \hat{\sigma} \boldsymbol{E}$, where $\hat{\sigma}$ is the conductivity tensor. For simplicity, we consider the isotropic case of $\xi_k = \hbar^2 k^2/(2m)$ and $\tau_{\boldsymbol{k}} = \tau_k$. The conductivity tensor now takes a diagonal form with $\sigma = \sigma_{xx} = \cdots = \sigma_{zz} = \text{Tr}(\hat{\sigma})/d$. We can then write

$$\sigma = \frac{2e^2}{d\,Na^d} \sum_{\boldsymbol{k}} v_k^2 \tau_k \left(-\frac{\partial f^0(\xi_k)}{\partial \xi_k} \right). \tag{7.19}$$

We then go to zero temperature, where the magnitude of the derivative of the Fermi distribution becomes a δ-function, producing

$$\sigma_e = \frac{2e^2 v_{k_F}^2 \tau_{k_F} D_0}{d\,N a^d}.$$

(7.20)

We then have that the conductivity depends on the electron relaxation time, group velocity, and density of states, all evaluated at the Fermi level. If we have many electrons around the Fermi level, a large Fermi velocity, as well as little scattering, we see that we end up with a large conductivity. Alternatively, one can also rewrite the expression for the conductivity on the form of the Drude formula [167].

7.1.3   Boltzmann equation for magnons

Similarly to the electron distribution function, we can also write down a Boltzmann equation for magnon distribution function $b_\gamma(\boldsymbol{r}, \boldsymbol{q}, t)$

$$\frac{\partial b}{\partial t} + \dot{\boldsymbol{r}} \cdot \frac{\partial b}{\partial \boldsymbol{r}} = \left[\frac{\partial b}{\partial t} \right]_{\mathrm{coll}}.$$

(7.21)

In this case we have not included a term proportional to $\dot{\boldsymbol{q}}$ as electric and magnetic fields do not couple to the motion of chargeless magnons. The time-derivative $\dot{\boldsymbol{r}}$ is simply the magnon group velocity $\boldsymbol{v}_{\boldsymbol{q}}^m = \frac{1}{\hbar} \frac{\partial \omega_{\boldsymbol{q}}}{\partial \boldsymbol{q}}$. The collision term can be treated in the relaxation time approximation, producing e.g.

$$\left[\frac{\partial b}{\partial t} \right]_{\mathrm{coll}} = -\frac{b_\gamma(\boldsymbol{r}, \boldsymbol{q}, t) - b_\gamma^0(\boldsymbol{r}, \boldsymbol{q}, t)}{\tau_{M,\gamma}(\boldsymbol{q})}.$$

(7.22)

In a magnetic insulator, the relaxation time should capture the dominant contributions from scattering of e.g. the types magnon-magnon, magnon-phonon, and magnon-impurity [168, 169].

7.2   Magnon drag in a metal-insulating antiferro-magnet bilayer

As we have introduced Boltzmann equations for both electrons and magnons, we are ready to face the problem of a coupled system of electrons and

magnons, which is the topic of Paper [7]. As we did earlier when investigating superconductivity, we consider a bilayer structure consisting of an antiferromagnetic insulator and a normal metal. A charge current is driven in the normal metal with direction parallel to the interface between the two layers. The antiferromagnetic interface can, again, be either compensated or uncompensated, tuned by the parameter $\Omega = \Omega_B$ as defined in Paper [4]. The question we wanted to answer was if it is possible to induce a magnon spin current in the antiferromagnet in this system setup.

The study was motivated by earlier studies of drag effects in magnetic metals, such as the study in Ref. [170] where the magnon spin current induced by an electron current was calculated for the case of a ferromagnetic metal. One might then expect that similar effects are possible in heterostructures involving magnetic insulators. A recent study of a spin-triplet superconductor coupled to a ferromagnetic insulator showed this to be the case [171], finding that an in-plane supercurrent could induce a magnon spin current in the ferromagnet. It could be of interest to realize a magnon spin current in an antiferromagnetic insulator in a similar way. One then, however, has to avoid that the two oppositely polarized α and β magnon modes are dragged along identically, leading to a finite magnon current, but a vanishing magnon spin current. In Paper [7], we attempted to solve this problem by tuning the asymmetry in the coupling between the normal metal and the two sublattices of the antiferromagnet.

Our main finding was that a magnon spin current can be induced in the antiferromagnet if the antiferromagnetic interface is uncompensated. Spin-splitting the magnon modes or increasing the spin fluctuations in the system by e.g. increasing the temperature can further enhance the magnon-spin current.

We start out from our usual description of electrons, magnons, and the coupling between them, introduced in Chap. 4. In order to simplify the calculations, we in this case go to the long-wavelength limit to obtain isotropic expressions for dispersion relations and magnon coherence factors. In line with this approximation, the Fermi surface for the electrons should be small and isotropic. Umklapp scattering processes can then be neglected. The dispersion relations take the form $\epsilon_{k\sigma} = t(ka)^2 - \mu - \sigma h_e$, and $\omega_{q\alpha} = \omega_q + h_m$, $\omega_{q\beta} = \omega_q - h_m$ with $\omega_q = \sqrt{\Delta_g^2 + \kappa^2(qa)^2}$. Here, we have included the possibility of spin-splitting of both electrons and magnons. We then introduce the normal interaction Hamiltonian,

$$H_{\text{int}} = \frac{\bar{V}}{\sqrt{N}} \sum_{\boldsymbol{kq}} \left(M_{\boldsymbol{q}}\, c^{\dagger}_{\boldsymbol{k+q},\downarrow} c_{\boldsymbol{k},\uparrow} + M^{\dagger}_{-\boldsymbol{q}}\, c^{\dagger}_{\boldsymbol{k+q},\uparrow} c_{\boldsymbol{k},\downarrow} \right), \qquad (7.23)$$

where we have now defined $\bar{V} = V\sqrt{N}$.

The Boltzmann equations are taken on the form

$$
\begin{aligned}
-eE\, v^e_{k_x} \frac{\partial f^0(\epsilon_{k,\sigma})}{\partial \epsilon_{k,\sigma}} &= -\frac{f_\sigma(\boldsymbol{k}) - \overline{f_\sigma}(k)}{\tau_\sigma} - \frac{f_\sigma(\boldsymbol{k}) - \overline{f_{-\sigma}}(k)}{\tau_{\uparrow\downarrow}} \\
&\quad + \left[\frac{\partial f_\sigma(\boldsymbol{k})}{\partial t} \right]_{\text{int}},
\end{aligned}
\qquad (7.24)
$$

and

$$\left[\frac{\partial b_\gamma(\boldsymbol{q})}{\partial t} \right]_{\text{int}} = \frac{b_\gamma(\boldsymbol{q}) - b^0_\gamma(q)}{\tau_{M,\gamma}(q)}, \qquad (7.25)$$

where we have assumed no spatial dependence, considering a stationary solution where a uniform electron current, arising from a uniform electric field, potentially gives rise to uniform magnon current. The effect of the electron-magnon scattering is included in the interaction terms in the Boltzmann equations and will be treated using Fermi's golden rule. The rest of the relevant scattering processes are treated in the relaxation time approximation and included in the different relaxation times. For the magnons, the remaining scattering processes are assumed to be taken into account by a single momentum dependent relaxation time. For the electrons, the dominant scattering processes are assumed to take place around the Fermi level, and the momentum dependence of the relaxation times is assumed to be of less importance. Further, for the electrons, we have also included a separate relaxation time for spin-flip scattering. As electron-magnon contributions to spin-flip scattering is captured in the interaction term, the remaining spin-flip scattering, arising from e.g. interaction with magnetic impurities, is expected to not be very strong. Further, the overline on the electron distributions denotes an angular average. If there are no even-in-momentum corrections to the electron distribution function, the overline simply produces the equilibrium distribution as we express

$$f_\sigma(\boldsymbol{k}) = f^0(\epsilon_{k,\sigma}) - \frac{\partial f^0(\epsilon_{k,\sigma})}{\partial \epsilon_{k,\sigma}} \big[\delta\mu_\sigma^e + g_\sigma^e(\boldsymbol{k})\big], \tag{7.26}$$

$$b_\gamma(\boldsymbol{q}) = b^0(\omega_{q,\gamma}) - \frac{\partial b^0(\omega_{q,\gamma})}{\partial \omega_{q,\gamma}} \big[\delta\mu_\gamma^m + g_\gamma^m(\boldsymbol{q})\big]. \tag{7.27}$$

The part of the functions g which is odd in momentum may give rise to electron and magnon currents. Moreover, the interaction terms in the Boltzmann equations take the form

$$\left[\frac{\partial f_\uparrow(\boldsymbol{k})}{\partial t}\right]_{\text{int}} = \frac{2\pi\bar{V}^2}{\hbar N} \sum_{\boldsymbol{q}} [Q_\alpha(\boldsymbol{k},\boldsymbol{q}) - Q_\beta^{\text{R}}(\boldsymbol{k},\boldsymbol{q})], \tag{7.28}$$

$$\left[\frac{\partial f_\downarrow(\boldsymbol{k})}{\partial t}\right]_{\text{int}} = \frac{2\pi\bar{V}^2}{\hbar N} \sum_{\boldsymbol{q}} [Q_\beta(\boldsymbol{k},\boldsymbol{q}) - Q_\alpha^{\text{R}}(\boldsymbol{k},\boldsymbol{q})], \tag{7.29}$$

and

$$\left[\frac{\partial b_\gamma(\boldsymbol{q})}{\partial t}\right]_{\text{int}} = \frac{2\pi\bar{V}^2}{\hbar N} \sum_{\boldsymbol{k}} Q_\gamma(\boldsymbol{k},\boldsymbol{q}), \tag{7.30}$$

with

$$\begin{aligned}
Q_\alpha(\boldsymbol{k},\boldsymbol{q}) =& \big(\Omega_A u_q + \Omega_B v_q\big)^2 \delta\big[\epsilon_{\boldsymbol{k},\uparrow} + \omega_{\boldsymbol{q},\alpha} - \epsilon_{\boldsymbol{k}+\boldsymbol{q},\downarrow}\big] \\
& \times \Big([b_\alpha(\boldsymbol{q}) + 1]\big[1 - f_\uparrow(\boldsymbol{k})\big]f_\downarrow(\boldsymbol{k}+\boldsymbol{q}) \\
& - b_\alpha(\boldsymbol{q})\big[1 - f_\downarrow(\boldsymbol{k}+\boldsymbol{q})\big]f_\uparrow(\boldsymbol{k})\Big),
\end{aligned} \tag{7.31}$$

$$\begin{aligned}
Q_\beta(\boldsymbol{k},\boldsymbol{q}) =& \big(\Omega_A v_q + \Omega_B u_q\big)^2 \delta\big[\epsilon_{\boldsymbol{k},\downarrow} + \omega_{\boldsymbol{q},\beta} - \epsilon_{\boldsymbol{k}+\boldsymbol{q},\uparrow}\big] \\
& \times \Big([b_\beta(\boldsymbol{q}) + 1]\big[1 - f_\downarrow(\boldsymbol{k})\big]f_\uparrow(\boldsymbol{k}+\boldsymbol{q}) \\
& - b_\beta(\boldsymbol{q})\big[1 - f_\uparrow(\boldsymbol{k}+\boldsymbol{q})\big]f_\downarrow(\boldsymbol{k})\Big).
\end{aligned} \tag{7.32}$$

Here, we have introduced $Q_\gamma^{\text{R}}(\boldsymbol{k},\boldsymbol{q})$, related to $Q_\gamma(\boldsymbol{k},\boldsymbol{q})$ by first sending $\boldsymbol{q} \to -\boldsymbol{q}$ and then sending $\boldsymbol{k} \to \boldsymbol{k}+\boldsymbol{q}$. We are here summing over all processes

that scatter particles in and out, weighted by the interaction strength, the relevant distribution factors, and with conservation of energy enforced.

We then introduce current densities for electron spin-current, electron current, magnon spin current, and magnon current

$$j_s = \frac{1}{(2\pi)^2} \int d\mathbf{k}\, v_{k_x}^e \big[f_\uparrow(\mathbf{k}) - f_\downarrow(\mathbf{k}) \big], \tag{7.33}$$

$$j_e = \frac{1}{(2\pi)^2} \int d\mathbf{k}\, v_{k_x}^e \big[f_\uparrow(\mathbf{k}) + f_\downarrow(\mathbf{k}) \big], \tag{7.34}$$

$$j_{sm} = \frac{1}{(2\pi)^2} \int d\mathbf{q}\, v_{q_x}^m \big[b_\beta(\mathbf{q}) - b_\alpha(\mathbf{q}) \big], \tag{7.35}$$

$$j_m = \frac{1}{(2\pi)^2} \int d\mathbf{q}\, v_{q_x}^m \big[b_\beta(\mathbf{q}) + b_\alpha(\mathbf{q}) \big]. \tag{7.36}$$

By starting from the Boltzmann equations and multiplying them by an electron or magnon velocity, as well as integrating over momentum, we can then obtain an approximate set of coupled equations relating the different currents [170]. We can further solve the set of equations to derive expressions for j_s, j_{sm}, j_m in terms of j_e

$$\begin{pmatrix} j_s \\ j_m \\ j_{sm} \end{pmatrix} = \begin{pmatrix} P_s \\ P_m \\ P_{sm} \end{pmatrix} j_e. \tag{7.37}$$

The main result of the article, considering the case without spin-splitting of the magnons and where spin-splitting of the electrons has been neglected, is presented in Fig. 7.1 (a). For $\Omega = 1$, there is no magnon spin current. Although the imbalanced population of left-moving and right-moving electrons in the normal metal leads to an imbalance of left-moving and right-moving magnons, the contributions from α and β magnons to P_{sm} cancel. For $\Omega < 1$, we find that there is an asymmetry in the coupling between the electrons and the two magnon modes. A magnon spin current is therefore possible, in particular for the case of $\Omega = 0$ corresponding to an uncompensated interface. The sign of the induced magnon spin current is in this case negative due to a stronger coupling to α magnons carrying a negative spin.

As discussed in detail in the article, the dependence of the drag coefficient P_{sm} on the relative importance of long-wavelength magnons further leads to the possibility that $\Omega > 0$ can maximize the induced magnon spin
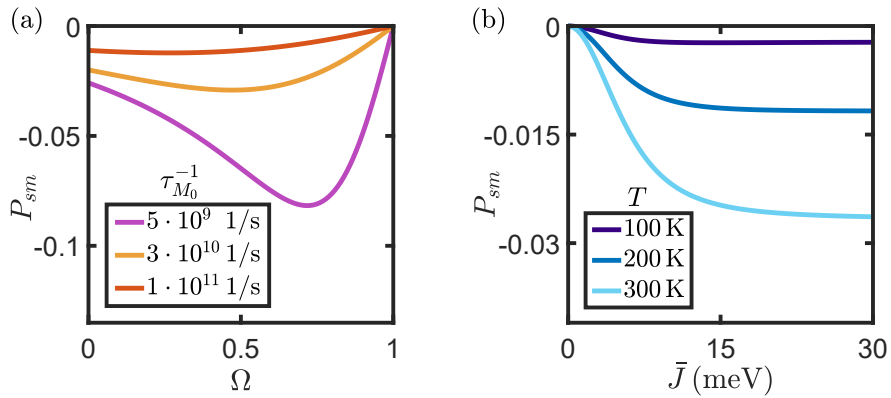
Figure 7.1: The ratio of magnon spin current to electron current as a function of (a) the sublattice coupling asymmetry parameter Ω and (b) the interfacial coupling strength $\bar{J}$. Further, $\tau_{M_0}^{-1}$ is here the inverse magnon relaxation time for the case of zero momentum and T is temperature.

current by reducing the relative importance of magnons with very small, but nonzero, momenta. The potential benefit of suppressing contribution from magnons with very small momenta arises from the asymmetry in the coupling between the electrons and the two magnon modes relying on a difference in magnitude between $u_{\boldsymbol{q}}$ and $v_{\boldsymbol{q}}$. As introduced in Chap. 2, $u_{\boldsymbol{q}}$ and $v_{\boldsymbol{q}}$ are most similar in magnitude for $\boldsymbol{q} \to 0$. Intermediate-strength sublattice asymmetry in the interfacial interaction may be possible experimentally if the two antiferromagnetic sublattices consist of different atoms.

We also find that the magnon spin current increases with temperature, as shown in Fig. 7.1 (b). Further, spin-splitting the magnon modes, increasing the asymmetry in the contributions from α and β magnons to the magnon spin current, may also enhance the magnon spin-current. While the induced magnon spin-current increases with temperature, there is, naturally, a limit to how far this effect can be exploited. In general, enhancing P_{sm} by amplifying the spin-fluctuations in the antiferromagnet only works up until the point where magnetic order is lost.

As highlighted in the article, the estimates for the magnitude of the induced magnon spin current are highly parameter dependent and should further also be expected to depend on the thicknesses of the materials. Keeping the normal metal thin might in this case be of less importance than in the case of magnon-mediated superconductivity discussed in Chap.

4 as a voltage applied to a thicker normal metal may generate a similar surface current affecting the antiferromagnet. Finite thickness of the antiferromagnet can help ensure magnetic order at convenient temperatures, but could also make it harder for the normal metal to induce magnon currents and should be expected to reduce the density of the magnon currents. Our simple modelling of the system, allowing for a treatment relying heavily on analytical calculations, can be well-suited for understanding under what general circumstances a magnon spin-current can be generated and how it may be enhanced. Our treatment is, however, not well-suited for reliably predicting the possible magnitude of the induced magnon spin current in specific system setups realizable in experiments. Further theoretical studies closer related to specific experimental setups would therefore clearly be of interest. A specific case to look into could also be biaxial antiferromagnets featuring non-degenerate magnons modes able to carry spin currents.

8

Conclusion and outlook

In this thesis, we first provided an introduction to magnetism and superconductivity, leading up to a discussion of Paper [1–4]. In these articles, we considered whether superconductivity can be induced in a conductor due to proximity to magnetic materials. We mainly focused on the case of indirect interaction between itinerant electrons in a normal metal mediated by magnons in antiferromagnetic insulators. The superconducting instability was found to depend intimately on the interplay between filling fraction in the metal and asymmetry in the coupling between the metal and the two sublattices of the antiferromagnets. In particular, for small Fermi surfaces, we found that a sublattice asymmetric interfacial coupling may be necessary to realize superconductivity, leading to spin-triplet p-wave pairing. Closer to half-filling, both spin-singlet d-wave pairing and spin-triplet pairing could be possible depending on the degree of sublattice asymmetry in the coupling between the materials. Our Eliashberg treatment of the system also revealed that the importance of long-wavelength magnons for the pairing can lead to the cutoff on the magnon spectrum not setting the relevant energy scale for the calculated critical temperature.

We next discussed indirect interaction between spins mediated by itinerant electrons, as well as the case of indirect interaction between ferromagnets mediated by superconductors. This brought us to Paper [5], where we found that the presence of zero-energy states on the surface of a d-wave superconductor could give rise to a preference for alignment of the magnetization of two metallic ferromagnets connected by the superconductor.

We then moved on to investigating the maximum spin-splitting field that a flatband superconductor can coexist with. For the model system with one dispersive band in addition to a flatband considered in Paper [6], we concluded that spin-singlet superconductivity might be able to survive spin-splitting fields larger than the superconducting gap at zero field and temperature.

Finally, we briefly discussed description of electron and magnon transport in the Boltzmann formalism. This lead us to a discussion of Paper [7], where it was found that an electron charge current in a normal metal layer, with direction parallel to an uncompensated antiferromagnetic interface, may give rise to a magnon spin current in the antiferromagnet.

All of the above summarized studies included in this thesis have one thing in common. They involve investigations of the physics that can arise in simple model systems, leading to prediction of, more or less interesting or useful, effects that could take place. These model systems are meant, to some approximation, to represent classes of realistic systems. Many of these realistic systems may be found to be in an unfavorable parameter regime or to be missing important components for our predicted effects to take place. Many of the systems may also introduce new physics not captured by our treatment. The goal is, however, that our simple modelling should capture something general that can show up in certain realistic systems, or inspire future studies predicting interesting effects realizable in experiments.

The next step for these studies is naturally either to go to experiments, or to perform further theoretical investigations in order to guide future experiments. The ideal scenario would likely be an iterative approach where both theory and experiments guide each other. For the magnon-mediated superconductivity in heterostructures, it is clear that further theoretical improvements can be done. This could include taking into account the full momentum-dependence of the electron-magnon interaction within Eliashberg theory, including lowest-order vertex corrections, and e.g. trying to take into account finite thickness of the materials. Before digging too deep into this, it would be great with some feedback from experiments. Although simply growing a seemingly appropriate heterostructure and cooling it down may not be sufficient to realize magnon-mediated superconductivity, a better understanding of the system resulting from targeted experimental investigation could be helpful for guiding further work. It is also possible that there could be more, already existing, experimental studies of relevant systems that it might be useful to take input from.

For the proposal in Paper [6], further theoretical work seems like a natural path ahead. Calculations for realistic systems featuring both a flat and dispersive band around the Fermi level could be performed. Twisted-trilayer graphene here seems like a good candidate.

For the magnon drag effect in Paper [7], it could be possible to try to connect the system closer to realistic systems, potentially relying more on

numerics and less on analytical calculations. Directly attempting to realize the effect in experiments, followed by optimization of the effect through theory-experiment collaboration could also be an option.

Bibliography

[1] E. Erlandsen, A. Kamra, A. Brataas, and A. Sudbø, Phys. Rev. B **100**, 100503 (2019).

[2] E. Erlandsen, A. Brataas, and A. Sudbø, Phys. Rev. B **101**, 094503 (2020).

[3] E. Erlandsen and A. Sudbø, Phys. Rev. B **102**, 214502 (2020).

[4] E. Thingstad, E. Erlandsen, and A. Sudbø, Phys. Rev. B **104**, 014508 (2021).

[5] A. Ghanbari, E. Erlandsen, and J. Linder, Phys. Rev. B **104**, 054502 (2021).

[6] A. Ghanbari, E. Erlandsen, A. Sudbø, and J. Linder, Phys. Rev. B **105**, L060501 (2022).

[7] E. Erlandsen and A. Sudbø, Phys. Rev. B **105**, 184434 (2022).

[8] E. Masanet, A. Shehabi, N. Lei, S. Smith, and J. Koomey, Science **367**, 984 (2020).

[9] L.-B. Desroches, H. Fuchs, J. Greenblatt, S. Pratt, H. Willem, E. Claybaugh, B. Beraki, M. Nagaraju, S. Price, and S. Young, "Computer usage and national energy consumption: Results from a field-metering study," (2015).

[10] M. Parizh, Y. Lvovsky, and M. Sumption, Superconductor Science and Technology **30**, 014007 (2016).

[11] P. Schmuser, Reports on Progress in Physics **54**, 683 (1991).

[12] M. Buchner, K. Höfler, B. Henne, V. Ney, and A. Ney, Journal of Applied Physics **124**, 161101 (2018).

[13] J. Maguire and J. Yuan, Physica C: Superconductivity **469**, 874 (2009), proceedings of the 21st International Symposium on Superconductivity (ISS 2008).

[14] P. Dai, B. Chakoumakos, G. Sun, K. Wong, Y. Xin, and D. Lu, Physica C: Superconductivity **243**, 201 (1995).

[15] L. P. Gor'kov and V. Z. Kresin, Rev. Mod. Phys. **90**, 011001 (2018).

[16] E. Snider, N. Dasenbrock-Gammon, R. McBride, M. Debessai, H. Vindana, K. Vencatasamy, K. V. Lawler, A. Salamat, and R. P. Dias, Nature **586**, 373 (2020).

[17] A. Hirohata, K. Yamada, Y. Nakatani, I.-L. Prejbeanu, B. Diény, P. Pirro, and B. Hillebrands, Journal of Magnetism and Magnetic Materials **509**, 166711 (2020).

[18] A. Fert, Rev. Mod. Phys. **80**, 1517 (2008).

[19] P. A. Grünberg, Rev. Mod. Phys. **80**, 1531 (2008).

[20] M. Dyakonov and V. Perel, Physics Letters A **35**, 459 (1971).

[21] J. E. Hirsch, Phys. Rev. Lett. **83**, 1834 (1999).

[22] A. Brataas, B. van Wees, O. Klein, G. de Loubens, and M. Viret, Physics Reports **885**, 1 (2020), spin Insulatronics.

[23] J. Linder and J. W. A. Robinson, Nature Physics **11**, 307 (2015).

[24] G. Yang, C. Ciccarelli, and J. W. A. Robinson, APL Materials **9**, 050703 (2021).

[25] M. Scheffler, A. Tkatchenko, P. Rinke, and F. Weg, Summer semester lecture course in theoretical solid state physics (2012).

[26] J. Stöhr and H. C. Siegmann, Solid-State Sciences. Springer, Berlin, Heidelberg **5**, 236 (2006).

[27] E. C. Stoner, Proceedings of the Royal Society of London. Series A. Mathematical and Physical Sciences **165**, 372 (1938).

[28] P. Bruno, Magnetismus von Festkörpern und grenzflächen **24**, 1 (1993).

[29] C. Kittel, *Quantum Theory of Solids, 2nd Revised Edition* (Wiley, New York, 1963).

[30] N. D. Mermin and H. Wagner, Phys. Rev. Lett. **17**, 1133 (1966).

[31] P. C. Hohenberg, Phys. Rev. **158**, 383 (1967).

[32] A. Auerbach and D. P. Arovas, "Schwinger bosons approaches to quantum antiferromagnetism," in *Introduction to Frustrated Magnetism: Materials, Experiments, Theory*, edited by C. Lacroix, P. Mendels, and F. Mila (Springer Berlin Heidelberg, Berlin, Heidelberg, 2011) pp. 365–377.

[33] D. P. Arovas and A. Auerbach, Phys. Rev. B **38**, 316 (1988).

[34] S. Sarker, C. Jayaprakash, H. R. Krishnamurthy, and M. Ma, Phys. Rev. B **40**, 5028 (1989).

[35] A. Kamra, E. Thingstad, G. Rastelli, R. A. Duine, A. Brataas, W. Belzig, and A. Sudbø, Phys. Rev. B **100**, 174407 (2019).

[36] J.-i. Igarashi and A. Watabe, Phys. Rev. B **43**, 13456 (1991).

[37] C. Wei and R. Tao, Phys. Rev. B **50**, 6840 (1994).

[38] H. A. Ceccatto, C. J. Gazza, and A. E. Trumper, Phys. Rev. B **47**, 12329 (1993).

[39] R. Flint and P. Coleman, Phys. Rev. B **79**, 014424 (2009).

[40] J. Merino, M. Holt, and B. J. Powell, Phys. Rev. B **89**, 245112 (2014).

[41] D.-V. Bauer and J. O. Fjærestad, Phys. Rev. B **96**, 165141 (2017).

[42] L. Messio, C. Lhuillier, and G. Misguich, Phys. Rev. B **87**, 125127 (2013).

[43] A. Auerbach, *Interacting Electrons and Quantum Magnetism*, Graduate Texts in Contemporary Physics (Springer New York, 2012).

[44] R. Haghshenas, W.-W. Lan, S.-S. Gong, and D. N. Sheng, Phys. Rev. B **97**, 184436 (2018).

[45] J. B. Parkinson and D. J. Farnell, *An introduction to quantum spin systems*, Vol. 816 (Springer, 2010).

[46] H. Kamerlingh Onnes, Koninklijke Nederlandse Akademie van Wetenschappen Proceedings Series B Physical Sciences **14**, 113 (1911).

[47] W. Meissner and R. Ochsenfeld, Naturwissenschaften **21**, 787 (1933).

[48] J. Bardeen, L. N. Cooper, and J. R. Schrieffer, Phys. Rev. **108**, 1175 (1957).

[49] H. Fröhlich, Proceedings of the Royal Society of London. Series A. Mathematical and Physical Sciences **215**, 291 (1952).

[50] L. N. Cooper, Phys. Rev. **104**, 1189 (1956).

[51] E. Maxwell, Phys. Rev. **78**, 477 (1950).

[52] C. A. Reynolds, B. Serin, W. H. Wright, and L. B. Nesbitt, Phys. Rev. **78**, 487 (1950).

[53] K. Fossheim and A. Sudbø, *Superconductivity: physics and applications* (John Wiley & Sons, 2004).

[54] D. Scalapino, "The electron-phonon interaction and strong-coupling superconductors," in *SUPERCONDUCTIVITY (IN TWO VOLUMES) VOLUME 1*, edited by R. Parks (Marcel Dekker, INC, New York, 1969) pp. 449–560.

[55] G. Eliashberg, Sov. Phys. JETP **11**, 696 (1960).

[56] A. B. Migdal, JETP **34**, 1438 (1958).

[57] C. Timm, "Theory of superconductivity," (2012).

[58] G. R. Stewart, Advances in Physics **66**, 75 (2017).

[59] V. Berezinskii, Sov. Phys. JETP **34**, 610 (1972).

[60] J. M. Kosterlitz and D. J. Thouless, Journal of Physics C: Solid State Physics **5**, L124 (1972).

[61] J. M. Kosterlitz and D. J. Thouless, Journal of Physics C: Solid State Physics **6**, 1181 (1973).

[62] M. R. Beasley, J. E. Mooij, and T. P. Orlando, Phys. Rev. Lett. **42**, 1165 (1979).

[63] M. Sigrist and K. Ueda, Rev. Mod. Phys. **63**, 239 (1991).

[64] M. Sigrist, AIP Conference Proceedings **789**, 165 (2005).

[65] J. R. Schrieffer and P. A. Wolff, Phys. Rev. **149**, 491 (1966).

[66] R. Heid, "Electron-phonon coupling," in *The Physics of Correlated Insulators, Metals, and Superconductors*, edited by E. Pavarini, E. Koch, R. Scalettar, and R. Martin (Forschungszentrum Jülich GmbH Zentralbibliothek, Verlag, Jülich, 2017) pp. 399–427.

[67] P. Morel and P. W. Anderson, Phys. Rev. **125**, 1263 (1962).

[68] P.-G. De Gennes and P. A. Pincus, *Superconductivity of metals and alloys* (CRC Press, 1999).

[69] F. S. Bergeret, M. Silaev, P. Virtanen, and T. T. Heikkilä, Rev. Mod. Phys. **90**, 041001 (2018).

[70] B. S. Chandrasekhar, Applied Physics Letters **1**, 7 (1962).

[71] A. M. Clogston, Phys. Rev. Lett. **9**, 266 (1962).

[72] B. J. Powell, J. F. Annett, and B. L. G. rffy, Journal of Physics A: Mathematical and General **36**, 9289 (2003).

[73] P. Fulde and R. A. Ferrell, Phys. Rev. **135**, A550 (1964).

[74] A. I. Larkin and Y. N. Ovchinnikov, Zh. Eksp. Teor. Fiz. **47**, 1136 (1964).

[75] R. C. Bruno and B. B. Schwartz, Phys. Rev. B **8**, 3161 (1973).

[76] J. A. Ouassou, T. D. Vethaak, and J. Linder, Phys. Rev. B **98**, 144509 (2018).

[77] E. Thingstad, "Collective effects in low-dimensional systems with coupled quasiparticles," (2021).

[78] P. Coleman, *Introduction to Many-Body Physics* (Cambridge University Press, 2015).

[79] G. D. Mahan, *Many-Particle Physics* (Springer Science & Business Media, 2000).

[80] J. Linder and A. V. Balatsky, Rev. Mod. Phys. **91**, 045005 (2019).

[81] P. B. Allen and B. Mitrović, *Theory of Superconducting Tc*, edited by H. Ehrenreich, F. Seitz, and D. Turnbull, Solid State Physics, Vol. 37 (Academic Press, 1983) pp. 1–92.

[82] P. B. Allen and R. C. Dynes, Phys. Rev. B **12**, 905 (1975).

[83] F. Marsiglio, Journal of Low Temperature Physics **87**, 659 (1992).

[84] A. Madhukar, Solid State Communications **24**, 11 (1977).

[85] F. Schrodi, P. M. Oppeneer, and A. Aperis, Phys. Rev. B **102**, 024503 (2020).

[86] S. V. Vonsovskiĭ and Y. A. Izyumov, Soviet Physics Uspekhi **5**, 723 (1963).

[87] G. Chen and W. A. Goddard, Science **239**, 899 (1988).

[88] H. Shimahara, Journal of the Physical Society of Japan **63**, 1861 (1994).

[89] P. Coleman, "Heavy fermions and the kondo lattice: a 21st century perspective," (2015), arXiv:1509.05769 [cond-mat.str-el] .

[90] F. Steglich, O. Stockert, S. Wirth, C. Geibel, H. Q. Yuan, S. Kirchner, and Q. Si, Journal of Physics: Conference Series **449**, 012028 (2013).

[91] A. J. Leggett, Rev. Mod. Phys. **47**, 331 (1975).

[92] D. J. Scalapino, Journal of Low Temperature Physics **117**, 179 (1999).

[93] M. Cyrot, Solid State Communications **60**, 253 (1986).

[94] D. J. Scalapino, E. Loh, and J. E. Hirsch, Phys. Rev. B **34**, 8190 (1986).

[95] K. Miyake, S. Schmitt-Rink, and C. M. Varma, Phys. Rev. B **34**, 6554 (1986).

[96] P. Monthoux, A. V. Balatsky, and D. Pines, Phys. Rev. Lett. **67**, 3448 (1991).

[97] P. Monthoux and D. Pines, Phys. Rev. Lett. **69**, 961 (1992).

[98] A. Abanov, A. V. Chubukov, and J. Schmalian, Advances in Physics **52**, 119 (2003).

[99] N. Rohling, E. L. Fjærbu, and A. Brataas, Phys. Rev. B **97**, 115401 (2018).

[100] X. Gong, M. Kargarian, A. Stern, D. Yue, H. Zhou, X. Jin, V. M. Galitski, V. M. Yakovenko, and J. Xia, Science Advances **3** (2017).

[101] M. Kargarian, D. K. Efimkin, and V. Galitski, Phys. Rev. Lett. **117**, 076806 (2016).

[102] H. G. Hugdal, S. Rex, F. S. Nogueira, and A. Sudbø, Phys. Rev. B **97**, 195438 (2018).

[103] M. Z. Hasan and C. L. Kane, Rev. Mod. Phys. **82**, 3045 (2010).

[104] K. Mæland, H. I. Røst, J. W. Wells, and A. Sudbø, Phys. Rev. B **104**, 125125 (2021).

[105] H. G. Hugdal and A. Sudbø, Phys. Rev. B **102**, 125429 (2020).

[106] E. L. Fjærbu, N. Rohling, and A. Brataas, Phys. Rev. B **100**, 125432 (2019).

[107] M. A. Ruderman and C. Kittel, Phys. Rev. **96**, 99 (1954).

[108] T. Kasuya, Progress of Theoretical Physics **16**, 45 (1956).

[109] K. Yosida, Phys. Rev. **106**, 893 (1957).

[110] S. S. P. Parkin, N. More, and K. P. Roche, Phys. Rev. Lett. **64**, 2304 (1990).

[111] E. Hirota, H. Sakakima, and K. Inomata, "Gmr devices of metallic multilayers," in *Giant Magneto-Resistance Devices* (Springer Berlin Heidelberg, Berlin, Heidelberg, 2002) pp. 47–70.

[112] P. W. Anderson and H. Suhl, Phys. Rev. **116**, 898 (1959).

[113] V. M. Galitski and A. I. Larkin, Phys. Rev. B **66**, 064526 (2002).

[114] D. N. Aristov, S. V. Maleyev, and A. G. Yashenkin, Zeitschrift für Physik B Condensed Matter **102**, 467 (1997).

[115] Y. Zhu, A. Pal, M. G. Blamire, and Z. H. Barber, Nature Materials **16**, 195 (2017).

[116] A. Di Bernardo, S. Komori, G. Livanas, G. Divitini, P. Gentile, M. Cuoco, and J. W. A. Robinson, Nature Materials **18**, 1194 (2019).

[117] F. S. Bergeret, A. L. Yeyati, and A. Martín-Rodero, Phys. Rev. B **72**, 064524 (2005).

[118] F. S. Bergeret, A. F. Volkov, and K. B. Efetov, Rev. Mod. Phys. **77**, 1321 (2005).

[119] A. Andreev, Soviet Physics-JETP **19**, 1228 (1964).

[120] P. De Gennes, Physics Letters **23**, 10 (1966).

[121] A. Ghanbari, V. K. Risinggård, and J. Linder, Scientific Reports **11**, 5028 (2021).

[122] C.-R. Hu, Phys. Rev. Lett. **72**, 1526 (1994).

[123] T. Löfwander, V. S. Shumeiko, and G. Wendin, Superconductor Science and Technology **14**, R53 (2001).

[124] A. Ghanbari, "Rkky interaction and coexistence with magnetism in superconducting systems," (2022).

[125] M. Covington, M. Aprili, E. Paraoanu, L. H. Greene, F. Xu, J. Zhu, and C. A. Mirkin, Phys. Rev. Lett. **79**, 277 (1997).

[126] J.-X. Zhu, *Bogoliubov-de Gennes method and its applications*, Vol. 924 (Springer, 2016).

[127] D. Leykam, A. Andreanov, and S. Flach, Advances in Physics: X **3**, 1473052 (2018).

[128] B. Sutherland, Phys. Rev. B **34**, 5208 (1986).

[129] E. H. Lieb, Phys. Rev. Lett. **62**, 1201 (1989).

[130] A. Mielke, Journal of Physics A: Mathematical and General **24**, 3311 (1991).

[131] H. Tasaki, Phys. Rev. Lett. **69**, 1608 (1992).

[132] S. Miyahara, K. Kubo, H. Ono, Y. Shimomura, and N. Furukawa, Journal of the Physical Society of Japan **74**, 1918 (2005).

[133] A. Ramachandran, A. Andreanov, and S. Flach, Phys. Rev. B **96**, 161104 (2017).

[134] A. Sil and A. K. Ghosh, Journal of Physics: Condensed Matter **31**, 245601 (2019).

[135] A. Tadjine, G. Allan, and C. Delerue, Phys. Rev. B **94**, 075441 (2016).

[136] W.-X. Qiu, S. Li, J.-H. Gao, Y. Zhou, and F.-C. Zhang, Phys. Rev. B **94**, 241409 (2016).

[137] M. R. Slot, T. S. Gardenier, P. H. Jacobse, G. C. P. van Miert, S. N. Kempkes, S. J. M. Zevenhuizen, C. M. Smith, D. Vanmaekelbergh, and I. Swart, Nature Physics **13**, 672 (2017).

[138] R. Drost, T. Ojanen, A. Harju, and P. Liljeroth, Nature Physics **13**, 668 (2017).

[139] S. Taie, T. Ichinose, H. Ozawa, and Y. Takahashi, Nature Communications **11**, 257 (2020).

[140] G.-B. Jo, J. Guzman, C. K. Thomas, P. Hosur, A. Vishwanath, and D. M. Stamper-Kurn, Phys. Rev. Lett. **108**, 045305 (2012).

[141] R. Bistritzer and A. H. MacDonald, Proceedings of the National Academy of Sciences **108**, 12233 (2011).

[142] Y. Cao, V. Fatemi, A. Demir, S. Fang, S. L. Tomarken, J. Y. Luo, J. D. Sanchez-Yamagishi, K. Watanabe, T. Taniguchi, E. Kaxiras, R. C. Ashoori, and P. Jarillo-Herrero, Nature **556**, 80 (2018).

[143] A. K. Geim and I. V. Grigorieva, Nature **499**, 419 (2013).

[144] K. S. Novoselov, A. Mishchenko, A. Carvalho, and A. H. C. Neto, Science **353**, aac9439 (2016).

[145] S. K. Behura, A. Miranda, S. Nayak, K. Johnson, P. Das, and N. R. Pradhan, Emergent Materials **4**, 813 (2021).

[146] L. Balents, C. R. Dean, D. K. Efetov, and A. F. Young, Nature Physics **16**, 725 (2020).

[147] L. Wang, E.-M. Shih, A. Ghiotto, L. Xian, D. A. Rhodes, C. Tan, M. Claassen, D. M. Kennes, Y. Bai, B. Kim, K. Watanabe, T. Taniguchi, X. Zhu, J. Hone, A. Rubio, A. N. Pasupathy, and C. R. Dean, Nature Materials **19**, 861 (2020).

[148] S. Miyahara, S. Kusuta, and N. Furukawa, Physica C: Superconductivity **460-462**, 1145 (2007).

[149] N. B. Kopnin, T. T. Heikkilä, and G. E. Volovik, Phys. Rev. B **83**, 220503 (2011).

[150] R. Ojajärvi, T. Hyart, M. A. Silaev, and T. T. Heikkilä, Phys. Rev. B **98**, 054515 (2018).

[151] A. Bussmann-Holder, H. Keller, A. Simon, and A. Bianconi, Condensed Matter **4** (2019), 10.3390/condmat4040091.

[152] S. Peotta and P. Törmä, Nature Communications **6**, 8944 (2015).

[153] F. Schrodi, A. Aperis, and P. M. Oppeneer, Phys. Rev. Research **2**, 012066 (2020).

[154] J. Herzog-Arbeitman, V. Peri, F. Schindler, S. D. Huber, and B. A. Bernevig, Phys. Rev. Lett. **128**, 087002 (2022).

[155] Y. Cao, V. Fatemi, S. Fang, K. Watanabe, T. Taniguchi, E. Kaxiras, and P. Jarillo-Herrero, Nature **556**, 43 (2018).

[156] H. Guo, X. Zhu, S. Feng, and R. T. Scalettar, Phys. Rev. B **97**, 235453 (2018).

[157] C.-C. Liu, L.-D. Zhang, W.-Q. Chen, and F. Yang, Phys. Rev. Lett. **121**, 217001 (2018).

[158] B. Roy and V. Juričić, Phys. Rev. B **99**, 121407 (2019).

[159] F. Wu, A. H. MacDonald, and I. Martin, Phys. Rev. Lett. **121**, 257001 (2018).

[160] Y. W. Choi and H. J. Choi, Phys. Rev. B **98**, 241412 (2018).

[161] B. Lian, Z. Wang, and B. A. Bernevig, Phys. Rev. Lett. **122**, 257002 (2019).

[162] W. Qin and A. H. MacDonald, Phys. Rev. Lett. **127**, 097001 (2021).

[163] J. M. Park, Y. Cao, K. Watanabe, T. Taniguchi, and P. Jarillo-Herrero, Nature **590**, 249 (2021).

[164] Y. Cao, J. M. Park, K. Watanabe, T. Taniguchi, and P. Jarillo-Herrero, Nature **595**, 526 (2021).

[165] Y. Cao, D. Rodan-Legrain, J. M. Park, N. F. Q. Yuan, K. Watanabe, T. Taniguchi, R. M. Fernandes, L. Fu, and P. Jarillo-Herrero, Science **372**, 264 (2021).

[166] H. Suhl, B. T. Matthias, and L. R. Walker, Phys. Rev. Lett. **3**, 552 (1959).

[167] J. Sólyom, *Fundamentals of the Physics of Solids: Volume II: Electronic Properties*, Vol. 2 (Springer Science & Business Media, 2008).

[168] S. S.-L. Zhang and S. Zhang, Phys. Rev. Lett. **109**, 096603 (2012).

[169] S. M. Rezende, R. L. Rodríguez-Suárez, and A. Azevedo, Phys. Rev. B **93**, 054412 (2016).

[170] Y. Cheng, K. Chen, and S. Zhang, Phys. Rev. B **96**, 024449 (2017).

[171] L. G. Johnsen, H. T. Simensen, A. Brataas, and J. Linder, Phys. Rev. Lett. **127**, 207001 (2021).

Enhancement of superconductivity mediated by antiferromagnetic squeezed magnons

Authors

Eirik Erlandsen
Akashdeep Kamra
Arne Brataas
Asle Sudbø

Enhancement of superconductivity mediated by antiferromagnetic squeezed magnons

Eirik Erlandsen, Akashdeep Kamra, Arne Brataas, and Asle Sudbø [*]

Center for Quantum Spintronics, Department of Physics, Norwegian University of Science and Technology, NO-7491 Trondheim, Norway

We theoretically investigate magnon-mediated superconductivity in a heterostructure consisting of a normal metal and a two-sublattice antiferromagnetic insulator. The attractive electron-electron pairing interaction is caused by an interfacial exchange coupling with magnons residing in the antiferromagnet, resulting in p-wave, spin-triplet superconductivity in the normal metal. Our main finding is that one may significantly enhance the superconducting critical temperature by coupling the normal metal to only one of the two antiferromagnetic sublattices employing, for example, an uncompensated interface. Employing realistic material parameters, the critical temperature increases from vanishingly small values to significantly larger values than 1 K as the interfacial coupling becomes strongly sublattice asymmetric. We provide a general physical picture of this enhancement mechanism based on the notion of squeezed bosonic eigenmodes.

Introduction. Hybrids consisting of a magnetic insulator coupled to a conducting layer allow for interconversion between magnonic and electronic spin currents [1–11]. The spin Hall effect [12,13] in the conductor has further been exploited to electrically control and detect magnonic spin currents [14], thereby enabling their integration with conventional electronics. The ensuing newly gained control over spin currents has instigated a wide range of magnon transport-based concepts and devices [5,8,9,15–18]. Conversely, magnons in the magnet can mediate the electron-electron attraction in the conducting layer. The resulting magnon-mediated superconductivity has been investigated theoretically in normal metals [19,20] as well as topological insulators [21,22], and experimentally [23]. Magnon-mediated indirect exciton condensation has also been predicted recently [24].

Interest in antiferromagnets (AFMs) has recently been invigorated [25–27] due to their distinct advantages over ferromagnets (FMs), such as minimization of stray fields, sensitivity to external magnetic noise, and low-energy magnons. The demonstration of electrically accessible memory cells based on AFMs [28,29] and spin transport across micrometers [18] corroborates their high application potential. Furthermore, their two-sublattice nature allows for unique phenomena [30,31], such as topological spintronics [32] and strong quantum fluctuations, not accommodated by FMs. AFMs with uncompensated interfaces, proven instrumental in exchange biasing [33–39] FMs for contemporary memory technology, have been predicted to amplify spin transfer to an adjacent conductor [40]. Recently, a theoretical proposal for proximity-inducing spin splitting in a superconductor using an uncompensated AFM, along with an experimental feasibility study based on existing literature, has also been put forward [41].

Within the standard theory of boson-mediated superconductivity [42,43], the superconducting critical temperature T_c is determined by an energy scale set by some high-frequency

cutoff ω_c on the boson spectrum, coupling of electrons with these bosons, and the single-particle electronic density of states on the Fermi surface. The latter two combine into an effective dimensionless coupling constant λ. In the simplest case, $T_c \sim \omega_c \exp(-1/\lambda)$. An enhancement of electron-phonon coupling, and thus λ, possibly due to a feedback loop involving strong correlation effects, typically results in a larger T_c [44]. An increase of λ caused by nonequilibrium squeezing [45] of phonons has been suggested [46,47] as a mechanism underlying experimentally observed, light-induced transient enhancement of T_c in some superconductors [48–50].

In this Rapid Communication, we theoretically demonstrate a drastically increased, attractive, magnon-mediated electron-electron (e-e) interaction, exploiting the two-sublattice nature of, and equilibrium squeezing-mediated strong quantum fluctuations (Fig. 1) in, an AFM [51,52]. We study a bilayer structure in which a normal metal (NM) exchange couples equally or differently to the two sublattices of an AFM insulator (AFMI), as depicted in Fig. 2, and find a significant enhancement of the attractive e-e interaction in the latter case. This is attributed to an amplification of the electron-magnon coupling that appears through magnon coherence factors acting constructively, instead of destructively as they do in the case of equal coupling to both sublattices. The resulting increase in λ produces a significant enhancement in T_c with sublattice symmetry breaking of the interfacial exchange coupling between the NM and AFMI (Fig. 3). We also comment on the experimental feasibility and optimal materials for realization of the predicted p-wave, spin-triplet superconducting state in these engineered bilayers.

A physical picture of this electron-magnon coupling enhancement, detailed elsewhere [51], is provided by the intrinsically squeezed nature of the antiferromagnetic magnons [51–53] (Fig. 1). Referring to a spin-flip residing on sublattice A (B) as a spin-up (spin-down) magnon, the antiferromagnetic eigenmodes are formed by two-mode squeezing [45] between these spin-up and spin-down magnons [52,53]. Thus, a

---

[*]Corresponding author: asle.sudbo@ntnu.no

FIG. 1. Representation of a spin-up antiferromagnetic squeezed magnon [51]. The squeezed excitation is a coherent superposition of states with $N + 1$ spin-up and N spin-down magnons. Each of the constituent states possesses a unit net spin, but varies in its spin content on each sublattice, thereby resulting in strong quantum fluctuations.

spin-up AFM squeezed magnon consists of a coherent superposition of states with $N + 1$ spin-up and N spin-down magnons, as depicted in Fig. 1, where N runs from zero to infinity [54,55]. The average spin on each sublattice associated with one squeezed magnon is thus much larger than its unit net spin. Any excitations, such as itinerant electrons, that exchange couple to only one of the sublattices thus experience a much stronger interaction proportional to the average spin residing on the particular sublattice. The exposure of itinerant electrons to a fully uncompensated antiferromagnetic interface accomplishes this effect.

We note that the mechanism proposed herein appears to be mathematically analogous [51,56,57] to the one based on nonequilibrium squeezing of phonons [46,47] proposed to explain the light-induced transient enhancement in T_c observed experimentally [48–50]. Our mechanism, however, exploits the intrinsic, equilibrium squeezed nature of the antiferromagnetic magnons [51] in contrast with the driven, transient squeezing achieved with phonons [46]. Moreover, our mechanism attributes the increase in λ to an enhanced electron-magnon coupling [51,56] while Knap and co-workers find a renormalized, reduced electron hopping which alters the density of states, to underpin a similar enhancement [46].

Model. We consider a bilayer consisting of a NM interfaced with an AFMI. The magnetic ground state is assumed to be an ordered staggered state where the staggered magnetization is taken to be along the z direction. The essential physics does not depend on whether the z direction is taken to be in or out of the interfacial plane. We take $\hbar = a = 1$, where a is the
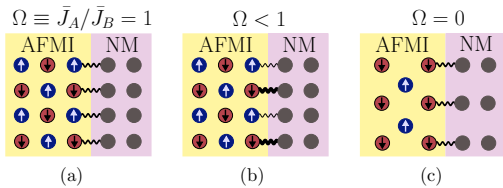
FIG. 2. Schematic depiction of the antiferromagnetic insulator (AFMI)/normal metal (NM) bilayer including its sublattice-asymmetric interfacial exchange coupling. (a) and (c), respectively, illustrate compensated and uncompensated interfaces that are realized in experiments, for example, via AFMI layer growth in a specific crystal orientation. (b) shows the model employed in our analysis, which conveniently allows capturing the full range of interfacial asymmetry via the parameter Ω.
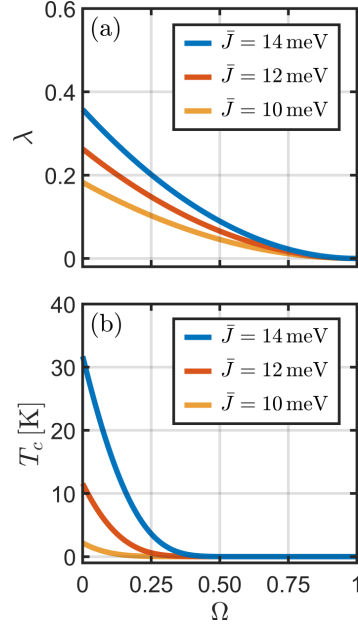
FIG. 3. (a) Dimensionless coupling constant λ and (b) superconducting critical temperature T_c vs coupling asymmetry parameter $\Omega \equiv \bar{J}_A/\bar{J}_B$, with $\bar{J} \equiv \bar{J}_B$. $\Omega = 1$ and 0, respectively, correspond to compensated and uncompensated antiferromagnetic interfaces (Fig. 2). An increase in both λ and T_c in the latter case constitutes our main result.

lattice constant. The system is modeled by a Hamiltonian $H = H_{AFMI} + H_{NM} + H_{int}$, with

$$H_{AFMI} = J \sum_{\langle i,j \rangle} \boldsymbol{S}_i \cdot \boldsymbol{S}_j - K \sum_i S_{iz}^2, \tag{1}$$

$$H_{NM} = -t \sum_{\langle i,j \rangle \sigma} c_{i\sigma}^\dagger c_{j\sigma} - \mu \sum_{i\sigma} c_{i\sigma}^\dagger c_{i\sigma}, \tag{2}$$

$$H_{int} = -2\bar{J}_A \sum_{i \in A} c_i^\dagger \boldsymbol{\tau} c_i \cdot \boldsymbol{S}_i - 2\bar{J}_B \sum_{i \in B} c_i^\dagger \boldsymbol{\tau} c_i \cdot \boldsymbol{S}_i, \tag{3}$$

consisting of a term describing the AFMI, a tight-binding Hamiltonian describing the NM, and a term accounting for exchange coupling between the two materials [5,7,19,31,53,58]. Here, J (>0) and K (>0) respectively parametrize the antiferromagnetic exchange and easy-axis anisotropy, and the sum over $\langle i, j \rangle$ includes all nearest neighbors for each i. Further, t is the tight-binding hopping parameter, the chemical potential is denoted by μ, and $c_i^\dagger \equiv (c_{i\uparrow}^\dagger, c_{i\downarrow}^\dagger)$, where $c_{i\sigma}^\dagger$ is a creation operator, creating an electron with spin σ on lattice site i. The Pauli matrices $\boldsymbol{\tau}$ act on the electron spin degree of freedom. Without loss of generality, the lattices on both sides of the interface are assumed to be square. The local exchange coupling between the NM electrons and AFMI spins across the interface is parametrized by sublattice-dependent strengths $\bar{J}_A$ and $\bar{J}_B$ [40,41].

Employing a Holstein-Primakoff transformation for the spin operators and switching to Fourier space, we obtain the magnetic Hamiltonian in terms of the sublattice magnons [59,60], which are not the eigenmodes. Executing a Bogoliubov transformation brings the AFMI Hamiltonian to its diagonal form [59,60], $H_{AFMI} = \sum_k \omega_k(\alpha_k^\dagger \alpha_k + \beta_k^\dagger \beta_k)$, where $\omega_k = 2s\sqrt{(zJ+K)^2 - z^2J^2\gamma_k^2}$, $\gamma_k = 2\sum_b \cos(k_b)/z$, and the sum over k covers the reduced Brillouin zone of the sublattices. Here, z is the number of nearest neighbors, s is the spin quantum number associated with the lattice site spins, and the sum over b covers the directions parallel to the interface. The magnon operators α_k and β_k are coherent superpositions of the individual sublattice magnons $\alpha_k = u_k a_k - v_k b_{-k}^\dagger$, $\beta_k = u_k b_k - v_k a_{-k}^\dagger$, where $u_k = \cosh(\theta_k)$, $v_k = \sinh(\theta_k)$, and $\theta_k = \frac{1}{2}\tanh^{-1}(-\frac{Jz\gamma_k}{zJ+K})$. Performing a Fourier transformation, the NM Hamiltonian becomes $H_{NM} = \sum_{k\sigma} \epsilon_k c_{k\sigma}^\dagger c_{k\sigma}$, where $\epsilon_k = -tz\gamma_k - \mu$. The sum over k here covers the full Brillouin zone.

As detailed in the Supplemental Material [59] (see also Refs. [61–66] therein), the interaction Hamiltonian [Eq. (3)] couples the NM electrons with the A and B sublattices of the AFMI,

$$H_{int}^{(A)} = \Omega V \sum_{kq}[(u_q\alpha_q + v_q\beta_{-q}^\dagger)c_{k+q,\downarrow}^\dagger c_{k\uparrow} + H.c.],$$

$$H_{int}^{(B)} = V \sum_{kq}[(u_q\beta_q + v_q\alpha_{-q}^\dagger)c_{k+q,\uparrow}^\dagger c_{k\downarrow} + H.c.],$$

where $V \equiv -\frac{2\bar{J}\sqrt{s}}{\sqrt{N}}$, N is the number of lattice sites in the interfacial plane, and $\bar{J} = \bar{J}_B$.

Effective pairing interaction. The full Hamiltonian now takes the form $H = H_{AFMI} + H_{NM} + H_{int}^{(A)} + H_{int}^{(B)}$. In order to obtain an effective interacting theory for electrons in NM, we integrate out the magnons, using a canonical transformation [60]. We then obtain an effective electronic Hamiltonian $H' = H_{NM} + H_{pair}$ [59]. The term H_{pair} contains the pairing interaction between electrons mediated by the antiferromagnetic magnons. Considering opposite momenta pairing [43], we obtain [59]

$$H_{pair} = \sum_{kk'} V_{kk'}c_{k\uparrow}^\dagger c_{-k\downarrow}^\dagger c_{-k'\downarrow}c_{k'\uparrow}, \tag{4}$$

where

$$V_{kk'} = -V^2\frac{2\omega_{k+k'}}{(\epsilon_{k'}-\epsilon_k)^2 - \omega_{k+k'}^2}A(k+k',\Omega), \tag{5}$$

and

$$A(q,\Omega) = \frac{1}{2}(\Omega^2+1)(u_q^2+v_q^2) + 2\Omega u_q v_q. \tag{6}$$

The interaction potential in Eq. (5) consists of two factors, in addition to a prefactor. The first is the standard expression that enters pairing mediated by bosons with a dispersion relation ω_k, familiar from phonon-mediated superconductivity [43]. The second factor $A(q,\Omega)$ [Eq. (6)] contains the effect of the constructive or destructive interference of squeezed magnons. For long-wavelength magnons, the coherence factors u_q and v_q grow large, but take on opposite signs. For the case of equal coupling to both sublattices, $\Omega = 1$, we have $A(q,\Omega) =$

$(u_q+v_q)^2$, and a near cancellation of the coherence factors. On the other hand, for the case of a fully uncompensated AFMI interface, $\Omega = 0$, the coherence factors combine to $A(q,\Omega) = (u_q^2+v_q^2)/2$, where u_q and v_q are squared separately. This represents a dramatic amplification of the pairing interaction in the latter case.

Mean-field theory and T_c. We now formulate the weak-coupling mean-field theory for the magnon-mediated superconductivity in the NM employing the standard methodology for unconventional superconductors [67]. Comparing our effective interaction potential [Eqs. (4) and (5)] with that for conventional s-wave superconductors [43], we note the additional multiplicative minus sign. This implies that the conventional spin-singlet pairing channel is repulsive and does not support condensation. We therefore consider $S_z = 0$ spin-triplet pairing which is the typical condensation channel for magnon-mediated superconductivity [19,68–70]. The corresponding gap function is defined as $\Delta_k = -\sum_{k'} V_{kk',O(k)}\langle c_{-k'\downarrow}c_{k'\downarrow} + c_{-k'\downarrow}c_{k'\uparrow}\rangle/2$, where $V_{kk',O(k)} = \frac{1}{2}(V_{kk'} - V_{-k,k'})$ is the odd part of the pairing potential [Eq. (5)]. The ensuing gap equation takes the form [67]

$$\Delta_k = -\sum_{k'} V_{kk',O(k)}\frac{\Delta_{k'}}{2E_{k'}}\tanh\left(\frac{E_{k'}}{2k_BT}\right), \tag{7}$$

where $E_k = \sqrt{\epsilon_k^2 + |\Delta_k|^2}$. Close to the critical temperature, we linearize the gap equation and compute an average over the Fermi surface $\lambda\Delta_k = -D_0\langle V_{kk',O(k)}\Delta_{k'}\rangle_{k',FS}$, in order to determine the critical temperature [59,67],

$$k_BT_c = 1.14\omega_c e^{-1/\lambda}. \tag{8}$$

Here, D_0 is the density of states on the Fermi surface and ω_c is the high-frequency cutoff on the magnon spectrum. As detailed in the Supplemental Material [59], the numerical solution of the eigenvalue problem for the dimensionless coupling constant λ yields a p-wave gap function. Employing experimentally obtained material parameters [59], the critical temperature T_c and dimensionless coupling constant λ are evaluated and presented as a function of the asymmetry parameter $\Omega \equiv \bar{J}_A/\bar{J}_B$ in Fig. 3. We now pause to comment on the results thus obtained.

Both λ and T_c are found to increase with the sublattice asymmetry of the interfacial exchange coupling, i.e., as Ω decreases (Fig. 3). Furthermore, a T_c of few tens of degrees Kelvin is obtained for a perfectly uncompensated interface, corresponding to $\Omega = 0$, employing realistic parameters [59]. However, T_c evaluations are notoriously unreliable on account of their sensitivity to the λ (exponential dependence on $1/\lambda$) evaluation method and related details. Within our model, altering the parameters by a few tens of percent leads to significantly smaller, or even larger, critical temperatures. The key lesson of our analysis is that uncompensated interfaces drastically enhance T_c to values potentially significantly larger than 1 K considering realistic materials.

Theoretical model assessment. Uncompensated AFM interfaces induce spin splitting in the adjacent conductor [41] that has not been included here. In conventional BCS superconductors this effect has been investigated in detail and is known to result in rich physics [71,72] including gapless

superconductivity [73], a Fulde-Ferrell-Larkin-Ovchinnikov (FFLO) state [74,75], and finally, destruction of the superconducting phase when spin splitting becomes significantly larger than T_c [76]. In the present case, the magnon-squeezing effect amplifies the electron-magnon coupling, and thus T_c, while leaving the spin splitting unchanged. Thus, the latter is expected to bear no significant effects on the predicted superconducting state [70] with T_c considerably larger than the typically induced spin splitting ~1 K [41,77]. Spin splitting may also be suppressed by applying an external compensating magnetic field [78]. The system considered in this Rapid Communication is far less susceptible to nontrivial feedback effects of the itinerant electrons on the antiferromagnet than the case studied in Ref. [79], particularly since the magnetic surface we consider is the surface of a bulk magnet and an Ising easy-axis anisotropy is included in the description. A strong spin-orbit interaction, also disregarded here, may reduce T_c [72]. Finally, all non-*s*-wave superconducting phases are suppressed by disorder. Therefore, we expect the inclusion of interfacial disorder to reduce T_c for our *p*-wave state [70]. A rigorous analysis of the effects mentioned above constitutes a promising avenue for future studies.

Experimental feasibility. The fabrication of proposed bilayers with uncompensated and low disorder interfaces, albeit challenging, is within the reach of contemporary state-of-the-art techniques [23,36]. The choice of materials is likely to be dictated by the growth, rather than theoretical, considerations. Nevertheless, we now outline the optimal materials requirements from a theory standpoint. Broadly speaking, a reasonably large Néel temperature for the AFM is beneficial. A metal with a high density of states at the Fermi level and a low spin-orbit interaction is desirable. The possibility of a strong exchange coupling across the interface seems to be supported by spin mixing conductance experiments for a wide range of bilayers [2,4,80]. Without an extensive comparison between many materials, hematite [18] or chromia [29,38] as AFM and copper or aluminum as the metal seem to be reasonable choices.

Summary. We have shown that magnons in an antiferromagnetic insulator mediate attractive electron-electron interactions in an adjacent normal metal. Exploiting the intrinsic squeezing of antiferromagnetic magnons, the electron-electron pairing potential is amplified by exchange coupling the normal metal asymmetrically to the two sublattices of the antiferromagnet. This, in turn, is found to result in a dramatic increase in the superconducting critical temperature, which is estimated to be significantly larger than 1 K employing experimentally obtained material parameters, when the normal metal is exposed to an uncompensated antiferromagnetic interface. Our results demonstrate the possibility of engineering heterostructures exhibiting superconductivity at potentially large temperatures.

[1] Y. Tserkovnyak, A. Brataas, and G. E. W. Bauer, Enhanced Gilbert Damping in Thin Ferromagnetic Films, Phys. Rev. Lett. **88**, 117601 (2002).

[2] Y. Kajiwara, K. Harii, S. Takahashi, J. Ohe, K. Uchida, M. Mizuguchi, H. Umezawa, H. Kawai, K. Ando, K. Takanashi, S. Maekawa, and E. Saitoh, Transmission of electrical signals by spin-wave interconversion in a magnetic insulator, Nature (London) **464**, 262 (2010).

[3] A. V. Chumak, V. I. Vasyuchka, A. A. Serga, and B. Hillebrands, Magnon spintronics, Nat. Phys. **11**, 453 (2015).

[4] M. Weiler, M. Althammer, M. Schreier, J. Lotze, M. Pernpeintner, S. Meyer, H. Huebl, R. Gross, A. Kamra, J. Xiao, Y.-T. Chen, H. J. Jiao, G. E. W. Bauer, and S. T. B. Goennenwein, Experimental Test of the Spin Mixing Interface Conductivity Concept, Phys. Rev. Lett. **111**, 176601 (2013).

[5] S. S.-L. Zhang and S. Zhang, Spin convertance at magnetic interfaces, Phys. Rev. B **86**, 214424 (2012).

[6] H. Adachi, K. ichi Uchida, E. Saitoh, and S. Maekawa, Theory of the spin Seebeck effect, Rep. Prog. Phys. **76**, 036501 (2013).

[7] S. Takahashi, E. Saitoh, and S. Maekawa, Spin current through a normal-metal/insulating-ferromagnet junction, J. Phys.: Conf. Ser. **200**, 062030 (2010).

[8] L. J. Cornelissen, J. Liu, R. A. Duine, J. Ben Youssef, and B. J. van Wees, Long-distance transport of magnon spin information in a magnetic insulator at room temperature, Nat. Phys. **11**, 1022 (2015).

[9] S. T. B. Goennenwein, R. Schlitz, M. Pernpeintner, K. Ganzhorn, M. Althammer, R. Gross, and H. Huebl, Non-local magnetoresistance in YIG/Pt nanostructures, Appl. Phys. Lett. **107**, 172405 (2015).

[10] S. Maekawa, S.O. Valenzuela, E. Saitoh, and T. Kimura, *Spin Current*, Series on Semiconductor Science and Technology (Oxford University Press, Oxford, UK, 2012).

[11] G. E. W. Bauer, E. Saitoh, and B. J. van Wees, Spin caloritronics, Nat. Mater. **11**, 391 (2012).

[12] J. E. Hirsch, Spin Hall Effect, Phys. Rev. Lett. **83**, 1834 (1999).

[13] J. Sinova, S. O. Valenzuela, J. Wunderlich, C. H. Back, and T. Jungwirth, Spin Hall effects, Rev. Mod. Phys. **87**, 1213 (2015).

[14] E. Saitoh, M. Ueda, H. Miyajima, and G. Tatara, Conversion of spin current into charge current at room temperature: Inverse spin-Hall effect, Appl. Phys. Lett. **88**, 182509 (2006).

[15] A. V. Chumak, A. A. Serga, and B. Hillebrands, Magnon transistor for all-magnon data processing, Nat. Commun. **5**, 4700 (2014).

[16] V. V. Kruglyak, S. O. Demokritov, and D. Grundler, Magnonics, J. Phys. D **43**, 264001 (2010).

[17] K. Ganzhorn, S. Klingler, T. Wimmer, S. Geprägs, R. Gross, H. Huebl, and S. T. B. Goennenwein, Magnon-based logic in a multi-terminal YIG/Pt nanostructure, Appl. Phys. Lett. **109**, 022405 (2016).

[18] R. Lebrun, A. Ross, S. A. Bender, A. Qaiumzadeh, L. Baldrati, J. Cramer, A. Brataas, R. A. Duine, and M.

Kläui, Tunable long-distance spin transport in a crystalline antiferromagnetic iron oxide, Nature (London) **561**, 222 (2018).

[19] N. Rohling, E. L. Fjærbu, and A. Brataas, Superconductivity induced by interfacial coupling to magnons, Phys. Rev. B **97**, 115401 (2018).

[20] E. L. Fjærbu, N. Rohling, and A. Brataas, Superconductivity at metal-antiferromagnetic insulator interfaces, arXiv:1904.00233 [Phys. Rev. B (to be published)].

[21] M. Kargarian, D. K. Efimkin, and V. Galitski, Amperean Pairing at the Surface of Topological Insulators, Phys. Rev. Lett. **117**, 076806 (2016).

[22] H. G. Hugdal, S. Rex, F. S. Nogueira, and A. Sudbø, Magnon-induced superconductivity in a topological insulator coupled to ferromagnetic and antiferromagnetic insulators, Phys. Rev. B **97**, 195438 (2018).

[23] X. Gong, M. Kargarian, A. Stern, Di Yue, H. Zhou, X. Jin, V. M. Galitski, V. M. Yakovenko, and J. Xia, Time-reversal symmetry-breaking superconductivity in epitaxial bismuth/nickel bilayers, Sci. Adv. **3**, e1602579 (2017).

[24] Ø. Johansen, A. Kamra, C. Ulloa, A. Brataas, and R. A. Duine, Magnon-mediated indirect exciton condensation through antiferromagnetic insulators, arXiv:1904.12699.

[25] T. Jungwirth, X. Marti, P. Wadley, and J. Wunderlich, Antiferromagnetic spintronics, Nat. Nanotechnol. **11**, 231 (2016).

[26] V. Baltz, A. Manchon, M. Tsoi, T. Moriyama, T. Ono, and Y. Tserkovnyak, Antiferromagnetic spintronics, Rev. Mod. Phys. **90**, 015005 (2018).

[27] O. Gomonay, V. Baltz, A. Brataas, and Y. Tserkovnyak, Antiferromagnetic spin textures and dynamics, Nat. Phys. **14**, 213 (2018).

[28] P. Wadley, B. Howells, J. Zelezný, C. Andrews, V. Hills, R. P. Campion, V. Novák, K. Olejník, F. Maccherozzi, S. S. Dhesi, S. Y. Martin, T. Wagner, J. Wunderlich, F. Freimuth, Y. Mokrousov, J. Kunes, J. S. Chauhan, M. J. Grzybowski, A. W. Rushforth, K. W. Edmonds, B. L. Gallagher, and T. Jungwirth, Electrical switching of an antiferromagnet, Science **351**, 587 (2016).

[29] T. Kosub, M. Kopte, R. Hühne, P. Appel, B. Shields, P. Maletinsky, R. Hübner, M. O. Liedke, J. Fassbender, O. G. Schmidt, and D. Makarov, Purely antiferromagnetic magnetoelectric random access memory, Nat. Commun. **8**, 13985 (2017).

[30] A. Kamra, R. E. Troncoso, W. Belzig, and A. Brataas, Gilbert damping phenomenology for two-sublattice magnets, Phys. Rev. B **98**, 184402 (2018).

[31] Y. Ohnuma, H. Adachi, E. Saitoh, and S. Maekawa, Spin Seebeck effect in antiferromagnets and compensated ferrimagnets, Phys. Rev. B **87**, 014423 (2013).

[32] L. Smejkal, Y. Mokrousov, B. Yan, and A. H. MacDonald, Topological antiferromagnetic spintronics, Nat. Phys. **14**, 242 (2018).

[33] J. Nogués and I. K. Schuller, Exchange bias, J. Magn. Magn. Mater. **192**, 203 (1999).

[34] J. Nogués, J. Sort, V. Langlais, V. Skumryev, S. Suriñach, J. S. Muñoz, and M. D. Baró, Exchange bias in nanostructures, Phys. Rep. **422**, 65 (2005).

[35] R. L. Stamps, Mechanisms for exchange bias, J. Phys. D **33**, R247 (2000).

[36] W. Zhang and K. M. Krishnan, Epitaxial exchange-bias systems: From fundamentals to future spin-orbitronics, Mater. Sci. Eng., R **105**, 1 (2016).

[37] P. K. Manna and S. M. Yusuf, Two interface effects: Exchange bias and magnetic proximity, Phys. Rep. **535**, 61 (2014).

[38] X. He, Y. Wang, N. Wu, A. N. Caruso, E. Vescovo, K. D. Belashchenko, P. A. Dowben, and C. Binek, Robust isothermal electric control of exchange bias at room temperature, Nat. Mater. **9**, 579 (2010).

[39] K. D. Belashchenko, Equilibrium Magnetization at the Boundary of a Magnetoelectric Antiferromagnet, Phys. Rev. Lett. **105**, 147204 (2010).

[40] A. Kamra and W. Belzig, Spin Pumping and Shot Noise in Ferrimagnets: Bridging Ferro- and Antiferromagnets, Phys. Rev. Lett. **119**, 197201 (2017).

[41] A. Kamra, A. Rezaei, and W. Belzig, Spin Splitting Induced in a Superconductor by an Antiferromagnetic Insulator, Phys. Rev. Lett. **121**, 247702 (2018).

[42] J. Bardeen, L. N. Cooper, and J. R. Schrieffer, Theory of superconductivity, Phys. Rev. **108**, 1175 (1957).

[43] J. R. Schrieffer, *Theory of Superconductivity*, 4th ed., Frontiers in Physics (Addison-Wesley, Boston, 1988).

[44] Y. He, M. Hashimoto, D. Song, S.-D. Chen, J. He, I. M. Vishik, B. Moritz, D.-H. Lee, N. Nagaosa, J. Zaanen, T. P. Devereaux, Y. Yoshida, H. Eisaki, D. H. Lu, and Z.-X. Shen, Rapid change of superconductivity and electron-phonon coupling through critical doping in Bi-2212, Science **362**, 62 (2018).

[45] C. Gerry and P. Knight, *Introductory Quantum Optics* (Cambridge University Press, Cambridge, UK, 2004).

[46] M. Knap, M. Babadi, G. Refael, I. Martin, and E. Demler, Dynamical Cooper pairing in nonequilibrium electron-phonon systems, Phys. Rev. B **94**, 214504 (2016).

[47] M. Babadi, M. Knap, I. Martin, G. Refael, and E. Demler, Theory of parametrically amplified electron-phonon superconductivity, Phys. Rev. B **96**, 014512 (2017).

[48] D. Fausti, R. I. Tobey, N. Dean, S. Kaiser, A. Dienst, M. C. Hoffmann, S. Pyon, T. Takayama, H. Takagi, and A. Cavalleri, Light-induced superconductivity in a stripe-ordered cuprate, Science **331**, 189 (2011).

[49] R. Mankowsky, A. Subedi, M. Först, S. O. Mariager, M. Chollet, H. T. Lemke, J. S. Robinson, J. M. Glownia, M. P. Minitti, A. Frano, M. Fechner, N. A. Spaldin, T. Loew, B. Keimer, A. Georges, and A. Cavalleri, Nonlinear lattice dynamics as a basis for enhanced superconductivity in YBa$_2$Cu$_3$O$_{6.5}$, Nature (London) **516**, 71 (2014).

[50] M. Mitrano, A. Cantaluppi, D. Nicoletti, S. Kaiser, A. Perucchi, S. Lupi, P. Di Pietro, D. Pontiroli, M. Riccò, S. R. Clark, D. Jaksch, and A. Cavalleri, Possible light-induced superconductivity in K$_3$C$_{60}$ at high temperature, Nature (London) **530**, 461 (2016).

[51] A. Kamra, E. Thingstad, G. Rastelli, R. A. Duine, A. Brataas, W. Belzig, and A. Sudbø, Antiferromagnetic magnons as highly squeezed Fock states underlying quantum correlations, arXiv:1904.04553.

[52] A. Kamra, U. Agrawal, and W. Belzig, Noninteger-spin magnonic excitations in untextured magnets, Phys. Rev. B **96**, 020411(R) (2017).

[53] A. Kamra and W. Belzig, Super-Poissonian Shot Noise of Squeezed-Magnon Mediated Spin Transport, Phys. Rev. Lett. **116**, 146601 (2016).

[54] P. Král, Displaced and squeezed Fock states, J. Mod. Opt. **37**, 889 (1990).

[55] M. M. Nieto, Displaced and squeezed number states, Phys. Lett. A **229**, 135 (1997).

[56] C. Leroux, L. C. G. Govia, and A. A. Clerk, Enhancing Cavity Quantum Electrodynamics via Antisqueezing: Synthetic Ultrastrong Coupling, Phys. Rev. Lett. **120**, 093602 (2018).

[57] W. Qin, A. Miranowicz, P.-B. Li, X.-Y. Lü, J. Q. You, and F. Nori, Exponentially Enhanced Light-Matter Interaction, Cooperativities, and Steady-State Entanglement using Parametric Amplification, Phys. Rev. Lett. **120**, 093601 (2018).

[58] S. A. Bender and Y. Tserkovnyak, Interfacial spin and heat transfer between metals and magnetic insulators, Phys. Rev. B **91**, 140402(R) (2015).

[59] See Supplemental Material at http://link.aps.org/supplemental/10.1103/PhysRevB.100.100503 for (i) a detailed derivation of the diagonalized Hamiltonian contributions describing the antiferromagnet, normal metal, and their mutual interaction, (ii) derivation of the effective electron-electron interaction, (iii) mean-field theory detailing the superconducting order parameter, (iv) formulation of the gap equation, (v) evaluation of T_c by solving the linearized gap equation, and (vi) the material parameters employed in obtaining the T_c and λ plots (Fig. 3).

[60] C. Kittel, *Quantum Theory of Solids* (Wiley, New York, 1963).

[61] E. L. Fjærbu, N. Rohling, and A. Brataas, Electrically driven Bose-Einstein condensation of magnons in antiferromagnets, Phys. Rev. B **95**, 144408 (2017).

[62] G. A. Burdick, Energy band structure of copper, Phys. Rev. **129**, 138 (1963).

[63] Z. Lin, L. V. Zhigilei, and V. Celli, Electron-phonon coupling and electron heat capacity of metals under conditions of strong electron-phonon nonequilibrium, Phys. Rev. B **77**, 075133 (2008).

[64] M. G. Ramchandani, Energy band structure of gold, J. Phys. C **3**, S1 (1970).

[65] E. J. Samuelsen, M. T. Hutchings, and G. Shirane, Inelastic neutron scattering investigation of spin waves and magnetic interactions in Cr_2O_3, Physica **48**, 13 (1970).

[66] U. Köbler, A. Hoser, and J.-U. Hoffmann, Crystal field effects in the 3d transition metal compounds, Physica B: Condens. Matter **382**, 98 (2006).

[67] M. Sigrist and K. Ueda, Phenomenological theory of unconventional superconductivity, Rev. Mod. Phys. **63**, 239 (1991).

[68] N. Karchev, Magnon exchange mechanism of ferromagnetic superconductivity, Phys. Rev. B **67**, 054416 (2003).

[69] C. Pfleiderer, Superconducting phases of f-electron compounds, Rev. Mod. Phys. **81**, 1551 (2009).

[70] A. P. Mackenzie and Y. Maeno, The superconductivity of Sr_2RuO_4 and the physics of spin-triplet pairing, Rev. Mod. Phys. **75**, 657 (2003).

[71] F. S. Bergeret, A. F. Volkov, and K. B. Efetov, Odd triplet superconductivity and related phenomena in superconductor-ferromagnet structures, Rev. Mod. Phys. **77**, 1321 (2005).

[72] F. S. Bergeret, M. Silaev, P. Virtanen, and T. T. Heikkilä, Colloquium: Nonequilibrium effects in superconductors with a spin-splitting field, Rev. Mod. Phys. **90**, 041001 (2018).

[73] K. Maki, Gapless superconductivity, in *Superconductivity: Vol. 2*, edited by R. D. Parks (Taylor & Francis, London, 1969).

[74] P. Fulde and R. A. Ferrell, Superconductivity in a strong spin-exchange field, Phys. Rev. **135**, A550 (1964).

[75] A. I. Larkin and Y. N. Ovchinnikov, Inhomogeneous state of superconductors, Sov. Phys. JETP **20**, 762 (1965).

[76] K. Maki and T. Tsuneto, Pauli paramagnetism and superconducting state, Prog. Theor. Phys. **31**, 945 (1964).

[77] B. Li, N. Roschewsky, B. A. Assaf, M. Eich, M. Epstein-Martin, D. Heiman, M. Münzenberg, and J. S. Moodera, Superconducting Spin Switch with Infinite Magnetoresistance Induced by an Internal Exchange Field, Phys. Rev. Lett. **110**, 097001 (2013).

[78] M. Lange, M. J. Van Bael, Y. Bruynseraede, and V. V. Moshchalkov, Nanoengineered Magnetic-Field-Induced Superconductivity, Phys. Rev. Lett. **90**, 197006 (2003).

[79] A. M. Tsvelik and O. M. Yevtushenko, Chiral Spin Order in Kondo-Heisenberg Systems, Phys. Rev. Lett. **119**, 247203 (2017).

[80] F. D. Czeschka, L. Dreher, M. S. Brandt, M. Weiler, M. Althammer, I.-M. Imort, G. Reiss, A. Thomas, W. Schoch, W. Limmer, H. Huebl, R. Gross, and S. T. B. Goennenwein, Scaling Behavior of the Spin Pumping Effect in Ferromagnet-Platinum Bilayers, Phys. Rev. Lett. **107**, 046601 (2011).

Supplementary material
Enhancement of superconductivity mediated by antiferromagnetic squeezed magnons

Eirik Erlandsen, Akashdeep Kamra, Arne Brataas, and Asle Sudbø

Center for Quantum Spintronics, Department of Physics,
Norwegian University of Science and Technology, NO-7491 Trondheim, Norway

(Dated: September 12, 2019)

In this supplement, we provide more details for the derivations of the results presented in the main paper. In the following we will take $\hbar = a = 1$.

MODEL

We consider a bilayer heterostructure consisting of a normal metal (NM) and an antiferromagnetic insulator (AFMI), as shown in Fig. 1. The staggered magnetization of the AFMI is assumed to be aligned with the z-direction, which could be either in-plane or out-of-plane.
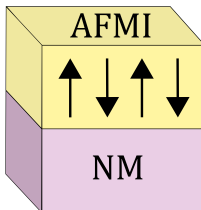
FIG. 1. The system consists of an antiferromagnetic insulator (AFMI) placed on top of a normal metal (NM).

The system is modeled by the Hamiltonian $H = H_{\text{AFMI}} + H_{\text{NM}} + H_{\text{int}}$ [1, 2], where

$$H_{\text{AFMI}} = J \sum_{\langle \boldsymbol{i}, \boldsymbol{j} \rangle} \boldsymbol{S_i} \cdot \boldsymbol{S_j} - K \sum_{\boldsymbol{i}} S_{\boldsymbol{i}z}^2, \tag{1}$$

$$H_{\text{NM}} = -t \sum_{\langle \boldsymbol{i}, \boldsymbol{j} \rangle \sigma} c_{\boldsymbol{i}\sigma}^\dagger c_{\boldsymbol{j}\sigma} - \mu \sum_{\boldsymbol{i}\sigma} c_{\boldsymbol{i}\sigma}^\dagger c_{\boldsymbol{i}\sigma}, \tag{2}$$

$$H_{\text{int}} = -2\bar{J}_A \sum_{\boldsymbol{i} \in A} c_{\boldsymbol{i}}^\dagger \boldsymbol{\tau} c_{\boldsymbol{i}} \cdot \boldsymbol{S_i} - 2\bar{J}_B \sum_{\boldsymbol{i} \in B} c_{\boldsymbol{i}}^\dagger \boldsymbol{\tau} c_{\boldsymbol{i}} \cdot \boldsymbol{S_i}. \tag{3}$$

Here, we have $c_i^\dagger = (c_{i\uparrow}^\dagger, c_{i\downarrow}^\dagger)$, where $c_{i\sigma}^\dagger$ is a creation operator, creating an electron with spin σ on lattice site $\boldsymbol{i}$ in the NM. The chemical potential is denoted by μ. The exchange coefficients J is assumed to be positive and therefore favors anti-alignment of neighboring lattice site spins $\boldsymbol{S_i}$. The easy-axis anisotropy coefficient K is also positive. The Pauli matrices $\boldsymbol{\tau}$ act on the fermionic spin degree of freedom, the lattices are taken to be square and we have periodic boundary conditions in the directions parallel to the interfacial plane. The sum over $\langle \boldsymbol{i}, \boldsymbol{j} \rangle$ includes all nearest neighbors for each $\boldsymbol{i}$, and the lattice site sums in the interaction Hamiltonian cover the interfacial plane between the two materials. The strength of the coupling between the electrons and the lattice site spins of sublattice A, B is determined by the parameters $\bar{J}_A$, $\bar{J}_B$. In the following, we will take $\bar{J}_B = \bar{J}$ and $\bar{J}_A = \Omega \bar{J}$, where Ω determines which AFMI sublattice couples strongest to the electrons on the surface of the NM. In this way of parametrizing the exchange-interaction across the AFMI-NM interface, we may without loss of generality set $0 \leq \Omega \leq 1$.

We introduce Holstein-Primakoff transformations for both sublattices in the AFMI

$$S_{i+}^A = \sqrt{2s - a_i^\dagger a_i}\, a_i \approx \sqrt{2s}\, a_i, \tag{4}$$

$$S_{i-}^A = a_i^\dagger \sqrt{2s - a_i^\dagger a_i} \approx \sqrt{2s}\, a_i^\dagger, \tag{5}$$

$$S_{iz}^A = s - a_i^\dagger a_i, \tag{6}$$

$$S_{j+}^B = b_j^\dagger \sqrt{2s - b_j^\dagger b_j} \approx \sqrt{2s}\, b_j^\dagger, \tag{7}$$

$$S_{j-}^B = \sqrt{2s - b_j^\dagger b_j}\, b_j \approx \sqrt{2s}\, b_j, \tag{8}$$

$$S_{jz}^B = -s + b_j^\dagger b_j, \tag{9}$$

and Fourier transformations for the magnon and electron operators

$$a_i = \frac{1}{\sqrt{N_A}} \sum_{\boldsymbol{k}\in\diamondsuit} a_{\boldsymbol{k}} e^{-i\boldsymbol{k}\cdot\boldsymbol{r}_i}, \qquad b_i = \frac{1}{\sqrt{N_B}} \sum_{\boldsymbol{k}\in\diamondsuit} b_{\boldsymbol{k}} e^{-i\boldsymbol{k}\cdot\boldsymbol{r}_i}, \tag{10}$$

$$c_{i\sigma} = \frac{1}{\sqrt{N}} \sum_{\boldsymbol{k}\in\diamondsuit} \left(c_{\boldsymbol{k}\sigma} e^{-i\boldsymbol{k}\cdot\boldsymbol{r}_i} + c_{\boldsymbol{k}+\boldsymbol{G},\sigma} e^{-i(\boldsymbol{k}+\boldsymbol{G})\cdot\boldsymbol{r}_i} \right), \tag{11}$$

where $\diamondsuit$ indicates that the sum over momenta covers the reduced Brillouin zone of the sublattices and $\boldsymbol{G} \equiv \frac{\pi(\hat{x}+\hat{y})}{a}$ is a reciprocal lattice vector for the sublattices. After performing a Bogoliubov transformation, the AFMI Hamiltonian becomes

$$H_{\mathrm{AFMI}} = \sum_{\boldsymbol{k}\in\diamondsuit} \omega_{\boldsymbol{k}} \left(\alpha_{\boldsymbol{k}}^\dagger \alpha_{\boldsymbol{k}} + \beta_{\boldsymbol{k}}^\dagger \beta_{\boldsymbol{k}} \right), \tag{12}$$

with

$$\omega_{\boldsymbol{k}} = 2s \sqrt{(zJ + K)^2 - z^2 J^2 \gamma_{\boldsymbol{k}}^2}, \tag{13}$$

$$\gamma_{\boldsymbol{k}} = \frac{2}{z} \sum_b \cos(k_b), \tag{14}$$

$$\alpha_{\boldsymbol{k}} = u_{\boldsymbol{k}} a_{\boldsymbol{k}} - v_{\boldsymbol{k}} b_{-\boldsymbol{k}}^\dagger, \qquad \beta_{\boldsymbol{k}} = u_{\boldsymbol{k}} b_{\boldsymbol{k}} - v_{\boldsymbol{k}} a_{-\boldsymbol{k}}^\dagger, \tag{15}$$

$$u_{\boldsymbol{k}} = \cosh(\theta_{\boldsymbol{k}}), \qquad v_{\boldsymbol{k}} = \sinh(\theta_{\boldsymbol{k}}), \tag{16}$$

$$\theta_{\boldsymbol{k}} = \frac{1}{2} \tanh^{-1} \left(-\frac{J z \gamma_{\boldsymbol{k}}}{zJ + K} \right). \tag{17}$$

The number of nearest neighbors is here denoted by z, and the sum over b in Eq. (14) goes over the directions parallel to the interface. For small k, compared to the size of the Brillouin zone, the parameters $u_{\boldsymbol{k}}$ and $v_{\boldsymbol{k}}$ grow large with similar magnitude, but opposite signs.

The NM Hamiltonian reduces to

$$H_{\mathrm{NM}} = \sum_{\substack{\boldsymbol{k}\in\square \\ \sigma}} \epsilon_{\boldsymbol{k}} c_{\boldsymbol{k}\sigma}^{\dagger} c_{\boldsymbol{k}\sigma}, \tag{18}$$

with

$$\epsilon_{\boldsymbol{k}} = -tz\gamma_{\boldsymbol{k}} - \mu. \tag{19}$$

From the interaction Hamiltonian we obtain, for coupling to sublattice A and B respectively [2, 3],

$$H_{\mathrm{int}}^{(A)} = \Omega V \sum_{\substack{\boldsymbol{k}\in\square \\ \boldsymbol{q}\in\Diamond}} \left(a_{\boldsymbol{q}} c_{\boldsymbol{k}+\boldsymbol{q},\downarrow}^{\dagger} c_{\boldsymbol{k}\uparrow} + a_{\boldsymbol{q}} c_{\boldsymbol{k}+\boldsymbol{q}+\boldsymbol{G},\downarrow}^{\dagger} c_{\boldsymbol{k}\uparrow} + \mathrm{h.c.} \right) - \Omega \bar{J} s \sum_{\substack{\boldsymbol{k}\in\square \\ \sigma}} \hat{\sigma} \left(c_{\boldsymbol{k}\sigma}^{\dagger} c_{\boldsymbol{k}\sigma} + c_{\boldsymbol{k}+\boldsymbol{G},\sigma}^{\dagger} c_{\boldsymbol{k}\sigma} \right), \tag{20}$$

$$H_{\mathrm{int}}^{(B)} = V \sum_{\substack{\boldsymbol{k}\in\square \\ \boldsymbol{q}\in\Diamond}} \left(b_{\boldsymbol{q}} c_{\boldsymbol{k}+\boldsymbol{q},\uparrow}^{\dagger} c_{\boldsymbol{k}\downarrow} - b_{\boldsymbol{q}} c_{\boldsymbol{k}+\boldsymbol{q}+\boldsymbol{G},\uparrow}^{\dagger} c_{\boldsymbol{k}\downarrow} + \mathrm{h.c.} \right) + \bar{J} s \sum_{\substack{\boldsymbol{k}\in\square \\ \sigma}} \hat{\sigma} \left(c_{\boldsymbol{k}\sigma}^{\dagger} c_{\boldsymbol{k}\sigma} - c_{\boldsymbol{k}+\boldsymbol{G},\sigma}^{\dagger} c_{\boldsymbol{k}\sigma} \right), \tag{21}$$

where $\hat{\sigma} = \pm 1$ depending on the spin being up or down. We have also defined

$$V \equiv -\frac{2\bar{J}\sqrt{s}}{\sqrt{N}}, \tag{22}$$

where N is the number of lattice sites in the interfacial plane and used $\square$ to mark the sums that cover the Brillouin zone of the full lattice. Quadratic or higher order terms in the magnon operators have been neglected. The relative minus signs between the two terms in each of the parentheses in the expression for $H_{\mathrm{int}}^{(B)}$ arise due to sublattice B being shifted in space one lattice constant away from sublattice A.

For our tight binding NM model, the different sides of the Fermi surface are connected by a reciprocal lattice vector $\boldsymbol{G}$, in the case of half-filling. The above Umklapp processes involving $\boldsymbol{G}$ are then important for the physics at the Fermi surface [2]. In the following, we focus on the case away from half-filling and neglect such processes. Moreover, based on experimental results, the effect of the potential Zeeman splitting is expected to be small and a rigorous treatment of the corrections to the superconducting state stemming from this effect is outside the scope of this letter. See the discussion in the main paper. We therefore neglect these terms as well and obtain

$$H_{\mathrm{int}} = V \sum_{\substack{\boldsymbol{k}\in\square \\ \boldsymbol{q}\in\Diamond}} \left(\Omega\, a_{\boldsymbol{q}} c_{\boldsymbol{k}+\boldsymbol{q},\downarrow}^{\dagger} c_{\boldsymbol{k}\uparrow} + b_{\boldsymbol{q}} c_{\boldsymbol{k}+\boldsymbol{q},\uparrow}^{\dagger} c_{\boldsymbol{k}\downarrow} + \mathrm{h.c.} \right). \tag{23}$$

Rewriting the magnon operators in terms of the quasiparticles that diagonalized the AFMI Hamiltonian, we then have

$$H_{\mathrm{int}} = V \sum_{\boldsymbol{k}\boldsymbol{q}} \left[\Omega\left(u_{\boldsymbol{q}}\alpha_{\boldsymbol{q}} + v_{\boldsymbol{q}}\beta_{-\boldsymbol{q}}^{\dagger} \right) c_{\boldsymbol{k}+\boldsymbol{q},\downarrow}^{\dagger} c_{\boldsymbol{k}\uparrow} + \left(u_{\boldsymbol{q}}\beta_{\boldsymbol{q}} + v_{\boldsymbol{q}}\alpha_{-\boldsymbol{q}}^{\dagger} \right) c_{\boldsymbol{k}+\boldsymbol{q},\uparrow}^{\dagger} c_{\boldsymbol{k}\downarrow} + \mathrm{h.c.} \right]. \tag{24}$$

Collecting the results, the total Hamiltonian takes the form $H = H_{\mathrm{AFMI}} + H_{\mathrm{NM}} + H_{\mathrm{int}}^{(A)} + H_{\mathrm{int}}^{(B)}$,

$$H_{\text{AFMI}} = \sum_{\boldsymbol{k}} \omega_{\boldsymbol{k}} \left(\alpha_{\boldsymbol{k}}^{\dagger} \alpha_{\boldsymbol{k}} + \beta_{\boldsymbol{k}}^{\dagger} \beta_{\boldsymbol{k}} \right), \tag{25}$$

$$H_{\text{NM}} = \sum_{\boldsymbol{k}\sigma} \epsilon_{\boldsymbol{k}} c_{\boldsymbol{k}\sigma}^{\dagger} c_{\boldsymbol{k}\sigma}, \tag{26}$$

$$H_{\text{int}}^{(A)} = \Omega V \sum_{\boldsymbol{k}\boldsymbol{q}} \left[\left(u_{\boldsymbol{q}} \alpha_{\boldsymbol{q}} + v_{\boldsymbol{q}} \beta_{-\boldsymbol{q}}^{\dagger} \right) c_{\boldsymbol{k}+\boldsymbol{q},\downarrow}^{\dagger} c_{\boldsymbol{k}\uparrow} + \text{h.c.} \right], \tag{27}$$

$$H_{\text{int}}^{(B)} = V \sum_{\boldsymbol{k}\boldsymbol{q}} \left[\left(u_{\boldsymbol{q}} \beta_{\boldsymbol{q}} + v_{\boldsymbol{q}} \alpha_{-\boldsymbol{q}}^{\dagger} \right) c_{\boldsymbol{k}+\boldsymbol{q},\uparrow}^{\dagger} c_{\boldsymbol{k}\downarrow} + \text{h.c.} \right]. \tag{28}$$

EFFECTIVE INTERACTION

We now perform a canonical transformation in order to eliminate the magnon operators from the problem and obtain an effective interacting theory for the electrons, with the electron-electron interaction mediated by virtual magnons. We define

$$H_0 \equiv \sum_{\boldsymbol{k}} \omega_{\boldsymbol{k}} \left(\alpha_{\boldsymbol{k}}^{\dagger} \alpha_{\boldsymbol{k}} + \beta_{\boldsymbol{k}}^{\dagger} \beta_{\boldsymbol{k}} \right) + \sum_{\boldsymbol{k}\sigma} \epsilon_{\boldsymbol{k}\sigma} c_{\boldsymbol{k}\sigma}^{\dagger} c_{\boldsymbol{k}\sigma} \tag{29}$$

$$\eta H_1 = \eta H_1^{(A)} + \eta H_1^{(B)} \equiv H_{\text{int}}^{(A)} + H_{\text{int}}^{(B)}, \tag{30}$$

and write

$$H'' = e^{-\eta S} H e^{\eta S} = H + \eta [H, S] + \frac{\eta^2}{2!} [[H, S], S] + \mathcal{O}(\eta^3)$$
$$= H_0 + \eta \left(H_1 + [H_0, S] \right) + \eta^2 \left([H_1, S] + \frac{1}{2} [[H_0, S], S] \right) + \mathcal{O}(\eta^3). \tag{31}$$

We then choose $\eta S = \eta S^{(A)} + \eta S^{(B)}$ such that we have

$$\eta H_1^{(L)} + \left[H_0, \eta S^{(L)} \right] = 0, \tag{32}$$

producing

$$H' = H_0 + \frac{1}{2} \sum_{LL'} \left[\eta H_1^{(L)}, \eta S^{(L')} \right] + \mathcal{O}(\eta^3), \tag{33}$$

where $L \in \{A, B\}$. Choosing

$$\eta S^{(A)} = \Omega V \sum_{\boldsymbol{k}\boldsymbol{q}} \left[\left(x_{\boldsymbol{k},\boldsymbol{q}} u_{\boldsymbol{q}} \alpha_{\boldsymbol{q}} + y_{\boldsymbol{k},\boldsymbol{q}} v_{\boldsymbol{q}} \beta_{-\boldsymbol{q}}^{\dagger} \right) c_{\boldsymbol{k}+\boldsymbol{q},\downarrow}^{\dagger} c_{\boldsymbol{k}\uparrow} + \left(z_{\boldsymbol{k},\boldsymbol{q}} u_{\boldsymbol{q}} \alpha_{-\boldsymbol{q}}^{\dagger} + w_{\boldsymbol{k},\boldsymbol{q}} v_{\boldsymbol{q}} \beta_{\boldsymbol{q}} \right) c_{\boldsymbol{k}+\boldsymbol{q},\uparrow}^{\dagger} c_{\boldsymbol{k}\downarrow} \right], \tag{34}$$

$$\eta S^{(B)} = V \sum_{\boldsymbol{k}\boldsymbol{q}} \left[\left(w_{\boldsymbol{k},\boldsymbol{q}} u_{\boldsymbol{q}} \beta_{\boldsymbol{q}} + z_{\boldsymbol{k},\boldsymbol{q}} v_{\boldsymbol{q}} \alpha_{-\boldsymbol{q}}^{\dagger} \right) c_{\boldsymbol{k}+\boldsymbol{q},\uparrow}^{\dagger} c_{\boldsymbol{k}\downarrow} + \left(y_{\boldsymbol{k},\boldsymbol{q}} u_{\boldsymbol{q}} \beta_{-\boldsymbol{q}}^{\dagger} + x_{\boldsymbol{k},\boldsymbol{q}} v_{\boldsymbol{q}} \alpha_{\boldsymbol{q}} \right) c_{\boldsymbol{k}+\boldsymbol{q},\downarrow}^{\dagger} c_{\boldsymbol{k}\uparrow} \right], \tag{35}$$

where

$$x_{k,q} = w_{k,q} = \frac{1}{\epsilon_k - \epsilon_{k+q} + \omega_q}, \qquad y_{k,q} = z_{k,q} = \frac{1}{\epsilon_k - \epsilon_{k+q} - \omega_q}, \tag{36}$$

and working out the commutators, one obtains

$$H_{\text{pair}}^{(A,A)} = \frac{1}{2}\Omega^2 V^2 \sum_{kqk'} c_{k+q\downarrow}^\dagger c_{k\uparrow} c_{k'-q\uparrow}^\dagger c_{k'\downarrow} \left[u_q^2 \left(\frac{1}{(\epsilon_{k'} - \epsilon_{k'-q}) - \omega_q} - \frac{1}{(\epsilon_k - \epsilon_{k+q}) + \omega_q} \right) \right.$$
$$\left. + v_q^2 \left(\frac{1}{(\epsilon_k - \epsilon_{k+q}) - \omega_q} - \frac{1}{(\epsilon_{k'} - \epsilon_{k'-q}) + \omega_q} \right) \right], \tag{37}$$

$$H_{\text{pair}}^{(B,B)} = \frac{1}{2} V^2 \sum_{kqk'} c_{k+q\downarrow}^\dagger c_{k\uparrow} c_{k'-q\uparrow}^\dagger c_{k'\downarrow} \left[v_q^2 \left(\frac{1}{(\epsilon_{k'} - \epsilon_{k'-q}) - \omega_q} - \frac{1}{(\epsilon_k - \epsilon_{k+q}) + \omega_q} \right) \right.$$
$$\left. + u_q^2 \left(\frac{1}{(\epsilon_k - \epsilon_{k+q}) - \omega_q} - \frac{1}{(\epsilon_{k'} - \epsilon_{k'-q}) + \omega_q} \right) \right], \tag{38}$$

$$H_{\text{pair}}^{(A,B)} + H_{\text{pair}}^{(B,A)} = \Omega V^2 \sum_{kqk'} c_{k+q\downarrow}^\dagger c_{k\uparrow} c_{k'-q\uparrow}^\dagger c_{k'\downarrow} \, u_q v_q \left(\frac{1}{(\epsilon_{k'} - \epsilon_{k'-q}) - \omega_q} \right.$$
$$\left. + \frac{1}{(\epsilon_k - \epsilon_{k+q}) - \omega_q} - \frac{1}{(\epsilon_{k'} - \epsilon_{k'-q}) + \omega_q} - \frac{1}{(\epsilon_k - \epsilon_{k+q}) + \omega_q} \right). \tag{39}$$

Here, we have defined $H_{\text{pair}}^{(L,L')}$ as the contribution from $\frac{1}{2}\left[\eta H_1^{(L)}, \eta S^{(L')}\right]$ that takes the form of an electron-electron interaction. Collecting together the different contributions and focusing on BCS-type pairing between electrons on opposite sides of the Fermi surface, the result can be written on the following form

$$H_{\text{pair}} = \sum_{kk'} V_{kk'} c_{k\uparrow}^\dagger c_{-k\downarrow}^\dagger c_{-k'\downarrow} c_{k'\uparrow}, \tag{40}$$

where

$$V_{kk'} = -V^2 \frac{2\omega_{k+k'}}{(\epsilon_{k'} - \epsilon_k)^2 - \omega_{k+k'}^2} A(k + k', \Omega), \tag{41}$$

and

$$A(k + k', \Omega) = \frac{1}{2}(\Omega^2 + 1)(u_{k+k'}^2 + v_{k+k'}^2) + 2\,\Omega\, u_{k+k'} v_{k+k'}. \tag{42}$$

The fraction in Eq. (41) is of the standard form for electron-electron interactions mediated by a boson. The A-factor quantifies the effect of the interference between squeezed magnon states [4, 5] on sublattices A and B. Assuming q significantly smaller than the size of the Brillouin zone, the term involving $u_q^2 + v_q^2$ grows large and positive, while the next term involving $u_q v_q$ grows large and negative, due to the opposite signs of the parameters u_q and v_q. The destructive interference between squeezed magnon states is in general maximal when $\Omega = 1$. Then, the factor within the square brackets simplify to $(u_q + v_q)^2$, which for general filling fractions is small due to a near cancellation of u_q and v_q. Setting instead $\Omega = 0$ eliminates the destructive interference between squeezed magnon states on sublattices A and B entirely.

GAP EQUATION

The potential can be divided into even and odd parts in $\boldsymbol{k}$

$$V_{\boldsymbol{k}\boldsymbol{k}'} = V_{\boldsymbol{k}\boldsymbol{k}',O(\boldsymbol{k})} + V_{\boldsymbol{k}\boldsymbol{k}',E(\boldsymbol{k})}, \tag{43}$$

where

$$V_{\boldsymbol{k}\boldsymbol{k}',O(\boldsymbol{k})} = \frac{1}{2}(V_{\boldsymbol{k}\boldsymbol{k}'} - V_{-\boldsymbol{k},\boldsymbol{k}'}), \tag{44}$$

$$V_{\boldsymbol{k}\boldsymbol{k}',E(\boldsymbol{k})} = \frac{1}{2}(V_{\boldsymbol{k}\boldsymbol{k}'} + V_{-\boldsymbol{k},\boldsymbol{k}'}). \tag{45}$$

Following the procedure of Ref. [6], we write the pairing Hamiltonian as

$$H_{\mathrm{pair}}^{(\mathrm{BCS})} = \frac{1}{2} \sum_{\boldsymbol{k}\boldsymbol{k}'} \sum_{s_1 s_2 s_3 s_4} V_{\boldsymbol{k}\boldsymbol{k}'}^{s_1 s_2 s_3 s_4} c_{\boldsymbol{k}s_1}^\dagger c_{-\boldsymbol{k}s_2}^\dagger c_{-\boldsymbol{k}'s_3} c_{\boldsymbol{k}'s_4}, \tag{46}$$

where

$$V_{\boldsymbol{k}\boldsymbol{k}'}^{\uparrow\downarrow\downarrow\uparrow} = V_{\boldsymbol{k}\boldsymbol{k}'}^{\downarrow\uparrow\uparrow\downarrow} = \frac{1}{2}\left[V_{\boldsymbol{k}\boldsymbol{k}',O(\boldsymbol{k})} + V_{\boldsymbol{k}\boldsymbol{k}',E(\boldsymbol{k})}\right] \tag{47}$$

$$V_{\boldsymbol{k}\boldsymbol{k}'}^{\downarrow\uparrow\downarrow\uparrow} = V_{\boldsymbol{k}\boldsymbol{k}'}^{\uparrow\downarrow\uparrow\downarrow} = \frac{1}{2}\left[V_{\boldsymbol{k}\boldsymbol{k}',O(\boldsymbol{k})} - V_{\boldsymbol{k}\boldsymbol{k}',E(\boldsymbol{k})}\right], \tag{48}$$

following from the fermionic anti-commutation relations of the electron operators. The potential vanishes for all other spin-combinations. We define a gap function

$$\Delta_{\boldsymbol{k},s_1 s_2} = -\sum_{\boldsymbol{k}',s_3 s_4} V_{\boldsymbol{k}\boldsymbol{k}'}^{s_1 s_2 s_3 s_4} b_{\boldsymbol{k}',s_3 s_4}, \tag{49}$$

where $b_{\boldsymbol{k},ss'} = \langle c_{-\boldsymbol{k}s} c_{\boldsymbol{k}s'} \rangle$. Following the usual mean-field approach, the gap equation then becomes

$$\Delta_{\boldsymbol{k},s_1 s_2} = -\sum_{\boldsymbol{k}',s_3 s_4} V_{\boldsymbol{k}\boldsymbol{k}'}^{s_1 s_2 s_3 s_4} \Delta_{\boldsymbol{k}',s_4 s_3} \chi_{\boldsymbol{k}'}, \tag{50}$$

where

$$\chi_{\boldsymbol{k}'} = \frac{1}{2E_{\boldsymbol{k}'}} \tanh\left(\frac{E_{\boldsymbol{k}'}}{2k_B T}\right), \tag{51}$$

and $E_{\boldsymbol{k}} = \sqrt{\epsilon_k^2 + |\Delta_{\boldsymbol{k}}|^2}$. Restricting to the spin singlet channel, we obtain

$$\Delta_{\boldsymbol{k},\uparrow\downarrow,O(s)} = -\sum_{\boldsymbol{k}'} V_{\boldsymbol{k}\boldsymbol{k}',E(\boldsymbol{k})} \Delta_{\boldsymbol{k}',\uparrow\downarrow,O(s)} \chi_{\boldsymbol{k}'}. \tag{52}$$

with

$$V_{\boldsymbol{k}\boldsymbol{k}',E(\boldsymbol{k})} = -V^2\left[\frac{\omega_{\boldsymbol{k}+\boldsymbol{k}'}}{(\epsilon_{\boldsymbol{k}'} - \epsilon_{\boldsymbol{k}})^2 - \omega_{\boldsymbol{k}+\boldsymbol{k}'}^2} A(\boldsymbol{k}+\boldsymbol{k}',\Omega) + \frac{\omega_{\boldsymbol{k}-\boldsymbol{k}'}}{(\epsilon_{\boldsymbol{k}'} - \epsilon_{\boldsymbol{k}})^2 - \omega_{\boldsymbol{k}-\boldsymbol{k}'}^2} A(\boldsymbol{k}-\boldsymbol{k}',\Omega)\right], \tag{53}$$

where $O(s)$ indicates that the gap function is odd in spin, and therefore even in momentum. Comparing with standard phonon-mediated s-wave BCS pairing, this potential has an additional minus sign in front. We therefore instead consider the spin triplet channel, where we find

$$\Delta_{\boldsymbol{k},\uparrow\downarrow,E(s)} = -\sum_{\boldsymbol{k}'} V_{\boldsymbol{k}\boldsymbol{k}',O(\boldsymbol{k})} \Delta_{\boldsymbol{k}',\uparrow\downarrow,E(s)} \chi_{\boldsymbol{k}'}, \tag{54}$$

with

$$V_{\boldsymbol{k}\boldsymbol{k}',O(\boldsymbol{k})} = -V^2 \left[\frac{\omega_{\boldsymbol{k}+\boldsymbol{k}'}}{(\epsilon_{\boldsymbol{k}'} - \epsilon_{\boldsymbol{k}})^2 - \omega_{\boldsymbol{k}+\boldsymbol{k}'}^2} A(\boldsymbol{k} + \boldsymbol{k}', \Omega) - \frac{\omega_{\boldsymbol{k}-\boldsymbol{k}'}}{(\epsilon_{\boldsymbol{k}'} - \epsilon_{\boldsymbol{k}})^2 - \omega_{\boldsymbol{k}-\boldsymbol{k}'}^2} A(\boldsymbol{k} - \boldsymbol{k}', \Omega) \right]. \tag{55}$$

Considering scattering exactly at the Fermi surface ($\epsilon_{\boldsymbol{k}'} = \epsilon_{\boldsymbol{k}} = \epsilon_F$), the potential simplifies to

$$V_{\boldsymbol{k}\boldsymbol{k}',O(\boldsymbol{k})} = V^2 \left[\frac{1}{\omega_{\boldsymbol{k}+\boldsymbol{k}'}} A(\boldsymbol{k} + \boldsymbol{k}', \Omega) - \frac{1}{\omega_{\boldsymbol{k}-\boldsymbol{k}'}} A(\boldsymbol{k} - \boldsymbol{k}', \Omega) \right]. \tag{56}$$

When $\boldsymbol{k} - \boldsymbol{k}'$ is small, i.e. when $\boldsymbol{k}$ and $\boldsymbol{k}'$ are almost parallel and $\Delta_{\boldsymbol{k}',\uparrow\downarrow,E(s)}$ has the same sign as $\Delta_{\boldsymbol{k},\uparrow\downarrow,E(s)}$, the second term in the potential dominates and the potential is attractive. When $\boldsymbol{k} + \boldsymbol{k}'$ is small, i.e. when $\boldsymbol{k}$ and $\boldsymbol{k}'$ are almost anti-parallel and $\Delta_{\boldsymbol{k}',\uparrow\downarrow,E(s)}$ has the opposite sign as $\Delta_{\boldsymbol{k},\uparrow\downarrow,E(s)}$, the first term in the potential dominates and the potential is repulsive. In both cases the signs in Eq. (54) work out in order to provide a non-trivial solution of the gap equation. The A-factor clearly strengthens the interaction, which increases the critical temperature of the superconducting instability.

In order to determine the critical temperature, we linearize the gap equation

$$d_{\boldsymbol{k}} = -\sum_{\boldsymbol{k}'} V_{\boldsymbol{k}\boldsymbol{k}',O(\boldsymbol{k})} \, d_{\boldsymbol{k}'} \frac{1}{2|\epsilon_{\boldsymbol{k}'}|} \tanh\left(\frac{|\epsilon_{\boldsymbol{k}'}|}{2k_B T_c} \right), \tag{57}$$

where we have defined $d_{\boldsymbol{k}} = \Delta_{\boldsymbol{k},\uparrow\downarrow,E(s)} = \Delta_{\boldsymbol{k},\downarrow\uparrow,E(s)}$. Following Ref. [6], we write

$$d_{\boldsymbol{k}} = -D_0 \langle V_{\boldsymbol{k}\boldsymbol{k}',O(\boldsymbol{k})} \, d_{\boldsymbol{k}'} \rangle_{\boldsymbol{k}',\mathrm{FS}} \int_{-\omega_c}^{\omega_c} \mathrm{d}\epsilon \frac{1}{2|\epsilon|} \tanh\left(\frac{|\epsilon|}{2\mathrm{k_B T_c}} \right), \tag{58}$$

where D_0 is the single-particle density of states at the Fermi level, ω_c is a cutoff energy for the boson spectrum and $\langle \ \rangle_{\boldsymbol{k}',\mathrm{FS}}$ is an angular average over the Fermi surface. Assuming $\omega_c/(k_B T_c) >> 1$, we can take

$$\frac{1}{\lambda} = \int_{-\omega_c}^{\omega_c} \mathrm{d}\epsilon \frac{1}{2|\epsilon|} \tanh\left(\frac{|\epsilon|}{2\mathrm{k_B T_c}} \right) \approx \ln\left(\frac{1.14 \, \omega_c}{\mathrm{k_B T_c}} \right), \tag{59}$$

implying

$$k_B T_c = 1.14 \, \omega_c \, e^{-1/\lambda}, \tag{60}$$

where the dimensionless coupling constant λ is the largest eigenvalue of the eigenvalue equation

$$\lambda \, d_{\boldsymbol{k}} = -D_0 \langle V_{\boldsymbol{k}\boldsymbol{k}',O(\boldsymbol{k})} \, d_{\boldsymbol{k}'} \rangle_{\boldsymbol{k}',\mathrm{FS}}. \tag{61}$$

By picking discrete points on the Fermi surface for $\boldsymbol{k}$ and $\boldsymbol{k}'$, this equation can be expressed as a matrix eigenvalue problem

$$\lambda \boldsymbol{d} = M\boldsymbol{d}, \tag{62}$$

which can be solved numerically for a given set of model parameters in order to determine λ as well as the corresponding eigenvector, which contains information about the structure of the gap function.

MATERIAL PARAMETERS

In the long-wavelength limit the density of states $D(\epsilon) = \sum_{\boldsymbol{k}} \delta(\epsilon - \epsilon_{\boldsymbol{k}})$ of the tight binding model is

$$D(\epsilon) = \frac{N}{4\pi t}. \tag{63}$$

Taking $t = 0.8\,\text{eV}$, produces

$$\frac{D_0}{N} = 1.4 \,\frac{1}{\text{atom}\,\text{Ry}}, \tag{64}$$

which is a typical magnitude for the long-wavelength density of states of metals such as Cu, Al and Au [7–9]. For the Fermi momentum, we take a small value of $k_F\,a = 0.07\,\pi$, which provides us with an approximately circular Fermi surface and makes the results less dependent on the lattice geometry. For the AFMI, we take $J = 5\,\text{meV}$, $J/K = 2000$ and $s = 1$ [10, 11]. The cutoff ω_c is set to the value at the Brillouine zone boundary $\omega_c = 2szJ$. Finally, the strength of the interfacial coupling is typically reported to be on the order of magnitude of $10\,\text{meV}$ [2, 12].

———————

[1] N. Rohling, E. L. Fjærbu, and A. Brataas, Phys. Rev. B **97**, 115401 (2018).
[2] E. L. Fjærbu, N. Rohling, and A. Brataas, ArXiv e-prints (2019), arXiv:1904.00233.
[3] E. L. Fjærbu, N. Rohling, and A. Brataas, Phys. Rev. B **95**, 144408 (2017).
[4] A. Kamra and W. Belzig, Phys. Rev. Lett. **116**, 146601 (2016).
[5] A. Kamra, U. Agrawal, and W. Belzig, Phys. Rev. B **96**, 020411 (2017).
[6] M. Sigrist and K. Ueda, Rev. Mod. Phys. **63**, 239 (1991).
[7] G. A. Burdick, Phys. Rev. **129**, 138 (1963).
[8] Z. Lin, L. V. Zhigilei, and V. Celli, Phys. Rev. B **77**, 075133 (2008).
[9] M. G. Ramchandani, Journal of Physics C: Solid State Physics **3**, S1 (1970).
[10] E. Samuelsen, M. Hutchings, and G. Shirane, Physica **48**, 13 (1970).
[11] U. Köbler, A. Hoser, and J.-U. Hoffmann, Physica B: Condensed Matter **382**, 98 (2006).
[12] Y. Kajiwara, K. Harii, S. Takahashi, J. Ohe, K. Uchida, M. Mizuguchi, H. Umezawa, H. Kawai, K. Ando, K. Takanashi, S. Maekawa, and E. Saitoh, Nature **464**, 262 EP (2010).

Magnon-mediated superconductivity on the surface of a topological insulator

Authors

Eirik Erlandsen
Arne Brataas
Asle Sudbø

Magnon-mediated superconductivity on the surface of a topological insulator

Eirik Erlandsen ⊙, Arne Brataas, and Asle Sudbø ⊙*

Center for Quantum Spintronics, Department of Physics, Norwegian University of Science and Technology, NO-7491 Trondheim, Norway

We study superconductivity on the surface of a topological insulator, mediated by magnetic fluctuations in an adjacent ferromagnetic or antiferromagnetic insulator. Superconductivity can arise from effective interactions between helical fermions induced by interfacial fermion-magnon interactions. For both ferromagnetic and antiferromagnetic insulators, these fermion-fermion interactions have the correct structure to facilitate pairing between particles located on the same side of the Fermi surface, also known as Amperean pairing. In antiferromagnets, the strength of the induced interactions can be enhanced by coupling the topological insulator asymmetrically to the two sublattices of the antiferromagnet. This effect is further amplified by next-nearest-neighbor frustration in the antiferromagnetic insulator. The enhancement makes the induced interactions significantly stronger in the antiferromagnetic case compared to the ferromagnetic case. These results indicate that an uncompensated antiferromagnetic interface might be a better candidate than a ferromagnetic interface for proximity-induced magnon-mediated superconductivity on the surface of a topological insulator.

I. INTRODUCTION

Heterostructures of ferro- and antiferromagnetic insulators, on the one hand, and superconductors, metals, and topological insulators, on the other hand, have received much interest both theoretically and experimentally over the last few decades [1–10]. They continue to be fruitful model systems for development of novel ideas in condensed-matter physics. Recently, the idea that magnons in a magnetic material can induce superconductivity across an interface when proximized with either a normal metal (NM) or a topological insulator (TI) was considered in some detail [11–16]. In NMs, the magnons mediate attractive interactions between electrons. On the surface of TIs the Cooper pairs are formed by helical fermions where the spin and momentum are locked together [17,18]. As a consequence, while the pairing in NMs is of the normal BCS type where Cooper pairs are formed by electrons on opposite sides of the Fermi surface, Kargarian *et al.* [11] predicted pairing between fermions with momenta in the same direction, named Amperean pairing [19], in a TI coupled to a ferromagnetic insulator (FMI). Amperean pairing, with finite-momentum Cooper pairs, should be experimentally distinguishable from normal BCS-type pairing through its nonuniform ground state [11]. In a subsequent related study, the cases of a TI coupled to a FMI and a TI coupled to an antiferromagnetic insulator (AFMI) were considered in Ref. [14]. Possible attractive interactions for both Amperean and BCS-type pairing were found.

Similar to Kargarian *et al.*, we study a TI coupled to a FMI. Instead of a continuum action model, we utilize a lattice model Hamiltonian to describe the system. Furthermore, Kargarian *et al.* applied a self-consistent strong-coupling approach, establishing that the fermionic states on the surface of the TI

can be strongly renormalized by the presence of the magnetic fluctuations through the fermion self-energy. Our objective is, however, not to perform an optimal analysis of the superconducting instability. Instead, we seek to reveal the qualitative difference between the effective fermionic interactions induced by ferromagnetic and antiferromagnetic fluctuations, arising from the magnon coherence factors not present in the ferromagnet. To illustrate this important aspect, we therefore find it sufficient to apply a simpler weak-coupling approach, neglecting the renormalization of the fermionic normal state.

Treating the magnetic subsystem in a quantum-mechanical fashion, we investigate the effect of coupling the TI symmetrically or asymmetrically to the two sublattices of the AFMI. An asymmetric coupling can be achieved through a fully uncompensated antiferromagnetic interface where only one of the two sublattices is exposed [20,21]. Such an asymmetric coupling has been predicted to significantly enhance the critical temperature for magnon-mediated superconductivity in a NM/AFMI heterostructure [16]. This enhancement can be understood from the picture of antiferromagnetic magnons as squeezed states, revealing that an antiferromagnetic magnon is associated with a large spin located at each sublattice [22]. Coupling to only one of the two sublattices of an AFMI thereby involves coupling to a large spin, leading to a strong enhancement of the coupling interaction [16,23].

For both FMIs and AFMIs, we find that the effective fermion-fermion interactions mediated by magnetic fluctuations cannot facilitate BCS-type chiral *p*-wave pairing. For Amperean pairing, on the other hand, we find that the effective potential has the correct form to produce a nontrivial solution to the gap equation in both the FMI and AFMI cases. For the FMI, the phase space is, within our weak-coupling approach, too small to produce a superconducting instability for realistic parameters, in contrast to the strong-coupling result of Kargarian *et al*. For the AFMI, when coupling asymmetrically to the two sublattices, we obtain a nontrivial solution to the
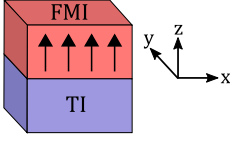
---

*Corresponding author: asle.sudbo@ntnu.no

FIG. 1. The system consists of a ferromagnetic insulator (FMI) on top of a topological insulator (TI).

gap equation. However, this solution arises from a strong interaction potential and small phase space. Combined with the strong renormalization of the fermionic states predicted by Kargarian *et al.*, this suggests that a strong-coupling approach, not performed here, is needed in order to provide stronger evidence for the existence of a superconducting instability and realistic estimates for the critical temperature.

The main result of this paper, which is expected to be robust, is that the strength of the fermion-fermion interaction mediated by antiferromagnetic magnons, analogously to the NM/AFMI case of Ref. [16], is enhanced by coupling asymmetrically to the two sublattices of the AFMI. The interaction strength is therefore significantly larger than for an FMI. Moreover, including an antiferromagnetic next-nearest-neighbor interaction term, frustrating the AFMI, is found to strengthen the enhancement effect. The result of this next-nearest-neighbor frustration is not limited to the case of a TI.

This paper is organized as follows. In Sec. II we consider the case of a TI coupled to a FMI, and in Sec. III we consider the case of a TI coupled to an AFMI. The results are summarized in Sec. IV. Additional details concerning the derivation of the self-consistent equation for the Amperean gap function are presented in the Appendix.

II. FERROMAGNETIC CASE

We consider a three-dimensional TI with a single Dirac cone such as Bi_2Se_3 or Bi_2Te_3 [24,25] proximity coupled to a FMI such as YIG, EuO, or EuS [6,26,27], as displayed in Fig. 1. The interface is placed in the xy plane. For the FMI we assume an ordered magnetic state with magnetization along the z axis. In the following, we take $\hbar = a = 1$, where a is the lattice constant.

A. Model

The system is modeled by the Hamiltonian [28,29] $H = H_{\text{FMI}} + H_{\text{TI}} + H_{\text{int}}$,

$$H_{\text{FMI}} = -J \sum_{\langle i,j \rangle} \boldsymbol{S}_i \cdot \boldsymbol{S}_j - K \sum_i S_{iz}^2, \tag{1a}$$

$$H_{\text{TI}} = \frac{v_F}{2} \sum_{i,\boldsymbol{b}} [c_i^\dagger (i\tau_y \delta_{\boldsymbol{b},\hat{x}} - i\tau_x \delta_{\boldsymbol{b},\hat{y}}) c_{i+\boldsymbol{b}} + \text{H.c.}]$$
$$+ \sum_i c_i^\dagger [2W\tau_z - \mu] c_i$$
$$- \frac{W}{2} \sum_{i,\boldsymbol{b}} [c_i^\dagger \tau_z c_{i+\boldsymbol{b}} + \text{H.c.}], \tag{1b}$$

$$H_{\text{int}} = -2\bar{J} \sum_i c_i^\dagger \boldsymbol{\tau} c_i \cdot \boldsymbol{S}_i. \tag{1c}$$

Here, the ferromagnetic exchange interaction between lattice site spins S_i is parametrized by the exchange constant $J > 0$, and the strength of the easy-axis anisotropy is determined by $K > 0$. Moreover, $c_i^\dagger = (c_{i\uparrow}^\dagger, c_{i\downarrow}^\dagger)$, where $c_{i\sigma}^\dagger$ is a creation operator for an electron with spin σ on lattice site $\boldsymbol{i}$ on the surface of the TI. The Pauli matrices $\boldsymbol{\tau}$ act on the spin degree of freedom of the electrons, and μ is the chemical potential. The first term in the TI Hamiltonian in Eq. (1b) describes the spin-momentum locking experienced by electrons on the surface of the TI, the strength of which is determined by the Fermi velocity v_F. The following Wilson terms W ensure that there is not more than one Dirac cone in the first Brillouin zone, avoiding the fermion-doubling problem which arises in the discretization of the continuum model $H(\boldsymbol{k}) = v_F(\boldsymbol{\tau} \times \boldsymbol{k}) \cdot \hat{z}$ [28–30]. The Wilson terms are phenomenologically added to the Hamiltonian in order to produce a lattice model that describes the correct physics. Their effect vanishes in the long-wavelength limit where the effective two-dimensional lattice model is expected to faithfully describe the surface states of the TI [28]. The electrons on the surface of the TI are exchange coupled to the lattice site spins on the surface of the FMI [13], with a strength determined by $\bar{J}$. The lattices are quadratic, and we assume periodic boundary conditions in the x and y directions in order to capture the physics at the interface between the two materials. The sum over $\langle \boldsymbol{i}, \boldsymbol{j} \rangle$ includes all nearest neighbors in both positive and negative directions, while $\boldsymbol{b} \in \{\hat{x}, \hat{y}\}$ includes only nearest neighbors in the positive directions.

B. Diagonalization of subsystems

We introduce a Holstein-Primakoff transformation [31] for the spin operators $S_{i+} = \sqrt{2s}\, a_i$, $S_{i-} = \sqrt{2s}\, a_i^\dagger$, $S_{iz} = s - a_i^\dagger a_i$. Including quadratic terms in the magnon operators and performing a Fourier transformation $a_i = \frac{1}{\sqrt{N}} \sum_k a_k e^{-ik \cdot r_i}$, the FMI Hamiltonian takes the form [32]

$$H_{\text{FMI}} = \sum_k \omega_k a_k^\dagger a_k, \tag{2}$$

where $\omega_k = 2sJz_1(1 - \gamma_k) + 2Ks$ and $\gamma_k = \frac{2}{z_1} \sum_b \cos(k_b)$. The number of nearest neighbors has here been denoted by z_1, the sum over b covers the spatial dimensions of the FMI lattice, and the number of lattice sites in the interfacial plane is denoted by N.

From the interaction Hamiltonian (1c), we obtain

$$H_{\text{int}} = -2\bar{J}\sqrt{2s} \sum_i (a_i c_{i\downarrow}^\dagger c_{i\uparrow} + \text{H.c.})$$
$$- 2\bar{J} \sum_{i\sigma} \sigma c_{i\sigma}^\dagger c_{i\sigma}(s - a_i^\dagger a_i), \tag{3}$$

where the first line originates with the x, y components of the coupling scalar product and the second line originates with the z component. The quantity σ in front of the electron operators in the second line is $+1$ for spin up and -1 for spin down. Fourier transforming the magnon and electron operators $c_{i\sigma} = \frac{1}{\sqrt{N}} \sum_k c_{k\sigma} e^{-ik \cdot r_i}$ then produces [13]

$$H_{\text{int}} = V \sum_{kq} (a_q c_{k+q,\downarrow}^\dagger c_{k\uparrow} + \text{H.c.}) - 2\bar{J}s \sum_{k\sigma} \sigma c_{k\sigma}^\dagger c_{k\sigma}, \tag{4}$$

with $V = \frac{-2J\sqrt{2s}}{\sqrt{N}}$. The first terms represent electron-magnon interactions involving a single magnon, and the second term originates with the exchange field that the electrons on the surface of the TI are exposed to due to the proximity to the FMI. Electron-magnon interactions involving more than one magnon have been neglected. Fourier transforming the electron operators in the TI Hamiltonian, as well as moving the exchange field contribution from the interaction Hamiltonian to the TI Hamiltonian, produces

$$H_{TI} = W \sum_{k\sigma} \sigma c_{k\sigma}^\dagger c_{k\sigma} \left[2 - \sum_b \cos(k_b) \right]$$
$$- v_F \sum_k \{ c_{k\uparrow}^\dagger c_{k\downarrow}[\sin(k_y) + i\sin(k_x)] + \text{H.c.} \}$$
$$- 2\bar{J}s \sum_{k\sigma} \sigma c_{k\sigma}^\dagger c_{k\sigma} - \mu \sum_{k\sigma} c_{k\sigma}^\dagger c_{k\sigma}. \quad (5)$$

As we are interested in pairing between long-lived excitations on the surface of the TI, mediated by magnetic fluctuations on the surface of the FMI, we diagonalize H_{TI}, where the presence of the exchange field now has been taken into account. The TI Hamiltonian then takes the form

$$H_{TI} = \sum_{k\alpha} E_{k\alpha} \psi_{k\alpha}^\dagger \psi_{k\alpha}, \quad (6)$$

where $\alpha = \pm$ is the helicity index of the quasiparticles $\psi_{k\alpha}$. Defining $A = -\mu$, $B_k = W[2 - \sum_b \cos(k_b)] - 2\bar{J}s$, $C_k = -v_F \sin(k_y)$, $D_k = -v_F \sin(k_x)$, $N_k = 2F_k(F_k + B_k)$, and $F_k = \sqrt{B_k^2 + C_k^2 + D_k^2}$, the excitation energies can be expressed as $E_{k\alpha} = -\mu + \alpha F_k$, and the original electron operators can be related to the new quasiparticle operators

$$c_{k\uparrow} = Q_{\uparrow+}(\boldsymbol{k}) \psi_{k+} + Q_{\uparrow-}(\boldsymbol{k}) \psi_{k-}, \quad (7a)$$
$$c_{k\downarrow} = Q_{\downarrow+}(\boldsymbol{k}) \psi_{k+} + Q_{\downarrow-}(\boldsymbol{k}) \psi_{k-}, \quad (7b)$$

where we have defined

$$Q_{\uparrow+} = -Q_{\downarrow-} = (B_k + F_k)/\sqrt{N_k}, \quad (8a)$$
$$Q_{\uparrow-} = Q_{\downarrow+}^* = (C_k + iD_k)/\sqrt{N_k}. \quad (8b)$$

The band structure of the TI surface states is presented in Fig. 2, displaying the two bands of opposite helicity. The exchange field from the FMI breaks time-reversal symmetry and introduces a gap in the dispersion relation [6,27,33], similar to the mass gap in the dispersion relation for massive Dirac fermions [34].

Expressing the interaction Hamiltonian in terms of the TI eigenexcitations, the full Hamiltonian becomes $H = H_{FMI} + H_{TI} + H_{int}$, with

$$H_{int} = V \sum_{kq} \sum_{\alpha\alpha'} Q_{\downarrow\alpha}^\dagger(k+q) Q_{\uparrow\alpha'}(\boldsymbol{k})$$
$$\times a_{\boldsymbol{q}} \psi_{k+q,\alpha}^\dagger \psi_{k\alpha'} + \text{H.c.} \quad (9)$$

In the following, we derive the effective fermion-fermion interaction arising from this magnon-fermion coupling.
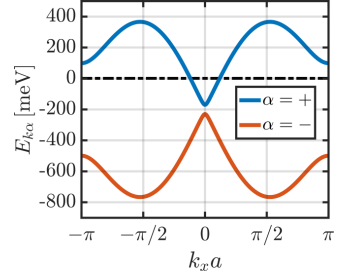

FIG. 2. The band structure of the topological insulator surface states in the presence of the exchange field from the adjacent ferromagnetic insulator for $k_y = 0$, Fermi velocity $v_F = 5 \times 10^5$ m/s, lattice constant $a = 0.6$ nm, Wilson term coefficient $W = 0.3\hbar v_F$ [28], interfacial exchange coupling strength $\bar{J} = 15$ meV, spin quantum number of the lattice site spins $s = 1$, and chemical potential $\mu = 200$ meV. In the long-wavelength limit, the dispersion relation is linear, in agreement with the continuum model. The Wilson terms open a gap at the Brillouin zone boundaries, removing the extra Dirac cones originating with the discretization of the continuum model.

C. Effective interaction

We proceed by integrating out the magnons in order to obtain an effective theory of interacting helical fermions. Examining the nature of the interaction between particles close to the Fermi surface, we can then determine whether a superconducting instability is possible. We take $H = H_0 + \eta H_1$, where $H_0 = H_{FMI} + H_{TI}$, $\eta H_1 = H_{int}$, and η is a smallness parameter. We then perform a canonical transformation [32]

$$H' = e^{-\eta S} H e^{\eta S} \quad (10)$$

and a second-order expansion

$$H' = H_0 + \eta(H_1 + [H_0 S]) + \eta^2 \left([H_1 S] + \tfrac{1}{2}[[H_0 S]S]\right). \quad (11)$$

Choosing

$$\eta S \equiv V \sum_{kq} \sum_{\alpha\alpha'} \left[x_{k,q}^{\alpha\alpha'} Q_{\downarrow\alpha}^\dagger(k+q) Q_{\uparrow\alpha'}(\boldsymbol{k}) a_{\boldsymbol{q}} \right.$$
$$\left. + y_{k,q}^{\alpha\alpha'} Q_{\uparrow\alpha}^\dagger(\boldsymbol{k}+\boldsymbol{q}) Q_{\downarrow\alpha'}(\boldsymbol{k}) a_{-\boldsymbol{q}}^\dagger \right] \psi_{k+q,\alpha}^\dagger \psi_{k\alpha'} \quad (12)$$

and

$$x_{k,q}^{\alpha\alpha'} = \frac{1}{E_{k\alpha'} - E_{k+q,\alpha} + \omega_q}, \quad (13a)$$

$$y_{k,q}^{\alpha\alpha'} = \frac{1}{E_{k\alpha'} - E_{k+q,\alpha} - \omega_q}, \quad (13b)$$

we have [35]

$$\eta H_1 + [H_0 \eta S] = 0 \quad (14)$$

and

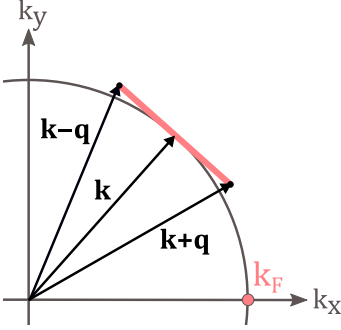$$H' = H_0 + \tfrac{1}{2}[\eta H_1 \eta S]. \quad (15)$$

FIG. 3. Amperean pairing with $\boldsymbol{k}' \approx \boldsymbol{k}$. In order for all momenta to stay close to the Fermi surface, the momentum transfer q needs to be small relative to the Fermi momentum k_F.

Computing the commutator and picking out the terms that involve four fermionic operators, we then obtain

$$
\begin{aligned}
H_{\text{pair}} = V^2 \sum_{\boldsymbol{k}\boldsymbol{q}\boldsymbol{k}'} \sum_{\alpha\alpha'} \sum_{\beta\beta'} Q_{\uparrow\beta}^{\dagger}(\boldsymbol{k}'-\boldsymbol{q}) Q_{\downarrow\beta'}(\boldsymbol{k}') \\
\times \; Q_{\downarrow\alpha}^{\dagger}(\boldsymbol{k}+\boldsymbol{q}) Q_{\uparrow\alpha'}(\boldsymbol{k}) \psi_{\boldsymbol{k}+\boldsymbol{q},\alpha}^{\dagger} \psi_{\boldsymbol{k}'-\boldsymbol{q},\beta}^{\dagger} \psi_{\boldsymbol{k}'\beta'} \psi_{\boldsymbol{k}\alpha'} \\
\times \left(\frac{1}{E_{\boldsymbol{k}'\beta'} - E_{\boldsymbol{k}'-\boldsymbol{q},\beta} - \omega_{\boldsymbol{q}}} - \frac{1}{E_{\boldsymbol{k}\alpha'} - E_{\boldsymbol{k}+\boldsymbol{q},\alpha} + \omega_{\boldsymbol{q}}} \right).
\end{aligned}
$$
(16)

In the formation of Cooper pairs, the fermions all have momenta close to the Fermi momentum k_F. In the case of Amperean pairing [11,19,36,37], Cooper pairs are formed by particles on the same side of the Fermi surface. In order for all particles to stay close to the Fermi surface, the momentum transfer in the processes, q, then needs to be small relative to k_F [14]. This is seen in Fig. 3. In the case of BCS-type pairing between particles on opposite sides of the Fermi surface [38], q is not necessarily small relative to k_F. If $\boldsymbol{k}+\boldsymbol{q}$ is close to the Fermi surface, then $\boldsymbol{k}'-\boldsymbol{q}$ is also close to the Fermi surface when $\boldsymbol{k}' = -\boldsymbol{k}$.

Consider next Eq. (16) in the long-wavelength limit. Assuming $\mu > 0$, we project down on the helicity band with index $+$, as this is the band that crosses the Fermi level. We then obtain for BCS-type pairing and Amperean pairing, respectively,

$$
\begin{aligned}
H_{\text{pair}}^{\text{(BCS)}} = -\frac{V^2}{4} \sum_{\boldsymbol{k}\boldsymbol{k}'} \frac{v_F(k_x - ik_y)}{\sqrt{(2\bar{J}s)^2 + v_F{}^2 k^2}} \frac{v_F(k_x' + ik_y')}{\sqrt{(2\bar{J}s)^2 + v_F^2 k'^2}} \\
\times \frac{2\omega_{\boldsymbol{k}-\boldsymbol{k}'}}{(E_{\boldsymbol{k}',+} - E_{\boldsymbol{k},+})^2 - \omega_{\boldsymbol{k}-\boldsymbol{k}'}^2} \psi_{\boldsymbol{k},+}^{\dagger} \psi_{-\boldsymbol{k},+}^{\dagger} \psi_{-\boldsymbol{k}',+} \psi_{\boldsymbol{k}',+},
\end{aligned}
$$
(17)

$$
\begin{aligned}
H_{\text{pair}}^{\text{(Amp)}} = \frac{V^2}{4} \sum_{\boldsymbol{k}\boldsymbol{k}'\boldsymbol{q}} \frac{v_F(k_x - ik_y)}{\sqrt{(2\bar{J}s)^2 + v_F^2 k^2}} \frac{v_F(k_x' + ik_y')}{\sqrt{(2\bar{J}s)^2 + v_F^2 k'^2}} \\
\times \left(\frac{1}{E_{\boldsymbol{k}',+} - E_{\boldsymbol{k}'-\boldsymbol{q},+} - \omega_{\boldsymbol{q}}} - \frac{1}{E_{\boldsymbol{k},+} - E_{\boldsymbol{k}+\boldsymbol{q},+} + \omega_{\boldsymbol{q}}} \right) \\
\times \; \psi_{\boldsymbol{k}+\boldsymbol{q},+}^{\dagger} \psi_{\boldsymbol{k}'-\boldsymbol{q},+}^{\dagger} \psi_{\boldsymbol{k}',+} \psi_{\boldsymbol{k},+}.
\end{aligned}
$$
(18)

Here, we have taken $q \ll k_F$ for the Amperean case. Both of the pairing Hamiltonians include the factors $(k_x - ik_y)(k_x' + ik_y')$, originating with the spin-momentum locking of the surface states. The denominator of these factors leads to the interaction strength being largest when the Fermi level is far away from the exchange-field-induced gap in the dispersion relation, $2\bar{J}s \ll v_F k_F$, in agreement with Ref. [14]. In the BCS case, the factor involving the bosonic and fermionic dispersion relations takes the same form as in phonon-mediated superconductivity [39].

D. BCS-type pairing

For BCS-type pairing, we define

$$
\begin{aligned}
V_{\boldsymbol{k}\boldsymbol{k}'}^{\text{(BCS)}} = -\frac{V^2}{2} \frac{v_F(k_x - ik_y)}{\sqrt{(2\bar{J}s)^2 + v_F{}^2 k^2}} \\
\times \frac{v_F(k_x' + ik_y')}{\sqrt{(2\bar{J}s)^2 + v_F^2 k'^2}} \frac{2\omega_{\boldsymbol{k}-\boldsymbol{k}'}}{(E_{\boldsymbol{k}',+} - E_{\boldsymbol{k},+})^2 - \omega_{\boldsymbol{k}-\boldsymbol{k}'}^2}.
\end{aligned}
$$
(19)

The potential of Eq. (19) can be split into even and odd parts with respect to momentum $V_{\boldsymbol{k}\boldsymbol{k}'}^{\text{(BCS)}} = V_{\boldsymbol{k}\boldsymbol{k}',E(k)}^{\text{(BCS)}} + V_{\boldsymbol{k}\boldsymbol{k}',O(k)}^{\text{(BCS)}}$, where $V_{\boldsymbol{k}\boldsymbol{k}',E(k)}^{\text{(BCS)}} = (V_{\boldsymbol{k}\boldsymbol{k}'}^{\text{(BCS)}} + V_{-\boldsymbol{k},\boldsymbol{k}'}^{\text{(BCS)}})/2$ and $V_{\boldsymbol{k}\boldsymbol{k}',O(k)}^{\text{(BCS)}} = (V_{\boldsymbol{k}\boldsymbol{k}'}^{\text{(BCS)}} - V_{-\boldsymbol{k},\boldsymbol{k}'}^{\text{(BCS)}})/2$. By anticommuting the first two fermionic operators and transforming $\boldsymbol{k} \to -\boldsymbol{k}$, it is seen directly from Eq. (17) that the even part of the potential vanishes. Only the odd part can then contribute to pairing. Defining $b_{\boldsymbol{k}} = \langle \psi_{-\boldsymbol{k},+} \psi_{\boldsymbol{k},+} \rangle$ and the superconducting gap $\Delta_{\boldsymbol{k}} = -\sum_{\boldsymbol{k}'} V_{\boldsymbol{k}\boldsymbol{k}',O(k)}^{\text{(BCS)}} b_{\boldsymbol{k}'}$, we observe that the superconducting gap function is even in pseudospin (helicity) and odd in momentum, analogous to a spin-polarized spin-triplet gap function. The symmetry of the gap function follows directly from the fact that there is only a single band crossing the Fermi level. Performing a standard mean-field procedure [40], we obtain a self-consistent equation for the superconducting gap function

$$
\Delta_{\boldsymbol{k}} = -\sum_{\boldsymbol{k}'} V_{\boldsymbol{k}\boldsymbol{k}',O(k)}^{\text{(BCS)}} \frac{\Delta_{\boldsymbol{k}'}}{2\tilde{E}_{\boldsymbol{k}'}} \tanh\left(\frac{\beta \tilde{E}_{\boldsymbol{k}'}}{2}\right),
$$
(20)

where $\tilde{E}_{\boldsymbol{k}} = \sqrt{E_{\boldsymbol{k}+}^2 + |\Delta_{\boldsymbol{k}}^2|}$ and $1/\beta = k_B T$, where k_B is the Boltzmann constant and T is the temperature. While the structure of the interaction potential clearly points to the possibility of a chiral p-wave solution, linearizing the gap equation and performing an average of $V_{\boldsymbol{k}\boldsymbol{k}',O(k)}^{\text{(BCS)}} \Delta_{\boldsymbol{k}'}$ over the Fermi surface [40] reveal that the sign of the real part of the potential should have been opposite in order to facilitate this opportunity. An indication of this can be seen directly by inspecting the interaction potential for $|\boldsymbol{k}| = |\boldsymbol{k}'| = k_F$, producing $\text{Re}(V_{\boldsymbol{k}\boldsymbol{k}',O(k)}^{\text{(BCS)}}) \sim \boldsymbol{k} \cdot \boldsymbol{k}'$, which is repulsive when $\boldsymbol{k}' \parallel \boldsymbol{k}$ and attractive when $\boldsymbol{k}' \parallel -\boldsymbol{k}$. From Eq. (20), it is clear that the signs of the two sides of the equation will be opposite in these cases. We conclude that BCS pairing is not possible. In accordance with [11], the interaction potential in the Amperean case appears to have a sign opposite the BCS case, arising from the Q factors generated by the spin-momentum

locking of the surface states. We therefore move on to the Amperean case.

E. Amperean pairing

Taking $\boldsymbol{k} = \boldsymbol{K} + \boldsymbol{p}'$ and $\boldsymbol{k}' = \boldsymbol{K} - \boldsymbol{p}'$, where $\boldsymbol{p}' \ll \boldsymbol{K}$ and $\boldsymbol{p} = \boldsymbol{p}' + \boldsymbol{q}$ [11,19,37], we obtain

$$H_{\text{pair}}^{(\text{Amp})} = \frac{1}{2} \sum_{\boldsymbol{K}\boldsymbol{p}\boldsymbol{p}'} V_{\boldsymbol{p}\boldsymbol{p}'}^{(\text{Amp})}(\boldsymbol{K})$$
$$\times \psi_{\boldsymbol{K}+\boldsymbol{p},+}^{\dagger} \psi_{\boldsymbol{K}-\boldsymbol{p},+}^{\dagger} \psi_{\boldsymbol{K}-\boldsymbol{p}',+} \psi_{\boldsymbol{K}+\boldsymbol{p}',+}, \quad (21)$$

where

$$V_{\boldsymbol{p}\boldsymbol{p}'}^{(\text{Amp})}(\boldsymbol{K}) = \frac{V^2}{2} \frac{v_F^2 K^2}{(2\bar{J}s)^2 + v_F^2 K^2}$$
$$\times \left(\frac{1}{E_{\boldsymbol{K}-\boldsymbol{p}',+} - E_{\boldsymbol{K}-\boldsymbol{p},+} - \omega_{\boldsymbol{p}-\boldsymbol{p}'}} \right.$$
$$\left. - \frac{1}{E_{\boldsymbol{K}+\boldsymbol{p}',+} - E_{\boldsymbol{K}+\boldsymbol{p},+} + \omega_{\boldsymbol{p}-\boldsymbol{p}'}} \right). \quad (22)$$

The momentum $\boldsymbol{K}$ should here be located at, or close to, the Fermi surface, restricting the interactions to act between particles located close to the Fermi surface. This potentially leads to the formation of Cooper pairs with center-of-mass momentum $2K \approx 2k_F$. By anticommuting operators and transforming $\boldsymbol{p} \rightarrow -\boldsymbol{p}$ and $\boldsymbol{p}' \rightarrow -\boldsymbol{p}'$, we find that the part of the potential that does not vanish is $\bar{V}_{\boldsymbol{p}\boldsymbol{p}'}(\boldsymbol{K}) \equiv V_{\boldsymbol{p}\boldsymbol{p}',O(\boldsymbol{p})}^{(\text{Amp})}(\boldsymbol{K}) = [V_{\boldsymbol{p}\boldsymbol{p}',O(\boldsymbol{p})}^{(\text{Amp})}(\boldsymbol{K}) - V_{\boldsymbol{p},-\boldsymbol{p}',O(\boldsymbol{p})}^{(\text{Amp})}(\boldsymbol{K})]/2$, which is odd in both $\boldsymbol{p}$ and $\boldsymbol{p}'$. Defining $b_{\boldsymbol{p}}(\boldsymbol{K}) = \langle \psi_{\boldsymbol{K}-\boldsymbol{p},+} \psi_{\boldsymbol{K}+\boldsymbol{p},+} \rangle$ and $\Delta_{\boldsymbol{p}}(\boldsymbol{K}) = -\sum_{\boldsymbol{p}'} \bar{V}_{\boldsymbol{p}\boldsymbol{p}'}(\boldsymbol{K}) b_{\boldsymbol{p}}(\boldsymbol{K})$, we now have a superconducting gap function that is even in pseudospin (helicity) and odd in the relative momentum $\boldsymbol{p}$.

Following the mean-field procedure outlined in the Appendix, the self-consistent equation for the gap function takes the form

$$\Delta_{\boldsymbol{p}}(\boldsymbol{K}) = -\sum_{\boldsymbol{p}'} \bar{V}_{\boldsymbol{p}\boldsymbol{p}'}(\boldsymbol{K})\Delta_{\boldsymbol{p}'}(\boldsymbol{K})\chi_{\boldsymbol{p}'}(\boldsymbol{K}). \quad (23)$$

Here,

$$\chi_{\boldsymbol{p}'}(\boldsymbol{K}) = \frac{1}{4\xi_{\boldsymbol{p}'}(\boldsymbol{K})} \left[\tanh\left(\frac{\beta[\xi_{\boldsymbol{p}'}(\boldsymbol{K}) + \epsilon_{\boldsymbol{p}'}^o(\boldsymbol{K})]}{2} \right) \right.$$
$$\left. + \tanh\left(\frac{\beta[\xi_{\boldsymbol{p}'}(\boldsymbol{K}) - \epsilon_{\boldsymbol{p}'}^o(\boldsymbol{K})]}{2} \right) \right], \quad (24)$$

with the quantities $\epsilon_{\boldsymbol{p}'}^o(\boldsymbol{K}) = (E_{\boldsymbol{K}+\boldsymbol{p}',+} - E_{\boldsymbol{K}-\boldsymbol{p}',+})/2$, $\epsilon_{\boldsymbol{p}'}^e(\boldsymbol{K}) = (E_{\boldsymbol{K}+\boldsymbol{p}',+} + E_{\boldsymbol{K}-\boldsymbol{p}',+})/2$, and $\xi_{\boldsymbol{p}'}(\boldsymbol{K}) = \sqrt{[\epsilon_{\boldsymbol{p}'}^e(\boldsymbol{K})]^2 + |\Delta_{\boldsymbol{p}'}(\boldsymbol{K})|^2}$.

For $\boldsymbol{K} = k_F \hat{x}$, which we will focus on in the following, the χ factor is presented in Fig. 4, showing that only processes in a small region around $\boldsymbol{K}$ give significant contributions to the gap equation. As the Fermi surface is approximately circular and $\boldsymbol{K} = k_F \hat{x}$, it is clear that processes where one of the particles ends up on the inside of the Fermi surface are suppressed as temperature is lowered. In order to single out the region of importance for temperatures of the order of a kelvin, we apply
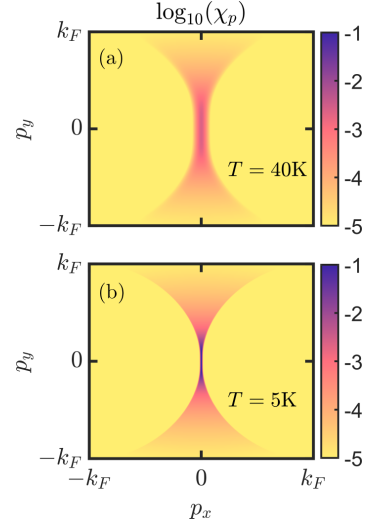

FIG. 4. The factor $\chi_{\boldsymbol{p}}(\boldsymbol{K})$ plotted on a logarithmic scale as a function of $\boldsymbol{p}$ for $\boldsymbol{K} = k_F \hat{x}$ for Fermi velocity $v_F = 5 \times 10^5$ m/s, lattice constant $a = 0.6$ nm, Fermi momentum $k_F a = \pi/8$, interfacial exchange coupling strength $\bar{J} = 10$ meV, and spin quantum number of the lattice site spins $s = 1$. In (a), the temperature is set to $T = 40$ K, while in (b) it is set to $T = 5$ K.

the same ansatz as Kargarian *et al.*, $|p_x| < p_y^2/k_F$, originating in Ref. [19], which is found to be a good approximation.

For processes where the fermionic quasiparticle energy differences can be neglected, the potential takes the simplified form

$$\bar{V}_{\boldsymbol{p}\boldsymbol{p}'}(\boldsymbol{K}) \sim \frac{1}{\omega_{\boldsymbol{p}+\boldsymbol{p}'}} - \frac{1}{\omega_{\boldsymbol{p}-\boldsymbol{p}'}}. \quad (25)$$

This potential is attractive for $\boldsymbol{p}' \parallel \boldsymbol{p}$ and repulsive for $\boldsymbol{p}' \parallel -\boldsymbol{p}$, which are the signs that are needed in order to obtain a p-wave solution for the gap equation. Note that this is p wave in the relative momentum. For reasonable parameters, the potential can, however, be approximated by this form in only a very limited region around $\boldsymbol{K}$. Outside of this region, the potential changes back and forth between being attractive and repulsive, making it harder to analyze and less favorable for superconductivity. Restricting the calculation of the gap function to the region where $|p_x| < p_y^2/k_F$ and the potential behaves similarly to Eq. (25), assuming that the gap function dies off sufficiently quickly outside of this region, a numerical solution of the linearized gap equation was attempted by picking points in k space within the relevant region and solving the matrix eigenvalue problem using the full potential. The phase space was found to be too small, and the potential was not strong enough to produce a solution, at least not for realistic parameters and reasonable temperatures. The conclusion is therefore that a superconducting instability is not possible within this weak-coupling mean-field theory. According to Kargarian *et al.*, a superconducting
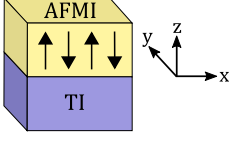
FIG. 5. The system consists of an antiferromagnetic insulator (AFMI) on top of a topological insulator (TI).

instability is, on the other hand, possible within a strong-coupling framework. Rather than performing a more advanced analysis of the TI/FMI case, our objective is to compare the results obtained in this section with those of the TI/AFMI case considered in the following section.

III. ANTIFERROMAGNETIC CASE

In this section, we consider the case of a TI coupled to an AFMI on a bipartite lattice, such as Cr_2O_3 or Fe_2O_3, as shown in Fig. 5. The interface is once again placed in the xy plane, and the staggered magnetization of the AFMI is assumed to be aligned with the z direction.

A. Model

The system is modeled by the Hamiltonian [28,29] $H = H_{AFMI} + H_{TI} + H_{int}$,

$$H_{AFMI} = J_1 \sum_{\langle i,j \rangle} \boldsymbol{S}_i \cdot \boldsymbol{S}_j + J_2 \sum_{\langle\langle i,j \rangle\rangle} \boldsymbol{S}_i \cdot \boldsymbol{S}_j - K \sum_i S_{iz}^2, \quad (26a)$$

$$H_{TI} = \frac{v_F}{2} \sum_{i,\boldsymbol{b}} [c_i^\dagger (i\tau_y \delta_{\boldsymbol{b},\hat{x}} - i\tau_x \delta_{\boldsymbol{b},\hat{y}}) c_{i+\boldsymbol{b}} + \text{H.c.}]$$
$$+ \sum_i c_i^\dagger [2W\tau_z - \mu] c_i - \frac{W}{2} \sum_{i,\boldsymbol{b}} [c_i^\dagger \tau_z c_{i+\boldsymbol{b}} + \text{H.c.}], \quad (26b)$$

$$H_{int} = -2\bar{J}_A \sum_{i \in A} c_i^\dagger \boldsymbol{\tau} c_i \cdot \boldsymbol{S}_i - 2\bar{J}_B \sum_{i \in B} c_i^\dagger \boldsymbol{\tau} c_i \cdot \boldsymbol{S}_i. \quad (26c)$$

Here, $J_1 > 0$ and J_2 are nearest-neighbor and next-nearest-neighbor exchange constants, and $K > 0$ parametrizes the easy-axis anisotropy of the AFMI. For $J_2 < 0$, the next-nearest-neighbor interaction stabilizes the staggered state, while for $J_2 > 0$ this term acts as a frustration. As long as $J_2 > 0$ is small compared to J_1, the magnetic ground state is assumed to be an ordered staggered state, while the magnons are influenced by the frustration [41,42]. The TI Hamiltonian is identical to the one in the previous section, and we still consider square lattices. The two subsystems are once again coupled through an exchange interaction, where we now allow for the interaction strength to differ for the A and B sublattices of the AFMI. Such a sublattice-asymmetric interfacial coupling can, e.g., be achieved using an experimentally realizable uncompensated antiferromagnetic interface [20,21], as depicted in Fig. 6.
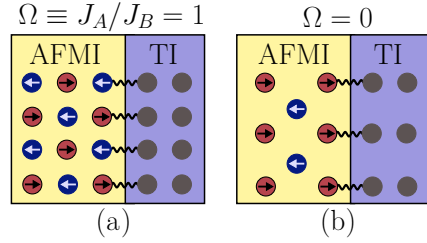
FIG. 6. Exchange coupling across the interface between an antiferromagnetic insulator (AFMI) and a topological insulator (TI). In (a) the antiferromagnetic interface is fully compensated, and the TI is coupled symmetrically to the two sublattices of the AFMI with exchange coupling strength $\bar{J}_A = \bar{J}_B$. In (b) the antiferromagnetic interface is fully uncompensated, resulting in the TI coupling to only one of the two sublattices of the AFMI.

B. Diagonalization of subsystems

We introduce Holstein-Primakoff transformations for the spin operators on the two sublattices of the AFMI $S_{i+}^A = \sqrt{2s}\, a_i$, $S_{i-}^A = \sqrt{2s}\, a_i^\dagger$, $S_{iz}^A = s - a_i^\dagger a_i$, $S_{j+}^B = \sqrt{2s}\, b_j^\dagger$, $S_{j-}^B = \sqrt{2s}\, b_j$, and $S_{jz}^B = -s + b_j^\dagger b_j$ and Fourier transformations of the magnon operators $a_i = \frac{1}{\sqrt{N_A}} \sum_{\boldsymbol{k} \in \diamond} a_{\boldsymbol{k}} e^{-i\boldsymbol{k}\cdot\boldsymbol{r}_i}$ and $b_i = \frac{1}{\sqrt{N_B}} \sum_{\boldsymbol{k} \in \diamond} b_{\boldsymbol{k}} e^{-i\boldsymbol{k}\cdot\boldsymbol{r}_i}$. Here, $\boldsymbol{k} \in \diamond$ indicates that the sum covers the reduced Brillouin zone of the sublattices, and the number of lattice sites in the interfacial plane is given by $N = N_A + N_B$. The AFMI Hamiltonian is then diagonalized by a Bogoliubov transformation, expressing the antiferromagnetic eigenexcitations in terms of the original sublattice magnons $\alpha_{\boldsymbol{k}} = u_{\boldsymbol{k}} a_{\boldsymbol{k}} - v_{\boldsymbol{k}} b_{-\boldsymbol{k}}^\dagger$ and $\beta_{\boldsymbol{k}} = u_{\boldsymbol{k}} b_{\boldsymbol{k}} - v_{\boldsymbol{k}} a_{-\boldsymbol{k}}^\dagger$. Here, $u_{\boldsymbol{k}} = \cosh(\theta_{\boldsymbol{k}})$, $v_{\boldsymbol{k}} = \sinh(\theta_{\boldsymbol{k}})$, $\tanh(2\theta_{\boldsymbol{k}}) = -\tilde{\gamma}_{\boldsymbol{k}}/\lambda_{\boldsymbol{k}}$, $\tilde{\gamma}_{\boldsymbol{k}} = 4J_1 s \sum_b \cos(k_b)$, $\lambda_{\boldsymbol{k}} = 2s[J_1 z_1 + K + J_2 z_2 (\gamma_{\boldsymbol{k},2} - 1)]$, and $\gamma_{\boldsymbol{k},2} = \frac{2}{z_2} \sum_{\substack{\sigma bb' \\ b < b'}} \cos(k_b + \sigma k_{b'})$. The number of next-nearest neighbors is denoted by z_2, and in two dimensions we have $\sum_{\substack{\sigma bb' \\ b < b'}} \cos(k_b + \sigma k_{b'}) = \cos(k_x + k_y) + \cos(k_x - k_y)$. The AFMI Hamiltonian then takes the form

$$H_{AFMI} = \sum_{\boldsymbol{k}} \omega_{\boldsymbol{k}} (\alpha_{\boldsymbol{k}}^\dagger \alpha_{\boldsymbol{k}} + \beta_{\boldsymbol{k}}^\dagger \beta_{\boldsymbol{k}}), \quad (27)$$

where $\omega_{\boldsymbol{k}} = \lambda_{\boldsymbol{k}} \sqrt{1 - \tilde{\gamma}_{\boldsymbol{k}}^2/\lambda_{\boldsymbol{k}}^2}$.

For the electron operators, we express the Fourier transformation as $c_{i\sigma} = \frac{1}{\sqrt{N}} \sum_{\boldsymbol{k} \in \diamond} (c_{\boldsymbol{k}\sigma} e^{-i\boldsymbol{k}\cdot\boldsymbol{r}_i} + c_{\boldsymbol{k}+\boldsymbol{G},\sigma} e^{-i(\boldsymbol{k}+\boldsymbol{G})\cdot\boldsymbol{r}_i})$, where $\boldsymbol{G} \equiv \pi(\hat{x} + \hat{y})/a$ is a reciprocal lattice vector for the sublattices. From the interaction Hamiltonian of Eq. (26c), we obtain for the two sublattices

$$H_{int}^{(A)} = U\,\Omega \sum_{\substack{\boldsymbol{k} \in \square \\ \boldsymbol{q} \in \diamond}} (a_{\boldsymbol{q}} c_{\boldsymbol{k}+\boldsymbol{q},\downarrow}^\dagger c_{\boldsymbol{k}\uparrow} + a_{\boldsymbol{q}} c_{\boldsymbol{k}+\boldsymbol{q}+\boldsymbol{G},\downarrow}^\dagger c_{\boldsymbol{k}\uparrow} + \text{H.c.})$$
$$- \bar{J}s\,\Omega \sum_{\substack{\boldsymbol{k} \in \square \\ \sigma}} \sigma (c_{\boldsymbol{k}\sigma}^\dagger c_{\boldsymbol{k}\sigma} + c_{\boldsymbol{k}+\boldsymbol{G},\sigma}^\dagger c_{\boldsymbol{k}\sigma}), \quad (28)$$

$$H_{\text{int}}^{(B)} = U \sum_{\substack{k \in \square \\ q \in \diamond}} (b_q c_{k+q,\uparrow}^\dagger c_{k\downarrow} - b_q c_{k+q+G,\uparrow}^\dagger c_{k\downarrow} + \text{H.c.})$$

$$+ \bar{J}s \sum_{\substack{k \in \square \\ \sigma}} \sigma (c_{k\sigma}^\dagger c_{k\sigma} - c_{k+G,\sigma}^\dagger c_{k\sigma}), \qquad (29)$$

respectively, where $k \in \square$ indicates that the sum covers the full Brillouin zone. There are additional contributions from two-magnon processes, which we once again neglect. We have here defined $U = -2\bar{J}\sqrt{s}/\sqrt{N}$, $\Omega \equiv \bar{J}_A/\bar{J}_B$, and $\bar{J} \equiv \bar{J}_B$. The parameter Ω, which is taken to be $0 \leqslant \Omega \leqslant 1$, then determines the degree of asymmetry in the coupling to the two sublattices of the AFMI. The processes where the momentum of the outgoing electron is shifted by a reciprocal lattice vector G are umklapp processes. These processes are expected to be important for inducing superconductivity mediated by antiferromagnetic magnons in normal metals at half-filling [15].

For a tight-binding model on a square lattice at half-filling, G connects different points on the Fermi surface. For the case of a TI with a Fermi surface close to the center of the Brillouin zone [24,25], on the other hand, the Fermi momentum is typically small compared to $|G|$, and these umklapp processes are expected to be less important as they scatter fermions far away from the Fermi surface. The umklapp processes are therefore neglected in the following.

We once again move the exchange field terms, which cancel only for $\Omega = 1$, over to the TI Hamiltonian and express the sublattice magnon operators in the interaction Hamiltonian in terms of the magnons that diagonalized the AFMI Hamiltonian. We then obtain

$$H_{\text{int}} = U \sum_{kq} [\Omega(u_q \alpha_q + v_q \beta_{-q}^\dagger) c_{k+q,\downarrow}^\dagger c_{k\uparrow}$$

$$+ (u_q \beta_q + v_q \alpha_{-q}^\dagger) c_{k+q,\uparrow}^\dagger c_{k\downarrow} + \text{H.c.}]. \qquad (30)$$

For the TI Hamiltonian, we now have

$$H_{\text{TI}} = W \sum_{k\sigma} \sigma c_{k\sigma}^\dagger c_{k\sigma} \left[2 - \sum_b \cos(k_b) \right] - v_F \sum_k \{ c_{k\uparrow}^\dagger c_{k\downarrow} [\sin(k_y) + i \sin(k_x)] + \text{H.c.} \}$$

$$- \bar{J}s(\Omega - 1) \sum_{k\sigma} \sigma c_{k\sigma}^\dagger c_{k\sigma} - \mu \sum_{k\sigma} c_{k\sigma}^\dagger c_{k\sigma}. \qquad (31)$$

Building on the results from the FMI case, we take $B_k \equiv W[2 - \sum_b \cos(k_b)] - \bar{J}s(\Omega - 1)$ and obtain

$$H_{\text{TI}} = \sum_{k\alpha} E_{k\alpha} \psi_{k\alpha}^\dagger \psi_{k\alpha}, \qquad (32)$$

with the rest of the definitions as in the previous section.

Expressing the electron operators in the interaction Hamiltonian in terms of the eigenexcitations of the TI Hamiltonian, we obtain

$$H_{\text{int}}^{(A)} = U \Omega \sum_{kq} \sum_{\alpha\alpha'} [(u_q \alpha_q + v_q \beta_{-q}^\dagger) Q_{\downarrow\alpha}^\dagger(k+q) Q_{\uparrow\alpha'}(k) \psi_{k+q,\alpha}^\dagger \psi_{k\alpha'} + \text{H.c.}], \qquad (33)$$

$$H_{\text{int}}^{(B)} = U \sum_{kq} \sum_{\alpha\alpha'} [(u_q \beta_q + v_q \alpha_{-q}^\dagger) Q_{\uparrow\alpha}^\dagger(k+q) Q_{\downarrow\alpha'}(k) \psi_{k+q,\alpha}^\dagger \psi_{k\alpha'} + \text{H.c.}]. \qquad (34)$$

We will, in the following section, derive the effective fermion-fermion interaction arising from this magnon-fermion coupling.

C. Effective interaction

We once again perform a canonical transformation in order to obtain a theory of fermions with interactions mediated by magnons. Taking, this time, $\eta H_1 = H_{\text{int}}^{(A)} + H_{\text{int}}^{(B)}$, we choose $\eta S = \eta S^{(A)} + \eta S^{(B)}$, with

$$\eta S^{(A)} = U \Omega \sum_{kq} \sum_{\alpha\alpha'} \left[\left(x_{k,q}^{\alpha\alpha'} u_q \alpha_q + y_{k,q}^{\alpha\alpha'} v_q \beta_{-q}^\dagger \right) Q_{\downarrow\alpha}^\dagger(k+q) Q_{\uparrow\alpha'}(k) + \left(y_{k,q}^{\alpha\alpha'} u_q \alpha_{-q}^\dagger + x_{k,q}^{\alpha\alpha'} v_q \beta_q \right) Q_{\uparrow\alpha}^\dagger(k+q) Q_{\downarrow\alpha'}(k) \right] \psi_{k+q,\alpha}^\dagger \psi_{k\alpha'},$$

$$\qquad (35)$$

$$\eta S^{(B)} = U \sum_{kq} \sum_{\alpha\alpha'} \left[\left(x_{k,q}^{\alpha\alpha'} u_q \beta_q + y_{k,q}^{\alpha\alpha'} v_q \alpha_{-q}^\dagger \right) Q_{\uparrow\alpha}^\dagger(k+q) Q_{\downarrow\alpha'}(k) + \left(y_{k,q}^{\alpha\alpha'} u_q \beta_{-q}^\dagger + x_{k,q}^{\alpha\alpha'} v_q \alpha_q \right) Q_{\downarrow\alpha}^\dagger(k+q) Q_{\uparrow\alpha'}(k) \right] \psi_{k+q,\alpha}^\dagger \psi_{k\alpha'},$$

$$\qquad (36)$$

where $x_{k,q}^{\alpha\alpha'}$ and $y_{k,q}^{\alpha\alpha'}$ are defined as in the FMI case.

Computing the commutator in Eq. (15), projecting down on the helicity band with index $+$, and taking the long-wavelength limit, we obtain for BCS-type pairing and Amperean pairing, respectively,

$$H_{\text{pair}}^{(\text{BCS})} = -\frac{U^2}{4} \sum_{kk'} \frac{v_F(k_x - ik_y)}{\sqrt{[\bar{J}s(\Omega-1)]^2 + v_F^2 k^2}} \frac{v_F(k_x' + ik_y')}{\sqrt{[\bar{J}s(\Omega-1)]^2 + v_F^2 k'^2}} \frac{2\omega_{k-k'}}{(E_{k',+} - E_{k,+})^2 - \omega_{k-k'}^2}$$

$$\times A(k - k', \Omega)\, \psi_{k,+}^{\dagger} \psi_{-k,+}^{\dagger} \psi_{-k',+} \psi_{k'+}, \tag{37}$$

$$A(q, \Omega) = \tfrac{1}{2}(\Omega^2 + 1)(u_q^2 + v_q^2) + 2\,\Omega\, u_q v_q, \tag{38}$$

$$H_{\text{pair}}^{(\text{AMP})} = \frac{U^2}{4} \sum_{kk'q} \frac{v_F(k_x - ik_y)}{\sqrt{[\bar{J}s(\Omega-1)]^2 + v_F^2 k^2}} \frac{v_F(k_x' + ik_y')}{\sqrt{[\bar{J}s(\Omega-1)]^2 + v_F^2 k'^2}} \left[\frac{1}{2}(\Omega^2 u_q^2 + v_q^2 + 2\,\Omega\, u_q v_q) \right.$$

$$\times \left(\frac{1}{E_{k'+} - E_{k'-q,+} - \omega_q} - \frac{1}{E_{k+} - E_{k+q,+} + \omega_q} \right)$$

$$\left. + \frac{1}{2}(\Omega^2 v_q^2 + u_q^2 + 2\,\Omega\, u_q v_q) \left(\frac{1}{E_{k+} - E_{k+q,+} - \omega_q} - \frac{1}{E_{k'+} - E_{k'-q,+} + \omega_q} \right) \right] \psi_{k+q,+}^{\dagger} \psi_{k'-q,+}^{\dagger} \psi_{k',+} \psi_{k+}, \tag{39}$$

where we once again have taken $q \ll k_F$ for the Amperean case.

The factor $A(q, \Omega)$ is the same as the one arising for asymmetric coupling of a normal metal to the two sublattices of a bipartite AFMI, providing a significant enhancement of the strength of the effective interactions and the superconducting critical temperature in that case [16]. For long-wavelength magnons, the magnon coherence factors u_q and v_q grow large with opposite signs, and $A(q, \Omega = 1) = (u_q + v_q)^2$ (equal coupling to both AFMI sublattices) is therefore a small quantity, while $A(q, \Omega = 0) = (u_q^2 + v_q^2)/2$ (coupling to only one AFMI sublattice) is a large quantity [16]. This enhancement of the interaction for $\Omega = 0$ and suppression for $\Omega = 1$ are a quantum effect not captured by the model in Ref. [14]. In the Amperean case, the magnon coherence factors do not combine directly to the same factor $A(q, \Omega)$, but as u_q and v_q grow large with opposite signs, the behavior is similar. For $\Omega = 1$, the negative terms $2\,\Omega\, u_q v_q$ and positive terms of the form $\Omega^2 u_q^2 + v_q^2$ work in opposite directions exactly as in $A(q, \Omega)$, while for $\Omega = 0$, the negative terms once again vanish, leading to stronger interaction.

The effect of the magnon coherence factors is influenced by the next-nearest-neighbor interaction term in the AFMI Hamiltonian. In Fig. 7, the magnon coherence factors u_q and v_q are presented as a function of q for different values of the next-nearest-neighbor interaction strength J_2. Figure 7 shows that frustrating the system, $J_2 > 0$, increases the magnon coherence factors and thereby also, e.g., $A(q, \Omega = 0) = (u_q^2 + v_q^2)/2$. On the other hand, taking $J_2 < 0$, stabilizing the staggered magnetic state, decreases the magnon coherence factors. This effect would be the same in the normal-metal case of Ref. [16], meaning that next-nearest-neighbor frustration could aid in the enhancement of the critical temperature also in this case.

D. Pairing

For the AFMI case, the gap equation for BCS-type pairing is exactly the same as in the FMI case. The only difference between the interaction potentials is the presence of the $A(q, \Omega)$ factor in the AFMI case. This factor does not change the sign

of the potential, and the conclusion is therefore, as for the FMI, that we do not get a chiral p-wave solution to the gap equation.

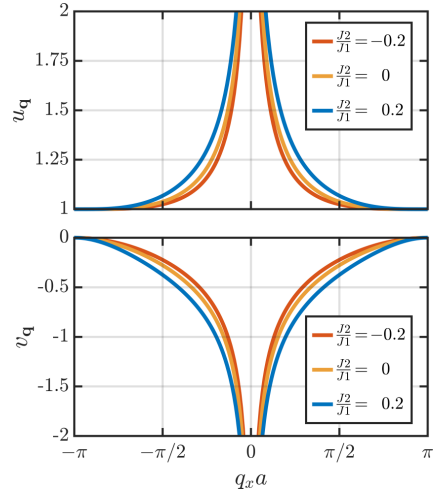For Amperean pairing, the AFMI case is also very similar to the FMI case, apart from the presence of the magnon

FIG. 7. The magnon coherence factors u_q and v_q are here presented as a function of the momentum q for different values of J_2/J_1, where J_1 and J_2 are the nearest-neighbor and next-nearest-neighbor interaction strengths between the lattice site spins of the antiferromagnetic insulator. We have here set $q_y = 0$, spin quantum number of the lattice site spins $s = 1$, and easy-axis anisotropy $K = J_1/10^4$ and taken fairly large values for $|J_2/J_1|$ in order to clearly display the effect of the frustration.
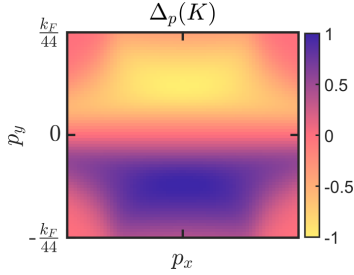
FIG. 8. Form of the gap function obtained as a solution to the linearized gap equation, obtained with Fermi velocity $v_F = 3.6 \times 10^5$ m/s, lattice constant $a = 0.7$ nm, Fermi momentum $k_F a = \pi/6$, $\boldsymbol{K} = k_F \hat{x}$, interfacial exchange coupling strength $\bar{J} = 18$ meV, nearest-neighbor exchange constant $J_1 = 7$ meV, next-nearest-neighbor exchange constant $J_2 = 0.05 J_1$, easy-axis anisotropy $K = J_1/10^5$, spin quantum number of the lattice site spins $s = 1$, and asymmetry parameter $\Omega = 0$. In the x direction, the points lie within $|p_x| < p_y^2/k_F$, meaning that the p_x value associated with each point depends on the value of p_y.

coherence factors. As for the FMI, we obtain a gap equation

$$\Delta_{\boldsymbol{p}}(\boldsymbol{K}) = -\sum_{\boldsymbol{p}'} \bar{U}_{\boldsymbol{p}\boldsymbol{p}'}(\boldsymbol{K}) \Delta_{\boldsymbol{p}'}(\boldsymbol{K}) \chi_{\boldsymbol{p}'}(\boldsymbol{K}), \quad (40)$$

where the potential $\bar{U}_{\boldsymbol{p}\boldsymbol{p}'}(\boldsymbol{K})$ is, once again, odd in both relative momenta. The gap function is, as before, defined as $\Delta_{\boldsymbol{p}}(\boldsymbol{K}) = -\sum_{\boldsymbol{p}'} \bar{U}_{\boldsymbol{p}\boldsymbol{p}'}(\boldsymbol{K}) b_{\boldsymbol{p}'}(\boldsymbol{K})$, and the χ factor is defined in Eq. (24). In a region close to $\boldsymbol{K}$, the potential now behaves as

$$\bar{U}_{\boldsymbol{p}\boldsymbol{p}'}(\boldsymbol{K}) \sim \frac{1}{\omega_{\boldsymbol{p}+\boldsymbol{p}'}} A(\Omega, \boldsymbol{p} + \boldsymbol{p}') - \frac{1}{\omega_{\boldsymbol{p}-\boldsymbol{p}'}} A(\Omega, \boldsymbol{p} - \boldsymbol{p}'). \quad (41)$$

We then still have the required signs in order to obtain a nontrivial solution to the gap equation and obtain a boosting from the A factor for $\Omega < 1$ in exactly the same way as was obtained in the NM/AFMI case of Ref. [16]. For $\Omega = 0$, the interaction potential is therefore much stronger than the potential we had in the FMI case.

Focusing on $\boldsymbol{K} = k_F \hat{x}$ and restricting the calculation of the gap function to the region where $|p_x| < p_y^2/k_F$ and the potential behaves similarly to Eq. (41), a numerical solution of the linearized gap equation was attempted by picking points in k space within the relevant region and solving the matrix eigenvalue problem using the full potential. The relevant phase space is now typically larger than the corresponding region for the FMI case, as the antiferromagnetic magnons have a linear, instead of quadratic, dispersion relation for small momenta. As the phase space is still small, a strong potential is needed in order to produce a nontrivial solution of the gap equation. Taking $\Omega = 0$ and sufficiently small easy-axis anisotropy, fully exploiting the boosting effect [22], the potential is found to be strong enough to provide a solution. As expected, the solution has a p-wave character, as displayed in Fig. 8. Since small phase space is compensated by large interaction strength, a strong-coupling approach would provide more solid evidence of the existence of a superconducting instability and realistic estimates for the critical temperature.
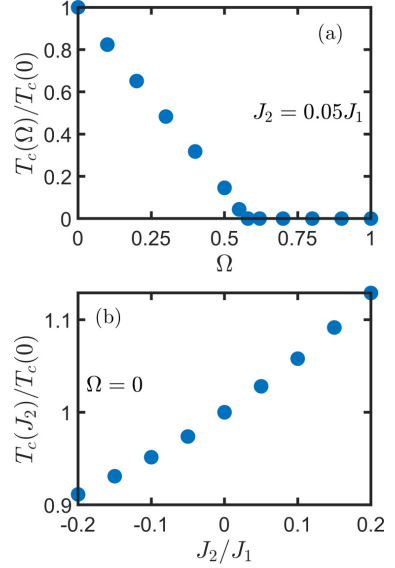
FIG. 9. Critical temperature as a function of (a) asymmetry parameter Ω and (b) next-nearest-neighbor exchange constant J_2, obtained with Fermi velocity $v_F = 8 \times 10^4$ m/s, lattice constant $a = 0.7$ nm, Fermi momentum $k_F a = \pi/6$, $\boldsymbol{K} = k_F \hat{x}$, interfacial exchange coupling strength $\bar{J} = 18$ meV, nearest-neighbor-exchange constant $J_1 = 7$ meV, easy-axis anisotropy $K = J_1/10^5$, and spin quantum number of the lattice site spins $s = 1$.

In order to display the effect of the asymmetry parameter Ω on the ability of inducing a superconducting instability, we reduce the Fermi velocity to about 20% of typical values [25] in order to obtain solutions for $\Omega > 0$. The dependence of the critical temperature on Ω is presented in Fig. 9(a), clearly showing that the interaction strength, and thereby the critical temperature, is significantly enhanced by coupling the TI asymmetrically to the AFMI. Similarly, the effect of the next-nearest-neighbor frustration on the critical temperature is displayed in Fig. 9(b).

IV. SUMMARY

We have investigated effective fermion-fermion interactions on the surface of a topological insulator, induced by magnetic fluctuations in a proximity-coupled ferromagnetic or antiferromagnetic insulator. Our main finding is that effective interactions induced by an uncompensated antiferromagnetic interface are significantly stronger than the interactions induced by a fully compensated antiferromagnetic interface or a ferromagnetic interface. This indicates that an uncompensated interface might be the optimal choice for proximity-induced magnon-mediated superconductivity on the surface of a topological insulator. Moreover, we find that the interaction amplification obtained by coupling asymmetrically to the two sublattices of the antiferromagnet can be further strengthened by next-nearest-neighbor frustration in the antiferromagnet. In

both the ferromagnetic and antiferromagnetic cases, we find that the interaction potential has the correct form to give rise to Amperean pairing formed between particles on the same side of the Fermi surface, but in our weak-coupling approach we find only a nontrivial solution of the gap equation in the antiferromagnetic case.

APPENDIX: DERIVATION OF AMPEREAN GAP EQUATION

We start from the effective Hamiltonian

$$
\begin{aligned}
H_{\text{eff}} = & \sum_{k\alpha} E_{k\alpha} \psi_{k\alpha}^{\dagger} \psi_{k\alpha} \\
& + \sum_{Kpp'} \frac{\bar{V}_{pp'}(\boldsymbol{K})}{2} \psi_{K+p,+}^{\dagger} \psi_{K-p,+}^{\dagger} \psi_{K-p',+} \psi_{K+p',+}, \quad \text{(A1)}
\end{aligned}
$$

where $\bar{V}_{pp'}(\boldsymbol{K})$ is real and odd in $\boldsymbol{p}$ and $\boldsymbol{p}'$ and $\bar{V}_{pp'}(\boldsymbol{K}) = \bar{V}_{p'p}(\boldsymbol{K})$. Defining $b_p(\boldsymbol{K}) = \langle \psi_{K-p,+} \psi_{K+p,+} \rangle$, we obtain the mean-field Hamiltonian

$$
\begin{aligned}
H_{\text{eff}}' = & \sum_{k\alpha} E_{k\alpha} \psi_{k\alpha}^{\dagger} \psi_{k\alpha} + \sum_{Kpp'} \frac{\bar{V}_{pp'}(\boldsymbol{K})}{2} [b_p^{\dagger}(\boldsymbol{K}) \psi_{K-p',+} \psi_{K+p',+} \\
& + b_{p'}(\boldsymbol{K}) \psi_{K+p,+}^{\dagger} \psi_{K-p,+}^{\dagger}], \quad \text{(A2)}
\end{aligned}
$$

where terms not affecting the gap equation have been neglected. Taking

$$
\Delta_p(\boldsymbol{K}) = -\sum_{p'} \bar{V}_{pp'}(\boldsymbol{K}) b_{p'}(\boldsymbol{K}) \quad \text{(A3)}
$$

produces

$$
\begin{aligned}
H_{\text{eff}}' = & \sum_{k\alpha} E_{k\alpha} \psi_{k\alpha}^{\dagger} \psi_{k\alpha} - \frac{1}{2} \sum_{Kp} [\Delta_p^{\dagger}(\boldsymbol{K}) \psi_{K-p,+} \psi_{K+p,+} \\
& + \Delta_p(\boldsymbol{K}) \psi_{K+p,+}^{\dagger} \psi_{K-p,+}^{\dagger}]. \quad \text{(A4)}
\end{aligned}
$$

As Cooper pairs with different $\boldsymbol{K}$ have different center-of-mass momenta, it is expected that they will, mainly, behave independently of each other. Focusing on a single $\boldsymbol{K}$, we can then write

$$
\begin{aligned}
H_{\text{eff}}'(\boldsymbol{K}) = & \sum_{k} E_{k-} \psi_{k-}^{\dagger} \psi_{k-} + \frac{1}{2} \sum_{p} (\psi_{K+p,+}^{\dagger} \quad \psi_{K-p,+}) \\
& \times \begin{pmatrix} E_{K+p,+} & -\Delta_p(\boldsymbol{K}) \\ -\Delta_p^{\dagger}(\boldsymbol{K}) & -E_{K-p,+} \end{pmatrix} \begin{pmatrix} \psi_{K+p,+} \\ \psi_{K-p,+}^{\dagger} \end{pmatrix}. \quad \text{(A5)}
\end{aligned}
$$

The second part of this equation, which is the one relevant for determining the gap equation, can be expressed as

$$
H''(\boldsymbol{K}) = \frac{1}{2} \sum_{p} \phi_p^{\dagger}(\boldsymbol{K}) M_p(\boldsymbol{K}) \phi_p(\boldsymbol{K}). \quad \text{(A6)}
$$

The matrix $M_p(\boldsymbol{K})$ can be transformed into diagonal form by a unitary transformation $P_p(\boldsymbol{K}) M_p(\boldsymbol{K}) P_p^{-1}(\boldsymbol{K})$, where

$$
P_p(\boldsymbol{K}) = \frac{1}{L_p(\boldsymbol{K})} \begin{pmatrix} \epsilon_p^e(\boldsymbol{K}) + \xi_p(\boldsymbol{K}) & -\Delta_p(\boldsymbol{K}) \\ -\Delta_p^{\dagger}(\boldsymbol{K}) & -\epsilon_p^e(\boldsymbol{K}) - \xi_p(\boldsymbol{K}) \end{pmatrix}, \quad \text{(A7)}
$$

$P_p^{-1}(\boldsymbol{K}) = P_p(\boldsymbol{K})$, $\epsilon_p^o(\boldsymbol{K}) = (E_{K+p,+} - E_{K-p,+})/2$, $\epsilon_p^e(\boldsymbol{K}) = (E_{K+p,+} + E_{K-p,+})/2$, $\xi_p(\boldsymbol{K}) = \sqrt{[\epsilon_p^e(\boldsymbol{K})]^2 + |\Delta_p(\boldsymbol{K})^2|}$, and $L_p^2(\boldsymbol{K}) = 2\xi_p(\boldsymbol{K})[\xi_p(\boldsymbol{K}) + \epsilon_p^e(\boldsymbol{K})]$. We then have

$$
H''(\boldsymbol{K}) = \sum_{p} [\xi_p(\boldsymbol{K}) + \epsilon_p^o(\boldsymbol{K})] \gamma_{K+p}^{\dagger} \gamma_{K+p}, \quad \text{(A8)}
$$

where the relationship between the original fermionic operators and the γ operators is

$$
\psi_{K+p,+} = \frac{\epsilon_p^e(\boldsymbol{K}) + \xi_p(\boldsymbol{K})}{L_p(\boldsymbol{K})} \gamma_{K+p} + \frac{\Delta_p(\boldsymbol{K})}{L_p(\boldsymbol{K})} \gamma_{K-p}^{\dagger}. \quad \text{(A9)}
$$

Plugging Eq. (A9) into the definition of the gap function in Eq. (A3), we obtain Eq. (23). This derivation is similar to the one performed in the Supplemental Material of Ref. [37].

[1] Y. Tserkovnyak, A. Brataas, and G. E. W. Bauer, Phys. Rev. Lett. **88**, 117601 (2002).

[2] A. I. Buzdin, Rev. Mod. Phys. **77**, 935 (2005).

[3] E. Saitoh, M. Ueda, H. Miyajima, and G. Tatara, Appl. Phys. Lett. **88**, 182509 (2006).

[4] J. Linder, Y. Tanaka, T. Yokoyama, A. Sudbø, and N. Nagaosa, Phys. Rev. Lett. **104**, 067001 (2010).

[5] I. Garate and M. Franz, Phys. Rev. Lett. **104**, 146802 (2010).

[6] P. Wei, F. Katmis, B. A. Assaf, H. Steinberg, P. Jarillo-Herrero, D. Heiman, and J. S. Moodera, Phys. Rev. Lett. **110**, 186807 (2013).

[7] R. Cheng, J. Xiao, Q. Niu, and A. Brataas, Phys. Rev. Lett. **113**, 057601 (2014).

[8] L. J. Cornelissen, J. Liu, R. A. Duine, J. B. Youssef, and B. J. van Wees, Nat. Phys. **11**, 1022 (2015).

[9] C. Du, T. van der Sar, T. X. Zhou, P. Upadhyaya, F. Casola, H. Zhang, M. C. Onbasli, C. A. Ross, R. L. Walsworth, Y. Tserkovnyak, and A. Yacoby, Science **357**, 195 (2017).

[10] R. Lebrun, A. Ross, S. A. Bender, A. Qaiumzadeh, L. Baldrati, J. Cramer, A. Brataas, R. A. Duine, and M. Kläui, Nature (London) **561**, 222 (2018).

[11] M. Kargarian, D. K. Efimkin, and V. Galitski, Phys. Rev. Lett. **117**, 076806 (2016).

[12] X. Gong, M. Kargarian, A. Stern, D. Yue, H. Zhou, X. Jin, V. M. Galitski, V. M. Yakovenko, and J. Xia, Sci. Adv. **3** e1602579 (2017).

[13] N. Rohling, E. L. Fjærbu, and A. Brataas, Phys. Rev. B **97**, 115401 (2018).

[14] H. G. Hugdal, S. Rex, F. S. Nogueira, and A. Sudbø, Phys. Rev. B **97**, 195438 (2018).

[15] E. L. Fjærbu, N. Rohling, and A. Brataas, Phys. Rev. B **100**, 125432 (2019).

[16] E. Erlandsen, A. Kamra, A. Brataas, and A. Sudbø, Phys. Rev. B **100**, 100503(R) (2019).

[17] M. Z. Hasan and C. L. Kane, Rev. Mod. Phys. **82**, 3045 (2010).

[18] X.-L. Qi and S.-C. Zhang, Rev. Mod. Phys. **83**, 1057 (2011).

[19] S.-S. Lee, P. A. Lee, and T. Senthil, Phys. Rev. Lett. **98**, 067006 (2007).

[20] A. Kamra and W. Belzig, Phys. Rev. Lett. **119**, 197201 (2017).

[21] A. Kamra, A. Rezaei, and W. Belzig, Phys. Rev. Lett. **121**, 247702 (2018).

[22] A. Kamra, E. Thingstad, G. Rastelli, R. A. Duine, A. Brataas, W. Belzig, and A. Sudbø, Phys. Rev. B **100**, 174407 (2019).

[23] O. Johansen, A. Kamra, C. Ulloa, A. Brataas, and R. A. Duine, Phys. Rev. Lett. **123**, 167203 (2019).

[24] Y. Xia, D. Qian, D. Hsieh, L. Wray, A. Pal, H. Lin, A. Bansil, D. Grauer, Y. S. Hor, R. J. Cava, and M. Z. Hasan, Nat. Phys. **5**, 398 (2009).

[25] Y. L. Chen, J. G. Analytis, J.-H. Chu, Z. K. Liu, S.-K. Mo, X. L. Qi, H. J. Zhang, D. H. Lu, X. Dai, Z. Fang, S. C. Zhang, I. R. Fisher, Z. Hussain, and Z.-X. Shen, Science **325**, 178 (2009).

[26] M. Li, C.-Z. Chang, B. J. Kirby, M. E. Jamer, W. Cui, L. Wu, P. Wei, Y. Zhu, D. Heiman, J. Li, and J. S. Moodera, Phys. Rev. Lett. **115**, 087201 (2015).

[27] Q. I. Yang, M. Dolev, L. Zhang, J. Zhao, A. D. Fried, E. Schemm, M. Liu, A. Palevski, A. F. Marshall, S. H. Risbud, and A. Kapitulnik, Phys. Rev. B **88**, 081407(R) (2013).

[28] Y.-F. Zhou, H. Jiang, X. C. Xie, and Q.-F. Sun, Phys. Rev. B **95**, 245137 (2017).

[29] Z.-Z. Li, F.-C. Zhang, and Q.-H. Wang, Sci. Rep. **4**, 6363 (2014).

[30] J. B. Kogut, Rev. Mod. Phys. **55**, 775 (1983).

[31] T. Holstein and H. Primakoff, Phys. Rev. **58**, 1098 (1940).

[32] C. Kittel, *Quantum Theory of Solids* (Wiley, New York, 1963).

[33] C. Tang, C.-Z. Chang, G. Zhao, Y. Liu, Z. Jiang, C.-X. Liu, M. R. McCartney, D. J. Smith, T. Chen, J. S. Moodera, and J. Shi, Sci. Adv. **3** e1700307 (2017).

[34] T. Wehling, A. Black-Schaffer, and A. Balatsky, Adv. Phys. **63**, 1 (2014).

[35] J. R. Schrieffer and P. A. Wolff, Phys. Rev. **149**, 491 (1966).

[36] P. A. Lee, Phys. Rev. X **4**, 031017 (2014).

[37] F. Schlawin, A. Cavalleri, and D. Jaksch, Phys. Rev. Lett. **122**, 133602 (2019).

[38] J. Bardeen, L. N. Cooper, and J. R. Schrieffer, Phys. Rev. **108**, 1175 (1957).

[39] J. Schrieffer, *Theory Of Superconductivity*, 4th ed., Frontiers in Physics (Addison-Wesley, Boca Raton, 1988).

[40] M. Sigrist and K. Ueda, Rev. Mod. Phys. **63**, 239 (1991).

[41] J. B. Parkinson and D. J. Farnell, *An Introduction to Quantum Spin Systems*, Lecture Notes in Physics Vol. 816 (Springer, Berlin, Heidelberg, 2010).

[42] J. Richter and J. Schulenburg, Eur. Phys. J. B **73**, 117 (2010).

Schwinger boson study of superconductivity mediated by antiferromagnetic spin fluctuations

Authors | Eirik Erlandsen
Asle Sudbø

Schwinger boson study of superconductivity mediated by antiferromagnetic spin fluctuations

Eirik Erlandsen and Asle Sudbø *

Center for Quantum Spintronics, Department of Physics, Norwegian University of Science and Technology, NO-7491 Trondheim, Norway

We study superconductivity in a normal metal, arising from effective electron-electron interactions mediated by spin fluctuations in a neighboring antiferromagnetic insulator. Introducing a frustrating next-nearest neighbor interaction in a Néel antiferromagnet with an uncompensated interface, the superconducting critical temperature is found to be enhanced as the frustration is increased. Further, for sufficiently large next-nearest neighbor interaction, the antiferromagnet is driven into a stripe phase, which can also give rise to attractive electron-electron interactions. For the stripe phase, as previously reported for the Néel phase, the superconducting critical temperature is found to be amplified for an uncompensated interface where the normal metal conduction electrons are coupled to only one of the two sublattices of the magnet. The superconducting critical temperature arising from fluctuations in the stripe phase antiferromagnet can be further enhanced by approaching the transition back to the Néel phase.

DOI: 10.1103/PhysRevB.102.214502

I. INTRODUCTION

Recent studies have investigated whether spin fluctuations in a magnetic material can induce attractive interactions between electrons in an adjacent conductor, leading to a superconducting instability [1–8]. Both ferromagnetic (FMIs) and antiferromagnetic insulators (AFMIs) have been considered as potential sources for the magnetic fluctuations. In order to ensure magnetic ordering, these materials typically ought to be of a three-dimensional nature [9,10]. Since a three-dimensional crystal has more than one crystal plane, the issue arises whether it makes a difference which crystal plane is exposed at the interface. For the simplest type of ferromagnet, all lattice sites can be considered to be identical, and the choice of crystal plane does not affect the coupling to an external system. For the simplest case of an antiferromagnet on a bipartite lattice, there are two different types of lattice sites. Depending on the chosen crystal plane, it is possible that either both sublattices (compensated interface) are exposed at the interface, or only one of the sublattices (uncompensated interface) is exposed at the interface [11–13].

As outlined in Ref. [14], the presence of an antiferromagnetic eigenexcitation with spin unity is associated with a large, and oppositely directed, spin located on each of the two sublattices. An external system that is only coupled to one of the two sublattices is then essentially interacting with a large spin, potentially leading to a strong coupling interaction. In accordance with this picture, uncompensated antiferromagnetic interfaces have been predicted to enhance the spin transfer to a neighboring conductor [15], and produce magnon-mediated indirect exciton condensation [16]. Moreover, importantly for our purposes, coupling a conductor to an uncompensated,

instead of compensated, antiferromagnetic interface might produce a stronger induced electron-electron interaction and higher superconducting critical temperature [6,7].

In view of the fact that the superconductivity arises from magnetic fluctuations, it is natural to ask whether amplifying the fluctuations can be favorable. One way of achieving such an amplification is to include next-nearest neighbor frustration in the AFMI. This type of frustration is common in antiferromagnets, and has been predicted to increase the critical temperature of superconductivity induced on the surface of a topological insulator [7]. Using the picture from Ref. [14], this increase in critical temperature can be understood from the amplified fluctuations increasing the average spin on each sublattice associated with an antiferromagnetic magnon. The effect of coupling to only one of the two sublattices then becomes stronger.

The previous study of the effect of frustration, however, employed a Holstein-Primakoff treatment of the AFMI, starting from a staggered Néel state [7]. This framework is expected to accurately describe the system when the antiferromagnetic next-nearest neighbor exchange coupling J_2 is relatively small compared to the nearest neighbor coupling J_1. The previous study therefore limited itself to this parameter region [7]. Hence, it is of interest to investigate the rest of the phase diagram of the J_1-J_2 Heisenberg model. On a square or cubic lattice, this model contains two distinct magnetically ordered phases, a Néel phase for $J_2/J_1 \ll 1$ and a stripe phase for $J_2/J_1 \gg 1$ [17,18]. In the stripe phase, the spins in, e.g., one column could be aligned with each other and antialigned with the spins in the neighboring columns, creating alternating stripes of spins. This state arises from two decoupled, interpenetrating, Néel ordered antiferromagnets ($J_2/J_1 \to \infty$), which align themselves and create a stripe pattern for finite J_1 [19,20]. Given the origin of the stripe phase, it could be possible that coupling to only the up/down spins of both Néel ordered antiferromagnets could give a similar effect as only

---

*Corresponding author: asle.sudbo@ntnu.no

coupling to one of the sublattices of a single Néel ordered antiferromagnet.

The transition between the Néel and stripe phases takes place in the vicinity of $J_2/J_1 = 0.5$, with variations depending on the spin quantum number and lattice structure [17,18,21,22]. For the spin-1/2 system on a square lattice, it is predicted that there is an intermediate region where the magnetic long-range order is destroyed by quantum fluctuations [17,23–25]. A similar intermediate region might also be present for the spin-1/2 system on a simple cubic lattice, in contrast to the case of a body-centered cubic lattice [18,26]. We will, however, focus on the properties of the ordered phases. While the Néel phase is more commonly encountered, the stripe configuration has attracted attention as the magnetic ground state of the iron oxypnictide LaOFeAs, which is the original undoped parent compound of the high-T_c iron pnictides [27]. This layered material has been found to be well described by the square lattice J_1-J_2 Heisenberg model with spin $S > 1/2$ and $J_2/J_1 > 1/2$ [28,29].

In this paper, we consider an AFMI, with both nearest-neighbor and next-nearest neighbor antiferromagnetic exchange interaction, which is proximity coupled to a normal metal (NM). The AFMI can be in either a Néel or stripe state, and the interface can be either compensated or uncompensated. In order to accurately describe the physics of the AFMI when the system is strongly frustrated, focusing on the case where the two magnetically ordered phases are separated by a direct phase transition, we perform a Schwinger boson study, rather than the usual Holstein-Primakoff treatment which has been employed for these systems in the past. Conventional spin-wave theory would in this case, e.g., incorrectly predict a vanishing magnetization close to $J_2/J_1 = 0.5$ instead of a direct phase transition between two magnetically ordered phases [21,30]. Moreover, the two subsystems are coupled through an interfacial exchange coupling, which produces effective electron-electron interactions in the NM. We explore the effect of the induced interactions through a BCS-type mean-field treatment, and numerically solve the gap equation in order to determine how the critical temperature depends on the properties of the AFMI.

For a Néel AFMI with small next-nearest neighbor frustration, the results for the superconductivity are similar to the results obtained through a Holstein-Primakoff treatment of the AFMI [6]. As before, the strength of the effective interactions is enhanced for an uncompensated interface, leading to an amplified critical temperature. Increasing the frustration, the effect of coupling to only one of the two sublattices of the AFMI becomes stronger, as expected [7]. Further, the increased frustration also lowers the cutoff on the boson spectrum, and reduces the sublattice magnetization in the AFMI, which is found to reduce the strength of the induced electron-electron interactions. The overall effect is, however, still typically a rise in the critical temperature when the frustration is increased. For the stripe phase, coupling to an uncompensated AFMI interface is found to enhance the critical temperature, like in the Néel case. Moreover, approaching the transition point between the two magnetic phases from the stripe side does, like from the Néel side, leads to a further increase in the critical temperature.
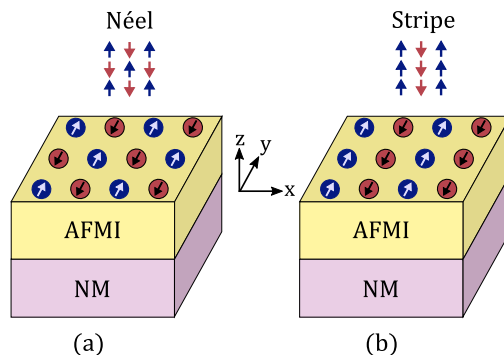

FIG. 1. The system consists of a normal metal (NM), which is proximity coupled to an antiferromagnetic insulator (AFMI). The AFMI can be either in a Néel phase (a) or a stripe phase (b).

The paper is organized as follows. In Sec. II we introduce the modeling of the system. In Sec. III the Schwinger boson treatment of the antiferromagnet is covered for both the Néel phase and the stripe phase. Next, the NM and the coupling between the two subsystems is treated in Sec. IV. In Sec. V, we derive an effective theory of interacting electrons, and in Sec. VI we investigate the possibility of a superconducting instability through a weak-coupling mean-field theory. The results from the numerical treatment of the gap equation are presented in Sec. VII. Finally, in Sec. VIII, we summarize our results. Additional details concerning the derivation of the interaction potential are included in the Appendix.

II. MODEL

The system, consisting of a NM proximity coupled to an AFMI, is displayed in Fig. 1. The real system we have in mind would consist of a three-dimensional AFMI grown on top of a thin NM layer. However, in order to capture the physics at the interface, we apply two-dimensional lattice models, with continuous boundary conditions, for the two subsystems. The AFMI is described by a Heisenberg Hamiltonian with nearest neighbor and next-nearest neighbor exchange interaction, as well as easy-axis anisotropy (K). By tuning the next-nearest neighbor interaction, the ground state of the AFMI can be changed from a Néel phase to a stripe phase. The NM is described by a tight-binding hopping model. The two subsystems are coupled together through an interfacial exchange coupling ($\bar{J}$) where the spins of the NM conduction electrons are coupled to the AFMI lattice site spins [3,5,31–33].

For each of the magnetic phases we define two sublattices. In Fig. 1, the lattice sites with blue spins constitute one sublattice, and the lattice sites with oppositely aligned red spins constitute the other sublattice. The sublattices are therefore defined differently for the Néel phase and the stripe phase. As mentioned earlier, depending on which crystal plane of the three-dimensional AFMI that constitutes the interface, it is possible that either both sublattices or only one of the sublattices is exposed at the interface. In order to describe this, we apply a model where the NM electrons are coupled to both

sublattices of the AFMI, but where the coupling strength is allowed to differ for the two sublattices ($\bar{J}_A/\bar{J}_B$) [6]. This model allows us to tune between the two cases of a compensated or uncompensated interface.

The system is modeled by a Hamiltonian $H = H_{\text{AFMI}} + H_{\text{NM}} + H_{\text{int}}$ where

$$H_{\text{AFMI}} = J_1 \sum_{\langle i,j \rangle} \boldsymbol{S}_i \cdot \boldsymbol{S}_j + J_2 \sum_{\langle\langle i,j \rangle\rangle} \boldsymbol{S}_i \cdot \boldsymbol{S}_j - K \sum_i S_{iz}^2, \quad \text{(1a)}$$

$$H_{\text{NM}} = -t \sum_{\langle i,j \rangle \sigma} c_{i\sigma}^\dagger c_{j\sigma} - \mu \sum_{i\sigma} c_{i\sigma}^\dagger c_{i\sigma}, \quad \text{(1b)}$$

$$H_{\text{int}} = -2\bar{J}_A \sum_{i \in A} c_i^\dagger \boldsymbol{\tau} c_i \cdot \boldsymbol{S}_i - 2\bar{J}_B \sum_{i \in B} c_i^\dagger \boldsymbol{\tau} c_i \cdot \boldsymbol{S}_i. \quad \text{(1c)}$$

Here, $c_i^\dagger = (c_{i\uparrow}^\dagger, c_{i\downarrow}^\dagger)$ and $c_{i\sigma}^\dagger$ creates an electron with spin σ on lattice site $\boldsymbol{i}$. The electron hopping amplitude is denoted by t, and μ is the chemical potential. The easy-axis anisotropy constant K is taken to be positive, favoring ordering of spins in the z direction in spin space, which could be either parallel with or normal to the interface. In the interaction part of the Hamiltonian, $\boldsymbol{\tau}$ is the vector of Pauli matrices, representing the NM electron spin which is coupled to the lattice site spin $\boldsymbol{S}_i$ in the AFMI. Further, it should be noted that the lattices are assumed to be square, the sums over nearest and next-nearest neighbors include the neighbors in both positive and negative spatial directions, and we have set $\hbar = a = 1$, where a is the lattice constant.

III. ANTIFERROMAGNET

In order to treat the AFMI, we will represent the lattice site spins in terms of Schwinger bosons [34–36]. For our purposes, where we will couple an external system to the two sublattices of the AFMI, it will be useful to define different Schwinger bosons for the two sublattices A and B [37]:

$$S_{i+}^A = a_{i\uparrow}^\dagger a_{i\downarrow}, \quad \text{(2a)}$$

$$S_{i-}^A = a_{i\downarrow}^\dagger a_{i\uparrow}, \quad \text{(2b)}$$

$$S_{iz}^A = \frac{1}{2}(a_{i\uparrow}^\dagger a_{i\uparrow} - a_{i\downarrow}^\dagger a_{i\downarrow}), \quad \text{(2c)}$$

$$S_{i+}^B = -b_{i\downarrow}^\dagger b_{i\uparrow}, \quad \text{(3a)}$$

$$S_{i-}^B = -b_{i\uparrow}^\dagger b_{i\downarrow}, \quad \text{(3b)}$$

$$S_{iz}^B = -\frac{1}{2}(b_{i\uparrow}^\dagger b_{i\uparrow} - b_{i\downarrow}^\dagger b_{i\downarrow}). \quad \text{(3c)}$$

An ordered Néel or stripe state can then be described through a condensation [35,36,38] of $\uparrow$-bosons with momentum $\boldsymbol{k} = 0$ on both the A and B sublattice, producing a spatially uniform state with opposite magnetization on the two sublattices. In order to fix the length of the spins, we have the condition [35],

$$n_{i,A} = \sum_\alpha a_{i\alpha}^\dagger a_{i\alpha} = 2S,$$

$$n_{j,B} = \sum_\alpha b_{j\alpha}^\dagger b_{j\alpha} = 2S, \quad \text{(4)}$$

on each lattice site. In the following mean-field treatment, this condition on the number of Schwinger bosons will be

enforced on the average. In order to rewrite the AFMI Hamiltonian in terms of Schwinger boson operators, we introduce bond operators quadratic in the boson operators. We follow the recipe of Ref. [39], as outlined in Refs. [38,40]. When the Schwinger boson operators have been defined equally on all lattice sites, the bond operators then take the form,

$$A_{ij} = \frac{1}{2}(a_{i\uparrow}a_{j\downarrow} - a_{i\downarrow}a_{j\uparrow}), \quad \text{(5a)}$$

$$B_{ij} = \frac{1}{2}(a_{i\uparrow}a_{j\uparrow}^\dagger + a_{i\downarrow}a_{j\downarrow}^\dagger). \quad \text{(5b)}$$

Here, A_{ij} corresponds to an antiferromagnetic bond and B_{ij} corresponds to a ferromagnetic bond [19,38]. This choice of bond operators captures the cost of frustrating bonds, which is essential for frustrated antiferromagnets, and has been shown to preserve the time-inversion properties of the spins [19]. As we have defined different Schwinger boson operators on the two sublattices, we should perform the following transformation on the operators living on the B sublattice in the above definitions of the bond operators,

$$a_{i\uparrow} \rightarrow -b_{i\downarrow},$$

$$a_{i\downarrow} \rightarrow b_{i\uparrow}.$$

A. Néel phase

For the Néel phase, the AFMI Hamiltonian can be expressed on the form,

$$H_{\text{AFMI}}^{\text{Néel}} = J_1 \sum_{\substack{i \in A \\ j\text{nn}i}} \boldsymbol{S}_i^A \cdot \boldsymbol{S}_j^B + J_1 \sum_{\substack{i \in B \\ j\text{nn}i}} \boldsymbol{S}_i^B \cdot \boldsymbol{S}_j^A$$

$$+ J_2 \sum_{\substack{i \in A \\ j\text{nnn}i}} \boldsymbol{S}_i^A \cdot \boldsymbol{S}_j^A + J_2 \sum_{\substack{i \in B \\ j\text{nnn}i}} \boldsymbol{S}_i^B \cdot \boldsymbol{S}_j^B$$

$$- K \sum_{i \in A} S_{iz}^2 - K \sum_{i \in B} S_{iz}^2. \quad \text{(6)}$$

We then introduce the bond operators,

$$A_{ij}^{1,A} = \frac{1}{2}(a_{i\uparrow}b_{j\uparrow} + a_{i\downarrow}b_{j\downarrow}), \quad \text{(7a)}$$

$$B_{ij}^{1,A} = \frac{1}{2}(a_{i\downarrow}b_{j\uparrow}^\dagger - a_{i\uparrow}b_{j\downarrow}^\dagger), \quad \text{(7b)}$$

$$A_{ij}^{1,B} = \frac{1}{2}(-b_{i\downarrow}a_{j\downarrow} - b_{i\uparrow}a_{j\uparrow}), \quad \text{(7c)}$$

$$B_{ij}^{1,B} = \frac{1}{2}(b_{i\uparrow}a_{j\downarrow}^\dagger - b_{i\downarrow}a_{j\uparrow}^\dagger), \quad \text{(7d)}$$

$$A_{ij}^{2,A} = \frac{1}{2}(a_{i\uparrow}a_{j\downarrow} - a_{i\downarrow}a_{j\uparrow}), \quad \text{(7e)}$$

$$B_{ij}^{2,A} = \frac{1}{2}(a_{i\uparrow}a_{j\uparrow}^\dagger + a_{i\downarrow}a_{j\downarrow}^\dagger), \quad \text{(7f)}$$

$$A_{ij}^{2,B} = \frac{1}{2}(b_{i\uparrow}b_{j\downarrow} - b_{i\downarrow}b_{j\uparrow}), \quad \text{(7g)}$$

$$B_{ij}^{2,B} = \frac{1}{2}(b_{i\uparrow}b_{j\uparrow}^\dagger + b_{i\downarrow}b_{j\downarrow}^\dagger), \quad \text{(7h)}$$

and write out the Hamiltonian as

$$
\begin{aligned}
H_{\mathrm{AFMI}}^{\mathrm{N\acute{e}el}} = {} & J_1 \sum_{\substack{i\in A \\ j\,\mathrm{nn}\,i}} \left[\left(B_{ij}^{1,A}\right)^{\dagger} B_{ij}^{1,A} - \left(A_{ij}^{1,A}\right)^{\dagger} A_{ij}^{1,A} - \frac{1}{4} n_{i,A} \right] \\
& + J_1 \sum_{\substack{i\in B \\ j\,\mathrm{nn}\,i}} \left[\left(B_{ij}^{1,B}\right)^{\dagger} B_{ij}^{1,B} - \left(A_{ij}^{1,B}\right)^{\dagger} A_{ij}^{1,B} - \frac{1}{4} n_{i,B} \right] \\
& + J_2 \sum_{\substack{i\in A \\ j\,\mathrm{nnn}\,i}} \left[\left(B_{ij}^{2,A}\right)^{\dagger} B_{ij}^{2,A} - \left(A_{ij}^{2,A}\right)^{\dagger} A_{ij}^{2,A} - \frac{1}{4} n_{i,A} \right] \\
& + J_2 \sum_{\substack{i\in B \\ j\,\mathrm{nnn}\,i}} \left[\left(B_{ij}^{2,B}\right)^{\dagger} B_{ij}^{2,B} - \left(A_{ij}^{2,B}\right)^{\dagger} A_{ij}^{2,B} - \frac{1}{4} n_{i,B} \right] \\
& - K \sum_{i\in A} S_{iz}^2 - K \sum_{i\in B} S_{iz}^2 + \lambda_A \sum_{i\in A} \left(n_{i,A} - \kappa \right) \\
& + \lambda_B \sum_{i\in B} \left(n_{i,B} - \kappa \right).
\end{aligned}
\tag{8}
$$

Here $\kappa = 2S$ and λ_A, λ_B are Lagrange multipliers that have been included in order to enforce the constraint on the number of Schwinger bosons per site. The choice of $\kappa = 2S$ seems sensible based on Eq. (4), and fixes the magnitude of the spins to the correct value. For this value of κ, the spin fluctuations are, however, somewhat overestimated [35]. Another possibility is therefore to adjust κ in order to obtain the correct result for the fluctuations, at the expense of the spin length [41]. We will mostly be interested in how the results vary depending on J_2 for typical values of the rest of the parameters, and the specific choice of κ therefore is not of great importance.

We next perform a mean-field decoupling of a bond variable C_{ij} as follows:

$$
\begin{aligned}
C_{ij} &= \langle C_{ij}\rangle + \left(C_{ij} - \langle C_{ij}\rangle\right) \equiv \langle C_{ij}\rangle + \delta(C_{ij}), \\
\left(C_{ij}\right)^{\dagger} C_{ij} &\approx \langle C_{ij}\rangle^{\dagger} C_{ij} + \langle C_{ij}\rangle \left(C_{ij}\right)^{\dagger} - |\langle C_{ij}\rangle|^2.
\end{aligned}
\tag{9}
$$

Here, we have neglected quadratic terms in the deviations from the mean-field values. Moreover, we choose an Ansatz for the expectation values of the bond operators that will produce a Néel-type state,

$$
\begin{aligned}
\langle B_{ij}^{1,A}\rangle &= \langle B_{ij}^{1,B}\rangle = 0, \\
\langle A_{ij}^{1,A}\rangle &= -\langle A_{ij}^{1,B}\rangle \equiv \mathcal{A}_{\delta_1}, \\
\langle B_{ij}^{2,A}\rangle &= \langle B_{ij}^{2,B}\rangle \equiv \mathcal{B}_{\delta_2}, \\
\langle A_{ij}^{2,A}\rangle &= \langle A_{ij}^{2,B}\rangle = 0,
\end{aligned}
\tag{10}
$$

where all quantities are assumed to be real [40,41]. We also take $\lambda_A = \lambda_B \equiv \lambda$. For the easy-axis terms we do the same mean-field treatment as above and take $\langle S_{iz}^C\rangle \equiv m_C$.

We introduce Fourier transformations for the Schwinger boson operators,

$$
a_{i\sigma} = \frac{1}{\sqrt{N_A}} \sum_{k\in\diamond} e^{ik\cdot r_i} a_{k\sigma},
\tag{11a}
$$
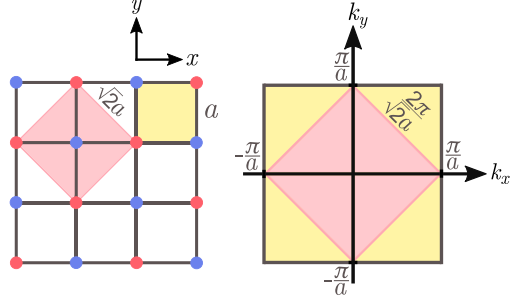
FIG. 2. Unit cell and Brillouin zone for the full lattice and the sublattices.

$$
b_{i\sigma} = \frac{1}{\sqrt{N_B}} \sum_{k\in\diamond} e^{ik\cdot r_i} b_{k\sigma},
\tag{11b}
$$

where N_A and N_B are the number of lattice sites in the A and B sublattices, respectively. The momenta live in the reduced Brillouin zone of the sublattices $\diamond$, as displayed in Fig. 2.

The AFMI Hamiltonian then takes the following form:

$$
\begin{aligned}
H_{\mathrm{AFMI}}^{\mathrm{N\acute{e}el}} = {} & 2N_A \left[J_1 \sum_{\delta_1} \left(\mathcal{A}_{\delta_1}\right)^2 - J_2 \sum_{\delta_2} \left(\mathcal{B}_{\delta_2}\right)^2 \right] \\
& + \left[\lambda - \frac{1}{4}(J_1 z_1 + J_2 z_2) \right] \sum_{\substack{k\in\diamond \\ \sigma}} \left(a_{k\sigma}^{\dagger} a_{k\sigma} + b_{k\sigma}^{\dagger} b_{k\sigma}\right) \\
& - K m_A \sum_{\substack{k\in\diamond \\ \sigma}} \sigma a_{k\sigma}^{\dagger} a_{k\sigma} + K m_B \sum_{\substack{k\in\diamond \\ \sigma}} \sigma b_{k\sigma}^{\dagger} b_{k\sigma} \\
& + \sum_{\substack{k\in\diamond \\ \sigma}} \gamma_k^{B_2} \left(a_{k\sigma}^{\dagger} a_{k\sigma} + b_{k\sigma} b_{k\sigma}^{\dagger}\right) + K N_A \left(m_A^2 + m_B^2\right) \\
& - \sum_{\substack{k\in\diamond \\ \sigma}} \gamma_k^{A_1} \left(b_{k\sigma}^{\dagger} a_{-k\sigma}^{\dagger} + a_{k\sigma} b_{-k\sigma}\right) - 2N_A \kappa \lambda,
\end{aligned}
\tag{12}
$$

where z_1 and z_2 are the number of nearest neighbors and next-nearest neighbors, respectively. Throughout this paper, the quantity $\sigma = \pm 1$ takes on a positive sign for spin-up, and a negative sign for spin-down. We have also introduced the form factors,

$$
\gamma_k^{A_1} \equiv J_1 \sum_{\delta_1} \mathcal{A}_{\delta_1} \cos(k\cdot\delta_1),
\tag{13a}
$$

$$
\gamma_k^{B_2} \equiv J_2 \sum_{\delta_2} \mathcal{B}_{\delta_2} \cos(k\cdot\delta_2),
\tag{13b}
$$

where the sums over nearest neighbors (δ_1) and next-nearest neighbors (δ_2) cover both positive and negative directions. We then define $\lambda' \equiv \lambda - \frac{1}{4}(J_1 z_1 + J_2 z_2)$, rename $\lambda' \to \lambda$, and neglect constant terms that do not contain any of the mean-field parameters.

In order to make progress, we split the Hamiltonian up into three parts $H_{\text{AFMI}}^{\text{Néel}} = E_0 + H^{\uparrow} + H^{\downarrow}$ where

$$E_0 = 2N_A \Big[J_1 \sum_{\delta_1} \big(\mathcal{A}_{\delta_1} \big)^2 - J_2 \sum_{\delta_2} \big(\mathcal{B}_{\delta_2} \big)^2 \Big]$$
$$- 2N_A \lambda(\kappa + 1) + KN_A \big(m_A^2 + m_B^2 \big), \qquad (14)$$

and

$$H^{\sigma} = \sum_{k \in \diamond} \big(\lambda + \gamma_k^{B_2} - \sigma K m_A \big) a_{k\sigma}^{\dagger} a_{k\sigma}$$
$$+ \sum_{k \in \diamond} \big(\lambda + \gamma_k^{B_2} + \sigma K m_B \big) b_{k\sigma} b_{k\sigma}^{\dagger}$$
$$- \sum_{k \in \diamond} \gamma_k^{A_1} \big(b_{k\sigma}^{\dagger} a_{-k\sigma}^{\dagger} + a_{k\sigma} b_{-k\sigma} \big). \qquad (15)$$

We can then perform a Bogoliubov transformation,

$$a_{k\sigma} = u_{k\sigma} \alpha_{k\sigma} - v_{k\sigma} \beta_{-k\sigma}^{\dagger},$$
$$b_{-k\sigma}^{\dagger} = v_{k\sigma} \alpha_{k\sigma} - u_{k\sigma} \beta_{-k\sigma}^{\dagger}. \qquad (16)$$

where $u_{k\sigma}$ and $v_{k\sigma}$ are taken to be real and are parametrized by $u_{k\sigma} = \cosh(\theta_{k\sigma})$, $v_{k\sigma} = \sinh(\theta_{k\sigma})$. The value of $\theta_{k\sigma}$ that diagonalizes the Hamiltonian is given by

$$\tanh(2\theta_{k\sigma}) = \frac{\gamma_k^{A_1}}{\lambda + \gamma_k^{B_2} + \sigma \frac{K}{2} \big(m_B - m_A \big)}. \qquad (17)$$

In order to simplify the expressions, we take $m_B = -m_A$, which is consistent with a Néel phase. The diagonalized Hamiltonian now takes the form,

$$H_{\text{AFMI}}^{\text{Néel}} = E_0' + \sum_{\substack{k \in \diamond \\ \sigma}} \omega_{k\sigma} \big(\alpha_{k\sigma}^{\dagger} \alpha_{k\sigma} + \beta_{k\sigma}^{\dagger} \beta_{k\sigma} \big), \qquad (18)$$

where

$$\omega_{k\sigma} = \sqrt{\big(\lambda + \gamma_k^{B_2} - \sigma K m_A \big)^2 - \big(\gamma_k^{A_1} \big)^2}, \qquad (19)$$

and $E_0' = E_0 + \sum_{k\sigma} \omega_{k\sigma}$.

The mean-field parameters should be determined self-consistently from minimization of the free energy. The free energy per lattice site is given by

$$f = \frac{E_0'}{N} + \frac{2}{\beta N} \sum_{\substack{k \in \diamond \\ \sigma}} \ln(1 - e^{-\beta \omega_{k\sigma}}). \qquad (20)$$

Minimizing the free energy with respect to $\mathcal{A}_{\delta_1}$, $\mathcal{B}_{\delta_2}$, λ, and m_A, we then obtain the following self-consistent equations for the mean-field parameters,

$$\mathcal{A}_{\delta_1} = \frac{1}{2N} \sum_{\substack{k \in \diamond \\ \sigma}} \frac{\gamma_k^{A_1}}{\omega_{k\sigma}} \big(1 + 2n_{k\sigma} \big) \cos(k \cdot \delta_1), \qquad (21a)$$

$$\mathcal{B}_{\delta_2} = \frac{1}{2N} \sum_{\substack{k \in \diamond \\ \sigma}} \frac{\big(\lambda + \gamma_k^{B_2} - \sigma K m_A \big)}{\omega_{k\sigma}} \big(1 + 2n_{k\sigma} \big) \cos(k \cdot \delta_2),$$
$$\qquad (21b)$$

$$\bar{\kappa} = \frac{1}{2N} \sum_{\substack{k \in \diamond \\ \sigma}} \frac{\big(\lambda + \gamma_k^{B_2} - \sigma K m_A \big)}{\omega_{k\sigma}} \big(1 + 2n_{k\sigma} \big), \qquad (21c)$$

$$m_A = \frac{1}{2N} \sum_{\substack{k \in \diamond \\ \sigma}} \frac{\sigma \big(\lambda + \gamma_k^{B_2} - \sigma K m_A \big)}{\omega_{k\sigma}} \big(1 + 2n_{k\sigma} \big). \qquad (21d)$$

The Bose-Einstein occupation factor is here denoted by $n_{k\sigma}$, and we have defined $\bar{\kappa} = \frac{1}{2}(\kappa + 1)$. As mentioned earlier, in our description of the system, a Néel-type state with $m_A > 0$ arises from condensation of $\uparrow$-bosons with $k = 0$. It should be noted that the condensation only takes place in the thermodynamic limit and that the bosonic energy cannot be taken to zero without also taking the system size to infinity. For condensation to take place, we need $|\lambda + \gamma_0^{B_2} - K m_A| = |\gamma_0^{A_1}|$. In the following, we will take A_{δ_1} to be positive. For the interaction potential that will enter into the Hamiltonian describing the effective theory of interacting electrons, we need the ground-state properties of the antiferromagnet. From the Bose-Einstein occupation factors, at zero temperature, we then only get a contribution from the condensate $n_{0\uparrow}$. Defining $\zeta_{k\sigma} \equiv \gamma_0^{A_1} - \gamma_0^{B_2} + \gamma_k^{B_2} + 2K m_A \delta_{\sigma,\downarrow}$, we now have

$$\bar{\kappa} = \frac{1}{2N} \sideset{}{'}\sum_{\substack{k \in \diamond \\ \sigma}} \frac{\zeta_{k\sigma}}{\omega_{k\sigma}} + \frac{1}{N} Q_0, \qquad (22a)$$

$$m_A = \frac{1}{2N} \sideset{}{'}\sum_{\substack{k \in \diamond \\ \sigma}} \frac{\sigma \zeta_{k\sigma}}{\omega_{k\sigma}} + \frac{1}{N} Q_0, \qquad (22b)$$

$$\mathcal{A}_{\delta_1} = \frac{1}{2N} \sideset{}{'}\sum_{\substack{k \in \diamond \\ \sigma}} \frac{\gamma_k^{A_1}}{\omega_{k\sigma}} \cos(k \cdot \delta_1) + \frac{1}{N} Q_0, \qquad (22c)$$

$$\mathcal{B}_{\delta_2} = \frac{1}{2N} \sum_{\substack{k \in \diamond \\ \sigma}} \frac{\zeta_{k\sigma}}{\omega_{k\sigma}} \cos(k \cdot \delta_2) + \frac{1}{N} Q_0, \qquad (22d)$$

where

$$Q_0 = \frac{\gamma_0^{A_1}}{\omega_{0\uparrow}} \Big(n_{0\uparrow} + \frac{1}{2} \Big). \qquad (23)$$

Note that the sums no longer include $k = 0$, $\sigma = \uparrow$. We can then eliminate

$$\tilde{Q}_0 \equiv \frac{1}{N} Q_0 = \bar{\kappa} - \frac{1}{2N} \sideset{}{'}\sum_{\substack{k \in \diamond \\ \sigma}} \frac{\zeta_{k\sigma}}{\omega_{k\sigma}}, \qquad (24)$$

and obtain

$$m_A - \bar{\kappa} + \frac{1}{N} \sideset{}{'}\sum_{k \in \diamond} \frac{\zeta_{k\downarrow}}{\omega_{k\downarrow}} = 0, \qquad (25a)$$

$$\mathcal{A} - \bar{\kappa} - \frac{1}{2N} \sideset{}{'}\sum_{\substack{k \in \diamond \\ \sigma}} \frac{\gamma_k^{A_1} \cos(k_x) - \zeta_{k\sigma}}{\omega_{k\sigma}} = 0, \qquad (25b)$$

$$\mathcal{B} - \bar{\kappa} - \frac{1}{2N} \sideset{}{'}\sum_{\substack{k \in \diamond \\ \sigma}} \frac{\zeta_{k\sigma}}{\omega_{k\sigma}} \Big[\cos(k_x + k_y) - 1 \Big] = 0, \qquad (25c)$$
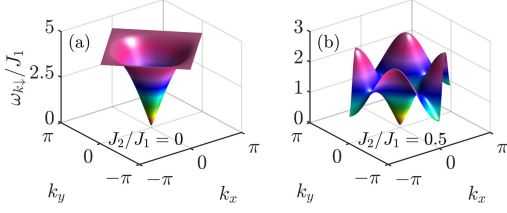
FIG. 3. Schwinger boson dispersion relations $\omega_{k\sigma}$ for $K = 0.001J_1$, $S = 1$, and $\sigma = \downarrow$. The value for J_2 varies between the two subfigures.

where we have taken $\mathcal{A} \equiv \mathcal{A}_{\delta_1}$ and $\mathcal{B} \equiv \mathcal{B}_{\delta_2}$. In the thermodynamic limit, we can convert the sums to integrals and solve the coupled set of equations numerically using a multidimensional root finder [42].

Solving the self-consistent equations for the mean-field parameters, the properties of the antiferromagnet can be determined, e.g., for different values of J_2. In Fig. 3, the Schwinger boson dispersion relation $\omega_{k\sigma}$ is presented both deep into the Néel regime and close to the transition to the stripe phase. Note how local minima have developed close to the zone edges of the Brillouin zone for $J_2/J_1 = 0.5$, which are nearly degenerate with the dispersion minimum at the zone center. This indicates the vicinity of an instability of the Néel state into a new spin-ordered state. For the same parameters, the Schwinger boson coherence factor $u_{k\sigma}$ is presented in Fig. 4. All quantities are displayed for $\sigma = \downarrow$, because, as we will see in the following, $\omega_{k\downarrow}$ and $u_{k\downarrow}$, $v_{k\downarrow}$ are the quantities, arising in the effective electron-electron interaction potential, that correspond to the magnon energies and coherence factors encountered in the Holstein-Primakoff treatment of the AFMI.

B. Stripe phase

For the stripe phase we write out the AFMI Hamiltonian as

$$H_{\text{AFMI}}^{\text{Stripe}} = J_1 \sum_{\substack{i \in A \\ j = i \pm \hat{x}}} S_i^A \cdot S_j^B + J_1 \sum_{\substack{i \in A \\ j = i \pm \hat{y}}} S_i^A \cdot S_j^A$$
$$+ J_1 \sum_{\substack{i \in B \\ j = i \pm \hat{x}}} S_i^B \cdot S_j^A + J_1 \sum_{\substack{i \in B \\ j = i \pm \hat{y}}} S_i^B \cdot S_j^B$$
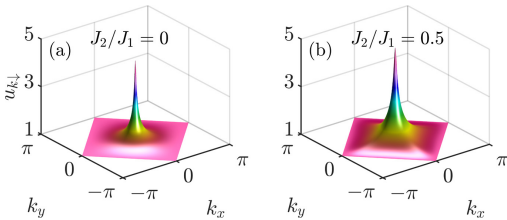
FIG. 4. Schwinger boson coherence factors $u_{k\sigma}$ for $K = 0.001J_1$, $S = 1$, and $\sigma = \downarrow$.

$$+ J_2 \sum_{\substack{i \in A \\ j \text{nnn} i}} S_i^A \cdot S_j^B + J_2 \sum_{\substack{i \in B \\ j \text{nnn} i}} S_i^B \cdot S_j^A$$
$$- K \sum_{i \in A} S_{iz}^2 - K \sum_{i \in B} S_{iz}^2, \tag{26}$$

where we have assumed that the stripes are oriented in the y direction. The results for the superconductivity are not expected to depend on the spatial direction of the stripes. The bond operators, this time, take the form,

$$A_{ij}^{A_x} = \frac{1}{2}\left(a_{i\uparrow}b_{j\uparrow} + a_{i\downarrow}b_{j\downarrow}\right) = A_{ij}^{2,A}, \tag{27a}$$

$$B_{ij}^{A_x} = \frac{1}{2}\left(a_{i\downarrow}b_{j\uparrow}^\dagger - a_{i\uparrow}b_{j\downarrow}^\dagger\right) = B_{ij}^{2,A}, \tag{27b}$$

$$A_{ij}^{A_y} = \frac{1}{2}\left(a_{i\uparrow}a_{j\downarrow} - a_{i\downarrow}a_{j\uparrow}\right), \tag{27c}$$

$$B_{ij}^{A_y} = \frac{1}{2}\left(a_{i\uparrow}a_{j\uparrow}^\dagger + a_{i\downarrow}a_{j\downarrow}^\dagger\right), \tag{27d}$$

$$A_{ij}^{B_x} = \frac{1}{2}\left(-b_{i\downarrow}a_{j\downarrow} - b_{i\uparrow}a_{j\uparrow}\right) = A_{ij}^{2,B}, \tag{27e}$$

$$B_{ij}^{B_x} = \frac{1}{2}\left(b_{i\uparrow}a_{j\downarrow}^\dagger - b_{i\downarrow}a_{j\uparrow}^\dagger\right) = B_{ij}^{2,B}, \tag{27f}$$

$$A_{ij}^{B_y} = \frac{1}{2}\left(b_{i\uparrow}b_{j\downarrow} - b_{i\downarrow}b_{j\uparrow}\right), \tag{27g}$$

$$B_{ij}^{B_y} = \frac{1}{2}\left(b_{i\downarrow}b_{j\downarrow}^\dagger + b_{i\uparrow}b_{j\uparrow}^\dagger\right). \tag{27h}$$

Including the Lagrange multiplier terms, the AFMI Hamiltonian can then be written out as

$$H_{\text{AFMI}}^{\text{Stripe}} = J_1 \sum_{\substack{i \in A \\ j = i \pm \hat{x}}} \left[\left(B_{ij}^{A_x}\right)^\dagger B_{ij}^{A_x} - \left(A_{ij}^{A_x}\right)^\dagger A_{ij}^{A_x} - \frac{1}{4}n_{i,A}\right]$$

$$+ J_1 \sum_{\substack{i \in A \\ j = i \pm \hat{y}}} \left[\left(B_{ij}^{A_y}\right)^\dagger B_{ij}^{A_y} - \left(A_{ij}^{A_y}\right)^\dagger A_{ij}^{A_y} - \frac{1}{4}n_{i,A}\right]$$

$$+ J_1 \sum_{\substack{i \in B \\ j = i \pm \hat{x}}} \left[\left(B_{ij}^{B_x}\right)^\dagger B_{ij}^{B_x} - \left(A_{ij}^{B_x}\right)^\dagger A_{ij}^{B_x} - \frac{1}{4}n_{i,B}\right]$$

$$+ J_1 \sum_{\substack{i \in B \\ j = i \pm \hat{y}}} \left[\left(B_{ij}^{B_y}\right)^\dagger B_{ij}^{B_y} - \left(A_{ij}^{B_y}\right)^\dagger A_{ij}^{B_y} - \frac{1}{4}n_{i,B}\right]$$

$$+ J_2 \sum_{\substack{i \in A \\ j \text{nnn} i}} \left[\left(B_{ij}^{2,A}\right)^\dagger B_{ij}^{2,A} - \left(A_{ij}^{2,A}\right)^\dagger A_{ij}^{2,A} - \frac{1}{4}n_{i,A}\right]$$

$$+ J_2 \sum_{\substack{i \in B \\ j \text{nnn} i}} \left[\left(B_{ij}^{2,B}\right)^\dagger B_{ij}^{2,B} - \left(A_{ij}^{2,B}\right)^\dagger A_{ij}^{2,B} - \frac{1}{4}n_{i,B}\right] \tag{28}$$

$$- K \sum_{i \in A} S_{iz}^2 - K \sum_{i \in B} S_{iz}^2 + \lambda_A \sum_{i \in A} \left(n_{i,A} - \kappa\right)$$

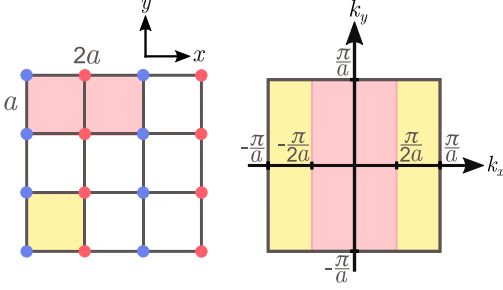$$+ \lambda_B \sum_{i \in B} \left(n_{i,B} - \kappa\right).$$

FIG. 5. Unit cell and Brillouin zone for the full lattice and the sublattices.

In order to make progress, we introduce the mean-field decoupling from Eq. (9), and choose an Ansatz for the mean-field parameters that will produce a stripe phase,

$$\langle A_{ij}^{A_x} \rangle = -\langle A_{ij}^{B_x} \rangle \equiv \mathcal{A}_{\delta_x}, \tag{29a}$$

$$\langle B_{ij}^{A_x} \rangle = \langle B_{ij}^{B_x} \rangle = 0, \tag{29b}$$

$$\langle A_{ij}^{A_y} \rangle = \langle A_{ij}^{B_y} \rangle = 0, \tag{29c}$$

$$\langle B_{ij}^{A_y} \rangle = \langle B_{ij}^{B_y} \rangle \equiv \mathcal{B}_{\delta_y}, \tag{29d}$$

$$\langle B_{ij}^{2,A} \rangle = \langle B_{ij}^{2,B} \rangle = 0, \tag{29e}$$

$$\langle A_{ij}^{2,A} \rangle = -\langle A_{ij}^{2,B} \rangle \equiv \mathcal{A}_{\delta_2}. \tag{29f}$$

As before, we take $\lambda_A = \lambda_B \equiv \lambda$ and treat the easy-axis anisotropy terms in the same mean-field fashion as for the Néel state. Next, we introduce Fourier transformations for the boson operators,

$$a_{i\sigma} = \frac{1}{\sqrt{N_A}} \sum_{k \in \square} e^{ik \cdot r_i} a_{k\sigma}, \tag{30a}$$

$$b_{i\sigma} = \frac{1}{\sqrt{N_B}} \sum_{k \in \square} e^{ik \cdot r_i} b_{k\sigma}, \tag{30b}$$

where the sum over momentum covers the reduced Brillouin zone of the sublattices $\square$, as displayed in Fig. 5. The Hamiltonian then takes the form,

$$
H_{\mathrm{AFMI}}^{\mathrm{Stripe}} = 2N_A \Big[J_1 \sum_{\delta_x} (\mathcal{A}_{\delta_x})^2 - J_1 \sum_{\delta_y} (\mathcal{B}_{\delta_y})^2
$$
$$
+ J_2 \sum_{\delta_2} (\mathcal{A}_{\delta_2})^2 \Big] - 2N_A \kappa \lambda + KN_A (m_A^2 + m_B^2)
$$
$$
+ \Big[\lambda - \frac{1}{4}(J_1 z_1 + J_2 z_2) \Big] \sum_{\substack{k \in \square \\ \sigma}} \big(a_{k\sigma}^\dagger a_{k\sigma} + b_{k\sigma}^\dagger b_{k\sigma} \big)
$$
$$
- Km_A \sum_{\substack{k \in \square \\ \sigma}} \sigma\, a_{k\sigma}^\dagger a_{k\sigma} + Km_B \sum_{\substack{k \in \square \\ \sigma}} \sigma\, b_{k\sigma}^\dagger b_{k\sigma}
$$

$$
+ \sum_{\substack{k \in \square \\ \sigma}} \gamma_k^{B_y} \big(a_{k\sigma}^\dagger a_{k\sigma} + b_{k\sigma} b_{k\sigma}^\dagger \big)
$$
$$
- \sum_{\substack{k \in \square \\ \sigma}} \big(\gamma_k^{A_x} + \gamma_k^{A_2} \big)\big(b_{k\sigma}^\dagger a_{-k\sigma}^\dagger + a_{k\sigma} b_{-k\sigma} \big), \tag{31}
$$

where we have defined

$$\gamma_k^{A_x} = J_1 \sum_{\delta_x} \mathcal{A}_{\delta_x} \cos(k \cdot \delta_x), \tag{32a}$$

$$\gamma_k^{B_y} = J_1 \sum_{\delta_y} \mathcal{B}_{\delta_y} \cos(k \cdot \delta_y), \tag{32b}$$

$$\gamma_k^{A_2} = J_2 \sum_{\delta_2} \mathcal{A}_{\delta_2} \cos(k \cdot \delta_2). \tag{32c}$$

The sums over nearest neighbors still cover both positive and negative directions. We then redefine λ as we did for the Néel phase and exclude constant terms not involving mean-field parameters. Splitting up the Hamiltonian in three parts $H_{\mathrm{AFMI}}^{\mathrm{Stripe}} = E_0 + H^\uparrow + H^\downarrow$, we write

$$
E_0 = 2N_A \Big[J_1 \sum_{\delta_x} (\mathcal{A}_{\delta_x})^2 - J_1 \sum_{\delta_y} (\mathcal{B}_{\delta_y})^2 + J_2 \sum_{\delta_2} (\mathcal{A}_{\delta_2})^2 \Big]
$$
$$
- 2N_A \lambda(\kappa + 1) + KN_A(m_A^2 + m_B^2), \tag{33}
$$

$$
H^\sigma = \sum_{k \in \square} \big(\lambda + \gamma_k^{B_y} - \sigma Km_A \big) a_{k\sigma}^\dagger a_{k\sigma}
$$
$$
+ \sum_{k \in \square} \big(\lambda + \gamma_k^{B_y} + \sigma Km_B \big) b_{k\sigma} b_{k\sigma}^\dagger
$$
$$
- \sum_{k \in \square} \big(\gamma_k^{A_x} + \gamma_k^{A_2} \big)\big(b_{k\sigma}^\dagger a_{-k\sigma}^\dagger + a_{k\sigma} b_{-k\sigma} \big). \tag{34}
$$

As in the Néel case, the Bogoliubov transformation of Eq. (16) diagonalizes the Hamiltonian, where $\theta_{k\sigma}$ this time is given by

$$
\tanh(2\theta_{k\sigma}) = \frac{\gamma_k^{A_x} + \gamma_k^{A_2}}{\lambda + \gamma_k^{B_y} + \sigma \frac{K}{2}(m_B - m_A)}. \tag{35}
$$

Taking $m_B = -m_A$, we obtain the following expression for the diagonalized Hamiltonian:

$$
H_{\mathrm{AFMI}}^{\mathrm{Stripe}} = E_0' + \sum_{\substack{k \in \square \\ \sigma}} \omega_{k\sigma} \big(\alpha_{k\sigma}^\dagger \alpha_{k\sigma} + \beta_{k\sigma}^\dagger \beta_{k\sigma} \big), \tag{36}
$$

where

$$
\omega_{k\sigma} = \sqrt{\big(\lambda + \gamma_k^{B_y} - \sigma Km_A \big)^2 - \big(\gamma_k^{A_x} + \gamma_k^{A_2} \big)^2}, \tag{37}
$$

and $E_0' = E_0 + \sum_{k\sigma} \omega_{k\sigma}$. Minimizing the free energy with respect to $\mathcal{A}_{\delta_x}$, $\mathcal{A}_{\delta_2}$, $\mathcal{B}_{\delta_y}$, λ, and m_A, we obtain

$$
\mathcal{A}_{\delta_x} = \frac{1}{2N} \sum_{\substack{k \in \square \\ \sigma}} \frac{\big(\gamma_k^{A_x} + \gamma_k^{A_2} \big)}{\omega_{k\sigma}} \big(1 + 2n_{k\sigma} \big) \cos(k \cdot \delta_x), \tag{38a}
$$

$$\mathcal{A}_{\delta_2} = \frac{1}{2N} \sum_{\substack{k \in \square \\ \sigma}} \frac{\left(\gamma_k^{A_x} + \gamma_k^{A_2}\right)}{\omega_{k\sigma}} (1 + 2n_{k\sigma}) \cos(k \cdot \delta_2), \quad (38b)$$

$$\mathcal{B}_{\delta_y} = \frac{1}{2N} \sum_{\substack{k \in \square \\ \sigma}} \frac{\left(\lambda + \gamma_k^{B_y} - \sigma K m_A\right)}{\omega_{k\sigma}} (1 + 2n_{k\sigma}) \cos(k \cdot \delta_y), \quad (38c)$$

$$\bar{\kappa} = \frac{1}{2N} \sum_{\substack{k \in \square \\ \sigma}} \frac{\left(\lambda + \gamma_k^{B_y} - \sigma K m_A\right)}{\omega_{k\sigma}} (1 + 2n_{k\sigma}), \quad (38d)$$

$$m_A = \frac{1}{2N} \sum_{\substack{k \in \square \\ \sigma}} \frac{\sigma\left(\lambda + \gamma_k^{B_y} - \sigma K m_A\right)}{\omega_{k\sigma}} (1 + 2n_{k\sigma}). \quad (38e)$$

Here, we have once again defined $\bar{\kappa} = \frac{1}{2}(\kappa + 1)$. For a stripe-type state with $m_A > 0$, we will have condensation of ↑-bosons with $k = 0$, and we then need $|\lambda + \gamma_0^{B_y} - K m_A| = |\gamma_0^{A_x} + \gamma_0^{A_2}|$. The mean-field parameters $\mathcal{A}_{\delta_x}$ and $\mathcal{A}_{\delta_2}$ will be assumed to be positive. At zero temperature, we once again only get contributions from $n_{k\sigma}$ from the condensate. We then define $\zeta_{k\sigma} = \gamma_0^{A_x} + \gamma_0^{A_2} - \gamma_0^{B_y} + \gamma_k^{B_y} + 2 K m_A \delta_{\sigma,\downarrow}$, and write

$$\bar{\kappa} = \frac{1}{2N} \sideset{}{'}\sum_{\substack{k \in \square \\ \sigma}} \frac{\zeta_{k\sigma}}{\omega_{k\sigma}} + \frac{1}{N} Q_0, \quad (39a)$$

$$m_A = \frac{1}{2N} \sideset{}{'}\sum_{\substack{k \in \square \\ \sigma}} \frac{\sigma \, \zeta_{k\sigma}}{\omega_{k\sigma}} + \frac{1}{N} Q_0, \quad (39b)$$

$$\mathcal{A}_x = \frac{1}{2N} \sideset{}{'}\sum_{\substack{k \in \square \\ \sigma}} \frac{\left(\gamma_k^{A_x} + \gamma_k^{A_2}\right)}{\omega_{k\sigma}} \cos(k_x) + \frac{1}{N} Q_0, \quad (39c)$$

$$\mathcal{A}_2 = \frac{1}{2N} \sideset{}{'}\sum_{\substack{k \in \square \\ \sigma}} \frac{\left(\gamma_k^{A_x} + \gamma_k^{A_2}\right)}{\omega_{k\sigma}} \cos(k_x + k_y) + \frac{1}{N} Q_0, \quad (39d)$$

$$\mathcal{B}_y = \frac{1}{2N} \sideset{}{'}\sum_{\substack{k \in \square \\ \sigma}} \frac{\zeta_{k\sigma}}{\omega_{k\sigma}} \cos(k_y) + \frac{1}{N} Q_0, \quad (39e)$$

where

$$Q_0 = \frac{\left(\gamma_0^{A_x} + \gamma_0^{A_2}\right)}{\omega_{0\uparrow}} \left(n_{0\uparrow} + \frac{1}{2}\right), \quad (40)$$

and we have taken $\mathcal{A}_x \equiv \mathcal{A}_{\delta_x}$, $\mathcal{A}_2 \equiv \mathcal{A}_{\delta_2}$, and $\mathcal{B}_y \equiv \mathcal{B}_{\delta_y}$. We can then once again eliminate Q_0,

$$\tilde{Q}_0 \equiv \frac{1}{N} Q_0 = \bar{\kappa} - \frac{1}{2N} \sideset{}{'}\sum_{k\sigma} \frac{\zeta_{k\sigma}}{\omega_{k\sigma}}, \quad (41)$$
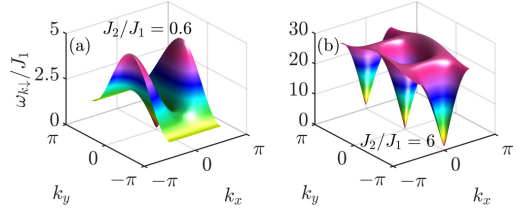
FIG. 6. Schwinger boson dispersion relations $\omega_{k\sigma}$ for $K = 0.001 J_1$, $S = 1$, and $\sigma = \downarrow$. The value for J_2 varies between the two subfigures.

and obtain the equations,

$$m_A = \bar{\kappa} - \frac{1}{N} \sideset{}{'}\sum_{k \in \square} \frac{\zeta_{k\downarrow}}{\omega_{k\downarrow}}, \quad (42a)$$

$$\mathcal{A}_x = \bar{\kappa} + \frac{1}{2N} \sideset{}{'}\sum_{\substack{k \in \square \\ \sigma}} \frac{\left(\gamma_k^{A_x} + \gamma_k^{A_2}\right) \cos(k_x) - \zeta_{k\sigma}}{\omega_{k\sigma}}, \quad (42b)$$

$$\mathcal{A}_2 = \bar{\kappa} + \frac{1}{2N} \sideset{}{'}\sum_{\substack{k \in \square \\ \sigma}} \frac{\left(\gamma_k^{A_x} + \gamma_k^{A_2}\right) \cos(k_x + k_y) - \zeta_{k\sigma}}{\omega_{k\sigma}}, \quad (42c)$$

$$\mathcal{B}_y = \bar{\kappa} + \frac{1}{2N} \sideset{}{'}\sum_{\substack{k \in \square \\ \sigma}} \frac{\zeta_{k\sigma}}{\omega_{k\sigma}} \left[\cos(k_y) - 1\right]. \quad (42d)$$

In the thermodynamic limit, we can then convert the sums into integrals and solve the coupled set of equations numerically.

As for the Néel phase, we present dispersion relations and coherence factors for values of J_2/J_1 deep into the stripe phase and close to the transition to the other magnetic phase. These results are displayed in Figs. 6 and 7. In addition, we also explore in Fig. 8 how the mean-field parameters depend on J_2/J_1 for the two phases. Notably, the factor $\tilde{Q}_0$, which is closely related to the sublattice magnetization, decreases towards the phase transition and is reduced more on the Néel side of the transition than on the stripe side. This factor will show up later in the effective electron-electron interaction potential.
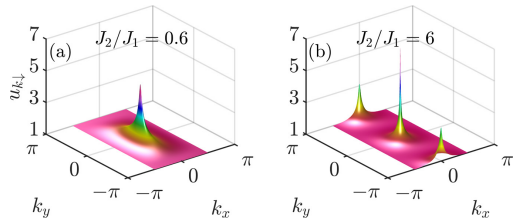

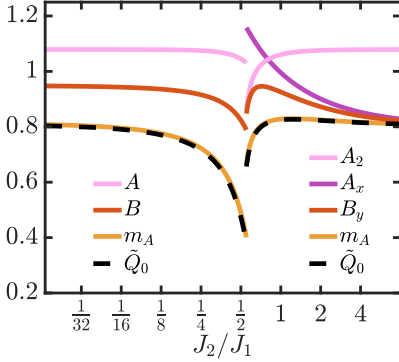FIG. 7. Schwinger boson coherence factors $u_{k\sigma}$ for $K = 0.001 J_1$, $S = 1$, and $\sigma = \downarrow$.

FIG. 8. Mean-field parameters for the Néel and stripe phase for $K/J_1 = 0.001$ and $S = 1$. The transition between the two phases is found to take place around $J_2/J_1 = 0.549$.
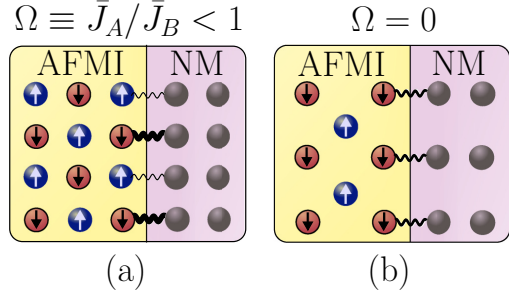

FIG. 9. (a) Illustration of our model where the coupling to the two sublattices is allowed to differ. The coupling asymmetry is parametrized by Ω. (b) Shown is an uncompensated interface, where only one of the two sublattices is present, producing a coupling corresponding to $\Omega = 0$.

IV. COUPLING TO THE NM

When considering the coupling to the normal metal (NM), we will treat both the Néel phase and stripe phase simultaneously as the calculation is identical for both phases. It should then be understood that the expressions for the factor $\tilde{Q}_0$, the Schwinger boson energies $\omega_{k\sigma}$, and the Schwinger boson coherence factors $u_{k\sigma}$, $v_{k\sigma}$, depend on the magnetic phase.

Through a Fourier transformation, the NM Hamiltonian is brought on diagonal form,

$$H_{\text{NM}} = \sum_{\substack{k \in \square \\ \sigma}} \epsilon_k c^\dagger_{k\sigma} c_{k\sigma}, \qquad (43)$$

with

$$\epsilon_k = -t z_1 \gamma_k - \mu. \qquad (44)$$

Here, the sum over momentum covers the Brillouin zone of the full lattice $\square$ and the number of nearest neighbors z_1 is the same as in the AFMI. In addition, the NM is exchange coupled to the two sublattices of the antiferromagnet, $H_{\text{int}} = H_{\text{int}}^{(A)} + H_{\text{int}}^{(B)}$,

$$H_{\text{int}}^{(A)} = -2\bar{J}\,\Omega \sum_{i \in A} (a^\dagger_{i\uparrow} a_{i\downarrow} c^\dagger_{i\downarrow} c_{i\uparrow} + a^\dagger_{i\downarrow} a_{i\uparrow} c^\dagger_{i\uparrow} c_{i\downarrow})$$
$$- \bar{J}\,\Omega \sum_{i \in A\sigma} \sigma c^\dagger_{i\sigma} c_{i\sigma} (a^\dagger_{i\uparrow} a_{i\uparrow} - a^\dagger_{i\downarrow} a_{i\downarrow}), \qquad (45)$$

$$H_{\text{int}}^{(B)} = 2\bar{J} \sum_{i \in B} (b^\dagger_{i\uparrow} b_{i\downarrow} c^\dagger_{i\downarrow} c_{i\uparrow} + b^\dagger_{i\downarrow} b_{i\uparrow} c^\dagger_{i\uparrow} c_{i\downarrow})$$
$$+ \bar{J} \sum_{\substack{i \in B \\ \sigma}} \sigma c^\dagger_{i\sigma} c_{i\sigma} (b^\dagger_{i\uparrow} b_{i\uparrow} - b^\dagger_{i\downarrow} b_{i\downarrow}). \qquad (46)$$

Here, we have defined $\Omega \equiv \bar{J}_A/\bar{J}_B$, as visualized in Fig. 9, and $\bar{J} \equiv \bar{J}_B$. For magnetic ordering in the z direction in spin space, the z component of the coupling gives rise to a staggered magnetic exchange field. For asymmetric coupling to

the two sublattices, the NM electrons are then exposed to a net magnetic field, which will influence the superconductivity. For an in-plane magnetic field, the dominant effect is the Pauli pair-breaking mechanism, rather than the orbital effect [43]. As described in Ref. [6], this paramagnetic effect, arising from the z component of the coupling, is not expected to destroy the superconductivity in the considered system, and can be counteracted by, e.g., applying an oppositely directed external magnetic field [44]. The effect of the z component of the coupling will therefore be neglected in the following.

We then perform Fourier transformations, where the electron operators are transformed as

$$c_{i\sigma} = \frac{1}{\sqrt{N}} \sum_{k \in \text{RBZ}} (c_{k\sigma} e^{i k \cdot r_i} + c_{k+G,\sigma} e^{i(k+G)\cdot r_i}), \qquad (47)$$

where $G \equiv \frac{\pi(\hat{x}+\hat{y})}{a}$ for the Néel phase and $G \equiv \frac{\pi \hat{x}}{a}$ for the stripe phase. The sum over momentum covers the reduced Brillouin zone (RBZ) of the sublattices. Umklapp processes where the momentum of the outgoing electron is shifted by a reciprocal lattice vector of the sublattices, will arise due to the electrons and Schwinger bosons living in different Brillouin zones [6,7]. These processes are expected to be important for induced superconductivity in the case of an AFMI coupled to a NM close to half-filling [5]. Away from half-filling, the Umklapp processes are, however, of less importance. In addition, for a real uncompensated interface, the NM will be lattice matched with the AFMI sublattice it is coupled to, removing the Umklapp processes from the coupling. The Umklapp processes will therefore not be included in our treatment of the system.

We are now left with the coupling terms,

$$H_{\text{int}}^{(A)} = -\frac{2\bar{J}\,\Omega}{N} \sum_{q \in \square} \sum_{\substack{k k' \\ \in \text{RBZ}}} (a^\dagger_{k\uparrow} a_{k'\downarrow} c^\dagger_{q\downarrow} c_{k+q-k'\uparrow} + \text{H.c.}),$$

$$(48)$$

$$H_{\text{int}}^{(B)} = \frac{2\bar{J}}{N} \sum_{q \in \square} \sum_{\substack{kk' \\ \in \text{RBZ}}} (b_{k\downarrow}^{\dagger} b_{k'\uparrow} c_{q\downarrow}^{\dagger} c_{k+q-k'\uparrow} + \text{H.c.}).$$

$$(49)$$

Expressing the the sublattice Schwinger boson operators in terms of the boson operators that diagonalized the AFMI Hamiltonian, we have the final expression for the electron-boson coupling,

$$H_{\text{int}}^{(A)} = -\frac{2\bar{J}\,\Omega}{N} \sum_{q \in \square} \sum_{\substack{kk' \\ \in \text{RBZ}}} [(u_{k\uparrow}\alpha_{k\uparrow}^{\dagger} - v_{k\uparrow}\beta_{-k\uparrow})$$

$$\times (u_{k'\downarrow}\alpha_{k'\downarrow} - v_{k'\downarrow}\beta_{-k'\downarrow}^{\dagger})c_{q\downarrow}^{\dagger} c_{k+q-k'\uparrow} + \text{H.c.}], \quad (50)$$

$$H_{\text{int}}^{(B)} = \frac{2\bar{J}}{N} \sum_{q \in \square} \sum_{\substack{kk' \\ \in \text{RBZ}}} \left[(v_{k\downarrow}\alpha_{-k\downarrow} - u_{k\downarrow}\beta_{k\downarrow}^{\dagger}) \right.$$

$$\left. \times (v_{k'\uparrow}\alpha_{-k'\uparrow}^{\dagger} - u_{k'\uparrow}\beta_{k'\uparrow})c_{q\downarrow}^{\dagger} c_{k+q-k'\uparrow} + \text{H.c.} \right]. \quad (51)$$

In the next section, we will derive effective electron-electron interactions, mediated by Schwinger bosons, arising from this electron-boson coupling.

V. EFFECTIVE INTERACTION

We now perform a Schrieffer-Wolff transformation [45] in order to integrate out the boson operators and obtain an effective theory of interacting electrons. As we have two boson operators in the initial electron-boson coupling, we will end up with electron-electron scattering processes where there are still two boson operators present. The remaining pair of boson operators will be replaced by its ground-state expectation value in order to obtain an effective theory of interacting electrons. We define $H = H_0 + \eta H_1$ with

$$H_0 \equiv E_0' + \sum_{\substack{k \in \text{RBZ} \\ \sigma}} \omega_{k\sigma}(\alpha_{k\sigma}^{\dagger}\alpha_{k\sigma} + \beta_{k\sigma}^{\dagger}\beta_{k\sigma})$$

$$+ \sum_{\substack{k \in \square \\ \sigma}} \epsilon_k c_{k\sigma}^{\dagger} c_{k\sigma}, \quad (52)$$

and

$$\eta H_1 = \eta H_1^{(A)} + \eta H_1^{(B)} \equiv H_{\text{int}}^{(A)} + H_{\text{int}}^{(B)}. \quad (53)$$

We then perform a canonical transformation,

$$H' = e^{-\eta S} H e^{\eta S} = H + \eta[H, S] + \frac{\eta^2}{2!}[[H, S], S] + \mathcal{O}(\eta^3)$$

$$= H_0 + \eta(H_1 + [H_0, S]) + \eta^2 \left([H_1, S] + \frac{1}{2}[[H_0, S], S] \right)$$

$$+ \mathcal{O}(\eta^3), \quad (54)$$

where we choose $\eta S = \eta S^{(A)} + \eta S^{(B)}$ such that we have

$$\eta H_1^{(L)} + [H_0, \eta S^{(L)}] = 0. \quad (55)$$

The result is then

$$H' = H_0 + \frac{1}{2} \sum_{LL'} [\eta H_1^{(L)}, \eta S^{(L')}] + \mathcal{O}(\eta^3), \quad (56)$$

where $L \in \{A, B\}$. We then make appropriate choices for ηS^A and ηS^B [46], compute the commutators, consider that we have condensation of $\uparrow$-bosons, and restrict ourselves to BCS-type scattering processes where the two incoming, as well as outgoing, electrons have opposite momenta. See Appendix for details. The pairing Hamiltonian then takes the form,

$$H_{\text{pair}} = \sum_{kk'} V_{kk'} c_{k\uparrow}^{\dagger} c_{-k\downarrow}^{\dagger} c_{-k'\downarrow} c_{k'\uparrow}, \quad (57)$$

where

$$V_{kk'} = -V^2 \tilde{Q}_0 \frac{2\omega_{k+k'\downarrow}}{(\epsilon_{k'} - \epsilon_k)^2 - \omega_{k+k'\downarrow}^2} A(k + k', \Omega)$$

$$- \frac{V^2}{N} \sum_{h \in \text{RBZ}}' B(k + k' + h, h, \Omega) \quad (58)$$

$$\times \frac{2(\omega_{k+k'+h\uparrow} + \omega_{h\downarrow})}{(\epsilon_{k'} - \epsilon_k)^2 - (\omega_{k+k'+h\uparrow} + \omega_{h\downarrow})^2},$$

and we have defined

$$A(q, \Omega) = \frac{1}{2}(\Omega^2 + 1)(u_{q\downarrow}^2 + v_{q\downarrow}^2) - 2\Omega u_{q\downarrow}v_{q\downarrow}, \quad (59)$$

as well as

$$B(q, h, \Omega) = \frac{1}{2}(\Omega^2 + 1)(u_{q\uparrow}^2 v_{h\downarrow}^2 + v_{q\uparrow}^2 u_{h\downarrow}^2)$$

$$- 2\Omega u_{q\uparrow}v_{h\downarrow}v_{q\uparrow}u_{h\downarrow}. \quad (60)$$

Here, we have introduced $V \equiv 2\bar{J}/\sqrt{N}$. The two momenta in the sum in Eq. (57) are restricted such that the separation between them is limited to a momentum living in the reduced Brillouin zone of the sublattices. The A factor is the same function as in Ref. [6], but due to different choices for the sign of the coherence factors, the sign in front of the $u_{q\downarrow}v_{q\downarrow}$ term is negative instead of positive in this case. Both coherence factors are, in this case, positive for small momenta for both the Néel and stripe phase. For $\Omega = 0$, the A factor then grows large, while for $\Omega = 1$, there is a near cancellation between the positive and negative contributions to the A factor. The interaction strength is therefore enhanced in the case of asymmetric coupling to the two sublattices, just like in Ref. [6]. The second part of the interaction potential includes a sum over momenta that covers the reduced Brillouin zone of the sublattices, apart from the point $h = -k - k'$. This term displays similar behavior as the first term in the interaction potential when Ω is varied. Importantly, the above expressions are valid for both the Néel and stripe phase, meaning that the previously reported enhancement of the critical temperature when coupling asymmetrically to the two sublattices of the AFMI should be expected also for the stripe phase.

Examining the first part of the interaction potential, where the $\uparrow$-bosons carry zero momentum, we see that the properties of the $\uparrow$-bosons that condense have been absorbed into

the prefactor $\tilde{Q}_0$. Comparing with the earlier obtained spin-wave result, it is then clear that the magnon energies and coherence factors from Ref. [6] have been replaced by the energies and coherence factors of Schwinger bosons with spin $\sigma = \downarrow$. These ↓-bosons have been gapped by the easy-axis anisotropy, ensuring ordering in the z direction. Taking the limit of $K \to 0$, the coherence factors in $A(\mathbf{q}, \Omega)$ diverge, producing a divergent interaction potential. This is consistent with the Holstein-Primakoff result in the limit of zero easy-axis anisotropy [6]. In order to treat the possibility of superconductivity, at least within a weak-coupling framework, one should then take finite easy-axis anisotropy. If both the ↑- and ↓-bosons had been gapped, as in a gapped spin liquid state, there would be no condensate and the remaining contributions to the interaction potential would be expected to take on a form similar to the current second term involving $B(\mathbf{q}, \mathbf{h}, \Omega)$. In that case, there could, however, also be extra contributions arising from the z component of the interfacial exchange coupling.

Making further comparisons with Ref. [6], the prefactor $V^2 \tilde{Q}_0$ is the same as Eq. (5) in Ref. [6] except that the AFMI spin quantum number S (representing the sublattice magnetization) has been replaced by $\tilde{Q}_0$ which is closely related to the sublattice magnetization m_A. As the sublattice magnetization, and therefore $\tilde{Q}_0$, is reduced by frustration, this replacement represents a correction that can strongly influence how the superconductivity depends on the introduction of frustration. In addition, the Schwinger boson energies and coherence factors also depend on m_A (instead of S), which will depend on the value of J_2 in this treatment of the system.

VI. GAP EQUATION

Performing a standard weak-coupling treatment of the superconducting instability [47], both terms in the interaction potential are found to be attractive for $S_z = 0$ spin-triplet pairing [6], with gap function,

$$\Delta_{\mathbf{k}} = -\sum_{\mathbf{k}'} V_{\mathbf{k}\mathbf{k}', O(\mathbf{k})} \langle c_{-\mathbf{k}'\uparrow} c_{\mathbf{k}'\downarrow} + c_{-\mathbf{k}'\downarrow} c_{\mathbf{k}'\uparrow} \rangle / 2. \quad (61)$$

Here $V_{\mathbf{k}\mathbf{k}', O(\mathbf{k})} = \frac{1}{2}(V_{\mathbf{k}\mathbf{k}'} - V_{-\mathbf{k},\mathbf{k}'})$ is the part of the effective interaction potential that is odd in momentum. The origin of the spin-triplet pairing is the spin-flip nature of the electron-boson scattering processes. When combining two electron-boson scattering processes to an effective pairing potential, the spin flips produce an operator ordering of the type $c_{\uparrow}^{\dagger} c_{\downarrow} c_{\uparrow}^{\dagger} c_{\uparrow}$, instead of $c_{\uparrow}^{\dagger} c_{\uparrow} c_{\downarrow}^{\dagger} c_{\downarrow}$ which is the case for conventional phonon-mediated singlet pairing. The exchange of the spin indices of the destruction operators, combined with the anticommutation relations of the electrons, introduce a relative minus sign compared with the case of phonon-mediated singlet pairing, meaning that the spin-singlet channel is therefore no longer attractive.

The resulting gap equation takes the form [47],

$$\Delta_{\mathbf{k}} = -\sum_{\mathbf{k}'} V_{\mathbf{k}\mathbf{k}', O(\mathbf{k})} \frac{\Delta_{\mathbf{k}'}}{2 E_{\mathbf{k}'}} \tanh\left(\frac{E_{\mathbf{k}'}}{2 k_B T}\right), \quad (62)$$
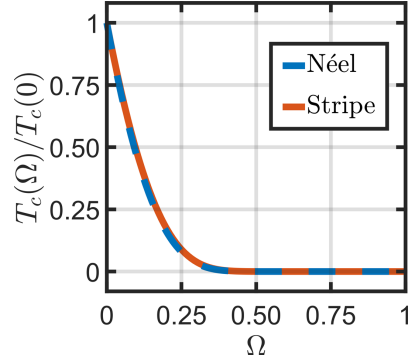

FIG. 10. Superconducting critical temperature T_c presented as a function of the coupling asymmetry parameter Ω for $J_1 = 5$ meV, $K = J_1/4000$, $S = 1$, $t = 0.8$ eV, $\mu = -3.5t$, and $\bar{J} = 13$ meV. The critical temperature has been normalized by its value for $\Omega = 0$ for the Néel phase ($J_2 = 0.5 J_1$) and the stripe phase ($J_2 = 0.6 J_1$), respectively.

where $E_{\mathbf{k}} = \sqrt{\epsilon_{\mathbf{k}}^2 + |\Delta_{\mathbf{k}}|^2}$, k_B is the Boltzmann constant, and T is the temperature. In order to determine the critical temperature, we consider the linearized gap equation and compute a Fermi surface average,

$$\lambda \Delta_{\mathbf{k}} = -D_0 \langle V_{\mathbf{k}\mathbf{k}', O(\mathbf{k})} \Delta_{\mathbf{k}'} \rangle_{\mathbf{k}', \text{FS}}. \quad (63)$$

The critical temperature is then given by [47]

$$k_B T_c = 1.14 \, \omega_c \, e^{-1/\lambda}, \quad (64)$$

where D_0 is the density of states at the Fermi level, ω_c is the boson spectrum cutoff, and the dimensionless coupling constant λ is the largest eigenvalue of the eigenvalue problem in Eq. (63).

The eigenvalue problem can be treated numerically by picking discrete points on the Fermi surface and solving the resulting matrix eigenvalue problem using a linear algebra library [48,49]. The density of states at the Fermi level is obtained from numerical evaluation of the elliptical integral derived in Ref. [50]. The second part of the interaction potential, involving the B factor, is found to have little influence on the dimensionless coupling constant and the critical temperature. Calculating this part of the potential is computationally costly as an integral over the Brillouin zone then needs to be computed for each independent set of momenta $\mathbf{k}$, $\mathbf{k}'$ in Eq. (63). In order to increase the momentum-space resolution, the following results are therefore obtained without the second part of the interaction potential.

VII. RESULTS

The critical temperature as a function of the asymmetry parameter Ω is presented in Fig. 10 for both the Néel and stripe phase. As expected, based on the discussion in Sec. V, the critical temperature rises up when $\Omega \to 0$ (uncompensated interface), as the A factor grows larger. The displayed values for each magnetic phase have been normalized by the critical

temperature corresponding to the same magnetic phase and $\Omega = 0$.

The chemical potential is here tuned to produce a small Fermi surface where the scattering processes close to the Fermi surface involve small momentum transfers, taking advantage of the Schwinger boson coherence factors that grow large for these processes. Increasing the chemical potential, the typical scattering processes become more short wavelength, and the effect of, e.g., the A factor in the interaction potential becomes smaller. Although a larger chemical potential leads to a larger electronic density of states, the result is still a decrease in the critical temperature. On the other hand, while lowering the chemical potential could produce a larger critical temperature, taking the chemical potential too low would challenge the validity of the theory, which, e.g., relies on the Fermi energy being significantly larger than the cutoff on the boson spectrum. Based on the result that an uncompensated interface provides an enhancement of the critical temperature for both magnetic phases, we focus on the case of $\Omega = 0$ in the following.

Next, we investigate how the dimensionless coupling constant and the critical temperature depend on the next-nearest neighbor interaction J_2 in the AFMI. These results are displayed in Fig. 11. For both magnetic phases, we find that approaching the phase transition leads to a larger dimensionless coupling constant and critical temperature. For the Néel phase, the introduction of frustration gives rise to a smaller cutoff on the boson spectrum (Fig. 3), and a smaller sublattice magnetization which leads to a reduction of the prefactor $\tilde{Q}_0$ (Fig. 8) in the interaction potential. On the other hand, the frustration produces larger coherence factors (Fig. 4) and a flatter boson dispersion relation, which enters in the denominator of the interaction potential. The overall effect is that the dimensionless coupling constant increases, which leads to a rise in the critical temperature despite the reduction in the boson spectrum cutoff. In the vicinity of the transition to the stripe phase, the T_c curve becomes flatter as the factor $\tilde{Q}_0$ drops more quickly. For smaller (larger) AFMI spin quantum number S, $\tilde{Q}_0$ will be reduced more (less) dramatically as one approaches the transition point. For the spin $S = 1/2$ case, where the long-range order can vanish for sufficiently strong frustration, the critical temperature resulting from the above calculation will dive down. However, for a three-dimensional system, with stronger tendency of ordering, the magnetization will generally be reduced less than for the two-dimensional model system considered here. The typical result for an actual three-dimensional AFMI with an uncompensated interface (potentially excluding the case of spin-1/2 on a simple cubic lattice [18]), is then expected to be similar to the above result (Fig. 11) where the dimensionless coupling constant increases as one approaches the stripe phase, leading to a higher critical temperature.

For the stripe phase, approaching the transition to the Néel phase, the cutoff on the boson spectrum (Fig. 6) and the factor $\tilde{Q}_0$ (Fig. 8) are once again reduced. In addition, the maximum value of the coherence factors also decreases (Fig. 7), in contrast to the Néel case. This could indicate that the induced electron-electron interactions are becoming weaker, potentially leading to a smaller λ and T_c. It is, however, the case that the region in k space where the coherence factors take
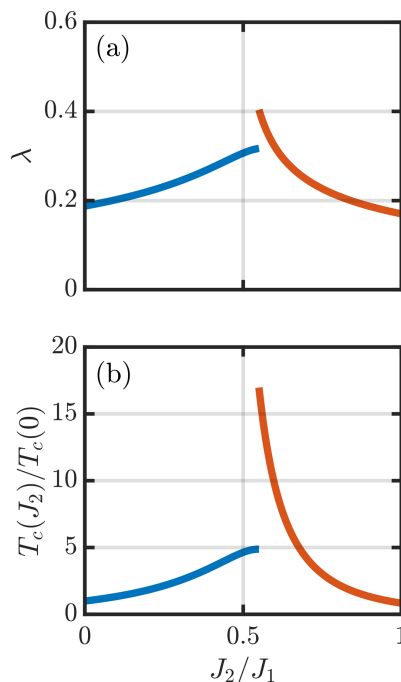

FIG. 11. Dimensionless coupling constant λ (a) and superconducting critical temperature T_c (b) presented as a function of the next-nearest neighbor exchange coupling J_2 in the antiferromagnet for $J_1 = 5$ meV, $K = J_1/4000$, $S = 1$, $t = 0.8$ eV, $\mu = -3.5t$, $\bar{J} = 13$ meV, and $\Omega = 0$.

on large values is stretched out in the direction of the stripes (the k_y direction), followed by a flattening of the dispersion relation in this direction. In order to take advantage of favorable scattering processes in the k_y direction, while keeping the involved electrons on the Fermi surface, the magnitude of the gap function is shifted towards the k_x axis compared to the standard p-wave gap function of the unfrustrated Néel state [6]. More scattering processes with large and moderately large contributions compensate for the reduction, instead of increase, in the maximum value of the coherence factors. The dimensionless coupling constant therefore still grows as one approaches the phase transition. As the sublattice magnetization is more robust for the stripe phase than the Néel phase (Fig. 8), the maximum value of λ actually ends up being slightly higher for the stripe phase due to a larger value for $\tilde{Q}_0$. As the critical temperature is very sensitive to λ, the critical temperature rises up quite dramatically on the stripe side of the transition in our calculation. The main conclusion from the stripe phase is that increasing the fluctuations by approaching the transition to the Néel phase can be favorable for the superconductivity and that the more stable sublattice magnetization of the stripe phase can be an advantage.

VIII. SUMMARY

We have investigated superconductivity in a normal metal, induced by an interfacial coupling to an antiferromagnetic insulator. We have shown that next-nearest neighbor frustration in a Néel antiferromagnet with an uncompensated interface can lead to an enhancement of the superconducting critical temperature. Moreover, coupling to an uncompensated antiferromagnetic interface is found to be favorable for the superconductivity regardless of whether the antiferromagnet is in a Néel phase or a stripe phase. For the stripe phase, arising from large next-nearest neighbor interaction in the antiferromagnet, we find that amplifying the magnetic fluctuations by approaching the transition to the Néel phase, once again, can lead to a rise in the critical temperature.

ACKNOWLEDGMENTS

APPENDIX: DERIVATION OF THE EFFECTIVE INTERACTION

In order to obtain an effective theory of interacting electrons, we choose

$$
\eta S^{(A)} = -\frac{2\bar{J}\,\Omega}{N} \sum_{q \in \square} \sum_{\substack{kk' \\ \in \mathrm{RBZ}}} \Big[\big(x_{k,k'q}^{\alpha,\uparrow\downarrow} u_{k\uparrow} u_{k'\downarrow} \alpha_{k\uparrow}^{\dagger} \alpha_{k'\downarrow}
$$
$$
+ y_{k,k'q}^{\beta,\downarrow\uparrow} v_{k\uparrow} v_{k'\downarrow} \beta_{-k'\downarrow}^{\dagger} \beta_{-k\uparrow} - z_{k,k'q}^{-,\uparrow\downarrow} u_{k\uparrow} v_{k'\downarrow} \alpha_{k\uparrow}^{\dagger} \beta_{-k'\downarrow}^{\dagger}
$$
$$
- w_{k,k'q}^{+,\downarrow\uparrow} v_{k\uparrow} u_{k'\downarrow} \alpha_{k'\downarrow} \beta_{-k\uparrow} \big) c_{q\downarrow}^{\dagger} c_{k+q-k'\uparrow}
$$
$$
+ \big(x_{k,k'q}^{\alpha,\downarrow\uparrow} u_{k\downarrow} u_{k'\uparrow} \alpha_{k\downarrow}^{\dagger} \alpha_{k'\uparrow} + y_{k,k'q}^{\beta,\uparrow\downarrow} v_{k\downarrow} v_{k'\uparrow} \beta_{-k'\uparrow}^{\dagger} \beta_{-k\downarrow}
$$
$$
- z_{k,k'q}^{-,\downarrow\uparrow} u_{k\downarrow} v_{k'\uparrow} \alpha_{k\downarrow}^{\dagger} \beta_{-k'\uparrow}^{\dagger}
$$
$$
- w_{k,k'q}^{+,\uparrow\downarrow} v_{k\downarrow} u_{k'\uparrow} \alpha_{k'\uparrow} \beta_{-k\downarrow} \big) c_{q\uparrow}^{\dagger} c_{k+q-k'\downarrow} \Big],
$$

(A1)

and

$$
\eta S^{(B)} = \frac{2\bar{J}}{N} \sum_{q \in \square} \sum_{\substack{kk' \\ \in \mathrm{RBZ}}} \Big[\big(y_{k,k'q}^{\alpha,\uparrow\downarrow} v_{k\downarrow} v_{k'\uparrow} \alpha_{-k'\uparrow}^{\dagger} \alpha_{-k\downarrow}
$$
$$
+ x_{k,k'q}^{\beta,\downarrow\uparrow} u_{k\downarrow} u_{k'\uparrow} \beta_{k\downarrow}^{\dagger} \beta_{k'\uparrow} - z_{k,k'q}^{+,\downarrow\uparrow} v_{k\downarrow} u_{k'\uparrow} \alpha_{-k\downarrow} \beta_{k'\uparrow}
$$
$$
- w_{k,k'q}^{-,\uparrow\downarrow} u_{k\downarrow} v_{k'\uparrow} \alpha_{-k'\uparrow}^{\dagger} \beta_{k\downarrow}^{\dagger} \big) c_{q\downarrow}^{\dagger} c_{k+q-k'\uparrow}
$$
$$
+ \big(y_{k,k'q}^{\alpha,\downarrow\uparrow} v_{k\uparrow} v_{k'\downarrow} \alpha_{-k'\downarrow}^{\dagger} \alpha_{-k\uparrow} + x_{k,k'q}^{\beta,\uparrow\downarrow} u_{k\uparrow} u_{k'\downarrow} \beta_{k\uparrow}^{\dagger} \beta_{k'\downarrow}
$$
$$
- z_{k,k'q}^{+,\uparrow\downarrow} v_{k\uparrow} u_{k'\downarrow} \alpha_{-k\uparrow} \beta_{k'\downarrow}
$$
$$
- w_{k,k'q}^{-,\downarrow\uparrow} u_{k\uparrow} v_{k'\downarrow} \alpha_{-k'\downarrow}^{\dagger} \beta_{k\uparrow}^{\dagger} \big) c_{q\uparrow}^{\dagger} c_{k+q-k'\downarrow} \Big],
$$

(A2)

where

$$
x_{k,k'q}^{\alpha,\uparrow\downarrow} = \frac{1}{\epsilon_{k+q-k'} - \epsilon_q + \omega_{k'\downarrow\alpha} - \omega_{k\uparrow\alpha}}, \tag{A3a}
$$

$$
y_{k,k'q}^{\beta,\downarrow\uparrow} = \frac{1}{\epsilon_{k+q-k'} - \epsilon_q + \omega_{k\uparrow\beta} - \omega_{k'\downarrow\beta}}, \tag{A3b}
$$

$$
z_{k,k'q}^{-,\uparrow\downarrow} = \frac{1}{\epsilon_{k+q-k'} - \epsilon_q - \omega_{k\uparrow\alpha} - \omega_{k'\downarrow\beta}}, \tag{A3c}
$$

$$
w_{k,k'q}^{+,\downarrow\uparrow} = \frac{1}{\epsilon_{k+q-k'} - \epsilon_q + \omega_{k'\downarrow\alpha} + \omega_{k\uparrow\beta}}, \tag{A3d}
$$

and, e.g.,

$$
z_{k,k'q}^{+,\uparrow\downarrow} = \frac{1}{\epsilon_{k+q-k'} - \epsilon_q + \omega_{k\uparrow\alpha} + \omega_{k'\downarrow\beta}}, \tag{A4a}
$$

$$
w_{k,k'q}^{-,\downarrow\uparrow} = \frac{1}{\epsilon_{k+q-k'} - \epsilon_q - \omega_{k'\downarrow\alpha} - \omega_{k\uparrow\beta}}. \tag{A4b}
$$

Prior to commencing a calculation of the commutators, it turns out to be advantageous to further split up the terms in the interaction Hamiltonian,

$$
H_{\mathrm{int}}^{(L)} = H_{\mathrm{int}}^{(L,+)} + H_{\mathrm{int}}^{(L,-)}, \tag{A5}
$$

where

$$
H_{\mathrm{int}}^{(A,+)} = -\frac{2\bar{J}\,\Omega}{N} \sum_{q \in \square} \sum_{\substack{kk' \\ \in \mathrm{RBZ}}} \big(u_{k\uparrow} u_{k'\downarrow} \alpha_{k\uparrow}^{\dagger} \alpha_{k'\downarrow}
$$
$$
+ v_{k\uparrow} v_{k'\downarrow} \beta_{-k\uparrow} \beta_{-k'\downarrow}^{\dagger} - u_{k\uparrow} v_{k'\downarrow} \alpha_{k\uparrow}^{\dagger} \beta_{-k'\downarrow}^{\dagger}
$$
$$
- v_{k\uparrow} u_{k'\downarrow} \beta_{-k\uparrow} \alpha_{k'\downarrow} \big) c_{q\downarrow}^{\dagger} c_{k+q-k'\uparrow},
$$

(A6)

$$
H_{\mathrm{int}}^{(A,-)} = -\frac{2\bar{J}\,\Omega}{N} \sum_{q \in \square} \sum_{\substack{kk' \\ \in \mathrm{RBZ}}} \big(u_{k\downarrow} u_{k'\uparrow} \alpha_{k\downarrow}^{\dagger} \alpha_{k'\uparrow}
$$
$$
+ v_{k\downarrow} v_{k'\uparrow} \beta_{-k\downarrow} \beta_{-k'\uparrow}^{\dagger} - u_{k\downarrow} v_{k'\uparrow} \alpha_{k\downarrow}^{\dagger} \beta_{-k'\uparrow}^{\dagger}
$$
$$
- v_{k\downarrow} u_{k'\uparrow} \beta_{-k\downarrow} \alpha_{k'\uparrow} \big) c_{q\uparrow}^{\dagger} c_{k+q-k'\downarrow},
$$

(A7)

$$
H_{\mathrm{int}}^{(B,+)} = \frac{2\bar{J}}{N} \sum_{q \in \square} \sum_{\substack{kk' \\ \in \mathrm{RBZ}}} \big(v_{k\downarrow} v_{k'\uparrow} \alpha_{-k\downarrow} \alpha_{-k'\uparrow}^{\dagger}
$$
$$
+ u_{k\downarrow} u_{k'\uparrow} \beta_{k\downarrow}^{\dagger} \beta_{k'\uparrow} - v_{k\downarrow} u_{k'\uparrow} \alpha_{-k\downarrow} \beta_{k'\uparrow}
$$
$$
- u_{k\downarrow} v_{k'\uparrow} \beta_{k\downarrow}^{\dagger} \alpha_{-k'\uparrow}^{\dagger} \big) c_{q\downarrow}^{\dagger} c_{k+q-k'\uparrow},
$$

(A8)

$$
H_{\mathrm{int}}^{(B,-)} = \frac{2\bar{J}}{N} \sum_{q \in \square} \sum_{\substack{kk' \\ \in \mathrm{RBZ}}} \big(v_{k\uparrow} v_{k'\downarrow} \alpha_{-k\uparrow} \alpha_{-k'\downarrow}^{\dagger}
$$
$$
+ u_{k\uparrow} u_{k'\downarrow} \beta_{k\uparrow}^{\dagger} \beta_{k'\downarrow} - v_{k\uparrow} u_{k'\downarrow} \alpha_{-k\uparrow} \beta_{k'\downarrow}
$$
$$
- u_{k\uparrow} v_{k'\downarrow} \beta_{k\uparrow}^{\dagger} \alpha_{-k'\downarrow}^{\dagger} \big) c_{q\uparrow}^{\dagger} c_{k+q-k'\downarrow}.
$$

(A9)

When calculating the boson commutators, leaving us with four electron operators and two boson operators, and exchanging the pair of remaining boson operators with its ground-state

expectation value, we find that only processes where the two incoming electrons have opposite spins give nonzero contributions. These processes then conserve the electron spin and are of the same type as the processes one obtains from a Holstein-Primakoff treatment of the magnetic system [3,5,6]. The pairing Hamiltonian can then be written as

$$H_{\text{pair}} = \frac{1}{2} \sum_{LL'\sigma} \left[H_{\text{int}}^{(L,\sigma)}, \eta S^{(L',-\sigma)} \right], \qquad (A10)$$

where

$$\eta S^{(A,+)} = -\frac{2\bar{J}\Omega}{N} \sum_{\substack{q\in\square}} \sum_{\substack{kk'\\ \in \text{RBZ}}} \left(x_{k,k'q}^{\alpha,\uparrow\downarrow} u_{k\uparrow} u_{k'\downarrow} \alpha_{k\uparrow}^\dagger \alpha_{k'\downarrow} \right.$$
$$+ y_{k,k'q}^{\beta,\downarrow\uparrow} v_{k\uparrow} v_{k'\downarrow} \beta_{-k'\downarrow}^\dagger \beta_{-k\uparrow} - z_{k,k'q}^{-,\uparrow\downarrow} u_{k\uparrow} v_{k'\downarrow} \alpha_{k\uparrow}^\dagger \beta_{-k'\downarrow}^\dagger$$
$$\left. - w_{k,k'q}^{+,\downarrow\uparrow} v_{k\uparrow} u_{k'\downarrow} \alpha_{k'\downarrow} \beta_{-k\uparrow} \right) c_{q\downarrow}^\dagger c_{k+q-k'\uparrow}, \qquad (A11)$$

$$\eta S^{(A,-)} = -\frac{2\bar{J}\Omega}{N} \sum_{\substack{q\in\square}} \sum_{\substack{kk'\\ \in \text{RBZ}}} \left(x_{k,k'q}^{\alpha,\downarrow\uparrow} u_{k\downarrow} u_{k'\uparrow} \alpha_{k\downarrow}^\dagger \alpha_{k'\uparrow} \right.$$
$$+ y_{k,k'q}^{\beta,\uparrow\downarrow} v_{k\downarrow} v_{k'\uparrow} \beta_{-k'\uparrow}^\dagger \beta_{-k\downarrow} - z_{k,k'q}^{-,\downarrow\uparrow} u_{k\downarrow} v_{k'\uparrow} \alpha_{k\downarrow}^\dagger \beta_{-k'\uparrow}^\dagger$$
$$\left. - w_{k,k'q}^{+,\uparrow\downarrow} v_{k\downarrow} u_{k'\uparrow} \alpha_{k'\uparrow} \beta_{-k\downarrow} \right) c_{q\uparrow}^\dagger c_{k+q-k'\downarrow}, \qquad (A12)$$

$$\eta S^{(B,+)} = \frac{2\bar{J}}{N} \sum_{\substack{q\in\square}} \sum_{\substack{kk'\\ \in \text{RBZ}}} \left(y_{k,k'q}^{\alpha,\uparrow\downarrow} v_{k\downarrow} v_{k'\uparrow} \alpha_{-k'\downarrow}^\dagger \alpha_{-k\downarrow} \right.$$
$$+ x_{k,k'q}^{\beta,\downarrow\uparrow} u_{k\downarrow} u_{k'\uparrow} \beta_{k\downarrow}^\dagger \beta_{k'\uparrow} - z_{k,k'q}^{+,\downarrow\uparrow} v_{k\downarrow} u_{k'\uparrow} \alpha_{-k\downarrow} \beta_{k'\uparrow}$$
$$\left. - w_{k,k'q}^{-,\uparrow\downarrow} u_{k\downarrow} v_{k'\uparrow} \alpha_{-k'\downarrow}^\dagger \beta_{k\downarrow}^\dagger \right) c_{q\downarrow}^\dagger c_{k+q-k'\uparrow}, \qquad (A13)$$

$$\eta S^{(B,-)} = \frac{2\bar{J}}{N} \sum_{\substack{q\in\square}} \sum_{\substack{kk'\\ \in \text{RBZ}}} \left(y_{k,k'q}^{\alpha,\downarrow\uparrow} v_{k\uparrow} v_{k'\downarrow} \alpha_{-k'\uparrow}^\dagger \alpha_{-k\uparrow} \right.$$
$$+ x_{k,k'q}^{\beta,\uparrow\downarrow} u_{k\uparrow} u_{k'\downarrow} \beta_{k\uparrow}^\dagger \beta_{k'\downarrow} - z_{k,k'q}^{+,\uparrow\downarrow} v_{k\uparrow} u_{k'\downarrow} \alpha_{-k\uparrow} \beta_{k'\downarrow}$$
$$\left. - w_{k,k'q}^{-,\downarrow\uparrow} u_{k\uparrow} v_{k'\downarrow} \alpha_{-k'\uparrow}^\dagger \beta_{k\uparrow}^\dagger \right) c_{q\uparrow}^\dagger c_{k+q-k'\downarrow}. \qquad (A14)$$

Computing the commutators, grouping together terms, and exchanging the boson operator pairs by their ground-state expectation value, we obtain

$$H_{\text{pair}} = H^{AA} + H^{BB} + H^{AB} + H^{BA}, \qquad (A15)$$

where

$$H^{AA} = \Omega^2 \frac{V^2}{2N} \sum_{\substack{ql}} \sum_{\substack{kk'\\ \in \square \; \in \text{RBZ}}} \left\{ \left(x_{k',k,l}^{\alpha,\uparrow\downarrow} - x_{k,k',q}^{\alpha,\uparrow\downarrow} \right) u_{k\uparrow}^2 u_{k'\downarrow}^2 \right.$$
$$\times \left(\langle \alpha_{k\uparrow}^\dagger \alpha_{k\uparrow} \rangle - \langle \alpha_{k'\downarrow}^\dagger \alpha_{k'\downarrow} \rangle \right) + \left(y_{k,k',q}^{\beta,\downarrow\uparrow} - y_{k',k,l}^{\beta,\uparrow\downarrow} \right) v_{k\uparrow}^2 v_{k'\downarrow}^2$$
$$\times \left(\langle \beta_{-k\uparrow}^\dagger \beta_{-k\uparrow} \rangle - \langle \beta_{-k'\downarrow}^\dagger \beta_{-k'\downarrow} \rangle \right) + \left(z_{k,k',q}^{-,\uparrow\downarrow} - w_{k',k,l}^{+,\uparrow\downarrow} \right)$$
$$\times u_{k\uparrow}^2 v_{k'\downarrow}^2 \left(\langle \alpha_{k\uparrow}^\dagger \alpha_{k\uparrow} \rangle + \langle \beta_{-k'\downarrow}^\dagger \beta_{-k'\downarrow} \rangle + 1 \right)$$

$$+ \left(z_{k',k,l}^{-,\downarrow\uparrow} - w_{k,k',q}^{+,\downarrow\uparrow} \right) v_{k\uparrow}^2 u_{k'\downarrow}^2 \left(\langle \beta_{-k\uparrow}^\dagger \beta_{-k\uparrow} \rangle \right.$$
$$\left. + \langle \alpha_{k'\downarrow}^\dagger \alpha_{k'\downarrow} \rangle + 1 \right) \right\} c_{q\downarrow}^\dagger c_{k+q-k'\uparrow} c_{l\uparrow}^\dagger c_{k'+l-k\downarrow}, \quad (A16)$$

$$H^{BB} = \frac{V^2}{2N} \sum_{\substack{ql}} \sum_{\substack{kk'\\ \in \square \; \in \text{RBZ}}} \left\{ \left(y_{k',k,l}^{\alpha,\downarrow\uparrow} - y_{k,k',q}^{\alpha,\uparrow\downarrow} \right) v_{k\downarrow}^2 v_{k'\uparrow}^2 \right.$$
$$\times \left(\langle \alpha_{-k'\uparrow}^\dagger \alpha_{-k'\uparrow} \rangle - \langle \alpha_{-k\downarrow}^\dagger \alpha_{-k\downarrow} \rangle \right) + \left(x_{k,k',q}^{\beta,\downarrow\uparrow} - x_{k',k,l}^{\beta,\uparrow\downarrow} \right)$$
$$\times u_{k\downarrow}^2 u_{k'\uparrow}^2 \left(\langle \beta_{k'\uparrow}^\dagger \beta_{k'\uparrow} \rangle - \langle \beta_{k\downarrow}^\dagger \beta_{k\downarrow} \rangle \right) + \left(w_{k',k,l}^{-,\downarrow\uparrow} - z_{k,k',q}^{+,\uparrow\downarrow} \right)$$
$$\times v_{k\downarrow}^2 u_{k'\uparrow}^2 \left(\langle \beta_{k'\uparrow}^\dagger \beta_{k'\uparrow} \rangle + \langle \alpha_{-k\downarrow}^\dagger \alpha_{-k\downarrow} \rangle + 1 \right)$$
$$+ \left(w_{k,k',q}^{-,\uparrow\downarrow} - z_{k',k,l}^{+,\downarrow\uparrow} \right) u_{k\downarrow}^2 v_{k'\uparrow}^2 \left(\langle \alpha_{-k'\uparrow}^\dagger \alpha_{-k'\uparrow} \rangle \right.$$
$$\left. + \langle \beta_{k\downarrow}^\dagger \beta_{k\downarrow} \rangle + 1 \right) \right\} c_{q\downarrow}^\dagger c_{k+q-k'\uparrow} c_{l\uparrow}^\dagger c_{k'+l-k\downarrow}, \qquad (A17)$$

$$H^{AB} = -\Omega \frac{V^2}{2N} \sum_{\substack{ql}} \sum_{\substack{kk'\\ \in \square \; \in \text{RBZ}}} \left\{ \left(y_{-k,-k',l}^{\alpha,\downarrow\uparrow} - y_{-k',-k,q}^{\alpha,\uparrow\downarrow} \right) u_{k\uparrow} u_{k'\downarrow} \right.$$
$$\times v_{k\uparrow} v_{k'\downarrow} \left(\langle \alpha_{k\uparrow}^\dagger \alpha_{k\uparrow} \rangle - \langle \alpha_{k'\downarrow}^\dagger \alpha_{k'\downarrow} \rangle \right) + \left(x_{-k',-k,q}^{\beta,\downarrow\uparrow} \right.$$
$$\left. - x_{-k,-k',l}^{\beta,\uparrow\downarrow} \right) v_{k\uparrow} v_{k'\downarrow} u_{k\uparrow} u_{k'\downarrow} \left(\langle \beta_{-k\uparrow}^\dagger \beta_{-k\uparrow} \rangle - \langle \beta_{-k'\downarrow}^\dagger \beta_{-k'\downarrow} \rangle \right)$$
$$+ \left(w_{-k',-k,q}^{-,\uparrow\downarrow} - z_{-k,-k',l}^{+,\uparrow\downarrow} \right) u_{k\uparrow} u_{k'\downarrow} v_{k\uparrow} u_{k'\downarrow} \left(\langle \alpha_{k\uparrow}^\dagger \alpha_{k\uparrow} \rangle \right.$$
$$\left. + \langle \beta_{-k'\downarrow}^\dagger \beta_{-k'\downarrow} \rangle + 1 \right) + \left(w_{-k,-k',l}^{-,\downarrow\uparrow} - z_{-k',-k,q}^{+,\downarrow\uparrow} \right) v_{k\uparrow} u_{k'\downarrow}$$
$$\times u_{k\uparrow} v_{k'\downarrow} \left(\langle \beta_{-k\uparrow}^\dagger \beta_{-k\uparrow} \rangle + \langle \alpha_{k'\downarrow}^\dagger \alpha_{k'\downarrow} \rangle + 1 \right) \right\}$$
$$\times c_{q\downarrow}^\dagger c_{k+q-k'\uparrow} c_{l\uparrow}^\dagger c_{k'+l-k\downarrow}, \qquad (A18)$$

$$H^{BA} = -\Omega \frac{V^2}{2N} \sum_{\substack{ql}} \sum_{\substack{kk'\\ \in \square \; \in \text{RBZ}}} \left\{ \left(x_{-k,-k',l}^{\alpha,\downarrow\uparrow} - x_{-k',-k,q}^{\alpha,\uparrow\downarrow} \right) v_{k\downarrow} v_{k'\uparrow} \right.$$
$$\times u_{k\downarrow} u_{k'\uparrow} \left(\langle \alpha_{-k'\uparrow}^\dagger \alpha_{-k'\uparrow} \rangle - \langle \alpha_{-k\downarrow}^\dagger \alpha_{-k\downarrow} \rangle \right) + \left(y_{-k',-k,q}^{\beta,\downarrow\uparrow} \right.$$
$$\left. - y_{-k,-k',l}^{\beta,\uparrow\downarrow} \right) u_{k\downarrow} u_{k'\uparrow} v_{k\downarrow} v_{k'\uparrow} \left(\langle \beta_{k'\uparrow}^\dagger \beta_{k'\uparrow} \rangle - \langle \beta_{k\downarrow}^\dagger \beta_{k\downarrow} \rangle \right)$$
$$+ \left(z_{-k,-k',l}^{-,\downarrow\uparrow} - w_{-k',-k,q}^{+,\downarrow\uparrow} \right) v_{k\downarrow} u_{k'\uparrow} u_{k\downarrow} v_{k'\uparrow} \left(\langle \beta_{k'\uparrow}^\dagger \beta_{k'\uparrow} \rangle \right.$$
$$\left. + \langle \alpha_{-k\downarrow}^\dagger \alpha_{-k\downarrow} \rangle + 1 \right) + \left(z_{-k',-k,q}^{-,\uparrow\downarrow} - w_{-k,-k',l}^{+,\uparrow\downarrow} \right) u_{k\downarrow} v_{k'\uparrow}$$
$$\times v_{k\downarrow} u_{k'\uparrow} \left(\langle \alpha_{-k'\uparrow}^\dagger \alpha_{-k'\uparrow} \rangle + \langle \beta_{k\downarrow}^\dagger \beta_{k\downarrow} \rangle + 1 \right) \right\}$$
$$\times c_{q\downarrow}^\dagger c_{k+q-k'\uparrow} c_{l\uparrow}^\dagger c_{k'+l-k\downarrow}. \qquad (A19)$$

Here, we have defined, $V \equiv 2\bar{J}/\sqrt{N}$.

When considering the ground-state expectation value of the boson operator pairs, we only get contributions from ↑-bosons with momentum $\boldsymbol{k} = 0$, as the ground state is a condensate of

↑-bosons. Further, restricting to the BCS case of incoming, as well as outgoing, particles with opposite momenta, the result for the effective interaction is $H_{\text{pair}} = H_{\text{pair}}^{(1)} + H_{\text{pair}}^{(2)}$ where

$$H_{\text{pair}}^{(1)} = \frac{V^2}{N}(u_{0\uparrow}^2 + v_{0\uparrow}^2)n_{0\uparrow} \sum_{\boldsymbol{q} \in \square} \sum_{\substack{\boldsymbol{k} \in \\ \text{RBZ}}} A(\boldsymbol{k}, \Omega)$$

$$\times \frac{2\omega_{\boldsymbol{k}\downarrow}}{(\epsilon_{\boldsymbol{q}+\boldsymbol{k}} - \epsilon_{\boldsymbol{q}})^2 - \omega_{\boldsymbol{k}\downarrow}^2} c_{\boldsymbol{q}\downarrow}^\dagger c_{\boldsymbol{q}+\boldsymbol{k}\uparrow} c_{-\boldsymbol{q}\uparrow}^\dagger c_{-\boldsymbol{q}-\boldsymbol{k}\downarrow}, \quad \text{(A20)}$$

and

$$H_{\text{pair}}^{(2)} = \frac{V^2}{N} \sum_{\substack{\boldsymbol{q} \\ \in \square}} \sum_{\substack{\boldsymbol{kk'} \\ \in \text{RBZ}}} B(\boldsymbol{k}, \boldsymbol{k'}, \Omega)$$

$$\times \frac{2(\omega_{\boldsymbol{k}\uparrow} + \omega_{\boldsymbol{k'}\downarrow})}{(\epsilon_{\boldsymbol{q}+\boldsymbol{k}-\boldsymbol{k'}} - \epsilon_{\boldsymbol{q}})^2 - (\omega_{\boldsymbol{k}\uparrow} + \omega_{\boldsymbol{k'}\downarrow})^2}$$

$$\times c_{\boldsymbol{q}\downarrow}^\dagger c_{\boldsymbol{q}+\boldsymbol{k}-\boldsymbol{k'}\uparrow} c_{-\boldsymbol{q}\uparrow}^\dagger c_{-\boldsymbol{q}+\boldsymbol{k'}-\boldsymbol{k}\downarrow}. \quad \text{(A21)}$$

The functions A and B are defined in the main text. The contributions to $H_{\text{pair}}^{(1)}$ come from the expectation value of the ↑-bosons with momentum $\boldsymbol{k} = 0$, $n_{0\uparrow}$, while the contributions to $H_{\text{pair}}^{(2)}$ originate with the terms without boson operators. Moving the contributions from $H_{\text{pair}}^{(2)}$ where $\boldsymbol{k} = 0$ over to $H_{\text{pair}}^{(1)}$, and using $u_{0\uparrow}^2, v_{0\uparrow}^2 \gg 1$, we can rewrite $H_{\text{pair}}^{(1)}$ as

$$H_{\text{pair}}^{(1)} = V^2 \tilde{Q}_0 \sum_{\boldsymbol{q} \in \square} \sum_{\substack{\boldsymbol{k} \in \\ \text{RBZ}}} A(\boldsymbol{k}, \Omega)$$

$$\times \frac{2\omega_{\boldsymbol{k}\downarrow}}{(\epsilon_{\boldsymbol{q}+\boldsymbol{k}} - \epsilon_{\boldsymbol{q}})^2 - \omega_{\boldsymbol{k}\downarrow}^2} c_{\boldsymbol{q}\downarrow}^\dagger c_{\boldsymbol{q}+\boldsymbol{k}\uparrow} c_{-\boldsymbol{q}\uparrow}^\dagger c_{-\boldsymbol{q}-\boldsymbol{k}\downarrow}, \quad \text{(A22)}$$

where $\tilde{Q}_0$ is a quantity of order unity, closely related to the sublattice magnetization.

[1] M. Kargarian, D. K. Efimkin, and V. Galitski, Phys. Rev. Lett. **117**, 076806 (2016).

[2] X. Gong, M. Kargarian, A. Stern, D. Yue, H. Zhou, X. Jin, V. M. Galitski, V. M. Yakovenko, and J. Xia, Sci. Adv. **3**, e1602579 (2017).

[3] N. Rohling, E. L. Fjærbu, and A. Brataas, Phys. Rev. B **97**, 115401 (2018).

[4] H. G. Hugdal, S. Rex, F. S. Nogueira, and A. Sudbø, Phys. Rev. B **97**, 195438 (2018).

[5] E. L. Fjærbu, N. Rohling, and A. Brataas, Phys. Rev. B **100**, 125432 (2019).

[6] E. Erlandsen, A. Kamra, A. Brataas, and A. Sudbø, Phys. Rev. B **100**, 100503(R) (2019).

[7] E. Erlandsen, A. Brataas, and A. Sudbø, Phys. Rev. B **101**, 094503 (2020).

[8] H. G. Hugdal and A. Sudbø, Phys. Rev. B **102**, 125429 (2020).

[9] N. D. Mermin and H. Wagner, Phys. Rev. Lett. **17**, 1133 (1966).

[10] P. C. Hohenberg, Phys. Rev. **158**, 383 (1967).

[11] J. Nogués and I. K. Schuller, J. Magn. Magn. Mater. **192**, 203 (1999).

[12] J. Nogués, J. Sort, V. Langlais, V. Skumryev, S. Suriñach, J. Muñoz, and M. Baró, Phys. Rep. **422**, 65 (2005).

[13] R. L. Stamps, J. Phys. D **33**, R247 (2000).

[14] A. Kamra, E. Thingstad, G. Rastelli, R. A. Duine, A. Brataas, W. Belzig, and A. Sudbø, Phys. Rev. B **100**, 174407 (2019).

[15] A. Kamra and W. Belzig, Phys. Rev. Lett. **119**, 197201 (2017).

[16] O. Johansen, A. Kamra, C. Ulloa, A. Brataas, and R. A. Duine, Phys. Rev. Lett. **123**, 167203 (2019).

[17] J. B. Parkinson and D. J. Farnell, *An Introduction to Quantum Spin Systems*, Vol. 816 (Springer, New York, 2010).

[18] D. J. J. Farnell, O. Götze, and J. Richter, Phys. Rev. B **93**, 235123 (2016).

[19] R. Flint and P. Coleman, Phys. Rev. B **79**, 014424 (2009).

[20] C. L. Henley, Phys. Rev. Lett. **62**, 2056 (1989).

[21] R. Haghshenas, W.-W. Lan, S.-S. Gong, and D. N. Sheng, Phys. Rev. B **97**, 184436 (2018).

[22] R. F. Bishop, P. H. Y. Li, R. Darradi, and J. Richter, Europhys. Lett. **83**, 47004 (2008).

[23] E. Dagotto and A. Moreo, Phys. Rev. Lett. **63**, 2148 (1989).

[24] F. Figueirido, A. Karlhede, S. Kivelson, S. Sondhi, M. Rocek, and D. S. Rokhsar, Phys. Rev. B **41**, 4619 (1990).

[25] L. Capriotti, F. Becca, A. Parola, and S. Sorella, Phys. Rev. Lett. **87**, 097201 (2001).

[26] R. Schmidt, J. Schulenburg, J. Richter, and D. D. Betts, Phys. Rev. B **66**, 224406 (2002).

[27] Y. Kamihara, T. Watanabe, M. Hirano, and H. Hosono, J. Am. Chem. Soc. **130**, 3296 (2008).

[28] Q. Si and E. Abrahams, Phys. Rev. Lett. **101**, 076401 (2008).

[29] F. Ma, Z.-Y. Lu, and T. Xiang, Phys. Rev. B **78**, 224517 (2008).

[30] P. Chandra and B. Doucot, Phys. Rev. B **38**, 9335 (1988).

[31] Y. Kajiwara, K. Harii, S. Takahashi, J. Ohe, K. Uchida, M. Mizuguchi, H. Umezawa, H. Kawai, K. Ando, K. Takanashi, S. Maekawa, and E. Saitoh, Nature (London) **464**, 262 (2010).

[32] S. Takahashi, E. Saitoh, and S. Maekawa, J. Phys.: Conf. Ser. **200**, 062030 (2010).

[33] S. A. Bender and Y. Tserkovnyak, Phys. Rev. B **91**, 140402(R) (2015).

[34] D. P. Arovas and A. Auerbach, Phys. Rev. B **38**, 316 (1988).

[35] A. Auerbach, *Interacting Electrons and Quantum Magnetism*, Graduate Texts in Contemporary Physics (Springer, New York, 2012).

[36] S. Sarker, C. Jayaprakash, H. R. Krishnamurthy, and M. Ma, Phys. Rev. B **40**, 5028 (1989).

[37] C. Wei and R. Tao, Phys. Rev. B **50**, 6840 (1994).

[38] J. Merino, M. Holt, and B. J. Powell, Phys. Rev. B **89**, 245112 (2014).

[39] H. A. Ceccatto, C. J. Gazza, and A. E. Trumper, Phys. Rev. B **47**, 12329 (1993).

[40] D.-V. Bauer and J. O. Fjærestad, Phys. Rev. B **96**, 165141 (2017).

[41] L. Messio, C. Lhuillier, and G. Misguich, Phys. Rev. B **87**, 125127 (2013).

[42] GNU Scientific Library, https://www.gnu.org/software/gsl/.

[43] F. S. Bergeret, M. Silaev, P. Virtanen, and T. T. Heikkilä, Rev. Mod. Phys. **90**, 041001 (2018).

[44] M. Lange, M. J. Van Bael, Y. Bruynseraede, and V. V. Moshchalkov, Phys. Rev. Lett. **90**, 197006 (2003).

[45] J. R. Schrieffer and P. A. Wolff, Phys. Rev. **149**, 491 (1966).

[46] C. Kittel, *Quantum Theory of Solids* (Wiley, New York, 1963).

[47] M. Sigrist and K. Ueda, Rev. Mod. Phys. **63**, 239 (1991).

[48] C. Sanderson and R. Curtin, J. Open Source Software **1**, 26 (2016).

[49] C. Sanderson and R. Curtin, *Mathematical Software-ICMS 2018* (Springer International Publishing, Cham, 2018), pp. 422–430.

[50] R. Piasecki, arXiv:0804.1037.

Eliashberg study of superconductivity induced by interfacial coupling to antiferromagnets

Authors

Even Thingstad*
Eirik Erlandsen*
Asle Sudbø

*These authors contributed equally to this work.

Eliashberg study of superconductivity induced by interfacial coupling to antiferromagnets

Even Thingstad ⬤,* Eirik Erlandsen ⬤,* and Asle Sudbø ⬤†

Center for Quantum Spintronics, Department of Physics, Norwegian University of Science and Technology, NO-7491 Trondheim, Norway

We perform Eliashberg calculations for magnon-mediated superconductivity in a normal metal, where the electron-magnon interaction arises from interfacial coupling to antiferromagnetic insulators. In agreement with previous studies, we find *p*-wave pairing for large doping when the antiferromagnetic interfaces are uncompensated and *d*-wave pairing close to half filling when the antiferromagnetic interfaces are compensated. However, for the *p*-wave phase, we find a considerable reduction in the critical temperature compared to previous weak-coupling results, as the effective frequency cutoff on the magnon propagator in this case is found to be much smaller than the cutoff on the magnon spectrum. The *d*-wave phase, on the other hand, relies less on long-wavelength magnons, leading to a larger effective cutoff on the magnon propagator. Combined with a large density of states close to half filling, this might allow the *d*-wave phase to survive up to higher critical temperatures. Based on our findings, we provide insight into how to realize interfacially induced magnon-mediated superconductivity in experiments.

I. INTRODUCTION

For conventional superconductors, the fluctuations responsible for Cooper pairing of electrons are provided by phonons [1]. As the role of the phonons is simply to introduce attractive interaction between electrons, superconductivity can in principle arise from exchange of any bosonic quasiparticle that is able to provide a similar attractive interaction [2–5]. One alternative that has received much attention is exchange of paramagnetic spin fluctuations [6,7]. The idea is that the spins in a paramagnet, close to magnetic ordering, can act like a medium that can be polarized by the spin of an electron. Another electron can then interact with the polarized medium, giving rise to an effective interaction between the electrons. The quasiparticle mediating the interaction, the paramagnon, represents a damped spin-wave propagating in an ordered patch of the paramagnet [8,9].

The paramagnon exchange mechanism has been proposed to be closely related to the superconductivity of heavy fermion materials [10–12] and high-T_c cuprates [13,14]. In the context of the Hubbard model, paramagnon exchange has been found to give rise to *p*-wave superconductivity for small isotropic Fermi surfaces and *d*-wave superconductivity closer to half filling [11]. This *d*-wave superconductivity arises from antiferromagnetic fluctuations, so that the interaction is peaked at finite momentum. Although the spin-singlet *s*-wave channel is repulsive, the *d*-wave channel is then able to become attractive by taking advantage of sign changes in the gap function [6].

In these systems, superconductivity arises from interactions between fermions due to their own collective spin excitations [13–15]. Spin-fluctuation mediated superconductivity may also occur in heterostructures with itinerant

fermions proximity coupled to the spins of insulating materials [16–24]. Since the spins and the itinerant fermions are then separate degrees of freedom, this provides a simpler context to study superconductivity mediated by spin fluctuations.

Magnon-mediated superconductivity induced in a normal metal (NM) due to proximity coupling to a magnetic insulator has so far been investigated within a weak-coupling BCS framework [18,20–22]. The first case to be considered was a NM coupled to ferromagnetic insulators, which was found to give rise to *p*-wave pairing [18]. Similarly, for a NM coupled to an antiferromagnetic insulator (AFMI), *p*-wave solutions were obtained for large dopings by exploiting the inherent squeezing of antiferromagnetic magnons [25] by coupling the conduction electrons in the NM asymmetrically to the two sublattices of the AFMI [21]. This sublattice coupling asymmetry suppresses sublattice interferences in the pairing potential, which are very unfavorable for the *p*-wave phase. A general asymmetry of this type can be realized by employing an antiferromagnetic interface where both sublattices are exposed (compensated interface), but further breaking the sublattice symmetry by using an antiferromagnetic material with two different atoms on the two sublattices. The particularly relevant case of coupling to only one of the two sublattices is, however, achieved through an uncompensated antiferromagnetic interface where only one of the two sublattices is exposed [26–28].

For the case of a compensated antiferromagnetic interface, the magnons live in a Brillouin zone which is reduced compared to the electron Brillouin zone. This introduces electron-magnon scattering processes of two types: regular and Umklapp [29,30]. In the regular processes, the electrons are scattered with a momentum within the first magnon Brillouin zone. In the Umklapp processes, on the other hand, the outgoing electron receives an additional momentum corresponding to a magnon reciprocal space lattice vector. The Umklapp processes are of little relevance for the small

---

*These authors contributed equally to this work.
†Corresponding author: asle.sudbo@ntnu.no

Fermi surfaces considered in Ref. [21], but closer to half filling they have been predicted to give rise to d-wave superconductivity in a normal metal sandwiched between two compensated antiferromagnetic interfaces [20]. Analogously to the case of paramagnon exchange in the Hubbard model, the d-wave pairing arises from a repulsive s-wave channel and an interaction that is peaked at finite momentum.

We also note that a normal metal coupled to a compensated antiferromagnetic interface is similar to a single material with antiferromagnetically ordered localized spins and itinerant electrons treated as separate degrees of freedom, considered, e.g., in Refs. [31–33]. While Ref. [31] simply found the spin singlet s-wave channel to be repulsive for magnon-mediated pairing, Ref. [32] also considered the spin triplet channel and found p-wave superconductivity due to their treatment not probing the interference effects discussed in Ref. [21]. Reference [33], on the other hand, found that two-magnon scattering processes were dominant for small Fermi surfaces due to the strong destructive interference for one-magnon processes, while spin singlet d-wave pairing driven by one-magnon processes could be possible for larger Fermi surfaces.

A notable difference between the electron-phonon coupling in common weak-coupling superconductors and the electron-magnon coupling considered in the present study is the behavior of the coupling matrix element in the limit of small momentum transfers. Since the electron-phonon coupling represents a coupling between electrons and spatial fluctuations of ion densities, it vanishes at zero momentum. In contrast, the coupling between the spins of itinerant electrons and the localized spins of the magnetic insulator is local and therefore constant in momentum space. For the magnon-mediated superconductivity discussed in the above references, this allows processes with small scattering momentum and small magnon frequencies to dominate the superconducting pairing. In turn, these small momentum processes can compensate for the relatively small interfacial coupling strength of order 10 meV [18,34], which is typically smaller than the energy scale for the electron-phonon coupling giving rise to phonon-mediated superconductivity [35,36].

When the dominant contributions to the pairing arise from long-wavelength magnons, one should expect that it may no longer be reasonable to use the cutoff on the boson spectrum as the characteristic boson energy setting the energy scale for the critical temperature. This is not captured in simple BCS theory, which does not consider the frequency dependence of the bosonic fluctuation spectrum responsible for pairing. Furthermore, renormalization of both electrons and bosons is neglected in BCS theory, and these effects could turn out to play a more essential role here. Although BCS theory explains phonon-mediated superconductivity in weak-coupling superconductors reasonably well, a more detailed analysis may be required when other pairing mechanisms are involved.

In this paper, we therefore investigate superconductivity induced in a NM by interfacial coupling to antiferromagnetic insulators using an Eliashberg theory framework. In addition to exploring how the existing results change when the electron renormalization and the proper frequency dependence of the electron-magnon interaction are taken into account, we also study the effect of magnon renormalization and discuss importance of vertex corrections. Instead of focusing only on

regular [21] or Umklapp processes [20], we simultaneously take both types of processes into account and examine how the superconductivity varies with both chemical potential and asymmetry in the coupling to the two sublattices of the antiferromagnet.

In agreement with earlier results, we find a p-wave phase for large sublattice coupling asymmetry and large doping, and a d-wave phase for small sublattice coupling asymmetry and small doping. For the p-wave phase, the critical temperature is considerably reduced compared to previous weak-coupling studies due to the reduction of the effective magnon frequency cutoff. However, the d-wave phase is found to be less reliant on exchange of long-wavelength magnons. This leads to a larger effective cutoff. Near half filling, the reduction in the contributions from long-wavelength magnons for the d-wave phase can be compensated by a larger density of states, opening up for the possibility of larger critical temperatures. For a strongly nested Fermi surface, however, one needs to consider, e.g., the possibility of a competing spin-density wave instability. Moreover, while a sufficiently large gap in the magnon spectrum may be necessary to protect the ordering of the magnet upon inclusion of magnon renormalization, the net effect on possible critical temperatures is found to be small.

In Sec. II, we present the model of our system. In Sec. III, we outline the Eliashberg theory for magnon-mediated superconductivity. We further derive the Fermi surface averaged Eliashberg equations in Sec. IV and present results for these equations in Sec. V. In Sec. VI we move on to the effect of renormalization of the magnons. Finally, we discuss the validity of the results as well as additional neglected effects in Sec. VII, and experimental considerations in Sec. VIII, before we summarize in Sec. IX. Additional details, as well as a discussion of the role of vertex corrections, can be found in the Appendices.

II. MODEL

We consider a trilayer heterostructure consisting of a normal metal sandwiched between two antiferromagnets, as shown in Fig. 1. The experimental realization of the system would consist of a thin NM layer between two thicker AFMI layers. For simplicity, we model the system using two-dimensional lattice models for the three distinct layers. We assume that the antiferromagnets have staggered magnetic order along the z direction in spin space and that this order is opposite in the two antiferromagnets. In general, the spin space z direction can be either in-plane or out-of-plane in real space for our model.

We model the system with the Hamiltonian $H = H_{\text{NM}} + H_{\text{AFMI}} + H_{\text{int}}$, where

$$H_{\text{NM}} = -\sum_{ij,\sigma} t_{ij} c_{i\sigma}^\dagger c_{j\sigma} - \mu \sum_{i\sigma} c_{i\sigma}^\dagger c_{i\sigma}, \tag{1a}$$

$$H_{\text{AFMI}} = \sum_{ij,\eta} J_{ij} \mathbf{S}_{i\eta} \cdot \mathbf{S}_{j\eta} - K \sum_{i,\eta} \left(S_{i\eta}^z\right)^2, \tag{1b}$$

$$H_{\text{int}} = -2\bar{J} \sum_{\eta,\Upsilon} \sum_{i \in \Upsilon} \Omega_\Upsilon^\eta c_i^\dagger \boldsymbol{\sigma} c_i \cdot \mathbf{S}_{i\eta}, \tag{1c}$$

and the terms describe the normal metal, the antiferromagnetic insulators, and the interfacial coupling between the materials.
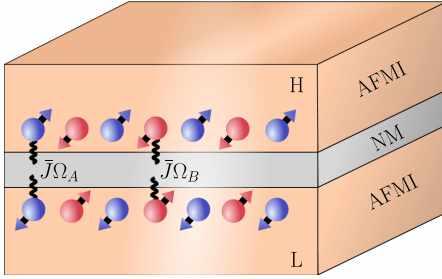
FIG. 1. A trilayer consisting of a normal metal (NM) layer sandwiched between two antiferromagnetic insulator (AFMI) layers. The A and B sublattices of the AFMIs consist of the blue and red lattice sites, respectively. The two AFMIs are oppositely ordered so that the spins associated with a specific sublattice are oppositely oriented for the highest (H) and lowest (L) AFMI. The coupling to the A sublattices of both AFMIs is taken to be of equal strength ($\bar{J}\Omega_A$), and similarly for the B sublattices, so that the itinerant electrons in the NM experience no net magnetic field. The coupling to the A sublattices is, however, allowed to differ from the coupling to the B sublattices.

The sums over i, j denote sums over lattice sites, the sum over $\eta \in \{H, L\}$ denotes a sum over the the two antiferromagnetic insulators, and the sum over $\Upsilon \in \{A, B\}$ denotes a sum over the sublattices. All three layers are modelled by square lattices with periodic boundary conditions. In the normal metal, our model describes spinful electrons with annihilation and creation operators $c_{i\sigma}$ and $c_{i\sigma}^\dagger$ for an electron on site i with spin σ. The electron chemical potential is expressed as μ, and t_{ij} is the hopping amplitude, which we set to t for nearest neighbors and zero otherwise. The AFMIs in our model consist of localized lattice site spins, where $S_{i\eta}$ denotes the spin on site i in antiferromagnet η. The exchange coupling between the spins on lattice sites i and j is J_{ij}, which we assume to take the value $J_1 > 0$ for nearest neighbor and J_2 for next-nearest neighbor sites. Moreover, $K > 0$ denotes the easy axis anisotropy. The interfacial coupling between the materials is included as an effective exchange interaction $\bar{J}$ between the lattice site spins in the antiferromagnets and the spins of the conduction band electrons that are confined to the normal metal [18,20,34,37,38]. We use the notation $c_i = (c_{i\uparrow}, c_{i\downarrow})^T$ and have taken $\boldsymbol{\sigma}$ to denote the Pauli matrix vector in spin space. In order to be able to introduce asymmetry in the coupling between the normal metal and the two sublattices of the antiferromagnets, we have included a dimensionless, sublattice- and layer-dependent, parameter Ω_Υ^η in the interaction Hamiltonian [21–23]. In order to eliminate any magnetic fields, we will be focusing on equal coupling to the two antiferromagnets [20] and therefore let $\Omega_\Upsilon^\eta \equiv \Omega_\Upsilon$. In the following, we set $\hbar = a = 1$, with a being the lattice constant.

The normal metal Hamiltonian can be diagonalized to obtain

$$H_{\text{NM}} = \sum_{\boldsymbol{k} \in \square, \sigma} \xi_{\boldsymbol{k}} c_{\boldsymbol{k}\sigma}^\dagger c_{\boldsymbol{k}\sigma}, \tag{2}$$
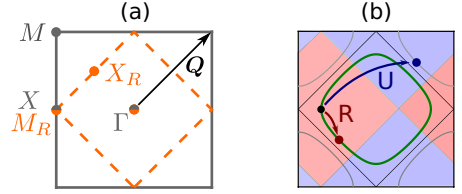
FIG. 2. (a) Electron (gray) and magnon (orange) Brillouin zones with labeling of high symmetry points. We refer to the magnon Brillouin zone as the reduced Brillouin zone (RBZ). The antiferromagnetic ordering vector $\boldsymbol{Q}$ is also indicated. (b) Fermi surface (green) at moderate doping. Electrons can be scattered from $\boldsymbol{k}$ (black) to points $\boldsymbol{k} + \boldsymbol{q}$ inside the shaded red part of the Brillouin zone through regular processes and to points $\boldsymbol{k} + \boldsymbol{q} + \boldsymbol{Q}$ in the shaded blue part of the Brillouin zone through Umklapp processes.

where the quasimomentum sum runs over the full Brillouin zone, we have defined $\xi_{\boldsymbol{k}} = \epsilon_{\boldsymbol{k}} - \mu$, and the single particle electron dispersion relation is given by $\epsilon_{\boldsymbol{k}} = -2t(\cos k_x + \cos k_y)$. To determine the eigenexcitations of the antiferromagnetic insulator, we introduce the linearized Holstein-Primakoff transformation to represent the spins in terms of bosons $a_{i\eta}$ and $b_{i\eta}$ on the two sublattices of the system. Further, introducing the Fourier transformed operators $a_{\boldsymbol{q}\eta}$ and $b_{\boldsymbol{q}\eta}$, one may diagonalize the AFMI Hamiltonian using a Bogoliubov transformation

$$a_{\boldsymbol{q}\eta} = u_{\boldsymbol{q}} \alpha_{\boldsymbol{q}\eta} + v_{\boldsymbol{q}} \beta_{-\boldsymbol{q}\eta}^\dagger, \tag{3a}$$

$$b_{-\boldsymbol{q}\eta}^\dagger = u_{\boldsymbol{q}} \beta_{-\boldsymbol{q}\eta}^\dagger + v_{\boldsymbol{q}} \alpha_{\boldsymbol{q}\eta}, \tag{3b}$$

as detailed in Appendix A. By suitable choice of coherence factors $u_{\boldsymbol{q}}$ and $v_{\boldsymbol{q}}$, the AFMI Hamiltonian takes the form

$$H_{\text{AFMI}} = \sum_{\boldsymbol{q} \in \diamond, \eta} \omega_{\boldsymbol{q}} (\alpha_{\boldsymbol{q}\eta}^\dagger \alpha_{\boldsymbol{q}\eta} + \beta_{\boldsymbol{q}\eta}^\dagger \beta_{\boldsymbol{q}\eta}), \tag{4}$$

with eigenmagnon operators $\alpha_{\boldsymbol{q}\eta}$ and $\beta_{\boldsymbol{q}\eta}$, magnon dispersion $\omega_{\boldsymbol{q}}$, and where the quasimomentum $\boldsymbol{q}$ runs over the reduced Brillouin zone, as illustrated in Fig. 2(a).

As shown in Refs. [21,23], the electron-magnon coupling in this system in general consists of staggered and net magnetic fields, as well as electron scattering processes of both regular and Umklapp type. In our case, all net and staggered magnetic fields from the two opposing antiferromagnetic layers cancel.

The interaction Hamiltonian then takes the form

$$H_{\text{int}} = V \sum_{\substack{\boldsymbol{k} \in \square \\ \boldsymbol{q} \in \diamond}} \left[M_{\boldsymbol{q}}^R c_{\boldsymbol{k}+\boldsymbol{q},\downarrow}^\dagger c_{\boldsymbol{k},\uparrow} + M_{\boldsymbol{q}}^U c_{\boldsymbol{k}+\boldsymbol{q}+\boldsymbol{Q},\downarrow}^\dagger c_{\boldsymbol{k},\uparrow} \right.$$
$$\left. + \left(M_{-\boldsymbol{q}}^R\right)^\dagger c_{\boldsymbol{k}+\boldsymbol{q},\uparrow}^\dagger c_{\boldsymbol{k},\downarrow} + \left(M_{-\boldsymbol{q}}^U\right)^\dagger c_{\boldsymbol{k}+\boldsymbol{q}+\boldsymbol{Q},\uparrow}^\dagger c_{\boldsymbol{k},\downarrow} \right], \tag{5}$$

where we have defined the magnon operators $M_{\boldsymbol{q}}^\kappa = M_{\boldsymbol{q}H}^\kappa + M_{\boldsymbol{q}L}^\kappa$ with

$$M_{\boldsymbol{q}H}^\kappa = \Omega_A a_{\boldsymbol{q}H} + \kappa \, \Omega_B b_{-\boldsymbol{q}H}^\dagger, \tag{6a}$$

$$M_{\boldsymbol{q}L}^\kappa = \Omega_A a_{-\boldsymbol{q}L}^\dagger + \kappa \, \Omega_B b_{\boldsymbol{q}L}. \tag{6b}$$

Here, $\kappa \in \{R, U\}$ is an index characterizing whether the corresponding electron scattering process is of regular or Umklapp type, which we associate with the values $R \to +1$ and $U \to -1$ in the definition of M_q^κ. Examples of regular and Umklapp scattering processes are shown in Fig. 2(b). We have also defined the momentum shift vector $\boldsymbol{Q} = \pi(\hat{x} + \hat{y})$ occurring in the Umklapp scattering processes, and the interaction strength parameter $V \equiv -2\bar{J}\sqrt{S/N}$, where S is the spin quantum number of the AFMI lattice site spins and N the number of lattice sites. In terms of the eigenmagnon operators $\alpha_{q\eta}$, $\beta_{q\eta}$, we may also express the magnon operators M_q^κ as

$$M_q^\kappa = (\Omega_A u_q + \kappa\,\Omega_B v_q)(\alpha_{qH} + \alpha_{-qL}^\dagger)$$
$$+ (\Omega_A v_q + \kappa\,\Omega_B u_q)(\beta_{-qH}^\dagger + \beta_{qL}), \qquad (7)$$

so that we may think of the magnon operators M_q^κ as linear combinations of antiferromagnetic eigenmagnon operators with a given spin and momentum.

III. ELIASHBERG THEORY

A. Magnon propagators

Since the magnon operators in the electron-magnon interaction only occur in the particular linear combinations M_q^κ, the propagators of M_q^κ will be key building blocks in our Eliashberg theory. In the imaginary time formalism, we therefore define the magnon propagator

$$\mathcal{D}^{\kappa\kappa'}(\boldsymbol{q}, \tau) = -\big\langle T_\tau M_q^\kappa(\tau)\big(M_q^{\kappa'}\big)^\dagger(0)\big\rangle, \qquad (8)$$

where T_τ is the time-ordering operator and the expectation value is computed with the full Hamiltonian. In the noninteracting theory, one may utilize the eigenmagnon propagators to show that

$$\mathcal{D}_0^{\kappa\kappa'}(\boldsymbol{q}, iv_m) = -2A_e^{\kappa\kappa'}(\boldsymbol{q})\frac{2\omega_q}{v_m^2 + \omega_q^2}, \qquad (9)$$

where $v_m = 2m\pi/\beta$ is a bosonic Matsubara frequency and β the inverse temperature. The boosting factors $A_e^{\kappa\kappa'}(\boldsymbol{q})$ are given by

$$A_e^{RR}(\boldsymbol{q}) = \tfrac{1}{2}[(\Omega_A u_q + \Omega_B v_q)^2 + (\Omega_A v_q + \Omega_B u_q)^2], \quad (10a)$$

$$A_e^{UU}(\boldsymbol{q}) = \tfrac{1}{2}[(\Omega_A u_q - \Omega_B v_q)^2 + (\Omega_A v_q - \Omega_B u_q)^2], \quad (10b)$$

$$A_e^{RU}(\boldsymbol{q}) = A_e^{UR}(\boldsymbol{q}) = \tfrac{1}{2}\big(\Omega_A^2 - \Omega_B^2\big)\big(u_q^2 + v_q^2\big). \quad (10c)$$

Here, u_q and v_q are the magnon coherence factors, arising from the Bogoliubov transformation, discussed in Appendix A. Inspecting the boosting factor corresponding to regular scattering processes, we see that it coincides with the boosting factor occurring from the canonical transformation used to obtain the effective interaction potential in Ref. [21].

From the expressions for the regular and Umklapp boosting factors $A_e^{RR}(\boldsymbol{q})$ and $A_e^{UU}(\boldsymbol{q})$, it is clear that in addition to contributions from only the A and B sublattices proportional to factors of Ω_A^2 and Ω_B^2, there are in general also interferences between contributions from the two sublattices. Since u_q is typically positive and v_q is typically negative, as discussed in Appendix A, we typically expect destructive interference in the regular process boosting factor $A_e^{RR}(\boldsymbol{q})$ [21] and constructive interference in the Umklapp process boosting

factor $A_e^{UU}(\boldsymbol{q})$. The significance of these interference effects is controlled by the asymmetry in the coupling to the two sublattices, where we find the strongest sublattice interferences when we couple equally to both sublattices, and that all interference effects are removed when we couple to only one sublattice. The mixed propagator boosting factors A_e^{RU} and A_e^{UR} do not experience similar interferences.

B. Spinor representations

To study magnon-mediated superconductivity, we now construct the Eliashberg theory for the system. To do this, we first introduce the Nambu spinor

$$\psi_k = \begin{pmatrix} c_{k\uparrow} \\ c_{k\downarrow} \\ c_{-k\uparrow}^\dagger \\ c_{-k\downarrow}^\dagger \\ c_{k+Q\uparrow} \\ c_{k+Q\downarrow} \\ c_{-k-Q\uparrow}^\dagger \\ c_{-k-Q\downarrow}^\dagger \end{pmatrix}. \qquad (11)$$

The corresponding Green's function can then in general be written as the 8×8 matrix

$$G(\boldsymbol{k}, \boldsymbol{k}', \tau) = -\langle T_\tau \psi_k(\tau)\psi_{k'}^\dagger(0)\rangle, \qquad (12)$$

where we will also be using the notation $G(\boldsymbol{k}, \boldsymbol{k}, \tau) = G(\boldsymbol{k}, \tau)$. After a Fourier transform, the imaginary time propagators can be expressed through the Fourier coefficients $G(\boldsymbol{k}, i\omega_n)$, with fermionic Matsubara frequencies $\omega_n = (2n + 1)\pi/\beta$. The 8×8 matrix can in general be spanned by the Pauli matrix outer products

$$\rho_\alpha \otimes \tau_\beta \otimes \sigma_\gamma, \qquad (13)$$

where $\alpha, \beta, \gamma \in \{0, 1, 2, 3\}$ and the Pauli matrix ρ_α acts on the momentum sector degree of freedom, τ_β on the particle/hole degree of freedom, and σ_γ on the spin degree of freedom.

We also introduce the magnon spinor

$$B_q = \begin{pmatrix} M_q^R & \big(M_{-q}^R\big)^\dagger & M_q^U & \big(M_{-q}^U\big)^\dagger \end{pmatrix}^T, \qquad (14)$$

where each magnon operator in the spinor corresponds to the destruction of an excitation with momentum $\boldsymbol{q}$ and spin -1, or the creation of an excitation with momentum $-\boldsymbol{q}$ and spin $+1$. The magnon operator propagators can now be collected in the magnon propagator matrix

$$D_{\gamma\gamma'}(\boldsymbol{q}, \tau) = -\big\langle T_\tau B_q^\gamma(\tau)B_{-q}^{\gamma'}(0)\big\rangle. \qquad (15)$$

After a Fourier transform, the propagator matrix takes the form

$$D(q) = \begin{pmatrix} 0 & \mathcal{D}^{RR}(q) & 0 & \mathcal{D}^{RU}(q) \\ \mathcal{D}^{RR}(-q) & 0 & \mathcal{D}^{UR}(-q) & 0 \\ 0 & \mathcal{D}^{UR}(q) & 0 & \mathcal{D}^{UU}(q) \\ \mathcal{D}^{RU}(-q) & 0 & \mathcal{D}^{UU}(-q) & 0 \end{pmatrix}, \qquad (16)$$
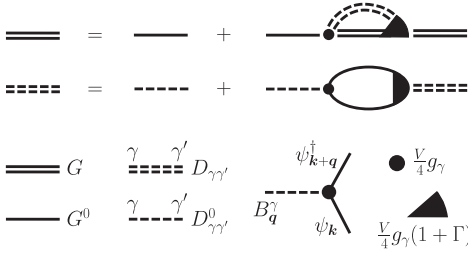
FIG. 3. Feynman diagram expansion for interacting electron and magnon propagators. Each vertex is associated with a factor $Vg_\gamma/4$, and electron and magnon propagators G and D are represented by solid and dashed lines.

in terms of the previously introduced propagators $\mathcal{D}^{\kappa\kappa'}$. Here, $q = (\boldsymbol{q}, iv_m)$ is a three-vector containing both momentum and the Matsubara frequency. As the magnon propagators respect time-reversal and inversion symmetry, we have $\mathcal{D}^{\kappa\kappa'}(-q) = \mathcal{D}^{\kappa\kappa'}(q)$. Further, the magnon propagators also satisfy $\mathcal{D}^{RU}(q) = \mathcal{D}^{UR}(q)$.

In spinor notation for the magnon and electron operators, the interaction Hamiltonian can be written on the form

$$H_{\text{int}} = \frac{V}{4} \sum_{\substack{\boldsymbol{k} \in \square \\ \boldsymbol{q} \in \diamond}} \sum_{\alpha\beta\gamma} g_\gamma^{\alpha\beta} B_{\boldsymbol{q}}^\gamma \psi_{\boldsymbol{k}+\boldsymbol{q}\alpha}^\dagger \psi_{\boldsymbol{k}\beta}, \qquad (17)$$

where the sum over $\boldsymbol{k}$ runs over the full Brillouin zone, the sum over $\boldsymbol{q}$ runs over the reduced Brillouin zone, and the index γ corresponds to the various operators in the magnon spinor $B_{\boldsymbol{q}}^\gamma$. The matrices g_γ are given by

$$g_1 = f_1 \otimes \rho_0, \quad g_2 = f_2 \otimes \rho_0, \qquad (18a)$$

$$g_3 = f_1 \otimes \rho_1, \quad g_4 = f_2 \otimes \rho_1, \qquad (18b)$$

where we have introduced the 4×4 matrices

$$f_1 = \tfrac{1}{2}(\sigma_1\tau_0 - i\sigma_2\tau_3), \qquad (19a)$$

$$f_2 = \tfrac{1}{2}(\sigma_1\tau_0 + i\sigma_2\tau_3), \qquad (19b)$$

acting on the spin and particle/hole degrees of freedom to simplify the notation.

C. S-matrix expansion

Starting from the noninteracting electron Hamiltonian and the spinor form of the interaction, we may now apply the S-matrix expansion and use Wicks theorem to obtain a Feynman diagram expansion for the electron Green's function $G(\boldsymbol{k}, i\omega_n)$, as shown in Fig. 3. The resulting equation can be solved for the electron Green's function to obtain the Dyson equation

$$G^{-1}(k) = G_0^{-1}(k) - \Sigma(k), \qquad (20)$$

where $\Sigma(k)$ is the self-energy, and $G_0(k)$ is the noninteracting electron Green's function given by

$$G_0^{-1}(\boldsymbol{k}, i\omega_n) = i\omega_n\rho_0\tau_0\sigma_0 - \epsilon_{\boldsymbol{k}}\rho_3\tau_3\sigma_0 + \mu\rho_0\tau_3\sigma_0. \qquad (21)$$

In the following, we neglect vertex corrections, which are discussed more in Appendix D. We may then consider only sunset type diagrams in the self-energy. Performing the S-matrix expansion, we extract the self-energy

$$\Sigma(k) = -\frac{V^2}{2\beta} \sum_{k'} \sum_{\gamma\gamma'} \theta_{\boldsymbol{k}-\boldsymbol{k}'} D_{\gamma\gamma'}(k-k') g_\gamma G(k') g_{\gamma'}, \qquad (22)$$

as evident from the diagrammatic representation in Fig. 3 up to signs and prefactors. Here, $\theta_{\boldsymbol{q}}$ is defined by

$$\theta_{\boldsymbol{q}} = \begin{cases} 1, & \boldsymbol{q} \in \text{RBZ} \\ 0, & \boldsymbol{q} \in \text{QBZ} \end{cases} \qquad (23)$$

and ensures that the magnon propagator momentum $\boldsymbol{q} = \boldsymbol{k} - \boldsymbol{k}'$ is restricted to the reduced Brillouin zone (RBZ) [39]. Here, QBZ refers to the conjugate Brillouin zone which, together with the RBZ, comprises the full electron Brillouin zone.

In the discussion so far, we have been using a Nambu spinor $\psi_{\boldsymbol{k}}$ containing electrons at both $\boldsymbol{k}$ and $\boldsymbol{k}+\boldsymbol{Q}$. Thus, the 8×8 matrix Green's function $G(k)$ may in general have correlations between electrons at momenta $\boldsymbol{k}$ and $\boldsymbol{k}+\boldsymbol{Q}$. In the following, we assume that the processes close to the Fermi surface dominate the self-energy. Away from half filling, we may then neglect the correlations which are off-diagonal in the momentum sector, as they are suppressed by the large electronic energy at momentum $\boldsymbol{k}+\boldsymbol{Q}$ when $\boldsymbol{k}$ is close to the Fermi surface. This is discussed in more detail in Appendix C. The Green's function $G(k)$ and the self-energy $\Sigma(k)$ then reduce to two uncoupled blocks of size 4×4 which are related by $\boldsymbol{k} \to \boldsymbol{k}+\boldsymbol{Q}$. In the following, we therefore consider only one of the two blocks.

D. Eliashberg equations

To derive the Eliashberg equations, we decompose the self-energy matrix into contributions corresponding to the various basis matrices $\sigma_\alpha \otimes \tau_\beta$ for Hermitian 4×4 matrices. We set

$$\Sigma = (1 - Z)i\omega_n\sigma_0\tau_0 + \chi\sigma_0\tau_3 + \phi_s\sigma_2\tau_2 + \phi_t\sigma_1\tau_1, \qquad (24)$$

where Z is the electron renormalization, χ is the quasiparticle energy shift, ϕ_s is the spin singlet pairing amplitude, and ϕ_t the amplitude for unpolarized spin triplet pairing.

Among the 16 possible terms on the form $\sigma_\alpha \otimes \tau_\beta$, we have kept only four. Of the remaining 12 combinations, the eight which do not conserve spin cannot occur because they are incompatible with the spin structure of the self energy diagram. The combinations $\tau_3\sigma_3$ and $\tau_0\sigma_3$ are disregarded because they introduce spin-dependent quasiparticle renormalization, which is not expected to be present due to the spin symmetry of the fermions in the system. Finally, we could have introduced terms $\tilde{\phi}_s\tau_1\sigma_2$ and $\tilde{\phi}_t\sigma_1\tau_2$. However, the associated fields $\tilde{\phi}_s$ and $\tilde{\phi}_t$ would play exactly the same roles as ϕ_s and ϕ_t, and we therefore set them to zero.

Due to symmetry relations between the electron correlations in the Nambu spinor Green's function matrix $G(k)$ [40], the normal Green's function fields satisfy

$$Z(-k) = Z(k), \quad Z(\boldsymbol{k}, i\omega_n) = Z(\boldsymbol{k}, -i\omega_n)^*, \quad (25)$$

$$\chi(-k) = \chi(k), \quad \chi(\boldsymbol{k}, i\omega_n) = \chi(\boldsymbol{k}, -i\omega_n)^*, \quad (26)$$

and the anomalous correlations satisfy

$$\phi_s(-k) = +\phi_s(k), \quad \phi_s(\boldsymbol{k}, i\omega_n) = \phi_s(\boldsymbol{k}, -i\omega_n)^*, \quad (27)$$

$$\phi_t(-k) = -\phi_t(k), \quad \phi_t(\boldsymbol{k}, i\omega_n) = \phi_t(\boldsymbol{k}, -i\omega_n)^*. \quad (28)$$

We may now derive equations for the fields Z, χ, ϕ_s, ϕ_t by inserting the form for Σ into the Dyson equation, inverting the inverse $G^{-1}(k)$ and inserting $G(k)$ into the self-energy in Eq. (22). Comparing term by term, we then obtain the equations

$$[1 - Z(k)]i\omega_n = -V^2 \frac{1}{\beta} \sum_{k'} \mathcal{D}(k - k') \frac{i\omega_{n'} Z(k')}{\Theta(k')}, \quad (29a)$$

$$\chi(k) = -V^2 \frac{1}{\beta} \sum_{k'} \mathcal{D}(k - k') \frac{\xi_{k'} + \chi(k')}{\Theta(k')}, \quad (29b)$$

$$\phi_s(k) = -V^2 \frac{1}{\beta} \sum_{k'} \mathcal{D}(k - k') \frac{\phi_s(k')}{\Theta(k')}, \quad (29c)$$

$$\phi_t(k) = +V^2 \frac{1}{\beta} \sum_{k'} \mathcal{D}(k - k') \frac{\phi_t(k')}{\Theta(k')}, \quad (29d)$$

under the assumption that a single symmetry channel dominates, so that either $\phi_s = 0$ or $\phi_t = 0$ [41]. We have also introduced the combined magnon propagator

$$\mathcal{D}(q) = \theta_{\boldsymbol{q}} \mathcal{D}^{RR}(\boldsymbol{q}, i\nu_m) + \theta_{\boldsymbol{q}+\boldsymbol{Q}} \mathcal{D}^{UU}(\boldsymbol{q} + \boldsymbol{Q}, i\nu_m), \quad (30)$$

where the argument $\boldsymbol{q}$ can now take on values in the full electron Brillouin zone. The submatrix determinant $\Theta(k)$ is given by

$$\Theta(k) = [i\omega_n Z(k)]^2 - \tilde{\xi}_k^2 - |\phi_{s,t}(k)|^2, \quad (31)$$

with anomalous correlation $\phi_{s,t}$ depending on whether we consider a singlet or triplet instability, and where have introduced $\tilde{\xi}_k = \xi_k + \chi(k)$. In the following, we will assume that the quasiparticle energy shift χ is small compared to the electron bandwidth and that it can be neglected. Note the opposite signs on the right hand side of the equations for ϕ_s and ϕ_t. This occurs because the spin flips in the vertices of the self-energy diagrams introduce a sign change for the spin singlet amplitude but not for the spin triplet amplitude.

IV. FERMI SURFACE AVERAGED EQUATIONS

When the electron energy scale is large compared to the magnon energy scale, the regions close to the Fermi surface dominate the momentum sums in the Eliashberg equations. We assume that the quasiparticle renormalization field close to the Fermi surface is weakly dependent on momentum, so that we may write $Z(\boldsymbol{k}, i\omega_n) = Z(i\omega_n)$. Furthermore, for a single dominant pairing symmetry channel, we assume that the anomalous correlations can be written in the product form

$\phi_{s,t}(\boldsymbol{k}, i\omega_n) = \psi(\boldsymbol{k})\phi_{s,t}(i\omega_n)$, where we assume some simple functional form $\psi(\boldsymbol{k})$ for the momentum dependence of the relevant anomalous correlation.

Since we expect regions close to the Fermi surface to dominate the momentum sum, we may split it into a perpendicular and a parallel part, and neglect the perpendicular momentum dependence of the magnon propagator. Close to the critical temperature, one may furthermore linearize the Eliashberg equations in the anomalous correlations. Converting the perpendicular momentum integration into an energy integral, one then obtains

$$(1 - Z)i\omega_n = \frac{1}{\beta N_F} \sum_{\omega_{n'}} \lambda_1(i\omega_n - i\omega_{n'}) i\omega_{n'} Z' \int d\xi \frac{N(\xi)}{\Theta(\xi, i\omega_{n'})}, \quad (32a)$$

$$\phi_{s,t} = -\frac{1}{\beta N_F} \sum_{\omega_{n'}} \lambda_2^{s,t}(i\omega_n - i\omega_{n'}) \phi'_{s,t}$$

$$\times \int d\xi \frac{N(\xi)}{\Theta(\xi, i\omega_{n'})}. \quad (32b)$$

We have here introduced the dimensionless electron-magnon coupling strength $\lambda_1(i\omega_n - i\omega_{n'})$ occurring in the quasiparticle renormalization equations and the modified coupling strength $\lambda_2^{s,t}(i\omega_n - i\omega_{n'})$ occurring in the anomalous correlation equations. We have further denoted $Z(k)$ by Z and $Z(k')$ by Z', with similar notation also for the remaining fields, and denoted the electron density of states by $N(\xi)$, which takes on the value N_F at the Fermi level. The dimensionless coupling strengths are given by

$$\lambda_1(i\omega_n - i\omega_{n'}) = -\frac{V^2}{N_F} \sum_{\boldsymbol{k}\boldsymbol{k}'} \delta(\xi_{\boldsymbol{k}})\delta(\xi_{\boldsymbol{k}'})\mathcal{D}(k - k'), \quad (33)$$

$$\lambda_2^{s,t}(i\omega_n - i\omega_{n'}) = -\zeta_{s,t} \frac{1}{\langle \psi^2(\boldsymbol{k})\rangle_{\text{FS}}} \frac{V^2}{N_F} \sum_{\boldsymbol{k}\boldsymbol{k}'} \delta(\xi_{\boldsymbol{k}})\delta(\xi_{\boldsymbol{k}'})$$

$$\times \psi(\boldsymbol{k})\mathcal{D}(k - k')\psi(\boldsymbol{k}'), \quad (34)$$

where $\zeta_s = -1$ for spin singlet and $\zeta_t = +1$ for spin triplet is the sign associated with a spin flip in the anomalous pairing. The brackets $\langle\ \rangle_{\text{FS}}$ denote a Fermi surface average.

In the following, we assume that the density of states can be approximated by a constant in the dominant region close to the Fermi surface. We may then perform the energy integral analytically to obtain

$$(1 - Z)i\omega_n = -\frac{i\pi}{\beta} \sum_{\omega_{n'}} \lambda_1(i\omega_n - i\omega_{n'}) \, \text{sgn}(\omega_{n'}), \quad (35)$$

$$\phi_{s,t} = +\frac{\pi}{\beta} \sum_{\omega_{n'}} \lambda_2^{s,t}(i\omega_n - i\omega_{n'}) \frac{\phi'_{s,t}}{|\omega_{n'} Z'|}. \quad (36)$$

We next assume that the magnon propagator $\mathcal{D}$ can be replaced by the noninteracting propagator $\mathcal{D}_0$. Solving the Eliashberg equations is then reduced to calculating dimensionless coupling strengths $\lambda_{1,2}$ and solving eigenvalue problems in the Matsubara frequencies. In Sec. VI, we investigate the effect of including the magnon self-energy.

In addition to introducing the dimensionless coupling strengths $\lambda_{1,2}$, we may follow the conventional routine and

also introduce frequency dependent functions $\alpha_{1,2}^2 F(\omega)$ defined such that

$$\lambda_{1,2}(i\omega_n - i\omega_{n'}) = \int d\omega \, \alpha_{1,2}^2 F(\omega) \frac{2\omega}{(\omega_n - \omega_{n'})^2 + \omega^2}. \quad (37)$$

Comparing with the definition of $\lambda_{1,2}$, this gives

$$\alpha_1^2 F(\omega) = \frac{V^2}{N_F} \sum_{kk'} \delta(\xi_k) \delta(\xi_{k'}) \delta(\omega - \omega_{k-k'}) \mathcal{A}_e(k - k'), \quad (38)$$

$$\alpha_2^2 F(\omega) = \zeta_{s,t} \frac{1}{\langle \psi^2(k) \rangle_{\text{FS}}} \frac{V^2}{N_F} \sum_{kk'} \delta(\xi_k) \delta(\xi_{k'}) \delta(\omega - \omega_{k-k'})$$
$$\times \psi(k) \mathcal{A}_e(k - k') \psi(k'), \quad (39)$$

where the boosting factor

$$\mathcal{A}_e(q) = \theta_q A_e^{RR}(q) + \theta_{q+Q} A_e^{UU}(q + Q), \quad (40)$$

has been defined analogously to $\mathcal{D}(q)$.

The Eliashberg functions $\alpha_{1,2}^2 F(\omega)$ and the electron-magnon coupling strengths $\lambda_{1,2}(i\nu_m)$ are central quantities in the Fermi surface averaged Eliashberg equations. Through the approximate formula

$$T_c^{\text{AD}} = \frac{\omega_{\log}}{1.2} \exp\left(-\frac{1.04[1 + \lambda_1(0)]}{\lambda_2(0)} \right), \quad (41)$$

they can therefore be used to qualitatively understand the critical temperatures resulting from actually solving the Eliashberg equations. The above formula was suggested by Allen and Dynes [42] for weak and intermediate electron-boson coupling. We have set the Coulomb pseudopotential to zero and use the logarithmic average

$$\omega_{\log} = \omega_a \exp\left[\frac{2}{\lambda_2(0)} \int d\omega \ln\left(\frac{\omega}{\omega_a} \right) \frac{\alpha_2^2 F(\omega)}{\omega} \right] \quad (42)$$

as the effective cutoff frequency, where ω_a is an arbitrary frequency scale.

V. SOLVING THE ELIASHBERG EQUATIONS

We now solve the Fermi surface averaged equations using realistic material parameters, as detailed in Appendix E. We set $\Omega_A = 1$ and use $\Omega_B \equiv \Omega \in [0, 1]$ to tune the sublattice coupling asymmetry.

In order to compute the dimensionless coupling strengths $\lambda_{1,2}$, the momentum sums are transformed into integrals over momenta on the Fermi surface. The quasiparticle renormalization field $Z(i\omega_n)$ can then be calculated using Eq. (35). Subsequently, we use Eq. (36) to determine the critical temperature for the superconducting instability by finding the temperature for which the largest eigenvalue of the eigenvalue problem becomes 1 [43,44]. This gives the critical temperature T_c of the superconducting instability. We consider three different ansätze for the superconducting pairing, namely even frequency spin triplet p-wave pairing, even frequency spin triplet f-wave pairing, and even frequency spin singlet d-wave pairing. These pairings dominate in different parts of the parameter space of our model. Other pairing symmetries like even frequency spin singlet s-wave and different odd frequency variants were not found to give rise to superconductivity. Figure 4(a) presents the phase diagram for our model in the Ω-μ plane, where critical temperature normalized to the maximum value within each phase is indicated
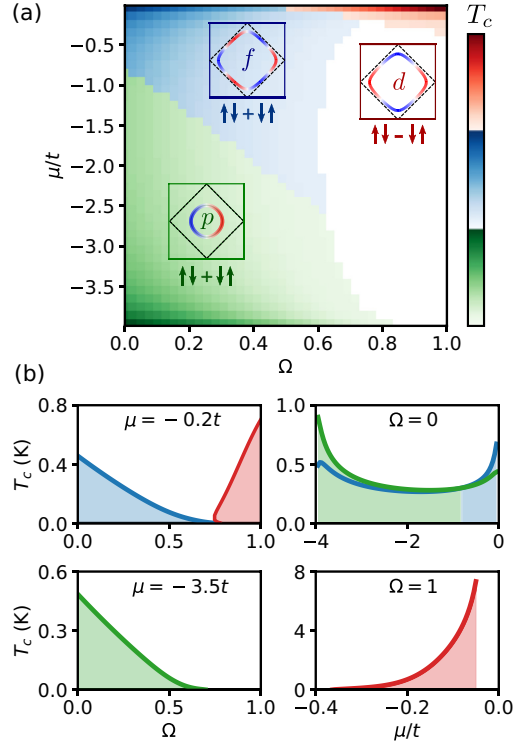
FIG. 4. (a) Phase diagram in terms of sublattice coupling asymmetry $\Omega = \Omega_B/\Omega_A$ and chemical potential μ below half filling. We find spin triplet p-wave, spin triplet f-wave, and spin singlet d-wave phases. The phase diagram is colored according to the critical temperature normalized to the largest value in the phase diagram within the same phase. Parameter regimes supporting multiple superconducting instabilities are colored according to the phase with the largest critical temperature. The insets show the spin structure and momentum structure on the Fermi surface for the various phases. The various subfigures in (b) show the critical temperature T_c as a function of Ω (left) and μ (right) along different lines in the phase diagram.

by color intensity. The type of pairing is indicated by choice of color (green/blue/red), where regimes supporting multiple solutions are colored according to the phase with the largest critical temperature. In the following, we discuss the different superconducting phases in the phase diagram in more detail.

A. Spin triplet p-wave and f-wave pairing

For the even frequency spin triplet p-wave and f-wave pairings, we consider anomalous pairing momentum dependence on the form

$$\psi_p(k) = \cos\phi_k, \quad (43a)$$
$$\psi_f(k) = \cos 3\phi_k, \quad (43b)$$

where ϕ_k is the polar angle between the quasimomentum $\boldsymbol{k}$ on the Fermi surface and the x axis. These momentum dependencies are shown in the insets of the phase diagram.

As expected, and in agreement with the results of Ref. [21], we find even frequency spin triplet p-wave superconductivity for small Fermi surfaces and large sublattice coupling asymmetry, corresponding to small μ and Ω. For small Fermi surfaces, all processes between points on the Fermi surface are of the regular type. Since the magnon energy is smallest for small $\boldsymbol{q}$, minimizing the denominator of the magnon propagator, the dominant contribution to the momentum sums in the Eliashberg equations originate from small $\boldsymbol{q}$. Without sublattice coupling asymmetry (i.e., $\Omega = 1$), coherence factor interference effects suppress the boosting factor $A_e^{RR}(\boldsymbol{q})$, whereas $\Omega = 0$ removes these interference effects completely and makes p-wave superconductivity possible.

Setting $\Omega = 0$, we also find an even frequency spin triplet f-wave solution in the entire chemical potential range we have considered. As shown in Fig. 4(b), the critical temperature of the p-wave solution is larger than the critical temperature of the f-wave solution for small Fermi surfaces. For Fermi surfaces approaching half filling, however, the situation is reversed due to emergence of subleading Umklapp processes. The interaction providing spin triplet pairing is attractive for scattering processes between $\boldsymbol{k}$ and $\boldsymbol{k}'$ only when $\phi(\boldsymbol{k}, i\omega_n)$ and $\phi(\boldsymbol{k}', i\omega_n)$ have the same sign. Consider now the scattering processes between points on the Fermi surface where the momentum transfer is closest to $\boldsymbol{Q}$, bringing the electron from one side of the Fermi surface to the opposing side. From the f-wave and p-wave momentum structure of the anomalous correlations shown in the insets of Fig. 4(a), it is clear that these processes are always repulsive in the p-wave phase and typically attractive in the f-wave phase. This explains why the f-wave phase has a higher critical temperature than the p-wave phase upon approaching half filling. As discussed in more detail in Sec. VIII, the combination of $\Omega = 0$ and the presence of Umklapp processes may, however, be challenging to access experimentally.

Compared with the results of Ref. [21], we find significantly lower critical temperatures for the p-wave phase. We attribute this difference to the magnon energy cutoff. As long-wavelength processes dominate, the characteristic magnon frequency in the pairing interaction is much smaller than the upper cutoff on the magnon spectrum. Since the characteristic frequency serves as the energy scale for the critical temperature, the critical temperature is then significantly reduced, which is captured in the Eliashberg theory analysis.

More quantitatively, this argument can be understood in terms of the Allen-Dynes formula of Eq. (41). Since the boosting factor $A_e^{RR}(\boldsymbol{q})$ is peaked for small momenta $\boldsymbol{q}$, and the electron-magnon coupling strength V is momentum independent, the electron-magnon coupling function $\alpha_2^2 F(\omega)$ is peaked at small frequencies. This is shown in Fig. 5(a), where the logarithmic average $\omega_{\log}$ is indicated with a dashed line. The effective magnon frequency for the superconducting pairing is therefore significantly reduced compared to the largest magnon frequency in the system. Further, the lower panel of Fig. 5(c) shows $\lambda_{1,2}(i v_m)$, which decays quickly beyond the effective cutoff. Solving the Eliashberg equations gives the solutions for the anomalous correlation $\phi(i\omega_n)$, which
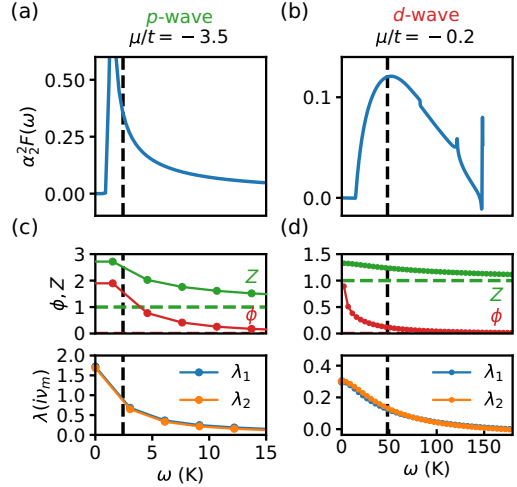
FIG. 5. Eliashberg functions and Eliashberg equation solutions for the p-wave regime ($\mu/t = -3.5$ and $\Omega = 0$) to the left and d-wave regime ($\mu/t = -0.2$ and $\Omega = 1$) to the right. Subfigures (a) and (b) show the Eliashberg function $\alpha_2^2 F(\omega)$. Subfigures (c) and (d) show the dimensionless electron-magnon coupling strengths $\lambda_{1,2}(i v_m)$ as well as the Matsubara frequency dependence of the quasiparticle renormalization $Z(i\omega_n)$ and the anomalous correlation $\phi(i\omega_n)$ at the critical temperatures for the respective superconducting instabilities. The logarithmic average $\omega_{\log}$ is shown with vertical dashed lines.

also decays quickly beyond the cutoff, and the quasiparticle renormalization $Z(i\omega_n)$, which decays to 1.

B. Spin singlet d-wave pairing

In the Eliashberg equations, the difference between the spin triplet case in Eq. (29d) and the singlet case in Eq. (29c) is the sign. Thus, the small momentum process pairing potential that was attractive for spin triplet pairing becomes repulsive for spin singlet pairing. To obtain singlet pairing attraction, we therefore need to rely on dominant processes with a relative sign between the anomalous pairing $\phi_s(k)$ on the left-hand side and right-hand side of the equation. Since small momentum processes cannot provide this sign change, we need to rely on Umklapp processes. As an s-wave ansatz does not change sign around the Fermi surface, we instead choose the d-wave ansatz

$$\psi_d(\boldsymbol{k}) = \frac{1}{2\pi}(\cos k_x - \cos k_y), \qquad (44)$$

shown in the inset of the phase diagram in Fig. 4(a). Since the d-wave phase relies on Umklapp processes, it occurs for chemical potentials μ approaching half filling in the phase diagram. Furthermore, the Umklapp processes benefit from the coherence factor interference in the boosting factor $A_e^{UU}(\boldsymbol{q})$, which is maximized for $\Omega = 1$. Crucially, these interferences also suppress the competing regular processes with small momentum $\boldsymbol{q}$, which would otherwise prevent

spin singlet superconductivity. The d-wave phase therefore occurs only for large Ω in the phase diagram. This picture is also verified in Fig. 4(b), which shows the critical temperature for the spin singlet d-wave phase as a function of coupling asymmetry and as a function of chemical potential at $\Omega = 1$.

The electron-magnon coupling strength function $\alpha_2^2 F(\omega)$ is shown in Fig. 5(b). With $\Omega = 1$, the regular small momentum processes are suppressed, and away from half filling, the Umklapp processes between points on the Fermi surface require the magnons to carry momentum which differs from $\boldsymbol{Q}$ by a finite amount. Therefore, $\alpha_2^2 F(\omega)$ takes on significant values only beyond a relatively large lower frequency cutoff. This cutoff corresponds to the magnon energy associated with the smallest momentum necessary to bring an Umklapp scattered electron with incoming momentum $\boldsymbol{k}$ from $\boldsymbol{k} + \boldsymbol{Q}$ and back to the Fermi surface. Moreover, it should be noted that this smallest momentum depends on where on the Fermi surface the electron was situated to begin with. At the lowest relevant frequencies in $\alpha_2^2 F(\omega)$, only a few momenta $\boldsymbol{k}$ bring $\boldsymbol{k} + \boldsymbol{Q}$ to a position where the momentum transfer necessary to get back to the Fermi surface is associated with a magnon energy that is small enough to match the frequency ω. The function $\alpha_2^2 F(\omega)$ then only obtains contributions from a few points $\boldsymbol{k}$ that bring $\boldsymbol{k} + \boldsymbol{Q}$ close enough to the Fermi surface. As the frequency ω increases, $\alpha_2^2 F(\omega)$ obtains contributions from more points $\boldsymbol{k}$ as the restriction on how close $\boldsymbol{k} + \boldsymbol{Q}$ needs to be to the Fermi surface is relaxed. Therefore, $\alpha_2^2 F(\omega)$ is not peaked at small frequencies. The situation should be contrasted with the p-wave case, where regular scattering on the Fermi surface with vanishing momentum is possible regardless of where on the Fermi surface the initial electron is situated. Denoting the magnon spectrum gap by ω_0, $\alpha_2^2 F(\omega \to \omega_0)$ therefore receives large contributions from $\boldsymbol{k} - \boldsymbol{k}' \approx 0$ regardless of where on the Fermi surface $\boldsymbol{k}$ is situated.

The reduced reliance of the d-wave pairing on processes with small magnon energy gives rise to a larger effective magnon frequency $\omega_{\log}$. This larger characteristic magnon frequency suppresses the magnon propagator occurring in $\lambda_{1,2}(i\nu_m)$ for small Matsubara frequencies but also increases the frequency scale over which the magnon propagator decays compared to the p-wave regime. Together with a large density of states close to half filling, this causes the significant critical temperatures that are observed for the d-wave regime in Fig. 4(b). As shown in Fig. 5(d), the dimensionless electron-magnon coupling strength $\lambda_{1,2}(i\nu_m)$ decays to zero beyond the effective cutoff frequency, whereas $\phi(i\omega_n)$ has a crossover from behavior $1/\omega_n$ to $1/\omega_n^3$.

C. Effect of frustration

Since the superconductivity in our system relies on spin fluctuations, we expect interactions in the AFMI spin model that enhance fluctuations to also enhance the critical temperature. Earlier weak-coupling studies have investigated the effect of a frustrating next-nearest neighbor exchange coupling $J_2 > 0$ in the antiferromagnet on superconductivity dominated by regular fermion-magnon scattering processes [22,23]. In Fig. 6(a),we show how the critical temperature
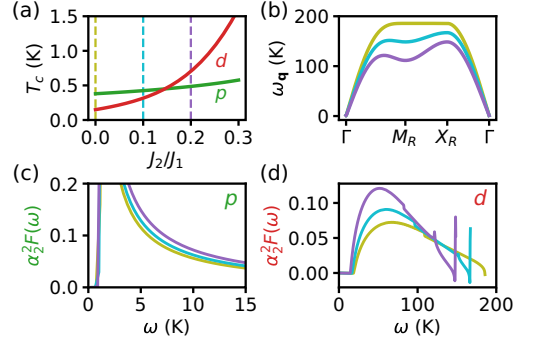
FIG. 6. Effect of frustrating the antiferromagnet with an next-to-nearest neighbor exchange coupling J_2. (a) Critical temperature for the p-wave (at $\mu = -3.5t$ and $\Omega = 0$) and d-wave (at $\mu = -0.2t$ and $\Omega = 1$) instabilities as a function of J_2 frustrating the antiferromagnet. (b) Magnon spectrum for different values of J_2, as indicated by the vertical dashed lines in (a), between Brillouin zone high symmetry points as shown in Fig. 2(a). (c) Electron-magnon coupling function $\alpha_2^2 F(\omega)$ in the p-wave regime. (d) $\alpha_2^2 F(\omega)$ in the d-wave regime. Frustration reduces the magnon excitation energies and enhance the spin fluctuations in the system. Thus, weight is shifted from high magnon energies to low magnon energies in the electron-magnon coupling function $\alpha_2^2 F(\omega)$, and this increases the critical temperature.

increases with J_2 for both the p-wave and d-wave instabilities. The effect of J_2 on the superconductivity can be understood in terms of the magnon excitation energies in Fig. 6(b), showing that the magnon bands are flattened as J_2 increases. As displayed in Figs. 6(c) and 6(d), this shifts weight from large to the more significant small frequencies in the electron-magnon coupling function $\alpha_2^2 F(\omega)$, leading to a higher critical temperature. Notably, increasing J_2 does not affect the gap in the magnon spectrum, meaning that the effective cutoff for the p-wave phase is not much affected. For the d-wave phase, the effective cutoff is somewhat reduced for larger J_2, but trading some cutoff for a larger dimensionless coupling strength $\lambda_2(0)$ is nevertheless found to be beneficial. As the d-wave phase has a smaller dimensionless coupling strength than the p-wave phase, the increase of the dimensionless coupling strength arising from J_2 leads to a more dramatic increase in critical temperature for the d-wave curve in Fig. 6(a).

VI. MAGNON RENORMALIZATION

To consider the effect of magnon renormalization, we consider the electron bubble diagram shown in Fig. 3 and once again neglect vertex corrections. Performing the S-matrix expansion, one may show that magnon propagators $D_{\gamma\gamma'}$ satisfy the Dyson equation

$$D^{-1}(q) = D_0^{-1}(q) - \Pi(q), \qquad (45)$$

where the polarization matrix is given by

$$\Pi_{\gamma\gamma'}(q) = \frac{V^2}{4\beta} \sum_k \text{Tr}\left[g_\gamma G(k+q) g_{\gamma'} G(k)\right]. \qquad (46)$$

From the matrix structure of the matrices g_γ, it follows that $\Pi_{\gamma\gamma'}$ takes the form

$$\Pi(q) = \begin{pmatrix} 0 & \Pi^{RR}(q) & 0 & \Pi^{RU}(q) \\ \Pi^{RR}(-q) & 0 & \Pi^{UR}(-q) & 0 \\ 0 & \Pi^{UR}(q) & 0 & \Pi^{UU}(q) \\ \Pi^{RU}(-q) & 0 & \Pi^{UU}(-q) & 0 \end{pmatrix}. \tag{47}$$

In principle, we should now solve the coupled equations for the electron and magnon propagators. However, to estimate the effect of magnon renormalization, we use the noninteracting electron Green's functions to calculate the polarizations. Using the previous assumption of neglecting terms in the electron Green's function which are off-diagonal in momentum sector, we may furthermore neglect the mixed process polarizations Π^{UR} and Π^{RU}. This leaves the regular and Umklapp polarizations Π^{RR} and Π^{UU}, which reduce to

$$\Pi_0^{RR}(q) = \frac{V^2}{\beta} \sum_k G_0^{11}(k+q) G_0^{22}(k), \tag{48}$$

$$\Pi_0^{UU}(q) = \frac{V^2}{\beta} \sum_k G_0^{11}(k+q+Q) G_0^{22}(k), \tag{49}$$

where G_0^{11} and G_0^{22} are matrix elements in the noninteracting electron Green's function G_0 corresponding to different spins.

Solving the Dyson equation for the magnon propagator, one may show that the regular and Umklapp propagators become

$$\mathcal{D}^{RR}(q) = \left[\left(\frac{1 - \mathcal{D}_0^{UU} \Pi_0^{UU}}{1 - r\mathcal{D}_0^{UU} \Pi_0^{UU}} \right) - \mathcal{D}_0^{RR} \Pi_0^{RR} \right]^{-1} \mathcal{D}_0^{RR}(q), \tag{50}$$

$$\mathcal{D}^{UU}(q) = \left[\left(\frac{1 - \mathcal{D}_0^{RR} \Pi_0^{RR}}{1 - r\mathcal{D}_0^{RR} \Pi_0^{RR}} \right) - \mathcal{D}_0^{UU} \Pi_0^{UU} \right]^{-1} \mathcal{D}_0^{UU}(q), \tag{51}$$

where we have introduced the quantity

$$r(\boldsymbol{q}) = 1 - \frac{A_e^{UR}(\boldsymbol{q}) A_e^{RU}(\boldsymbol{q})}{A_e^{RR}(\boldsymbol{q}) A_e^{UU}(\boldsymbol{q})}. \tag{52}$$

Here, the Umklapp polarization occurs in the regular propagator and vice versa due to the presence of mixed magnon propagators.

We note that in the special case $\Omega = 0$ where we found spin triplet pairing, we have $r = 0$ since all the boosting factors are equal. In the opposite limit of $\Omega = 1$ where we found spin singlet d-wave pairing approaching half filling, the mixed propagators vanish, so that $r = 1$ and each of the two magnon propagators $\mathcal{D}^{\kappa\kappa}(q)$ are just renormalized by the corresponding polarization $\Pi^{\kappa\kappa}(q)$.

We may now calculate the regular and the Umklapp polarizations. Performing the Matsubara frequency sums in Eqs. (48) and (49), we obtain the standard result

$$\Pi_0^{RR}(\boldsymbol{q}, iv_m) = V^2 \sum_{\boldsymbol{p}} \left(\frac{n_F(\xi_{\boldsymbol{p}}) - n_F(\xi_{\boldsymbol{p}+\boldsymbol{q}})}{iv_m + \xi_{\boldsymbol{p}} - \xi_{\boldsymbol{p}+\boldsymbol{q}}} \right), \tag{53}$$

$$\Pi_0^{UU}(\boldsymbol{q}, iv_m) = V^2 \sum_{\boldsymbol{p}} \left(\frac{n_F(\xi_{\boldsymbol{p}}) - n_F(\xi_{\boldsymbol{p}+\boldsymbol{q}+\boldsymbol{Q}})}{iv_m + \xi_{\boldsymbol{p}} - \xi_{\boldsymbol{p}+\boldsymbol{q}+\boldsymbol{Q}}} \right), \tag{54}$$
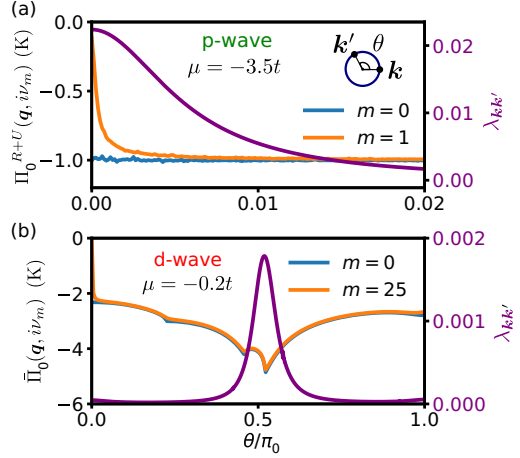
FIG. 7. Polarization renormalizing the magnon propagator for magnon scattering momenta $\boldsymbol{q}$ between points $\boldsymbol{k}$ and $\boldsymbol{k}'$ on the Fermi surface, corresponding to angles 0 and θ, as shown in the inset of (a). The relative contributions $\lambda_{\boldsymbol{k}\boldsymbol{k}'}$ from the various points on the Fermi surface to $\lambda_2(iv_m = 0)$ is shown in purple. (a) shows the combined polarization $\Pi_0^{R+U}(\boldsymbol{q}, iv_m)$ and the contributions to $\lambda_2(0)$ for $\mu/t = -3.5$ and $\Omega = 0$, where we expect p-wave superconductivity. The dominant contributions to $\lambda_2(0)$ come from small momentum processes close to $\theta = 0$. (b) shows the polarization $\bar{\Pi}(\boldsymbol{q}, iv_m)$, corresponding to Π^{RR} when $\boldsymbol{k} - \boldsymbol{k}' = \boldsymbol{q}$ is inside, and Π^{UU} when $\boldsymbol{k} - \boldsymbol{k}' = \boldsymbol{q}$ is outside the reduced Brillouin zone. Dominant contributions to $\lambda_2(0)$ come from Umklapp processes in vicinity to $\boldsymbol{k} - \boldsymbol{k}' = \boldsymbol{Q}$. The temperature has been set to $T = 1\text{K}$ in both subfigures.

where the momentum sums are evaluated in the thermodynamic limit through numerical integration [45]. Using that $\xi_{\boldsymbol{p}} = \xi_{-\boldsymbol{p}}$, one may show that the imaginary part of the polarization vanishes, so that only the real part remains.

For $\Omega = 0$ and a small Fermi surface, the relevant processes are regular processes. The renormalization of the regular propagator then depends on $\Pi_0^{R+U}(\boldsymbol{q}, iv_m) \equiv \Pi_0^{RR}(\boldsymbol{q}, iv_m) + \Pi_0^{UU}(\boldsymbol{q}, iv_m)$, where the Umklapp polarization Π_0^{UU} is small. In Fig. 7(a) we present the polarization $\Pi_0^{R+U}(\boldsymbol{k} - \boldsymbol{k}', iv_m)$ together with the contributions to $\lambda_2(iv_m = 0)$ from the various momenta $\boldsymbol{k}'$ on the Fermi surface given incoming electron momentum $\boldsymbol{k}$ as shown in the inset. The dominant contributions to $\lambda_2(iv_m = 0)$ arise from $\theta \approx 0$, which corresponds to scattering processes with small momentum $\boldsymbol{q} = \boldsymbol{k} - \boldsymbol{k}'$. In this region, the zero frequency polarization is more or less constant. Consistent with what we expect from Eq. (53), the finite frequency polarizations approach zero as $\boldsymbol{q} \to 0$. The region where the finite frequency polarizations deviate significantly from the zero frequency polarization is, however, small compared to the region over which we expect the dominant contributions to λ_2 [46]. Hence we may approximate the polarization for $\Omega = 0$ and small Fermi surface by a constant value $\Pi_C \approx \Pi_0^{RR}(\boldsymbol{q} \to 0, iv_m = 0) = -N_F V^2$.

For $\Omega = 1$, the regular and Umklapp propagators are simply renormalized by the regular and Umklapp polarizations, respectively. Figure 7(b) therefore presents the polarization $\bar{\Pi}_0(\boldsymbol{q}, iv_m) \equiv \theta_q \Pi_0^{RR}(\boldsymbol{q}, iv_m) + \theta_{q+Q} \Pi_0^{UU}(\boldsymbol{q} + \boldsymbol{Q}, iv_m)$, which is relevant for the d-wave phase. Also shown are the contributions to $\lambda_2(iv_m = 0)$ as in Fig. 7(a). The polarization is now weakly dependent on frequency, but it varies somewhat with momentum in the relevant region. Qualitatively, it should also in this case be possible to extract the effect of magnon renormalization by setting the polarization to a constant value.

In the following, we consider the same two special cases as above. For $\Omega = 0$ and large doping, where we found p-wave superconductivity, the relevant magnon propagator is $\mathcal{D}^{RR}(q)$, which can be written

$$\mathcal{D}^{RR}(q) = -\frac{4\omega_q A_e^{RR}(\boldsymbol{q})}{v_m^2 + \omega_q^2 + 4\omega_q A_e^{RR}(\boldsymbol{q})\Pi_C}. \tag{55}$$

Thus, the magnon frequency in the denominator has been replaced by an effective magnon frequency ω_q^{eff}, given by

$$\left(\omega_q^{\mathrm{eff}}\right)^2 = \omega_q^2 + 4\omega_q A_e^{RR}(\boldsymbol{q})\Pi_C. \tag{56}$$

Since the polarization is negative, the effective magnon frequency may turn imaginary, indicating that it is no longer reasonable to start out from a Néel ordered state. At $\boldsymbol{q} = 0$, where the magnon energy is the smallest, it happens for

$$|\Pi_C| \geqslant 2KS\left(\frac{1 + K/2z_1 J_1}{1 + K/z_1 J_1}\right), \tag{57}$$

where z_1 is the number of nearest neighbors.

For $\Omega = 1$ and large Fermi surface, where we found d-wave superconductivity, the two relevant propagators $\mathcal{D}^{RR}$ and $\mathcal{D}^{UU}$ are given by

$$\mathcal{D}^{\kappa\kappa}(q) = -\frac{4\omega_q A_e^{\kappa\kappa}(\boldsymbol{q})}{v_m^2 + \omega_q^2 + 4\omega_q A_e^{\kappa\kappa}(\boldsymbol{q})\Pi_0^{\kappa\kappa}}, \tag{58}$$

with $\kappa \in \{R, U\}$. Similar to the previous special case, we may now introduce an effective magnon frequency. Since the unrenormalized magnon frequency is the smallest for $\boldsymbol{q} = 0$ and the regular boosting factor $A_e^{RR}(\boldsymbol{q} = 0)$ is suppressed due to coherence factor interference, we expect that the effective magnon frequency may primarily turn imaginary for Umklapp processes close to $\boldsymbol{q} = 0$. One may show that this happens for

$$\left|\Pi_0^{UU}\right| \geqslant \frac{1}{2}KS. \tag{59}$$

Although the coupling to the electrons may therefore in principle destroy the magnetic order in the antiferromagnet, unsurprisingly, this does not happen as long as the easy axis anisotropy is sufficiently large compared to the polarization. A picture now emerges where the easy-axis anisotropy and the magnon renormalization play opposite roles stabilizing and destabilizing the magnetic order in the antiferromagnet, respectively. Retaining magnetic order upon inclusion of magnon renormalization requires a larger easy axis anisotropy. The larger easy axis anisotropy has little effect on the numerator of the magnon propagator but shifts the square of the magnon energies in the denominator upwards by an almost constant value with respect to momentum when J_2/J_1 is small. By choice of the easy-axis anisotropy, the effect of the magnon renormalization on the effective magnon

frequencies can then be compensated. Superconductivity may therefore still occur at critical temperatures similar to those obtained by disregarding magnon renormalization.

VII. DISCUSSION

The Eliashberg equation solutions in this paper are obtained using Fermi surface averaged equations, thus neglecting the dependence of the magnon propagator and the fields appearing in the Eliashberg equations on momentum perpendicular to the Fermi surface. The justification for this is as follows: Although the magnon propagator is momentum dependent, the behavior of the right-hand side of the Eliashberg equations when moving $\boldsymbol{k}'$ away from the Fermi surface is still dominated by the suppression arising from the fermion energies in the denominator due to the large energy scale of the electrons. In this case there are additional variations arising from the momentum dependence of the magnon propagator. Thus, a possible avenue for further work could be to take the full momentum dependence in the Eliashberg equations into account in order to test the accuracy of our approximation.

The results also rely on vertex corrections being small, so that the series of vertex diagrams can be cut off after the zeroth-order contribution. For phonon-mediated superconductivity, the smallness of the higher-order vertex diagrams is ensured by Migdal's theorem [47], which states that higher-order diagrams are smaller by a factor ω_E/E_F, where ω_E is a characteristic phonon frequency. Migdal's theorem is, however, known to break down for long-wavelength phonons [47,48] and in systems with strong Fermi surface nesting [49–51]. Moreover, for reduced spatial dimensionality, the reduction of the higher-order diagrams should be expected to be less dramatic [51,52]. As the superconductivity studied in this work relies on long-wavelength magnons and/or a two-dimensional Fermi surface close to half filling, it then seems plausible that vertex corrections could be of importance. A discussion of the effect of vertex corrections in the present system is presented in Appendix D. For large doping, we find that vertex corrections can become of relevant magnitude but that the region in momentum space where the corrections are large might be small enough to limit their effect. Exactly at half filling, the vertex corrections are expected to be quite large, but their effect can be reduced by moving away from half filling.

Upon approaching half filling, we would also at some point expect onset of spin density wave correlations. Exactly at half filling, one may straightforwardly generalize the above Eliashberg theory to accommodate the expected commensurate spin density wave instability. Previously, this has been done for the phonon-induced instability [53]. Below half filling, the commensurate wave vector $\boldsymbol{Q}$ does not connect points on the Fermi surface. We therefore expect the commensurate spin density wave to be suppressed relative to superconductivity due to the large electronic energy for processes between states which are not on the Fermi surface. However, we may still have incommensurate spin density waves, which are far more challenging to investigate theoretically. In this paper, we have been investigating the properties of the superconducting phases, and the highly nontrivial interplay between superconducting

and spin density wave orders that we could potentially obtain is beyond the scope of the present study.

Another effect that could be included is the effect of the quasiparticle energy shift χ. For the present system, χ was found to be small compared to the Fermi energy for chemical potentials ranging from half filling and down towards the vicinity of the bottom of the band. Apart from the limit where the Fermi level approaches the bottom of the band, inclusion of χ would typically amount to a small, weakly frequency-dependent shift of the effective chemical potential in the Eliashberg equations, and it was therefore neglected in the presented calculations.

The effect of Coulomb interactions on the electron self-energy is in general challenging to calculate [48]. Their effect on the Fermi surface averaged Eliashberg equations for the anomalous pairing amplitudes is typically included by neglecting vertex corrections and including an extra repulsive and frequency-independent potential in the equations. The Coulomb repulsion will then have a limited effect on the critical temperatures as long as $\lambda_2(i\nu_m = 0)$ is somewhat larger than the Coulomb pseudopotential μ^* [48]. Moreover, taking the Coulomb interaction to be momentum independent, its contributions to the gap equation will cancel for unconventional pairing symmetries like the ones considered in this work. For a momentum dependent Coulomb potential, the Coulomb contributions to the gap equation no longer cancel identically for unconventional pairing symmetries, but μ^* will still be reduced compared to the s-wave case.

In the system setup we have considered, the antiferromagnetic order and interfacial coupling to the two antiferromagnets has been chosen such that any magnetic fields cancel. If we instead consider a single antiferromagnetic layer and $\Omega \neq 1$, there would be a net magnetic field, as shown in Eqs. (B1c) and (B1d). In addition, there would also be a term in the magnon propagator that is odd in frequency, as shown in Eq. (B4). The odd part of the propagator would renormalize and reduce the magnetic field h and produce an effective magnetic field $\tilde{h}$. Together with the odd part of the propagator, this effective magnetic field could in principle give rise to an exotic coexistence of odd and even frequency superconductivity [54]. For the experimentally most relevant parameters, we would, however, expect the magnetic field to be too strong to give significant critical temperatures.

We also note that a previously studied system consisting of a normal metal sandwiched between two ferromagnetic insulators [18] gives rise to a p-wave phase that bears many similarities with the p-wave phase considered in the present study. The main difference between the two systems is the absence of the magnon coherence factors in the ferromagnetic case. The numerator of the magnon propagator (or effective potential in a weak-coupling framework) for the ferromagnet therefore scales as $\omega_q^{FM} \sim K$ for long-wavelength magnons, while the numerator of the magnon propagator for the antiferromagnet scales as $A_e^{RR}(q)\,\omega_q \sim J_1$. For superconductivity dominated by long-wavelength magnons, with $K/J_1 \ll 1$, the dimensionless electron-magnon coupling $\lambda_2(i\nu_m = 0)$ may, however, still be of the same magnitude in both cases, corresponding to similar dimensionless coupling constants in a weak-coupling framework. This is because the ferromagnet propagator can simply rely on having a smaller gap in the magnon spectrum, making the denominator of the propagator smaller for the long-wavelength processes. As the critical temperature in a simple weak-coupling framework only depends on the dimensionless coupling constant and the cutoff on the boson spectrum, sizable critical temperatures can then be obtained for both ferromagnets and antiferromagnets. Within an Eliashberg framework, on the other hand, the effective cutoff frequency is determined by the characteristic magnon energies in the pairing interaction. Since, with ferromagnets, the large values for $\lambda_2(i\nu_m = 0)$ were obtained by relying on smaller magnon energies in the denominator of the propagator, the effective frequency cutoff will be smaller, and the critical temperatures obtainable with ferromagnets should be smaller than with antiferromagnets.

In the current antiferromagnetic case, magnon renormalization was found to have little effect on the available critical temperatures. This is because the larger easy axis anisotropy K, required to protect magnetic order in the AFMIs, is compensated by the magnon energy renormalization in the denominator of the propagator. The larger easy-axis anisotropy has little effect on the numerator of the propagator. For the case of the ferromagnet, on the other hand, increasing K so that it compensates the renormalization would also lead to a larger numerator in the propagator. Magnon renormalization could then open the way for slightly higher critical temperatures.

VIII. EXPERIMENTAL CONSIDERATIONS

The model employed in this study allows us to tune the interfacial coupling between the normal metal and the two different sublattices of the antiferromagnet independently. In principle, such a general asymmetric coupling could be engineered, as discussed in the introduction. However, the experimentally most promising route to realizing superconductivity in systems well described by our model appears to be through fully compensated and uncompensated interfaces, where the conduction band electrons in the normal metal are coupled to only one AFMI sublattice ($\Omega = 0$) or equally to both AFMI sublattices ($\Omega = 1$). There is, however, a significant difference between our model and the intended realization with an uncompensated interface for the case $\Omega = 0$. In the intended realization, the square lattice of the normal metal matches the exposed sublattice of the antiferromagnet and not the square lattice of the antiferromagnet itself, as in our model. Thus, the electron Brillouin zone coincides with the Brillouin zone of the antiferromagnet. Although it is possible to imagine a compensated interface where the magnons at the interface live in a smaller Brillouin zone than the electrons, this would not be the typical case.

Within our model, Umklapp processes are included for both $\Omega = 0$ and $\Omega = 1$. In the intended realization for $\Omega = 0$, however, Umklapp processes are absent. For a small Fermi surface, the effect of Umklapp processes in our model is small, since all processes between points on the Fermi surface are of the regular type. The p-wave phase we expect for uncompensated interfaces and large doping is therefore well represented by our model. For small doping, however, the f-wave phase of our model takes precedence over the p-wave phase

precisely because of the Umklapp processes. The f-wave phase is therefore of less experimental relevance, and we expect that the p-wave phase would dominate regardless of doping for a normal metal sandwiched between two uncompensated interfaces.

For the p-wave phase with $\Omega = 0$, having a trilayer heterostructure in order to cancel all magnetic fields seems necessary, as the critical temperature is significantly reduced compared to previous predictions [21]. For the d-wave phase with $\Omega = 1$, the result of coupling to a single antiferromagnet would lead to the presence of a staggered field. As a staggered field might be less detrimental to superconductivity than a uniform spin splitting [55], a bilayer heterostructure might be a viable option in this case.

When it comes to choice of parameters, it is clear that a strategy of simply taking a very small gap in the magnon spectrum in order to increase the dimensionless coupling strength $\lambda_2(0)$ has its limitations, as this leads to a very small effective cutoff frequency and slow increase in critical temperature with dimensionless coupling strength. In order to realize superconductivity in this system it is then essential that the constant prefactor that appears in the gap equation is sufficiently large. A sizable interfacial exchange coupling and electron density of states is then preferable. Moreover, as the effective induced interaction experienced by the electrons in the normal metal might be reduced with the thickness of the normal metal [18], the metallic layer should be kept quite thin.

The easy-axis anisotropy governs the size of the gap in the magnon spectrum and appears to play a crucial role in realizing superconductivity. A sufficiently large gap in the magnon spectrum could be important for both the p-wave and d-wave phases in order to stabilize the antiferromagnet. The p-wave phase does, however, rely more heavily on fine tuning of the easy-axis anisotropy in order to produce a nonzero, but sufficiently small, effective magnon gap producing a sizable critical temperature. This could make the p-wave phase more difficult to realize experimentally. The d-wave pairing receives contributions from a wider range of magnon energies, and the critical temperature is therefore more robust to a shift of the magnon energies. For larger Fermi surfaces, a larger easy-axis anisotropy is, however, needed to preserve magnetic order in the antiferromagnet, which could in itself be an experimental complication. However, using a magnetically more stable three-dimensional antiferromagnet instead of the two-dimensional magnet considered in our model could potentially lead to a reduction in the easy-axis anisotropy required to stabilize the magnets.

In contrast to earlier results, the present study indicates that the d-wave phase may be able to produce higher critical temperatures than the p-wave phase. However, the d-wave phase is, in our model, dependent on proximity to half filling, where it, e.g., needs to compete with spin-density wave order. This competition may push the superconducting phase down towards lower filling fractions associated with lower critical temperatures. It should also be noted that since the d-wave phase relies on Umklapp processes, it is more sensitive to the detailed structure of the Fermi surface. In comparison with the p-wave phase, the d-wave phase may therefore place stricter requirements on the electron band structure of the normal metal in the experimental realization. Compared with the third

option of coupling to ferromagnetic insulators, however, both phases considered in the present study seem more promising.

IX. SUMMARY

We use Eliashberg theory to study interfacially induced magnon-mediated superconductivity in a normal metal-antiferromagnet heterostructure. For large doping and uncompensated antiferromagnetic interfaces, we find p-wave superconductivity, while for small doping and compensated antiferromagnetic interfaces, we find d-wave superconductivity. This can be understood in terms of sublattice interferences suppressing and enhancing scattering processes in the system. Although the qualitative results are in accordance with earlier weak-coupling studies, the critical temperature achievable for the p-wave phase is found to be significantly reduced as the characteristic magnon frequency in the pairing interaction is much smaller than the cutoff on the magnon spectrum. The d-wave phase, on the other hand, is found to rely less on long-wavelength magnons and can therefore potentially produce larger critical temperatures when approaching half filling. Close to half filling the d-wave instability may however have to compete with a spin-density wave instability, potentially reducing the available critical temperatures. A sufficiently large gap in the magnon spectrum might be necessary to stabilize the magnetic order in the antiferromagnets due to feedback from the electrons, but this is found to have limited effect on the critical temperatures.

APPENDIX A: ANTIFERROMAGNETIC MAGNONS

Starting from the AFMI Hamiltonian, we introduce the linearized Holstein-Primakoff transformation [56]

$$S_{i\in A,H}^+ = \sqrt{2S}a_{iH} \quad S_{i\in A,L}^+ = \sqrt{2S}a_{iL}^\dagger \tag{A1a}$$

$$S_{j\in B,H}^+ = \sqrt{2S}b_{jH}^\dagger \quad S_{j\in B,L}^+ = \sqrt{2S}b_{jL} \tag{A1b}$$

$$S_{i\in A,H}^- = \sqrt{2S}a_{iH}^\dagger \quad S_{i\in A,L}^- = \sqrt{2S}a_{iL} \tag{A1c}$$

$$S_{j\in B,H}^- = \sqrt{2S}b_{jH} \quad S_{j\in B,L}^- = \sqrt{2S}b_{jL}^\dagger \tag{A1d}$$

$$S_{i\in A,H}^z = S - a_{iH}^\dagger a_{iH} \quad S_{i\in A,L}^z = -S + a_{iL}^\dagger a_{iL} \tag{A1e}$$

$$S_{j\in B,H}^z = -S + b_{jH}^\dagger b_{jH} \quad S_{j\in B,L}^z = S - b_{jL}^\dagger b_{jL}, \tag{A1f}$$

where we have assumed oppositely aligned antiferromagnetic order in the spin space z direction for the two antiferromagnets. Inserting this into the AFMI Hamiltonian and expressing it in terms of sublattice magnon Fourier modes $a_{q\eta}$ and $b_{q\eta}$, the

AFMI Hamiltonian takes the form

$$H_{\text{AFMI}} = \sum_{\boldsymbol{q},\eta} C_{\boldsymbol{q}}(a_{\boldsymbol{q}\eta}^\dagger a_{\boldsymbol{q}\eta} + b_{\boldsymbol{q}\eta}^\dagger b_{\boldsymbol{q}\eta}) + D_{\boldsymbol{q}}(a_{\boldsymbol{q}\eta}b_{-\boldsymbol{q}\eta} + a_{\boldsymbol{q}\eta}^\dagger b_{-\boldsymbol{q}\eta}^\dagger),$$
(A2)

where $C_{\boldsymbol{q}}$ and $D_{\boldsymbol{q}}$ are given by

$$C_{\boldsymbol{q}} = 2z_1 J_1 S - 2z_2 J_2 S(1 - \tilde{\gamma}_{\boldsymbol{q}}) + 2KS,$$
(A3a)

$$D_{\boldsymbol{q}} = 2z_1 J_1 S \gamma_{\boldsymbol{q}},$$
(A3b)

and we have defined

$$\gamma_{\boldsymbol{q}} = \frac{1}{z_1}\sum_{\boldsymbol{\delta}_1} e^{i\boldsymbol{q}\cdot\boldsymbol{\delta}_1}, \quad \tilde{\gamma}_{\boldsymbol{q}} = \frac{1}{z_2}\sum_{\boldsymbol{\delta}_2} e^{i\boldsymbol{q}\cdot\boldsymbol{\delta}_2}.$$
(A4)

Here, z_1 and z_2 are the number of nearest and next-nearest neighbor vectors, which are summed over and denoted by $\boldsymbol{\delta}_1$ and $\boldsymbol{\delta}_2$. The Hamiltonian is diagonalized through the Bogoliubov transform

$$a_{\boldsymbol{q}\eta} = u_{\boldsymbol{q}}\alpha_{\boldsymbol{q}\eta} + v_{\boldsymbol{q}}\beta_{-\boldsymbol{q}\eta}^\dagger,$$
(A5a)

$$b_{-\boldsymbol{q}\eta}^\dagger = u_{\boldsymbol{q}}\beta_{-\boldsymbol{q}\eta}^\dagger + v_{\boldsymbol{q}}\alpha_{\boldsymbol{q}\eta},$$
(A5b)

where the coherence factors $u_{\boldsymbol{q}}$ and $v_{\boldsymbol{q}}$ can be written as

$$u_{\boldsymbol{q}} = \cosh\tilde{\theta}_{\boldsymbol{q}}, \quad v_{\boldsymbol{q}} = \sinh\tilde{\theta}_{\boldsymbol{q}},$$
(A6)

in terms of the hyperbolic angle

$$\tilde{\theta}_{\boldsymbol{q}} = -\frac{1}{2}\tanh^{-1}\left(\frac{D_{\boldsymbol{q}}}{C_{\boldsymbol{q}}}\right).$$
(A7)

The resulting magnon spectrum is

$$\omega_{\boldsymbol{q}} = \sqrt{C_{\boldsymbol{q}}^2 - D_{\boldsymbol{q}}^2}.$$
(A8)

By expressing the inverse hyperbolic tangent in terms of a logarithm, one may show the relations

$$u_{\boldsymbol{q}}^2 + v_{\boldsymbol{q}}^2 = +C_{\boldsymbol{q}}/\omega_{\boldsymbol{q}},$$
(A9a)

$$2u_{\boldsymbol{q}}v_{\boldsymbol{q}} = -D_{\boldsymbol{q}}/\omega_{\boldsymbol{q}},$$
(A9b)

for the coherence factor combinations which appear in the magnon propagator.

Whereas $u_{\boldsymbol{q}}$ is positive, $v_{\boldsymbol{q}}$ is typically negative. Furthermore, we notice that when K and J_2 are small compared to J_1, $|\tilde{\theta}_{\boldsymbol{q}}|$ becomes large when $\boldsymbol{q} \to 0$, as $D_{\boldsymbol{q}}$ approaches $C_{\boldsymbol{q}}$. This causes $u_{\boldsymbol{q}}$ to grow large and positive and $v_{\boldsymbol{q}}$ to grow large and negative in this limit.

APPENDIX B: INTERFACIAL COUPLING HAMILTONIAN

In the main text, we presented expressions for the interfacial coupling and the magnon propagators under the assumption that the two antiferromagnets couple to the normal metal with equal strength. In this Appendix, we generalize the results beyond this assumption.

The interfacial coupling Hamiltonian describing the coupling to a single antiferromagnetic insulator labeled by η can be written $H_{\text{int}}^\eta = H_{\text{int}}^{h,\eta} + H_{\text{int}}^{V,\eta}$, where the magnetic exchange

field contributions $H_{\text{int}}^{h,\eta} = H_{\text{int}}^{h,A,\eta} + H_{\text{int}}^{h,B,\eta}$ from the two sublattices are

$$H_{\text{int}}^{h,A,H} = -\bar{J}\,\Omega_A^H S \sum_{\boldsymbol{k}\in\square,\sigma}\sigma(c_{\boldsymbol{k}\sigma}^\dagger c_{\boldsymbol{k}\sigma} + c_{\boldsymbol{k}+\boldsymbol{Q},\sigma}^\dagger c_{\boldsymbol{k}\sigma}),$$
(B1a)

$$H_{\text{int}}^{h,B,H} = +\bar{J}\,\Omega_B^H S \sum_{\boldsymbol{k}\in\square,\sigma}\sigma(c_{\boldsymbol{k}\sigma}^\dagger c_{\boldsymbol{k}\sigma} - c_{\boldsymbol{k}+\boldsymbol{Q},\sigma}^\dagger c_{\boldsymbol{k}\sigma}),$$
(B1b)

$$H_{\text{int}}^{h,A,L} = +\bar{J}\,\Omega_A^L S \sum_{\boldsymbol{k}\in\square,\sigma}\sigma(c_{\boldsymbol{k}\sigma}^\dagger c_{\boldsymbol{k}\sigma} + c_{\boldsymbol{k}+\boldsymbol{Q},\sigma}^\dagger c_{\boldsymbol{k}\sigma}),$$
(B1c)

$$H_{\text{int}}^{h,B,L} = -\bar{J}\,\Omega_B^L S \sum_{\boldsymbol{k}\in\square,\sigma}\sigma(c_{\boldsymbol{k}\sigma}^\dagger c_{\boldsymbol{k}\sigma} - c_{\boldsymbol{k}+\boldsymbol{Q},\sigma}^\dagger c_{\boldsymbol{k}\sigma}),$$
(B1d)

and where the exchange coupling strengths $\bar{J}\Omega_\Upsilon^\eta$ are in general different for the two antiferromagnets. Coupling to only one antiferromagnet can be realized by, e.g., setting $\Omega_\Upsilon^L = 0$. Assuming $\Omega_\Upsilon^H = \Omega_\Upsilon^L$, however, all magnetic fields cancel.

The electron-magnon interaction is given by

$$H_{\text{int}}^{V,\eta} = V\sum_{\substack{\boldsymbol{k}\in\square\\\boldsymbol{q}\in\diamond}}\left[M_{\boldsymbol{q}\eta}^R c_{\boldsymbol{k}+\boldsymbol{q},\downarrow}^\dagger c_{\boldsymbol{k},\uparrow} + M_{\boldsymbol{q}\eta}^U c_{\boldsymbol{k}+\boldsymbol{q}+\boldsymbol{Q},\downarrow}^\dagger c_{\boldsymbol{k},\uparrow}\right.$$
$$\left. + \left(M_{-\boldsymbol{q}\eta}^R\right)^\dagger c_{\boldsymbol{k}+\boldsymbol{q},\uparrow}^\dagger c_{\boldsymbol{k},\downarrow} + \left(M_{-\boldsymbol{q}\eta}^U\right)^\dagger c_{\boldsymbol{k}+\boldsymbol{q}+\boldsymbol{Q},\uparrow}^\dagger c_{\boldsymbol{k},\downarrow}\right],$$
(B2)

where we have defined magnon operators $M_{\boldsymbol{q}\eta}^\kappa$ associated with the antiferromagnet η as

$$M_{\boldsymbol{q}H}^\kappa = \Omega_A^H a_{\boldsymbol{q}H} + \kappa\,\Omega_B^H b_{-\boldsymbol{q}H}^\dagger,$$
(B3a)

$$M_{\boldsymbol{q}L}^\kappa = \Omega_A^L a_{-\boldsymbol{q}L}^\dagger + \kappa\,\Omega_B^L b_{\boldsymbol{q}L},$$
(B3b)

so that the operator $M_{\boldsymbol{q}}^\kappa$ introduced in the main text is given by $M_{\boldsymbol{q}}^\kappa = M_{\boldsymbol{q}H}^\kappa + M_{\boldsymbol{q}L}^\kappa$. Expressing the magnon operators in terms of the eigenmagnon operators resulting from the Bogoliubov transformation, the corresponding magnon propagators are

$$\mathcal{D}_{0,\eta}^{\kappa\kappa'}(\boldsymbol{q}, i\omega_n) = -A_{e,\eta}^{\kappa\kappa'}(\boldsymbol{q})\frac{2\omega_{\boldsymbol{q}}}{\omega_n^2 + \omega_{\boldsymbol{q}}^2} - A_{o,\eta}^{\kappa\kappa'}\frac{2i\omega_n}{\omega_n^2 + \omega_{\boldsymbol{q}}^2}.$$
(B4)

Here, the first term is even under the three-vector transformation $q \to -q$, and the second term is odd. The expressions for $A_{e,\eta}^{\kappa\kappa'}(\boldsymbol{q})$ can be obtained from Eq. (10) in the main text by the simple generalization $A_e^{\kappa\kappa'}(\boldsymbol{q}) \to A_{e,\eta}^{\kappa\kappa'}(\boldsymbol{q})$ and $\Omega_\Upsilon \to \Omega_\Upsilon^\eta$. The odd part prefactor $A_{o,\eta}^{\kappa\kappa'}$ is $\boldsymbol{q}$ independent and given by

$$A_{o,\eta}^{\kappa\kappa'} = \frac{1}{2}\eta\left[\left(\Omega_A^\eta\right)^2 - \kappa\kappa'\left(\Omega_B^\eta\right)^2\right],$$
(B5)

where we associate the index η with the values $H \to 1$ and $L \to -1$. We notice that the odd part of the propagator has different signs for the two antiferromagnets, so that their contributions cancel out when we couple equally to the two antiferromagnets.

APPENDIX C: SUPPRESSION OF ELECTRON CORRELATIONS WHICH ARE OFF-DIAGONAL IN MOMENTUM

In this Appendix, we argue that terms in the electron Green's function which are off-diagonal in momentum are suppressed as long as the electron propagator renormalization is small compared to the difference in electron energies at the

momenta k and $k + Q$. The self-energy is in general an 8×8 matrix in the momentum, particle/hole, and spin degrees of freedom. The self-energy can then be written

$$\Sigma = \begin{pmatrix} \Sigma_{11} & \Sigma_{12} \\ \Sigma_{21} & \Sigma_{22} \end{pmatrix}, \tag{C1}$$

where Σ_{ij} is now a 4×4 submatrix in the particle/hole and spin degrees of freedom corresponding to momentum sector (i, j). The self-energy is related to the Green's function through the Dyson equation, so that

$$G^{-1}(k) = \begin{pmatrix} G_0^{-1}(k) - \Sigma_{11}(k) & -\Sigma_{12}(k) \\ -\Sigma_{21}(k) & G_0^{-1}(k + Q) - \Sigma_{22}(k) \end{pmatrix}. \tag{C2}$$

Away from half filling, both k and $k + Q$ cannot both be on the Fermi surface, so one of the submatrices on the diagonal will have a term proportional to the identity matrix and prefactor of the same order as the electron energy scale. We now assume that k is close to the Fermi surface, so that this applies to $G_0^{-1}(k + Q)$. To obtain the Green's function $G(k)$, we then make use of the following matrix inversion identity [57]: Given a matrix G^{-1} which can be partitioned into submatrices and written on the form

$$G^{-1} = \begin{pmatrix} N_{11} & N_{12} \\ N_{21} & N_{22} \end{pmatrix}, \tag{C3}$$

where N_{11} and N_{22} are invertible matrices [58], the inverse can similarly be expressed

$$G = \begin{pmatrix} M_{11} & M_{12} \\ M_{21} & M_{22} \end{pmatrix}, \tag{C4}$$

with submatrices

$$M_{11} = (N_{11} - N_{12} N_{22}^{-1} N_{21})^{-1}, \tag{C5a}$$

$$M_{12} = -(N_{11} - N_{12} N_{22}^{-1} N_{21})^{-1} N_{12} N_{22}^{-1}, \tag{C5b}$$

$$M_{21} = -N_{22}^{-1} N_{21} (N_{11} - N_{12} N_{22}^{-1} N_{21})^{-1}, \tag{C5c}$$

$$M_{22} = (N_{22} - N_{21} N_{11}^{-1} N_{12})^{-1}. \tag{C5d}$$

In our case, N_{22} can now be thought of as an electronic energy that is much larger than the other submatrices, which have contributions from the self-energy and the noninteracting Green's function close to the Fermi surface. As long as the renormalization is small compared to the electron energy scale in the problem, $N_{22}^{-1} N_{21}$ is then small, and M_{21} and M_{12} are suppressed relative to M_{11}. By similar reasoning, M_{22} is also small, and M_{11} can be approximated by N_{11}^{-1}.

When $k + Q$ is close to the Fermi surface, we may similarly neglect M_{11} and the off-diagonal terms but not $M_{22} \approx N_{22}^{-1}$. For a general k, we may therefore neglect the off-diagonal terms, which is exactly what we use in the main text.

APPENDIX D: VERTEX CORRECTIONS

In order to obtain some insight into the importance of vertex corrections, we will attempt to estimate the magnitude of the lowest-order vertex corrections. Focusing on regular processes for the time being, a magnon equivalent of the
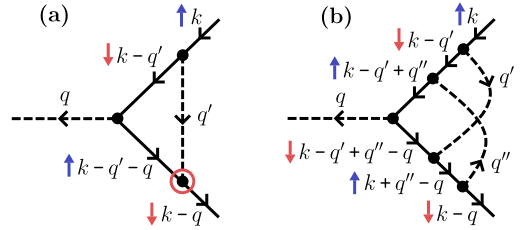
FIG. 8. (a) Typical lowest-order vertex correction, which vanishes in this case due to conservation of spin. (b) Lowest-order vertex correction for our model.

lowest-order vertex correction for phonon-mediated superconductivity is presented in Fig. 8(a). Due to conservation of spin, this diagram vanishes for our system. Starting with the upper vertex of the vertical magnon line, we see that the electron spin is flipped from $\uparrow$ to $\downarrow$, meaning that the outgoing magnon carries a spin $+1$. In the lower vertex of the vertical magnon line, this spin needs to be returned to the electrons, but the incoming electron already has spin $\uparrow$ instead of spin $\downarrow$, and spin can therefore not be conserved in this vertex. Including Umklapp processes, the momentum structure of Fig. 8(a) will differ, but the spin structure stays the same. The lowest-order vertex corrections are therefore of the type represented by the diagram in Fig. 8(b). As the diagram in (b) is of higher order, the effect of vertex corrections should then be expected to be smaller than what would have been the case if the diagram in (a) had not vanished.

The diagram in Fig. 8(b) represents a correction to the electron-magnon vertex $\frac{V}{4} g_\gamma \to \frac{V}{4} g_\gamma (1 + \Gamma)$, where

$$\Gamma(k, q) \sim \frac{V^4}{\beta^2} \sum_{q', q''} \mathcal{D}_0^{RR}(q') \mathcal{D}_0^{RR}(q'') G_0^{11}(k + q'' - q)$$
$$\times G_0^{22}(k - q' + q'' - q) G_0^{11}$$
$$\times (k - q' + q'') G_0^{22}(k - q'). \tag{D1}$$

A quick estimate for Γ can be obtained in the following way [36]. We approximate the magnon propagators as

$$\mathcal{D}_0^{RR}(q) \sim -\frac{A_e^{RR}(0)}{\omega_c}, \tag{D2}$$

for Matsubara frequency q_m less than some cutoff frequency $\omega_c \sim \omega_0$, where ω_0 is the magnon gap. For $q_m > \omega_c$, we take the magnon propagator to be zero. The number of terms that should be included in each of the Matsubara sums is then roughly $\beta \omega_c$. When performing the sums over momentum, the fermions will typically be away from the Fermi surface. We then approximate the momentum sums with the number of lattice sites N, and the electron Green's functions by $G_0^{aa} \sim 1/E_F$, where E_F is the Fermi energy, which is taken as a measure of the electron energy scale ~ 1 eV. We then obtain

$$\Gamma \sim \left(\frac{V^2 N A_e^{RR}(0)}{E_F^2} \right)^2 \sim \left(\frac{1}{100} \right)^2, \tag{D3}$$
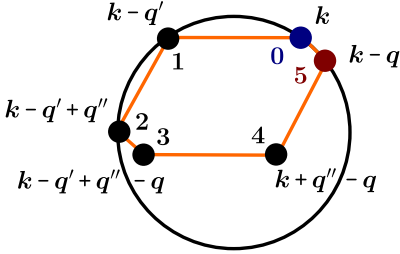
FIG. 9. The momentum scattering processes in the simplest non-vanishing vertex correction of Fig. 8(b) can be represented as a hexagon. Opposing sides in the hexagon are parallel and equally long due to conservation of momentum. The Fermi surface (assuming large doping) is shown as a circle.

where we have inserted typical values for the relevant energy scales, and taken $\Omega = 0$ which is suitable for the case of a relatively small Fermi surface where regular processes dominate. This estimate would indicate that vertex corrections are typically small. It does, however, not take into account that there can be large contributions arising from fermions being close to the Fermi surface when $q \to 0$. In order to pick up such contributions, we need to perform a more detailed estimate.

Starting from Eq. (D1), we can perform the Matsubara sums. Following Ref. [59], we focus on the term that arises from the poles of the boson propagators, limiting the number of factors with fermion energies in the denominator. At zero temperature, this term becomes

$$
\Gamma_1(k, q)
$$

$$
= -4V^4 \sum_{q',q''} A_e^{RR}(q') A_e^{RR}(q'')
$$

$$
\times \left(\frac{1}{\omega_{q'} + ik_n - \xi_{k-q'}} \right) \left(\frac{1}{\omega_{q''} + \xi_{k+q''-q} - i(k_n - q_m)} \right)
$$

$$
\times \left(\frac{1}{\omega_{q'} + i(k_n - q_m) - \omega_{q''} - \xi_{k-q'+q''-q}} \right)
$$

$$
\times \left(\frac{1}{\omega_{q'} + ik_n - \omega_{q''} - \xi_{k-q'+q''}} \right). \qquad (D4)
$$

To estimate this term in the limit of small q, we need to analyze which regions of the Brillouin zone that dominate the momentum sums. The momentum scattering processes in the vertex correction diagram can be represented by a hexagon where opposing sides are parallel and equally long due to conservation of momentum, as shown in Fig. 9. Each vertex in the hexagon represents the momentum of an electron propagator in the Feynman diagram. We consider processes where k and $k - q$ are close to the Fermi surface. Consider the variables q' and $q' - q'' \equiv \pi$ to be the integration variables of our momentum sums. For small q, the vertices 2 and 3 in Fig. 9 are reasonably close to each other. The dominant contributions to the diagram should therefore arise when $k - q' + q''$ is close to the Fermi surface. With $q' - q''$ fixed, the position

of the remaining two vertices 1 and 4 is fixed by choosing q'. Taking vertex 1 to be close to the Fermi surface, vertex 4 will now typically end up away from the Fermi surface. The number of terms in the sum over q' where vertex 1 is close to the Fermi surface is of order $N_F \omega_c$. The Green's functions corresponding to points 1 and 4 in the hexagon can then be approximated by $1/\omega_c$ and $1/E_F$, respectively. By also approximating the boosting factors by their maximum values $A_e^{RR}(\mathbf{0})$ and the remaining magnon energies by ω_c, we may then approximate the vertex correction by

$$
\Gamma_1(k, q) = -\frac{4N_F \left[V^2 A_e^{RR}(\mathbf{0}) \right]^2}{E_F} \sum_{\pi} \left(\frac{1}{ik_n - \xi_{k-\pi}} \right)
$$

$$
\times \left(\frac{1}{i(k_n - q_m) - \xi_{k-\pi-q}} \right). \qquad (D5)
$$

Alternatively, one can attempt to further restrict the sum over q' in order to keep all the fermions close to the Fermi surface, producing a similar result as in Eq. (D5).

Introducing $\mathbf{p} = \mathbf{k} - \mathbf{\pi}$, the diagram can now be calculated by Taylor expanding in small q, using

$$
\xi_{\mathbf{p}-\mathbf{q}} \approx \xi_{\mathbf{p}} - (\nabla \xi_{\mathbf{p}}) \cdot \mathbf{q} = \xi_{\mathbf{p}} - v_F q \cos(\theta_q(\mathbf{p})), \qquad (D6)
$$

where v_F is the Fermi velocity and $\theta_q(\mathbf{p})$ is the angle between $\nabla \xi_{\mathbf{p}}$ and $\mathbf{q}$. Writing the momentum integral in terms of polar coordinates and integrating out the radial momentum, we then obtain

$$
\Gamma_1(k, q) \approx -i \frac{4 \left[N_F V^2 A_e^{RR}(\mathbf{0}) \right]^2}{E_F} [\Theta(k_n) - \Theta(k_n - q_m)]
$$

$$
\times \int_0^{2\pi} d\theta \left(\frac{1}{iq_m - v_F q \cos(\theta)} \right). \qquad (D7)
$$

Performing also the angular integration, one may show that the vertex correction contribution for nonzero bosonic Matsubara frequency is of order

$$
\Gamma_1(k, q) \sim \left(\frac{N_F V^2 A_e^{RR}(0)}{E_F} \right)^2 \left(\frac{E_F}{\sqrt{v_F^2 q^2 + q_m^2}} \right). \qquad (D8)
$$

In short, this result can be interpreted as follows: Dominant contributions to Eq. (D4) arise from $N_F \omega_c$ terms in each of the momentum sums where two of the electron propagators then are of order $1/\omega_c$ as these electrons are close to the Fermi surface. One of the electron propagators is replaced by a factor $1/E_F$, as the electron in this case is not close to the Fermi surface. The last propagator momentum is reasonably close to the Fermi surface due to the small momentum scattering q. This propagator is found to be of order $1/\sqrt{(v_F q)^2 + q_m^2}$, where the square root can be interpreted as an interpolation between the frequency and the momentum energy scales for the scattering process with three-momentum $(\mathbf{q}, q_m)$.

For $q \to 0$, $q_m \sim 1$ K, and typical values for the remaining energy scales, the expression in Eq. (D8) is found to be of order 1, indicating that vertex corrections could become important for long-wavelength magnons. As $v_F q$ in the denominator grows quickly with q, the momentum region where our estimate for the vertex corrections is of importance is

quite limited. Whereas the above expression is quickly reduced when q surpasses q_m/v_F, the corresponding momentum cutoff for the magnon propagator depends on the magnon group velocity close to the bottom of the band, meaning that the momentum region where the estimated vertex corrections are of importance is typically significantly smaller than the momentum region where we obtain large contributions to the Eliashberg equations. A more rigorous treatment of the vertex corrections would treat both momentum sums in detail and could potentially give rise to contributions that are larger and/or less quickly reduced with increasing q.

As the diagram in Fig. 8(a) vanishes for our model, one might imagine that it could be possible to obtain significant vertex corrections by going to higher order in magnon operators in the electron-magnon interaction, giving rise to electron-magnon scattering processes without spin flips. Including higher-order terms in the interaction Hamiltonian arising from the z component of the antiferromagnetic spins, one may construct a diagram like the one in Fig. 8(a) where the vertical magnon line has been replaced with a magnon loop and the vertices of the magnon loop do not involve an electron spin flip, conserving the electron spin in the diagram. Performing estimates like those presented above, such diagrams are found to be of similar magnitude and displaying a similar suppression with increasing momentum q as the diagram in Fig. 8(b).

For larger Fermi surfaces and $\Omega = 1$, the regular processes are of little importance and the physics is dominated by Umklapp processes. Modifying the diagram of Fig. 8(b) to only include Umklapp processes, all spin-↓ electron propagators therefore attain an additional momentum shift Q. Below half filling, for k on the Fermi surface, placing $k - q + Q$ on the Fermi surface now requires a finite momentum q. Contrary

to the case with regular processes and $q \to 0$, choosing the hexagon vertex 2 reasonably close to the Fermi surface does therefore not necessarily mean that the hexagon vertex 3 is also reasonably close.

Exactly at half filling, the Fermi surface is perfectly nested, and the electron momenta can all be chosen reasonably close to the Fermi surface for a wide range of integration momenta and relevant values of q. Thus, we would get large vertex corrections [49,50,60]. Moving away from half filling, the nesting of the Fermi surface is no longer perfect. Our simplest estimate in Eq. (D3) will then eventually be restored, where $A_e^{RR}(\mathbf{0})$ needs to be replaced with the maximum value of $A_e^{UU}(\mathbf{q})$ for scattering processes on the Fermi surface. Thus, we would expect vertex corrections to become unimportant sufficiently far away from half filling.

APPENDIX E: MATERIAL PARAMETERS

Typical parameter values are shown in Table I. The electron density of states is calculated by numerical evaluation of the elliptical integral in Ref. [61].

TABLE I. Parameter values used in the numerical results. We refer to the main text for an explanation of their meanings.

Quantity	Value
J_1	2 meV
J_2	$0.2 J_1$
K	$1 \times 10^{-4} J_1$
$\bar{J}$	15 meV
S	1
t	1eV

[1] J. Bardeen, L. N. Cooper, and J. R. Schrieffer, Phys. Rev. **108**, 1175 (1957).

[2] F. Schlawin, A. Cavalleri, and D. Jaksch, Phys. Rev. Lett. **122**, 133602 (2019).

[3] A. Kavokin and P. Lagoudakis, Nat. Mater. **15**, 599 (2016).

[4] F. P. Laussy, A. V. Kavokin, and I. A. Shelykh, Phys. Rev. Lett. **104**, 106402 (2010).

[5] Y. Takada, J. Phys. Soc. Jpn. **45**, 786 (1978).

[6] D. J. Scalapino, J. Low Temp. Phys. **117**, 179 (1999).

[7] T. Moriya and K. Ueda, Rep. Prog. Phys. **66**, 1299 (2003).

[8] N. F. Berk and J. R. Schrieffer, Phys. Rev. Lett. **17**, 433 (1966).

[9] S. Doniach and S. Engelsberg, Phys. Rev. Lett. **17**, 750 (1966).

[10] M. Cyrot, Solid State Commun. **60**, 253 (1986).

[11] D. J. Scalapino, E. Loh, and J. E. Hirsch, Phys. Rev. B **34**, 8190 (1986).

[12] K. Miyake, S. Schmitt-Rink, and C. M. Varma, Phys. Rev. B **34**, 6554 (1986).

[13] P. Monthoux, A. V. Balatsky, and D. Pines, Phys. Rev. Lett. **67**, 3448 (1991).

[14] P. Monthoux and D. Pines, Phys. Rev. Lett. **69**, 961 (1992).

[15] A. Abanov, A. V. Chubukov, and J. Schmalian, Adv. Phys. **52**, 119 (2003).

[16] M. Kargarian, D. K. Efimkin, and V. Galitski, Phys. Rev. Lett. **117**, 076806 (2016).

[17] X. Gong, M. Kargarian, A. Stern, D. Yue, H. Zhou, X. Jin, V. M. Galitski, V. M. Yakovenko, and J. Xia, Sci. Adv. **3**, e1602579 (2017).

[18] N. Rohling, E. L. Fjærbu, and A. Brataas, Phys. Rev. B **97**, 115401 (2018).

[19] H. G. Hugdal, S. Rex, F. S. Nogueira, and A. Sudbø, Phys. Rev. B **97**, 195438 (2018).

[20] E. L. Fjærbu, N. Rohling, and A. Brataas, Phys. Rev. B **100**, 125432 (2019).

[21] E. Erlandsen, A. Kamra, A. Brataas, and A. Sudbø, Phys. Rev. B **100**, 100503(R) (2019).

[22] E. Erlandsen and A. Sudbø, Phys. Rev. B **102**, 214502 (2020).

[23] E. Erlandsen, A. Brataas, and A. Sudbø, Phys. Rev. B **101**, 094503 (2020).

[24] H. G. Hugdal and A. Sudbø, Phys. Rev. B **102**, 125429 (2020).

[25] A. Kamra, E. Thingstad, G. Rastelli, R. A. Duine, A. Brataas, W. Belzig, and A. Sudbø, Phys. Rev. B **100**, 174407 (2019).

[26] J. Nogués and I. K. Schuller, J. Magn. Magn. Mater. **192**, 203 (1999).

[27] J. Nogués, J. Sort, V. Langlais, V. Skumryev, S. Suriñach, J. Muñoz, and M. Baró, Phys. Rep. **422**, 65 (2005).

[28] R. L. Stamps, J. Phys. D **33**, R247 (2000).

[29] S. Takei, B. I. Halperin, A. Yacoby, and Y. Tserkovnyak, Phys. Rev. B **90**, 094408 (2014).

[30] E. L. Fjærbu, N. Rohling, and A. Brataas, Phys. Rev. B **95**, 144408 (2017).

[31] S. V. Vonsovskĭ and Y. A. Izyumov, Sov. Phys. Usp. **5**, 723 (1963).

[32] G. Chen and W. A. Goddard, Science **239**, 899 (1988).

[33] H. Shimahara, J. Phys. Soc. Jpn. **63**, 1861 (1994).

[34] Y. Kajiwara, K. Harii, S. Takahashi, J. Ohe, K. Uchida, M. Mizuguchi, H. Umezawa, H. Kawai, K. Ando, K. Takanashi, S. Maekawa, and E. Saitoh, Nature (London) **464**, 262 (2010).

[35] F. Mazzola, T. Frederiksen, T. Balasubramanian, P. Hofmann, B. Hellsing, and J. W. Wells, Phys. Rev. B **95**, 075430 (2017).

[36] P. Coleman, *Introduction to Many-Body Physics* (Cambridge University Press, Cambridge, UK, 2015).

[37] S. Takahashi, E. Saitoh, and S. Maekawa, J. Phys.: Conf. Ser. **200**, 062030 (2010).

[38] S. A. Bender and Y. Tserkovnyak, Phys. Rev. B **91**, 140402(R) (2015).

[39] In general, the electron can be scattered with any momentum, however, upon explicitly introducing regular (R) and Umklapp (U) magnon operators, all magnon scattering processes can be described within the reduced Brillouin zone.

[40] J. Linder and A. V. Balatsky, Rev. Mod. Phys. **91**, 045005 (2019).

[41] One may derive equations also when this is not the case, but they will be somewhat more involved, as there will be interference terms in the submatrix determinant Θ.

[42] P. B. Allen and R. C. Dynes, Phys. Rev. B **12**, 905 (1975).

[43] C. Sanderson and R. Curtin, Journal of Open Source Software **1**, 26 (2016).

[44] C. Sanderson and R. Curtin, *Mathematical Software – ICMS 2018* (Springer International Publishing, Cham, 2018), pp. 422–430.

[45] GNU Scientific Library, https://www.gnu.org/software/gsl/

[46] It should be noted that although the size of the region with significant deviations from the zero frequency polarization increases with Matsubara frequency ν_m, so does also the width of the region over which we expect the dominant contributions to the corresponding $\lambda_2(i\nu_m)$. Thus, we still expect to be able to approximate the polarization by a constant for larger Matsubara frequencies ν_m.

[47] A. B. Migdal, Sov. Phys. JETP **7**, 996 (1958).

[48] P. B. Allen and B. Mitrović, *Theory of Superconducting Tc*, edited by H. Ehrenreich, F. Seitz, and D. Turnbull, Solid State Physics, Vol. 37 (Academic Press, New York, 1983), pp. 1–92.

[49] A. Virosztek and J. Ruvalds, Phys. Rev. B **42**, 4064 (1990).

[50] A. Virosztek and J. Ruvalds, Phys. Rev. B **59**, 1324 (1999).

[51] F. Schrodi, P. M. Oppeneer, and A. Aperis, Phys. Rev. B **102**, 024503 (2020).

[52] A. Madhukar, Solid State Commun. **24**, 11 (1977).

[53] R. Szczęśniak, Phys. Lett. A **336**, 402 (2005).

[54] M. Matsumoto, M. Koga, and H. Kusunose, J. Phys. Soc. Jpn. **81**, 033702 (2012).

[55] A. Cebula, J. Zieliński, and J. Biesiada, J. Supercond. **13**, 479 (2000).

[56] C. Kittel, *Quantum Theory of Solids* (John Wiley & Sons, New York, 1987).

[57] R. A. Horn and C. R. Johnson, *Matrix Analysis* (Cambridge University Press, Cambridge, 2012).

[58] The identity can also be formulated more generally, but this will be sufficient for our purposes.

[59] B. Roy, J. D. Sau, and S. Das Sarma, Phys. Rev. B **89**, 165119 (2014).

[60] D. Djajaputra and J. Ruvalds, Int. J. Mod. Phys. B **13**, 25 (1999).

[61] R. Piasecki, arXiv:0804.1037.

Effect of midgap states on the magnetic exchange interaction mediated by a d-wave superconductor

Authors

Atousa Ghanbari
Eirik Erlandsen
Jacob Linder

Effect of midgap states on the magnetic exchange interaction mediated by a d-wave superconductor

Atousa Ghanbari, Eirik Erlandsen, and Jacob Linder

Center for Quantum Spintronics, Department of Physics, Norwegian University of Science and Technology, NO-7491 Trondheim, Norway

We theoretically study the indirect interaction between two ferromagnetic contacts located on the surface of a d-wave superconductor. When the magnets are connected to a {010} edge of the superconductor we find an oscillating RKKY interaction that varies in sign as the distance between the magnetic contacts is varied. However, when coupling the magnets to an {110} edge of the superconductor, we find that the presence of midgap states qualitatively changes the results. The ground state of the system is then found to always favor alignment of the magnets as this configuration most strongly suppresses the midgap states, leading to a larger condensation energy, which dominates over the intrinsic RKKY interaction.

I. INTRODUCTION

Superconductors with d-wave symmetry have an anisotropic order parameter, which drops to zero along some nodal directions [1–3]. A {110} edge of a $d_{x^2-y^2}$ superconductor has been shown to feature dispersionless surface states with zero energy, called midgap states [4]. The appearance of midgap states for such an edge is related to the fact that the order parameter in a 45° rotated coordinate system takes the form d_{xy}, introducing opposite signs for the pair potential experienced by particles undergoing specular and Andreev reflections at the surface. The {110} edge also gives rise to a zero bias conductance peak [5], which is a result of the presence of the midgap states [6]. Such a zero-bias conductance peak has been experimentally observed in the high-T_c cuprate superconductors [7–10] and has been important in determining the pairing symmetry of these superconductors.

The indirect exchange interaction between two localized spins, mediated by the itinerant electrons of a host material, was first introduced by Ruderman, Kittel, Kasuya, and Yosida, and is known as the RKKY interaction [11–13]. In this indirect exchange interaction, itinerant electrons of the host material scatter off a localized spin, and the wave functions of the scattered electrons interfere with each other giving rise to alternating regions with high density of spin up/down. This leads to the well-known RKKY oscillations in the spin-spin interaction strength, which decrease with the distance R between the two localized spins as R^{-D}, where D is the dimensionality of the system. RKKY interaction has been investigated in various materials ranging from normal metals [11,13], to one- and two-dimensional electron gases [14,15], two-dimensional structures like graphene [16–20], and topological insulators [21–23].

For a system consisting of magnetic impurities embedded in a superconductor, the influence of superconductivity on the indirect impurity-impurity interaction has also been studied [24,25]. For a conventional s-wave superconductor, when the distance between the impurities is larger than the superconducting coherence length, the interaction between them is found to be antiferromagnetic in character and suppressed compared to the normal metal case. The suppression is caused by the superconducting gap reducing the number of states close to the Fermi level that can mediate the interaction. Below the coherence length, the behavior is similar to the normal metal case with an oscillatory RKKY interaction that changes sign with distance. However, nonperturbative treatments have shown that Yu-Shiba-Rusinov (YSR) bound states can give rise to mainly antiferromagnetic behavior even at distances shorter than the coherence length [26]. Further, for impurities on the surface of a three-dimensional topological insulator with proximity-induced s-wave superconductivity, the RKKY interaction favors the impurity spins to be in-plane and antiparallel [27]. For a spin-valve structure consisting of two ferromagnetic insulators connected by an s-wave superconductor, experiments have shown that anti-alignment of the magnets is still favored [28].

Conventional s-wave superconductors do however typically have coherence lengths far exceeding the decay length of the RKKY interaction. On the other hand, d-wave superconductors can feature very short coherence lengths of the order of nanometers [29], offering an intriguing platform for studying the interplay between superconductivity and RKKY interaction, as the characteristic length scales of both phenomena are comparable. RKKY interaction between magnetic impurities mediated by a d-wave superconductor with an anisotropic order parameter of the type $d_{x^2-y^2}$ has lead to similar behavior as in the s-wave case [30]. Further, for a spin-valve structure involving a $d_{x^2-y^2}$ superconductor, nodal quasiparticles close to the Fermi surface have been observed to mediate interaction that favors anti-alignment of the magnetic insulators for a sufficiently large superconductor thickness [31].

As the gapped band structure of a superconductor suppresses the RKKY interaction, it is of interest to investigate the effect the presence of midgap states have on the
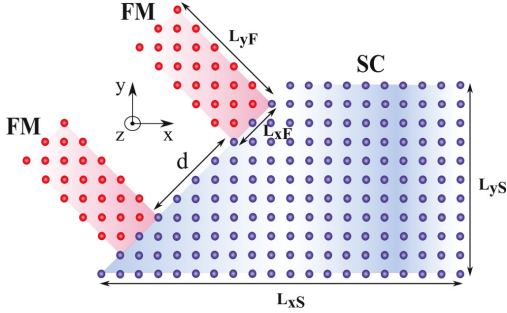
FIG. 1. Schematic illustration of a d-wave superconductor with midgap surface states mediating the indirect exchange interaction between two ferromagnetic contacts. We will consider configurations where the magnetization of the two magnets is either parallel (P) or antiparallel (AP). For comparison, the ferromagnetic contacts will also be attached to the lower, nondiagonal edge of the superconductor. The lengths indicated on the figure will in the main text be specified by the number of atomic distances.

interaction. We therefore consider a $d_{x^2-y^2}$ superconductor and calculate the exchange interaction between two ferromagnetic contacts located on a diagonal {110} edge, as illustrated in Fig. 1. The superconductor is modelled by an extended BCS tight-binding Hamiltonian on a square lattice and connected to the metallic magnets through a hopping term across the interface. The results are obtained through a self-consistent solution of the Bogoliubov-de Gennes (BdG) equations [32]. To put the results into context, we consider the cases of a normal metal and an isotropic s-wave superconductor, in addition to the d-wave superconductor. In all three cases, we investigate the interaction between ferromagnetic contacts located on both diagonal and nondiagonal edges.

For magnetic contacts located on a diagonal edge of a d-wave superconductor, we find that the system always favors alignment of the two magnets. The variation in the strength of the magnetic exchange interaction as we vary the distance between the magnets is small compared to the magnitude of the interaction itself. We attribute these results to the aligned magnets more efficiently suppressing the midgap states than the anti-aligned configuration. Although the aligned magnets induce a stronger spin splitting in the superconductor, suppressing the gap, the reduction of the midgap states leads to an overall larger gap and increased condensation energy. The parallel magnet configuration is therefore the ground state of the system.

The paper is organized as follows. In Sec. II we introduce the model and methodology. Then, in Sec. III we present and discuss the results. Finally, in Sec. IV we provide a summary of the findings. The phase diagram of our d-wave superconductor model for a square system with continuous boundary conditions is included in the Appendix.

II. MODEL AND METHODS

By means of a tight-binding Hamiltonian on a square lattice, we model the attractive electron-electron interaction in a

superconductor:

$$
H^{\text{SC}} = -\sum_{\langle i,j \rangle, \alpha} t_{ij} c_{i\alpha}^{\dagger} c_{j\alpha} - \sum_{i,\alpha} \mu_i n_{i\alpha} - \sum_i U_i n_{i\uparrow} n_{i\downarrow}
$$
$$
+ \sum_{\langle ij \rangle, \alpha \neq \alpha'} V_{ij} n_{i\alpha} n_{j\alpha'} + \sum_{\langle ij \rangle, \alpha} V'_{ij} n_{i\alpha} n_{j\alpha}. \quad (1)
$$

Here, $c_{i\alpha}^{\dagger}$ is a creation operator creating an electron with spin α on lattice site $i = (i_x, i_y)$. The hopping amplitude is denoted by t_{ij}, and μ_i is the chemical potential. The third term represents on-site attractive interactions between opposite spins, where the number operator is $n_{i\alpha} = c_{i\alpha}^{\dagger} c_{i\alpha}$. This term gives rise to conventional spin singlet isotropic s-wave superconductivity. The fourth and fifth terms represent nearest-neighbor interaction between opposite or equal spins, respectively. These terms can give rise to d-wave, p-wave, or extended s-wave pairing for an attractive interaction potential. For the purposes of this paper, we will set V'_{ij} to zero as we will not be interested in the possibility of equal spin pairing. As shown in the Appendix, the above model without V'_{ij} can give rise to a d-wave superconductor for a suitable choice of chemical potential.

A. Analytical methods

Through a mean-field treatment, we simplify the interaction terms. The on-site part of the interaction becomes

$$
-\sum_i U_i n_{i\uparrow} n_{i\downarrow} = -\sum_i U_i (c_{i\uparrow}^{\dagger} c_{i\downarrow}^{\dagger} \langle c_{i\downarrow} c_{i\uparrow} \rangle + c_{i\downarrow} c_{i\uparrow} \langle c_{i\uparrow}^{\dagger} c_{i\downarrow}^{\dagger} \rangle
$$
$$
- \langle c_{i\downarrow} c_{i\uparrow} \rangle \langle c_{i\uparrow}^{\dagger} c_{i\downarrow}^{\dagger} \rangle). \quad (2)
$$

Defining the superconducting gap for the on-site interaction as $\Delta_i = -U_i \langle c_{i\downarrow} c_{i\uparrow} \rangle$, we obtain

$$
-\sum_i U_i n_{i\uparrow} n_{i\downarrow} = \sum_i (c_{i\uparrow}^{\dagger} c_{i\downarrow}^{\dagger} \Delta_i + c_{i\downarrow} c_{i\uparrow} \Delta_i^*) + H_0^S, \quad (3)
$$

where we have defined

$$
H_0^S = \sum_i \frac{|\Delta_i|^2}{U_i}. \quad (4)
$$

The on-site interaction U_i will be taken to a constant $U \geqslant 0$ in the superconductor, and zero elsewhere. Once again, performing a mean-field treatment, the attractive nearest-neighbor interaction term becomes

$$
\sum_{\langle ij \rangle, \alpha \neq \alpha'} V_{ij} n_{i\alpha} n_{j\alpha'} = \sum_{\langle ij \rangle, \alpha \neq \alpha'} V_{ij} (c_{j\alpha'}^{\dagger} c_{i\alpha}^{\dagger} \langle c_{i\alpha} c_{j\alpha'} \rangle
$$
$$
+ c_{i\alpha} c_{j\alpha'} \langle c_{j\alpha'}^{\dagger} c_{i\alpha}^{\dagger} \rangle - \langle c_{j\alpha'}^{\dagger} c_{i\alpha}^{\dagger} \rangle \langle c_{i\alpha} c_{j\alpha'} \rangle). \quad (5)
$$

We then define the nearest-neighbor pairing amplitude

$$
F_{ij}^{\alpha\alpha'} = \langle c_{i\alpha} c_{j\alpha'} \rangle, \quad (6)
$$

transforming Eq. (5) into

$$
\sum_{\langle ij \rangle, \alpha \neq \alpha'} V_{ij} (c_{j\alpha'}^{\dagger} c_{i\alpha}^{\dagger} F_{ij}^{\alpha\alpha'} + c_{i\alpha} c_{j\alpha'} (F_{ij}^{\alpha\alpha'})^{\dagger}) + H_0^d, \quad (7)
$$

where

$$H_0^d = - \sum_{\langle i,j \rangle, \alpha \neq \alpha'} V_{ij} |F_{ij}^{\alpha\alpha'}|^2. \qquad (8)$$

As $\sum_{\langle i,j \rangle} V_{ij}|F_{ij}^{\uparrow\downarrow}|^2 = \sum_{\langle i,j \rangle} V_{ji}|F_{ij}^{\downarrow\uparrow}|^2$, we can rewrite $H_0^d = - \sum_{\langle i,j \rangle} |F_{ij}^{\uparrow\downarrow}|^2 (V_{ij} + V_{ji})$, and similarly

$$\sum_{\langle ij \rangle, \alpha \neq \alpha'} V_{ij}(c_{j\alpha}^\dagger c_{i\alpha}^\dagger F_{ij}^{\alpha\alpha'} + c_{i\alpha} c_{j\alpha'} (F_{ij}^{\alpha\alpha'})^\dagger)$$
$$= \sum_{\langle ij \rangle} (c_{j\downarrow}^\dagger c_{i\uparrow}^\dagger F_{ij}^{\uparrow\downarrow} + c_{i\uparrow} c_{j\downarrow} (F_{ij}^{\uparrow\downarrow})^\dagger)(V_{ij} + V_{ji}). \quad (9)$$

In the following, we will take the nearest-neighbor interaction to be $V_{ji} = V_{ij} = V \leqslant 0$ (corresponding to an attractive interaction) in the superconductor and zero elsewhere. The mean-field extended tight-binding Hamiltonian now takes the form

$$\begin{aligned} H_{mf}^{SC} = H_0 &- \sum_{\langle i,j \rangle, \alpha} t_{ij} c_{i\alpha}^\dagger c_{j\alpha} - \sum_{i,\alpha} \mu_i n_{i\alpha} \\ &+ \sum_i (c_{i\uparrow}^\dagger c_{i\downarrow}^\dagger \Delta_i + c_{i\downarrow} c_{i\uparrow} \Delta_i^*) \\ &+ 2\sum_{\langle ij \rangle} V(c_{j\downarrow}^\dagger c_{i\uparrow}^\dagger F_{ij}^{\uparrow\downarrow} + c_{i\uparrow} c_{j\downarrow}(F_{ij}^{\uparrow\downarrow})^\dagger), \quad (10) \end{aligned}$$

where $H_0 = H_0^S + H_0^d$.

The metallic ferromagnets that are attached to the superconductor are described by the following tight-binding Hamiltonian:

$$\begin{aligned} H^{FM} = &- \sum_{\langle i,j \rangle, \alpha} t_{ij} c_{i\alpha}^\dagger c_{j\alpha} - \sum_{i,\alpha} \mu_i n_{i\alpha} \\ &- \sum_{i\delta\alpha\beta} h_i^\delta (\sigma_z)_{\alpha\beta} \, c_{i\alpha}^\dagger c_{i\beta}. \quad (11) \end{aligned}$$

The last term represents the coupling between the spin of an electron at site i and the local magnetic exchange field, giving rise to ferromagnetism. The local exchange field h_i^δ is taken to produce a spin splitting in the z direction in spin space, giving rise to a magnetization that could in general be either in-plane or out-of-plane in real space. Our model does not separate these cases as the magnetism is simply introduced through a spin splitting. Orbital effects on the superconductor arising from the magnets, not considered in this model, can be limited by keeping the magnetization in-plane [33]. The Pauli matrices are denoted by σ, and the index δ separates the local

exchange field of each of the two magnets with $\delta = L, R$ for the leftmost and rightmost magnet, respectively. The sign of the local exchange field can be either the same or opposite for the two magnets, giving rise to parallel (P) or antiparallel (AP) ferromagnets. Outside of the magnets, the local magnetic exchange field is set to zero. The coupling between the magnets and the superconductor is introduced by having a nonzero hopping amplitude t_{ij} across the ferromagnet-superconductor interfaces. The region outside of the superconductor and magnets is considered to be vacuum and decoupled from the rest of the system with a vanishing hopping amplitude.

After diagonalization, the free energy of the system will be expressed as

$$F = H_0 - \frac{1}{2} \sum_{n=1}^{2N} E_n - \frac{1}{\beta} \sum_{n=1}^{2N} \ln(1 + e^{-\beta E_n}), \quad (12)$$

where E_n is the quasiparticle energy associated with quantum number n, and N is the number of lattice sites. The magnetic exchange interaction is computed as the difference in free energy between the configurations with parallel and antiparallel magnets

$$J = F^{\uparrow\uparrow} - F^{\uparrow\downarrow}, \quad (13)$$

which includes both the RKKY interaction mediated by the quasiparticles as well as the effect of the magnetic configurations on the condensation energy of the superconductor.

The Hamiltonian $H = H^{SC} + H^{FM}$ is diagonalized by means of the BdG method in order to compute the eigenvalues E_n and eigenstates γ_n. The diagonalized Hamiltonian will then take the form

$$H = H_0 - \frac{1}{2} \sum_{n=1}^{2N} E_n + \sum_{n=1}^{2N} E_n \gamma_n^\dagger \gamma_n. \quad (14)$$

In order to perform the diagonalization, we start by rewriting the Hamiltonian as $H = H_0 + \frac{1}{2} \sum_{ij} B_i^\dagger h_{ij} B_j$ where we have introduced the basis

$$B_i^\dagger = [c_{i\uparrow}^\dagger \quad c_{i\downarrow}^\dagger \quad c_{i\uparrow} \quad c_{i\downarrow}]. \quad (15)$$

Here, h_{ij} is a 4×4 matrix that takes the following form for $i \neq j$

$$h_{ij} = \begin{bmatrix} -t & 0 & 0 & -2VF_{ij} \\ 0 & -t & 2VF_{ji} & 0 \\ 0 & 2V(F_{ij})^* & +t & 0 \\ -2V(F_{ji})^* & 0 & 0 & +t \end{bmatrix}, \quad (16)$$

and for $i = j$

$$h_{ij} = \begin{bmatrix} -\mu_i + \sum_\delta h_i^\delta & 0 & 0 & \Delta_i \\ 0 & -\mu_i - \sum_\delta h_i^\delta & -\Delta_i & 0 \\ 0 & -(\Delta_i)^* & +\mu_i - \sum_\delta h_i^\delta & 0 \\ (\Delta_i)^* & 0 & 0 & +\mu_i + \sum_\delta h_i^\delta \end{bmatrix}. \quad (17)$$

Writing the Hamiltonian on matrix form $H = H_0 + \frac{1}{2}W^\dagger SW$, and introducing the matrix P, we diagonalize the Hamiltonian $H = H_0 + \frac{1}{2}W^\dagger P^\dagger PSP^\dagger PW = H_0 + \frac{1}{2}\tilde{W}^\dagger S_d \tilde{W}$. The eigenvectors of S

are

$$\Phi_n^\dagger = [\varphi_{1n}^* \quad \cdots \quad \varphi_{in}^* \quad \cdots \quad \varphi_{Nn}^*],$$
$$\varphi_{in}^* = [v_{in}^* \quad v_{in}^* \quad \omega_{in}^* \quad \chi_{in}^*], \quad (18)$$

such that

$$P^\dagger = [\Phi_1 \quad \Phi_2 \quad \dots \quad \Phi_{4N}]. \tag{19}$$

We next use $P^\dagger \tilde{W} = W$ along with

$$\tilde{W}^\dagger = [\gamma_1^\dagger \dots \gamma_{4N}^\dagger], \tag{20}$$

and the relations between the quasiparticle operators that are not independent of each other. There are then $2N$ remaining independent quasiparticle operators with corresponding eigenvalues. The creation and annihilation operators $\{c^\dagger, c\}$ can then be expressed in terms of quasiparticle creation and annihilation operators $\{\gamma^\dagger, \gamma\}$:

$$c_{i\uparrow} = \sum_{n=1}^{2N} \upsilon_{i,n} \gamma_n + \omega_{i,n}^* \gamma_n^\dagger, \quad c_{i\downarrow} = \sum_{n=1}^{2N} \nu_{i,n} \gamma_n + \chi_{i,n}^* \gamma_n^\dagger,$$

$$c_{i\uparrow}^\dagger = \sum_{n=1}^{2N} \omega_{i,n} \gamma_n + \upsilon_{i,n}^* \gamma_n^\dagger, \quad c_{i\downarrow}^\dagger = \sum_{n=1}^{2N} \chi_{i,n} \gamma_n + \nu_{i,n}^* \gamma_n^\dagger. \tag{21}$$

Inserting these relations into the definition of the gap for the on-site interaction, we obtain the self-consistent gap equation

$$\Delta_i = -U_i \sum_{n=1}^{2N} [(\chi_{i,n}^* \upsilon_{i,n} - \nu_{i,n} \omega_{i,n}^*) f(E_n) + \nu_{i,n} \omega_{i,n}^*]. \tag{22}$$

For the nearest-neighbor pairing amplitudes, we introduce a simplified notation $F_{ij}^{\uparrow\downarrow} = F_{ij}$. Further, $F_{i,i+\hat{x}}$ is expressed as $F_i^{\hat{x}+}$ and likewise $F_{i+\hat{x},i} \equiv F_i^{+\hat{x}}$ and so on. Inserting the expressions from Eq. (21) into the definitions of the pairing amplitudes, we obtain

$$F_i^{x\pm} = \sum_{n=1}^{2N} [(\omega_{i,n}^* \nu_{i\pm\hat{x},n} - \nu_{i,n} \chi_{i\pm\hat{x},n}^*) f(E_n) + \nu_{i,n} \chi_{i\pm\hat{x},n}^*],$$

$$F_i^{\pm x} = \sum_{n=1}^{2N} [(\omega_{i\pm\hat{x},n}^* \nu_{i,n} - \nu_{i\pm\hat{x},n} \chi_{i,n}^*) f(E_n) + \nu_{i\pm\hat{x},n} \chi_{i,n}^*],$$

$$F_i^{y\pm} = \sum_{n=1}^{2N} [(\omega_{i,n}^* \nu_{i\pm\hat{y},n} - \nu_{i,n} \chi_{i\pm\hat{y},n}^*) f(E_n) + \nu_{i,n} \chi_{i\pm\hat{y},n}^*],$$

$$F_i^{\pm y} = \sum_{n=1}^{2N} [(\omega_{i\pm\hat{y},n}^* \nu_{i,n} - \nu_{i\pm\hat{y},n} \chi_{i,n}^*) f(E_n) + \nu_{i\pm\hat{y},n} \chi_{i,n}^*]. \tag{23}$$

As we are interested in the effect of the midgap states on the indirect interaction between two ferromagnetic leads connected to the superconductor, establishing the presence of midgap states is of importance. This can be achieved by calculating the single particle local density of states (LDOS), which should have a peak around zero energy in the presence of midgap states. The number of charges on lattice site i is given by $\rho_i = \sum_\alpha \langle c_{i\alpha}^\dagger c_{i\alpha} \rangle$, but this quantity can also be expressed as $\rho_i = \int_{-\infty}^{+\infty} N_i(E) f(E) dE$. Here $N_i(E)$ is the local density of states at site i, and $f(E)$ is the Fermi-Dirac distribution with energy E measured relative to the chemical potential. At $T = 0$, we have $f(E) = 1$ for $E < 0$ and $f(E) = 0$ when $E > 0$. Comparing the above two expressions for the number

of charges on lattice site i, the LDOS can then be expressed as

$$N_i(E) = \sum_{n=1}^{2N} [(|\omega_{i,n}|^2 + |\chi_{i,n}|^2) \delta(E + E_n)$$

$$+ (|\upsilon_{i,n}|^2 + |\nu_{i,n}|^2) \delta(E - E_n)]. \tag{24}$$

Another quantity of interest is the magnetization on lattice site i, $\boldsymbol{M}_i = \langle \boldsymbol{S}_i \rangle$. Here, the spin operator is defined as $\boldsymbol{S}_i = \sum_{\alpha\beta} c_{i\alpha}^\dagger \boldsymbol{\sigma}_{\alpha\beta} c_{i\beta}$. The magnetization in the z direction can then be expressed as

$$M_i^z = \sum_{n=1}^{2N} [(|\upsilon_{i,n}|^2 + |\chi_{i,n}|^2 - |\omega_{i,n}|^2 - |\nu_{i,n}|^2) f(E_n)$$

$$+ |\omega_{i,n}|^2 - |\chi_{i,n}|^2]. \tag{25}$$

B. Computational methods

The computational part of this study consists of numerically diagonalizing the Hamiltonian and self-consistently solving the equations for either the on-site superconducting gap [Eq. (22)] or the nearest-neighbor pairing amplitudes [Eq. (23)], depending on whether the superconductor is taken to be of the isotropic s-wave type or the d-wave type. Iterative solution of these equations require an initial value for the gap function/pairing amplitudes, and a convergence criterion in order to determine when a solution has been obtained. In this paper, the convergence criterion was that the relative change in the gap/pairing amplitudes from one iteration to the next should be less than 1×10^{-4} for the d-wave and 1×10^{-3} for the s-wave state. The initial values for the d-wave state are listed in the Appendix and the initial value for the s-wave gap Δ was set to $0.5t$.

III. RESULTS AND DISCUSSION

We first investigate the presence of midgap surface states, i.e., zero-energy states existing on an edge of a superconductor. As displayed in Fig. 2, we calculate the LDOS for different points on an s-wave and a d-wave superconductor without magnetic contacts. One of the points is located at the diagonal edge, one of the points is in the bulk, and the third point is on the lower horizontal edge. Only on the diagonal edge of the d-wave superconductor, Fig. 2(b1), there is a peak around zero-energy signaling the presence of midgap states. In this figure, the chemical potential has been set to $\mu_S = 0.7t$, which gives rise to an asymmetric density of states around $E = 0$ for our tight-binding model as the gap in the electron spectrum is opened away from the middle of the band.

As the presence of midgap states has been established, we move on to results for the indirect interaction between magnetic leads attached to a normal metal, an s-wave superconductor, and finally a d-wave superconductor.

A. Normal state

To put the results for the superconductors into context, we start with the case of magnetic leads connected by a normal metal ($V = U = 0$). The indirect exchange interaction J is presented in Fig. 3. For the horizontal edge, the result is the expected RKKY oscillations that are damped with increasing
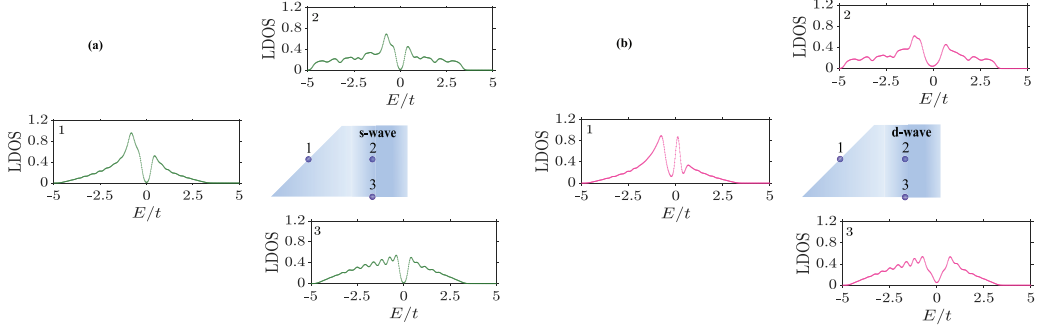
FIG. 2. Local density of states (LDOS) for different points of an *s*-wave superconductor (a) and a *d*-wave superconductor (b), showing the presence of midgap states on the diagonal edge of the *d*-wave superconductor. In both cases the size of the structure is $L_{xS} = 34$ and $L_{yS} = 30$. For the *s*-wave results we have taken $U/t = 2$ and $V = 0$, while for the *d*-wave results we have taken $U = 0$ and $V/t = -1$. In both cases we have set the chemical potential $\mu_S = 0.7t$.

distance between the magnets. For the diagonal edge, the results are more peculiar, showing an enhanced interaction when the electrodes are close to the endpoints of the diagonal edge. Investigating the LDOS for $E = 0$ in Fig. 4, the reason becomes clear. Close to the edges of the system, the LDOS increases in magnitude and exhibits Friedel-like oscillations due to the abruptly vanishing charge density at the edge. The oscillatory and increased LDOS close to the edges correspondingly affects the RKKY interaction when the electrodes are close to the edge.
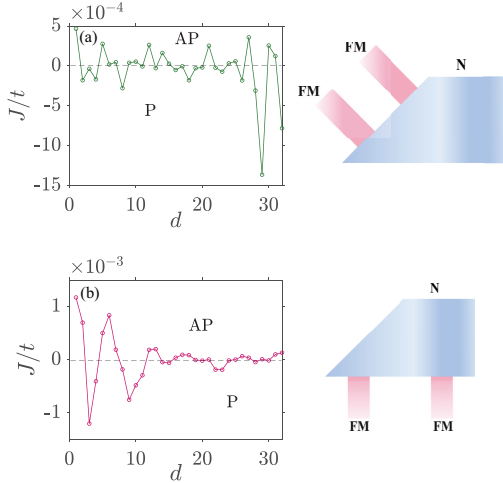
FIG. 3. Normal metal: Indirect exchange interaction between magnetic leads connected to a diagonal (a) and a horizontal (b) edge of a normal metal, presented as a function of the distance between the leads. Here, the chemical potential in the normal metal is set to $\mu_N = 0.9t$ and the chemical potential in the ferromagnets is set to $\mu_F = 1.2t$. Further, $h_i = 2t$, $L_{xN} = 40$, $L_{yN} = 40$, $L_{xF} = 2$, $L_{yF} = 10$, and $V = U = 0$. In both subfigures, the leftmost magnet was fixed two lattice points away from the endpoint of the edge.

B. *s*-Wave pairing

We then move on to the case of magnetic leads connected by an isotropic *s*-wave superconductor ($V = 0$). The results for the indirect exchange interaction are presented in Fig. 5. In this case, there are two competing effects: The conventional RKKY interaction and the blocking of the states that can mediate the interaction due to the gap around the Fermi level in the band structure. For a weak attractive interaction U in the superconductor, the RKKY interaction dominates, giving rise to an oscillating behavior. For larger U, the gap becomes larger and can block more of the states that can mediate the interaction between the magnets. The interaction then displays a damping behavior instead of oscillations, and an antiparallel configuration of the magnets is preferred [34]. For the diagonal edge, the electrodes have been kept further away from the endpoints of the edge. For a weak attractive interaction U, the enhanced RKKY oscillations occurring when the electrodes are close to the end-points can, however, still be observed, as explained previously. On the other hand, when the strength of
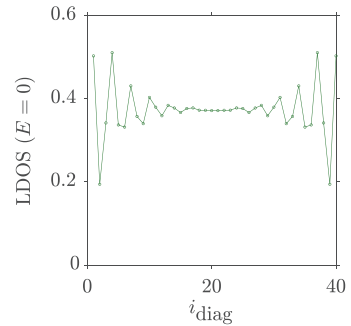
FIG. 4. Normal metal: Local density of states (LDOS) for $E = 0$ at the diagonal edge in the absence of magnetic contacts. The system size is $L_{xN} = 40$ and $L_{yN} = 40$, $V = U = 0$, and the chemical potential in the normal metal is $0.9t$.
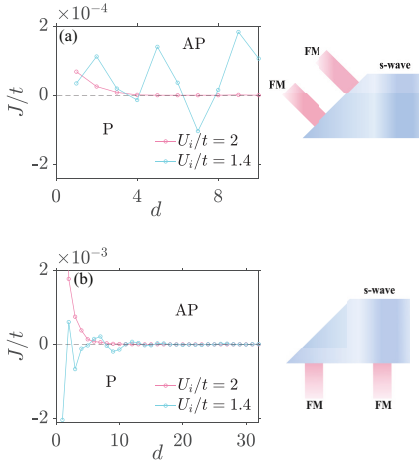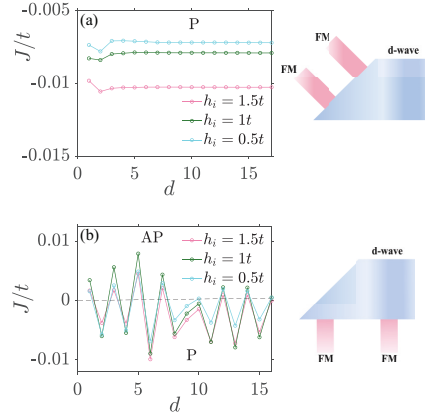
FIG. 5. s-Wave : Indirect exchange interaction between magnetic leads connected to a diagonal (a) and a horizontal (b) edge of a s-wave superconductor. Here $\mu_S = 0.9t$, $\mu_F = 1.2t$, $h_i = 2t$, $L_{xS} = 40$, $L_{yS} = 40$, $L_{xF} = 2$, $L_{yF} = 10$, and $V = 0$. For the diagonal edge, the leftmost magnet is fixed 13 lattice points away from the endpoint of the edge, while for the horizontal edge, the leftmost magnet is fixed 2 lattice points away from the endpoint.

FIG. 6. d-Wave : Indirect exchange interaction between magnetic leads connected to a diagonal (a) and a horizontal (b) edge of a d-wave superconductor. Here $\mu_S = 0.7t$, $\mu_F = 1t$, $V/t = -1$, $L_{xF} = 2$, $L_{yF} = 10$, and $U = 0$. For the diagonal edge, the leftmost magnet is fixed only 2 lattice points away from the endpoint of the edge in order to maximize the number of data points. The d-wave diagonal edge results are not sensitive to how close the magnets are to the endpoints of the edge. Further $L_{xS} = 34$, $L_{yS} = 30$. For the horizontal edge, the leftmost magnet is fixed 10 lattice points away from the endpoint, and $L_{xS} = 40$, $L_{yS} = 20$.

the attractive interaction is increased, increasing the superconducting gap, we see that J is damped to zero for sufficiently large magnet separation also for the diagonal edge. Thus, in the s-wave case, the qualitative behavior of J is the same regardless of which edge we consider.

C. d-Wave pairing

Finally, we consider the main result of this paper, which is how the magnetic leads interact when separated by a d-wave superconductor ($U = 0$). The results for the indirect interaction between the magnetic leads is presented in Fig. 6. For the horizontal edge, the interaction displays an oscillating behavior and varies in sign as a function of the distance between the magnetic contacts. The results for the diagonal edge, on the other hand, show a qualitatively different behavior. The system now always prefers alignment of the ferromagnets and the interaction varies little with distance. Further, increasing h_i now leads to a larger difference in free energy between the parallel and antiparallel magnet configurations.

The result that a parallel magnet configuration is strongly favored for the diagonal edge is surprising as one would expect that the parallel configuration induces a larger magnetization in the superconductor, which suppresses the gap and lowers the condensation energy. A particularly large induced magnetization in the superconductor should be expected in the presence of midgap states, which can give rise to a giant magnetic moment when subjected to a spin splitting [4,35,36]. In accordance with this, we find a sizable induced magnetization on the diagonal edge. As previously discussed in the literature, the magnetization induced in a superconductor due to

proximity to a ferromagnet can be either aligned or anti-aligned with the magnetization of the ferromagnet [37–39]. A physical picture for the origin of an anti-aligned induced magnetization is that there are contributions from Cooper pairs where one of the two electrons is located in the ferromagnet, aligned with the local magnetization, leaving a Cooper pair partner with opposite spin in the superconductor. In the present system the induced magnetization tends to be anti-aligned with the magnetization of the magnetic contacts, as displayed in Figs. 7(a) and 7(b).

The effect of introducing the magnets is, however, not solely to reduce the gap due to an induced effective spin splitting in the superconductor. The induced spin splitting also splits the midgap states away from their resonance point at zero energy, suppressing the midgap states. As the gap close to the edge to begin with is strongly suppressed by the midgap states, the effect of reducing the midgap states, causing the superconducting order parameter to recover at the edge, is stronger than the effect of the spin splitting on the condensation energy. As the parallel configuration most effectively produces a spin splitting in the superconductor, this configuration features the largest condensation energy, giving rise to the behavior that is observed in Fig. 6(a).

Investigating the constant term in the Hamiltonian $H_0 = \sum_i H_{0,i}$, the difference between $H_{0,i}$ for the parallel and antiparallel configurations is presented in Fig. 7(c). The figure shows that H_0, which is a positive quantity, is largest for the parallel configuration, corresponding to a larger gap. In turn, this produces a larger condensation energy that lowers the free energy of the system. From the figure, it is clear that the
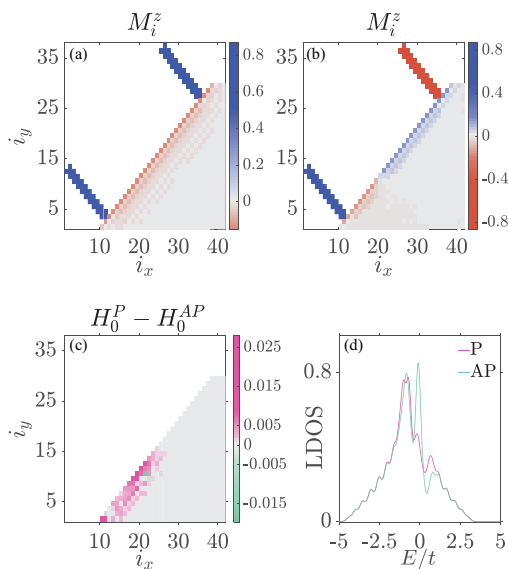
FIG. 7. d-Wave: Magnetization on each lattice site for the parallel (a) and antiparallel (b) configuration of magnets. The difference in $H_{0,i}$ between the parallel and antiparallel configurations is presented in (c). The local density of states (LDOS) for the 11th lattice site (from the left) of the diagonal edge is presented in (d), showing that the midgap states are more suppressed for the parallel magnet configuration. Here we have taken the same parameters as in Fig. 6(a), apart from a larger exchange field of $h_i = 2t$ in order to more clearly show the differences between the two configurations.

main contribution to the difference in condensation energy between the magnetic configurations comes from the transition region where the antiparallel configuration has a reduced edge magnetization. LDOS results from this region are presented in Fig. 7(d). While the AP configuration in this region has a clear midgap peak around zero energy, the midgap states for the P configuration have been split and suppressed by the induced spin splitting.

We close by discussing briefly experimental considerations and possible choices of materials for observation of the d-wave results presented in this paper. While the system sizes in the presented calculations are limited by computational considerations, the presented results are expected to be robust also for larger systems. As RKKY interaction typically decays below experimentally accessible values over short length scales of the order of nanometers, the separation between the magnetic contacts typically needs to be kept small. This might however only apply to the RKKY dominated indirect interaction that we observe for the horizontal edge of the d-wave superconductor. The preference of alignment of the ferromagnets when attached to a diagonal edge of a d-wave superconductor is expected to also be observable for larger magnet separation as the indirect interaction in this case is not dominated by itinerant carriers, but rather arises from the parallel configuration more efficiently inducing a spin

splitting, suppressing the localized midgap states. The distance the magnets can interact over is then limited by the length scale determining how far away from a magnet the midgap states still experience a spin splitting. If the magnet separation is much larger than this decay length of the induced spin splitting along the edge, the spin splitting arising from each magnet decays before interacting with the spin splitting arising from the other magnet. There is then no difference between the two magnet configurations when it comes to suppression of midgap states, and the parallel configuration is no longer favored. For an s-wave superconductor in proximity to a ferromagnet, the proximity-induced magnetization decays over a length scale of the superconducting coherence length [40]. A natural length scale for the decay of the induced spin splitting would then be the effective coherence length corresponding to the strongly suppressed order parameter at the edge. As the coherence length is inversely proportional to the order parameter, the magnets will then be able to interact over distances considerably larger than the bulk coherence length.

Experimental investigation of our main finding would consist of attaching magnetic leads to a {110} edge of a d-wave superconductor. The indirect interaction between the magnets can then be established by determining the energy barrier of switching between the two magnet configurations through an external magnetic field. Our prediction is that ferromagnetic alignment of the magnets will be preferred for a wide range of magnet separation distances. Possible material choices could be YBCO [2,7,29] for the d-wave superconductor featuring midgap states, and a nickel-alloy-like $Ni_{80}Co_{20}$ [41] for the magnetic contacts.

IV. SUMMARY

We have investigated the indirect exchange interaction between two ferromagnetic leads connected to a superconductor as a function of the separation between the magnets, showing that the presence of zero-energy surface states in a d-wave superconductor can qualitatively change the results. When the magnets are connected to an edge without zero-energy surface states we find a normal oscillating RKKY behavior. However, when the magnets are connected to an edge featuring zero-energy surface states, the strength of the magnetic exchange interaction is shifted away from zero, always favoring alignment of the magnetization in the two magnets, as the aligned configuration produces a larger superconducting condensation energy.

APPENDIX: PHASE DIAGRAM

In order to choose the parameters such that the superconductor used in the study is in a d-wave state, we obtain a starting point by considering a square system with continuous boundary conditions in both the x and y directions and no

attached magnetic leads. The relevant Hamiltonian is the one in Eq. (1) with $U_i = V'_{ij} = 0$. We introduce Fourier transformations for the electron operators $c_{i\alpha} = \frac{1}{\sqrt{N}} \sum_k e^{ik \cdot i} c_{k,\alpha}$ where $i = (i_x, i_y)$ and N is the number of lattice sites. After the mean-field approximation, Eq. (1) then becomes

$$
\begin{aligned}
H^{SC} = &-\sum_{\langle i,j \rangle, \alpha} t c_{i\alpha}^\dagger c_{j\alpha} - \sum_{i,\alpha} \mu_i n_{i\alpha} \\
&+ \sum_{i, \alpha \neq \alpha'} V[n_{i\alpha} n_{i+\hat{x}, \alpha'} + n_{i\alpha} n_{i-\hat{x}, \alpha'} + n_{i\alpha} n_{i+\hat{y}, \alpha'} \\
&+ n_{i\alpha} n_{i-\hat{y}, \alpha'}] \\
= &\sum_{k,\sigma} \zeta_k c_{k,\sigma}^\dagger c_{k,\sigma} + \sum_k [(\Gamma_k)^\dagger c_{k\downarrow}^\dagger c_{-k\uparrow}^\dagger + \Upsilon_k c_{k\uparrow} c_{-k\downarrow}] \\
&+ H_0^{SC}.
\end{aligned}
\tag{A1}
$$

Here $H_0^{SC} = -2NV(|F^{\hat{x}+}|^2 + |F^{\hat{x}-}|^2 + |F^{\hat{y}+}|^2 + |F^{\hat{y}-}|^2)$,

$$
\begin{aligned}
F^{x\pm} &= \frac{1}{N} \sum_k e^{\mp ik \cdot \hat{x}} \langle c_{k,\uparrow} c_{-k,\downarrow} \rangle, \\
F^{y\pm} &= \frac{1}{N} \sum_k e^{\mp ik \cdot \hat{y}} \langle c_{k,\uparrow} c_{-k,\downarrow} \rangle,
\end{aligned}
\tag{A2}
$$

and we have defined,

$$
\begin{aligned}
\Upsilon_k = 2V &(e^{-ik \cdot \hat{x}} (F^{\hat{x}+})^\dagger + e^{ik \cdot \hat{x}} (F^{\hat{x}-})^\dagger \\
&+ e^{-ik \cdot \hat{y}} (F^{\hat{y}+})^\dagger + e^{ik \cdot \hat{y}} (F^{\hat{y}-})^\dagger), \\
\Gamma_k = 2V &(e^{ik \cdot \hat{x}} (F^{\hat{x}+})^\dagger + e^{-ik \cdot \hat{x}} (F^{\hat{x}-})^\dagger \\
&+ e^{ik \cdot \hat{y}} (F^{\hat{y}+})^\dagger + e^{-ik \cdot \hat{y}} (F^{\hat{y}-})^\dagger), \\
\varepsilon_k = &-2t[\cos(k \cdot \hat{x}) + \cos(k \cdot \hat{y})] - \mu.
\end{aligned}
\tag{A3}
$$

Further, $t = t_{ij}$ and $V = V_{ij}$.

Following the BdG method [32], we consider the following basis in order to diagonalize the Hamiltonian

$$
B_k^\dagger = [c_{k\uparrow}^\dagger \quad c_{k\downarrow}^\dagger \quad c_{-k\uparrow} \quad c_{-k\downarrow}].
\tag{A4}
$$

Then full Hamiltonian can be written as $H = H_0 + \frac{1}{2} \sum_k B_k^\dagger H_k B_k$, where $H_0 = H_0^{SC} + \sum_k \varepsilon_k$ and H_k is

$$
H_k = \begin{bmatrix}
\varepsilon_k & 0 & 0 & -(\Upsilon_k)^\dagger \\
0 & \varepsilon_k & (\Gamma_k)^\dagger & 0 \\
0 & \Gamma_k & -\varepsilon_k & 0 \\
-\Upsilon_k & 0 & 0 & -\varepsilon_k
\end{bmatrix}.
\tag{A5}
$$

Using the unitary matrix P_k the diagonalized form of the Hamiltonian will be $H^{SC} = H_0 + \frac{1}{2} \sum_k B_k^\dagger P_k^\dagger P_k H_k P_k^\dagger P_k B_k = H_0 + \frac{1}{2} \sum_k \tilde{B}_k^\dagger \tilde{H}_k \tilde{B}_k = H_0 - \frac{1}{2} \sum_{k,\sigma} E_{k,\sigma} + \sum_{k,\sigma} E_{k,\sigma} \gamma_{k\sigma}^\dagger \gamma_{k\sigma}$. The relationship between the normal electron operators

TABLE I. Sets of initial values.

	$F^{\hat{x}+}$	$F^{\hat{x}-}$	$F^{\hat{y}+}$	$F^{\hat{y}-}$
d-wave	1	1	−1	−1
s-wave extended	1	1	1	1
$p_x + ip_y$	1	−1	i	$-i$
Normal state	0	0	0	0

and the quasiparticle operators is then

$$
\begin{bmatrix}
\upsilon_{k,\uparrow} & \upsilon_{k,\downarrow} & \omega_{k,\uparrow}^* & \omega_{k,\downarrow}^* \\
\nu_{k,\uparrow} & \upsilon_{k,\downarrow} & \chi_{-k,\uparrow}^* & \chi_{-k,\downarrow}^* \\
\omega_{k,\uparrow} & \omega_{k,\downarrow} & \upsilon_{-k,\uparrow}^* & \upsilon_{-k,\downarrow}^* \\
\chi_{k,\uparrow} & \chi_{k,\downarrow} & \nu_{-k,\uparrow}^* & \nu_{-k,\downarrow}^*
\end{bmatrix}
\begin{bmatrix}
\gamma_{k\uparrow} \\
\gamma_{k\downarrow} \\
\gamma_{-k\uparrow}^\dagger \\
\gamma_{-k\downarrow}^\dagger
\end{bmatrix}
=
\begin{bmatrix}
c_{k\uparrow} \\
c_{k\downarrow} \\
c_{-k\uparrow}^\dagger \\
c_{-k\downarrow}^\dagger
\end{bmatrix},
\tag{A6}
$$

where the columns are the eigenvectors of H_k. The pairing amplitudes can then be expressed as

$$
\begin{aligned}
F^{x\pm} = \frac{1}{N} \sum_{k,\sigma} &[e^{\mp ik \cdot \hat{x}} \upsilon_{k,\sigma} \chi_{k,\sigma}^* (1 - f(E_{k,\sigma})) \\
&+ e^{\pm ik \cdot \hat{x}} \omega_{k,\sigma}^* \nu_{k,\sigma} f(E_{k,\sigma})], \\
F^{y\pm} = \frac{1}{N} \sum_{k,\sigma} &[e^{\mp ik \cdot \hat{y}} \upsilon_{k,\sigma} \chi_{k,\sigma}^* (1 - f(E_{k,\sigma})) \\
&+ e^{\pm ik \cdot \hat{y}} \omega_{k,\sigma}^* \nu_{k,\sigma} f(E_{k,\sigma})].
\end{aligned}
\tag{A7}
$$

Finally, the free energy of the system is

$$
F = H_0 - \frac{1}{2} \sum_{k,\sigma} E_{k,\sigma} - \frac{1}{\beta} \sum_{k,\sigma} \ln(1 + e^{-\beta E_{k,\sigma}}).
\tag{A8}
$$

For different values of chemical potential and temperature, we then solve the self-consistent equations for the pairing amplitudes through iteration, using the different sets of initial values listed in Table I. We then compare the resulting free energies [Eq. (A8)] and determine the favored phase of the system. The phase diagram is presented in Fig. 8. The choices for the initial values are determined by the expressions for the
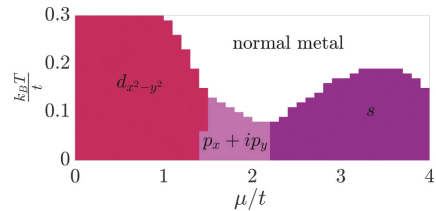

FIG. 8. Phase diagram for the tight-binding Hamiltonian with attractive nearest-neighbor interaction between opposite spins $V = -1t$. Here, T is the temperature, k_B is the Boltzmann constant, μ is the chemical potential, and t is the hopping amplitude.

gap functions [42]

$$\Delta_d = (V/4)(F^{\hat{x}+} + F^{\hat{x}-} - F^{\hat{y}+} - F^{\hat{y}-}),$$

$$\Delta_s = (V/4)(F^{\hat{x}+} + F^{\hat{x}-} + F^{\hat{y}+} + F^{\hat{y}-}),$$

$$\Delta_{p_x} = (V/2)(F^{\hat{x}+} - F^{\hat{x}-}),$$

$$\Delta_{p_y} = (V/2)(F^{\hat{y}+} - F^{\hat{y}-}). \tag{A9}$$

[1] P. Monthoux, A. V. Balatsky, and D. Pines, Phys. Rev. B **46**, 14803 (1992).

[2] D. A. Wollman, D. J. Van Harlingen, W. C. Lee, D. M. Ginsberg, and A. J. Leggett, Phys. Rev. Lett. **71**, 2134 (1993).

[3] C. C. Tsuei, J. R. Kirtley, C. C. Chi, Lock See Yu-Jahnes, A. Gupta, T. Shaw, J. Z. Sun, and M. B. Ketchen, Phys. Rev. Lett. **73**, 593 (1994).

[4] C.-R. Hu, Phys. Rev. Lett. **72**, 1526 (1994).

[5] Y. Tanaka and S. Kashiwaya, Phys. Rev. Lett. **74**, 3451 (1995).

[6] S. Kashiwaya, Y. Tanaka, M. Koyanagi, H. Takashima, and K. Kajimura, Phys. Rev. B **51**, 1350 (1995).

[7] J. Geerk, X. Xi, and G. Linker, Z. Phys. B **73**, 329 (1988).

[8] J. Lesueur, L. Greene, W. Feldmann, and A. Inam, Physica C: Superconductivity **191**, 325 (1992).

[9] I. Iguchi, W. Wang, M. Yamazaki, Y. Tanaka, and S. Kashiwaya, Phys. Rev. B **62**, R6131(R) (2000).

[10] J. Y. T. Wei, N.-C. Yeh, D. F. Garrigus, and M. Strasik, Phys. Rev. Lett. **81**, 2542 (1998).

[11] K. Yosida, Phys. Rev. **106**, 893 (1957).

[12] M. A. Ruderman and C. Kittel, Phys. Rev. **96**, 99 (1954).

[13] T. Kasuya, Prog. Theor. Phys. **16**, 45 (1956).

[14] Y. Yafet, Phys. Rev. B **36**, 3948 (1987).

[15] H. Imamura, P. Bruno, and Y. Utsumi, Phys. Rev. B **69**, 121303(R) (2004).

[16] A. M. Black-Schaffer, Phys. Rev. B **81**, 205416 (2010).

[17] E. Kogan, Phys. Rev. B **84**, 115119 (2011).

[18] S. Saremi, Phys. Rev. B **76**, 184430 (2007).

[19] M. Sherafati and S. Satpathy, Phys. Rev. B **83**, 165425 (2011).

[20] E. H. Hwang and S. Das Sarma, Phys. Rev. Lett. **101**, 156802 (2008).

[21] M. Shiranzaei, H. Cheraghchi, and F. Parhizgar, Phys. Rev. B **96**, 024413 (2017).

[22] J.-J. Zhu, D.-X. Yao, S.-C. Zhang, and K. Chang, Phys. Rev. Lett. **106**, 097201 (2011).

[23] Q. Liu, C.-X. Liu, C. Xu, X.-L. Qi, and S.-C. Zhang, Phys. Rev. Lett. **102**, 156603 (2009).

[24] V. M. Galitski and A. I. Larkin, Phys. Rev. B **66**, 064526 (2002).

[25] P. W. Anderson and H. Suhl, Phys. Rev. **116**, 898 (1959).

[26] N. Y. Yao, L. I. Glazman, E. A. Demler, M. D. Lukin, and J. D. Sau, Phys. Rev. Lett. **113**, 087202 (2014).

[27] A. A. Zyuzin and D. Loss, Phys. Rev. B **90**, 125443 (2014).

[28] Y. Zhu, A. Pal, M. G. Blamire, and Z. H. Barber, Nat. Mater. **16**, 195 (2017).

[29] U. Welp, W. K. Kwok, G. W. Crabtree, K. G. Vandervoort, and J. Z. Liu, Phys. Rev. Lett. **62**, 1908 (1989).

[30] D. Aristov, S. Maleyev, and A. Yashenkin, Z. Phys. B **102**, 467 (1997).

[31] A. Di Bernardo, S. Komori, G. Livanas, G. Divitini, P. Gentile, M. Cuoco, and J. W. Robinson, Nat. Mater. **18**, 1194 (2019).

[32] P. G. De Gennes, *Superconductivity Of Metals And Alloys* (CRC Press, Boca Raton, FL, 1999).

[33] F. S. Bergeret, M. Silaev, P. Virtanen, and T. T. Heikkilä, Rev. Mod. Phys. **90**, 041001 (2018).

[34] A. Ghanbari, V. K. Risinggård, and J. Linder, Sci. Rep. **11**, 5028 (2021).

[35] C.-R. Hu and X.-Z. Yan, Phys. Rev. B **60**, R12573(R) (1999).

[36] J.-X. Zhu and C. S. Ting, Phys. Rev. B **61**, 1456 (2000).

[37] F. S. Bergeret, A. F. Volkov, and K. B. Efetov, Rev. Mod. Phys. **77**, 1321 (2005).

[38] F. S. Bergeret, A. Levy Yeyati, and A. Martín-Rodero, Phys. Rev. B **72**, 064524 (2005).

[39] M. Y. Kharitonov, A. F. Volkov, and K. B. Efetov, Phys. Rev. B **73**, 054511 (2006).

[40] F. S. Bergeret, A. F. Volkov, and K. B. Efetov, Phys. Rev. B **69**, 174504 (2004).

[41] S. S. P. Parkin and D. Mauri, Phys. Rev. B **44**, 7131 (1991).

[42] K. Kuboki, J. Phys. Soc. Jpn. **70**, 2698 (2001).

Going beyond the Chandrasekhar-Clogston limit in a flatband superconductor

Authors

Atousa Ghanbari*
Eirik Erlandsen*
Asle Sudbø
Jacob Linder

*These authors contributed equally to this work.

Going beyond the Chandrasekhar-Clogston limit in a flatband superconductor

Atousa Ghanbari,[*] Eirik Erlandsen [●],[*] Asle Sudbø [●], and Jacob Linder[†]

Center for Quantum Spintronics, Department of Physics, Norwegian University of Science and Technology, NO-7491 Trondheim, Norway

The Chandrasekhar-Clogston limit normally places stringent conditions on the magnitude of the magnetic field that can coexist with spin-singlet superconductivity, restricting the critical induced Zeeman shift to a fraction of the superconducting gap. Here, we consider a model system where the spin-singlet Cooper pairing in a dispersive band crossing the Fermi level is boosted by an additional flat-band located away from the Fermi level. The boosting of the pairing in the dispersive band allows for nontrivial solutions to the coupled gap equations for spin-splitting fields considerably larger than the superconducting gaps at zero field. Further, the additional Cooper pairing in the flat-band, away from the Fermi level, can increase the superconducting condensation energy without affecting the paramagnetic susceptibility of the system, making the free energy favor the superconducting state. This opens up the possibility for spin-singlet superconductivity beyond the standard Chandrasekhar-Clogston limit.

I. INTRODUCTION

Coexistence of superconductivity and magnetism is essential within the field of superconducting spintronics [1–8], which relies on stabilizing superconductors in proximity to magnetic materials and realizing phenomena such as spin-polarized supercurrents [9–11]. Moreover, spin-split superconductors can give rise to very large thermoelectric effects [12–17], which can be used to convert excess heat into useful energy.

Magnetism is, however, usually detrimental to superconductivity. Orbital effects induced in a superconductor due to a magnetic field can be suppressed by making the superconductor sufficiently thin and applying the magnetic field in-plane [16,18,19]. The critical magnetic field is then determined by the Zeeman-splitting that the superconducting state can survive [20,21]. As the normal state of the system has a nonzero density of states at the Fermi level, the free energy can be lowered in the presence of a spin-splitting field by spin-polarizing the system. A spin-singlet superconductor with a gap around the Fermi level [22], however, has no zero-temperature paramagnetic susceptibility and is unable to lower its energy in the same way. When the Zeeman energy gain in the normal state becomes as large as the superconducting condensation energy, the system therefore transitions to the normal state. This places an upper bound on the spin-splitting field that a conventional superconductor can coexist with $h = \Delta_0/\sqrt{2} \approx 0.7\,\Delta_0$ [20,21], referred to as the Chandrasekhar-Clogston limit. Here, Δ_0 is the superconducting gap at zero field. Bypassing the Chandrasekhar-Clogston limit requires, e.g., spin-triplet or Fulde-Ferrell-Larkin-Ovchinnikov (FFLO) pairing [23,24], introduction of spin-orbit coupling in the system [25], or an

applied voltage bias driving the superconductor out of equilibrium [26].

Fermionic flat-band systems are systems containing one or more fermionic energy bands with weak or no dependence on momentum [27,28]. Such bands can be generated by realizing particular tight-binding models [29–35] in, e.g., artificial electronic lattices [36–39] or optical lattices filled with ultracold fermionic atoms [40,41]. For instance, spin-imbalanced superfluidity in lattices featuring flat bands, such as Lieb and kagome lattices, have been studied in Refs. [42,43]. Flat-bands can also be realized in twisted or lattice mismatched multilayers such as twisted bilayer graphene [28,44–47], where the flat-bands are defined in a mini-Brillouin zone corresponding to a long-wavelength superlattice arising from the mismatch between the periodic structures in the separate layers. Flat-band systems are appealing for superconductivity as a larger density of states at the Fermi level normally leads to a larger superconducting transition temperature. Early studies identified that the presence of a flat-band could in fact give rise to a linear dependence of the transition temperature on the strength of the attractive interactions [48,49], generating hope of achieving high critical temperatures. With the discovery of superconductivity in magic-angle twisted-bilayer graphene [45], interest in flat-band superconductivity rocketed [50–54]. Recently, it has also been shown that superconductivity in twisted trilayer graphene can survive in-plane magnetic fields beyond the Chandrasekhar-Clogston limit [55], which has been interpreted as an indication of spin-triplet pairing [55,56].

In this Letter, we consider a two-band model system for a spin-split superconductor, in which a dispersive band crosses the Fermi level and a flat-band is located in the vicinity of the Fermi level. We consider both attractive intra- and interband scattering, giving rise to two coupled self-consistency equations for the spin-singlet pairing amplitudes associated with the two bands. The additional Cooper pairing in the flat-band

---

*These authors contributed equally to this work.

†jacob.linder@ntnu.no

gives rise to an increase in the condensation energy, without affecting the zero-temperature paramagnetic susceptibility of the system as long as the flat-band does not cross the Fermi level. The free energy is therefore minimized by the super-conducting state beyond the Chandrasekhar-Clogston limit. Moreover, as the flat-band is located away from the Fermi level, quasiparticle excitations associated with the flat-band are energetically costly also for large spin-splitting, making the flat-band contributions to the gap equations more resilient to spin-splitting fields than the contributions from the dispersive band. We therefore find that the spin-singlet pairing in this system can survive spin-splitting fields significantly larger than the superconducting gaps at zero field. We close by discussing how the physics captured by our model can be realized in experiments.

II. MODEL

Our system is described by an interacting two-band Hamiltonian on the form

$$H = \sum_{i,\boldsymbol{k},\sigma} \varepsilon_{i,\boldsymbol{k},\sigma} c_{i,\boldsymbol{k},\sigma}^{\dagger} c_{i,\boldsymbol{k},\sigma}$$
$$- \frac{1}{N} \sum_{i,j,\boldsymbol{k},\boldsymbol{k}'} V_{ij}(\boldsymbol{k},\boldsymbol{k}') c_{i,\boldsymbol{k},\uparrow}^{\dagger} c_{i,-\boldsymbol{k},\downarrow}^{\dagger} c_{j,-\boldsymbol{k}',\downarrow} c_{j,\boldsymbol{k}',\uparrow}. \quad (1)$$

Here, $c_{i,\boldsymbol{k},\sigma}$ is an annihilation operator for an electron in band i with momentum $\boldsymbol{k}$, and spin σ. The noninteracting part of the Hamiltonian describes the dispersive band with energies $\varepsilon_{1,\boldsymbol{k},\sigma} = -2t[\cos(k_x) + \cos(k_y)] - \mu - \sigma h$ and the flat-band with energies $\varepsilon_{2,\boldsymbol{k},\sigma} = -\mu_0 - \sigma h$. The strength of the spin-splitting field is still h, the number of lattice sites is denoted by N, and μ is the chemical potential. Further, μ_0 is the shift of the flat band away from the Fermi-level, where a positive μ_0 corresponds to the flat-band being located below the Fermi level. With this parametrization, the Fermi level is moved relative to the dispersive band when μ is varied, while the separation of the flat-band and the Fermi level is fixed. The band structure in the absence of spin-splitting is illustrated in Figs. 1(a) and 1(b). The Hamiltonian in Eq. (1) is similar to the one used in Ref. [48], which discussed boosting of the pairing in a dispersive band through the presence of a flat-band. However, no spin-splitting field was considered in Ref. [48].

The interaction term in the Hamiltonian allows for attractive BCS-type intraband and interband scattering [57]. The interaction is taken to be attractive in a thin shell of width $2\hbar\omega_c$ around the Fermi level

$$V_{ij}(\boldsymbol{k},\boldsymbol{k}') = \begin{cases} V_{ij} > 0, & |\varepsilon_{i,\boldsymbol{k}}|, |\varepsilon_{j,\boldsymbol{k}'}| \leqslant \hbar\omega_c, \\ 0, & \text{otherwise.} \end{cases} \quad (2)$$

Here, $\varepsilon_{i,\boldsymbol{k}}$ is defined from $\varepsilon_{i,\boldsymbol{k},\sigma} = \varepsilon_{i,\boldsymbol{k}} - \sigma h$, and V_{ij} is the band-dependent attractive interaction strength. In the following, we neglect any hybridization between the bands or other changes to the normal state band structure arising from the interaction, and investigate up to what values of h the attractive interaction can give rise to superconductivity.

Performing a standard mean-field theory, defining spin-singlet gaps $\Delta_i(\boldsymbol{k}) = \frac{1}{N} \sum_{j,\boldsymbol{k}'} V_{ij}(\boldsymbol{k},\boldsymbol{k}') \langle c_{j,-\boldsymbol{k}',\downarrow} c_{j,\boldsymbol{k}',\uparrow} \rangle$, and
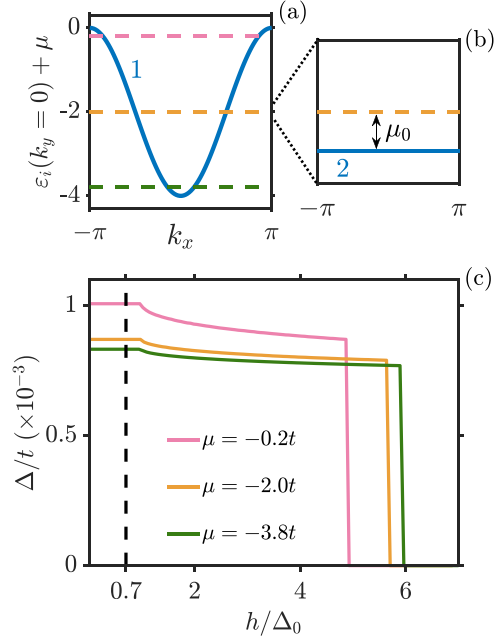

FIG. 1. (a), (b) Illustration of the band structure of the two-band model in the absence of spin-splitting. Dashed lines represent three different values of the chemical potential $\mu = -0.2t$, $-2t$, and $-3.8t$. The flat-band is fixed μ_0 below the Fermi level, which is illustrated by the blue line 2 in panel (b) for a specific choice of the chemical potential. (c) Superconducting gap versus the ratio between the strength of the spin-splitting field and the gap at zero field for the three different chemical potentials in (a). The Chandrasekhar-Clogston limit is indicated by the vertical dashed line. The parameters have been set to $T = 0$, $V_{11} = V_{12} = V_{21} = V_{22} = 0.01t$, $\mu_0 = 0.00495t$, and $\hbar\omega_c = 0.05t$.

introducing the necessary Bogoliubov-de Gennes transformation, the coupled gap equations take the form

$$\Delta_i(\boldsymbol{k}) = \frac{1}{N} \sum_{j,\boldsymbol{k}'} V_{ij}(\boldsymbol{k},\boldsymbol{k}') \frac{\Delta_j(\boldsymbol{k}')}{2E_{j,\boldsymbol{k}'}}$$
$$\times \frac{1}{2} \left[\tanh\left(\frac{\beta}{2} E_{j,\boldsymbol{k}',\uparrow}\right) + \tanh\left(\frac{\beta}{2} E_{j,\boldsymbol{k}',\downarrow}\right) \right]. \quad (3)$$

Here, $E_{i,\boldsymbol{k}} = \sqrt{\varepsilon_{i,\boldsymbol{k}}^2 + |\Delta_i(\boldsymbol{k})|^2}$, the quasiparticle energies are $E_{i,\boldsymbol{k},\sigma} = E_{i,\boldsymbol{k}} - \sigma h$, and $\beta = 1/(k_B T)$ is inverse temperature. The free energy, which determines whether the superconducting state minimizes the free energy, is expressed as

$$F = \frac{1}{4} \sum_{i,\boldsymbol{k},\sigma} \frac{\Delta_i^2(\boldsymbol{k})}{E_{i,\boldsymbol{k}}} \tanh\left(\frac{\beta}{2} E_{i,\boldsymbol{k},\sigma}\right)$$
$$+ \sum_{i,\boldsymbol{k}} (\varepsilon_{i,\boldsymbol{k}} - E_{i,\boldsymbol{k}}) - \frac{1}{\beta} \sum_{i,\boldsymbol{k},\sigma} \ln(1 + e^{-\beta E_{i,\boldsymbol{k},\sigma}}). \quad (4)$$

The first term in this expression is simply a generalization of the term $N\Delta^2/V$, which it reduces to for the case of a single electron band.

III. RESULTS

For simplicity, we start with the case where all the interaction strengths are equal ($V_{11} = V_{12} = V_{21} = V_{22} = V$). In this case, the two coupled gap equations in Eq. (3) reduce to a single self-consistent equation for the gap $\Delta = \Delta_1 = \Delta_2$. By numerically solving this gap equation and ensuring that the free energy in Eq. (4) is minimized, we determine the value of the gap as a function of the strength of the spin-splitting field h. The results at zero-temperature are presented in Fig. 1(c) for different values of the chemical potential μ. As displayed in this figure, a nonzero superconducting gap can exist for spin-splitting fields significantly larger than the gap at zero field Δ_0.

In the more familiar case of a superconductor with a single dispersive band crossing the Fermi level, the superconducting gap vanishes when the field strength reaches the Chandrasekhar-Clogston limit and the normal state minimizes the free energy. In Fig. 1(c), this limit is indicated by a vertical dashed line. The mechanism for this transition is easily seen from the expression for the free energy in Eq. (4) if we limit ourselves to the contributions from $i = 1$, corresponding to the dispersive band. For the superconductor, as long as the spin-splitting is smaller than the gap, all the quasiparticle energies are positive and the last term in the free energy vanishes at zero temperature. For the normal state, however, there is no gap in the excitation spectrum and the energies $E_{1,\mathbf{k},\sigma} = |\varepsilon_{1,\mathbf{k}}| - \sigma h$ can turn negative, giving rise to negative contributions from the last term in the free energy. This corresponds to a lowering of the normal state free energy through the system becoming spin-polarized. Comparing the rest of the free energy for the two phases gives rise to the condensation energy, favoring the superconducting state. When the strength of the spin-splitting field is increased, the lowering of the free energy of the normal state eventually dominates over the condensation energy, and the normal state prevails.

In the present case, there are additional contributions to the free energy arising from the flat band. As long as the quasiparticle energies $E_{2,\mathbf{k},\sigma}$ are shifted away from the Fermi level by $|\mu_0| > h$, these energies will always be positive even without a gap. At zero temperature there are then no contributions from the last term in the free energy arising from the flat-band, regardless of whether the system is in the superconducting or normal state. The effect of the flat-band on the free energy is then simply to significantly increase the condensation energy due to its large density of states. We therefore find that having a nonzero gap minimizes the free energy also beyond the Chandrasekhar-Clogston limit. Moreover, considering the dispersive band, when the spin-splitting becomes larger than Δ_0, the gaps in the separate spin-bands no longer overlap and the superconducting state is able to lower its free energy by spin-polarizing the quasiparticles as discussed in Ref. [58]. Such "gapless" superconductivity arises from time-reversal symmetry breaking [59,60] and has been encountered in, e.g., systems with magnetic impurities [61,62] and in the presence of a magnetic field [63,64]. For a model with two bands

crossing the Fermi level, the state where the spin-splitting is larger than the superconducting order parameter of both bands was discussed, but not found to be stable, in Ref. [65].

Turning to the gap equation, for a spin-splitting field larger than the gap, the energies $E_{1,\mathbf{k}',\uparrow}$ and $E_{1,\mathbf{k}',\downarrow}$ on the right-hand side of Eq. (3) can end up with opposite signs, leading to a cancellation of the contributions. The first contributions to go are those with the smallest energies $E_{1,\mathbf{k}'}$, i.e., the most important contributions from the dispersive band. For the flat-band, however, the quasiparticle energies are always positive for $h < \sqrt{\mu_0^2 + \Delta^2}$. The flat-band contributions to the gap equation are therefore robust towards spin-splitting. By having the flat-band sufficiently close to the Fermi level ($|\mu_0| < V/2$), nontrivial solutions to the gap equation can then be guaranteed as long as the field is not large enough to change the sign of quasiparticle energies.

Closer investigation of the free energy reveals that, when contributions from the dispersive band are neglected, the superconducting state is no longer favored for $h > \sqrt{\mu_0^2 + \Delta^2} - \frac{1}{2}\Delta^2/\sqrt{\mu_0^2 + \Delta^2}$. This expression is larger than or equal to $|\mu_0|$ and arises from the paramagnetic energy gain of the normal state compensating the energy gain associated with the superconducting gap. Moreover, the expression is smaller than $\sqrt{\mu_0^2 + \Delta^2}$, meaning that at this field strength there still exists a nontrivial solution to the gap equation if $|\mu_0| < V/2$. The critical field is then limited by the free energy, giving rise to a first-order transition where the gap suddenly vanishes. Further, for $\mu_0^2 \gg \Delta^2$, the critical spin-splitting field simply becomes $h_c \approx |\mu_0|$, where the maximum value of $|\mu_0|$ that can produce a nontrivial solution to the gap equation is limited by the interaction strength V.

The dependence of the gap equation on the strength of the spin-splitting field can be observed in Fig. 1(c), and is most easily seen by considering the pink curve corresponding to $\mu = -0.2t$. For $h < \Delta_0$, the curve is flat as the spin-splitting has no effect on the contributions to the gap equation. Then, as $h > \Delta_0$, contributions from the dispersive band start canceling out, leading to a decrease in the gap. This corresponds to the minimum energy of breaking a Cooper pair becoming zero, as discussed by Abrikosov in the context of gapless superconductivity in the presence of magnetic impurities [66]. In the present case, a nonzero superconducting gap exists until around $h > |\mu_0|$, beyond which the free energy favors the normal state.

Taking $\mu = -2t$ as an example, $h_c/\Delta_0 = 5.7$ and, calculating the critical temperature at zero field, $\Delta_0/T_c = 0.87$. For these parameters, we then obtain $h_c/\mu_B = 7.4\,\text{T/K} \times T_c$, where μ_B is the Bohr magneton. For $\mu = -0.2t$, the ratio Δ_0/T_c becomes larger as the dispersive band contributes more to the gap equation, and oppositely for $\mu = -3.8t$. Reducing $|\mu_0|$ can give rise to higher values for Δ_0/T_c. Further, the temperature dependence of the results for $\mu = -2t$ are presented in Fig. 2. As displayed in Fig. 2(b), the superconductor to normal state transition becomes a second-order transition at higher temperature. The change from a first-order to a second-order transition is found to take place slightly above $T/T_c = 0.06$. This ratio can be increased by moving the flat-band closer to the Fermi level.

We next demonstrate how our results are influenced by band-dependence of the interaction strengths. We first
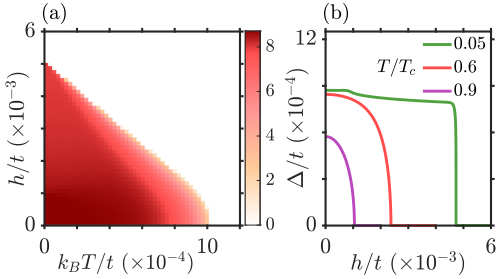
FIG. 2. (a) Superconducting gap Δ as a function of temperature T and the strength of the spin-splitting field h for the parameters in Fig. 1 with $\mu = -2t$. (b) Curves showing $\Delta(h)$ for a selection of temperatures.
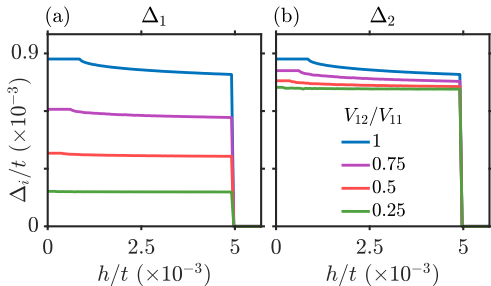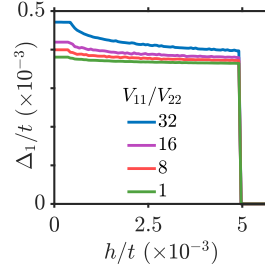

FIG. 4. The gap Δ_1 as a function of the strength of the spin-splitting field h for four different ratios of V_{11}/V_{22}. The parameters are set to $T = 0$, $\mu_0 = 0.00495t$, $V_{22} = 0.01t$, $V_{12} = V_{21} = 0.005t$, $\hbar\omega_c = 0.05t$, and $\mu = -2t$.

consider the effect of reducing the interband scattering by taking $V_{12} = V_{21}$ smaller than $V_{11} = V_{22}$. Solving the coupled gap equations and checking the free energy, we obtain the results in Fig. 3 . As the dominant contributions to the gap equations arise from the flat-band, we find that Δ_2, which obtains contributions from $V_{21}\Delta_1$ and $V_{22}\Delta_2$, is not strongly affected by a reduction of V_{21}. However, Δ_1 obtains contributions from $V_{11}\Delta_1$ and $V_{12}\Delta_2$, and a reduction of V_{12} therefore leads to a significant reduction of Δ_1. Substantial pairing in the dispersive band crossing the Fermi level therefore requires a sufficiently large interband interaction strength. In all cases, the gaps survive until around $h > |\mu_0|$, which is considerably larger than the gaps at zero field.

Finally, we consider the case where we also increase the intraband interaction in the dispersive band compared to the intraband interaction in the flat-band. The results for Δ_1 are displayed in Fig. 4, showing that significantly increasing V_{11} only leads to a moderate increase in Δ_1 as the dominant contributions to the gap equations still arise from the flat-band due to its large density of states. A moderate increase in Δ_1 has little impact on the results for Δ_2 which therefore varies little when we increase V_{11}. The gaps once again survive until around $h > |\mu_0|$, where the magnitude of $|\mu_0|$ that can still

provide a nontrivial solution to the gap equations is determined by how large we take V_{22}.

IV. OUTLOOK

We have presented a mechanism for how a spin-singlet superconductor can survive beyond the Chandrasekhar-Clogston limit. The mechanism relies on having a sufficiently dispersive band crossing the Fermi level, an additional flat-band nearby, sufficient intraband interaction in the flat-band, and some interband scattering. Experimental realization would typically be through a thin-film superconductor with a, preferably tunable, induced spin-splitting. The spin-splitting can be achieved by exposing the superconductor to a strong in-plane magnetic field, or to a combination of a ferromagnet and an external field where the additional external field provides the tunability of the strength of the spin-splitting [26]. The necessary band structure could be realized in twisted multilayers, artificial electronic lattices or alternatively in optical lattices. The especially relevant case of a dispersive band on top of a flat-band corresponds to the limiting case where the chemical potential in Fig. 1 is taken almost down to the bottom of the band, e.g., $\mu = -4t + \mu_0$. Importantly, the flatness of the flat-band should be stable in the presence of spin-splitting. Finally, the interactions could originate with phonons in twisted multilayers or be engineered in artificial systems. The choice of interactions in Fig. 1 could, e.g., in principle correspond to the electrons in both bands coupling similarly to Einstein phonons. As shown in Figs. 3 and 4, the results for the critical field are, however, quite robust to band-dependence of the interaction strengths, allowing for reduction of the interband scattering as well as for a much larger intraband scattering in the dispersive band than in the flat-band.

More exhaustive studies of realistic systems with similar properties as our model system, taking into account the details of the band structure and the interactions, should be performed to more closely relate the results to experiments. Special attention should be paid to the theoretical approach when a flat-band is present and when the Fermi energy is not dominating the other energy scales in the system, which, e.g., can be the case when the chemical potential is close to the bottom of the conduction band. Future work could also include analysis

FIG. 3. (a) Δ_1 (b) Δ_2 as a function of the strength of the spin-splitting field h for four different ratios of V_{12}/V_{11}. The parameters are set to $T = 0$, $\mu_0 = 0.00495t$, $V_{11} = V_{22} = 0.01t$, $V_{12} = V_{21}$, $\hbar\omega_c = 0.05t$, and $\mu = -2t$.

of the stability of other superconducting phases such as FFLO states, or investigation of, e.g., single-band models featuring bands that are partially flat and partially dispersive [67], where our mechanism in principle also could be applicable.

V. SUMMARY

Our results demonstrate that spin-singlet superconductivity beyond the Chandrasekhar-Clogston limit could be possible in flat-band systems. Future studies should perform more detailed calculations for realistic systems to more closely connect the findings to experiments.

ACKNOWLEDGMENTS

[1] J. Linder and J. W. A. Robinson, Nat. Phys. **11**, 307 (2015).

[2] M. Eschrig, Phys. Today **64**(1), 43 (2011).

[3] A. Singh, S. Voltan, K. Lahabi, and J. Aarts, Phys. Rev. X **5**, 021019 (2015).

[4] Y. C. Tao and J. G. Hu, J. Appl. Phys. **107**, 041101 (2010).

[5] A. I. Buzdin, Rev. Mod. Phys. **77**, 935 (2005).

[6] S. Takahashi and S. Maekawa, Phys. Rev. Lett. **88**, 116601 (2002).

[7] T. Wakamura, H. Akaike, Y. Omori, Y. Niimi, S. Takahashi, A. Fujimaki, S. Maekawa, and Y. Otani, Nat. Mater. **14**, 675 (2015).

[8] S. Takahashi and S. Maekawa, Jpn. J. Appl. Phys. **51**, 010110 (2011).

[9] R. S. Keizer, S. T. B. Goennenwein, T. M. Klapwijk, G. Miao, G. Xiao, and A. Gupta, Nature (London) **439**, 825 (2006).

[10] T. S. Khaire, M. A. Khasawneh, W. P. Pratt, and N. O. Birge, Phys. Rev. Lett. **104**, 137002 (2010).

[11] J. W. A. Robinson, J. D. S. Witt, and M. G. Blamire, Science **329**, 59 (2010).

[12] A. Ozaeta, P. Virtanen, F. S. Bergeret, and T. T. Heikkilä, Phys. Rev. Lett. **112**, 057001 (2014).

[13] P. Machon, M. Eschrig, and W. Belzig, Phys. Rev. Lett. **110**, 047002 (2013).

[14] F. Giazotto, J. W. A. Robinson, J. S. Moodera, and F. S. Bergeret, Appl. Phys. Lett. **105**, 062602 (2014).

[15] P. Machon, M. Eschrig, and W. Belzig, New J. Phys. **16**, 073002 (2014).

[16] F. S. Bergeret, M. Silaev, P. Virtanen, and T. T. Heikkilä, Rev. Mod. Phys. **90**, 041001 (2018).

[17] S. Kolenda, M. J. Wolf, and D. Beckmann, Phys. Rev. Lett. **116**, 097001 (2016).

[18] R. Meservey, P. M. Tedrow, and P. Fulde, Phys. Rev. Lett. **25**, 1270 (1970).

[19] R. Meservey, P. M. Tedrow, and R. C. Bruno, Phys. Rev. B **11**, 4224 (1975).

[20] B. S. Chandrasekhar, Appl. Phys. Lett. **1**, 7 (1962).

[21] A. M. Clogston, Phys. Rev. Lett. **9**, 266 (1962).

[22] J. Bardeen, L. N. Cooper, and J. R. Schrieffer, Phys. Rev. **108**, 1175 (1957).

[23] P. Fulde and R. A. Ferrell, Phys. Rev. **135**, A550 (1964).

[24] A. I. Larkin and Y. N. Ovchinnikov, Zh. Eksp. Teor. Fiz. **47**, 1136 (1964). [Sov. Phys. JETP **20**, 762 (1965)].

[25] R. C. Bruno and B. B. Schwartz, Phys. Rev. B **8**, 3161 (1973).

[26] J. A. Ouassou, T. D. Vethaak, and J. Linder, Phys. Rev. B **98**, 144509 (2018).

[27] D. Leykam, A. Andreanov, and S. Flach, Adv. Phys.: X **3**, 1473052 (2018).

[28] L. Balents, C. R. Dean, D. K. Efetov, and A. F. Young, Nat. Phys. **16**, 725 (2020).

[29] B. Sutherland, Phys. Rev. B **34**, 5208 (1986).

[30] E. H. Lieb, Phys. Rev. Lett. **62**, 1201 (1989).

[31] A. Mielke, J. Phys. A: Math. Gen. **24**, 3311 (1991).

[32] H. Tasaki, Phys. Rev. Lett. **69**, 1608 (1992).

[33] S. Miyahara, K. Kubo, H. Ono, Y. Shimomura, and N. Furukawa, J. Phys. Soc. Jpn. **74**, 1918 (2005).

[34] A. Ramachandran, A. Andreanov, and S. Flach, Phys. Rev. B **96**, 161104(R) (2017).

[35] A. Sil and A. K. Ghosh, J. Phys.: Condens. Matter **31**, 245601 (2019).

[36] A. Tadjine, G. Allan, and C. Delerue, Phys. Rev. B **94**, 075441 (2016).

[37] W.-X. Qiu, S. Li, J.-H. Gao, Y. Zhou, and F.-C. Zhang, Phys. Rev. B **94**, 241409(R) (2016).

[38] M. R. Slot, T. S. Gardenier, P. H. Jacobse, G. C. P. van Miert, S. N. Kempkes, S. J. M. Zevenhuizen, C. M. Smith, D. Vanmaekelbergh, and I. Swart, Nat. Phys. **13**, 672 (2017).

[39] R. Drost, T. Ojanen, A. Harju, and P. Liljeroth, Nat. Phys. **13**, 668 (2017).

[40] S. Taie, T. Ichinose, H. Ozawa, and Y. Takahashi, Nat. Commun. **11**, 257 (2020).

[41] G.-B. Jo, J. Guzman, C. K. Thomas, P. Hosur, A. Vishwanath, and D. M. Stamper-Kurn, Phys. Rev. Lett. **108**, 045305 (2012).

[42] K.-E. Huhtinen, M. Tylutki, P. Kumar, T. I. Vanhala, S. Peotta, and P. Törmä, Phys. Rev. B **97**, 214503 (2018).

[43] M. Tylutki and P. Törmä, Phys. Rev. B **98**, 094513 (2018).

[44] R. Bistritzer and A. H. MacDonald, Proc. Natl. Acad. Sci. USA **108**, 12233 (2011).

[45] Y. Cao, V. Fatemi, S. Fang, K. Watanabe, T. Taniguchi, E. Kaxiras, and P. Jarillo-Herrero, Nature (London) **556**, 43 (2018).

[46] Z. Zhang, Y. Wang, K. Watanabe, T. Taniguchi, K. Ueno, E. Tutuc, and B. J. LeRoy, Nat. Phys. **16**, 1093 (2020).

[47] J. M. Park, Y. Cao, K. Watanabe, T. Taniguchi, and P. Jarillo-Herrero, Nature (London) **590**, 249 (2021).

[48] S. Miyahara, S. Kusuta, and N. Furukawa, Physica C: Superconductivity **460–462**, 1145 (2007).

[49] N. B. Kopnin, T. T. Heikkilä, and G. E. Volovik, Phys. Rev. B **83**, 220503(R) (2011).

[50] R. Ojajärvi, T. Hyart, M. A. Silaev, and T. T. Heikkilä, Phys. Rev. B **98**, 054515 (2018).

[51] A. Bussmann-Holder, H. Keller, A. Simon, and A. Bianconi, Condensed Matter **4**, 91 (2019).

[52] Y. W. Choi and H. J. Choi, Phys. Rev. B **98**, 241412(R) (2018).

[53] B. Lian, Z. Wang, and B. A. Bernevig, Phys. Rev. Lett. **122**, 257002 (2019).

[54] F. Schrodi, A. Aperis, and P. M. Oppeneer, Phys. Rev. Res. **2**, 012066(R) (2020).

[55] Y. Cao, J. M. Park, K. Watanabe, T. Taniguchi, and P. Jarillo-Herrero, Nature (London) **595**, 526 (2021).

[56] W. Qin and A. H. MacDonald, Phys. Rev. Lett. **127**, 097001 (2021).

[57] H. Suhl, B. T. Matthias, and L. R. Walker, Phys. Rev. Lett. **3**, 552 (1959).

[58] G. Sarma, J. Phys. Chem. Solids **24**, 1029 (1963).

[59] K. H. Bennemann and J. B. Ketterson, *Superconductivity—Conventional and Unconventional Superconductors* (Springer-Verlag, Berlin, 2008).

[60] G. Sun, D. Y. Xing, J. Dong, and M. Liu, Phys. Rev. B **65**, 174508 (2002).

[61] A. A. Abrikosov and L. P. Gor'kov, Zh. Eksp. i Teor. Fiz. **39**, 1781 (1960).

[62] F. Reif and M. A. Woolf, Rev. Mod. Phys. **36**, 238 (1964).

[63] K. Maki, Phys. Phys. Fiz. **1**, 127 (1964).

[64] P. G. de Gennes and M. Tinkham, Phys. Phys. Fiz. **1**, 107 (1964).

[65] L. He and P. Zhuang, Phys. Rev. B **79**, 024511 (2009).

[66] A. A. Abrikosov, *Fundamentals of the Theory of Metals* (Elsevier Science Publishers, Amsterdam, 1988).

[67] H. Aoki, J. Supercond. Novel Magn. **33**, 2341 (2020).

Magnon drag in a metal-insulating antiferromagnet bilayer

Authors

Eirik Erlandsen
Asle Sudbø

Magnon drag in a metal–insulating antiferromagnet bilayer

Eirik Erlandsen and Asle Sudbø[*]

Center for Quantum Spintronics, Department of Physics, Norwegian University of Science and Technology, NO-7491 Trondheim, Norway

We study a bilayer structure consisting of an antiferromagnetic insulator and a normal metal. An electron current is driven in the normal metal with direction parallel to the interface between the materials. Due to interfacial exchange coupling between the localized spins in the antiferromagnet and the itinerant electrons in the normal metal, a magnon current can then be induced in the antiferromagnet. Using an uncompensated antiferromagnetic interface, creating an asymmetry in the interfacial coupling to the two degenerate magnon modes, we find that it is possible to generate a magnon spin current. The magnon spin current can be enhanced by increasing the temperature or by spin-splitting the magnon modes.

I. INTRODUCTION

A key element in spin-based electronics is the possibility of using spin currents to transport information. The spin currents should be efficiently generated, capable of propagating with low loss of energy, and reliably detected. An interesting avenue for low-loss transportation of spin signals is provided by magnetic insulators where spin currents are associated with fluctuations in magnetic order rather than a spin-polarized flow of electrons [1–4]. Information can thus be transferred without the need of moving charge carriers. Detection of spin currents propagating through magnetic insulators can, e.g., be achieved through conversion to electron spin currents at metal interfaces, which can then be detected through the inverse spin Hall effect [5–7]. Conversely, the generation of spin currents can be achieved through injection from a neighboring material, such as a material exhibiting the spin Hall effect [1,2,5,8–12]. Alternatively, spin currents in magnetic insulators can also result from, e.g., a temperature gradient through the spin Seebeck effect [13,14].

Antiferromagnetic insulators, specifically, have recently gathered interest as alternatives to ferromagnetic insulators as active components in spintronics applications [4,15–17]. An additional complication for spin transport in antiferromagnetic insulators is, however, that their ability to carry spin currents can be reduced by competing contributions from the two oppositely polarized magnon modes, often giving rise to a vanishing spin current for an easy-axis antiferromagnet with two degenerate magnon modes [18]. Potential solutions to this problem include splitting the magnon modes through, e.g., the application of an external magnetic field [19,20], or utilizing hard-axis antiferromagnets, naturally featuring nondegenerate magnon modes [21]. The latter solution relies on the net spin angular momentum of the magnons not vanishing [18].

Going in a different direction, it is also possible to work with degenerate magnon modes, but inducing a magnon spin

current through a coupling to another material where one mode is more affected than the other. Such an asymmetry in the coupling can, e.g., arise from the other material exhibiting a spin accumulation at the interface [22–26], or from the antiferromagnetic interface itself being uncompensated, meaning that only one antiferromagnetic sublattice is exposed at the interface [24]. In addition to a potential asymmetry in the coupling to the two magnon modes, uncompensated interfaces can also provide an enhancement of electron-magnon interactions through suppressed sublattice interference [27,28]. This has been exploited in proposals for magnon-mediated superconductivity in heterostructures consisting of antiferromagnets and conductors [29–32], as well as indirect exciton condensation [33].

Spin currents associated with fluctuations in magnetic order can also arise in metallic magnets featuring both ordered localized magnetic moments and itinerant electrons. In this case, the coupling between the localized spins and itinerant electrons can give rise to a rich phenomenology pertaining to transport phenomena [34–38]. For instance, a voltage-induced electron current, naturally giving rise to an electron spin current in a metallic ferromagnet due to the spin nondegeneracy of the system, can transfer momentum to the magnon population in the system. This gives rise to a magnon spin current [39]. Likewise, a ferromagnetic metal with a temperature gradient will host flow of both electrons and magnons coupled together through drag effects [40–43]. Coupling of flow of electrons and magnons has also been investigated in noncollinear antiferromagnetic metals [44]. This type of interplay between electron and magnon currents is not naturally present in magnetic insulators. It can, however, be realized in heterostructures involving magnetic insulators and conducting materials.

Recently, it has been proposed that an in-plane charge current carried by spin-triplet Cooper pairs in a superconducting thin film can induce a magnon spin current in a neighboring ferromagnetic insulator layer due to interfacial exchange coupling [45]. This study, considering the coupling between localized spins and an imbalanced population of left-moving

---

*Corresponding author: asle.sudbo@ntnu.no

and right-moving particles in an adjacent material, represents a new way of inducing a spin current in a ferromagnetic insulator. A natural question to ask is then whether it is possible to induce a spin current in an antiferromagnetic insulator in a similar way. Moreover, as a normal metal subjected to a voltage also can host an imbalance of right-moving and left-moving particles, exchanging the superconductor in Ref. [45] with a normal metal could allow for the mechanism to be extended to higher temperatures in a simpler system setup.

In the present article, we investigate a system consisting of an antiferromagnetic insulator (AFMI) layer located on top of a normal metal (NM) layer, where an in-plane current is driven in the normal metal. Our modeling allows us to tune between a compensated and uncompensated AFMI interface, as well as to introduce spin splitting of both electrons and magnons. Through interfacial scattering processes, momentum can be transferred from the itinerant electrons of the NM to the magnons in the AFMI, potentially giving rise to magnon currents. Applying semiclassical Boltzmann theory, we here derive a relationship between the macroscopic currents flowing in the system.

For the case of spin-degenerate quasiparticles in both subsystems and a compensated antiferromagnetic interface, we find that the charge current in the NM induces a magnon current in the AFMI, but no magnon spin current as the contributions from the two magnon modes cancel. Applying instead an uncompensated AFMI interface, a magnon spin current is produced. Interestingly, we find that the magnitude of the induced magnon spin current is not always maximized for a fully uncompensated interface. A weaker asymmetry in the coupling between the NM and the two AFMI sublattices can actually be more favorable, despite the fact that this weakens the typical strength of the electron-magnon coupling. It is further found that the magnon spin current increases with temperature and that it can be enhanced by spin-splitting the magnon modes.

II. MODEL

The system setup is illustrated in Fig. 1. An experimental realization of the system will typically feature thin films of some finite thickness. For simplicity, we consider the layers to be two-dimensional and apply square lattice models. We start out from a tight-binding description of electrons hopping between lattice sites in the NM. For the AFMI, we consider localized spins with easy-axis anisotropy K, interacting with each other through a nearest-neighbor exchange interaction J_1 and a next-nearest-neighbor interaction J_2. We perform a Holstein-Primakoff transformation in order to describe spin fluctuations in terms of magnons. Additionally, there is an interfacial exchange coupling $\bar{J}\Omega_\Upsilon$ between the localized spins of the $\Upsilon = A, B$ sublattice in the AFMI and the spins of the itinerant electrons in the NM, which gives rise to electron-magnon scattering [32]. Importantly, we can, e.g., set $\Omega_A = 1$, $\Omega_B = \Omega$ and tune our way from $\Omega = 1$ (compensated interface) to $\Omega = 0$ (uncompensated interface). As discussed in Appendix A, we go to the long-wavelength limit to obtain isotropic expressions for the dispersion relations and magnon coherence factors, which will simplify our further calcula-
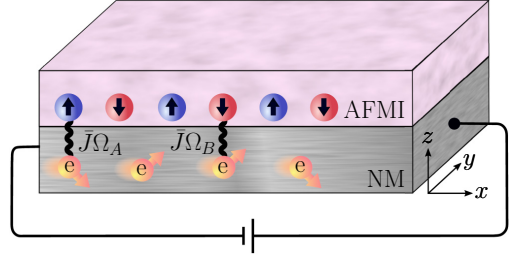

FIG. 1. A bilayer structure consisting of an antiferromagnetic insulator (AFMI) on top of a normal metal (NM). A voltage bias is applied to the normal metal in order to produce an electron current directed along the x axis. The itinerant electrons in the NM can interact with the spins in the AFMI, potentially leading to an induced magnon spin current. The coupling between the electrons in the NM and the A sublattice of the AFMI is $\bar{J}\Omega_A$, while the coupling to the B sublattice is $\bar{J}\Omega_B$.

tions. For a sufficiently small and isotropic Fermi surface in the NM, our modeling should be suitable.

The Hamiltonian describing the electrons then takes the form

$$H_{\text{NM}} = \sum_{k\sigma} \epsilon_{k\sigma} c_{k\sigma}^\dagger c_{k\sigma}, \quad (1)$$

where $\epsilon_{k\sigma} = t(ka)^2 - \mu - \sigma h_e$. Here, $c_{k\sigma}^\dagger$ is a creation operator for an electron with momentum $\boldsymbol{k}$ and spin $\sigma = \uparrow, \downarrow = +, -$. Further, t is the electron hopping amplitude, a is the lattice constant, μ is the chemical potential, and h_e is a spin-splitting field. The electron spin splitting can arise from either asymmetric coupling to the two sublattices of the AFMI, an external applied field, or a combination of these two sources, as discussed in Appendix A.

The Hamiltonian describing the magnons is expressed as

$$H_{\text{AFMI}} = \sum_{q} (\omega_{q\alpha} \alpha_q^\dagger \alpha_q + \omega_{q\beta} \beta_q^\dagger \beta_q), \quad (2)$$

where $\omega_{q\alpha} = \omega_q + h_m$, $\omega_{q\beta} = \omega_q - h_m$, and

$$\omega_q = \sqrt{\Delta_g^2 + \kappa^2(qa)^2}. \quad (3)$$

Here, $\alpha_q^\dagger$ is a creation operator for an α magnon (spin down) with momentum $\boldsymbol{q}$, and $\beta_q^\dagger$ is a creation operator for a β magnon (spin up). The gap in the magnon spectrum is Δ_g, while the dispersiveness of the spectrum is parametrized by κ. A splitting of the magnon modes h_m could, e.g., be introduced through an external field. Similarly to the electrons, we will use a short-form notation $\omega_{q,\gamma} = \omega_q - \gamma h_m$, where $\gamma = \alpha, \beta = -, +$.

Finally, the electron-magnon scattering arising from the coupling between the materials is described by [32]

$$H_{\text{int}} = \frac{V}{\sqrt{N}} \sum_{kq} (M_q c_{k+q,\downarrow}^\dagger c_{k,\uparrow} + M_{-q}^\dagger c_{k+q,\uparrow}^\dagger c_{k,\downarrow}), \quad (4)$$

where N is the number of lattice sites in each layer, $V = -2\bar{J}\sqrt{S}$, and

$$M_q = (\Omega_A u_q + \Omega_B v_q)\alpha_q + (\Omega_A v_q + \Omega_B u_q)\beta^{\dagger}_{-q}. \quad (5)$$

Here, S is the spin quantum number of the lattice site spins in the AFMI, and the magnon coherence factors u_q and v_q are defined in Appendix A. Importantly, u_q and v_q have opposite signs and grow large in magnitude when $q \to 0$, while always satisfying $u_q^2 - v_q^2 = 1$. The coupling between electron and long-wavelength magnons can therefore be enhanced by taking $\Omega_A \neq \Omega_B$ [28,29]. In addition to the scattering processes included in (4), there can also be additional umklapp scattering processes where the outgoing electron has its momentum shifted by a magnon reciprocal lattice vector [46]. Such scattering processes arise because the magnon Brillouin zone is reduced compared to the electron Brillouin zone. For a small electron Fermi surface, umklapp processes will take electrons far away from the Fermi surface, and such scattering processes can therefore be neglected [29,32]. Moreover, umklapp processes will typically not be present for a real uncompensated interface where the NM is lattice matched with one of the two sublattices of the AFMI.

In order to describe transport introduced by a voltage bias applied to the NM, we utilize coupled Boltzmann equations for electrons and magnons. We express the linearized Boltzmann equation for the electrons as [39,47]

$$-eE\, v^e_{k_x} \frac{\partial f^0(\epsilon_{k,\sigma})}{\partial \epsilon_{k,\sigma}} = -\frac{f_\sigma(\boldsymbol{k}) - \overline{f_\sigma}(\boldsymbol{k})}{\tau_\sigma} - \frac{f_\sigma(\boldsymbol{k}) - \overline{f_{-\sigma}}(\boldsymbol{k})}{\tau_{\uparrow\downarrow}}$$
$$+ \left[\frac{\partial f_\sigma(\boldsymbol{k})}{\partial t}\right]_{\text{int}}. \quad (6)$$

Here, e is the elementary charge, E is the electric field applied to the normal metal in the x direction, and $v^e_{k_x}$ is the x component of the electron group velocity. Further, $f_\sigma(\boldsymbol{k})$ is the electron distribution function, $f^0(\epsilon_{k,\sigma}) = 1/(e^{\beta\epsilon_{k,\sigma}} + 1)$ is the equilibrium electron distribution function, and $\bar{f}_\sigma$ represents a momentum average over the angular coordinate. In the absence of even-in-momentum corrections to the equilibrium distribution, the angularly averaged distribution is equivalent to the equilibrium distribution. Finally, τ_σ is the spin-conserving electron relaxation time for electrons with spin σ, and $\tau_{\uparrow\downarrow}$ is the spin-flip relaxation time for electrons. We have assumed that the electron distribution function is independent of in-plane position. An applied, uniform, electric field gives rise to spatially uniform corrections to the electron distribution functions, giving rise to flow of electrons. Interaction with magnons, represented by the last term [48], can modify, and potentially spin-polarize, the electron current. These effects are also assumed to be spatially uniform.

Furthermore, we express the linearized Boltzmann equation for the magnons as [21,39]

$$\left[\frac{\partial b_\gamma(\boldsymbol{q})}{\partial t}\right]_{\text{int}} = \frac{b_\gamma(\boldsymbol{q}) - b^0_\gamma(q)}{\tau_{M,\gamma}(q)}. \quad (7)$$

Here, the magnon distribution function is denoted by $b_\gamma(\boldsymbol{q})$, while $b^0_\gamma(q) = 1/(e^{\beta\omega_{q,\gamma}} - 1)$ is an equilibrium magnon distribution function. Moreover, $\tau_{M,\gamma}(q)$ is a momentum-dependent magnon-relaxation time. While the left-hand sides of the

Boltzmann equations for the electrons contain an external driving term, any net magnon motion will have to result from interaction with the electrons in the metal.

The electron and magnon distribution functions appearing in the Boltzmann equations will be expressed as sums of the equilibrium distributions and deviations from the equilibrium distributions of the form [39,49,50]

$$f_\sigma(\boldsymbol{k}) = f^0(\epsilon_{k,\sigma}) - \frac{\partial f^0(\epsilon_{k,\sigma})}{\partial \epsilon_{k,\sigma}} \left[\delta\mu^e_\sigma + g^e_\sigma(\boldsymbol{k})\right], \quad (8a)$$

$$b_\gamma(\boldsymbol{q}) = b^0(\omega_{q,\gamma}) - \frac{\partial b^0(\omega_{q,\gamma})}{\partial \omega_{q,\gamma}} \left[\delta\mu^m_\gamma + g^m_\gamma(\boldsymbol{q})\right]. \quad (8b)$$

While $\delta\mu$ represents a uniform shift of the chemical potential, any deviations associated with momentum-dependent corrections to the excitation energies are captured by the functions $\{g^e_\sigma(\boldsymbol{k}), g^m_\gamma(\boldsymbol{q})\}$. The part of these functions which is odd in momentum may generate a net flow of particles and will therefore be of relevance for this study. Moreover, the interaction terms in the electron Boltzmann equations can, using the interaction Hamiltonian together with Fermi's golden rule, be expressed as

$$\left[\frac{\partial f_\uparrow(\boldsymbol{k})}{\partial t}\right]_{\text{int}} = \frac{2\pi V^2}{\hbar N} \sum_{\boldsymbol{q}} \left[Q_\alpha(\boldsymbol{k}, \boldsymbol{q}) - Q^{\text{R}}_\beta(\boldsymbol{k}, \boldsymbol{q})\right], \quad (9a)$$

$$\left[\frac{\partial f_\downarrow(\boldsymbol{k})}{\partial t}\right]_{\text{int}} = \frac{2\pi V^2}{\hbar N} \sum_{\boldsymbol{q}} \left[Q_\beta(\boldsymbol{k}, \boldsymbol{q}) - Q^{\text{R}}_\alpha(\boldsymbol{k}, \boldsymbol{q})\right], \quad (9b)$$

while the interaction terms in the magnon Boltzmann equations similarly may be expressed as

$$\left[\frac{\partial b_\gamma(\boldsymbol{q})}{\partial t}\right]_{\text{int}} = \frac{2\pi V^2}{\hbar N} \sum_{\boldsymbol{k}} Q_\gamma(\boldsymbol{k}, \boldsymbol{q}). \quad (10)$$

Here, we have defined

$$Q_\alpha(\boldsymbol{k}, \boldsymbol{q}) = (\Omega_A u_q + \Omega_B v_q)^2 \delta[\epsilon_{k,\uparrow} + \omega_{q,\alpha} - \epsilon_{k+q,\downarrow}]$$
$$\times ([b_\alpha(\boldsymbol{q}) + 1][1 - f_\uparrow(\boldsymbol{k})]f_\downarrow(\boldsymbol{k} + \boldsymbol{q})$$
$$- b_\alpha(\boldsymbol{q})[1 - f_\downarrow(\boldsymbol{k} + \boldsymbol{q})]f_\uparrow(\boldsymbol{k})), \quad (11a)$$

$$Q_\beta(\boldsymbol{k}, \boldsymbol{q}) = (\Omega_A v_q + \Omega_B u_q)^2 \delta[\epsilon_{k,\downarrow} + \omega_{q,\beta} - \epsilon_{k+q,\uparrow}]$$
$$\times ([b_\beta(\boldsymbol{q}) + 1][1 - f_\downarrow(\boldsymbol{k})]f_\uparrow(\boldsymbol{k} + \boldsymbol{q})$$
$$- b_\beta(\boldsymbol{q})[1 - f_\uparrow(\boldsymbol{k} + \boldsymbol{q})]f_\downarrow(\boldsymbol{k})), \quad (11b)$$

as well as introduced $Q^{\text{R}}_\gamma(\boldsymbol{k}, \boldsymbol{q})$, which is related to $Q_\gamma(\boldsymbol{k}, \boldsymbol{q})$ by sending $\boldsymbol{q} \to -\boldsymbol{q}$ followed by sending $\boldsymbol{k} \to \boldsymbol{k} + \boldsymbol{q}$. We see that, with some necessary relabeling of momentum indices, conservation of spin dictates the structure of the equations. Processes increasing/decreasing the number of α magnons contribute in the same way to the number of spin-$\uparrow$ electrons, and conversely to the number of spin-$\downarrow$ electrons. For the β magnons, the situation is the same, except for reversal of the spin directions.

III. DERIVING MACROSCOPIC EQUATIONS

Starting from the coupled Boltzmann equations, we derive a set of macroscopic equations relating the spin-polarized

magnon current density j_{sm}, magnon current density j_m, and spin-polarized electron current density j_s to the electron current density j_e. The particle current densities are defined as [19,39,51]

$$j_s = \frac{1}{(2\pi)^2} \int dk \, v_{k_x}^e [f_\uparrow(\boldsymbol{k}) - f_\downarrow(\boldsymbol{k})], \quad (12a)$$

$$j_e = \frac{1}{(2\pi)^2} \int dk \, v_{k_x}^e [f_\uparrow(\boldsymbol{k}) + f_\downarrow(\boldsymbol{k})], \quad (12b)$$

$$j_{sm} = \frac{1}{(2\pi)^2} \int dq \, v_{q_x}^m [b_\beta(\boldsymbol{q}) - b_\alpha(\boldsymbol{q})], \quad (12c)$$

$$j_m = \frac{1}{(2\pi)^2} \int dq \, v_{q_x}^m [b_\beta(\boldsymbol{q}) + b_\alpha(\boldsymbol{q})], \quad (12d)$$

where we in the thermodynamic limit have introduced integration over momentum. In the following, j_s and j_{sm} will be referred to as the electron and magnon spin currents, while j_m and j_e will be referred to as simply the magnon and electron currents. Notably, we consider currents in the x direction in real space, and the spin-space z component of the spin currents. Further, the electron and magnon velocities appearing in the definitions of the currents are given by

$$v_{k_x}^e = \frac{1}{\hbar} \frac{\partial \epsilon_k}{\partial k} \hat{k} \cdot \hat{x}, \qquad v_{q_x}^m = \frac{1}{\hbar} \frac{\partial \omega_q}{\partial q} \hat{q} \cdot \hat{x}. \quad (13)$$

As the velocities are odd under inversion of momentum (odd in the x direction and even in the y direction), only the corresponding odd part of the distribution functions $f_\sigma(\boldsymbol{k})$ and $b_\gamma(\boldsymbol{q})$ contributes to the currents. Denoting the odd part of $g_\sigma^e(\boldsymbol{k})$ and $g_\gamma^m(\boldsymbol{q})$ by an index o, we can then write

$$j_s = \frac{1}{(2\pi)^2} \int dk \, v_{k_x}^e \sum_\sigma \sigma \left[-\frac{\partial f^0(\epsilon_{k,\sigma})}{\partial \epsilon_{k,\sigma}} \right] g_{\sigma,o}^e(\boldsymbol{k}), \quad (14a)$$

$$j_e = \frac{1}{(2\pi)^2} \int dk \, v_{k_x}^e \sum_\sigma \left[-\frac{\partial f^0(\epsilon_{k,\sigma})}{\partial \epsilon_{k,\sigma}} \right] g_{\sigma,o}^e(\boldsymbol{k}), \quad (14b)$$

$$j_{sm} = \frac{1}{(2\pi)^2} \int dq \, v_{q_x}^m \sum_\gamma \gamma \left[-\frac{\partial b^0(\omega_{q,\gamma})}{\partial \omega_{q,\gamma}} \right] g_{\gamma,o}^m(\boldsymbol{q}), \quad (14c)$$

$$j_m = \frac{1}{(2\pi)^2} \int dq \, v_{q_x}^m \sum_\gamma \left[-\frac{\partial b^0(\omega_{q,\gamma})}{\partial \omega_{q,\gamma}} \right] g_{\gamma,o}^m(\boldsymbol{q}). \quad (14d)$$

The next step is to multiply the electron Boltzmann equations by an electron velocity $v_{k_x}^e$ and integrate over momentum $\boldsymbol{k}$ [39]. Similarly, we multiply the magnon Boltzmann equations by a magnon velocity $v_{q_x}^m$ and integrate over momentum $\boldsymbol{q}$. Once again, any even-in-momentum corrections to the distribution functions drop out of the equations so that the remaining terms can be expressed in terms of the currents. Adding or subtracting the two equations for the electrons, we end up with

$$E T_+ = \tfrac{1}{2} P_0 \tau_e^{-1} j_s - \tfrac{1}{2} Y_0 \tau_e^{-1} j_e + [F_\uparrow + F_\downarrow], \quad (15a)$$

$$E T_- = \tfrac{1}{2} P_0 \tau_e^{-1} j_e - \tfrac{1}{2} Y_0 \tau_e^{-1} j_s + [F_\uparrow - F_\downarrow]. \quad (15b)$$

We have here defined $\tau_e^{-1} = \tau_\uparrow^{-1} + \tau_\downarrow^{-1}$, $P_0 = (\tau_\uparrow - \tau_\downarrow)/(\tau_\uparrow + \tau_\downarrow)$, $Y_0 = 1 + 2\tau_e/\tau_{\uparrow\downarrow}$,

$$T_\pm = \frac{-e}{(2\pi)^2} \int dk \, (v_{k_x}^e)^2 \left[\frac{\partial f^0(\epsilon_{k,\uparrow})}{\partial \epsilon_{k,\uparrow}} \pm \frac{\partial f^0(\epsilon_{k,\downarrow})}{\partial \epsilon_{k,\downarrow}} \right], \quad (16)$$

and

$$F_\sigma = \frac{1}{(2\pi)^2} \int dk \, v_{k_x}^e \left[\frac{\partial f_\sigma(\boldsymbol{k})}{\partial t} \right]_{\text{int}}. \quad (17)$$

As $\tau_{\uparrow\downarrow}$ shows up in the equations of the form $1 + 2\tau_e/\tau_{\uparrow\downarrow}$, its effect can be neglected for $\tau_{\uparrow\downarrow} \gg \tau_e$. Similarly, for the magnons, we obtain

$$B_\beta + B_\alpha = \tau_{M_0}^{-1} j_m, \quad (18a)$$

$$B_\beta - B_\alpha = \tau_{M_0}^{-1} j_{sm}, \quad (18b)$$

where

$$B_\gamma = \frac{1}{(2\pi)^2} \int dq \, v_{q_x}^m \, v(q) \left[\frac{\partial b_\gamma(\boldsymbol{q})}{\partial t} \right]_{\text{int}}. \quad (19)$$

We have here neglected the γ dependence of the magnon relaxation time [19,21], and written $\tau_M(q) = \tau_{M_0} v(q)$, where we take $v(q)$ to be of the form $v(q) = 1/[1 + \sum_n d_n(qa)^n]$. Setting some coefficient d_n nonzero, we can then capture the effect of momentum dependence of the magnon relaxation time. Further, it is worth noting that if both electrons and magnons are spin degenerate, the left-hand side of (18b) can vanish. A natural result would then be a nonzero magnon current, but no magnon spin current. However, for $\Omega_A \neq \Omega_B$, the asymmetry between u_q and v_q can give rise to $Q_\alpha \neq Q_\beta$, producing $B_\alpha \neq B_\beta$. In order to evaluate the interaction terms F_σ and M_σ, we insert the expressions for the distribution functions from Eqs. (8a) and (8b). We then have

$$F_\uparrow = \frac{V^2 a^2}{\hbar(2\pi)^3} \int dk \, v_{k_x}^e \int dq \, [Q_\alpha(\boldsymbol{k},\boldsymbol{q}) - Q_\beta^R(\boldsymbol{k},\boldsymbol{q})], \quad (20a)$$

$$F_\downarrow = \frac{V^2 a^2}{\hbar(2\pi)^3} \int dk \, v_{k_x}^e \int dq \, [Q_\beta(\boldsymbol{k},\boldsymbol{q}) - Q_\alpha^R(\boldsymbol{k},\boldsymbol{q})], \quad (20b)$$

$$B_\gamma = \frac{V^2 a^2}{\hbar(2\pi)^3} \int dq \, v_{q_x}^m \, v(q) \int dk \, Q_\gamma(\boldsymbol{k},\boldsymbol{q}), \quad (20c)$$

now with

$$\begin{aligned} Q_\alpha(\boldsymbol{k},\boldsymbol{q}) = {} & \beta(\Omega_A u_q + \Omega_B v_q)^2 \delta[\epsilon_{k,\uparrow} + \omega_{q,\alpha} - \epsilon_{k+q,\downarrow}] \\ & \times b^0(\omega_{q,\alpha})[1 - f^0(\epsilon_{k+q,\downarrow})] f^0(\epsilon_{k,\uparrow}) \\ & \times \big([\delta\mu_\downarrow^e - \delta\mu_\uparrow^e - \delta\mu_\alpha^m] \\ & + [g_\downarrow^e(\boldsymbol{k}+\boldsymbol{q}) - g_\uparrow^e(\boldsymbol{k}) - g_\alpha^m(\boldsymbol{q})] \big), \quad (21a) \end{aligned}$$

$$\begin{aligned} Q_\beta(\boldsymbol{k},\boldsymbol{q}) = {} & \beta(\Omega_A v_q + \Omega_B u_q)^2 \delta[\epsilon_{k,\downarrow} + \omega_{q,\beta} - \epsilon_{k+q,\uparrow}] \\ & \times b^0(\omega_{q,\beta})[1 - f^0(\epsilon_{k+q,\uparrow})] f^0(\epsilon_{k,\downarrow}) \\ & \times \big([\delta\mu_\uparrow^e - \delta\mu_\downarrow^e - \delta\mu_\beta^m] \\ & + [g_\uparrow^e(\boldsymbol{k}+\boldsymbol{q}) - g_\downarrow^e(\boldsymbol{k}) - g_\beta^m(\boldsymbol{q})] \big). \quad (21b) \end{aligned}$$

Here, $\beta = 1/(k_B T)$, where T is the temperature of the system and k_B is the Boltzmann constant. Redefining $\boldsymbol{k} \to -\boldsymbol{k}$ and $\boldsymbol{q} \to -\boldsymbol{q}$, we see that we, once again, are left with only contributions from terms involving $g_{\sigma,o}^e$ and $g_{\gamma,o}^m$. The factors $g_{\sigma,o}^e$ and $g_{\gamma,o}^m$ will be used in order to obtain F_σ and B_γ expressed in terms of currents multiplied by some prefactors. Depending on the order of the g's in the square brackets in (21a) and (21b), we give each term an index $a = 1, 2, 3$. Further, we also give terms arising from F_σ an index γ depending on whether they arise from Q_α or Q_β. We then have a total of 16 terms to evaluate: 12 terms $F_{\sigma,\gamma}^{(a)}$ and 6 terms $B_\gamma^{(a)}$, giving rise to $F_\sigma = \sum_{\gamma,a} F_{\sigma,\gamma}^{(a)}$ and $B_\gamma = \sum_a B_\gamma^{(a)}$. Each term should be expressed in terms of a combination of currents multiplied by some prefactor Γ. As outlined in Appendix B, we achieve this goal by, for each term, first performing one of the two momentum integrals. For each term, we are then left with an integral over $g_{\sigma,o}^e$ or $g_{\gamma,o}^m$ which can be related to a combination of currents by replacing additional momentum-dependent factors by some characteristic value determined by the rest of the integral. Along the way, we assume that the electron

energy scale is much larger than $k_B T$. The energy $k_B T$ is again assumed to be much larger than the typical magnon energies that contribute to the integrals, which we find to typically be a good approximation for our antiferromagnetic magnons living in two dimensions.

Inserting the resulting expressions for the interaction terms into Eqs. (18a), (18b), (15a), and (15b), we obtain

$$
\begin{aligned}
\tau_{M_0}^{-1} j_m = &\left[\Gamma_\beta^{(1)} + \Gamma_\alpha^{(1)} - \Gamma_\beta^{(2)} - \Gamma_\alpha^{(2)} \right] j_e \\
&+ \left[\Gamma_\beta^{(1)} - \Gamma_\alpha^{(1)} + \Gamma_\beta^{(2)} - \Gamma_\alpha^{(2)} \right] j_s \\
&- \left[\Gamma_\beta^{(3)} + \Gamma_\alpha^{(3)} \right] j_m - \left[\Gamma_\beta^{(3)} - \Gamma_\alpha^{(3)} \right] j_{sm},
\end{aligned} \tag{22}
$$

$$
\begin{aligned}
\tau_{M_0}^{-1} j_{sm} = &\left[\Gamma_\beta^{(1)} - \Gamma_\alpha^{(1)} - \Gamma_\beta^{(2)} + \Gamma_\alpha^{(2)} \right] j_e \\
&+ \left[\Gamma_\beta^{(1)} + \Gamma_\alpha^{(1)} + \Gamma_\beta^{(2)} + \Gamma_\alpha^{(2)} \right] j_s \\
&- \left[\Gamma_\beta^{(3)} - \Gamma_\alpha^{(3)} \right] j_m - \left[\Gamma_\beta^{(3)} + \Gamma_\alpha^{(3)} \right] j_{sm},
\end{aligned} \tag{23}
$$

$$
\begin{aligned}
E\, T_+ = &-\left[\tfrac{1}{2} Y_0 \tau_e^{-1} - \left[\Gamma_{\uparrow,\alpha}^{(1)} + \Gamma_{\downarrow,\alpha}^{(1)} - \Gamma_{\uparrow,\alpha}^{(2)} - \Gamma_{\downarrow,\alpha}^{(2)} - \Gamma_{\uparrow,\beta}^{(1)} - \Gamma_{\downarrow,\beta}^{(1)} + \Gamma_{\uparrow,\beta}^{(2)} + \Gamma_{\downarrow,\beta}^{(2)} \right] \right] j_e \\
&+ \left[\tfrac{1}{2} P_0 \tau_e^{-1} - \left[\Gamma_{\uparrow,\alpha}^{(1)} - \Gamma_{\downarrow,\alpha}^{(1)} + \Gamma_{\uparrow,\alpha}^{(2)} - \Gamma_{\downarrow,\alpha}^{(2)} + \Gamma_{\uparrow,\beta}^{(1)} - \Gamma_{\downarrow,\beta}^{(1)} + \Gamma_{\uparrow,\beta}^{(2)} - \Gamma_{\downarrow,\beta}^{(2)} \right] \right] j_s \\
&+ \left[\Gamma_{\uparrow,\beta}^{(3)} + \Gamma_{\downarrow,\alpha}^{(3)} - \Gamma_{\uparrow,\alpha}^{(3)} - \Gamma_{\downarrow,\beta}^{(3)} \right] j_m + \left[\Gamma_{\uparrow,\beta}^{(3)} - \Gamma_{\downarrow,\alpha}^{(3)} + \Gamma_{\uparrow,\alpha}^{(3)} - \Gamma_{\downarrow,\beta}^{(3)} \right] j_{sm},
\end{aligned} \tag{24}
$$

and

$$
\begin{aligned}
E\, T_- = &\left[\tfrac{1}{2} P_0 \tau_e^{-1} + \left[\Gamma_{\uparrow,\alpha}^{(1)} - \Gamma_{\downarrow,\alpha}^{(1)} - \Gamma_{\uparrow,\alpha}^{(2)} + \Gamma_{\downarrow,\alpha}^{(2)} - \Gamma_{\uparrow,\beta}^{(1)} + \Gamma_{\downarrow,\beta}^{(1)} + \Gamma_{\uparrow,\beta}^{(2)} - \Gamma_{\downarrow,\beta}^{(2)} \right] \right] j_e \\
&- \left[\tfrac{1}{2} Y_0 \tau_e^{-1} + \left[\Gamma_{\uparrow,\alpha}^{(1)} + \Gamma_{\downarrow,\alpha}^{(1)} + \Gamma_{\uparrow,\alpha}^{(2)} + \Gamma_{\downarrow,\alpha}^{(2)} + \Gamma_{\uparrow,\beta}^{(1)} + \Gamma_{\downarrow,\beta}^{(1)} + \Gamma_{\uparrow,\beta}^{(2)} + \Gamma_{\downarrow,\beta}^{(2)} \right] \right] j_s \\
&+ \left[\Gamma_{\uparrow,\beta}^{(3)} - \Gamma_{\downarrow,\alpha}^{(3)} - \Gamma_{\uparrow,\alpha}^{(3)} + \Gamma_{\downarrow,\beta}^{(3)} \right] j_m + \left[\Gamma_{\uparrow,\beta}^{(3)} + \Gamma_{\downarrow,\alpha}^{(3)} + \Gamma_{\uparrow,\alpha}^{(3)} + \Gamma_{\downarrow,\beta}^{(3)} \right] j_{sm}.
\end{aligned} \tag{25}
$$

The coefficients Γ are defined in Appendix C, and their indices relate them to one of the terms $F_{\sigma,\gamma}^{(a)}$ or $B_\gamma^{(a)}$. For a given set of parameters, these coefficients can be determined through numerical integration.

Solving Eq. (25) for E and inserting this into Eq. (24), we obtain

$$
j_s = A_{e \to s}\, j_e + A_{m \to s}\, j_m + A_{sm \to s}\, j_{sm}, \tag{26}
$$

where $A_{e \to s}$, $A_{m \to s}$, and $A_{sm \to s}$ are defined in Appendix D. Inserting the expression in Eq. (26) into Eq. (22), we further obtain

$$
j_m = C_{e \to m}\, j_e + C_{sm \to m}\, j_{sm}, \tag{27}
$$

where the expressions for the coefficients are once again provided in Appendix D.

Finally, combining Eqs. (27) and (26) with Eq. (23), we can obtain an expression for j_{sm} in terms of j_e. We can then use this expression to also obtain expressions for j_m and j_s in terms of j_e.

IV. RESULTS

The final result of our calculation is

$$
\begin{pmatrix} j_s \\ j_m \\ j_{sm} \end{pmatrix} = \begin{pmatrix} P_s \\ P_m \\ P_{sm} \end{pmatrix} j_e. \tag{28}
$$

Here, the magnon spin-current drag coefficient is

$$
\begin{aligned}
P_{sm} = &A_{e \to sm} + C_{e \to m} A_{m \to sm} \\
&+ (A_{e \to s} + C_{e \to m} A_{m \to s}) A_{s \to sm},
\end{aligned} \tag{29}
$$

where

$$
A_{e \to sm} = \left[\Gamma_\beta^{(1)} - \Gamma_\alpha^{(1)} - \Gamma_\beta^{(2)} + \Gamma_\alpha^{(2)} \right]/X_{sm}, \tag{30a}
$$

$$
A_{s \to sm} = \left[\Gamma_\beta^{(1)} + \Gamma_\alpha^{(1)} + \Gamma_\beta^{(2)} + \Gamma_\alpha^{(2)} \right]/X_{sm}, \tag{30b}
$$

$$
A_{m \to sm} = -\left[\Gamma_\beta^{(3)} - \Gamma_\alpha^{(3)} \right]/X_{sm}, \tag{30c}
$$

and

$$
\begin{aligned}
X_{sm} = &\tau_{M_0}^{-1} + \left[\Gamma_\beta^{(3)} + \Gamma_\alpha^{(3)} \right] + C_{sm \to m}\left[\Gamma_\beta^{(3)} - \Gamma_\alpha^{(3)} \right] \\
&- (A_{sm \to s} + C_{sm \to m} A_{m \to s})\left[\Gamma_\beta^{(1)} + \Gamma_\alpha^{(1)} + \Gamma_\beta^{(2)} + \Gamma_\alpha^{(2)} \right].
\end{aligned} \tag{31}
$$

The indices of the coefficients have been chosen to highlight the origin of the different contributions. The role played by the coefficients in Eqs. (26) and (27), can, e.g., provide some information about the the origin of the different terms in the numerator of P_{sm}. If $A_{e \to sm}$ is nonzero, there can, e.g., be a nonzero j_{sm} even if $C_{e \to m}$ and $A_{e \to s}$ vanish, meaning that a nonzero numerator of $A_{e \to sm}$ represents contributions to j_{sm} that can be interpreted as arising directly from j_e. The other terms in the numerator of P_{sm} can be interpreted as arising indirectly from j_e via j_m or j_s. Similarly, some understanding of the terms in the denominator of P_{sm} can be obtained. For vanishing $C_{sm \to m}$, $A_{sm \to s}$, and $\tau_{M_0}^{-1}$, there is still a remaining term $[\Gamma_\beta^{(3)} + \Gamma_\alpha^{(3)}]$ in X_{sm}, associated with direct conversion of magnon spin current into electron current.

Further, the magnon current drag coefficient can be expressed as

$$P_m = C_{e \to m} + P_{sm} C_{sm \to m}, \tag{32}$$

and the ratio between the electron spin current and the normal electron current is

$$P_s = A_{e \to s} + P_m A_{m \to s} + P_{sm} A_{sm \to s}. \tag{33}$$

The two latter expressions for P_m and P_s have some room for simplification, but their current form is convenient for understanding the numerical results.

Setting $\Omega_B = \Omega$ and $\Omega_A = 1$, results for P_{sm} and P_m as a function of Ω are presented in Fig. 2. We have here neglected any spin splitting of magnons and electrons and taken $\tau_\uparrow = \tau_\downarrow$. For $\Omega = 1$, we see that there is a finite induced magnon current, but no magnon spin current. In order to obtain a magnon spin current, we need to introduce an asymmetry between the coupling between the electrons and the two magnon modes. This can be achieved by taking $\Omega < 1$, producing a nonzero magnon spin current. From the figure, we see that P_m simply increases as we reduce Ω. The behavior of P_{sm} is a bit more peculiar. For sufficiently large $\tau_{M_0}^{-1}$, reducing Ω generally leads to an increase in $|P_{sm}|$ (or at least not a strong reduction), but for smaller $\tau_{M_0}^{-1}$ we see that $|P_{sm}|$ has a clear peak at some $\Omega > 0$. Taking $\Omega = 0$, maximizing the typical strength of the electron-magnon coupling, does, in other words, not necessarily maximize the induced magnon spin-current. We also note that P_s is found to be small in all cases.

These results can be understood by inspecting the expressions for the drag coefficients. Starting with P_{sm}, the behavior is mainly dominated by $A_{e \to sm}$, where the dominant parts of the denominator of $A_{e \to sm}$ are the terms related to magnon relaxation and direct conversion of magnon spin current into electron current. We can then inspect the resulting simplified expression

$$P_{sm} \sim \frac{\left[\Gamma_\beta^{(1)} - \Gamma_\alpha^{(1)} - \Gamma_\beta^{(2)} + \Gamma_\alpha^{(2)}\right]}{\tau_{M_0}^{-1} + \left[\Gamma_\beta^{(3)} + \Gamma_\alpha^{(3)}\right]}. \tag{34}$$

Here, asymmetry between $\Gamma_\gamma^{(1)}$ and $\Gamma_\gamma^{(2)}$ is related to asymmetry between different scattering processes involving a specific magnon mode, arising from an imbalance of electrons moving in opposite directions. Moreover, an asymmetry between $\Gamma_\alpha^{(a)}$ and $\Gamma_\beta^{(a)}$ has to arise from an asymmetry between scattering processes involving α and β magnons. As we see from the
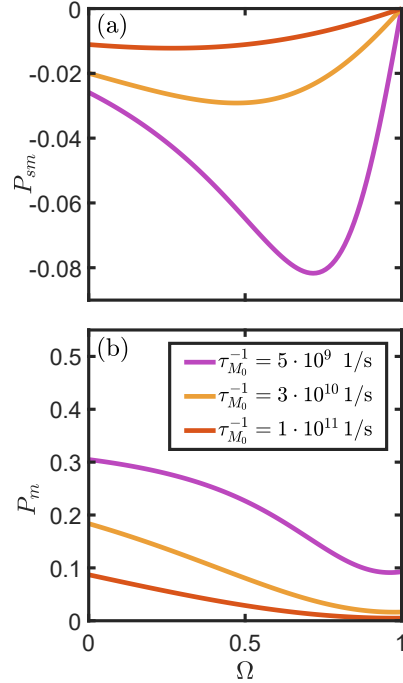

FIG. 2. The ratio of magnon spin current (a) and magnon current (b) to electron current as a function of the asymmetry in the coupling between the normal metal and the two sublattices of the antiferromagnet. Here, $\Omega = 1$ corresponds to a compensated interface, and $\Omega = 0$ corresponds to an uncompensated interface. Three different curves are displayed for different values of the inverse magnon relaxation time at zero momentum $\tau_{M_0}^{-1}$. The rest of the parameters are set to $t = 1.6$ eV, $k_F a = 0.6$, $S = 3/2$, $J_1 = 6$ meV, $J_2 = 0$, $K/J_1 = 1.0 \times 10^{-3}$, $\bar{J} = 15$ meV, $T = 300$ K, $\tau_\uparrow = \tau_\downarrow = 1.0 \times 10^{-14}$ s, $d_3 = 5$, and $h_e = h_m = 0$.

simplified expression, asymmetries of both types are necessary in order to obtain a magnon spin current.

Starting from large $\tau_{M_0}^{-1}$, this term dominates the denominator, and the effect of Ω will enter through the numerator of P_{sm}. Here, $\Omega < 1$ will typically act to make $(|u_q| - \Omega|v_q|)^2$ (for α magnons) and $(|v_q| - \Omega|u_q|)^2$ (for β magnons) larger and more different from each other, increasing the difference between α and β contributions to the numerator of P_{sm}. We therefore see that $|P_{sm}|$ increases with reduced Ω. As α magnons, for $\Omega < 1$, couple more strongly to electrons due to $|u_q| > |v_q|$, the negative direction of the spin carried by the α magnons makes P_{sm} negative.

However, if we reduce $\tau_{M_0}^{-1}$ so that the bracket in the denominator of P_{sm} also starts playing a role, the picture becomes more complicated. In order to have $P_{sm} \neq 0$, we still need $\Omega \neq 1$. Starting from $\Omega = 0$ and increasing Ω, we again have that $\Gamma_\gamma^{(a)}$ becomes smaller. Importantly, this reduction mainly stems from suppression of dominant long-wavelength

contributions with small $q > 0$. For such contributions $|u_q|$ and $|v_q|$ are large. Since $|u_q|^2 - |v_q|^2 = 1$, we have that $(|u_q| - |v_q|) = 1/(|u_q| + |v_q|)$, meaning that the difference between $|u_q|$ and $|v_q|$ is smaller for long-wavelength magnons. This means that when we increase Ω, we most efficiently suppress the long-wavelength contributions as, e.g., $(|u_q| - \Omega|v_q|)^2$ is more efficiently suppressed with increasing Ω when $|u_q|$ and $|v_q|$ are very similar. The key point to understanding the behavior of $P_{sm}(\Omega)$ is then that long-wavelength contributions are even more important for the denominator than the numerator of P_{sm}. In contrast to the denominator, the numerator relies on $|u_q| \neq |v_q|$, not allowing the magnon coherence factors to have their normal boosting effect and making contributions from somewhat larger q values more important. A simple example is $\Omega = 0$. Then, the magnon coherence factors of $\Gamma_\alpha^{(a)} - \Gamma_\beta^{(a)}$ show up in the form $u_q^2 - v_q^2 = 1$, while the coherence factors of $\Gamma_\alpha^{(3)} + \Gamma_\beta^{(3)}$ show up in the form $u_q^2 + v_q^2$, favoring long-wavelength magnons. By taking $\Omega > 0$, we then strongly suppress the bracket in the denominator through its long-wavelength contributions, while the numerator of P_{sm} is less strongly affected. This makes it possible for $|P_{sm}|$ to increase until the denominator becomes dominated by $\tau_{M_0}^{-1}$, or the suppression of the numerator of P_{sm} due to $\Omega \to 1$ eventually becomes too strong.

A similar increase in $|P_{sm}|$, for sufficiently small $\tau_{M_0}^{-1}$, can also be obtained by reducing the importance of long-wavelength contributions to the Γ's in other ways. One option is to increase the easy-axis anisotropy, which both reduces the value of u_q and v_q for small q and increases the excitation energy of long-wavelength magnons. It is, however, worth noting that, within our approximation scheme, one should be careful with suppressing the importance of long-wavelength magnons too much. For this reason, one should also not put too much trust in, e.g., the results for P_m when $\Omega \to 1$, in contrast to the result $P_{sm}(\Omega = 1) = 0$ which follows from symmetry. Further, taking the magnon relaxation time to decay faster with increasing momentum has an opposite effect, pushing contribution weights toward smaller momenta. If $\tau_{M_0}^{-1}$ is sufficiently small, we can compensate this effect by, e.g., taking a larger easy-axis anisotropy. However, if $\tau_{M_0}^{-1}$ is too large and/or $v(q)$ decays too quickly with momentum, there can be a reduction in the achievable values of P_{sm}. Increasing, e.g., both d_3 and K by an order of magnitude, the magnitude of $P_{sm}(\Omega = 0)$ for $\tau_{M_0}^{-1} = 5 \times 10^9$ 1/s is reduced by around 30%.

Similarly to P_{sm}, the behavior of P_m in Fig. 2 can also be understood from a simplified expression

$$P_m \sim \frac{\left[\Gamma_\beta^{(1)} + \Gamma_\alpha^{(1)} - \Gamma_\beta^{(2)} - \Gamma_\alpha^{(2)}\right]}{\tau_{M_0}^{-1} + \left[\Gamma_\beta^{(3)} + \Gamma_\alpha^{(3)}\right]}. \quad (35)$$

We see that the contributions from α and β magnons add, in contrast to the case of Eq. (34), where they were subtracted. In this case, also for small $\tau_{M_0}^{-1}$, there is typically no benefit of increasing Ω as also the combination of magnon coherence factors in, e.g., $\Gamma_\alpha^{(1)} + \Gamma_\beta^{(1)}$ in the numerator still favors long-wavelength magnons. Increasing Ω then simply leads to a rapid suppression of the numerator.

Finally, we also comment on the smallness of P_s in the simple case of no spin splitting of the electrons. The easiest
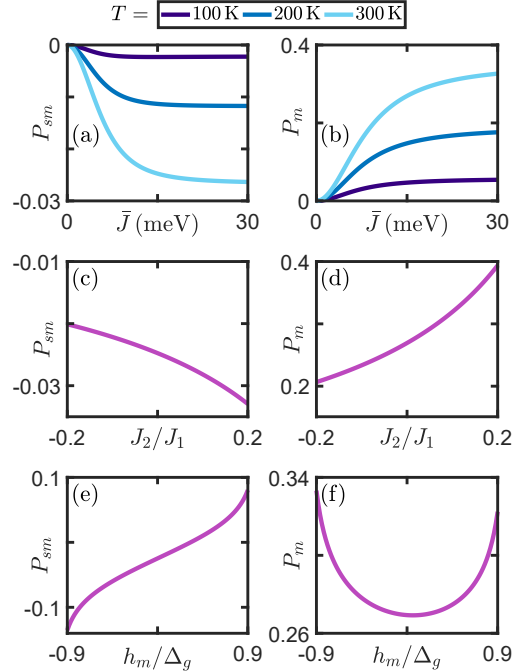

FIG. 3. The ratio of magnon spin current to electron current, P_{sm}, and the ratio of magnon current to electron current, P_m, are here presented. In (a) and (b) we vary the interfacial coupling between the materials, $\bar{J}$, as well as the temperature, T. In (c) and (d) we vary the next-nearest-neighbor interaction in the antiferromagnet, J_2, where $J_2 > 0$ corresponds to a frustration. In (e) and (f) we vary the splitting of the magnon modes h_m. Unless otherwise specified in the panels, we have set $h_m = J_2 = 0$, $\bar{J} = 15$ meV, and $T = 300$ K. We have also taken $\Omega = 0$ and $\tau_{M_0}^{-1} = 1 \times 10^{10}$ 1/s, while the rest of the parameters are set to their values in Fig. 2.

case to analyze is if we simply take τ_e^{-1} to be very large. In that case, the denominator of $A_{e \to s}$, $A_{m \to s}$, and $A_{sm \to s}$ contains a term τ_e^{-1} that is not matched in the numerators. As there, in this case, is assumed to be no intrinsic spin-current source in the normal metal, an electron spin current will have to arise from interaction with magnons. However, if the electron relaxation time is too short, the effect of interaction with magnons is washed away and the resulting electron spin current becomes small.

We next consider, for $\Omega = 0$, how the induced magnon spin current and magnon current depend on some other important parameters of the system. In Figs. 3(a) and 3(b), we show, for three different temperatures, how P_{sm} and P_m vary with the strength of the interfacial exchange coupling $\bar{J}$. For $\bar{J} = 0$, there is, of course, no induced magnon currents. As all coefficients $\Gamma \sim \bar{J}^2$, increasing $\bar{J}$ makes $\tau_{M_0}^{-1}$ less important until $|P_{sm}|$ and P_m reach their saturation values equivalent to $\tau_{M_0}^{-1} = 0$. The shape of the curves resemble a function $a_1/(1/x^2 + a_2)$, as expected from the simplified expressions

for P_{sm} and P_m. Further, increasing the temperature leads to more spin fluctuations, which enter the expressions through the Bose-Einstein distribution factors in $\Gamma_\gamma^{(1/2)}$. This increases the magnitude of the numerators of P_{sm} and P_m, leading to the results in Figs. 3(a) and 3(b). How much the magnon currents actually can be enlarged by increasing the temperature will necessarily be limited by how large temperature the order in the antiferromagnetic material can survive. In order to obtain larger drags at a given temperature, one can, e.g., reduce the energy scale of the antiferromagnet by reducing J_1, making it easier to excite magnons. Oppositely, increasing J_1 will make it harder to excite magnons and increase the stability of the magnetic ordering. Setting, e.g., $J_1 = 10$ meV in Fig. 2 leads to $P_{sm}(\Omega = 0) = 0.009$ and $P_m(\Omega = 0) = 0.15$ for the purple curves corresponding to $\tau_{M_0}^{-1} = 5 \times 10^9$ 1/s.

The behavior of P_{sm} and P_m as a function of next-nearest-neighbor interaction in the antiferromagnet is shown in Figs. 3(c) and 3(d). Positive J_2/J_1 here corresponds to an antiferromagnetic coupling between next-nearest neighbors, acting as a frustration. Similarly to increasing the temperature, frustrating the system leads to more spin fluctuations producing larger induced magnon currents. Notably, frustration, in contrast to a temperature increase, influences the magnon energies. Frustration therefore also affects the magnon coherence factors, with the particular effect of making them decay more slowly with increasing momentum without affecting their values at zero momentum [30,31]. The latter effect actually favors the denominator of P_{sm}, but the effect of increased number of magnons dominates and makes P_{sm} increase with increasing J_2.

Finally, in Figs. 3(e) and 3(f), we display how splitting of the magnon modes influences the drag coefficients. Taking $h_m < 0$ lowers the excitation energies of α magnons, increasing the asymmetry favoring contributions to P_{sm} associated with α magnons. This leads to an enhancement of the induced magnon spin current, which is quite significant because the splitting of the magnon modes allows for long-wavelength magnons to better contribute to P_{sm}. Taking $h_m > 0$ works in the opposite direction of the asymmetry between α and β magnons introduced by $\Omega = 0$. Moreover, while P_m is also influenced by h_m, the effect is much weaker as P_m does not rely on an asymmetry between contributions associated with α and β magnons. Taking, e.g., $h_m < 0$, the effect is that the α contributions become larger while the β contributions are suppressed. The growth of the α contributions slightly outweighs the decrease in the β contributions, leading to a weak enhancement of P_m. We also note that, if the results are extended to $|h_m|$ even closer to Δ_g, the magnitudes of the drag coefficients continue to grow larger, but they are not found to diverge.

In order to attempt to describe the induced magnon currents in a real system featuring a sufficiently thick NM layer, neglecting spin splitting of the electrons arising from $\Omega \neq 1$ (and/or an external field applied to the antiferromagnet) and taking $\tau_\uparrow = \tau_\downarrow$ might be a reasonable approximation. At least for a thinner NM layer, these effects could, however, play a larger role. We therefore investigate how the drag coefficients depend on h_e and $\tau_\uparrow \neq \tau_\downarrow$. The relationship between these parameters is not evident, especially when the electron density of states has weak or no energy dependence, and
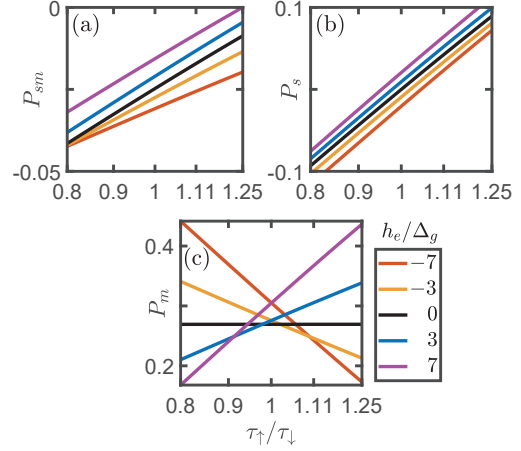

FIG. 4. The ratio of magnon spin current (a), electron spin current (b), and magnon current (c) to electron current as a function of $\tau_\uparrow/\tau_\downarrow$ for different values of h_e, where τ_σ is the spin-conserving relaxation time for electrons with spin σ and h_e represents a spin splitting of the electron energies. The x axis is here logarithmic in order to highlight symmetries between $\tau_\uparrow < \tau_\downarrow$ and $\tau_\uparrow > \tau_\downarrow$. For the parameters, we have set $\Omega = 0$, $\tau_\downarrow = 1.0 \times 10^{-14}$ s, $\tau_{M_0}^{-1} = 1 \times 10^{10}$ 1/s, while the rest of the parameters are equal to their values in Fig. 2.

the relationship should be expected to vary strongly with the details of the system. We therefore simply treat h_e and τ_σ as independent parameters and display how their separate and combined effects can influence the results.

In Fig. 4, we present P_{sm}, P_s, and P_m as a function of $\tau_\uparrow/\tau_\downarrow$ for different values of h_e. As we now introduce an asymmetry between spin-↑ and spin-↓ electrons, we have that, e.g., $A_{e \rightarrow s}$ starts to grow as T_-/T_+ and P_0 can become nonzero. We are then, of course, generating a spin current, as displayed in Fig. 4(b). For, e.g., $\tau_\uparrow < \tau_\downarrow$, the spin current becomes negative, which is quite natural. Moving on to the magnon spin current, the last term in the numerator of P_{sm} of the form $(A_{e \rightarrow s} + C_{e \rightarrow m} A_{m \rightarrow s}) A_{s \rightarrow sm}$ now starts becoming more active. This term can be viewed as converting electron spin current into magnon spin current. The general trend is therefore that the changes to P_{sm} in Fig. 4(a) follow the variations in P_s. We also see that a spin-splitting field h_e presumably will need to be somewhat larger than Δ_g in order to have a real effect on the induced magnon spin current, meaning that the effect on the electrons of applying an external field to split the magnons modes might not be that important for the resulting induced magnon spin current, even for a thin NM layer. Discussing next the results for P_m in Fig. 4(c), we see that P_m can be substantially affected by the combination of splitting of the electron energies and asymmetry in τ_σ. Taking $\tau_\uparrow \neq \tau_\downarrow$ alone is enough to create a spin current through $A_{e \rightarrow s}$, but in order for this spin current to influence the induced magnon current, we also need a sufficiently large $A_{s \rightarrow m} \sim [\Gamma_\beta^{(1)} - \Gamma_\alpha^{(1)} + \Gamma_\beta^{(2)} - \Gamma_\alpha^{(2)}]$. While the electron spin

current is naturally able to influence the magnon spin current, we find that, e.g., the related asymmetry between ↑ and ↓ electrons introduced through h_e is needed in order to enhance $A_{s \to m}$, allowing the electron spin-current to influence the spin-unpolarized magnon current.

V. DISCUSSION

As mentioned in the beginning of Sec. II, an experimental realization of our system would typically involve thin films of finite thickness. In particular, an experimentally realized uncompensated interface naturally relies on an AFMI with more than one layer. For a given material, the AFMI should be sufficiently thick to, in a real system, stabilize magnetic ordering in the presence of intrinsic quantum and thermal fluctuations, as well as interfacial interaction with the electrons from the metal. While a larger thickness can provide a necessary increase in stability, as well as simply more spins that can fluctuate, the added stability might also make it harder for the electrons of the normal metal to induce magnon currents. The density of the magnon currents should also be expected to decrease as only the surface layer couples directly to the electrons in the normal metal. The present study simply demonstrates that driving an in-plane electron current in an adjacent metal is a potential mechanism for creating a spin current in an AFMI and highlights that increasing the temperature and splitting the magnon modes are possible ways of increasing the magnon spin current in an ordered AFMI. In order to obtain reliable estimates for the magnitude of the induced magnon currents in a real system, one would need to take into account the effect of the thickness of the AFMI. Taking properly into account finite thickness of the normal metal layer could potentially also influence the results.

Moreover, the model we have used to study the system is, also in other ways, relatively simple, motivated by a goal of exploring some of the key physics that can arise in this system. We have therefore been able to rely on, quite involved, analytical calculations in order to interpret the origin of the results obtainable within the boundaries set by our approximation scheme. A natural extension of this work would be investigations more tailored toward specific material choices. The magnitude of the induced magnon spin current, intimately related to, e.g., the competition between effects pushing contribution weights towards smaller or larger momenta, should be expected to depend considerably on the details of the system.

For a larger and more anisotropic Fermi surface, umklapp processes, not considered in this study, could also become of importance. For such scattering processes, $\Omega = 1$ actually maximizes the electron-magnon coupling [32,46]. However, an induced magnon spin current relies on an asymmetry between α and β magnons. Hence, in the absence of splitting of the magnon modes, having a compensated interface and relying on umklapp processes to generate a magnon spin-current does not seem like a viable option.

As the induced magnon spin current is found to be enhanced through splitting of the magnon modes, antiferromagnets with intrinsically nondegenerate magnon modes present an interesting possibility. Nondegenerate magnon modes that are still able to carry a spin current may be realized

in biaxial antiferromagnets, featuring both a hard axis and an additional in-plane easy axis, such as NiO [21,52]. As long as long-wavelength magnons are dominant, it might not be problematic if the splitting of the magnon modes is only significant near the Brillouin zone center. Moreover, as we find that intermediate values of Ω could be more favorable than $\Omega = 0$, it could be worth considering other options than a fully uncompensated interface. One option could be a compensated interface where the two sublattices are made up of different atoms, potentially introducing an intermediate-strength asymmetry in the coupling between the normal metal and the two sublattices of the AFMI.

VI. SUMMARY

Applying semiclassical Boltzmann theory, we have investigated the possibility of inducing magnon currents in an antiferromagnetic insulator layer through proximity coupling to a normal metal layer where a charge current is driven parallel to the interface. We find that an asymmetry in the coupling between the electrons and the two sublattices of the antiferromagnet can allow for a magnon spin current to be generated. The magnitude of the induced magnon spin current depends intimately on the relative importance of long-wavelength magnons, leading to the somewhat surprising result that a more weakly asymmetric antiferromagnetic interface can be a better choice than a fully uncompensated interface. We also find that the induced magnon currents increase with temperature, and that magnon mode splitting can be beneficial for the magnon spin current. Future work could include more application-oriented studies, as well as experimentally investigation of our proposed mechanism for generating a magnon spin current in an antiferromagnetic insulator.

APPENDIX A: STARTING MODEL

Following Ref. [32] we start out from a Hamiltonian describing an antiferromagnet

$$H_{\text{AFMI}} = J_1 \sum_{\langle i,j \rangle} \boldsymbol{S}_i \cdot \boldsymbol{S}_j + J_2 \sum_{\langle\langle i,j \rangle\rangle} \boldsymbol{S}_i \cdot \boldsymbol{S}_j$$
$$- K \sum_i S_{iz}^2 - h_m \sum_i S_{i,z}, \quad \text{(A1)}$$

where we have added an additional term splitting the magnon modes. Our modeling is not sensitive to whether the spin-space z direction is taken to align with the real-space z direction or not. Performing a Holstein-Primakoff transformation, this Hamiltonian can be diagonalized and put in the form

of Eq. (2) with [32]

$$\omega_q = \sqrt{C_q^2 - D_q^2}, \tag{A2}$$

where

$$C_q = 2z_1 J_1 S - 2z_2 J_2 S(1 - \tilde{\gamma}_q) + 2KS, \tag{A3}$$

$$D_q = 2z_1 J_1 S \gamma_q. \tag{A4}$$

Here,

$$\gamma_k = \frac{2}{z_1}[\cos(k_x a) + \cos(k_y a)], \tag{A5}$$

$$\tilde{\gamma}_k = \frac{2}{z_2}[\cos(k_x a + k_y a) + \cos(k_x a - k_y a)], \tag{A6}$$

where z_1 is the number of nearest neighbors, and z_2 is the number of next-nearest neighbors.

For the coupling between the electrons and magnons, we start out from

$$H_{\text{int}} = -2\bar{J} \sum_{\Upsilon} \sum_{i \in \Upsilon} \Omega_{\Upsilon} \, c_i^\dagger \boldsymbol{\sigma} c_i \cdot \boldsymbol{S}_i, \tag{A7}$$

where the sum over $\Upsilon \in \{A, B\}$ is a sum over the two sublattices of the AFMI, and $\boldsymbol{\sigma}$ is a vector of Pauli matrices. We then, again, perform a Holstein-Primakoff transformation, as well as Fourier transformations. Neglecting umklapp scattering processes and moving electron spin-splitting terms to the NM Hamiltonian, we arrive at the expression in Eq. (4) [32]. Here, the magnon coherence factors, relating the AFMI eigenexcitations to the original sublattice spin-flip magnons introduced in the Holstein-Primakoff transformation, take the form

$$u_q = \frac{1}{\sqrt{2}} \sqrt{\frac{C_q}{\omega_q} + 1}, \tag{A8}$$

$$v_q = \frac{-1}{\sqrt{2}} \sqrt{\frac{C_q}{\omega_q} - 1}. \tag{A9}$$

Finally, for the electrons, we start out from

$$H_{\text{NM}} = -t \sum_{\langle i,j \rangle \sigma} c_{i\sigma}^\dagger c_{j\sigma} - \mu \sum_{i\sigma} c_{i\sigma}^\dagger c_{i\sigma} - h'_e \sum_{i\sigma} \sigma c_{i\sigma}^\dagger c_{i\sigma}, \tag{A10}$$

where h'_e is a spin-splitting arising from an externally applied field. Diagonalizing the Hamiltonian and including the potential additional spin splitting of the electrons arising from the antiferromagnetic interface, we end up with the Hamiltonian in Eq. (1). Here,

$$\epsilon_{k\sigma} = -t z_1 \gamma_k - \mu - \sigma h_e. \tag{A11}$$

The additional spin splitting of the electrons arising from the interaction term has a strength $\bar{J}S(\Omega_B - \Omega_A)$. However, if we consider a NM of finite thickness, delivering a similar surface current affecting the antiferromagnet, the effective spin-splitting of the electrons due to proximity to the AFMI will be reduced. We therefore treat the spin splitting of the electrons as an adjustable parameter.

Finally, the last step is to consider the long-wavelength limit in order to obtain isotropic expressions for ω_q, $\epsilon_{k\sigma}$, u_q,

and v_q. For $\omega_q = \sqrt{\Delta_g^2 + \kappa^2(qa)^2}$, we have defined $\Delta_g = 2S\sqrt{K(K + 8J_1)}$, and $\kappa = 4S\sqrt{2J_1^2 - J_2(K + 4J_1)}$. Further, the magnon coherence factors now take the form

$$u_q = \frac{1}{\sqrt{2}} \sqrt{\frac{8J_1 S - 4J_2 S(qa)^2 + 2KS}{\omega_q} + 1}, \tag{A12}$$

$$v_q = -\frac{1}{\sqrt{2}} \sqrt{\frac{8J_1 S - 4J_2 S(qa)^2 + 2KS}{\omega_q} - 1}. \tag{A13}$$

As we are working in the long-wavelength limit, under the assumption that large-momentum processes are negligible, it will not be of importance that the magnons live in a reduced Brillouin zone compared to the electrons. Momentum integrals for both magnons and electrons will be performed over circular Brillouin zones of radius π/a, where we make sure that contributions from large momenta have little or no influence on the results. In particular, by taking a sufficiently small Fermi surface, we make sure that all integrands containing magnon coherence factors vanish before the isotropic expression for v_q turns imaginary.

APPENDIX B: EVALUATING THE INTERACTION TERMS

As discussed above, in order to evaluate the interaction terms, we start out from Eqs. (20a), (20b), (20c) and divide these expressions up into terms involving a single factor $g_{\sigma,o}^e$ or $g_{\gamma,o}^m$. For terms involving $g_{\sigma,o}^e(\boldsymbol{k} + \boldsymbol{q})$ or $g_{\sigma,o}^m(\boldsymbol{k} + \boldsymbol{q})$, we send $\boldsymbol{k} \to \boldsymbol{k} - \boldsymbol{q}$. We then proceed to do the angular part of the integral over the momentum that the involved factor g does not depend on. If g depends on $\boldsymbol{q}$, we can next do the radial integral over $\boldsymbol{k}$ and use the remaining integral over $\boldsymbol{q}$ to form a combination of magnon currents after having replaced some additional $\boldsymbol{q}$-dependent factors by characteristic values. If g depends on $\boldsymbol{k}$, we use the assumption that the important magnon energies are significantly smaller $k_B T$ in order to decouple the two integrals. Replacing some additional $\boldsymbol{k}$-dependent factors by characteristic values, we are then left with a combination of electron currents with a prefactor that depends on a radial integral over q.

In this Appendix we outline the evaluation of two specific terms. The rest of the terms can be evaluated in a similar manner. We start with $B_\alpha^{(2)}$, which can be written out as

$$\begin{aligned}
B_\alpha^{(2)} = -\beta &\frac{V^2 a^2}{\hbar(2\pi)^3} \int d\boldsymbol{k} \, f^0(\epsilon_{k,\uparrow}) g_{\uparrow,o}^e(\boldsymbol{k}) \\
&\times \int d\boldsymbol{q} \, v_{q_x}^m v(q)(\Omega_A u_q + \Omega_B v_q)^2[1 - f^0(\epsilon_{k+q,\downarrow})] \\
&\times b^0(\omega_{q,\alpha})\delta[\epsilon_{k,\uparrow} + \omega_{q,\alpha} - \epsilon_{k+q,\downarrow}].
\end{aligned} \tag{B1}$$

We next proceed to perform the angular part of the integral over $\boldsymbol{q}$. For a given $\boldsymbol{k}$, we then introduce a new coordinate system for $\boldsymbol{q}$ where θ' is the angle between $\boldsymbol{q}$ and the x axis of the new coordinate system which is taken to be aligned with $\boldsymbol{k}$. The angle between $\boldsymbol{k}$ and the x axis of the original coordinate system is denoted by θ. We can then express $B_\alpha^{(2)}$

in the following form:

$$
\begin{aligned}
B_\alpha^{(2)} = -\beta \frac{V^2 a^2}{\hbar(2\pi)^3} \int d\mathbf{k}\, f^0(\epsilon_{\mathbf{k},\uparrow}) g_{\uparrow,o}^e(\mathbf{k}) \int dq\, q\, v_q^m v(q) \\
\times (\Omega_A u_q + \Omega_B v_q)^2 [1 - f^0(\epsilon_{\mathbf{k},\uparrow} + \omega_{q,\alpha})] b^0(\omega_{q,\alpha}) \\
\times \int_0^{2\pi} d\theta' \left[\cos(\theta')\cos(\theta) - \sin(\theta')\sin(\theta) \right] \\
\times \delta[\omega_{q,\alpha} - 2h_e - 2t(qa)(ka)\cos(\theta') - t(qa)^2],
\end{aligned}
\tag{B2}
$$

where the square bracket of cosine factors arises because we need the component of the magnon velocity in the x direction of the original coordinate system. Performing the angular integral, we obtain

$$
\begin{aligned}
B_\alpha^{(2)} = -\beta \frac{V^2}{2t\hbar(2\pi)^3} \int d\mathbf{k}\, \frac{\cos(\theta)}{k}\, f^0(\epsilon_{\mathbf{k},\uparrow}) g_{\uparrow,o}^e(\mathbf{k}) \\
\times \int dq\, v_q^m (\Omega_A u_q + \Omega_B v_q)^2 [1 - f^0(\epsilon_{\mathbf{k},\uparrow} + \omega_{q,\alpha})] \\
\times b^0(\omega_{q,\alpha}) \frac{2\,v(q)\Lambda_{q,\alpha,2}(k)}{\sqrt{1 - \Lambda_{q,\alpha,2}^2(k)}} \Theta(1 - |\Lambda_{q,\alpha,2}(k)|). \quad (B3)
\end{aligned}
$$

Using the assumption that the important magnon energies are significantly smaller than $k_B T$, we next approximate $f^0(\epsilon_{\mathbf{k},\uparrow} + \omega_{q,\alpha}) \approx f^0(\epsilon_{\mathbf{k},\uparrow})$. We also use that $v_k^e = 2tka^2/\hbar$, as well as $\beta[1 - f^0(\epsilon)]f^0(\epsilon) = -\partial f^0(\epsilon)/\partial\epsilon$. Finally, approximating loose factors of k by k_F, motivated by the combination of Fermi distributions, we end up with

$$
\begin{aligned}
B_\alpha^{(2)} = \frac{-V^2}{8\pi t^2 (k_F a)^2} \int dq\, (\Omega_A u_q + \Omega_B v_q)^2 \\
\times b^0(\omega_{q,\alpha})\, v_q^m \frac{2\,v(q)\Lambda_{q,\alpha,2}}{\sqrt{1 - \Lambda_{q,\alpha,2}^2}} \Theta(1 - |\Lambda_{q,\alpha,2}|) \\
\times \frac{1}{(2\pi)^2} \int d\mathbf{k}\, v_{k_x}^e \left[-\frac{\partial f^0(\epsilon_{\mathbf{k},\uparrow})}{\partial \epsilon_{\mathbf{k},\uparrow}} \right] g_{\uparrow,o}^e(\mathbf{k}), \quad (B4)
\end{aligned}
$$

where now

$$
\Lambda_{q,\alpha,2} = \frac{1}{2t(qa)(k_F a)}[\omega_{q,\alpha} - 2h_e - t(qa)^2]. \tag{B5}
$$

Writing the integral over $\mathbf{k}$ as a combination of electron currents and inserting $v_q^m = \kappa^2 qa^2/(\omega_q \hbar)$, we then obtain

$$
B_\alpha^{(2)} = -\Gamma_\alpha^{(2)}[j_e + j_s], \tag{B6}
$$

where we have defined

$$
\begin{aligned}
\Gamma_\alpha^{(2)} = \frac{1}{\hbar} \frac{(k_F a)^2 V^2}{8\pi E_F^2} \int d(qa)\,(\Omega_A u_q + \Omega_B v_q)^2 \\
\times b^0(\omega_{q,\alpha}) \frac{\kappa^2(qa)}{\omega_q} \frac{v(q)\Lambda_{q,\alpha,2}\,\Theta(1 - |\Lambda_{q,\alpha,2}|)}{\sqrt{1 - \Lambda_{q,\alpha,2}^2}}. \quad (B7)
\end{aligned}
$$

The integral included in $\Gamma_\alpha^{(2)}$ is somewhat complicated, but can, for a given set of parameters, be calculated numerically.

We next evaluate $B_\alpha^{(3)}$, which is of the form

$$
\begin{aligned}
B_\alpha^{(3)} = -\beta \frac{V^2 a^2}{\hbar(2\pi)^3} \int d\mathbf{q}\, v_{q_x}^m b^0(\omega_{q,\alpha}) g_{\alpha,o}^m(\mathbf{q}) \\
\times v(q)(\Omega_A u_q + \Omega_B v_q)^2 \int d\mathbf{k}\, [1 - f^0(\epsilon_{\mathbf{k}+\mathbf{q},\downarrow})] \\
\times f^0(\epsilon_{\mathbf{k},\uparrow})\, \delta[\epsilon_{\mathbf{k},\uparrow} + \omega_{q,\alpha} - \epsilon_{\mathbf{k}+\mathbf{q},\downarrow}]. \quad (B8)
\end{aligned}
$$

Following similar steps to those above, we proceed to, this time, perform the angular part of the integral over $\mathbf{k}$,

$$
\begin{aligned}
B_\alpha^{(3)} = -\beta \frac{V^2 a^2}{\hbar(2\pi)^3} \int d\mathbf{q}\, v_{q_x}^m g_{\alpha,o}^m(\mathbf{q}) \\
\times v(q)(\Omega_A u_q + \Omega_B v_q)^2 b^0(\omega_{q,\alpha}) \int dk\, k \\
\times f^0(\epsilon_{\mathbf{k},\uparrow})[1 - f^0(\epsilon_{\mathbf{k},\uparrow} + \omega_{q,\alpha})] \int_0^{2\pi} d\theta' \\
\times \delta[\omega_{q,\alpha} - 2h_e - 2t(qa)(ka)\cos(\theta') - t(qa)^2], \quad (B9)
\end{aligned}
$$

where we have introduced a rotated coordinate system for $\mathbf{k}$ where the new x axis is aligned with $\mathbf{q}$, and θ' is the angle between $\mathbf{k}$ and $\mathbf{q}$. The result after the angular integration becomes

$$
\begin{aligned}
B_\alpha^{(3)} = -\beta \frac{V^2}{2t\hbar(2\pi)^3} \int d\mathbf{q}\, \frac{v_{q_x}^m}{q} b^0(\omega_{q,\alpha}) g_{\alpha,o}^m(\mathbf{q}) \\
\times (\Omega_A u_q + \Omega_B v_q)^2 \frac{2\,v(q)\Theta(1 - |\Lambda_{q,\alpha,3}|)}{\sqrt{1 - \Lambda_{q,\alpha,3}^2}} \\
\times \int dk\, [1 - f^0(\epsilon_{\mathbf{k},\uparrow} + \omega_{q,\alpha})] f^0(\epsilon_{\mathbf{k},\uparrow}), \quad (B10)
\end{aligned}
$$

with

$$
\Lambda_{q,\alpha,3} = \frac{1}{2t(qa)(k_F a)}[\omega_{q,\alpha} - 2h_e - t(qa)^2], \tag{B11}
$$

where we have taken $k \approx k_F$ in $\Lambda_{q,\alpha,3}$, once again motivated by the combination of Fermi distributions. We then transform the radial integral over k into an integral over electron energy, producing a factor $1/\sqrt{\epsilon_k + \mu}$ which we approximate by its value at the Fermi level. Further, using the assumption $E_F \gg k_B T, h_e$, we end up with

$$
\begin{aligned}
B_\alpha^{(3)} = -\beta \frac{V^2}{2t\hbar(2\pi)^3} \int d\mathbf{q}\, \frac{v_{q_x}^m}{q} b^0(\omega_{q,\alpha}) g_{\alpha,o}^m(\mathbf{q}) \\
\times (\Omega_A u_q + \Omega_B v_q)^2 \frac{2\,v(q)\Theta(1 - |\Lambda_{q,\alpha,3}|)}{\sqrt{1 - \Lambda_{q,\alpha,3}^2}} \\
\times \frac{1}{2a\sqrt{t}} \frac{1}{\sqrt{E_F}} \frac{e^{\beta\omega_{q,\alpha}}}{e^{\beta\omega_{q,\alpha}} - 1} \omega_{q,\alpha}. \quad (B12)
\end{aligned}
$$

This expression can further be put in the form

$$
B_\alpha^{(3)} = \frac{-V^2}{4at^{\frac{3}{2}}\hbar(2\pi)^3\sqrt{E_F}} \int d\boldsymbol{q}\, v_{q_x}^m \left[-\frac{\partial b^0(\omega_{q,\alpha})}{\partial \omega_{q,\alpha}} \right] g_{\alpha,o}^m(\boldsymbol{q})
$$
$$
\times (\Omega_A u_q + \Omega_B v_q)^2 \frac{\omega_{q,\alpha}}{q} \frac{2\, v(q)\Theta(1 - |\Lambda_{q,\alpha,3}|)}{\sqrt{1 - \Lambda_{q,\alpha,3}^2}}.
$$

(B13)

The integral can here be rewritten as a combination of magnon currents multiplied by the expectation value of the second line of additional momentum-dependent factors calculated using the first part of the integral as the distribution function. When the first part of the integral is a sufficiently peaked function with respect to momentum, and the second part varies slowly with momentum, this procedure approaches simply approximating the second part by its value at the momentum corresponding to the peak of the first part. Assuming that radial momentum dependence of $g_{\alpha,o}^m(\boldsymbol{q})$ only has a weak effect on the important momentum region for the integral, the result for $B_\alpha^{(3)}$ can be expressed as

$$
B_\alpha^{(3)} = -\Gamma_\alpha^{(3)}[j_m - j_{sm}],
$$

(B14)

where

$$
\Gamma_\alpha^{(3)} = \frac{1}{\hbar}\frac{(k_F a)^3 V^2}{8\pi E_F^2}\frac{1}{I_\alpha} \int d(qa)(qa)\frac{\kappa^2(qa)}{\omega_q}\left[-\frac{\partial b^0(\omega_{q,\alpha})}{\partial \omega_{q,\alpha}} \right]
$$
$$
\times (\Omega_A u_q + \Omega_B v_q)^2 \frac{\omega_{q,\alpha}}{qa} \frac{v(q)\Theta(1 - |\Lambda_{q,\alpha,3}|)}{\sqrt{1 - \Lambda_{q,\alpha,3}^2}},
$$

(B15)

and

$$
I_\alpha = \int d(qa)\,(qa)\frac{\kappa^2(qa)}{\omega_q}\left[-\frac{\partial b^0(\omega_{q,\alpha})}{\partial \omega_{q,\alpha}} \right].
$$

(B16)

Like $\Gamma_\alpha^{(2)}$, the expression for $\Gamma_\alpha^{(3)}$ can also be evaluated numerically.

APPENDIX C: FINAL EXPRESSIONS FOR INTERACTION TERMS

Performing the necessary calculations for all interaction terms, we end up with

$$
B_\alpha^{(1)} = \Gamma_\alpha^{(1)}[j_e - j_s],
$$
$$
B_\alpha^{(2)} = -\Gamma_\alpha^{(2)}[j_e + j_s],
$$
$$
B_\alpha^{(3)} = -\Gamma_\alpha^{(3)}[j_m - j_{sm}],
$$

(C1)

$$
B_\beta^{(1)} = \Gamma_\beta^{(1)}[j_e + j_s],
$$
$$
B_\beta^{(2)} = -\Gamma_\beta^{(2)}[j_e - j_s],
$$
$$
B_\beta^{(3)} = -\Gamma_\beta^{(3)}[j_m + j_{sm}],
$$

(C2)

$$
F_{\uparrow,\alpha}^{(1)} = \Gamma_{\uparrow,\alpha}^{(1)}[j_e - j_s],
$$
$$
F_{\uparrow,\alpha}^{(2)} = -\Gamma_{\uparrow,\alpha}^{(2)}[j_e + j_s],
$$
$$
F_{\uparrow,\alpha}^{(3)} = -\Gamma_{\uparrow,\alpha}^{(3)}[j_m - j_{sm}],
$$

(C3)

$$
F_{\uparrow,\beta}^{(1)} = -\Gamma_{\uparrow,\beta}^{(1)}[j_e + j_s],
$$
$$
F_{\uparrow,\beta}^{(2)} = \Gamma_{\uparrow,\beta}^{(2)}[j_e - j_s],
$$
$$
F_{\uparrow,\beta}^{(3)} = \Gamma_{\uparrow,\beta}^{(3)}[j_m + j_{sm}],
$$

(C4)

$$
F_{\downarrow,\alpha}^{(1)} = \Gamma_{\downarrow,\alpha}^{(1)}[j_e + j_s],
$$
$$
F_{\downarrow,\alpha}^{(2)} = -\Gamma_{\downarrow,\alpha}^{(2)}[j_e - j_s],
$$
$$
F_{\downarrow,\alpha}^{(3)} = \Gamma_{\downarrow,\alpha}^{(3)}[j_m - j_{sm}],
$$

(C5)

$$
F_{\downarrow,\beta}^{(1)} = -\Gamma_{\downarrow,\beta}^{(1)}[j_e - j_s],
$$
$$
F_{\downarrow,\beta}^{(2)} = \Gamma_{\downarrow,\beta}^{(2)}[j_e + j_s],
$$
$$
F_{\downarrow,\beta}^{(3)} = -\Gamma_{\downarrow,\beta}^{(3)}[j_m + j_{sm}],
$$

(C6)

where

$$
\Gamma_\alpha^{(1/2)} = \frac{1}{\hbar}\frac{(k_F a)^2 V^2}{8\pi E_F^2}\int d(qa)\,(\Omega_A u_q + \Omega_B v_q)^2
$$
$$
\times b^0(\omega_{q,\alpha})\frac{\kappa^2(qa)}{\omega_q}\frac{v(q)\Lambda_{q,\alpha,1/2}\,\Theta(1 - |\Lambda_{q,\alpha,1/2}|)}{\sqrt{1 - \Lambda_{q,\alpha,1/2}^2}},
$$

(C7)

$$
\Gamma_\alpha^{(3)} = \frac{1}{\hbar}\frac{(k_F a)^3 V^2}{8\pi E_F^2}\frac{1}{I_\alpha}\int d(qa)(qa)\frac{\kappa^2(qa)}{\omega_q}\left[-\frac{\partial b^0(\omega_{q,\alpha})}{\partial \omega_{q,\alpha}} \right]
$$
$$
\times (\Omega_A u_q + \Omega_B v_q)^2 \frac{\omega_{q,\alpha}}{qa}\frac{v(q)\Theta(1 - |\Lambda_{q,\alpha,3}|)}{\sqrt{1 - \Lambda_{q,\alpha,3}^2}},
$$

(C8)

$$
\Gamma_\beta^{(1/2)} = \frac{1}{\hbar}\frac{(k_F a)^2 V^2}{8\pi E_F^2}\int d(qa)\,(\Omega_A v_q + \Omega_B u_q)^2
$$
$$
\times b^0(\omega_{q,\beta})\frac{\kappa^2(qa)}{\omega_q}\frac{v(q)\Lambda_{q,\beta,1/2}\,\Theta(1 - |\Lambda_{q,\beta,1/2}|)}{\sqrt{1 - \Lambda_{q,\beta,1/2}^2}},
$$

(C9)

$$
\Gamma_\beta^{(3)} = \frac{1}{\hbar}\frac{(k_F a)^3 V^2}{8\pi E_F^2}\frac{1}{I_\beta}\int d(qa)(qa)\frac{\kappa^2(qa)}{\omega_q}\left[-\frac{\partial b^0(\omega_{q,\beta})}{\partial \omega_{q,\beta}} \right]
$$
$$
\times (\Omega_A v_q + \Omega_B u_q)^2 \frac{\omega_{q,\beta}}{qa}\frac{v(q)\Theta(1 - |\Lambda_{q,\beta,3}|)}{\sqrt{1 - \Lambda_{q,\beta,3}^2}},
$$

(C10)

$$
\Gamma_{\sigma,\alpha}^{(1)} = \frac{1}{\hbar}\frac{(k_F a)V^2}{4\pi E_F}\int d(qa)\,(\Omega_A u_q + \Omega_B v_q)^2 b^0(\omega_{q,\alpha})
$$
$$
\times \frac{\Theta(1 - |\Lambda_{q,\sigma,\alpha,1}|)}{\sqrt{1 - \Lambda_{q,\sigma,\alpha,1}^2}}\left[1 - \frac{qa}{k_F a}\Lambda_{q,\sigma,\alpha,1} \right],
$$

(C11)

$$
\Gamma_{\sigma,\alpha}^{(2)} = \frac{1}{\hbar}\frac{(k_F a)V^2}{4\pi E_F}\int d(qa)\,(\Omega_A u_q + \Omega_B v_q)^2 b^0(\omega_{q,\alpha})
$$
$$
\times \frac{\Theta(1 - |\Lambda_{q,\sigma,\alpha,2}|)}{\sqrt{1 - \Lambda_{q,\sigma,\alpha,2}^2}},
$$

(C12)

$$\Gamma_{\sigma,\alpha}^{(3)} = \frac{1}{\hbar}\frac{(k_F a)^2 V^2}{4\pi E_F}\frac{1}{I_\alpha}\int d(qa)(qa)\left[-\frac{\partial b^0(\omega_{q,\alpha})}{\partial \omega_{q,\alpha}}\right]\Lambda_{q,\sigma,\alpha,3}$$

$$\times (\Omega_A u_q + \Omega_B v_q)^2 \frac{\omega_{q,\alpha}}{qa}\frac{\Theta(1-|\Lambda_{q,\sigma,\alpha,3}|)}{\sqrt{1-\Lambda_{q,\sigma,\alpha,3}^2}}, \quad (C13)$$

$$\Gamma_{\sigma,\beta}^{(1)} = \frac{1}{\hbar}\frac{(k_F a) V^2}{4\pi E_F}\int d(qa)\,(\Omega_A v_q + \Omega_B u_q)^2 b^0(\omega_{q,\beta})$$

$$\times \frac{\Theta(1-|\Lambda_{q,\sigma,\beta,1}|)}{\sqrt{1-\Lambda_{q,\sigma,\beta,1}^2}}, \quad (C14)$$

$$\Gamma_{\sigma,\beta}^{(2)} = \frac{1}{\hbar}\frac{(k_F a) V^2}{4\pi E_F}\int d(qa)\,(\Omega_A v_q + \Omega_B u_q)^2 b^0(\omega_{q,\beta})$$

$$\times \frac{\Theta(1-|\Lambda_{q,\sigma,\beta,2}|)}{\sqrt{1-\Lambda_{q,\sigma,\beta,2}^2}}\left[1 - \frac{qa}{k_F a}\Lambda_{q,\sigma,\beta,2}\right], \quad (C15)$$

$$\Gamma_{\sigma,\beta}^{(3)} = \frac{1}{\hbar}\frac{(k_F a)^2 V^2}{4\pi E_F}\frac{1}{I_\beta}\int d(qa)(qa)\left[-\frac{\partial b^0(\omega_{q,\beta})}{\partial \omega_{q,\beta}}\right]\Lambda_{q,\sigma,\beta,3}$$

$$\times (\Omega_A v_q + \Omega_B u_q)^2 \frac{\omega_{q,\beta}}{qa}\frac{\Theta(1-|\Lambda_{q,\sigma,\beta,3}|)}{\sqrt{1-\Lambda_{q,\sigma,\beta,3}^2}}. \quad (C16)$$

We have here defined

$$I_\gamma = \int d(qa)\,(qa)\,\frac{\kappa^2(qa)}{\omega_q}\left[-\frac{\partial b^0(\omega_{q,\gamma})}{\partial \omega_{q,\gamma}}\right], \quad (C17)$$

as well as

$$\Lambda_{q,\gamma,1} = \frac{1}{2t(qa)(k_F a)}[\omega_{q,\gamma} + 2\gamma h_e + t(qa)^2],$$

$$\Lambda_{q,\gamma,2} = \frac{1}{2t(qa)(k_F a)}[\omega_{q,\gamma} + 2\gamma h_e - t(qa)^2], \quad (C18)$$

$$\Lambda_{q,\gamma,3} = \Lambda_{q,\gamma,2},$$

$$\Lambda_{q,\uparrow,\alpha,1} = \frac{1}{2t(qa)(k_F a)}[\omega_{q,\alpha} - 2h_e + t(qa)^2],$$

$$\Lambda_{q,\uparrow,\alpha,2} = \frac{1}{2t(qa)(k_F a)}[\omega_{q,\alpha} - 2h_e - t(qa)^2],$$

$$\Lambda_{q,\uparrow,\alpha,3} = \Lambda_{q,\uparrow,\alpha,2},$$

$$\Lambda_{q,\uparrow,\beta,1} = \frac{1}{2t(qa)(k_F a)}[\omega_{q,\beta} + 2h_e + t(qa)^2],$$

$$\Lambda_{q,\uparrow,\beta,2} = \frac{-1}{2t(qa)(k_F a)}[\omega_{q,\beta} + 2h_e - t(qa)^2], \quad (C19)$$

$$\Lambda_{q,\uparrow,\beta,3} = \Lambda_{q,\uparrow,\beta,1},$$

$$\Lambda_{q,\downarrow,\alpha,1} = -\Lambda_{q,\uparrow,\alpha,2}, \quad \Lambda_{q,\downarrow,\alpha,2} = -\Lambda_{q,\uparrow,\alpha,1},$$
$$\Lambda_{q,\downarrow,\alpha,3} = \Lambda_{q,\uparrow,\alpha,1}, \quad \Lambda_{q,\downarrow,\beta,1} = -\Lambda_{q,\uparrow,\beta,2},$$
$$\Lambda_{q,\downarrow,\beta,2} = \Lambda_{q,\uparrow,\beta,1}, \quad \Lambda_{q,\downarrow,\beta,3} = -\Lambda_{q,\uparrow,\beta,2}. \quad (C20)$$

APPENDIX D: DEFINITION OF COEFFICIENTS

The coefficients in Eq. (26) are given by

$$A_{e\to s} = \frac{1}{X_s}\left[\frac{1}{2}\left(Y_0\frac{T_-}{T_+} + P_0\right)\tau_e^{-1}\right.$$

$$+ \left(1 + \frac{T_-}{T_+}\right)\left(-\Gamma_{\downarrow,\alpha}^{(1)} + \Gamma_{\downarrow,\alpha}^{(2)} + \Gamma_{\downarrow,\beta}^{(1)} - \Gamma_{\downarrow,\beta}^{(2)}\right)$$

$$\left.+ \left(1 - \frac{T_-}{T_+}\right)\left(\Gamma_{\uparrow,\alpha}^{(1)} - \Gamma_{\uparrow,\alpha}^{(2)} - \Gamma_{\uparrow,\beta}^{(1)} + \Gamma_{\uparrow,\beta}^{(2)}\right)\right], \quad (D1)$$

$$A_{m\to s} = \frac{1}{X_s}\left[\left(1 - \frac{T_-}{T_+}\right)\left(\Gamma_{\uparrow,\beta}^{(3)} - \Gamma_{\uparrow,\alpha}^{(3)}\right)\right.$$

$$\left.+ \left(1 + \frac{T_-}{T_+}\right)\left(-\Gamma_{\downarrow,\alpha}^{(3)} + \Gamma_{\downarrow,\beta}^{(3)}\right)\right], \quad (D2)$$

and

$$A_{sm\to s} = \frac{1}{X_s}\left[\left(1 - \frac{T_-}{T_+}\right)\left(\Gamma_{\uparrow,\beta}^{(3)} + \Gamma_{\uparrow,\alpha}^{(3)}\right)\right.$$

$$\left.+ \left(1 + \frac{T_-}{T_+}\right)\left(\Gamma_{\downarrow,\alpha}^{(3)} + \Gamma_{\downarrow,\beta}^{(3)}\right)\right], \quad (D3)$$

where

$$X_s = \frac{1}{2}\left(P_0\frac{T_-}{T_+} + Y_0\right)\tau_e^{-1}$$

$$- \left(\frac{T_-}{T_+} - 1\right)\left(\Gamma_{\uparrow,\alpha}^{(1)} + \Gamma_{\uparrow,\alpha}^{(2)} + \Gamma_{\uparrow,\beta}^{(1)} + \Gamma_{\uparrow,\beta}^{(2)}\right)$$

$$+ \left(\frac{T_-}{T_+} + 1\right)\left(\Gamma_{\downarrow,\alpha}^{(1)} + \Gamma_{\downarrow,\alpha}^{(2)} + \Gamma_{\downarrow,\beta}^{(1)} + \Gamma_{\downarrow,\beta}^{(2)}\right). \quad (D4)$$

Further, the coefficients in Eq. (27) take the form

$$C_{e\to m} = A_{e\to m} + A_{e\to s}A_{s\to m},$$
$$C_{sm\to m} = A_{sm\to m} + A_{sm\to s}A_{s\to m}, \quad (D5)$$

where

$$A_{e\to m} = \left[\Gamma_\beta^{(1)} + \Gamma_\alpha^{(1)} - \Gamma_\beta^{(2)} - \Gamma_\alpha^{(2)}\right]/X_m,$$

$$A_{s\to m} = \left[\Gamma_\beta^{(1)} - \Gamma_\alpha^{(1)} + \Gamma_\beta^{(2)} - \Gamma_\alpha^{(2)}\right]/X_m, \quad (D6)$$

$$A_{sm\to m} = \left[\Gamma_\alpha^{(3)} - \Gamma_\beta^{(3)}\right]/X_m,$$

and

$$X_m = \tau_{M_0}^{-1} + \left[\Gamma_\beta^{(3)} + \Gamma_\alpha^{(3)}\right]$$

$$- A_{m\to s}\left[\Gamma_\beta^{(1)} - \Gamma_\alpha^{(1)} + \Gamma_\beta^{(2)} - \Gamma_\alpha^{(2)}\right]. \quad (D7)$$

[1] Y. Kajiwara, K. Harii, S. Takahashi, J. Ohe, K. Uchida, M. Mizuguchi, H. Umezawa, H. Kawai, K. Ando, K. Takanashi, S. Maekawa, and E. Saitoh, Nature (London) **464**, 262 (2010).

[2] L. J. Cornelissen, J. Liu, R. A. Duine, J. B. Youssef, and B. J. van Wees, Nat. Phys. **11**, 1022 (2015).

[3] A. V. Chumak, V. I. Vasyuchka, A. A. Serga, and B. Hillebrands, Nat. Phys. **11**, 453 (2015).

[4] A. Brataas, B. van Wees, O. Klein, G. de Loubens, and M. Viret, Phys. Rep. **885**, 1 (2020).

[5] J. E. Hirsch, Phys. Rev. Lett. **83**, 1834 (1999).

[6] E. Saitoh, M. Ueda, H. Miyajima, and G. Tatara, Appl. Phys. Lett. **88**, 182509 (2006).

[7] C. W. Sandweg, Y. Kajiwara, A. V. Chumak, A. A. Serga, V. I. Vasyuchka, M. B. Jungfleisch, E. Saitoh, and B. Hillebrands, Phys. Rev. Lett. **106**, 216601 (2011).

[8] M. Dyakonov and V. Perel, Phys. Lett. A **35**, 459 (1971).

[9] Y. K. Kato, R. C. Myers, A. C. Gossard, and D. D. Awschalom, Science **306**, 1910 (2004).

[10] J. Sinova, S. O. Valenzuela, J. Wunderlich, C. H. Back, and T. Jungwirth, Rev. Mod. Phys. **87**, 1213 (2015).

[11] J. Li, Y. Xu, M. Aldosary, C. Tang, Z. Lin, S. Zhang, R. Lake, and J. Shi, Nat. Commun. **7**, 10858 (2016).

[12] H. Wu, C. H. Wan, X. Zhang, Z. H. Yuan, Q. T. Zhang, J. Y. Qin, H. X. Wei, X. F. Han, and S. Zhang, Phys. Rev. B **93**, 060403(R) (2016).

[13] K. Uchida, S. Takahashi, K. Harii, J. Ieda, W. Koshibae, K. Ando, S. Maekawa, and E. Saitoh, Nature (London) **455**, 778 (2008).

[14] K. Uchida, J. Xiao, H. Adachi, J. Ohe, S. Takahashi, J. Ieda, T. Ota, Y. Kajiwara, H. Umezawa, H. Kawai, G. E. W. Bauer, S. Maekawa, and E. Saitoh, Nat. Mater. **9**, 894 (2010).

[15] T. Jungwirth, X. Marti, P. Wadley, and J. Wunderlich, Nat. Nanotechnol. **11**, 231 (2016).

[16] V. Baltz, A. Manchon, M. Tsoi, T. Moriyama, T. Ono, and Y. Tserkovnyak, Rev. Mod. Phys. **90**, 015005 (2018).

[17] M. B. Jungfleisch, W. Zhang, and A. Hoffmann, Phys. Lett. A **382**, 865 (2018).

[18] Y. Ohnuma, H. Adachi, E. Saitoh, and S. Maekawa, Phys. Rev. B **87**, 014423 (2013).

[19] S. M. Rezende, R. L. Rodríguez-Suárez, and A. Azevedo, Phys. Rev. B **93**, 014425 (2016).

[20] S. M. Wu, W. Zhang, A. KC, P. Borisov, J. E. Pearson, J. S. Jiang, D. Lederman, A. Hoffmann, and A. Bhattacharya, Phys. Rev. Lett. **116**, 097204 (2016).

[21] S. M. Rezende, R. L. Rodríguez-Suárez, and A. Azevedo, Phys. Rev. B **93**, 054412 (2016).

[22] H. Wang, C. Du, P. C. Hammel, and F. Yang, Phys. Rev. B **91**, 220410(R) (2015).

[23] W. Lin, K. Chen, S. Zhang, and C. L. Chien, Phys. Rev. Lett. **116**, 186601 (2016).

[24] S. A. Bender, H. Skarsvåg, A. Brataas, and R. A. Duine, Phys. Rev. Lett. **119**, 056804 (2017).

[25] R. Lebrun, A. Ross, S. A. Bender, A. Qaiumzadeh, L. Baldrati, J. Cramer, A. Brataas, R. A. Duine, and M. Kläui, Nature (London) **561**, 222 (2018).

[26] K. Shen, Phys. Rev. B **100**, 094423 (2019).

[27] A. Kamra and W. Belzig, Phys. Rev. Lett. **119**, 197201 (2017).

[28] A. Kamra, E. Thingstad, G. Rastelli, R. A. Duine, A. Brataas, W. Belzig, and A. Sudbø, Phys. Rev. B **100**, 174407 (2019).

[29] E. Erlandsen, A. Kamra, A. Brataas, and A. Sudbø, Phys. Rev. B **100**, 100503(R) (2019).

[30] E. Erlandsen, A. Brataas, and A. Sudbø, Phys. Rev. B **101**, 094503 (2020).

[31] E. Erlandsen and A. Sudbø, Phys. Rev. B **102**, 214502 (2020).

[32] E. Thingstad, E. Erlandsen, and A. Sudbø, Phys. Rev. B **104**, 014508 (2021).

[33] O. Johansen, A. Kamra, C. Ulloa, A. Brataas, and R. A. Duine, Phys. Rev. Lett. **123**, 167203 (2019).

[34] J. Slonczewski, J. Magn. Magn. Mater. **159**, L1 (1996).

[35] L. Berger, Phys. Rev. B **54**, 9353 (1996).

[36] D. Ralph and M. Stiles, J. Magn. Magn. Mater. **320**, 1190 (2008).

[37] G. Tatara, H. Kohno, and J. Shibata, Phys. Rep. **468**, 213 (2008).

[38] A. Hirohata, K. Yamada, Y. Nakatani, I.-L. Prejbeanu, B. Diény, P. Pirro, and B. Hillebrands, J. Magn. Magn. Mater. **509**, 166711 (2020).

[39] Y. Cheng, K. Chen, and S. Zhang, Phys. Rev. B **96**, 024449 (2017).

[40] F. J. Blatt, D. J. Flood, V. Rowe, P. A. Schroeder, and J. E. Cox, Phys. Rev. Lett. **18**, 395 (1967).

[41] M. E. Lucassen, C. H. Wong, R. A. Duine, and Y. Tserkovnyak, Appl. Phys. Lett. **99**, 262506 (2011).

[42] D. Miura and A. Sakuma, J. Phys. Soc. Jpn. **81**, 113602 (2012).

[43] T. Yamaguchi, H. Kohno, and R. A. Duine, Phys. Rev. B **99**, 094425 (2019).

[44] Y. Cheng and S. Zhang, Phys. Rev. B **102**, 134403 (2020).

[45] L. G. Johnsen, H. T. Simensen, A. Brataas, and J. Linder, Phys. Rev. Lett. **127**, 207001 (2021).

[46] E. L. Fjærbu, N. Rohling, and A. Brataas, Phys. Rev. B **100**, 125432 (2019).

[47] A. Fert, J. Phys. C **2**, 1784 (1969).

[48] T. Kasuya, Prog. Theor. Phys. **22**, 227 (1959).

[49] T. Valet and A. Fert, Phys. Rev. B **48**, 7099 (1993).

[50] Steven S.-L. Zhang and S. Zhang, Phys. Rev. Lett. **109**, 096603 (2012).

[51] S. M. Rezende, A. Azevedo, and R. L. Rodríguez-Suárez, J. Phys. D: Appl. Phys. **51**, 174004 (2018).

[52] S. M. Rezende, A. Azevedo, and R. L. Rodríguez-Suárez, J. Appl. Phys. **126**, 151101 (2019).

NTNU

Norwegian University of
Science and Technology